Tailored Chain Sequences of Brominated Syndiotactic Polystyrene Copolymers via Post-Polymerization Functionalization in the Heterogeneous Gel State

Kristen Felice Noble

Dissertation submitted to the faculty of the Virginia Polytechnic Institute and State University in partial fulfillment of the requirements for the degree of

Doctor of Philosophy
In
Chemistry

Robert B. Moore, Chair
Paul A. Deck
John R. Morris
James M. Tanko

August 13, 2019
Blacksburg, VA

Keywords: gel-state, post-polymerization functionalization, bromination, heterogeneous, blocky, microstructure, comonomer sequence, degree of blockiness, syndiotactic polystyrene

Tailored Chain Sequences of Brominated Syndiotactic Polystyrene Copolymers via Post-Polymerization Functionalization in the Heterogeneous Gel State

Kristen Felice Noble

ABSTRACT

This dissertation demonstrates the preparation of blocky brominated syndiotactic polystyrene (sPS-*co*-sPS-Br) copolymers with tailored chain sequences using a simple, post-polymerization functionalization method conducted in the heterogeneous gel state, and investigates the effect of sPS reaction state and sPS/solvent gel morphology on the copolymer microstructure and thermal properties. Gel-state (Blocky) brominated copolymers were prepared from a 10 w/v% sPS/carbon tetrachloride (CCl_4) gel and a 10 w/v% sPS/chloroform ($CHCl_3$) gel in a matched set containing 6−32 mol% *p*-bromostyrene (Br-Sty) units. For comparison, a matched set of randomly brominated copolymers was prepared using a homogeneous solution-state (Random) reaction method and a set of brominated copolymers was prepared using a heterogenous powder-state (Powder) reaction method. The degree of bromination was evaluated using ^{1}H nuclear magnetic resonance (NMR) spectroscopy. Powder-state bromination produced copolymers with a limited degree of functionalization of up to 12 mol% Br and required a threefold longer reaction time than the gel-state method conducted on the sPS/$CHCl_3$ gel, demonstrating that the powder-state method is time-consuming and the dense sPS powder is incapable of producing copolymers with high Br-content. Microstructural characterization provided by ^{13}C NMR spectroscopy, showed that bromination of sPS produces multiple peaks in the quaternary carbon region of the NMR spectrum, signifying through-bond communication between neighboring styrene and Br-Sty monomers. This work provides the first high-resolution comonomer sequencing of brominated sPS copolymers. Characterization of the quaternary carbon spectrum,

assisted by band selective gradient heteronuclear multiple bond correlation (bsgHMBC) spectroscopy, electronic structure calculations, and simulated statistically random copolymer chains, revealed that each resonance peak could be assigned to a styrene or Br-Sty unit that exists in the center of a unique sequence of five monomers (i.e., a pentad) along the copolymer chain (e.g., ssssb where s = styrene and b = brominated styrene). Our comonomer sequencing method demonstrated that the Blocky and Powder copolymers have block-like character. Remarkably, the Blocky copolymers exhibit notably higher degrees of blockiness and larger fractions of sssss and bbbbb pentads at low Br-contents (i.e., 32 mol% Br), relative to the Powder copolymers, confirming their blocky microstructure. Quenched films of the Blocky copolymers, analyzed using ultra-small-angle (USAXS) and small-angle X-ray scattering (SAXS), show micro-phase separated morphologies that are reminiscent of conventional block copolymer phase behavior, supporting that the Blocky copolymers contain distinct segments of pure sPS and segments of randomly brominated sPS. Crystallization behavior of the copolymers, examined using differential scanning calorimetry (DSC), demonstrates that the Blocky copolymers are more crystallizable and crystallize faster at lower supercooling compared to their Random analogs. Simulations of blocky copolymers were developed based on the semicrystalline gel morphology to rationalize the effect of gel-state functionalization on copolymer microstructure and crystallization behavior. The simulations confirm that restricting the accessibility of the brominating reagent to monomers well removed from the crystalline fraction of the gel network produces copolymers with a greater prevalence of long runs of pure sPS that is advantageous for preserving desired crystallizability of the resulting blocky copolymers. To investigate the effect of sPS/solvent gel morphology on copolymer microstructure and crystallization behavior, the sPS/CCl_4 and sPS/$CHCl_3$ copolymers were compared directly. Characterization of the sPS/solvent gels using USAXS/SAXS, revealed

that the gels exhibit different morphologies and average lamella thicknesses. Microstructural analysis showed that the sPS/$CHCl_3$ copolymers contain larger fractions of sssss pentad and a greater degree of blockiness. The sPS/$CHCl_3$ copolymers contain larger phase domains, supporting that these copolymers contain longer distinct segments of pure sPS and randomly brominated sPS in a multiblock-like microstructure. In addition, the sPS/$CHCl_3$ copolymers are more crystallizable during conditions of rapid cooling and crystallize faster at low supercooling relative to their sPS/CCl_4 analogs. Simulated average chains of the Blocky copolymers, generated from the empirical pentad sequence distributions, provide strong evidence that the runs of pure sPS in the Blocky copolymers originate from the crystalline stems within the crystalline lamellae. Thus, the simulations support that semicrystalline blocky brominated copolymers with tailored chain sequences, phase behavior, and crystallization properties and can be prepared simply by changing the gelation solvent.

Tailored Chain Sequences of Brominated Syndiotactic Polystyrene Copolymers via Post-Polymerization Functionalization in the Heterogeneous Gel State

Kristen Felice Noble

GENERAL AUDIENCE ABSTRACT

Block copolymers are a class of large molecules (polymers) that are made up of two or more chains (blocks) of different smaller units (monomers) linked together at one of each of the chain ends. When the monomers that make up each block have distinctly different chemical properties, the blocks may be capable of self-assembling into well-ordered physical structures, which give the block copolymer unique material properties that are different, and often better than the properties of the individual blocks alone (homopolymers). Block copolymers have thus received tremendous attention with respect to controlled preparation, tailored structure development, and customized physical properties, for their potential use in self-assembled, nanostructured materials. Nevertheless, the generally difficult procedures and conditions required to make (polymerize) block copolymers with controlled sequences limits the scope of their commercial application. As an alternative to conventional polymerization methods, this dissertation demonstrates a comparatively simple physical method to make copolymers that contain significantly non-random (blocky) monomer sequences, starting with a homopolymer and using a reagent to modify units along the polymer chain. This post-polymerization method is conducted in the homopolymer's gel state, in which segments of the homopolymer chains are effectively shielded from the reagent. The homopolymer, syndiotactic polystyrene (sPS), was used as a model to conduct a fundamentical investigation into the effects of the polymer reaction state, i.e., gel, solution, or powder, and the gel structure (morphology) on the copolymer structure and properties. The gel-state was found to produce copolymers with a high degree of modification and

a greater degree of blockiness than the solution-state and powder-state. Copolymers prepared from the gel state exhibited properties that are characteristic of conventional block copolymers. Furthermore, using the gel-state method, blocky copolymers with tailored chain sequences and properties were prepared by simply changing the gel morphology. Thus, reaction in the gel-state is demonstrated as a simple physical approach to polymer design and synthesis that will be useful in the development of next-generation functionalized materials through the modification of low-cost commodity polymers. As an advancement to the manner in which nanostructured materials are created, these tailored materials will greatly enhance the convenience of block copolymers for a wide variety of applications including structural and biomechanical materials, and polymeric membranes for energy conversion and water purification systems.

In memory of Professor Karen J. Brewer.

You were an inspirational teacher. Your magic, leadership, selflessness, and support helped me to find my voice and myself.

Acknowledgements

First and foremost, I would like to express my thanks and greatest appreciation to my Ph.D. advisor, Professor Bob Moore. I owe my deepest gratitude to you for recognizing when I needed help and for guiding me through a difficult transition between research topics. Thank you for the time we spent discussing crystallization, chain folding, gelation, and comonomer sequencing. I can honestly say that I have enjoyed my graduate work and have enjoyed discussing our research findings. I am very proud of what we have been able to accomplish. Also, I want to thank you for encouraging me to pursue a career in teaching and for fostering my commitment to adolescent outreach.

I would like to thank my committee members, Professor Paul Deck, Professor John Morris, and Professor Jim Tanko, for your positive and constructive feedback, guidance, and recommendations, which have greatly improved the quality of this dissertation. Also, thank you all for being welcoming and for always having an open door for professional and personal conversations. I would also like to thank Professor Diego Troya for your intellectual contribution to this research as well as your constructive feedback, positive attitude, and genuine expression of interest in this work. Thank you to the Chemistry Department's NMR facility staff, especially Dr. Narasimhamurthy Shanaiah and Mr. Ken Knott for your intellectual contributions to this research and your support.

A heartfelt thank you is expressed to my Brewer Group family, especially Dr. Elise Naughton, Dr. Ted Canterbury, Dr. José Rodríguez Corrales, Dr. Alec Wagner, Dr. Hannah Sayre, Dr. Jie Zhu, Mrs. Candace Wall, Dr. Shamindri Arachchige, and Dr. Marwa Abdel Latif (honorary). I know that I have benefited from our intellectual conversations and your insightful comments and suggestions. More importantly, I have always felt that you have been my family

and that you have always looked out for me. Your unwavering encouragement, guidance, and friendship have been greatly appreciated. I would like to offer my special thanks to Elise, Ted, and José. From the beginning, you have been wonderful teachers, mentors, and friends. I am thankful to have you in my life. Special thanks to Shami for fostering my passion for outreach and providing me with opportunities to continue to share my love of chemistry with young people.

Thank you to previous and current members of the Moore Group, especially Dr. Samantha J. Talley, Christina Orsino, Lin Ju, Dr. Lindsey Anderson, and Greg Fahs. I am grateful for our many conversations. You also made graduate school fun. I enjoyed coming to work every day. Special thanks to Sam who was always willing to listen to my problems, always had an answer for my scattering questions, and was a great hiking partner and friend. Special thanks to Dr. Rachael Parker and Dr. Spencer Ahrenholtz for encouraging me to have fun outside of graduate school. Also, thank you for our continued friendship.

Special thanks to Ms. Joli Hyunh, the Chemistry Department's Graduate Student Coordinator. Thank you for answering all of my frantic emails promptly with a detailed list of answers to all of my questions. Also, thank you for always having an open door for questions or friendly conversation. Thank you to the Chemistry Department Administrative Office staff and Business Office staff, especially Susan Saxe, Corrin Lundquist, Beth Kast, and EMillie Shephard for answering my many questions, making sure I had everything I needed, and for our polite conversation. You all deserve tremendous credit and acknowledgement for the work that you do.

My deepest heartfelt appreciation goes to my Mom and Dad. Thank you for being supportive, encouraging me, listening to me, and expressing interest in my work. That is all I could have asked for.

I am deeply grateful to Professor Karen Brewer who invited me to join her laboratory, which started me on this amazing, challenging, and memorable journey. I wish you could have seen it through to the end.

To my wife Alex, thank you for your encouraging me to start this journey, and your continuous love and support throughout.

Attributions

Professor Robert B. Moore – Research advisor

Professor of Chemistry at Virginia Tech

Professor Karen J. Brewer (deceased 2014) – Former research co-advisor

Late Professor of Chemistry at Virginia Tech. Contributed her knowledge and expertise in the area of inorganic photochemistry to the work described in **Appendix D**.

Dr. Diego Troya – Professor of Chemistry at Virginia Tech

Contributed to **Chapter 3** and **Chapter 4** by writing a computer code using Fortran software that simulates average chains of the brominated copolymers by minimizing the residuals between the pentad sequence distribution of the empirical results and the intermediate simulated chain. Contributed to Chapter 5 by writing a computer code using Fortran programming software that simulates copolymer chains with blocky microstructures by randomly placing inaccessible blocks along the chains before using random number generation to functionalize the blocks up to a specified degree. Provided invaluable constructive feedback on the manuscript preparation of **Chapter 3**.

Alexandria M. Noble – Wife and graduate student in Industrial Systems and Engineering at Virginia Tech

Contributed to **Chapter 2** and **Chapter 3** by writing a computer code using MATLAB® programming software that simulates copolymer chains with random and blocky microstructures and calculates the prevalence of triad and pentad sequences within each chain and the length and frequency of runs of consecutive like units along each chain.

Dr. Samantha J. Talley – Former graduate student in Chemistry at Virginia Tech

Contributed to **Chapter 2** by characterizing the radius of gyration of the scattering features in the USAXS/SAXS profiles of the sPS homopolymer and brominated copolymers. Contributed to **Chapter 3** by recording and analyzing the SAXS profiles of the sPS homopolymer and brominated copolymers.

Gregory J. Fahs – Former graduate student in Chemistry at Virginia Tech

Contributed to **Chapter 2**, **Chapter 3**, and **Chapter 4** by writing a computer code using Mathematica software that applies the 1-D correlation function method to estimate the average lamella thickness in an sPS/solvent gel and the sPS homopolymer and brominated copolymers.

Dr. Narasimhamurthy Shanaiah – VT Chemistry Department's NMR facility staff employee

Provided his knowledge and expertise in quantitative ^{13}C NMR spectroscopy, which contributed to the NMR spectra reported in **Chapter 2**, **Chapter 3**, **Chapter 4**, and **Chapter 5**. Performed the spin-lattice relaxation time, T_1, experiments reported in **Chapter 3**.

Mr. Ken Knott − VT Chemistry Department's NMR facility staff employee

Provided his knowledge and expertise in two-dimensional (2D) NMR spectroscopy, which contributed to the 2D NMR spectra reported in **Chapter 3**.

Helen T. Tran – Undergraduate student at Virginia Tech

Contributed to **Chapter 4** by assisting in the preparation of brominated copolymers using a post-polymerization functionalization method carried out in the heterogeneous powder state. Characterized the microstructure of the brominated copolymers using NMR spectroscopy.

Peter M. Moberg – Undergraduate student at Virginia Tech

Contributed to **Chapter 3** by assisting in the preparation of brominated copolymers using a post-polymerization functionalization method carried out in the heterogeneous gel state on sPS/$CHCl_3$ gels.

Dr. Congcong Wu – Postdoctoral Associate in Professor Shashank Priya's research group at Virginia Tech

Collaborator on **Appendix E**.

Table of Contents

List of Figures

List of Tables

List of abbreviations and chemical formulas

$\%X_c$	percent crystallinity (either by vol or weight)
aPS	atactic polystyrene
APS	Advanced Photon Source
BL	bridging ligand
Blocky	gel-state brominated copolymers
B_o	static magnetic field
bpy	2,2′-bipyridine
Br_2	Bromine
Br-Sty	brominated styrene
bsgHMBC	band-selective gradient heteronuclear multiple bond correlation
CCl_4	carbon tetrachloride
$CHCl_3$	Chloroform
cm	Centimeter
$Đ$	polydispersity index
d_{Bragg}	Bragg spacing
dcbpy	2,2′-bipyridine-4,4′-dicarboxylic acid
DCM	1,2-dichloromethane
DOE	Department of Energy
dpp	2,3-bis(2-pyridyl)pyrazine
DSC	differential scanning calorimetry
ED	electron donor
ER	electron relay
eV	electronvolt
$F_c(t)$	bulk fractional crystallinity
$FeCl_3$	ferric(III) chloride
fid	free induction decay
g	gram
gDQCOSY	gradient double quantum filtered correlation spectroscopy
Gel	gel-state brominated copolymers prepared from a 10 w/v% sPS/$CHCl_3$ gel
gHSQC	gradient heteronuclear single quantum coherence
h	hour
HOMO	highest occupied molecular orbital
$I(q)$	intensity
iPS	isotactic polystyrene
j_{Sty}	fraction of styrene units occurring in j sequences
kV	kilovolt
L	liter
L_a	amorphous thickness
L_c	lamella thickness
L_p	long period
LUMO	lowest unoccupied molecular orbital
$LW_{1/2}$	line-width at half maximum
mA	milliampere
mg	milligram

min	minute
mL	milliliter
MLCT	metal-to-ligand charge transfer
mmol	millimole
M_w	weight average molecular weight
N	average number of blocks per 100 monomer units
n	block length
n_B	average length of consecutive brominated styrene units
nm	nanometer
NMR	nuclear magnetic resonance
NOE	nuclear Overhauser effect
n_S	average length of consecutive styrene units
P_a	fraction of crystallites in the α-form
PEC	photoinitiated electron collector
PEEK	poly(ether ketone)
Ph_2phen	4,7-diphenyl-1,10-phenanthroline
Powder	powder-state brominated copolymers
ppm	parts per million
PS	polystyrene
P_ζ	probability that a randomly selected styrene unit along a chain exists in a crystallizable chain segment of at least ζ styrene units
q	momentum difference between the incident and diffracted photons
R	block character (degree of blockiness)
RAF	rigid amorphous fraction
Random	solution-state brominated copolymers
R_g	radius of gyration
RMSD	root-means-square deviation
s	second
SANS	small-angle neutron scattering
SAXS	small-angle X-ray scattering
sec	second
sPBrS	syndiotactic poly(4-bromostyrene)
sPS	syndiotactic polystyrene
sPS-*co*-sPS-Br	brominated syndiotactic polystyrene
T_1	spin-lattice relaxation time
$t_{1/2}$	crystallization half-time
T_2	spin-spin relaxation time
T_c	temperature at maximum endothermic heat flow
TCB	1,2,4-trichlorobenzene
TCE	1,1,2,2-tetrachloroethane
T_g	glass transition temperature
TGA	thermogravimetric analysis
TL	terminal ligand
T_m	temperature at maximum exothermic heat flow
TOF	turnover frequency
TON	turnover number

USAXS	ultra-small angle X-ray scattering
UV	ultraviolet
Vis	visible
w/v%	weight per volume percent
WAXD	wide-angle X-ray diffraction
w_j	probability that a unit chosen at random is a styrene in a sequence of length *j*
WOC	water oxidation catalyst
WRC	water reduction catalyst
w_{Sty}	weight fraction of styrene units
wt	weight
XRD	X-ray diffraction
X_{Sty}	molar fraction of styrene units
ΔH_f	heat of fusion
$\Delta H_f°$	heat of fusion of 100% crystalline pure sPS
ζ	length of consecutive styrene units
θ	one-half of the scattering angle
λ	wavelength
μmol	micromole

Chapter 1.

Introduction to heterogeneous gel-state reaction schemes

1.1. Motivation

Block copolymers are a unique class of macromolecules, characterized by two or more chemically distinct polymer segments (i.e., blocks) linked together through covalent bonds at one of each of the segment ends.[1,2] The simplest and most thoroughly investigated block copolymer architecture is the linear *AB* diblock copolymer, which consists of a linear sequence of *A* monomer units covalently attached to a linear sequence of *B* monomer units. Modern living chain growth polymerization methods, free radical polymerization methods, and two-step oligomer coupling reactions used to control the sequencing of monomers have also led to more complex block copolymer architectures including *ABA* triblock copolymers, segmented/multiblock $(AB)_n$ copolymers, graft-branched copolymers, and a variety of star block systems. In comparison to random copolymers of identical comonomer composition, which exhibit properties that are intermediate between those of the parent homopolymers, and often predictable based on comonomer content obeying a simple rule-of-mixtures, block copolymers exhibit remarkable properties that stem from the individual character or function of their discrete blocks. The chemical nature of the different repeating monomers in the blocks, the number of blocks, block lengths, comonomer sequence distributions, and chain architectures (e.g., linear, graft-branched, star, etc.) define the copolymer's operative physical and chemical properties.[3-5] Moreover, thermodynamic immiscibility among chemically dissimilar blocks often drives self-assembly into well-ordered, micro-phase separated morphologies, as depicted in **Figure 1.1**, that can significantly enhance the

material properties. Block copolymers have thus received tremendous attention with respect to controlled synthesis, tailored morphological development, and customized physical properties with potential uses in self-assembled, nanostructured materials including structural and biomechanical materials, polymeric membranes for energy conversion and water purification systems, and blend compatibilization.[6-8] The technological applicability of block copolymers is promising; however the generally arduous procedures required for block copolymer synthesis that often involve inert atmospheric conditions, well-controlled, sequential reaction timings, specialized initiators, and high purity monomers and solvents, often limits the utilization of block copolymers in commercial products.[9,10] As a distinct alternative to the complex polymerization mechanisms and synthetic protocols employed in the conventional formation of block copolymers, this dissertation demonstrates that blocky copolymers with tailored chain sequences and micro-phase separated morphologies can be achieved using a comparatively simple post-polymerization functionalization method carried out on a semicrystalline homopolymer in its heterogeneous gel state. This review begins with an overview of gradient copolymers and polydisperse block copolymer architectures, which can demonstrate similar physical properties to conventional monodisperse block copolymers. Post-polymerization functionalization methods carried out in heterogeneous reaction states are discussed. Semicrystalline polymer gels, gelation mechanisms, and gel morphology are discussed in detail, with particular emphasis on syndiotactic polystyrene (sPS) as a model semicrystalline homopolymer for the heterogeneous gel-state functionalization method.

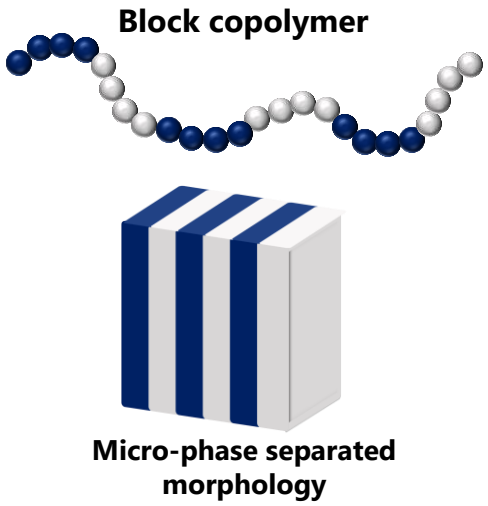

Figure 1.1. Pictorial representation of a segmented/multiblock copolymer and the micro-phase separated morphology into which the block copolymer can self-assemble.

1.2. Ordered domains in gradient and polydisperse block copolymers

The precise block copolymer architecture is not required to obtain copolymers with micro-phase separated morphologies. For example, gradient copolymers differ from conventional block copolymers in that the transition from one monomer sequence to the other comonomer is gradual along the chain (gradient or tapered) as opposed to the abrupt transition between comonomers in block copolymers. Nevertheless, gradient copolymers can demonstrate similar physical properties to block copolymers, including their ability to self-assemble into ordered domains.[11-16] Micro-phase separation in block copolymers is governed by thermodynamic incompatibility between the dissimilar comonomer segments, copolymer composition, volume fraction of the monomer species, and the Flory-Huggins interaction parameter (χ). In addition, linear gradient copolymers must exhibit relatively high molecular weights, sufficiently narrow gradient segment lengths, and a critical segregation strength, χN, (where N is the chain length) of ca. 30 (relative to 10.5 in block copolymer), in order to phase separate.[15] High molecular weights can actually be advantageous in copolymers because they improve the mechanical strength of the copolymer and adjust the order-

disorder transition temperature (i.e., the transition from the ordered phase to the homogenous disordered phase, χ_{ODT}) to more industrially-feasible processing temperatures, which can be challenging to achieve in block copolymer systems through modern synthetic methods. Gradient copolymers with strong gradients, similar to the comonomer sequence of block copolymers, generally phase separate more-readily than gradient copolymers with weak gradients. Gradated sequence structure tends to increase the size of phase domains and generates diffuse "blurred" interfacial regions between the chemically distinct domains that vary in breadth depending upon gradient strength, copolymer composition, and sample heterogeneity (i.e., polydispersity).[17-20] In gradient copolymer-based membranes, the diffuse phase boundary generates highly continuous phase domains, which improves the membrane's transport properties over random and block copolymers without destroying the membrane's mechanical integrity.[21] Dispersity in the composition of gradient copolymers results in increased phase domain sizes, which suggests that the effective segregation between monomer components increases with greater polydispersity.[14,17,18]

Block length polydispersity has also been reported to play a significant role in the phase behavior of block copolymers. Much of the understanding of the physical and morphological properties of polydisperse block copolymers is based on physical theories of polymer solutions and mixing.[22-26] Dobrynin and Leibler[22] simulated polydisperse multiblock copolymers and observed that increasing the block length polydispersity reduced the Flory-Huggins interaction parameter (χ) of the order-disorder transition (χ_{ODT}). Furthermore, self-consistent field theory and random phase approximation have provided insight into the phase behavior of simulated multiblock copolymers, and support that χ_{ODT} decreases significantly with increasing polydispersity at a fixed volume fraction of *A* units (ϕ_A).[23,24] A decrease in χ_{ODT} demonstrates an

increase in the order-disorder transition temperature through stabilization of the ordered phase.[25,26] Greater polydispersity was also found to lower the critical molar mass required to bring about micro-phase separation and leads to increased phase domain sizes.[24,26-28] Empirical investigations of the effect of polydispersity on phase behavior have primarily employed *AB* diblock copolymers that contain a polydisperse *A* block and a monodisperse *B* block.[29-32] Other studies have focused on multicomponent blends of monodisperse block copolymers, in which the blend compositions are varied systematically to control the polydispersity while maintaining a constant ϕ_A.[33-36] These investigations demonstrate that polydisperse copolymers contain large phase domain sizes, consistent with the behavior predicted by the theoretical findings.[37,38] The intriguing phase behavior of gradient copolymers and polydisperse multiblock copolymers reveals the relevance of developing new, straightforward, technologically-feasible methods to prepare copolymers with polydisperse, block-like distributions of comonomers.

1.3. Heterogeneous reaction states to prepare non-random copolymers

1.1.1. Heterogeneous powder state modification

Heterogeneous reaction states are often employed in post-polymerization functionalization reaction schemes, in order to introduce functional groups to polymers that are insoluble in common reaction solvents.[39] Unlike in a homogeneous solution where monomer units have an equal likelihood of reacting with a functionalizing reagent resulting in a statistically random copolymer, in the heterogeneous reaction state, monomer units that are far removed from the solid-liquid phase boundary are inaccessible to the functionalizing reagent, resulting in a non-random (i.e., blocky) distribution of functional groups along the chains. Copolymers prepared using heterogeneous reaction methods often exhibit properties that differ from solution-state (random) copolymers of

similar functional group content, attributed to their blocky microstructure.[40,41] Genzer and co-workers,[40-45] used results from experiments and simulations to extensively investigate the non-homogeneous bromination of atactic polystyrene (aPS) in poor solvents, where polymer chains are in a collapsed conformation. In the collapsed state, portions of the chains were effectively shielded from the brominating reagent, resulting in blocky brominated styrene sequences. The copolymers prepared in poor solvents adsorbed to a silica surface more strongly than copolymers prepared in good solvents. Simulations of the heterogeneous post-polymerization functionalization reaction supported that introducing a brominating reagent to aPS in its collapsed state produces copolymer chains that contain more consecutive styrene monomers and more segments of consecutive brominated styrene monomers that are capable of adsorbing to a suitable surface.

In addition to exhibiting properties that differ from their solution-state analogs, simulations by Khokhlov and Khalatur[46,47] suggest that copolymers prepared using a heterogeneous post-polymerization functionalization method will exhibit properties that depend on the polymer morphology. In their study, simulated protein-like *AB* copolymers were prepared by reassigning surface units in a dense *A* homopolymer globule to *B* units. The folding properties of the protein-like *AB* copolymers were compared to that of simulated random copolymers and simulated random-block copolymers of the same A/B composition. The simulated random-block copolymers contained the same average length of *A* and *B* sequences (blocks) as the protein-like copolymers, however the *A* and *B* blocks were distributed along the chains based on a Poisson distribution. In simulations, the protein-like copolymers transitioned from a globular state to a coil state at higher temperatures and with faster kinetics than the analogous random and random-block copolymers, demonstrating that the protein-like copolymers inherited properties of the parent homopolymer globule.

1.1.2. Heterogeneous surface modification

Surface treatment of polymer films with a functionalizing reagent can be used to impart useful functionalities that enhance the physicochemical properties (e.g., adhesion, wettability, etc.) of the material.[48] The strength of the reagent, inherent properties of the polymer (e.g., porosity), and duration of the reaction influence the extent and depth of the polymer modification. For example, Borriello and coworkers[49] investigated the post-polymerization sulfonation of solution cast and compression-molded sPS films, evaluating the interplay between sulfonating reagent diffusion and polymer phase morphology on sulfonation heterogeneity across the films. Solution cast films of sPS, which contain a porous crystalline phase and solvent swollen amorphous phase, demonstrate uniform sulfonation, attributed to rapid diffusion of sulfonating reagent through nanoporous phases in the film. In contrast, compression-molded films, which contain non-porous crystallites in a densely-packed amorphous chain matrix, exhibited a decreasing sulfonation gradient from the film's surface to interior, consistent with slow diffusion of sulfonating reagent into the dense, non-porous, solid-state "bulk" film. The results of their analysis were similar to that observed for the sulfonation of atactic (amorphous) polystyrene films.[50] Though the copolymer microstructures were not investigated, the heterogeneous reaction conditions used in these studies are expected to produce copolymers with a non-random distribution of functional groups whose sequence distributions depend on the film morphology.

1.1.3. Heterogeneous gel-state functionalization reaction schemes

Semicrystalline polymer gels are composed of lamellar crystallites that act as physical cross-links linking together a percolating network of solvent swollen amorphous chains.[51] Reports of heterogeneous gel-state functionalization reactions in the literature set a precedent for utilizing gel-state reaction conditions to produce blocky copolymers.[52,53] For example, we recently

demonstrated that the heterogeneous sulfonation of sPS and the sulfonation and bromination of poly(ether ketone) (PEEK) gels yields copolymers with blocky copolymer microstructures.[52,53] The gel-state functionalized sPS and PEEK copolymers demonstrated superior crystallizability and faster crystallization kinetics compared to their solution-state random analogs. In addition, quenched films of the gel-state brominated PEEK copolymers exhibited micro-phase separated morphology, similar to the phase behavior of conventional block copolymers. In contrast, solution-state brominated PEEK copolymer analogs displayed a phase-mixed state. Based on a random phase approximation, the critical value of the χ_{ODT}, above which the homogeneous mixed phase becomes unstable, is inversely proportional to the blockiness, referring to the state of segregation of comonomer units along the chains.[22,54] Thus, phase separation is favored for copolymers with a high degree of blockiness, while a homogeneous, phase-mixed state is favored for copolymers with a low degree of blockiness. The gel-state brominated PEEK copolymers must therefore contain a highly blocky microstructure. Venditto and coworkers[55] showed that exposing an aerogel of semicrystalline sPS to chlorosulfonic acid results in preferential sulfonation of the gel's amorphous component. While copolymer microstructure was not directly explored in their investigation, the sulfonated aerogel was found to maintain the original gel morphology and showed superior water uptake relative to an unsulfonated analog. Ultimately, these results demonstrate that copolymers with a blocky microstructure can retain the properties of the pure homopolymer with the added advantage of distinct properties attributed to the functional component.

Gel-state functionalized blocky copolymers are anticipated to have unique phase-separated morphologies unattainable in diblock copolymers, random copolymers, and monodisperse multiblock copolymers, stemming from block length polydispersity and blockiness that originates

from the gel morphology.[56,57] The rest of this introduction will focus on the gelation mechanisms of semicrystalline polymers and gel morphology, starting with a brief overview of polymer gels and giving particular emphasis to sPS/solvent gels.

1.4. Semicrystalline polymer gels

1.1.4. Polymer gels

Polymer gels are dilute or moderately dilute, three-dimensional (3D) continuous polymer networks that display solid-like behavior while physically confining a liquid or gas within the continuous network structure.[58] Gels can be handled and placed in an excess of solvent without irreversibly damaging the gel network.[59] Flory established a widely used classification system for polymer gels that is based on the network structures shown in **Figure 1.2**.[60] Soaps and clays are examples of Type 1 gels, consisting of well-ordered lamellae arranged in parallel through electrostatic or van der Waals forces or dipolar interactions. Type 2 gels are covalent, i.e., chemically cross-linked, polymer networks. Covalent polymer gels (e.g., thermosets) are formed by reacting a polymer with a polyfunctional cross-linking agent or through a photochemical reaction between polymer chains that is often initiated by ultraviolet light (curing). Suitable liquids or gases can then adsorb into the pores of the cross-linked 3D network. Polymer gels with networks that form through the physical aggregation of polymer chains, i.e., physically cross-linked gels, are classified as Type 3 gels. Type 4 gels are particulate disordered structures consisting of liquid-swollen, overlapping supramolecular particles. Protein aggregates are an example of supramolecules that form Type 4 gels.

Physical polymer gels (Type 3) achieve an interconnected network structure through the formation of intermolecular physical bonds that act as junction points, i.e., physical cross-links, in

the continuous gel network. Physical cross-links can form *via* hydrogen bonding, ionic aggregation, host-guest interactions, complex formation, crystallization, helix formation, or phase separation.[51] The physical cross-links are often thermally labile and are created and destroyed by simply cooling and heating, respectively. Thus, physical polymer gels are often termed thermoreversible gels.

Semicrystalline polymer gels are formed from miscible mixtures of a semicrystalline polymer and a suitable solvent. Crystallization packs chain segments tightly together in lamellar crystallites that act as physical cross-links, confining the solvent molecules within the amorphous component of the polymer network. Heating the semicrystalline gel to a sufficiently high temperature melts the crystallites, destroying the interconnected network. Conversely, lowering the solution temperature to a suitable crystallization temperature induces crystallization, reconstructing the physically cross-linked network of crystallites. Examples of homopolymers that form semicrystalline gels include syndiotactic poly(methyl methacrylate),[61] poly(phenylene sulfide),[62] poly(vinyl chloride),[63] poly(vinylidene fluoride),[64] isotactic polypropylene[65] and stereoregular polystyrene.[66-69] The tactically pure syndiotactic polystyrene (sPS) is an ideal model homopolymer for gel-state functionalization chemistries because it forms semicrystalline thermoreversible gels with a broad range of halogenated and aromatic hydrocarbon solvents.[70]

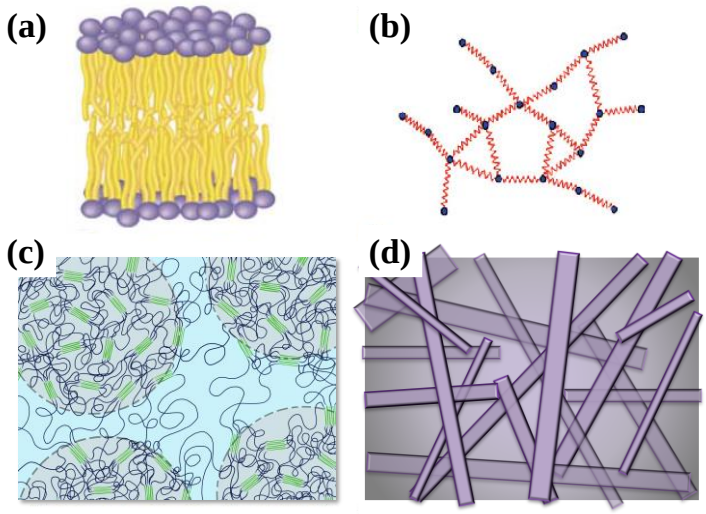

Figure 1.2. Pictorial representations of Flory's gel classifications: (a) Type 1: well-ordered lamellar gel (bilayer sheet); (b) Type 2: covalent polymer network (chemically cross-linked); (c) Type 3: polymer network formed through physical aggregation of polymer chains (physically cross-linked); and (4) Type 4: particulate disordered structure.

1.1.5. Syndiotactic polystyrene

Polystyrene is a well-recognized commercial plastic used in applications that include food and general storage containers and protective packaging materials.[71] This processable form of polystyrene consists of phenyl groups that are randomly distributed on either side of the carbon backbone, which is designated as atactic, where tacticity refers to the configuration of monomer units along the chain. In 1986, the synthesis of syndiotactic polystyrene with high tactic purity was first reported.[72] Syndiotactic polystyrene is a semicrystalline stereoregular form of polystyrene consisting of styrene units that alternate from side to side with respect to the carbon chain backbone.

Syndiotactic polystyrene exhibits complex polymorphic behavior that is based on four main crystalline forms.[73-76] The molecular chain conformations of the crystalline forms are shown in **Figure 1.3**. In the α- and β-forms, chain segments arrange in an all-trans-planar zigzag (T_4) conformation. The α-form has a hexagonal unit cell of nine chains that are arranged in three-chain clusters in hexagonal columns, while the β-form is characterized by an orthorhombic unit cell of

four chains.[77] Crystallites in the α- and β-form consist of chain-folded lamellae. The α-form crystallites are reported to be thinner than the β-form crystallites on average, and are expected to exhibit loosely looped (fringed micelle-like) surface chain folds, based on the relatively low density of the α-form (ρ = 1.033 g cm^{-3}).[78] Conversely, the higher density β-form crystallites (ρ = 1.067 g cm^{-3}) are expected to exhibit non-adjacently re-entering (switchboard-like) surface chain folds.[78] Crystal structures of the trans-planar zigzag conformation form by annealing from the glass (cold-crystallization) or upon cooling from the melt (melt-crystallization). The α-form is kinetically favorable and is formed preferentially from amorphous sPS upon annealing above 200 °C, or by melt-crystallization at temperatures well below the melting temperature (ca. 270 °C).[79] Crystallization from the melt at high temperatures (> 260 °C) favors the formation of the thermodynamically stable β-form.

The δ- and γ-forms are defined by chain segments in a s(2/1)2 helical (TTGG) conformation. Solvent molecules induce the formation of the helical conformation through polymer-solvent (host-guest) interactions. The δ-form crystal structure has a monoclinic unit cell and can be further characterized by a co-crystalline molecular complex phase wherein solvent molecules reside either in the cavities of the helix between the chains (clathrate) or in continuous channels between the helical chains (intercalate, also referred to as the ϵ-form).[70,77,80,81] The chemical nature of the guest molecule, which effects the polymer-solvent interactions, has been reported to influence the size of the δ-form crystallites. In particular, the correlation length (i.e., the distance over which structural order is maintained) along the axis perpendicular to the chain axis in the crystal has been reported by Daniel and co-workers to increase with increasing strength of the polymer-solvent interactions.[82,83] In these reports, however, the relationship between the guest chemical nature and the strength of the interactions is not well understood.

Solvent extraction by supercritical carbon dioxide ($scCO_2$) removes the guest solvent molecules from the cavities, resulting in a nanoporous emptied δ-form (δ_e).[84-86] Evaporative drying processes (e.g., annealing above the glass transition temperature) also remove the guest solvent molecules, however tension at the solvent-vapor interface collapses the nanopores resulting in a new monoclinic unit cell, designated as the γ-form.[87] The γ-form is also formed directly using solvents that are incapable of intercalating into the cavities between the helical chains (e.g., acetone, 1,1,2,2-tetrachloroethane).[77] The helical crystal structures are believed to be chain-extended due to enhanced chain rigidity that results from the formation of polymer-solvent molecular complexes.[75] The thermal and solvent processing conditions that can be used to obtain the crystalline forms of sPS are summarized in **Scheme 1.1**.

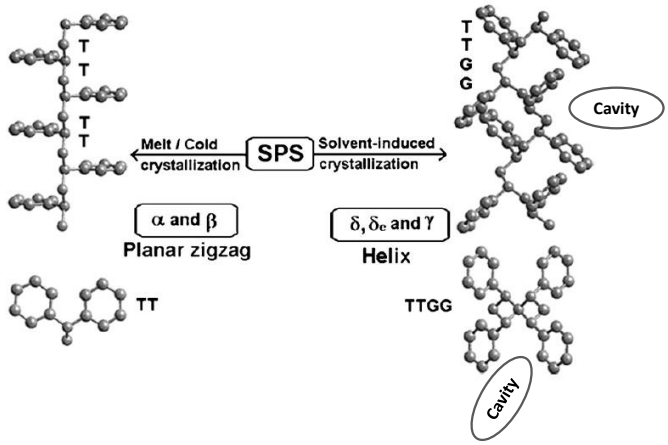

Figure 1.3. Molecular chain conformations of the crystalline forms of sPS. The TTGG helical conformation contains cavities into which suitable guest molecules can be adsorbed. Adapted with permission from Elsevier.[77]

Crystallites of the α-form transform to the δ-form upon exposure to solvent. The β-form crystallites do not transform to the δ-form, and thus can potentially co-exist with crystallites in the δ-form.[77] The β-form has also been reported to form during solvent processing conditions.[70,74,82,88] Gowd et al.[77] speculate that the mechanism for crystallization to the β-form in the presence of solvent molecules proceeds at elevated temperatures by way of a transformation of δ-form crystallites to the thermodynamically more stable β-form. However, temperature versus polymer

concentration phase diagrams of sPS in a broad range of solvents suggest that the β-form crystallites form through a nucleation and growth process, which is discussed in more detail below in subsection **1.1.7.**[74,88] The helical δ-form crystallites form the crystalline physical cross-links observed in sPS/solvent gels.

Scheme 1.1. Schematic representation of the crystallization and interconversion pathways between the polymorphs of sPS. Dotted lines indicate transitions that occur either in the presence of supercritical CO_2 ($\gamma \rightarrow \beta$) or excess solvent in the amorphous phase. Reprinted with permission from Elsevier.[77]

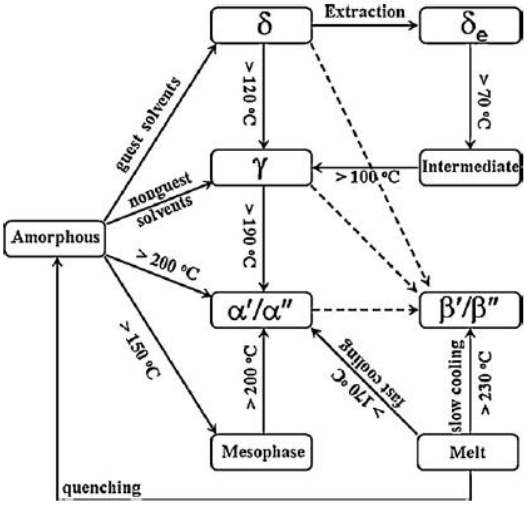

1.1.6. Gelation mechanisms

Syndiotactic polystyrene gels, like many other semicrystalline polymer gels,[61-65,67,69] form from homogeneous solutions of the polymer and a suitable solvent upon cooling the solution (monophasic) below the solution-gelation (sol-gel) transition, which induces a liquid-liquid phase separation (biphasic) that is followed by crystallization.[59,68] Gelation is dependent on solvent, polymer content, and temperature. **Figure 1.4** shows a typical temperature versus polymer concentration phase diagram for a semicrystalline polymer that displays liquid-liquid phase separation with an upper critical solution temperature (UCST).[89] The phase diagram is divided into three regions. In the monophasic region, above the binodal (coexistence) curve, the polymer/solvent system exists as a homogenous mixture. Below the binodal curve, two biphasic

regions emerge that derive from a liquid-liquid phase separation, the metastable region between the binodal and spinodal curves and the unstable region below the spinodal curve. Within the unstable region, infinitesimal fluctuations in composition and density result in spinodal decomposition (i.e., rapid unmixing), generating a continuous polymer-rich phase and a continuous polymer-poor phase of interconnected morphology. Crystallization occurs in the polymer-rich phase, establishing a gel network structure. In the metastable region, liquid-liquid phase separation proceeds via a nucleation and growth mechanism at localized nucleation sites. At low polymer concentration, the nucleation sites exist in polymer-rich regions that are dispersed by a polymer-poor solvent matrix, resulting in a morphology of disconnected globules of semicrystalline polymer. At high polymer concentration, polymer-poor regions are dispersed within a polymer-rich phase, producing a continuous semicrystalline network that contains dispersed solvent clusters. Thus, the gel morphology is highly dependent on temperature, polymer concentration, and the mechanism of liquid-liquid phase separation.

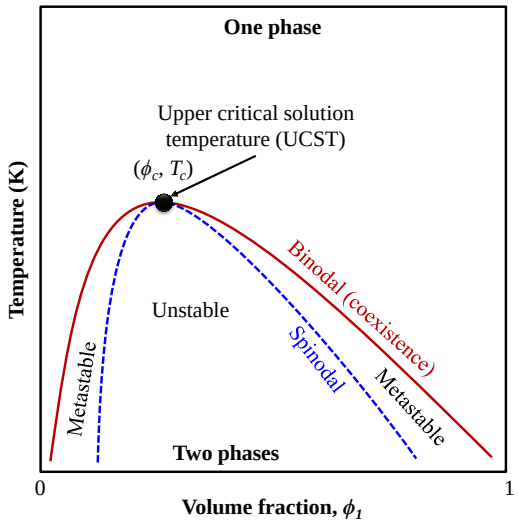

Figure 1.4. Temperature versus polymer concentration phase diagram for a polymer solution that exhibits an upper critical solution temperature (T_c) at a critical concentration (ϕ_c).

1.1.7. Syndiotactic polystyrene/solvent gelation and gel morphology

Syndiotactic polystyrene gels consist of fibrillar network structures that form via liquid-liquid phase separation followed by crystallization in the polymer-rich phase, generating a continuous gel network. Crystallization occurs through a solvent induced process in which polymer-solvent interactions transform randomly coiled chain segments into short s(2/1)2 helical segments.[74,77] Over time, the short helical segments form longer helical segments and aggregate into δ-form crystalline lamellae that act as junction points in the physical gel network. The fibrillar crystalline component that constitutes the gel network is often referred to as the δ phase or molecular complex phase, based on the presence of the helical δ-form co-crystalline polymorph.

The temperature versus polymer concentration phase diagram of sPS/solvent gels is complicated by the polymorphic behavior of sPS. **Figure 1.5** shows a typical temperature versus polymer concentration phase diagram for sPS. The sPS in bromoform ($CHBr_3$) phase diagram was constructed by De Rudder and co-workers[88] using thermal transition information obtained from differential scanning calorimetry (DSC). In this study, sPS/$CHBr_3$ samples of varying polymer content were homogenized at high temperature, cooled to a low temperature to observe the exothermic transitions (gelation or crystallization), and then reheated to observe the endothermic transition (melting). Gelation was evident at polymer contents between 10−50 mol%, indicated by a low temperature exotherm (open circles) and a relatively low temperature endotherm (filled circles) ascribed to the s(2/1)2 helical δ phase. At intermediate polymer content, in the range 50−70 mol% sPS, both gelation and crystallization are observed, demonstrated by the coexistence of the s(2/1)2 helical δ phase and trans-planar zigzag β-form crystallites. This behavior appears to suggest the occurrence of competing processes of spinodal decomposition and nucleation and growth in a transition toward the metastable region of the phase diagram. Above 70 mol% sPS, the phase

diagram shows only crystallization and melting of β-form crystallites. sPS/solvent systems that contain a trans-planar zigzag β phase have been reported to exhibit a lamellar morphology of interconnected lamella crystallites. Though the sPS/solvent systems that display a lamellar morphology have been reported as paste-like gels in the literature, these systems appear to be better defined as a suspension of crystallites rather than a semicrystalline polymer gel.[60,70,82,90]

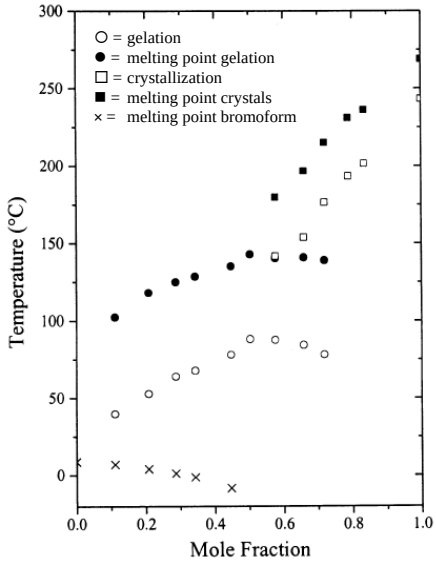

Figure 1.5. Phase diagram of sPS in bromoform. Adapted with permission from De Rudder, J.; Berghmans, H.; De Schryver, F. C.; Bosco, M.; Paoletti, S., *Macromolecules* 2002, *35* (25), 9529-9535.[88] Copyright 2002 American Chemical Society.

The stability of the helical δ phase, and thus the fibrillar gel network structure in sPS/solvent systems, is dependent on solvent quality. In good solvents, like $CHBr_3$, the helical δ phase is observed even at high polymer content.[88] As solvent quality decreases, the stability of the helical δ phase has been reported to also decrease.[74] For example, in the sPS/$CHCl_3$ solvent system, a very good solvent for sPS, the melting of β-form crystallites is not observed until polymer concentrations of at least 40 mol%. Meanwhile, in the sPS/TCB solvent system, a reportedly poor solvent for sPS, the melting of β-form crystallites was observed at just 20 mol% sPS. In non-complexing solvents, the β phase has been found to form preferentially.[70,90] This gelation behavior suggests that polymer-solvent interactions between the polymer chains and a good solvent leads

to the preferential formation of helical chain conformations that consist of co-crystalline molecular complexes.

The ability of a solvent to form molecular complexes with sPS is dependent on the size of the solvent molecule and the solvent quality. Mochizuki et al.[70] conducted a broad investigation of solvents that are able to form gels with sPS. Remarkably, out of the 62 solvents tested, 38 formed polymer-solvent molecular complexes with sPS that resulted in a fibrillar gel network of the s(2/1)2 helical δ phase. Syndiotactic polystyrene is capable of forming polymer-solvent molecular complexes with solvents whose molecular volume ranges from 69−153 $Å^3$ and whose Fedors' solubility parameter (*SP*) value ranges from 8.8−12.3 $(cal/cm^3)^{1/2}$, around the calculated *SP* value of sPS (10.4 $(cal/cm^3)^{1/2}$).

Depending on solvent quality, the morphology of a sPS/solvent system can change significantly over a relatively narrow concentration range.[70] As discussed above, good solvents like $CHBr_3$ and $CHCl_3$ form continuous fibrillar gel network structures even at high polymer concentrations of ca. 50 and 40 mol% sPS, respectively.[74,88] **Figure 1.6** compares the morphology of sPS/benzyl alcohol systems ranging in polymer concentration from 0.9 w/w% to 13.6 w/w%. Benzyl alcohol is a relatively poor solvent for sPS and exhibits an SP value of ca. 12 $(cal/cm^3)^{1/2}$ and a molecular volume of 110 $Å^3$.[70] At low polymer content, 0.9 w/w% and 2.7 w/w%, the morphology of the sPS/solvent system consists of a continuous fibrillar network ascribed to the s(2/1)2 helical δ phase.[70] In contrast, at concentrations of just 4 w/w% and above the morphology is remarkably different, consisting of lamellar spherulitic structures of the β-form crystalline phase. Thus, the morphology of the sPS/solvent system is clearly dependent on the polymer content and again, on the solvent quality.

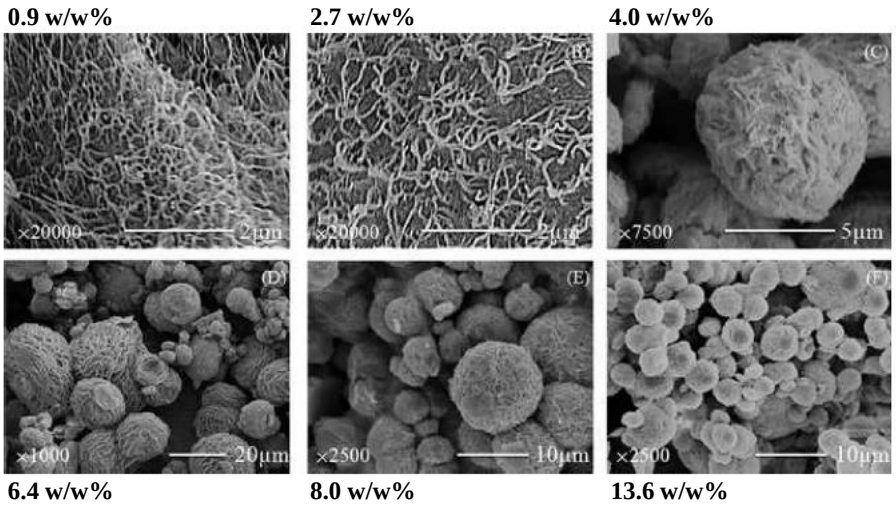

Figure 1.6. SEM micrographs of sPS/benzyl alcohol systems after drying under vacuum. Initial polymer concentrations are included above or below the images. The 0.9 w/w% and 2.7 w/w% systems are gels with fibrillar network structure. The 4.0−13.6 w/w% systems are paste-like particle suspensions and contain lamellar structures. Adapted with permission from Elsevier.[70]

For sPS/solvent systems that are capable of forming gels with sPS, the polymer-solvent interactions strongly impact the gel morphology, e.g., the structural order, size, and thickness of the crystallites, and the clustering of crystallites in the polymer-rich phase of the gel network. Kobayashi et al.[91] investigated the structure formation and gelation of sPS/solvent systems using Fourier transform infrared spectroscopy (FTIR). They observed that solutions of sPS in benzene, carbon tetrachloride (CCl_4), and 1,2-dichlorobenzene (*o*-DCB) contained aggregates of ordered s(2/1)2 helical conformations (i.e., crystal clusters) at concentrations below the critical concentration required for the formation of a continuous physical gel network, i.e., below concentrations of 0.2 w/v%. The authors termed these stable s(2/1)2 helical aggregate structures "microgels." Solutions of sPS in $CHCl_3$, a better solvent for sPS, were also investigated. Microgels were not observed in the sPS/$CHCl_3$ systems and the critical concentration for gelation was higher (2.2 w/v%) than in the sPS/CCl_4 and sPS/*o*-DCB systems. In addition, the evolution of conformational order (i.e., gelation) in the sPS/$CHCl_3$ system required a long period of time. The mechanisms of conformational ordering were classified into types. In the sPS/$CHCl_3$ system

conformational order arose from the aggregation of several helical chain segments, where the number of helical chain segments required to form a stable aggregate was reported to increase with temperature. In the poor solvent systems, a self-organization mechanism involving a single helical chain segment was recognized at temperatures below room temperature. Morphological characterization of the sPS/$CHCl_3$ gels provided by small angle neutron scattering (SANS) and Fourier transform infrared (FTIR) spectroscopy experiments revealed that the sPS/$CHCl_3$ gel morphology was remarkably different from that of the sPS/CCl_4 and sPS/*o*-DCB gels.[92] At early times, the sPS/$CHCl_3$ demonstrated sol-type behavior, characterized by small star-like segmental aggregates that were connected to each other over long distances. Over a long period of time, several hours to days, an immobilized gel structure developed. The SANS profiles and infrared spectra strongly suggested that the aggregates of helical chain segments in the sPS/$CHCl_3$ were poorly developed, the s(2/1)2 helical conformations were disordered, and the gel morphology consisted of loosely packed helical chain aggregates. Specifically, they described the sPS/$CHCl_3$ gel morphology as being situated "in between those of a well-developed cluster (a continuous fractal object) and an ensemble of starlike segmental coagulates which entangle each other."[92] Conversely, the sPS/CCl_4 and sPS/*o*-DCB systems exhibited typical gel-type behavior and well-ordered s(2/1)2 helical chain segments. Thus, lower polymer solubility appears to favor polymer aggregation. When a high density of aggregation states is present in the polymer-rich phase, faster gelation rates are observed.

The impact that solvent quality has on the sPS/solvent gel morphology is evidenced by the observable differences in the sPS/solvent gel turbidity.[82,83] The visible light transmittance of sPS/solvent gels has been reported to range from 0.6% to 79% depending on the gelation solvent.[83] Daniel and co-workers[82,83] compared the gel light transmittance of a broad range of sPS/solvent

gels to the size of crystallites in the direction perpendicular to the chain axis provided by wide-angle X-ray diffraction (WAXD). Gel transparency was reported to decrease with increasing crystallite size; though, the largest crystallite sizes were found to be ca. 14 nm, too small to effectively scatter visible light (ca. 380 nm < λ_{Vis} < 470 nm). The authors therefore suggested that gel turbidity must also indicate an increase in the size of the crystalline domains along the direction perpendicular to the chain axis. Based on the findings of Kobayashi et al., the visible light scattering in the sPS/solvent gels appears to be caused by clusters of crystallites within the gel network, whose presence depends on the gelation solvent.[91,92] Morphological characterization of sPS/solvent gels using ultra-small-angle X-ray scattering (USAXS) experiments to investigate large structural features in the gel network has not been reported in the literature.

1.5. Post-polymerization functionalization in the heterogeneous gel state

As discussed previously, the semicrystalline polymer gel is composed of tightly packed chain segments in lamella crystallites that act as physical cross-links bound together by a percolating network of solvent swollen amorphous chains. When a functionalizing reagent is introduced to the heterogeneous gel network, it is sterically excluded from the crystalline component, and thus only reacts with monomer units in the accessible interconnecting amorphous component. Using this straightforward post-polymerization functionalization approach, the resulting copolymer is likely to contain a blocky copolymer microstructure of separate segments of randomly functionalized "blocks" and un-functionalized "blocks" originating from monomer units that were isolated within the crystalline domains of the gel network, represented in **Scheme 1.2**. Here, the term "blocky copolymer" is used as a description of gel-state functionalized copolymers, implying a significant degree of non-randomness in the distribution of comonomers

along the copolymer chain, as well as significant block length polydispersity relative to that of conventional segmented/multiblock copolymers. Gel-state functionalized blocky copolymers are anticipated to have unique phase-separated morphologies unattainable in diblock copolymers, random copolymers, and monodisperse segmented/multiblock copolymers, stemming from their block length polydispersity and blockiness that originates from the gel morphology. Given the ability to control the precise morphology of the semicrystalline gel network, specifically through changing the polymer concentration, gelation solvent, and/or gelation conditions, copolymers that contain distinct blocks of highly functionalized segments with tunable sequence distributions, chemical composition, and copolymer properties are anticipated.

Scheme 1.2. Schematic representation of the post-polymerization functionalization of a semicrystalline polymer in the (left) homogeneous solution-state (Random) and (right) heterogeneous gel-state (Blocky).

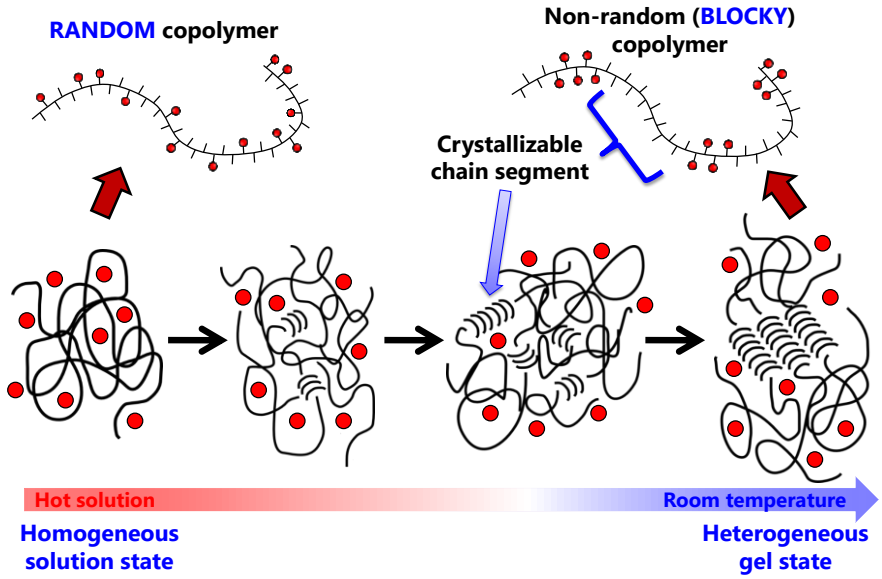

1.6. Conclusion and scope of thesis

Block copolymers are a unique class of macromolecules that have received tremendous attention with respect to controlled synthesis, tailored morphological development, and customized physical properties. The self-assembly of block copolymers into well-ordered, micro-phase separated morphologies, driven by thermodynamic immiscibility between the chemically

dissimilar blocks, can significantly enhance the material properties of block copolymers, rendering them useful for a broad range of potential applications in self-assembled, nanostructured materials. Nevertheless, the arduous procedures required for block copolymer synthesis generally limits the scope of their commercial application. As a distinct alternative to the complex polymerization mechanisms and synthetic protocols employed in the conventional formation of block copolymers, a physical polymer chemistry approach is proposed to produce blocky copolymer microstructures in semicrystalline polymers using a post-polymerization functionalization method carried out in a heterogenous gel state. Reports of heterogeneous reaction schemes in the literature set a precedent for utilizing gel-state reaction conditions to produce copolymers with blocky microstructures and tailored chain sequences. Semicrystalline thermoreversible polymer gels are composed of a physically cross-linked network of tightly packed chain segments in lamella crystallites tied together by a percolating network of solvent swollen amorphous chains. When a functionalizing reagent is introduced to the heterogeneous gel network, it is sterically excluded from the crystalline component, and thus only reacts with monomer units in the accessible interconnecting amorphous component. The resulting copolymer is thus likely to contain a blocky distribution of functional groups with un-functionalized "blocks" originating from monomer units that were isolated within the crystalline domains of the gel network. Copolymers that contain a highly blocky microstructures are expected to show similar physical properties to block copolymers, including their ability to self-assemble into ordered domains. Syndiotactic polystyrene is an ideal model polymer for this simple gel-state functionalization approach because of its ability to form semicrystalline thermoreversible gels in a broad range of solvents. Given the ability to control the precise gel morphology, specifically through changing the polymer concentration, gelation solvent, and gelation conditions, copolymers that contain distinct blocks of highly functionalized

segments with tunable sequence distributions, chemical composition, and copolymer properties are anticipated.

This dissertation demonstrates the bromination of sPS in the homogeneous solution-state and the heterogeneous gel and powder states to produce random and blocky brominated sPS (sPS-co-sPS-Br) copolymers, respectively. The purpose of this research was to investigate the use of gel-state bromination as a simple and facile post-polymerization functionalization method to prepare *semicrystalline* blocky copolymers with relatively high degrees of functionality. **Chapter 2** reports the first post-polymerization bromination of sPS in solution and in the heterogeneous gel-state to produce a matched set of random and blocky brominated copolymers. In **Chapter 3**, the first high-resolution comonomer sequencing of brominated sPS copolymers is reported, based on pentad assignments of the quaternary carbon region of the quantitative ^{13}C NMR spectrum. Described in **Chapter 3** is the development of a comonomer sequencing method for brominated sPS copolymers that has been used to obtain a deeper understanding of the relationship between the sPS/solvent gel morphology and the copolymer microstructure and degree of blockiness that results from gel-state functionalization. The structure-property relationship between the sPS/solvent gel morphology and the copolymer microstructure and thermal properties is further investigated in **Chapter 4** through the comparison of a matched set of gel-state brominated copolymers prepared from an sPS/CCl_4 gel and an sPS/$CHCl_3$ gel. **Chapter 5** describes the blocky bromination of sPS copolymers using a post-polymerization functionalization method carried out in the heterogeneous powder state to investigate the effect of the heterogeneous reaction state on the copolymer microstructure, degree of blockiness, and crystallization behavior. Finally, conclusions of this research, its broader impacts, and suggested future work are provided in **Chapter 6**.

1.7. References

1. Hadjichristidis, N.; Pispas, S.; Floudas, G. A., *Block Copolymers: Synthetic Strategies, Physical Properties, and Applications*. John Wiley and Sons: New York, 2002.
2. Hamley, I. W., *The Physics of Block Copolymers*. Oxford University Press: New York, 1998.
3. Lee, M.; Park, J. K.; Lee, H.-S.; Lane, O.; Moore, R. B.; McGrath, J. E.; Baird, D. G., Effects of Block Length and Solution-Casting Conditions on the Final Morphology and Properties of Disulfonated Poly(Arylene Ether Sulfone) Multiblock Copolymer Films for Proton Exchange Membranes. *Polymer* **2009,** *50*, 6129-6138.
4. Leibler, L., Theory of Microphase Separation in Block Copolymers. *Macromolecules* **1980,** *13* (6), 1602-1617.
5. Dobrynin, A. V.; Leibler, L., Theory of Polydisperse Multiblock Copolymers. *Macromolecules* **1997,** *30*, 4756-4765.
6. Bates, F. S.; Fredrickson, G. H., Block Copolymers - Designer Soft Materials. *Phys. Today* **1999,** *52* (2), 32-38.
7. Lodge, T. P., Block Copolymers: Past Successes and Future Challenges. *Macromol. Chem. Phys.* **2003,** *204* (2), 265-273.
8. Ruzette, A.-V.; Leibler, L., Block Copolymers in Tomorrow's Plastics. *Nat. Mater.* **2005,** *4* (1), 19-31.
9. Domski, G. J.; Rose, J. M.; Coates, G. W.; Bolig, A. D.; Brookhart, M., Living Alkene Polymerization: New Methods for the Precision Synthesis of Polyolefins. *Prog. Polym. Sci.* **2007,** *32* (1), 30-92.
10. Govorun, E. N.; Chertovich, A. V., Microphase Separation in Random Multiblock Copolymers. *J. Chem. Phys.* **2017,** *146*, 034903.
11. Shull, K. R., Interfacial Activity of Gradient Copolymers. *Macromolecules* **2002,** *35* (22), 8631-8639.
12. Lefebvre, M. D.; Dettmer, C. M.; McSwain, R. L.; Xu, C.; Davila, J. R.; Composto, R. J.; Nguyen, S. T.; Shull, K. R., Effect of Sequence Distribution on Copolymer Interfacial Activity. *Macromolecules* **2005,** *38* (25), 10494-10502.
13. Wylie, K.; Bennett, I.; Marić, M., Self-Assembly of Gradient Copolymers Synthesized in Semi-Batch Mode by Nitroxide Mediated Polymerization. *Soft Matter* **2017,** *13*, 2836-2843.

14. Beginn, U., Gradient Copolymers. *Colloid Polym. Sci.* **2008,** *286* (13), 1465-1474.
15. Mok, M. M.; Ellison, C. J.; Torkelson, J. M., Effect of Gradient Sequencing on Copolymer Order–Disorder Transitions: Phase Behavior of Styrene/ N -Butyl Acrylate Block and Gradient Copolymers. *Macromolecules* **2011,** *44*, 6220-6226.
16. Pakula, T.; Matyjaszewski, K., Copolymers with Controlled Distribution of Comonomers Along the Chain, 1. Structure, Thermodynamics and Dynamic Properties of Gradient Copolymers. Computer Simulation. *Macromol. Theory Simul.* **1996,** *5* (5), 987-1006.
17. Jiang, R.; Wang, Z.; Yin, Y.; Li, B.; Shi, A.-C., Effects of Compositional Polydispersity on Gradient Copolymer Melts. *J. Chem. Phys.* **2013,** *138* (7), 074906.
18. Ganesan, V.; Kumar, N. A.; Pryamitsyn, V., Blockiness and Sequence Polydispersity Effects on the Phase Behavior and Interfacial Properties of Gradient Copolymers. *Macromolecules* **2012,** *45* (15), 6281-6297.
19. Pandav, G.; Pryamitsyn, V.; Gallow, K. C.; Loo, Y.-L.; Genzer, J.; Ganesan, V., Phase Behavior of Gradient Copolymer Solutions: A Monte Carlo Simulation Study. *Soft Matter* **2012,** *8*, 6471.
20. Sigle, J. L.; Clough, A.; Zhou, J.; White, J. L., Controlling Macroscopic Properties by Tailoring Nanoscopic Interfaces in Tapered Copolymers. *Macromolecules* **2015,** *48* (16), 5714-5722.
21. Zheng, Z.; Gao, X.; Luo, Y.; Zhu, S., Employing Gradient Copolymer to Achieve Gel Polymer Electrolytes with High Ionic Conductivity. *Macromolecules* **2016,** *49* (6), 2179-2188.
22. Dobrynin, A. V.; Leibler, L., Theory of Polydisperse Multiblock Copolymers. *Macromolecules* **1997,** *30* (16), 4756-4765.
23. Burger, C.; Ruland, W.; Semenov, A. N., Polydispersity Effects on the Microphase-Separation Transition in Block Copolymers. *Macromolecules* **1990,** *23* (13), 3339-3346.
24. Sides, S. W.; Fredrickson, G. H., Continuous Polydispersity in a Self-Consistent Field Theory for Diblock Copolymers. *J. Chem. Phys.* **2004,** *121* (10), 4974-4986.
25. Beardsley, T. M.; Matsen, M. W., Monte Carlo Phase Diagram for a Polydisperse Diblock Copolymer Melt. *Macromolecules* **2011,** *44* (15), 6209-6219.
26. Cooke, D. M.; Shi, A.-C., Effects of Polydispersity on Phase Behavior of Diblock Copolymers. *Macromolecules* **2006,** *39* (19), 6661-6671.

27. Spontak, R. J.; Williams, M. C., Prediction of Microstructures for Polydisperse Block Copolymers, Using Continuous Thermodynamics. *J. Polym. Sci., Part B: Polym. Phys.* **1990,** *28* (8), 1379-1407.
28. Matsen, M. W., Effect of Large Degrees of Polydispersity on Strongly Segregated Block Copolymers. *Eur. Phys. J. E* **2006,** *21* (3), 199-207.
29. Lynd, N. A.; Hillmyer, M. A., Influence of Polydispersity on the Self-Assembly of Diblock Copolymers. *Macromolecules* **2005,** *38* (21), 8803-8810.
30. Lynd, N. A.; Hamilton, B. D.; Hillmyer, M. A., The Role of Polydispersity in the Lamellar Mesophase of Model Diblock Copolymers. *J. Polym. Sci., Part B: Polym. Phys.* **2007,** *45* (24), 3386-3393.
31. Lynd, N. A.; Hillmyer, M. A., Effects of Polydispersity on the Order−Disorder Transition in Block Copolymer Melts. *Macromolecules* **2007,** *40* (22), 8050-8055.
32. Kumar, R.; Lokitz, B. S.; Sides, S. W.; Chen, J.; Heller, W. T.; Ankner, J. F.; Browning, J. F.; Kilbey II, S. M.; Sumpter, B. G., Microphase Separation in Thin Films of Lamellar Forming Polydisperse Di-Block Copolymers. *RSC Advances* **2015,** *5* (27), 21336-21348.
33. Nguyen, D.; Zhong, X.-F.; Williams, C. E.; Eisenberg, A., Effect of Ionic Chain Polydispersity on the Size of Spherical Ionic Microdomains in Diblock Ionomers. *Macromolecules* **1994,** *27* (18), 5173-5181.
34. Matsushita, Y.; Noro, A.; Iinuma, M.; Suzuki, J.; Ohtani, H.; Takano, A., Effect of Composition Distribution on Microphase-Separated Structure from Diblock Copolymers. *Macromolecules* **2003,** *36* (21), 8074-8077.
35. Noro, A.; Iinuma, M.; Suzuki, J.; Takano, A.; Matsushita, Y., Effect of Composition Distribution on Microphase-Separated Structure from Bab Triblock Copolymers. *Macromolecules* **2004,** *37* (10), 3804-3808.
36. Noro, A.; Okuda, M.; Odamaki, F.; Kawaguchi, D.; Torikai, N.; Takano, A.; Matsushita, Y., Chain Localization and Interfacial Thickness in Microphase-Separated Structures of Block Copolymers with Variable Composition Distributions. *Macromolecules* **2006,** *39* (22), 7654-7661.
37. Noro, A.; Cho, D.; Takano, A.; Matsushita, Y., Effect of Molecular Weight Distribution on Microphase-Separated Structures from Block Copolymers. *Macromolecules* **2005,** *38* (10), 4371-4376.

38. Widin, J. M.; Schmitt, A. K.; Schmitt, A. L.; Im, K.; Mahanthappa, M. K., Unexpected Consequences of Block Polydispersity on the Self-Assembly of Aba Triblock Copolymers. *J. Am. Chem. Soc.* **2012,** *134*, 3834-3844.
39. Gao, Y.; Li, H. M., Synthesis and Characterization of Acetylated Syndiotactic Polystyrene. *Polym. Int.* **2004,** *53* (10), 1436-1441.
40. Jhon, Y. K.; Semler, J. J.; Genzer, J., Effect of Solvent Quality and Chain Confinement on the Kinetics of Polystyrene Bromination. *Macromolecules* **2008,** *41* (18), 6719-6727.
41. Jhon, Y. K.; Semler, J. J.; Genzer, J.; Beevers, M.; Gus' kova, O. A.; Khalatur, P. G.; Khokhlov, A. R., Effect of Comonomer Sequence Distribution on the Adsorption of Random Copolymers onto Impenetrable Flat Surfaces. *Macromolecules* **2009,** *42*, 2843-2853.
42. Semler, J. J.; Jhon, Y. K.; Tonelli, A.; Beevers, M.; Krishnamoorti, R.; Genzer, J., Facile Method of Controlling Monomer Sequence Distributions in Random Copolymers. *Adv. Mater.* **2007,** *19* (19), 2877-2883.
43. Strickland, L. A.; Hall, C. K.; Genzer, J., Design of Copolymers with Tunable Randomness Using Discontinuous Molecular Dynamics Simulation. *Macromolecules* **2009,** *42* (22), 9063-9071.
44. Han, J.; Jeon, B. H.; Ryu, C. Y.; Semler, J. J.; Jhon, Y. K.; Genzer, J., Discriminating among Co-Monomer Sequence Distributions in Random Copolymers Using Interaction Chromatography. *Macromol. Rapid Comm.* **2009,** *30* (18), 1543-1548.
45. Gurarslan, R.; Hardrict, S.; Roy, D.; Galvin, C.; Hill, M. R.; Gracz, H.; Sumerlin, B. S.; Genzer, J.; Tonelli, A., Beyond Microstructures: Using the Kerr Effect to Characterize the Macrostructures of Synthetic Polymers. *J. Polym. Sci. B Polym. Phys.* **2015,** *53* (3), 155-166.
46. Khokhlov, A. R.; Khalatur, P. G., Protein-Like Copolymers: Computer Simulation. *Physica A* **1998,** *249* (1–4), 253-261.
47. Khokhlov, A. R.; Khalatur, P. G. J. P. r. l., Conformation-Dependent Sequence Design (Engineering) of Ab Copolymers. *Phys. Rev. Lett.* **1999,** *82* (17), 3456.
48. Nemani, S. K.; Annavarapu, R. K.; Mohammadian, B.; Raiyan, A.; Heil, J.; Haque, M. A.; Abdelaal, A.; Sojoudi, H., Surface Modification of Polymers: Methods and Applications. *Advanced Materials Interfaces* **2018,** *5* (24).

49. Borriello, A.; Agoretti, P.; Ambrosio, L.; Fasano, G.; Pellegrino, M.; Venditto, V.; Guerra, G., Syndiotactic Polystyrene Films with Sulfonated Amorphous Phase and Nanoporous Crystalline Phase. *Chem. Mater.* **2009,** *21* (14), 3191-3196.
50. Gibson, H. W.; Bailey, F. C., Chemical Modification of Polymers. 13. Sulfonation of Polystyrene Surfaces. *Macromolecules* **1980,** *13* (1), 34-41.
51. Sundararajan, P. R., *Physical Aspects of Polymer Self-Assembly*. John Wiley & Sons, Inc.: 2016.
52. Fahs, G. B.; Benson, S. D.; Moore, R. B., Blocky Sulfonation of Syndiotactic Polystyrene: A Facile Route toward Tailored Ionomer Architecture Via Postpolymerization Functionalization in the Gel State. *Macromolecules* **2017,** *50* (6), 2387-2396.
53. Anderson, L. J.; Yuan, X.; Fahs, G. B.; Moore, R. B., Blocky Ionomers Via Sulfonation of Poly(Ether Ether Ketone) in the Semicrystalline Gel State. *Macromolecules* **2018,** *51* (16), 6226-6237.
54. Vanderwoude, G.; Shi, A.-C., Effects of Blockiness and Polydispersity on the Phase Behavior of Random Block Copolymers. *Macromol. Theory Simul.* **2017,** *26*, 1600044.
55. Venditto, V.; Pellegrino, M.; Califano, R.; Guerra, G.; Daniel, C.; Ambrosio, L.; Borriello, A., Monolithic Polymeric Aerogels with Vocs Sorbent Nanoporous Crystalline and Water Sorbent Amorphous Phases. *ACS Appl. Mater. Inter.* **2015,** *7* (2), 1318-1326.
56. Li, S.; Register, R. A.; Weinhold, J. D.; Landes, B. G., Melt and Solid-State Structures of Polydisperse Polyolefin Multiblock Copolymers. *Macromolecules* **2012,** *45*, 5773-5781.
57. Xu, C.-L.; Zeng, J.-B.; Zhu, Q.-Y.; Wang, Y.-Z., Poly(Ethylene Succinate)-B-Poly(Butylene Succinate) Multiblock Copolyesters: The Effects of Block Length and Composition on Physical Properties. *Ind. Eng. Chem. Res.* **2013,** *52*, 13669-13676.
58. Talley, S. J.; Yuan, X.; Moore, R. B., Thermoreversible Gelation of Poly (Ether Ether Ketone). *ACS Macro Lett.* **2017,** *6*, 262-266.
59. Daniel, C.; Dammer, C.; Guenet, J.-M., On the Definition of Thermoreversible Gels: The Case of Syndiotactic Polystyrene. *Polymer* **1994,** *35* (19), 4243-4246.
60. Flory, P. J., Introductory Lecture. *Faraday Discuss.* **1974,** *57* (0), 7-18.
61. Berghams, H.; Donkers, A.; Frenay, L.; Stoks, W.; De Schryver, F. E.; Moldenaers, P.; Mewis, J., Thermoreversible Gelation of Syndiotactic Poly(Methyl Methacrylate). *Polymer* **1987,** *28* (1), 97-102.

62. Ding, H.; Zeng, Y.; Meng, X.; Tian, Y.; Shi, Y.; Jiao, Q.; Zhang, S., Porous Polyphenylene Sulfide Membrane with High Durability against Solvents by the Thermally Induced Phase-Separation Method. *J. Appl. Polym. Sci.* **2006,** *102* (3), 2959-2966.
63. Mutin, P. H.; Guenet, J. M., Physical Gels from Pvc: Aging and Solvent Effects on Thermal Behavior, Swelling, and Compression Modulus. *Macromolecules* **1989,** *22* (2), 843-848.
64. Tazaki, M.; Wada, R.; Abe, M. O.; Homma, T., Crystallization and Gelation of Poly(Vinylidene Fluoride) in Organic Solvents. *J. Appl. Polym. Sci.* **1997,** *65* (8), 1517-1524.
65. Matsuda, H.; Inoue, T.; Okabe, M.; Ukaji, T., Study of Polyolefin Gel in Organic Solvents I. Structure of Isotactic Polypropylene Gel in Organic Solvents. *Polym. J.* **1987,** *19* (3), 323-329.
66. Prasad, A.; Mandelkern, L., The Thermoreversible Gelation of Syndiotactic Polystyrene. *Macromolecules* **1990,** *23* (23), 5041-5043.
67. Aubert, J. H., Isotactic Polystyrene Phase Diagrams and Physical Gelation. *Macromolecules* **1988,** *21* (12), 3468-3473.
68. Prasad, A.; Marand, H.; Mandelkern, L., Supermolecular Morphology of Thermoreversible Gels Formed from Homogeneous and Heterogeneous Solutions. *J. Polym. Sci., Part B: Polym. Phys.* **1993,** *31* (12), 1819-1835.
69. Wellinghoff, S.; Shaw, J.; Baer, E., Polymeric Materials from the Gel State. The Development of Fringed Micelle Structure in a Glass. *Macromolecules* **1979,** *12* (5), 932-939.
70. Mochizuki, J.; Sano, T.; Tokami, T.; Itagaki, H., Decisive Properties of Solvent Able to Form Gels with Syndiotactic Polystyrene. *Polymer* **2015,** *67*, 118-127.
71. Jaymand, M., Recent Progress in the Chemical Modification of Syndiotactic Polystyrene. *Polym. Chem.* **2014,** *5* (8), 2663-2690.
72. Ishihara, N.; Seimiya, T.; Kuramoto, M.; Uoi, M., Crystalline Syndiotactic Polystyrene. *Macromolecules* **1986,** *19* (9), 2464-2465.
73. De Rudder, J.; Bergé, B.; Berghmans, H., Competition between Gelation and Crystallization in Solutions of Syndiotactic Polystyrene in Cis-Decalin. *Macromol. Chem. Phys.* **2002,** *203* (14), 2083-2088.
74. Roels, T.; Deberdt, F.; Berghmans, H., Solvent Quality and Phase-Stability in Syndiotactic Polystyrene-Solvent Systems. *Macromolecules* **1994,** *27* (21), 6216-6220.
75. Daniel, C.; Menelle, A.; Brulet, A.; Guenet, J.-M., Thermoreversible Gelation of Syndiotactic Polystyrene in Toluene and Chloroform. *Polymer* **1997,** *38* (16), 4193-4199.

76. Ray, B.; Elhasri, S.; Thierry, A.; Marie, P.; Guenet, J.-M., Solvent-Induced Crystallization of Syndiotactic Polystyrene: Thermodynamics and Morphology. *Macromolecules* **2002,** *35* (26), 9730-9736.
77. Gowd, E. B.; Tashiro, K.; Ramesh, C., Structural Phase Transitions of Syndiotactic Polystyrene. *Prog. Polym. Sci.* **2009,** *34* (3), 280-315.
78. Su, C.; Jeng, U.; Chen, S.; Cheng, C.-Y.; Lee, J.-J.; Lai, Y.-H.; Su, W.; Tsai, J.; Su, A., Thermodynamic Characterization of Polymorphs in Bulk-Crystallized Syndiotactic Polystyrene Via Small/Wide-Angle X-Ray Scattering and Differential Scanning Calorimetry. *Macromolecules* **2009,** *42* (12), 4200-4207.
79. Guerra, G.; Vitagliano, V. M.; De Rosa, C.; Petraccone, V.; Corradini, P., Polymorphisms in Melt Crystallized Syndiotactic Polystyrene Samples. *Macromolecules* **1990,** *23* (5), 1539-1544.
80. Itagaki, H.; Tokami, T.; Mochizuki, J., A Trial to Clarify a Cause of Forming Physical Gels: Morphology of Syndiotactic Polystyrene in N-Alkylbenzene. *Polymer* **2012,** *53* (23), 5304-5312.
81. Petraccone, V.; Ruiz de Ballesteros, O.; Tarallo, O.; Rizzo, P.; Guerra, G., Nanoporous Polymer Crystals with Cavities and Channels. *Chem. Mater.* **2008,** *20* (11), 3663-3668.
82. Daniel, C.; Avallone, A.; Guerra, G., Syndiotactic Polystyrene Physical Gels: Guest Influence on Structural Order in Molecular Complex Domains and Gel Transparency. *Macromolecules* **2006,** *39* (22), 7578-7582.
83. Daniel, C.; Avallone, A.; Rizzo, P.; Guerra, G., Control of Crystal Size and Orientation in Polymer Films by Host−Guest Interactions. *Macromolecules* **2006,** *39* (14), 4820-4823.
84. Daniel, C.; Longo, S.; Ricciardi, R.; Reverchon, E.; Guerra, G., Monolithic Nanoporous Crystalline Aerogels. *Macromol. Rapid Commun.* **2013,** *34* (15), 1194-1207.
85. Daniel, C.; Giudice, S.; Guerra, G., Syndiotatic Polystyrene Aerogels with B, Γ, and E Crystalline Phases. *Chem. Mater.* **2009,** *21* (6), 1028-1034.
86. De Rosa, C.; Guerra, G.; Petraccone, V.; Pirozzi, B., Crystal Structure of the Emptied Clathrate Form (Δe Form) of Syndiotactic Polystyrene. *Macromolecules* **1997,** *30* (14), 4147-4152.
87. Wang, H.; Wu, C.-J.; Cui, D.-M.; Men, Y.-F., Equilibrium Crystallization Temperature of Syndiotactic Polystyrene Γ Form. *Chin. J. Polym. Sci.* **2018,** *36* (6), 749-755.

88. De Rudder, J.; Berghmans, H.; De Schryver, F. C.; Bosco, M.; Paoletti, S., Gelation Mechanism of Syndiotactic Polystyrene in Bromoform. *Macromolecules* **2002,** *35* (25), 9529-9535.
89. Hu, W., *Polymer Physics: A Molecular Approach*. Springer Science & Business Media: 2012.
90. Daniel, C., Structural Organization and Properties of Syndiotactic Polystyrene Gels. *Macromol. Symp.* **2007,** *251* (1), 1-10.
91. Kobayashi, M.; Kozasa, T., Conformational Ordering Process on Physical Gelation of Syndiotactic Polystyrene/Solvent Systems Revealed by Time-Resolved Infrared Spectroscopy. *Appl. Spectrosc.* **1993,** *47* (9), 1417-1424.
92. Kobayashi, M.; Yoshioka, T.; Kozasa, T.; Tashiro, K.; Suzuki, J.; Funahashi, S.; Izumi, Y., Structure of Physical Gels Formed in Syndiotactic Polystyrene/Solvent Systems Studied by Small-Angle Neutron Scattering. *Macromolecules* **1994,** *27* (6), 1349-1354.

Chapter 2.

Blocky Bromination of Syndiotactic Polystyrene via Post-Polymerization Functionalization in the Heterogeneous Gel State

(*Published: Noble, K. F.; Noble, A. M.; Talley, S. J.; Moore, R. B., Blocky bromination of syndiotactic polystyrene via post-polymerization functionalization in the heterogeneous gel state. Polym. Chem.* ***2018,*** *9 (41), 5095-5106.*)

Kristen F. Noble, Alexandria M. Noble, Samantha J. Talley, and Robert B. Moore*

*To whom correspondence should be addressed: rbmoore3@vt.edu

2.1. Abstract

This work demonstrates the successful blocky bromination of syndiotactic polystyrene (sPS-co-sPS-Br) copolymers containing 6-30 mol% *p*-bromostyrene units, using a post-polymerization functionalization method conducted in the heterogeneous gel state. For comparison, a matched set of randomly brominated sPS-co-sPS-Br copolymers was prepared using homogeneous (solution-state) reaction conditions. The degree of bromination and copolymer microstructure were evaluated using ^{1}H and ^{13}C nuclear magnetic resonance (NMR) spectroscopy. The NMR spectra of gel-state (Blocky) and solution-state (Random) copolymers exhibit strikingly different resonance frequencies and peak intensities above 6 mol% Br and provide direct evidence that functionalization in the gel state produces copolymers with non-random "blocky" microstructures. Quenched films of the Blocky copolymers, analyzed using ultra-small-angle X-ray scattering (USAXS) and small-angle X-ray scattering (SAXS), show micro-phase separated morphologies, which further supports that the Blocky copolymers contain distinct segments of

pure sPS and segments of randomly brominated sPS unlike their completely Random analogs. Crystallization behavior of the copolymers, examined using differential scanning calorimetry (DSC), demonstrates that the Blocky copolymers are more crystallizable and crystallize faster at lower supercooling compared to their Random analogs. Computer simulations of the blocky copolymers were developed based on the semicrystalline morphology of a 10 w/v% sPS/CCl_4 gel, to rationalize the effect of heterogeneous functionalization on copolymer microstructure and crystallization behavior. The simulations were found to agree with the microstructural analysis based on the NMR results and confirm that restricting the accessibility of the brominating reagent to monomers well removed from the crystalline fraction of the gel network produces copolymers with a greater prevalence of long, uninterrupted sPS homopolymer sequences. Thus, the blocky microstructure is advantageous for preserving desired crystallizability of the resulting blocky copolymers.

2.2. Introduction

Block copolymers are a class of macromolecules, characterized by two or more chemically distinct polymer segments linked together through covalent bonds.[1, 2] The individual characteristics of the discrete block segments, for example the chemical nature of the repeating monomers, block lengths and distribution, number of blocks, and chain architectures, govern the chemical and physical properties of the block copolymer. Moreover, the thermodynamic immiscibility between chemically dissimilar blocks often drives self-assembly into well-ordered, micro-phase separated morphologies that can significantly enhance the material properties. The technological applicability of block copolymers is promising; however, the generally arduous procedures for block copolymer synthesis, often involving inert atmospheric conditions, well-

controlled, sequential reaction timings, specialized initiators, and high purity monomers and solvents, generally limits the scope of their commercial application. To achieve crystallizable block copolymers, stereo/regiocontrolled living polymerization mechanisms are generally necessary, which presents an additional challenge that often requires the development of system-specific catalysts and significant synthetic skill.[3]

As a distinct alternative to the complex polymerization mechanisms and synthetic protocols employed in the conventional formation of block copolymers, our recent efforts have demonstrated that blocky copolymer microstructures can be achieved using comparatively simple post-polymerization functionalization chemistries carried out on semicrystalline homopolymers in their heterogeneous gel state.[4, 5] Herein, the term "blocky copolymer" will be used as a description of gel-state functionalized copolymers, implying a significant degree of non-randomness in the distribution of comonomers along the copolymer chain.

Gels of crystallizable homopolymers (e.g., sPS) are composed of tightly packed chain segments in lamella crystallites that act as physical cross-links bound together by a percolating network of solvent swollen amorphous chains.[6-10] When a functionalizing reagent is introduced to the heterogeneous gel network, it is sterically excluded from the crystalline component, and thus only reacts with monomer units in the accessible interconnecting amorphous component. Using this straightforward post-polymerization functionalization approach, the resulting copolymer is likely to contain separate segments of randomly functionalized "blocks" and un-functionalized "blocks" originating from monomer units that were isolated within the crystalline domains of the gel. By controlling the precise morphology of the semicrystalline gel, specifically the crystallite dimensions and degree of crystallinity, distinct blocks of highly functionalized segments with tunable sequence distributions and chemical compositions are anticipated.

Heterogeneous functionalization reaction schemes reported in the literature set a precedent for utilizing gel-state reaction conditions to produce copolymers with blocky microstructures. For example, we recently demonstrated that the heterogeneous sulfonation of sPS[4] and poly(ether ether ketone)[5] (PEEK) gels, yields ionomers with a blocky distribution of functionalities along the chains. The gel-state sulfonated sPS and PEEK ionomers demonstrated superior crystallizability and faster crystallization kinetics compared to their solution-state sulfonated random analogs, consistent with copolymers with blocky microstructures. Similarly, Venditto and coworkers[11] showed that exposing a gel of semicrystalline syndiotactic polystyrene (sPS) to chlorosulfonic acid results in preferential sulfonation of the gel's amorphous component. While evidence of a blocky microstructure was not directly explored, their heterogeneous method is effectively equivalent to our gel-state sulfonation approach[4, 12, 13] to produce blocky copolymers. In earlier work, Borriello and coworkers[14] investigated the post-polymerization sulfonation of solution cast or compression-molded sPS films, evaluating the interplay between sulfonating reagent diffusion and reaction processes on sulfonation heterogeneity across the films. Solution cast films demonstrated uniform sulfonation, attributed to rapid diffusion of sulfonating reagent through nanoporous phases in the film. In contrast, compression-molded films exhibited a decreasing sulfonation gradient from the film's surface to interior, consistent with slow diffusion of sulfonating reagent into the non-porous, solid-state "bulk" film. This result is also similar to that observed for the sulfonation of atactic polystyrene (aPS) films.[15] Genzer and coworkers[16-21] used experimental and theoretical results to extensively investigate the bromination of aPS in poor solvents, where polymer chains are in a collapsed conformation. In this collapsed state, portions of the chains were effectively shielded from the brominating reagent, resulting in blocky brominated styrene sequences. Others have performed post-polymerization bromination[22] or acetylation[23] on suspended sPS powders, though

copolymer microstructure was not investigated in these studies. Ultimately, to produce sPS-based copolymers that retain crystallizability of the sPS component with the added advantage of distinct properties attributed to the functional component, block or blocky copolymer microstructures are required.[24-26]

This work reports the first post-polymerization bromination of sPS in solution and in the heterogeneous gel-state to produce a matched set of random and blocky brominated sPS (sPS-co-sPS-Br) copolymers (**Scheme 2.1**). The purpose of this research was to prepare *semicrystalline* blocky copolymers with relatively high degrees of functionality using a facile, post-polymerization functionalization method. To investigate how the specific distribution of functional groups along the chains effects copolymer properties, NMR spectroscopy was used to evaluate the copolymer microstructure, X-ray scattering techniques were used to investigate the copolymer film morphology, and differential scanning calorimetry (DSC) was used to probe the crystallizability and crystallization kinetics of the copolymers. In order to obtain further insight into the effect of gel-state bromination on copolymer microstructure and to rationalize the effect of copolymer microstructure on the observed crystallization behavior, computer simulations of the random and blocky copolymers have been developed. Through this work, post-polymerization functionalization carried out in the gel state is proven to be a facile approach to prepare semicrystalline sPS-co-sPS-Br copolymers with blocky microstructures and tunable crystallization properties. Given a wealth of aromatic Br substitution chemistries,[27-29] the broader scope of this work is to use these blocky brominated sPS copolymers as templates to produce new functional materials with desirable physical and chemical properties that originate from the easily obtained blocky microstructure.

Scheme 2.1 Schematic representation of sPS bromination via post-polymerization functionalization in solution and in the heterogeneous gel state. Reproduced by permission of The Royal Society of Chemistry.

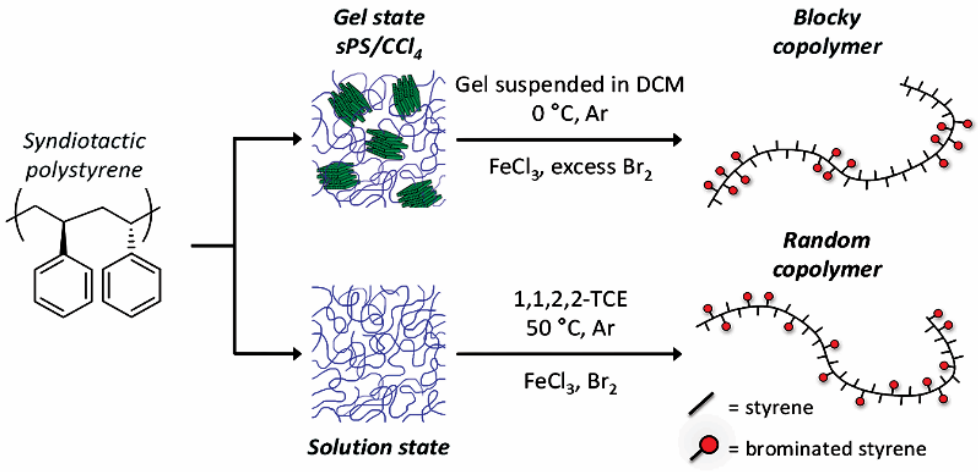

2.3. Experimental Section

2.3.1. Materials

Syndiotactic polystyrene (Questra® 102) of 300,000 g mol^{-1} weight average molecular weight (M_w) was obtained from Dow Chemical Company. Carbon tetrachloride (CCl_4), 1,1,2,2-tetrachloroethane (TCE), and 1,2-dichloromethane (DCM) were purchased from Fischer Scientific Company. Bromine (Br_2) was obtained from Sigma Aldrich®. The Lewis acid catalyst, ferric (III) chloride ($FeCl_3$), was purchased from VWR International LLC. All chemicals and reagents were used as received.

2.3.2. Gel-state bromination to produce Blocky copolymers

To prepare the gel, sPS (2.5 g, 0.83 μmol) pellets were first dissolved in CCl_4 (25 mL) in a pressure vessel at 120-140 °C, then removed from heat to promote gel formation. The gel formed within a period of one hour and was stored at room temperature for ca. 24 h prior to use. Using a spatula, the gel was broken into small pieces (ca. 1-3 mm), transferred to a round bottom flask and dispersed in DCM (final sPS concentration of 3 w/v%). After addition of $FeCl_3$ (68 mg, 0.42

mmol), the flask was placed in an ice bath and purged with argon for 30 min. To brominate the sPS gel, a stock solution of 50 w/w% Br_2 in DCM (4.3 mL Br_2, 0.084 mol) was added dropwise to the reaction vessel over two hours. In order to minimize bromination of the backbone by bromine radicals ($Br^{\bullet}$), the reaction was carried out in the dark under argon at room temperature.[27] To control the degree of bromination, reactions were halted after 6, 18, 24, or 51 hours by pouring the suspensions into stirred methanol. All samples were purified by dissolving in TCE, filtering, and precipitating in methanol to recover a white product. Prior to analysis, samples were ground into homogenous powders, washed by soxhlet extraction in hot methanol for ca. 24 h, and dried under vacuum at 110 °C for ca. 18 h.

2.3.3. Bromination in the solution-state to produce Random copolymers

To prepare the solution, sPS pellets (2.0 g, 0.67 μmol) were dissolved in TCE (25 mL) at 130 °C. The solution temperature was lowered to 50 °C, $FeCl_3$ (5 mol% based on the amount of Br_2) was added, and the solution was purged with argon for ca. 30 min. Bromine stock solution was added dropwise and the reaction was allowed to proceed for 2 h in the dark under argon at a final sPS concentration of 1 w/v%. To control the degree of bromination, reactions were carried out using mol ratios of Br_2 to styrene monomer of 0.10:1, 0.30:1, 0.40:1, or 0.70:1. Reaction solutions were poured into stirring methanol, filtered, washed, and dried to yield an off-white product. Samples were purified by dissolving in TCE and precipitating in methanol. All samples were homogenized by grinding, washed by soxhlet extraction in hot methanol for ca. 24 h, and dried under vacuum at 110 °C for ca. 18 h.

2.3.4. NMR spectroscopy

Microstructure analysis was carried out using nuclear magnetic resonance (NMR) spectroscopy. ^{1}H NMR, ^{1}H-^{13}C heteronuclear single quantum coherence (gHSQC), and ^{1}H-^{13}C band-selective heteronuclear multiple bond correlation (bsgHMBC) experiments were recorded at room temperature in $CDCl_3$ or TCE-d_2 on an Agilent U4-DD2 400 MHz spectrometer. Quantitative ^{13}C NMR experiments were recorded at room temperature in TCE-d_2 on a Bruker Avance II 500 MHz spectrometer (C13IG parameter set, proton decoupled, relaxation delay of 6 sec, O1P of 95, and sweep width of 150 ppm). Determination of the degree of bromination (mol% Br) from the ^{1}H NMR spectrum is described in the Results and Discussion section.

2.3.5. Thermal properties and crystallization kinetics

Copolymer thermal transitions and crystallization kinetics were probed using differential scanning calorimetry (DSC, TA Instruments DSC Q2000) under continuous nitrogen flow to minimize polymer degradation. To investigate crystallizability under specific cooling conditions, samples were first annealed at 300 °C for 3 min to erase thermal history, then cooled to 0 °C at −60 °C min^{-1} (rapid cool) or −10 °C min^{-1} (slow cool). Isothermal crystallization from the melt (300 °C held for 5 min and cooled at −60 °C min^{-1}) was carried out at 190 °C for 2 h. All heating scans were recorded at 10 °C min^{-1}. TA Instruments Universal Analysis software was used to determine glass transition temperatures (T_g), crystallization temperatures at maximum exothermic heat flow (T_c), and melting temperatures at maximum endothermic heat flow (T_m). To ascertain crystallization half-times ($t_{1/2}$), defined as the time at which a material attains 50% of its maximum crystallinity, samples were subjected to isothermal crystallization at specific crystallization temperatures below T_m. The isothermal crystallization profiles (heat flow versus time) were analyzed using the following approach:

$$F_c(t) = \frac{\int_0^t \frac{dH}{dt}\,dt}{\int_0^\infty \frac{dH}{dt}\,dt} \qquad (1)$$

where $F_c(t)$ is the bulk fractional crystallinity of the functionalized copolymer systems, equal to the heat evolved during isothermal crystallization at a specific time t divided by the total heat evolved during the isothermal crystallization process. The resulting crystallization isotherms (F_c versus time) were used to determine $t_{1/2}$ by extrapolating F_c at 0.5 to the time axis, and these $t_{1/2}$ values were used as a comparative measure of the overall rate of bulk crystallization.

2.3.6. Ultra-small-angle and small-angle X-ray scattering

Films were prepared from powders of the sPS homopolymer and Random and Blocky copolymers by melt pressing between Kapton sheets at 30 °C above T_m for 20 s at 2200 psi then for 20 s at 4500 psi, followed by quenching in ice water to prevent sPS crystallization. Ultra-small-angle X-ray scattering (USAXS) and small-angle X-ray scattering (SAXS) experiments were performed at the Advanced Photon Source beamline 9ID-C at Argonne National Laboratory.[30-32] The USAXS instrument was configured in standard mode with an X-ray energy of 21 keV (λ = 0.5895 Å), X-ray photon flux of ca. 1013 mm^{-2} s^{-1}, and a combined q range of 0.0001–1.3 $Å^{-1}$ ($q = 4\pi/\lambda \sin(\theta)$, where λ is the wavelength and θ is one-half of the scattering angle). The USAXS and SAXS profiles were acquired sequentially and merged into a single data set using the Irena SAS package.[33] The observed scattering features in the desmeared USAXS/SAXS profiles were analyzed using the Unified Fit, described in the Irena tool suite.[33]

2.3.7. Wide-angle X-ray diffraction

Wide-angle X-ray diffraction (WAXD) experiments were performed using a Rigaku MiniFlex II X-ray diffractometer emitting X-rays with a wavelength of 0.154 nm (Cu K_α). Samples

were scanned from 5° to 35° 2θ at a scan rate of 0.250° 2θ min^{-1} and a sampling window of 0.050° 2θ at a potential of 30 kV and current of 15 mA. All WAXD data were analyzed using the PDXL 2 software package to obtain WAXD intensity versus 2θ profiles.

2.3.8. Simulations of random and blocky copolymer microstructures

Representative chain microstructures resulting from the homogeneous and heterogeneous reaction states for sPS bromination were simulated using a code created with MATLAB® R2017a programming software (the code used for these simulations is provided in **section 2.8**). For each degree of functionalization, the MATLAB® code simulates 1000 homopolymer chains of 1442 monomer units (based on our sPS sample, M_w = 300K; Đ = 2.0). To simulate the random microstructure resulting from homogeneous solution-state functionalization, monomers along the chain are selected at random up to the desired degree of bromination. To simulate the blocky microstructure resulting from functionalization in the semicrystalline gel state, an inaccessible fraction of monomers, representing crystalline chain segments in the physical gel, was first established prior to random bromination of the remaining accessible fraction, representing the amorphous chain segments of the gel. The rationalization for the specific inaccessible fraction of monomers used in these simulations is based on the measured degree of crystallinity in a 10 w/v% sPS/CCl_4 gel and is discussed in more detail below in the Results and Discussion section. For each simulated polymer chain, the length and frequency of consecutive styrene (S) and Br-styrene (B) units, and the prevalence of each unique triad sequence (e.g., SSS, BBB, etc.) is calculated.

2.4. Results and Discussion

2.4.1. Microstructure analysis using NMR spectroscopy

To investigate the sPS-co-sPS-Br copolymer microstructure, gel-state (Blocky, B-x%) and solution-state (Random, R-x%) copolymers were prepared in a matched set of approximately x = 6, 15, 20, and 30 mol% brominated styrene (Br-Sty) units and analyzed by NMR spectroscopy. **Figure 2.1** shows the aromatic region of the ^{1}H NMR spectra of the Random and Blocky copolymers (for full spectra, see **Figure S2.1**). Compared to pure sPS, new proton resonances appear in the ^{1}H NMR spectrum of the sPS-co-sPS-Br copolymers at 1.23, 1.58−1.75, 6.27−6.38, and 7.11−7.22 ppm, corresponding to the methylene (H(b′)) and methine (H(a′)) protons, and the aromatic protons (H(2′) and H(3′)) of Br-Sty monomers, respectively. Resonance assignments were verified by homonuclear and heteronuclear two-dimensional (2D) NMR experiments included in **Figure S2.3** and **Figure S2.4**. To verify the absence of backbone bromination, the total peak areas of the methylene (H(b), H(b′)) and methine (H(a), H(a′)) group resonances for brominated and un-brominated monomers were compared and found to be consistent with the expected 2:1 ratio. The mol% Br was derived from the fraction of ortho-proton resonances of Br-Sty monomers (H(2′), 6.27−6.38 ppm) to the total area of styrene (H(2)) and Br-Sty ortho-proton resonances (6.27−6.60 ppm). Notably, the degree of bromination increased with increasing mol ratio of Br_2 to styrene monomer when the polymer was dissolved in solution and increasing reaction time in the presence of homopolymer gel, validating that the reaction methods effectively control the degree of functionalization.

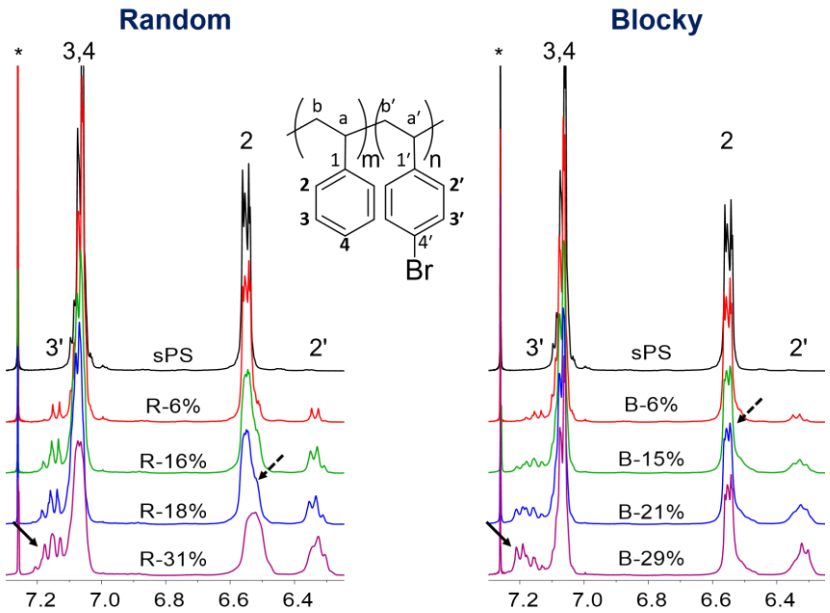

Figure 2.1. Aromatic region of the ^{1}H NMR spectra of (left) solution-state Random and (right) gel-state Blocky copolymers increasing in mol% Br from top to bottom. For comparison, spectra are referenced to $CDCl_3$ and normalized over 6.27−6.60 ppm. The asterisk (*) indicates solvent resonance. The arrows highlight differences between spectra. Reproduced by permission of The Royal Society of Chemistry.

Comparing the ^{1}H NMR spectra of Random and Blocky copolymers reveals significant differences in their peak intensities and proton chemical shifts, despite their similar Br-contents. For the Random copolymers, resonances attributed to un-brominated styrene units (e.g. H(2) and H(3,4)) broaden with increasing functionalization, consistent with a decrease in the sequence length of pure homopolymer segments (dashed arrows in **Figure 2.1**). In contrast, the Blocky copolymers exhibit sharp proton resonances similar to that of pure sPS even at high mol% Br. This behavior suggests that the Blocky copolymers contain a greater fraction of uninterrupted sPS segments compared to their Random analogs. In addition, the H(3′) proton resonances of Blocky Br-Sty units appear to shift downfield with increasing degree of functionalization, indicated by the solid arrows in **Figure 2.1**. The high frequencies and strong intensities of the H(3′) resonances in Blocky B-21% and B-29% are consistent with an accumulation of neighboring electronegative *p*-bromostyrene units, a strong indicator that these copolymers have numerous dyads and triad sequences of Br-Sty monomers. Notably, the shape of the H(3′) peak in B-29% is also consistent

with that observed for a highly brominated (59 mol% Br) sPS-co-sPS-Br copolymer prepared via copolymerization by Guo and co-workers.[34] Overall, the microstructural information provided by ^{1}H NMR yields strong evidence that gel-state bromination produces copolymers with long segments of consecutive styrene units and segments of densely brominated sPS, characteristic of a blocky copolymer microstructure.

Quantitative ^{13}C NMR spectroscopy was used to provide a deeper insight into the microstructure of the Random and Blocky copolymers. **Figure 2.2** shows the aromatic carbon spectral region of the sPS homopolymer and sPS-co-sPS-Br copolymers (for full spectra see **Figure S2.2**). Upon para-substitution of the phenyl rings with bromine, new carbon resonances appear in the ^{13}C NMR spectrum. The new resonances at 40.0 and 43.6 ppm are attributed, respectively, to the methine (C(a′)) and methylene (C(b′)) carbons of Br-Sty monomers. The resonances at 129.2 and 130.9 ppm are assigned, respectively, to the ortho- (C(2′)) and meta-carbons (C(3′)) of brominated phenyl rings. Multiple peaks are observed between 118.8−119.3 and 142.9−144.9 ppm, attributed to the Br-substituted phenyl carbons (C–Br, C(4′)) and the quaternary phenyl carbons of brominated (C(1′)) and un-brominated (C(1)) monomers, respectively. Throughout the Blocky copolymer series, carbon resonances of un-brominated styrene monomers are sharp and intense compared to their Random analogs, indicated by arrows in **Figure 2.2**. Similar to the behavior observed in the ^{1}H spectra above, this further suggests that the blocky copolymer microstructure is comprised of long segments of pure sPS, even at high Br-contents.

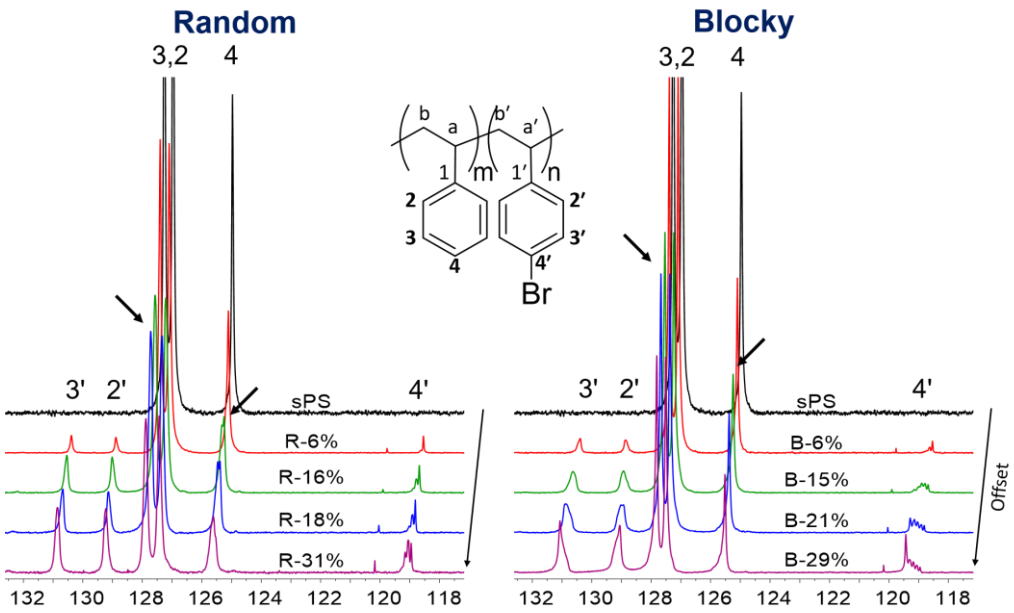

Figure 2.2 Aromatic C(2-4) and C(2′-4′) resonances in the ^{13}C NMR spectra of the (left) Random and (right) Blocky copolymers increasing in mol% Br from top to bottom. For comparison, spectra are referenced to TCE-d_2 and normalized over 127.0−132.5 ppm. Reproduced by permission of The Royal Society of Chemistry.

Chemical shifts in ^{13}C NMR spectra are highly dependent on the electronic environments of the carbon nuclei, which can be used to evaluate comonomer sequence distribution and provide insight into the short-range microstructure of a copolymer.[35, 36] For the sPS-co-sPS-Br copolymers, the C(4′) resonance appears to be sensitive to copolymer microstructure, demonstrated by the appearance of multiple peaks in the ^{13}C NMR spectra of the Random and Blocky samples with increasing mol% Br (**Figure 2.2**). The C(4′) region of Blocky B-29% exhibits five distinct peaks. The sharp C(4′) peak at 119.4 ppm in Blocky B-29% does not appear in the spectrum of Random R-31%, but is consistent with the chemical shift of C(4′) observed in sPBrS homopolymers.[34] Thus, this peak is characteristic of a copolymer with long segments of consecutive Br-Sty units. Interestingly, prior to this research, only chemical shifts of the backbone and C(1) carbons of polystyrene and poly(styrene-co-bromostyrene) copolymers were thought to be sensitive to copolymer microstructure.[35] Due to complexities arising from stereoirregularity, attempts by others to evaluate copolymer "blockiness" and comonomer sequence distribution in halogenated[21,

[36, 37] and sulfonated[38, 39] *atactic* polystyrene-based copolymers by NMR have been generally unsuccessful.[35, 39, 40] However, with the high tactic purity of *syndiotactic* polystyrene, this work further demonstrates that ^{13}C NMR spectroscopy can be used to evaluate comonomer sequence distribution.[41, 42]

The most profound evidence for microstructural differences between the Random and Blocky copolymers is observed by comparing the quaternary C(1) and C(1′) carbon spectra, shown in **Figure 2.3**. For the Random samples, bromination of sPS produces multiple new peaks that increase in intensity with increasing Br-content. The multiple peaks signify through-bond communication between neighboring brominated and un-brominated styrene monomers, and likely provide a unique fingerprint of the copolymer microstructure originating from the specific comonomer sequence distribution. For the Blocky samples, the quaternary carbon peak distributions and intensities differ strikingly from their Random analogs at all degrees of bromination, which is emphasized by the new resonance in Blocky B-21% and B-29% at 143.1−143.3 ppm. Based on the C(1′) chemical shift of the sPBrS homopolymer[34] which occurs at 143.1 ppm, our assignment of this new peak is to a Br-Sty triad (BBB). By integrating this peak relative to the full range of the C(1) and C(1′) resonances, the prevalence of the BBB triad in Blocky B-29% is found to be approximately 17%. This high prevalence for the Blocky sample is remarkable given that the quaternary carbon spectrum of Random R-31% does not exhibit a distinct peak at 143.1−143.3 ppm, demonstrating that random bromination results in a relatively low abundance of BBB triad. Our efforts to assign the remaining quaternary carbon peaks in the Random and Blocky copolymers to triad and pentad sequences and with comparison to simulations of random and blocky copolymer microstructures is discussed in **Chapter 3**. In summary, our initial microstructural analysis using NMR spectroscopy proves that the bromination method can

be used to manipulate copolymer sequence; solution-state bromination produces random copolymers while gel-state bromination clearly produces sPS-co-sPS-Br copolymers with blocky microstructures.

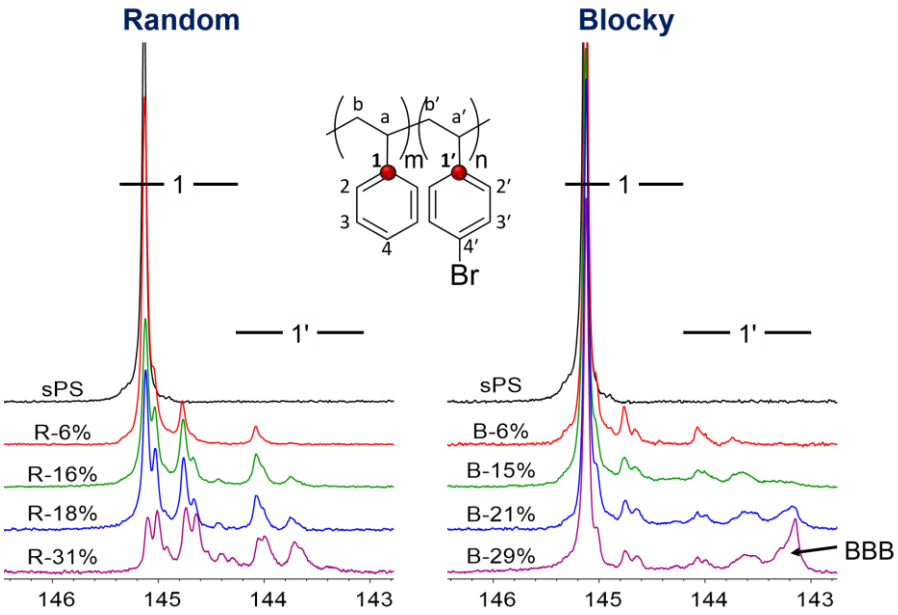

Figure 2.3 C(1) and C(1′) NMR spectra of the (left) Random and (right) Blocky copolymers increasing in mol% Br from top to bottom. For comparison, spectra are referenced to TCE-d_2 and normalized over 127.0−132.5 ppm. Reproduced by permission of The Royal Society of Chemistry.

2.4.2. Thermal transitions

DSC thermograms of the sPS homopolymer and the Random and Blocky copolymers after rapid cooling from the melt to 0 °C at −60 °C min^{-1} are shown in **Figure 2.4**. The heating trace of pure sPS displays two endothermic events, the glass transition at 98 °C and an intense melting endotherm at 272 °C. At approximately 6 mol% Br, both the Random and Blocky copolymers crystallize during cooling and exhibit similar depression in their melting temperatures, T_m, relative to pure sPS. Bromine groups attached to a crystallizable polymer can act as physical defects along the polymer chains, limiting crystallizability and lamella thickness. It is not surprising then that both copolymer series show a depression in T_m with increasing Br-content as a consequence of shorter crystallizable chain segments and thus thinner crystallites.[23, 26, 27, 43] Nonetheless, it is

important to note that the melting point depression for the Random copolymers occurs to a much greater extent compared to the Blocky copolymers, despite their analogous Br-contents (see **Figure S2.5**).

Above 6 mol% Br, the Blocky copolymers show an exothermic event observed between 150-200 °C (**Figure 2.4**), ascribed to cold crystallization during heating. Cold crystallization during the heating scan following a rapid cool is attributed to a reduction in the rate of crystallization.[23, 26] During conditions of slow cooling (−10 °C min^{-1}), the crystallization exotherm, T_c, decreases in temperature and intensity with increasing Br-content, which also reflects a reduction in the rate of crystallization (see **Figure S2.6**). In distinct contrast to the behavior of the Blocky samples, the 18 mol% Br and above Random samples do not crystallize under the thermal conditions of this experiment. This behavior demonstrates that the Blocky samples are much more crystallizable throughout the copolymer series. Remarkably, the Blocky B-29%, which has approximately one Br-Sty for every three styrene monomers, is still crystallizable and exhibits a melting endotherm at 210 °C. This result strongly implies a blocky distribution of Br-Sty units along the copolymer chains.

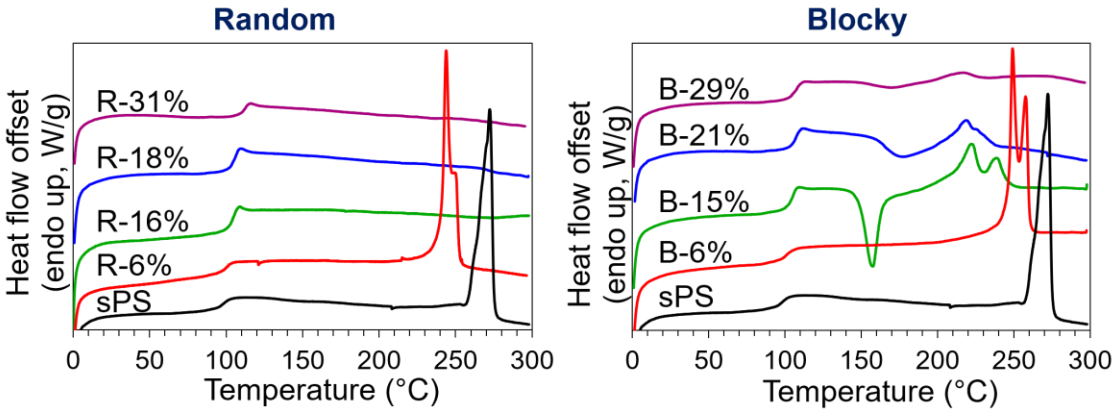

Figure 2.4 DSC heating scans of the sPS homopolymer and the (left) Random and (right) Blocky copolymers after rapid cooling from the melt (300 °C) at −60 °C min^{-1}. Heating rate: 10 °C min^{-1}. Reproduced by permission of The Royal Society of Chemistry.

To further examine the effect of blocky versus random microstructure on crystallizability, the weight percent crystallinity (%X_c) was calculated from the area under the melting endotherm (ΔH_f) with respect to the heat of fusion of 100% crystalline pure sPS[44] (ΔH_f° = 82.6 J g^{-1}). **Table 2.1** summarizes the thermal properties and %X_c of the sPS homopolymer and the Random and Blocky samples after slow cooling (−10 °C min^{-1}) and 2 h isothermal crystallization at 190 °C. Consistent with findings of Genzer et al.[45], the glass transition temperatures for both the Random and Blocky copolymers increase with degree of bromination, which is attributed to hindered rotations of the bulky *p*-bromostyrene units. For the Random copolymers, it is clear that the crystallizability is severely limited at degrees of bromination of 16% or more, in agreement with the work of Bae et al.[27] In contrast, the Blocky copolymers demonstrate a much greater aptitude for crystallization. For example, after isothermal crystallization at 190 °C, the Blocky B-21% yields a degree of crystallinity of X_c = 18% that constitutes 58% of the crystallinity of pure sPS, compared to only X_c = < 1% for the lower Br-content Random R-18% sample. Again, the much greater crystallizability for the Blocky samples is strongly suggestive of a highly blocky microstructure[23, 27]. For WAXD profiles of the sPS homopolymer and sPS-co-sPS-Br copolymers after isothermal crystallization, see **Figure S2.7**.

Table 2.1 Thermal properties and weight percent crystallinity of the sPS homopolymer and the Random and Blocky copolymers measured using DSC. Reproduced by permission of The Royal Society of Chemistry.

	After slow cooling at −10 °C min^{-1}				After 2 h isothermal crystallization at 190 °C	
Sample	**T_g(°C)**	**T_m(°C)**	**T_c(°C)[a]**	**X_c(%)**	**T_m(°C)**	**X_c(%)**
sPS	100	270	237	31	270	31
B-6%	102	249	215	24	249	28
B-15%	106	234	187	17	234	21
B-21%	105	222	180	16	222	18
B-29%	107	213	--	4	218	5
R-6%	100	245	204	23	245	28
R-11%	96	227	175	25	230	27
R-16%	105	215	--	<1	216	18
R-18%	106	--	--	0	213	<1
R-31%	111	--	--	0	--	0

T_g = glass transition temperature; T_m = temperature at maximum endothermic heat flow; [a]T_c = temperature at maximum exothermic heat flow during the cooling scan; X_c = weight percent crystallinity derived from the area under the melting endotherm (ΔH_f) and the heat of fusion of 100% crystalline pure sPS (ΔH_f°) according to the relationship $X_c = \frac{\Delta H_f}{\Delta H_f^\circ} \times 100\%$. Dashes (--) indicate no thermal transition detected. All samples were heated to 300 °C and annealed for 3-5 min prior to cooling to erase thermal history. Reproduced by permission of The Royal Society of Chemistry**.**

2.4.3. Crystallization kinetics

To investigate how the distribution of bromine defects along the chains affects the crystallization kinetics of the brominated copolymers, the Random and Blocky samples were subjected to isothermal crystallization at specific temperatures below T_m. To achieve rapid crystallization, chain segments of sufficient length, i.e., stems, of uninterrupted styrene units are required to assemble into stable crystalline domains. Br-Sty monomers encountered at the crystal growth front are structural defects that are consequently excluded from attaching to the growing crystallite. This process of rejection of a defective stem and diffusion of a new stem to the melt-crystal interface ultimately slows the rate of crystallization. **Figure 2.5** shows the $t_{1/2}$ versus temperature profiles for the Random and Blocky copolymers. At approximately 6 mol% Br, both the Random and Blocky samples crystallize relatively fast; although, the Blocky B-6% sample exhibits shorter $t_{1/2}$ values than the Random R-6% (note the different y-axis scales). Above 6 mol%

Br, the Blocky copolymers crystallize much faster, in under 15 min, and at lower supercooling compared to their Random analogs. For the highly brominated Blocky B-29% sample, the $t_{1/2}$ at 190 °C is 8 min. In contrast, the Random R-27% sample (not shown) was unable to crystallize during the isothermal crystallization experiments, even at high supercooling (2h at 140 °C). These differences in crystallization kinetics between the Random and Blocky samples are attributed to the effect of microstructure on the probability of encountering a defective stem. As will be demonstrated below in the Simulations subsection, the blocky microstructure provides a greater prevalence of crystallizable segments (i.e., runs of consecutive styrene units of sufficient length) along the polymer chains compared to the random microstructure. With more crystallizable stems, the blocky microstructure minimizes the time-consuming rejection/replacement process, and thus is capable of crystallizing in a shorter period of time.

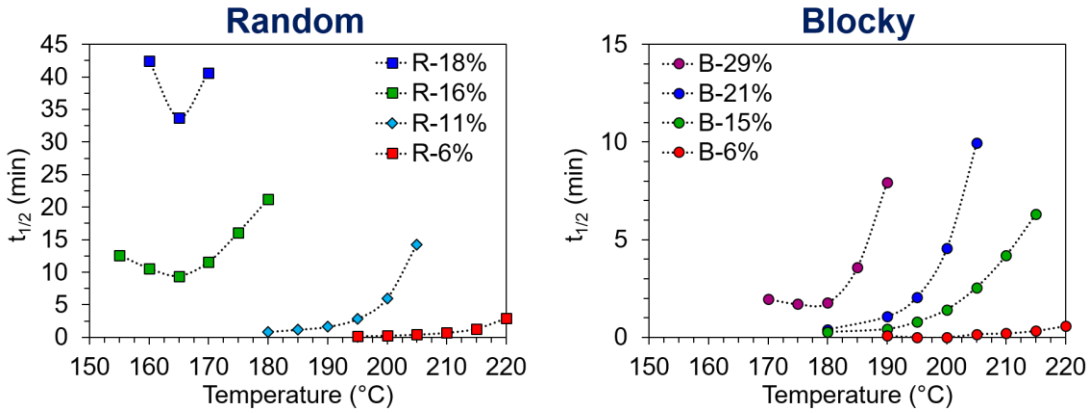

Figure 2.5 Crystallization half-time ($t_{1/2}$) versus temperature profiles for the (left) Random and (right) Blocky copolymers. The $t_{1/2}$ scales are different to clearly demonstrate the rapid crystallization kinetics, small $t_{1/2}$ times, exhibited by the Blocky samples. Reproduced by permission of The Royal Society of Chemistry.

2.4.4. Morphological characterization

USAXS/SAXS experiments were used to investigate the morphology of quenched films of the sPS-co-sPS-Br copolymers. The USAXS/SAXS profiles of the sPS homopolymer and the Random and Blocky copolymers are shown in Error! Reference source not found.. The scattering p rofiles of the Random copolymers are featureless with a q^{-4} dependence between 0.04 – 0.4 nm^{-1},

which is consistent with the profile of the sPS homopolymer. In contrast, the Blocky copolymers exhibit excess scattering from a large-scale morphological feature at low *q*, between 0.03 – 0.1 nm^{-1}. The Blocky B-29% sample also exhibits a second scattering feature at higher *q*, between 0.1 – 1 nm^{-1}. The dimensions of the features were determined using the Unified Fit model, summarized in **Table S2.1**. The low *q* scattering feature, present only in the Blocky copolymers, fits to a dimension of ca. 30 nm and is consistent with a micro-phase separated morphology. The presence of this feature suggests that the "blockiness" originating from the gel-state functionalization is sufficient to drive phase development that is somewhat reminiscent of conventional block copolymer phase behavior. The physical and molecular origins of this large-scale feature observed in the USAXS profiles of the Blocky copolymers are attributed to a thermodynamic immiscibility between the electron-dense brominated sPS segments and the pure runs of sPS within the blocky microstructure of the functionalized chains.

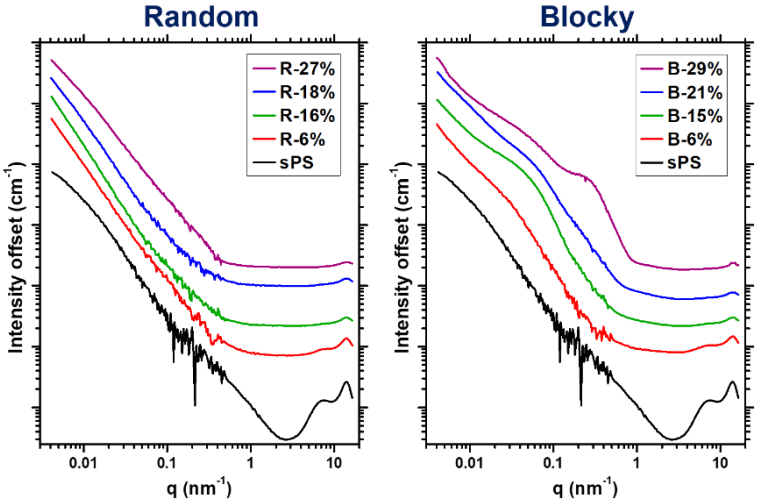

Figure 2.6 USAXS/SAXS profiles of quenched films of the sPS homopolymer and the (left) Random and (right) Blocky copolymers. Films were prepared from powders of the homopolymer or copolymers by melt pressing between Kapton sheets at 30 °C above T_m for 20 s at 2200 psi then for 20 s at 4500 psi, followed by quenching in ice water to prevent sPS crystallization. For clarity, data points are connected and vertically offset. Reproduced by permission of The Royal Society of Chemistry.

The high *q* feature near $q = 0.2\ nm^{-1}$, present only in the SAXS profile of the Blocky B-29% sample, fits to a dimension of 5.1 nm, which is surprisingly the same as the lamella thickness of

semicrystalline sPS[46] (5.1 nm). However, since this sample was quenched from T_m + 30 °C (250 °C), it is not expected to contain crystalline sPS lamella. To investigate the origin of the high *q* scattering feature, the melt-quenched samples of Blocky B-29%, Random R-27%, and the sPS homopolymer were analyzed using WAXD. As expected, the WAXD data in **Figure 2.7(a)** shows that the Random R-27% and the sPS homopolymer are completely amorphous. In distinct contrast, however, the Blocky B-29% sample exhibits a sharp crystalline reflection at 19.1° 2θ. It is important to note that this prominent reflection is not typically observed for melt-crystallized sPS.[47] Interestingly, the new prominent crystalline reflection at 19.1° 2θ, is similar to that previously observed in the diffractogram of an sPS copolymer that was polymerized with a high content (83 mol%) of *p*-chlorostyrene (19.4° 2θ), which was attributed to crystallization of the *p*-chlorostyrene units.[48] In addition, Guo et al.[34] reported that an sPS copolymer polymerized with a high content (59 mol%) of *p*-bromostyrene exhibits a high melting point of T_m = 317 °C, attributed to crystalline *p*-bromostyrene segments. In the DSC data for the Blocky B-29% sample, **Figure 2.7(b)**, a distinct melting endotherm is observed at 304 °C. It is important to note that this melting endotherm is above the equilibrium melting point of pure sPS[47] and well above the temperature from which the WAXD and SAXS samples were quenched. Based on these WAXD and DSC data and the previous evidence of crystallization of halogenated sPS,[48] it appears that runs of Br-Sty units in the Blocky B-29% sample are capable of crystallizing even at this relatively low Br-content. While further analysis of this intriguing observation will be the subject for future investigations, these data strongly suggest that the gel-state bromination process is capable of producing a copolymer microstructure that can contain distinct sequences of Br-Sty units in segments of significant length. Consequently, we tentatively propose that the high *q* SAXS

scattering feature observed in the melt quenched Blocky B-29% sample is attributed to the long period of crystalline Br-Sty segments.

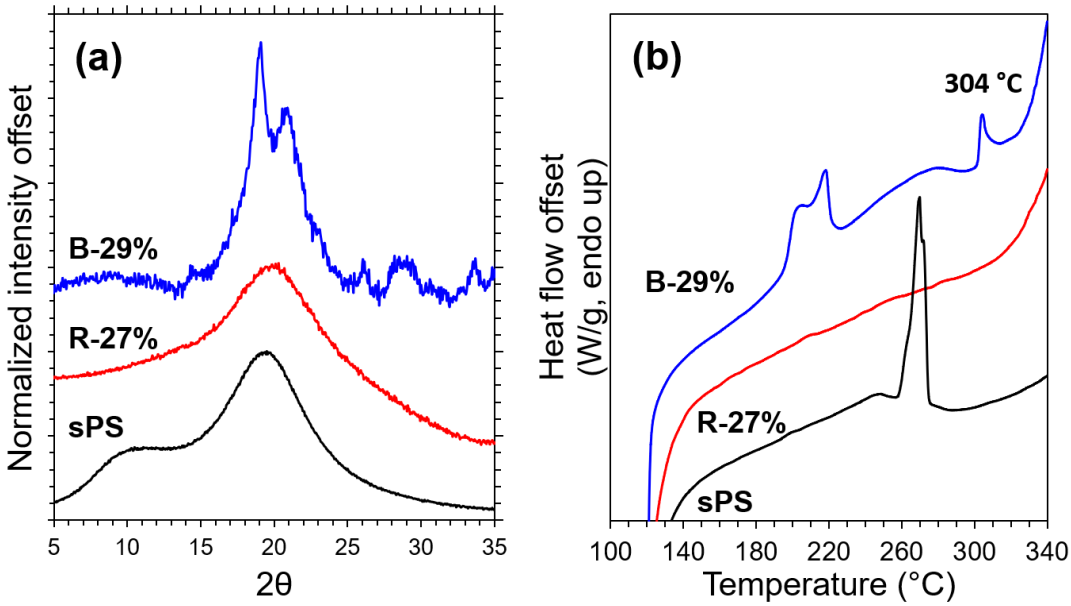

Figure 2.7 (a) Wide-angle X-ray diffraction profiles of the melt-quenched Blocky B-29%, Random R-27%, and the sPS homopolymer samples, and (b) DSC heating scans of the Blocky B-29%, Random R-27%, and the sPS homopolymer samples following 1 h isothermal crystallization at 190 °C. Reproduced by permission of The Royal Society of Chemistry.

2.4.5. Simulations of copolymer microstructure

To help rationalize the effect of copolymer microstructure on crystallization behavior after solution-state and gel-state functionalization, simulations of random and blocky copolymers were developed. The random microstructure resulting from homogeneous solution-state functionalization, is simulated by selecting monomers along a chain by random choice up to the desired degree of bromination. To simulate the blocky microstructure resulting from functionalization in the gel state, an inaccessible fraction of the total monomers in a chain is first established prior to random bromination of the remaining accessible fraction. Based on our hypothesis that the functionalizing reagent is sterically restricted to the solvent swollen amorphous chains within the semicrystalline gel, the inaccessible fraction of monomers is chosen to represent the fraction of monomers that are isolated within and in close proximity to the crystalline

component of the gel network. From our XRD analysis (**Figure S2.8**), the degree of crystallinity, $\%X_c$, of a 10 w/v% sPS/CCl_4 gel was determined to be 44%. In addition, it should also be recognized that chain segments in close proximity to the crystallites that emanate directly from the basal surfaces of the crystalline lamella may be locally restricted in their conformations (i.e., a rigid amorphous fraction), which could also limit reagent accessibility. Based on the measurements of Cebe and coworkers,[49] the rigid amorphous fraction for sPS is estimated to be 11%. Thus, combining the measured $\%X_c$ of the gel with the estimated rigid amorphous fraction, our first approximation for the inaccessible fraction within the heterogeneous gel network is estimated (for the purposes of this preliminary simulation) to be 55%.

With the inaccessible fraction set, the blocky chain microstructure is constructed by first randomly selecting a monomer along the polymer chain of a given length (1442 monomer units long based on our sPS sample, M_w = 300K; Đ = 2.0). Next, that monomer and its ± 26 neighboring monomers are removed from the list of functionalizable monomers, resulting in an inaccessible block of 53 monomers. This chosen number of monomers in the inaccessible block is based on (1) an average lamella thickness for solvent-crystallized sPS[46] of 5.1 nm; (2) the s(2/1)2 helical structure of the δ-form crystal structure of sPS[50] with 4 monomer units per identity period (c-axis dimension of the unit cell = 0.77 nm); and (3) the reasonable assumption that an attached stem has at least one fold. The process of selecting monomers for the inaccessible fraction is repeated until 55% of the monomers are marked inaccessible. Lastly, the remaining monomers within the accessible fraction are functionalized by random choice up to the desired degree of bromination.

For each degree of functionalization, the simulation generates 1000 polymer chains of 1442 monomers and calculates the frequency of a sequence length of *j* consecutive styrene units along each simulated chain. According to Flory's theory of crystallization in copolymers[51], the

probability (P_ζ) that a randomly selected styrene unit in the chain exists in a crystallizable chain segment of at least ζ styrene units is given by:

$$P_\zeta = \sum_j P_{\zeta,j} = \sum_{j=\zeta}^{\infty} \frac{(j-\zeta+1)\times w_j}{j} \qquad \textbf{(2)}$$

where w_j is the probability that a unit chosen at random is a styrene unit in a sequence of length j, calculated by multiplying the mole fraction of styrene units (X_{Sty}) by the fraction of styrene units occurring in j sequences (j_{Sty}). For this work, ζ is defined as 26 monomer units, the average number of styrene monomers in one crystalline stem of an sPS crystallite.[10] (Note that the probability of consecutive brominated styrene units can also be computed. For an example, see **Figure S2.9**.)

As shown in **Figure 2.8**, the probability of selecting a crystallizable styrene monomer (i.e., a monomer within a defect-free sequence of 26 monomer units) rapidly declines with increasing degree of bromination for the simulated random copolymers and falls below 1% at 18 mol% Br. This infrequency of crystallizable styrene monomers at 18 mol% Br is in excellent agreement with the experimentally-determined crystallizability of Random R-18%, which exhibits less than 1 wt% crystallinity after 2 h isothermal crystallization at 190 °C (**Table 2.1**) and very slow crystallization at high supercooling (**Figure 2.5**). Above 18 mol% Br, the probability of encountering a defect-free stem is very low, and thus the random copolymers are not predicted to be crystallizable. This prediction is in agreement with the amorphous nature of the Random R-31% sample; however, it is recognized that crystallization of styrene segments shorter than 26 units is possible, which is supported by the significant crystallizability (**Table 2.1**) observed in the Random R-16% sample.

In contrast to the predicted behavior of the random copolymers, the simulated blocky copolymers retain approximately 38% of their styrene monomers in crystallizable segments, even at 30 mol% Br. This result of the blocky simulation is in excellent agreement with the high

crystallizability and rapid crystallization kinetics observed for the empirical Blocky copolymers. For example, the Blocky B-21% sample is capable of rapidly crystallizing ($t_{1/2}$ less than 2 min) to a degree of 18 wt% during isothermal crystallization at 190 °C. Thus, the agreement between these simulated copolymers and experiment validates the basis of our blocky copolymer simulation and confirms our hypothesis that restricting accessibility of the functionalizing reagent to monomers in the amorphous component of the gel network produces copolymers with a high prevalence of crystallizable homopolymer segments.

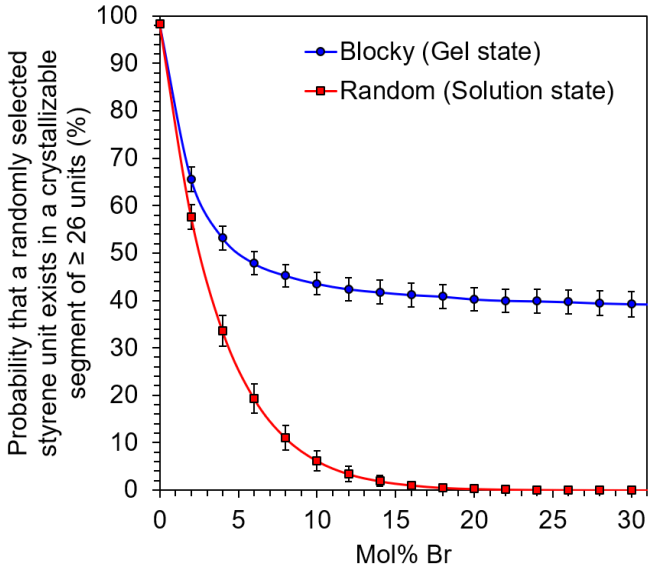

Figure 2.8 Probability that a styrene unit selected at random exists in a crystallizable segment of at least 26 consecutive styrene units from simulations of theoretical blocky (gel-state) or random (solution-state) copolymers. Results based on 1000 polymer chains of 1442 monomer units. Error bars represent one standard deviation. Reproduced by permission of The Royal Society of Chemistry.

Another valuable outcome of these simulations is the ability to construct representative copolymer chain sequences for qualitative and quantitative comparison of the random and blocky microstructures. From the simulations, representative 29 mol% Br random and blocky copolymer chains were created, shown in **Figure 9**. By inspection, it is clear that the simulated blocky 29 mol% Br copolymer exhibits longer segments of consecutive styrene units (open circles) compared to the simulated random copolymer. It is worth emphasizing that the distribution of these styrene

"blocks" along the chain depends only on the position of the units that were randomly selected for the inaccessible fraction. For a quantitative comparison, the triad sequences can be counted along the simulated chains and grouped into one of the six possible unique triad combinations (i.e., SSS, [SSB/BSS], BSB, SBS, [SBB/BBS], or BBB). The prevalence of encountering a given triad sequence is then calculated as a percentage of all unique triads counted along the simulated chains. For the simulated 29 mol% Br blocky copolymer shown in **Figure 2.9**, this analysis yields a %BBB of 12% and %SSS of 57%. As noted above, the ^{13}C NMR results for the empirical Blocky B-29% sample yielded a BBB prevalence of 17% from spectral integration of the resonance at 143.1−143.3 ppm. Similarly, the SSS prevalence for this sample was measured by integration of the C(1) NMR spectrum at 144.8−145.4 ppm and found to be 57%. These empirical values are in good agreement with the values determined from the simulations, which further supports the validity of this simulation approach. An initial assessment of the difference between 12% (simulation) and 17% (empirical) for the BBB prevalence suggests that the empirical samples are more "blocky" than our preliminary model predicts. We are currently exploring a detailed analysis of the ^{13}C NMR results from these copolymers aimed at developing a high-resolution sequencing protocol for further refinement of a microstructural model for blocky copolymers.

1. Hadjichristidis, N.; Pispas, S.; Floudas, G. A., *Block Copolymers: Synthetic Strategies, Physical Properties, and Applications*. John Wiley and Sons: New York, 2002.
2. Hamley, I. W., *The Physics of Block Copolymers*. Oxford University Press: New York, 1998.
3. Lee, M.; Park, J. K.; Lee, H.-S.; Lane, O.; Moore, R. B.; McGrath, J. E.; Baird, D. G., Effects of Block Length and Solution-Casting Conditions on the Final Morphology and Properties of Disulfonated Poly(Arylene Ether Sulfone) Multiblock Copolymer Films for Proton Exchange Membranes. *Polymer* **2009,** *50*, 6129-6138.

4. Leibler, L., Theory of Microphase Separation in Block Copolymers. *Macromolecules* **1980,** *13* (6), 1602-1617.
5. Dobrynin, A. V.; Leibler, L., Theory of Polydisperse Multiblock Copolymers. *Macromolecules* **1997,** *30*, 4756-4765.
6. Bates, F. S.; Fredrickson, G. H., Block Copolymers - Designer Soft Materials. *Phys. Today* **1999,** *52* (2), 32-38.
7. Lodge, T. P., Block Copolymers: Past Successes and Future Challenges. *Macromol. Chem. Phys.* **2003,** *204* (2), 265-273.
8. Ruzette, A.-V.; Leibler, L., Block Copolymers in Tomorrow's Plastics. *Nat. Mater.* **2005,** *4* (1), 19-31.
9. Domski, G. J.; Rose, J. M.; Coates, G. W.; Bolig, A. D.; Brookhart, M., Living Alkene Polymerization: New Methods for the Precision Synthesis of Polyolefins. *Prog. Polym. Sci.* **2007,** *32* (1), 30-92.
10. Govorun, E. N.; Chertovich, A. V., Microphase Separation in Random Multiblock Copolymers. *J. Chem. Phys.* **2017,** *146*, 034903.
11. Shull, K. R., Interfacial Activity of Gradient Copolymers. *Macromolecules* **2002,** *35* (22), 8631-8639.
12. Lefebvre, M. D.; Dettmer, C. M.; McSwain, R. L.; Xu, C.; Davila, J. R.; Composto, R. J.; Nguyen, S. T.; Shull, K. R., Effect of Sequence Distribution on Copolymer Interfacial Activity. *Macromolecules* **2005,** *38* (25), 10494-10502.
13. Wylie, K.; Bennett, I.; Marić, M., Self-Assembly of Gradient Copolymers Synthesized in Semi-Batch Mode by Nitroxide Mediated Polymerization. *Soft Matter* **2017,** *13*, 2836-2843.
14. Beginn, U., Gradient Copolymers. *Colloid Polym. Sci.* **2008,** *286* (13), 1465-1474.
15. Mok, M. M.; Ellison, C. J.; Torkelson, J. M., Effect of Gradient Sequencing on Copolymer Order–Disorder Transitions: Phase Behavior of Styrene/ N -Butyl Acrylate Block and Gradient Copolymers. *Macromolecules* **2011,** *44*, 6220-6226.
16. Pakula, T.; Matyjaszewski, K., Copolymers with Controlled Distribution of Comonomers Along the Chain, 1. Structure, Thermodynamics and Dynamic Properties of Gradient Copolymers. Computer Simulation. *Macromol. Theory Simul.* **1996,** *5* (5), 987-1006.
17. Jiang, R.; Wang, Z.; Yin, Y.; Li, B.; Shi, A.-C., Effects of Compositional Polydispersity on Gradient Copolymer Melts. *J. Chem. Phys.* **2013,** *138* (7), 074906.

18. Ganesan, V.; Kumar, N. A.; Pryamitsyn, V., Blockiness and Sequence Polydispersity Effects on the Phase Behavior and Interfacial Properties of Gradient Copolymers. *Macromolecules* **2012,** *45* (15), 6281-6297.
19. Pandav, G.; Pryamitsyn, V.; Gallow, K. C.; Loo, Y.-L.; Genzer, J.; Ganesan, V., Phase Behavior of Gradient Copolymer Solutions: A Monte Carlo Simulation Study. *Soft Matter* **2012,** *8*, 6471.
20. Sigle, J. L.; Clough, A.; Zhou, J.; White, J. L., Controlling Macroscopic Properties by Tailoring Nanoscopic Interfaces in Tapered Copolymers. *Macromolecules* **2015,** *48* (16), 5714-5722.
21. Zheng, Z.; Gao, X.; Luo, Y.; Zhu, S., Employing Gradient Copolymer to Achieve Gel Polymer Electrolytes with High Ionic Conductivity. *Macromolecules* **2016,** *49* (6), 2179-2188.
22. Dobrynin, A. V.; Leibler, L., Theory of Polydisperse Multiblock Copolymers. *Macromolecules* **1997,** *30* (16), 4756-4765.
23. Burger, C.; Ruland, W.; Semenov, A. N., Polydispersity Effects on the Microphase-Separation Transition in Block Copolymers. *Macromolecules* **1990,** *23* (13), 3339-3346.
24. Sides, S. W.; Fredrickson, G. H., Continuous Polydispersity in a Self-Consistent Field Theory for Diblock Copolymers. *J. Chem. Phys.* **2004,** *121* (10), 4974-4986.
25. Beardsley, T. M.; Matsen, M. W., Monte Carlo Phase Diagram for a Polydisperse Diblock Copolymer Melt. *Macromolecules* **2011,** *44* (15), 6209-6219.
26. Cooke, D. M.; Shi, A.-C., Effects of Polydispersity on Phase Behavior of Diblock Copolymers. *Macromolecules* **2006,** *39* (19), 6661-6671.
27. Spontak, R. J.; Williams, M. C., Prediction of Microstructures for Polydisperse Block Copolymers, Using Continuous Thermodynamics. *J. Polym. Sci., Part B: Polym. Phys.* **1990,** *28* (8), 1379-1407.
28. Matsen, M. W., Effect of Large Degrees of Polydispersity on Strongly Segregated Block Copolymers. *Eur. Phys. J. E* **2006,** *21* (3), 199-207.
29. Lynd, N. A.; Hillmyer, M. A., Influence of Polydispersity on the Self-Assembly of Diblock Copolymers. *Macromolecules* **2005,** *38* (21), 8803-8810.
30. Lynd, N. A.; Hamilton, B. D.; Hillmyer, M. A., The Role of Polydispersity in the Lamellar Mesophase of Model Diblock Copolymers. *J. Polym. Sci., Part B: Polym. Phys.* **2007,** *45* (24), 3386-3393.

31. Lynd, N. A.; Hillmyer, M. A., Effects of Polydispersity on the Order−Disorder Transition in Block Copolymer Melts. *Macromolecules* **2007,** *40* (22), 8050-8055.
32. Kumar, R.; Lokitz, B. S.; Sides, S. W.; Chen, J.; Heller, W. T.; Ankner, J. F.; Browning, J. F.; Kilbey II, S. M.; Sumpter, B. G., Microphase Separation in Thin Films of Lamellar Forming Polydisperse Di-Block Copolymers. *RSC Advances* **2015,** *5* (27), 21336-21348.
33. Nguyen, D.; Zhong, X.-F.; Williams, C. E.; Eisenberg, A., Effect of Ionic Chain Polydispersity on the Size of Spherical Ionic Microdomains in Diblock Ionomers. *Macromolecules* **1994,** *27* (18), 5173-5181.
34. Matsushita, Y.; Noro, A.; Iinuma, M.; Suzuki, J.; Ohtani, H.; Takano, A., Effect of Composition Distribution on Microphase-Separated Structure from Diblock Copolymers. *Macromolecules* **2003,** *36* (21), 8074-8077.
35. Noro, A.; Iinuma, M.; Suzuki, J.; Takano, A.; Matsushita, Y., Effect of Composition Distribution on Microphase-Separated Structure from Bab Triblock Copolymers. *Macromolecules* **2004,** *37* (10), 3804-3808.
36. Noro, A.; Okuda, M.; Odamaki, F.; Kawaguchi, D.; Torikai, N.; Takano, A.; Matsushita, Y., Chain Localization and Interfacial Thickness in Microphase-Separated Structures of Block Copolymers with Variable Composition Distributions. *Macromolecules* **2006,** *39* (22), 7654-7661.
37. Noro, A.; Cho, D.; Takano, A.; Matsushita, Y., Effect of Molecular Weight Distribution on Microphase-Separated Structures from Block Copolymers. *Macromolecules* **2005,** *38* (10), 4371-4376.
38. Widin, J. M.; Schmitt, A. K.; Schmitt, A. L.; Im, K.; Mahanthappa, M. K., Unexpected Consequences of Block Polydispersity on the Self-Assembly of Aba Triblock Copolymers. *J. Am. Chem. Soc.* **2012,** *134*, 3834-3844.
39. Gao, Y.; Li, H. M., Synthesis and Characterization of Acetylated Syndiotactic Polystyrene. *Polym. Int.* **2004,** *53* (10), 1436-1441.
40. Jhon, Y. K.; Semler, J. J.; Genzer, J., Effect of Solvent Quality and Chain Confinement on the Kinetics of Polystyrene Bromination. *Macromolecules* **2008,** *41* (18), 6719-6727.
41. Jhon, Y. K.; Semler, J. J.; Genzer, J.; Beevers, M.; Gus' kova, O. A.; Khalatur, P. G.; Khokhlov, A. R., Effect of Comonomer Sequence Distribution on the Adsorption of Random Copolymers onto Impenetrable Flat Surfaces. *Macromolecules* **2009,** *42*, 2843-2853.

42. Semler, J. J.; Jhon, Y. K.; Tonelli, A.; Beevers, M.; Krishnamoorti, R.; Genzer, J., Facile Method of Controlling Monomer Sequence Distributions in Random Copolymers. *Adv. Mater.* **2007,** *19* (19), 2877-2883.
43. Strickland, L. A.; Hall, C. K.; Genzer, J., Design of Copolymers with Tunable Randomness Using Discontinuous Molecular Dynamics Simulation. *Macromolecules* **2009,** *42* (22), 9063-9071.
44. Han, J.; Jeon, B. H.; Ryu, C. Y.; Semler, J. J.; Jhon, Y. K.; Genzer, J., Discriminating among Co-Monomer Sequence Distributions in Random Copolymers Using Interaction Chromatography. *Macromol. Rapid Comm.* **2009,** *30* (18), 1543-1548.
45. Gurarslan, R.; Hardrict, S.; Roy, D.; Galvin, C.; Hill, M. R.; Gracz, H.; Sumerlin, B. S.; Genzer, J.; Tonelli, A., Beyond Microstructures: Using the Kerr Effect to Characterize the Macrostructures of Synthetic Polymers. *J. Polym. Sci. B Polym. Phys.* **2015,** *53* (3), 155-166.
46. Khokhlov, A. R.; Khalatur, P. G., Protein-Like Copolymers: Computer Simulation. *Physica A* **1998,** *249* (1–4), 253-261.
47. Khokhlov, A. R.; Khalatur, P. G. J. P. r. l., Conformation-Dependent Sequence Design (Engineering) of Ab Copolymers. *Phys. Rev. Lett.* **1999,** *82* (17), 3456.
48. Nemani, S. K.; Annavarapu, R. K.; Mohammadian, B.; Raiyan, A.; Heil, J.; Haque, M. A.; Abdelaal, A.; Sojoudi, H., Surface Modification of Polymers: Methods and Applications. *Advanced Materials Interfaces* **2018,** *5* (24).
49. Borriello, A.; Agoretti, P.; Ambrosio, L.; Fasano, G.; Pellegrino, M.; Venditto, V.; Guerra, G., Syndiotactic Polystyrene Films with Sulfonated Amorphous Phase and Nanoporous Crystalline Phase. *Chem. Mater.* **2009,** *21* (14), 3191-3196.
50. Gibson, H. W.; Bailey, F. C., Chemical Modification of Polymers. 13. Sulfonation of Polystyrene Surfaces. *Macromolecules* **1980,** *13* (1), 34-41.
51. Sundararajan, P. R., *Physical Aspects of Polymer Self-Assembly*. John Wiley & Sons, Inc.: 2016.
52. Fahs, G. B.; Benson, S. D.; Moore, R. B., Blocky Sulfonation of Syndiotactic Polystyrene: A Facile Route toward Tailored Ionomer Architecture Via Postpolymerization Functionalization in the Gel State. *Macromolecules* **2017,** *50* (6), 2387-2396.

53. Anderson, L. J.; Yuan, X.; Fahs, G. B.; Moore, R. B., Blocky Ionomers Via Sulfonation of Poly(Ether Ether Ketone) in the Semicrystalline Gel State. *Macromolecules* **2018,** *51* (16), 6226-6237.
54. Vanderwoude, G.; Shi, A.-C., Effects of Blockiness and Polydispersity on the Phase Behavior of Random Block Copolymers. *Macromol. Theory Simul.* **2017,** *26*, 1600044.
55. Venditto, V.; Pellegrino, M.; Califano, R.; Guerra, G.; Daniel, C.; Ambrosio, L.; Borriello, A., Monolithic Polymeric Aerogels with Vocs Sorbent Nanoporous Crystalline and Water Sorbent Amorphous Phases. *ACS Appl. Mater. Inter.* **2015,** *7* (2), 1318-1326.
56. Li, S.; Register, R. A.; Weinhold, J. D.; Landes, B. G., Melt and Solid-State Structures of Polydisperse Polyolefin Multiblock Copolymers. *Macromolecules* **2012,** *45*, 5773-5781.
57. Xu, C.-L.; Zeng, J.-B.; Zhu, Q.-Y.; Wang, Y.-Z., Poly(Ethylene Succinate)-B-Poly(Butylene Succinate) Multiblock Copolyesters: The Effects of Block Length and Composition on Physical Properties. *Ind. Eng. Chem. Res.* **2013,** *52*, 13669-13676.
58. Talley, S. J.; Yuan, X.; Moore, R. B., Thermoreversible Gelation of Poly (Ether Ether Ketone). *ACS Macro Lett.* **2017,** *6*, 262-266.
59. Daniel, C.; Dammer, C.; Guenet, J.-M., On the Definition of Thermoreversible Gels: The Case of Syndiotactic Polystyrene. *Polymer* **1994,** *35* (19), 4243-4246.
60. Flory, P. J., Introductory Lecture. *Faraday Discuss.* **1974,** *57* (0), 7-18.
61. Berghams, H.; Donkers, A.; Frenay, L.; Stoks, W.; De Schryver, F. E.; Moldenaers, P.; Mewis, J., Thermoreversible Gelation of Syndiotactic Poly(Methyl Methacrylate). *Polymer* **1987,** *28* (1), 97-102.
62. Ding, H.; Zeng, Y.; Meng, X.; Tian, Y.; Shi, Y.; Jiao, Q.; Zhang, S., Porous Polyphenylene Sulfide Membrane with High Durability against Solvents by the Thermally Induced Phase-Separation Method. *J. Appl. Polym. Sci.* **2006,** *102* (3), 2959-2966.
63. Mutin, P. H.; Guenet, J. M., Physical Gels from Pvc: Aging and Solvent Effects on Thermal Behavior, Swelling, and Compression Modulus. *Macromolecules* **1989,** *22* (2), 843-848.
64. Tazaki, M.; Wada, R.; Abe, M. O.; Homma, T., Crystallization and Gelation of Poly(Vinylidene Fluoride) in Organic Solvents. *J. Appl. Polym. Sci.* **1997,** *65* (8), 1517-1524.
65. Matsuda, H.; Inoue, T.; Okabe, M.; Ukaji, T., Study of Polyolefin Gel in Organic Solvents I. Structure of Isotactic Polypropylene Gel in Organic Solvents. *Polym. J.* **1987,** *19* (3), 323-329.

66. Prasad, A.; Mandelkern, L., The Thermoreversible Gelation of Syndiotactic Polystyrene. *Macromolecules* **1990,** *23* (23), 5041-5043.
67. Aubert, J. H., Isotactic Polystyrene Phase Diagrams and Physical Gelation. *Macromolecules* **1988,** *21* (12), 3468-3473.
68. Prasad, A.; Marand, H.; Mandelkern, L., Supermolecular Morphology of Thermoreversible Gels Formed from Homogeneous and Heterogeneous Solutions. *J. Polym. Sci., Part B: Polym. Phys.* **1993,** *31* (12), 1819-1835.
69. Wellinghoff, S.; Shaw, J.; Baer, E., Polymeric Materials from the Gel State. The Development of Fringed Micelle Structure in a Glass. *Macromolecules* **1979,** *12* (5), 932-939.
70. Mochizuki, J.; Sano, T.; Tokami, T.; Itagaki, H., Decisive Properties of Solvent Able to Form Gels with Syndiotactic Polystyrene. *Polymer* **2015,** *67*, 118-127.
71. Jaymand, M., Recent Progress in the Chemical Modification of Syndiotactic Polystyrene. *Polym. Chem.* **2014,** *5* (8), 2663-2690.
72. Ishihara, N.; Seimiya, T.; Kuramoto, M.; Uoi, M., Crystalline Syndiotactic Polystyrene. *Macromolecules* **1986,** *19* (9), 2464-2465.
73. De Rudder, J.; Bergé, B.; Berghmans, H., Competition between Gelation and Crystallization in Solutions of Syndiotactic Polystyrene in Cis-Decalin. *Macromol. Chem. Phys.* **2002,** *203* (14), 2083-2088.
74. Roels, T.; Deberdt, F.; Berghmans, H., Solvent Quality and Phase-Stability in Syndiotactic Polystyrene-Solvent Systems. *Macromolecules* **1994,** *27* (21), 6216-6220.
75. Daniel, C.; Menelle, A.; Brulet, A.; Guenet, J.-M., Thermoreversible Gelation of Syndiotactic Polystyrene in Toluene and Chloroform. *Polymer* **1997,** *38* (16), 4193-4199.
76. Ray, B.; Elhasri, S.; Thierry, A.; Marie, P.; Guenet, J.-M., Solvent-Induced Crystallization of Syndiotactic Polystyrene: Thermodynamics and Morphology. *Macromolecules* **2002,** *35* (26), 9730-9736.
77. Gowd, E. B.; Tashiro, K.; Ramesh, C., Structural Phase Transitions of Syndiotactic Polystyrene. *Prog. Polym. Sci.* **2009,** *34* (3), 280-315.
78. Su, C.; Jeng, U.; Chen, S.; Cheng, C.-Y.; Lee, J.-J.; Lai, Y.-H.; Su, W.; Tsai, J.; Su, A., Thermodynamic Characterization of Polymorphs in Bulk-Crystallized Syndiotactic Polystyrene Via Small/Wide-Angle X-Ray Scattering and Differential Scanning Calorimetry. *Macromolecules* **2009,** *42* (12), 4200-4207.

79. Guerra, G.; Vitagliano, V. M.; De Rosa, C.; Petraccone, V.; Corradini, P., Polymorphisms in Melt Crystallized Syndiotactic Polystyrene Samples. *Macromolecules* **1990,** *23* (5), 1539-1544.
80. Itagaki, H.; Tokami, T.; Mochizuki, J., A Trial to Clarify a Cause of Forming Physical Gels: Morphology of Syndiotactic Polystyrene in N-Alkylbenzene. *Polymer* **2012,** *53* (23), 5304-5312.
81. Petraccone, V.; Ruiz de Ballesteros, O.; Tarallo, O.; Rizzo, P.; Guerra, G., Nanoporous Polymer Crystals with Cavities and Channels. *Chem. Mater.* **2008,** *20* (11), 3663-3668.
82. Daniel, C.; Avallone, A.; Guerra, G., Syndiotactic Polystyrene Physical Gels: Guest Influence on Structural Order in Molecular Complex Domains and Gel Transparency. *Macromolecules* **2006,** *39* (22), 7578-7582.
83. Daniel, C.; Avallone, A.; Rizzo, P.; Guerra, G., Control of Crystal Size and Orientation in Polymer Films by Host−Guest Interactions. *Macromolecules* **2006,** *39* (14), 4820-4823.
84. Daniel, C.; Longo, S.; Ricciardi, R.; Reverchon, E.; Guerra, G., Monolithic Nanoporous Crystalline Aerogels. *Macromol. Rapid Commun.* **2013,** *34* (15), 1194-1207.
85. Daniel, C.; Giudice, S.; Guerra, G., Syndiotatic Polystyrene Aerogels with B, Γ, and E Crystalline Phases. *Chem. Mater.* **2009,** *21* (6), 1028-1034.
86. De Rosa, C.; Guerra, G.; Petraccone, V.; Pirozzi, B., Crystal Structure of the Emptied Clathrate Form (Δe Form) of Syndiotactic Polystyrene. *Macromolecules* **1997,** *30* (14), 4147-4152.
87. Wang, H.; Wu, C.-J.; Cui, D.-M.; Men, Y.-F., Equilibrium Crystallization Temperature of Syndiotactic Polystyrene Γ Form. *Chin. J. Polym. Sci.* **2018,** *36* (6), 749-755.
88. De Rudder, J.; Berghmans, H.; De Schryver, F. C.; Bosco, M.; Paoletti, S., Gelation Mechanism of Syndiotactic Polystyrene in Bromoform. *Macromolecules* **2002,** *35* (25), 9529-9535.
89. Hu, W., *Polymer Physics: A Molecular Approach*. Springer Science & Business Media: 2012.
90. Daniel, C., Structural Organization and Properties of Syndiotactic Polystyrene Gels. *Macromol. Symp.* **2007,** *251* (1), 1-10.
91. Kobayashi, M.; Kozasa, T., Conformational Ordering Process on Physical Gelation of Syndiotactic Polystyrene/Solvent Systems Revealed by Time-Resolved Infrared Spectroscopy. *Appl. Spectrosc.* **1993,** *47* (9), 1417-1424.

92. Kobayashi, M.; Yoshioka, T.; Kozasa, T.; Tashiro, K.; Suzuki, J.; Funahashi, S.; Izumi, Y., Structure of Physical Gels Formed in Syndiotactic Polystyrene/Solvent Systems Studied by Small-Angle Neutron Scattering. *Macromolecules* **1994,** *27* (6), 1349-1354.
1. Claridge, T. D. W., Chapter 2 - Introducing High-Resolution NMR. In *High-Resolution NMR Techniques in Organic Chemistry (Third Edition)*, Claridge, T. D. W., Ed. Elsevier: Boston, 2016; pp 11-59.
2. *NMR Spectroscopy of Polymers*. 1st ed.; Springer Science+Business Media Dordrecht: New Delhi, 1993.
3. Magnetic resonance. In *Encyclopædia Britannica*, Encyclopædia Britannica, inc.: 2011.
4. Boltzmann factor. $P(\alpha)/P(\beta) = e^{(\Delta E/kT)}$ where, $P(\alpha)$ and $P(\beta)$ are the probabilities of the two states, ΔE is the energy difference between states, k is the Boltzmann constant, and T is temperature.
5. Bain, A.; Eaton, D.; Hamielec, A.; Mlekuz, M.; Sayer, B., Line broadening in the carbon-13 NMR spectra of cross-linked polymers. *Macromolecules* **1989,** *22* (9), 3561-3564.
6. Gronski, W.; Quack, G.; Murayama, N.; Elgert, K. F., Dependence of local chain motions on the sequence structure of cis-(1,4-1,2)-polybutadiene as revealed by 13c spin-lattice relaxation. *Die Makromolekulare Chemie* **1975,** *176* (12), 3605-3608.
7. Claridge, T. D. W., Chapter 4 - One-Dimensional Techniques. In *High-Resolution NMR Techniques in Organic Chemistry (Third Edition)*, Claridge, T. D. W., Ed. Elsevier: Boston, 2016; pp 133-169.
8. Claridge, T. D. W., Chapter 9 - Correlations Through Space: The Nuclear Overhauser Effect. In *High-Resolution NMR Techniques in Organic Chemistry (Third Edition)*, Claridge, T. D. W., Ed. Elsevier: Boston, 2016; pp 315-380.
9. Ziaee, F.; Salehi Mobarakeh, H., Effect of temperature on polystyrene tacticity through para aromatic carbon splitting in 13C NMR spectroscopy. *Iran Polym J* **2011,** *20*, 213-221.
10. Randall, J. C., The distribution of stereochemical configurations in polystyrene as observed with 13C NMR. *J. Polym. Sci., Part B: Polym. Phys.* **1975,** *13* (5), 889-899.
11. Randall, J. C.; Ruff, C. J.; Kelchtermans, M., 13C NMR microstructure determinations of low-density polyethylene homopolymers and copolymers. *Recl. Trav. Chim. Pays-Bas* **1991,** *110* (12), 543-552.

1. Claridge, T. D. W., Chapter 2 - Introducing High-Resolution NMR. In *High-Resolution NMR Techniques in Organic Chemistry (Third Edition)*, Claridge, T. D. W., Ed. Elsevier: Boston, 2016; pp 11-59.
2. *NMR Spectroscopy of Polymers*. 1st ed.; Springer Science+Business Media Dordrecht: New Delhi, 1993.
3. Magnetic resonance. In *Encyclopædia Britannica*, Encyclopædia Britannica, inc.: 2011.
4. Boltzmann factor. $P(\alpha)/P(\beta) = e^{(\Delta E/kT)}$ where, $P(\alpha)$ and $P(\beta)$ are the probabilities of the two states, ΔE is the energy difference between states, k is the Boltzmann constant, and T is temperature.
5. Bain, A.; Eaton, D.; Hamielec, A.; Mlekuz, M.; Sayer, B., Line broadening in the carbon-13 NMR spectra of cross-linked polymers. *Macromolecules* **1989,** *22* (9), 3561-3564.
6. Gronski, W.; Quack, G.; Murayama, N.; Elgert, K. F., Dependence of local chain motions on the sequence structure of cis-(1,4-1,2)-polybutadiene as revealed by 13c spin-lattice relaxation. *Die Makromolekulare Chemie* **1975,** *176* (12), 3605-3608.
7. Claridge, T. D. W., Chapter 4 - One-Dimensional Techniques. In *High-Resolution NMR Techniques in Organic Chemistry (Third Edition)*, Claridge, T. D. W., Ed. Elsevier: Boston, 2016; pp 133-169.
8. Claridge, T. D. W., Chapter 9 - Correlations Through Space: The Nuclear Overhauser Effect. In *High-Resolution NMR Techniques in Organic Chemistry (Third Edition)*, Claridge, T. D. W., Ed. Elsevier: Boston, 2016; pp 315-380.
9. Ziaee, F.; Salehi Mobarakeh, H., Effect of temperature on polystyrene tacticity through para aromatic carbon splitting in 13C NMR spectroscopy. *Iran Polym J* **2011,** *20*, 213-221.
10. Randall, J. C., The distribution of stereochemical configurations in polystyrene as observed with 13C NMR. *J. Polym. Sci., Part B: Polym. Phys.* **1975,** *13* (5), 889-899.
11. Randall, J. C.; Ruff, C. J.; Kelchtermans, M., 13C NMR microstructure determinations of low-density polyethylene homopolymers and copolymers. *Recl. Trav. Chim. Pays-Bas* **1991,** *110* (12), 543-552.
1. Claridge, T. D. W., Chapter 2 - Introducing High-Resolution NMR. In *High-Resolution NMR Techniques in Organic Chemistry (Third Edition)*, Claridge, T. D. W., Ed. Elsevier: Boston, 2016; pp 11-59.

2. *NMR Spectroscopy of Polymers*. 1st ed.; Springer Science+Business Media Dordrecht: New Delhi, 1993.
3. Magnetic resonance. In *Encyclopædia Britannica*, Encyclopædia Britannica, inc.: 2011.
4. Boltzmann factor. $P(\alpha)/P(\beta) = e^{(\Delta E/kT)}$ where, $P(\alpha)$ and $P(\beta)$ are the probabilities of the two states, ΔE is the energy difference between states, k is the Boltzmann constant, and T is temperature.
5. Bain, A.; Eaton, D.; Hamielec, A.; Mlekuz, M.; Sayer, B., Line broadening in the carbon-13 NMR spectra of cross-linked polymers. *Macromolecules* **1989,** *22* (9), 3561-3564.
6. Gronski, W.; Quack, G.; Murayama, N.; Elgert, K. F., Dependence of local chain motions on the sequence structure of cis-(1,4-1,2)-polybutadiene as revealed by 13c spin-lattice relaxation. *Die Makromolekulare Chemie* **1975,** *176* (12), 3605-3608.
7. Claridge, T. D. W., Chapter 4 - One-Dimensional Techniques. In *High-Resolution NMR Techniques in Organic Chemistry (Third Edition)*, Claridge, T. D. W., Ed. Elsevier: Boston, 2016; pp 133-169.
8. Claridge, T. D. W., Chapter 9 - Correlations Through Space: The Nuclear Overhauser Effect. In *High-Resolution NMR Techniques in Organic Chemistry (Third Edition)*, Claridge, T. D. W., Ed. Elsevier: Boston, 2016; pp 315-380.
9. Ziaee, F.; Salehi Mobarakeh, H., Effect of temperature on polystyrene tacticity through para aromatic carbon splitting in 13C NMR spectroscopy. *Iran Polym J* **2011,** *20*, 213-221.
10. Randall, J. C., The distribution of stereochemical configurations in polystyrene as observed with 13C NMR. *J. Polym. Sci., Part B: Polym. Phys.* **1975,** *13* (5), 889-899.
11. Randall, J. C.; Ruff, C. J.; Kelchtermans, M., 13C NMR microstructure determinations of low-density polyethylene homopolymers and copolymers. *Recl. Trav. Chim. Pays-Bas* **1991,** *110* (12), 543-552.

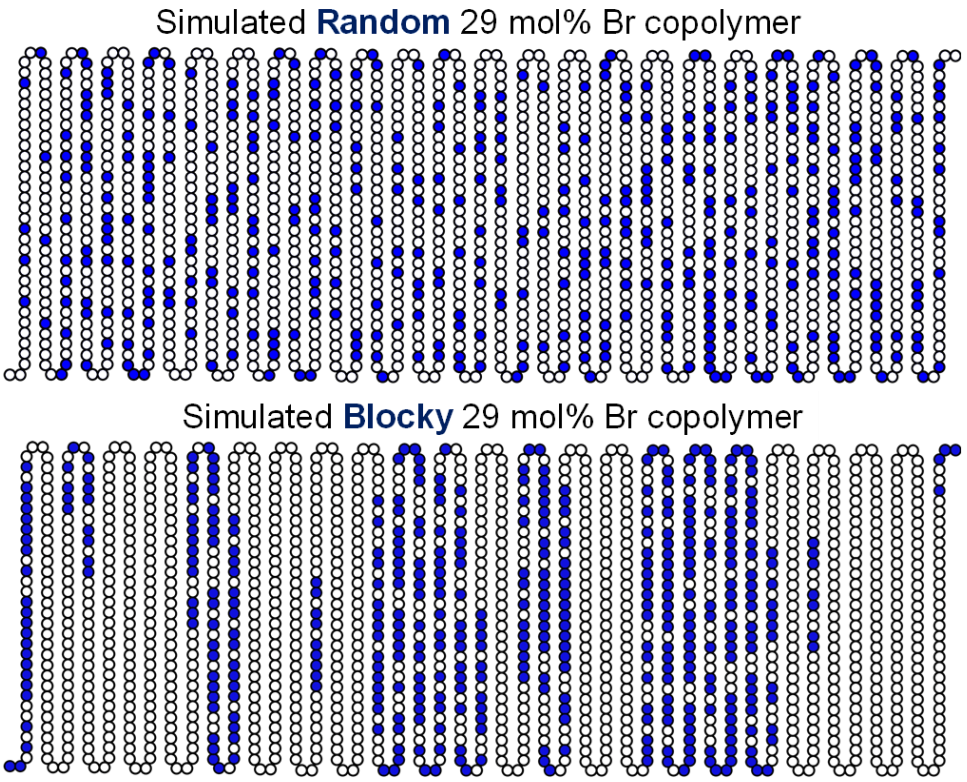

Figure 2.9 Representative 29 mol% Br (top) random and (bottom) blocky copolymer chains derived from simulations. Each comonomer sequence is 1 of the 1000 copolymer chains of 1442 monomer units generated in the simulations. The particular sequence selected has a prevalence of pure styrene pentads (SSSSS, where S = styrene) that is most similar to the average number of SSSSS for all 1000 simulated chains. Open circles = styrene; Filled circles = Br-Sty. Reproduced by permission of The Royal Society of Chemistry.

2.5. Conclusions

This work demonstrates the bromination of sPS in solution and in the heterogeneous gel state to produce random and blocky sPS-co-sPS-Br copolymers, respectively. The purpose of this research was to prepare semicrystalline blocky copolymers with relatively high degrees of functionality using a facile, post-polymerization functionalization method. Using our heterogeneous gel-state bromination method, a crystallizable 29 mol% Br sPS-co-sPS-Br copolymer was produced, demonstrating that this method favorably affects the bromination reaction to produce a blocky microstructure. When the brominating reagent is introduced into the heterogeneous gel network, it is excluded from the crystalline component and reacts with styrene monomers in the amorphous component. Based on the microstructural analysis of the Random and

Blocky samples provided by NMR spectroscopy, gel-state bromination produces sPS-co-sPS-Br copolymers with long segments of un-functionalized styrene "blocks" and segments of randomly functionalized "blocks" in a blocky microstructure. The USAXS/SAXS profiles of quenched films of the Blocky copolymers support that these distinct segments of pure sPS and randomly brominated sPS are capable of producing a micro-phase separated morphology attributed to thermodynamic immiscibility. The Blocky copolymers demonstrate superior crystallizability and faster crystallization kinetics at lower supercooling compared to their Random analogs. The microstructure of representative random and blocky copolymers generated from simulations of the homogeneous/heterogeneous bromination methods, affirms that restricting access of the functionalizing reagent to monomers well removed from the crystalline fraction of the gel network, produces copolymers with a greater prevalence of crystallizable sPS segments, which is advantageous for preserving desired crystallizability of the resulting blocky copolymers.

This work provides a fundamental investigation of the post-polymerization bromination of sPS, demonstrating that blocky sPS-co-sPS-Br copolymers can be prepared using a straightforward physical method of post-polymerization functionalization in the heterogeneous gel state. Given the high tactic purity and sequence specific ^{13}C NMR resonances, sPS is an ideal investigatory polymer for the gel-state functionalization reaction scheme. Future efforts will be focused on developing a deeper understanding of the relationship between gel morphology and the resulting copolymer microstructure in order to ultimately control the comonomer sequence distribution of sPS-co-sPS-Br copolymers. We anticipate that the dependence of sPS gel morphology on gelation solvent[7, 8, 52] will present avenues of further investigation into controlling the degree of blockiness in sPS-based copolymers. This research also lays the groundwork to synthesize other sPS-based

blocky copolymers with useful functionalities through simple substitution of the labile bromine functional groups.

2.6. Acknowledgements

This material is based upon work supported by the National Science Foundation under Grant No. DMR-1507245 and DMR-1809291. This research used resources of the Advanced Photon Source, a U.S. Department of Energy (DOE) Office of Science User Facility operated for the DOE Office of Science by Argonne National Laboratory under Contract No. DE-AC02-06CH11357. The authors would like to thank Dr. Jan Ilavsky and acknowledge the use of beamline 9ID-C for all USAXS and SAXS experiments.

2.7. Supplementary Information I

^{1}H NMR spectra were recorded using the following parameters: pulse sequence s2pul, 5 sec relaxation delay, 64 scans, 1.6622 μsec pulse width, and an acquisition time of 2.5559 sec. The full ^{1}H NMR spectra of the sPS homopolymer, Random R-31%, and Blocky B-29% are shown in **Figure S2.1**. Between 1.58-1.75 ppm, there are two distinct chemical shifts assigned to H(a′) protons based on the heteronuclear single quantum coherence (HSQC) NMR spectra (see **Figure S2.3**). The two H(a′) resonances are indicative of two different nuclei environments of the Br-Sty monomers. Based on the HSQC spectra, the more downfield resonance (H(a′1)) is assigned to a Br-Sty with one neighboring Br-Sty and the more upfield (H(a′2)) resonance is assigned to a Br-Sty with two Br-Sty neighbors. For Blocky B-29%, the relative intensity of the H(a′2) peak to the H(a′1) peak is greater than that of Random R-31%, indicating a greater prevalence of Br-Sty triads in the Blocky copolymer.

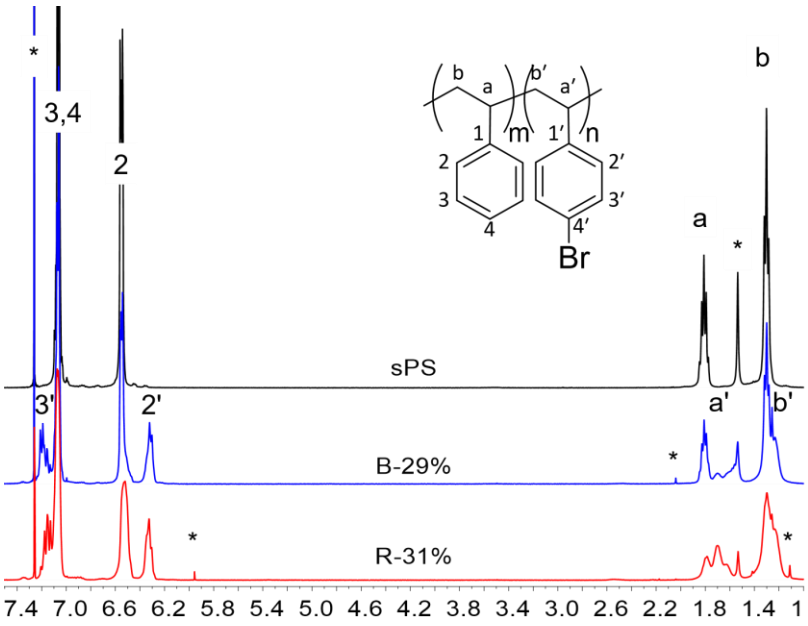

Figure S2.1 Full ^{1}H NMR spectra of pure sPS and the Blocky B-29% and Random R-31% sPS-co-sPS-Br copolymers. ^{1}H NMR spectra were recorded at room temperature and are referenced to $CDCl_3$ and normalized over the range 6.27-6.60 ppm. Asterisks (*) indicate solvent resonances. Reproduced by permission of The Royal Society of Chemistry.

The full quantitative ^{13}C NMR spectra of the sPS homopolymer, Random R-31%, and Blocky B-29%, recorded using a C13IG pulse program, proton decoupled (NOE−), 6 sec relaxation delay, 7680 scans, O1P of 95, and sweep width of 150 ppm, are shown in **Figure S2.2**.

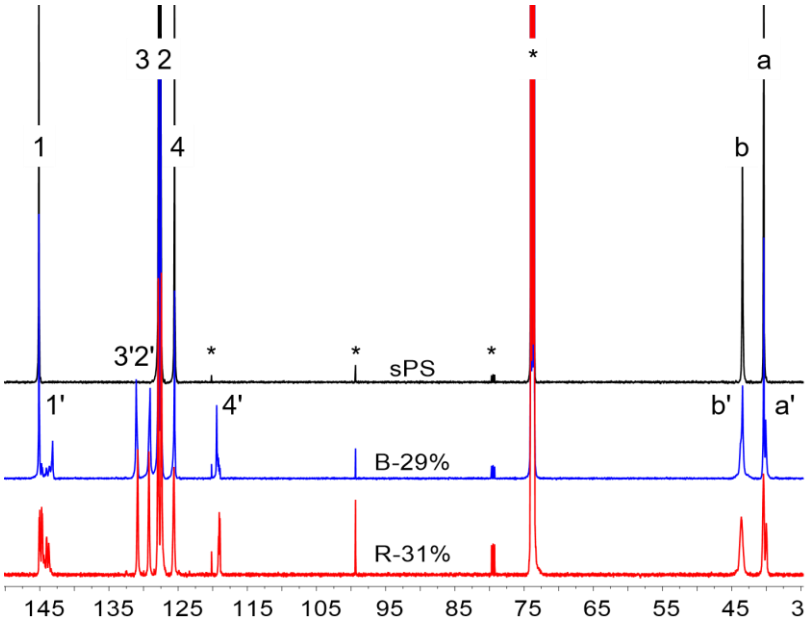

Figure S2.2 Full ^{13}C NMR of pure sPS and the Blocky B-29% and Random R-31% sPS-co-sPS-Br copolymers. The spectra were recorded at room temperature and are referenced to TCE-d_2 and normalized over the range 127.0-132.5 ppm. Asterisks (*) indicate solvent resonances. Reproduced by permission of The Royal Society of Chemistry.

The gHSQC and band-selective heteronuclear multiple bond correlation (bsgHMBC) spectra of Random R-30% and Blocky B-29%, shown respectively in **Figure S2.3** and **Figure S2.4**, were used to assign peaks in the ^{1}H and ^{13}C NMR spectra.

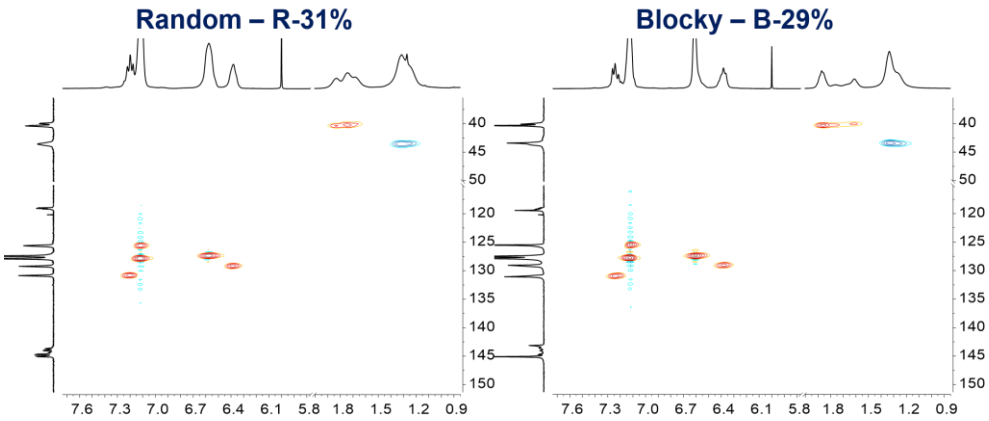

Figure S2.3 ^{1}H-^{13}C gHSQC NMR spectra of (a) Random R-31% and (b) Blocky B-29% referenced to $CDCl_3$. The spectra are cut to improve the clarity of the aromatic and aliphatic regions. Reproduced by permission of The Royal Society of Chemistry.

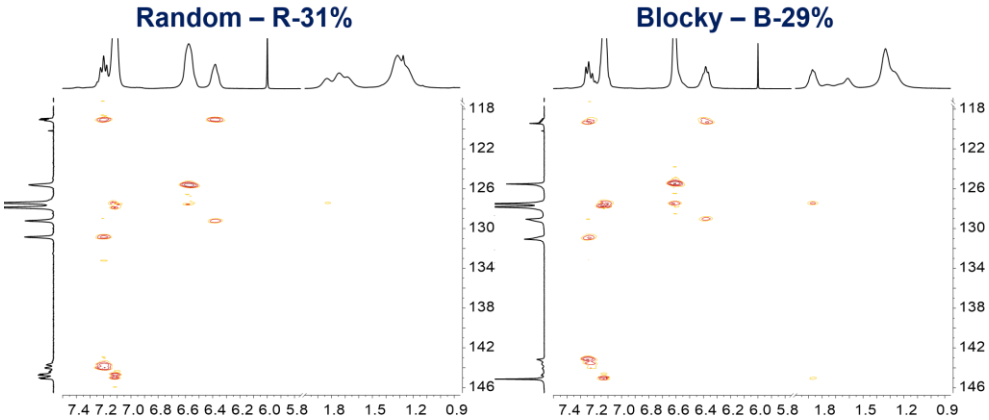

Figure S2.4 bsgHMBC NMR spectra of (left) Random R-31% and (right) Blocky B-29% referenced to TCE-d_2. The spectra are cut to improve the clarity of the aromatic and aliphatic regions. Reproduced by permission of The Royal Society of Chemistry.

The relationship between melting temperature and degree of bromination for the sPS homopolymer and Random and Blocky copolymers is shown in **Figure S2.5**. The reported multiple T_m per sample represent each endothermic peak maximum in the differential scanning calorimetry (DSC) heating scans shown in **Figure 2.4**. Melting point depression is greater in the Random samples, which is consistent with thinner crystallites and supports that the Random copolymers have shorter segments of consecutive styrene units relative to their Blocky analogs.

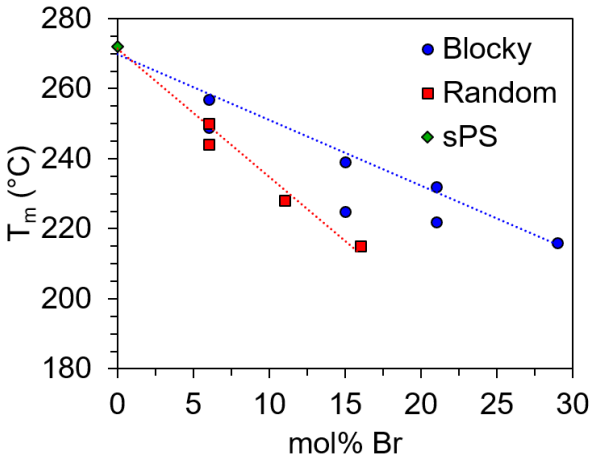

Figure S2.5 Melting temperature (T_m) versus degree of bromination for the Random and Blocky copolymers after the samples were rapidly cooled from the melt at −60 °C min^{-1}. The melting temperature is defined here as the temperature in the heating scan at the peak(s) of the melting endotherm. Dashed lines are linear fits to the highest melting temperatures and are shown to guide the eye. Reproduced by permission of The Royal Society of Chemistry.

The DSC thermograms of the sPS homopolymer and Random and Blocky copolymers during slow cooling from the melt to 0 °C at −10 °C min^{-1} are shown in **Figure S2.6**. For both series, the crystallization exotherm, T_c, decreases in temperature and intensity with increasing Br-content, which reflects a reduction in the rate of crystallization[23, 26]. For the Blocky samples, the T_c occur at lower supercooling compared to their Random analogs, demonstrating that these blocky copolymers crystallize at a faster rate. The faster crystallization kinetics is also supported by the ability of Blocky B-21% to crystallize during the slow cooling conditions. In contrast, at and above 16 mol% Br, the Random samples do not crystallize under these conditions.

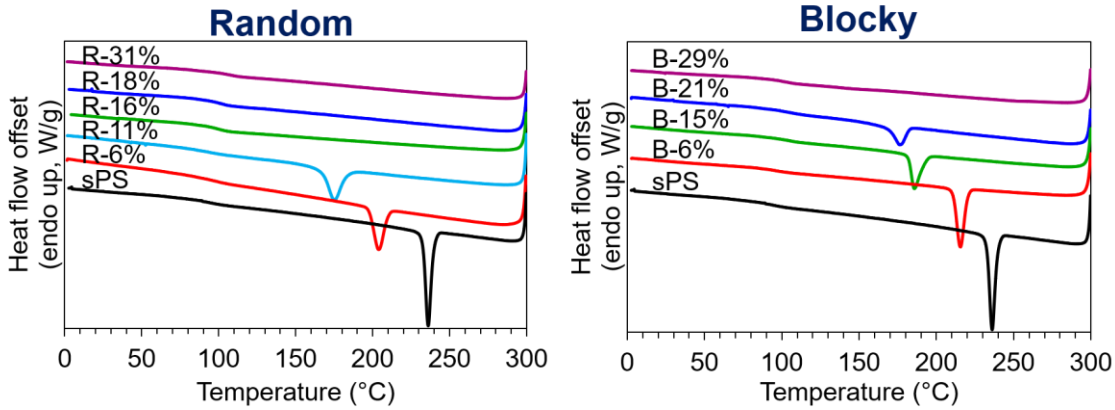

Figure S2.6 DSC slow cooling scans (−10 °C min^{-1}) for the sPS homopolymer and the (left) Random and (right) Blocky copolymers. Reproduced by permission of The Royal Society of Chemistry.

To further investigate the crystallinity of the copolymers, samples were melt crystallized at 190 °C for 2 h and analyzed using wide-angle X-ray diffraction (WAXD). **Figure S2.7** shows the diffraction patterns of the sPS homopolymer and the Random and Blocky copolymers after isothermal crystallization. Observed in the diffractograms of the Random copolymers with 6-16 mol% Br-content and the Blocky copolymers with 6-21 mol% Br-content are crystalline reflections that are consistent with the diffraction pattern of the melt-crystallized sPS homopolymer sample. For the highly brominated Random samples, above 16 mol% Br, the copolymers are completely amorphous. Observed in the diffraction pattern of Blocky B-29% is a new crystalline reflection at 19.3°, which we discuss in further detail in the Morphological characterization subsection.

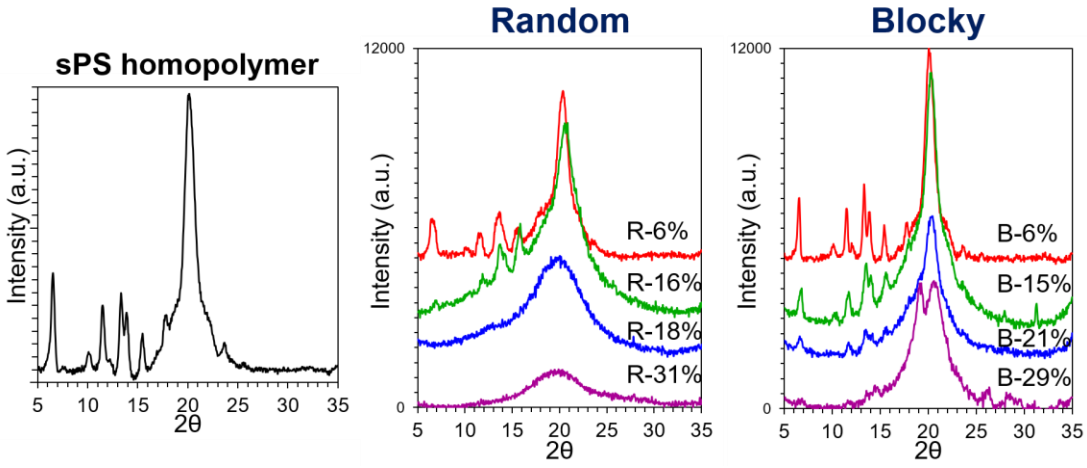

Figure S2.7 Wide-angle X-ray diffractograms of the (left) sPS homopolymer and the (center) Random and (right) Blocky copolymers, after 2 h isothermal crystallization at 190 °C. The powder samples were heated to 300 °C, held for 5 min to erase the thermal history, cooled to 190 °C at −60 °C min^{-1}, held for 2 h, then cooled to 0 °C at −60 °C min^{-1}, and held for 5 min. The WAXD profiles are vertically offset to facilitate a comparison of the peak positions and arranged top to bottom in order of increasing Br-content. Reproduced by permission of The Royal Society of Chemistry.

The WAXD profiles of an sPS quenched film, prepared from sPS pellets by melt pressing between Kapton sheets at 300 °C followed by quenching in ice water to prevent sPS crystallization, and a 10 w/v% sPS/CCl_4 gel that was dried under vacuum at 80 °C for 24 h, are shown in **Figure S2.8**. Microsoft Excel software with Solver was used to fit the amorphous and crystalline

components of the diffractograms to Gaussian distributions. The fit of the amorphous component of the sPS film was used to fit the amorphous component of the 10 w/v% sPS/CCl_4 gel by keeping the position of the Gaussian peaks constant and adjusting the peak amplitude and width. The percentage of the crystalline component in the gel was calculated from the total area of the crystalline component relative to the area of the full diffractogram and found to be 44%.

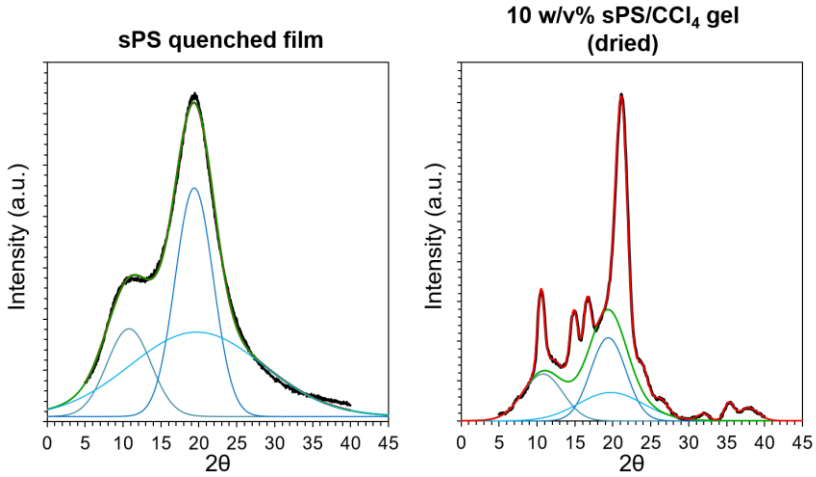

Figure S2.8 In black, diffractograms of (left) an sPS quenched film and (right) a 10 w/v% sPS gel from CCl_4 dried under vacuum at 80 °C for 24 h. Red curve = overall curve fitting; green curve = fit of the amorphous component; Blue curves = individual Gaussian distributions composing the amorphous component. Reproduced by permission of The Royal Society of Chemistry.

The probability of selecting a Br-Sty monomer that exists in a sequence of at least three consecutive Br-Sty monomers (i.e., BBB triads) in the simulated random and blocky copolymer chains of 0-30 mol% Br is shown in **Figure S2.9**. For the simulated 30 mol% Br random copolymer, the percentage of Br-Sty monomers in BBB triads or longer is less than 5%. In contrast, the simulated 30 mol% Br blocky copolymer has a significantly higher prevalence of Br-Sty monomers in sequences of at least three consecutive Br-Sty, demonstrating that the simulated blocky copolymer chains have segments that are densely brominated.

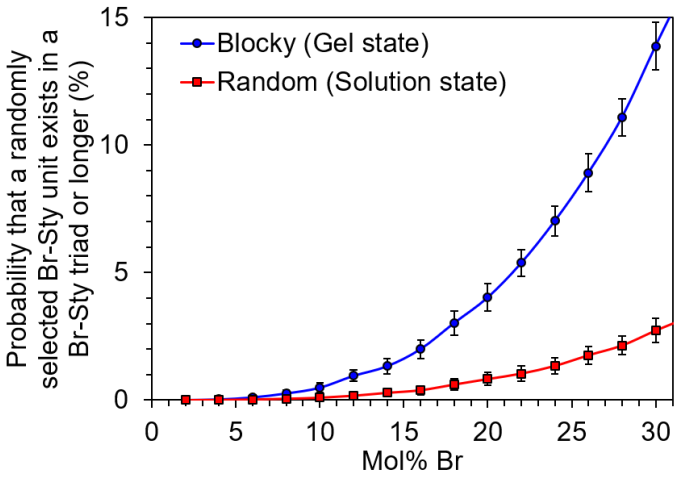

Figure S2.9 Probability that a Br-Sty monomer selected at random exists in a segment of at least three consecutive Br-Sty units from simulations of the theoretical blocky (gel state) or random (solution state) copolymer microstructures. Results based on 1000 polymer chains of 1442 monomer units each. Error bars represent one standard deviation. Reproduced by permission of The Royal Society of Chemistry.

The dimensions of the scattering features in the USAXS/SAXS profiles of the Blocky copolymer samples (**Figure 2.6**) were calculated using the Unified Fit model and are summarized in **Table S2.1**.

Table S2.1. Dimensions of the scattering features in the USAXS/SAXS profiles of semicrystalline sPS and the Blocky copolymers. Reproduced by permission of The Royal Society of Chemistry.

Sample	low *q* (nm)	high *q* (nm)
sPS (semicrystalline)[a]		5.1
B-15%	31.9 ± 0.1	
B-21%	29.7 ± 0.2	
B-29%	34.4 ± 0.2	5.12 ± 0.02

[a]Obtained from Wang et al.[46]
The low *q* feature is between 0.0003 – 0.001 nm^{-1} and the high *q* feature is between 0.001 – 0.01 nm^{-1}.

2.8. Supplementary Information II

```
% This code simulates copolymers with specified degrees of functionalization
%and random or blocky microstructures and then calculates (1) the sequence
%length and frequency of consecutive units; (2) the probability that a unit
%exists in a crystallizable segment; and (3) the prevalence of unique triad
%sequences in the copolymer chain
% This code was created using MATLAB® R2017a programming software

% Authors: Alexandria M. Noble & Kristen F. Noble

%% Variables
chain_length = 1442;  % number of units in one chain
amt = 0.55;  % fraction of inaccessible styrene units (for a random copolymer
      amt = 0)
keep_size = 5;  % units in the inaccessible block (Note: for the purpose of
      demonstrating how the inaccessible block is created the below code is
      written for a keep_size of 5, however the code can be modified for any
      desired keep_size by following the format of
      Block_InaccessibleFraction.m, shown below. This work used a %keep_size of
      53.
r = 1000;  % defines the iterative process that generates r number of chains
ts = 3;  % defines that triad sequences will be counted (Note: the code can be
      modified for any desired sequence (e.g., pentads, heptads, etc.) by
      following the format of TriadSequenceCounting.m, shown below.
l = 26;  % units in one crystallizable segment
percent_functionalization = transpose(0.0:0.02:0.40);  % Simulated degrees of
      functionalization (0-40% at intervals of 2%)

% The copolymer chain will contain 1's to represent styrene (s) units and 0's
      to represent brominated (b) styrene units.

%% Outputs
keep = [];  % stores the fixed styrene indices to create the inaccessible
      fraction
chain_matrix = [];  % stores all chains for one degree of functionalization
store_avg = [];  % stores the average prevalence for each degree of
      functionalization
store_sd = []; % stores the standard deviation of the prevalences for each
      degree of functionalization
P = [];  % stores the probability that a 1 exists in a segment length of j
      consecutive 1 units
store_P = [];  % stores the probability that a 1 exists in a crystallizable
      segment for each chain
Table = [];  % stores the average and standard deviation of the probability
      that a 1 exists in a crystallizable segment for each degree of
      functionalization

for vt = 1:size(percent_functionalization,1)    % for each degree of
      functionalization
    store_P = [];
    for uu = 1:r  % generates r number of chains and performs the following on
      each chain
```

```
  chain = transpose(ones(1,chain_length));  % creates a chain of 1's of
length chain_length
  q  =  round(amt*floor(chain_length));    % defines the number of
inaccessible 1's by the predefined amount (amt)

  fixed_styrene = randsample(chain_length,q);  % selects the inaccessible
1's by random chance

%% run Blocky_InaccessibleFraction.m  % code below
```

%% Blocky_InaccessibleFraction.m

```
% This code establishes the monomer units in the inaccessible fraction
% Note that for the purpose of demonstrating how the inaccessible block is
%created the below code is written for a keep_size of 5, however the code can
%be modified for any desired keep_size by following the format below. %This
%work used a keep_size of 53.
% This code was created using MATLAB® R2017a programming software

% Authors: Alexandria M. Noble & Kristen F. Noble
```

%% -- Begin Code Blocky_InaccessibleFraction -- %%

```
  keep = [];  % stores the fixed styrene indices to create the inaccessible
fraction

  for k = 1:size(fixed_styrene,1)  % repeat until k is the size of the
fixed  styrene  matrix  (based  on  the  predetermined  percent
functionalization and chain length)
      while size(keep,1)< q  % while the size of the keep matrix is less
than the number of inaccessible 1's (q) established above
          if keep_size == 5
              if fixed_styrene(k)-1<1  % prevents the styrene index from
being less than 1 (if fixed_styrene = 1 then keep 1,2,3)
                  keep                                                  =
[keep;fixed_styrene(k);fixed_styrene(k)+1;fixed_styrene(k)+2];
              elseif fixed_styrene(k)-1<2
                  keep            =            [keep;fixed_styrene(k)-
1;fixed_styrene(k);fixed_styrene(k)+1;fixed_styrene(k)+2];
              elseif fixed_styrene(k)+1 > chain_length  % prevents the
styrene index from being greater than the chain length (if chain_length
= 1442 and fixed_styrene = 1442 then keep 1440,1441,1442)
                  keep   =   [keep;fixed_styrene(k)-2;fixed_styrene(k)-
1;fixed_styrene(k)];
              elseif fixed_styrene(k)+2 > chain_length
                  keep   =   [keep;fixed_styrene(k)-2;fixed_styrene(k)-
1;fixed_styrene(k);fixed_styrene(k)+1];
              else
                  keep   =   [keep;fixed_styrene(k)-2;fixed_styrene(k)-
1;fixed_styrene(k);fixed_styrene(k)+1;fixed_styrene(k)+2];
              end
          end
      end
      keep = unique(keep);
  end
```

%% -- End Code Blocky_InaccessibleFraction -- %%

```
  q2 = round(percent_functionalization(vt)*floor(chain_length)); % gives
integer value for the percent functionalization (e.g., 40%*length of
chain)
  I2 = transpose(1:1:chain_length);  % converts a row of integer values
into a column

  xr = [];  % specifies which indices are in the accessible fraction based
on indices in the inaccessible fraction
  for n = 1:size(keep,1)
      xr = [xr;find(I2 == keep(n))];
  end

  I2(xr) = [];  % stores the indices not in keep

  rand_bromine = randsample(I2,q2);    % selects at random without
replacement indices in the chain

  chain(rand_bromine,1) = 0;  % changes specified indices in rand_bromine
to zeros
  chain_matrix(:,uu) = chain;

  x1 = find(chain == 0);  % identify bromines
  x2 = find(chain == 1);  % identify indices where chain is equal to 1

  chain_f(x1,1)={'b'};  % change all 0's in the chain to 'b' for bromine
  chain_f(x2,1)={'s'};  % change all 1's in the chain to 's' for styrene

  %% run TriadSequenceCounting.m  %code below
```

%% TriadSequenceCounting.m

```
% This code indexes the triad combinations in the chain, calculates the
%frequency and prevalence of the unique triad sequences, and creates a matrix
%of the average and standard deviation of the triad sequence prevalences
%calculated from all generated chains
% Note: this code can be modified for any sequence length (e.g., pentad, heptad,
%etc.)
% This code was created using MATLAB® R2017a programming software

% Authors: Alexandria M. Noble & Kristen F. Noble
```

%% -- Begin Code TriadSequenceCounting -- %%

```
  tpseq = {};  % stores the triad sequences identified in the loop below
  for i = 1:chain_length  % loop that repeats based on the chain length
      if i <= chain_length-(ts-1)  % if the step (i) is less than or equal
to the (chain length)-ts-1
          indices =  i:1:i+(ts-1);  % then indices are selected as shown
          if ts == 3
              tpseq                    =                    [tpseq;
[char(chain_f(indices(1))),char(chain_f(indices(2))),char(chain_f(indic
es(3)))], {indices}]; % makes triad sequences from the chain
          end
      end
  end

  if ts == 3  % if calculating the prevalence of triad sequences
```

```
      k = 8;  % there are 8 possible sequences

      C = {'sss'; 'ssb'; 'sbs'; 'sbb'; 'bss'; 'bsb'; 'bbs'; 'bbb'};  %
creates an array of the 8 possible triad sequences
      C = table(C,C,zeros(size(C,1),1),zeros(size(C,1),1));  % creates a
table to store the triad sequences, their frequency, and their prevalence
      C.Properties.VariableNames = {'SeqA','SeqB','Freq','Theo_Prev'};

      for i = 1:size(C,1)   % for each triad sequence in column SeqA,
identify the unique triad sequences in the chain and count their frequency
(e.g., C.SeqA(i))
          flipped = {fliplr(C.SeqA{i,1})};  % flip C.SeqA in order to
count forward and reverse variants of the sequence

          if strcmp(C.SeqA(i),flipped)  % if SeqA equals the flipped SeqA
(e.g., SeqA = 'sss')
              x = find(strcmp(C.SeqA(i),tpseq(:,1)));  % identify the
indices in tpseq where SeqA(i) occurs
              C.SeqB(i) = C.SeqA(i);  % SeqA == SeqB
              C.Freq(i) = size(x,1);  % obtain the size of x, which is
the frequency of each of the symmetric triad sequences without double
counting

          else  % if SeqA does not equal the flipped SeqA (SeqA(i) is
asymmetric)
              C.SeqB(i) = flipped; % populate column SeqB with the
appropriate variant from SeqA (e.g., 'ssb' = 'bss')
              x = size(find(strcmp(C.SeqA(i),tpseq(:,1))),1)+...
                  size(find(strcmp(flipped,tpseq(:,1))),1); % obtain the
size of tpseq for the locations of C.SeqA(i) and the variant in C.SeqB(i)
and add the two size functions together to determine the overall frequency
              C.Freq(i) = x ;   % records the overall frequency of
asymmetric SeqA(i) and its variant
          end
      end
  end

  C.Theo_Prev = C.Freq/size(tpseq,1);  % calculates the prevalence of
each triad sequence as the ratio of the frequency to the total number of
triads in the chain (size of tpseq)

  prev(:,uu) = C{:,4};  % stores the prevalences for each triad sequence
from all generated chains
  avg_prev = mean(prev,2);  % calculates the average of the prevalences
  sd_prev = std(prev,[],2);  % calculates the standard deviation of the
prevalence
```

%% -- End Code TriadSequenceCounting -- %%

```
% Length and frequency of consecutive units

  string = sprintf('%d',chain);  % Converts the chain matrix into a string
with no spaces
```

```
  t1=textscan(string,'%s','delimiter','0','multipleDelimsAsOne',1);    % reads the consecutive 1's from the string using 0's as delimiters (to calculate the segment length of consecutive bromine, the delimiter should be changed from 0 to 1)
  s = t1;  % computes the length of each consecutive segment in the string
  data = cellfun('length',s);  % assigns the length of each segment (e.g., 111 = 3, 111111 = 6)

  [number_times segment_length] = hist(data, 1:(chain_length));  % makes matrices of the segment_lengths and their frequencies in the string

  Table1 = transpose([segment_length;number_times]);   % converts the above arrays into one matrix of segment length and frequency

% Calculate the probability that a 1 is from a segment of at least the crystallizable segment

  j = Table1(:,1);  % segment lengths of consecutive styrene units
  P = [];  % stores the probability that a 1 exists in a segment length of j consecutive 1 units

  for t = 1:size(j,1)  % for each segment length
      S = Table1(:,1).*Table1(:,2);  % calculates the number of 1's in each segment length (segment length*frequency)
      wj    =    (1-percent_functionalization(vt))*(S/(chain_length*(1-percent_functionalization(vt))));  % probability that a unit chosen at random is a 1 and is a member of a sequence of j consecutive units

      if j(t) < l  % if the segment length is less than that of the defined crystallizable segment (l) then P = 0
          P = [P; 0];  % Probability based on Flory, P. J., Theory of Crystallization in Copolymers. T. Faraday Soc. 1955, 51 (0), 848-857.
      elseif j(t) >= l

          P = [P;((j(t)-l+1)/j(t))*wj(t)];  % if the segment length is at least that of the defined crystallizable segment (l) then calculates probability based on Flory, P. J., Theory of Crystallization in Copolymers. T. Faraday Soc. 1955, 51 (0), 848-857.

      end
  end

  sumP = sum(P);  % sums all of the P's to determine the probability that a unit chosen at random is a 1 from a crystallizable segment
  store_P = [store_P;sumP];  % stores the probability that a 1 exists in a crystallizable segment for each chain

end

store_avg = [store_avg, avg_prev];  % stores the average of the prevalences (rows) for each degree of functionalization (columns)
store_sd = [store_sd, sd_prev];  % stores the standard deviation of the prevalences (rows) for each degree of functionalization (columns)
p1 = 100.*(mean(store_P));  % calculates the average of the store_P's for each degree of functionalization
```

```
    p2 = 100.*(std(store_P));   % calculates the standard deviation of the
      store_P's for each degree of functionalization
    Table = [Table; percent_functionalization(vt).*100,p1,p2];   % stores the
      degree of functionalization and the average and standard deviation of the
      probability that a 1 exists in a crystallizable segment

end
```

2.9. References

1. Hadjichristidis, N.; Pispas, S.; Floudas, G. A., *Block Copolymers: Synthetic Strategies, Physical Properties, and Applications*. John Wiley and Sons: New York, 2002.
2. Hamley, I. W., *The Physics of Block Copolymers*. Oxford University Press: New York, 1998.
3. Domski, G. J.; Rose, J. M.; Coates, G. W.; Bolig, A. D.; Brookhart, M., Living Alkene Polymerization: New Methods for the Precision Synthesis of Polyolefins. *Prog. Polym. Sci.* **2007,** *32* (1), 30-92.
4. Fahs, G. B.; Benson, S. D.; Moore, R. B., Blocky Sulfonation of Syndiotactic Polystyrene: A Facile Route toward Tailored Ionomer Architecture via Postpolymerization Functionalization in the Gel State. *Macromolecules* **2017,** *50* (6), 2387-2396.
5. Anderson, L. J.; Yuan, X.; Fahs, G. B.; Moore, R. B., Blocky Ionomers via Sulfonation of Poly(ether ether ketone) in the Semicrystalline Gel State. *Macromolecules* **2018,** *51* (16), 6226-6237.
6. Mochizuki, J.; Sano, T.; Tokami, T.; Itagaki, H., Decisive Properties of Solvent Able to Form Gels with Syndiotactic Polystyrene. *Polymer* **2015,** *67*, 118-127.
7. Shimizu, H.; Wakayama, T.; Wada, R.; Okabe, M.; Tanaka, F., Solvent Effect on Junction Size in Syndiotactic Polystyrene Physical Gel. *Polym. J.* **2005,** *37* (4), 294-298.
8. Kobayashi, M.; Yoshioka, T.; Kozasa, T.; Tashiro, K.; Suzuki, J.; Funahashi, S.; Izumi, Y., Structure of Physical Gels Formed in Syndiotactic Polystyrene/Solvent Systems Studied by Small-Angle Neutron Scattering. *Macromolecules* **1994,** *27* (6), 1349-1354.
9. Roels, T.; Deberdt, F.; Berghmans, H., Solvent Quality and Phase-Stability in Syndiotactic Polystyrene-Solvent Systems. *Macromolecules* **1994,** *27* (21), 6216-6220.
10. Daniel, C.; Guerra, G.; Musto, P., Clathrate Phase in Syndiotactic Polystyrene Gels. *Macromolecules* **2002,** *35* (6), 2243-2251.
11. Venditto, V.; Pellegrino, M.; Califano, R.; Guerra, G.; Daniel, C.; Ambrosio, L.; Borriello, A., Monolithic Polymeric Aerogels with VOCs Sorbent Nanoporous Crystalline and Water Sorbent Amorphous Phases. *ACS Appl. Mater. Inter.* **2015,** *7* (2), 1318-1326.
12. Benson, S. D.; Moore, R. B., Crystallization Behavior of Non-Random Sulfonated Syndiotactic Polystyrene. *Polymer Prepr.* **2009,** *50* (2), 182.

13. Benson, S. D. The Effect of Nanoscale Particles and Ionomer Architecture on the Crystallization Behavior of Sulfonated Syndiotactic Polystyrene. Dissertation, Virginia Polytechnic Institute and State University, Blacksburg, VA, 2010.
14. Borriello, A.; Agoretti, P.; Ambrosio, L.; Fasano, G.; Pellegrino, M.; Venditto, V.; Guerra, G., Syndiotactic Polystyrene Films with Sulfonated Amorphous Phase and Nanoporous Crystalline Phase. *Chem. Mater.* **2009,** *21* (14), 3191-3196.
15. Gibson, H. W.; Bailey, F. C., Chemical Modification of Polymers. 13. Sulfonation of Polystyrene Surfaces. *Macromolecules* **1980,** *13* (1), 34-41.
16. Semler, J. J.; Jhon, Y. K.; Tonelli, A.; Beevers, M.; Krishnamoorti, R.; Genzer, J., Facile Method of Controlling Monomer Sequence Distributions in Random Copolymers. *Adv. Mater.* **2007,** *19* (19), 2877-2883.
17. Jhon, Y. K.; Semler, J. J.; Genzer, J., Effect of Solvent Quality and Chain Confinement on the Kinetics of Polystyrene Bromination. *Macromolecules* **2008,** *41* (18), 6719-6727.
18. Strickland, L. A.; Hall, C. K.; Genzer, J., Design of Copolymers with Tunable Randomness Using Discontinuous Molecular Dynamics Simulation. *Macromolecules* **2009,** *42* (22), 9063-9071.
19. Han, J.; Jeon, B. H.; Ryu, C. Y.; Semler, J. J.; Jhon, Y. K.; Genzer, J., Discriminating Among Co-monomer Sequence Distributions in Random Copolymers Using Interaction Chromatography. *Macromol. Rapid Comm.* **2009,** *30* (18), 1543-1548.
20. Jhon, Y. K.; Semler, J. J.; Genzer, J.; Beevers, M.; Gus' kova, O. A.; Khalatur, P. G.; Khokhlov, A. R., Effect of Comonomer Sequence Distribution on the Adsorption of Random Copolymers onto Impenetrable Flat Surfaces. *Macromolecules* **2009,** *42*, 2843-2853.
21. Gurarslan, R.; Hardrict, S.; Roy, D.; Galvin, C.; Hill, M. R.; Gracz, H.; Sumerlin, B. S.; Genzer, J.; Tonelli, A., Beyond Microstructures: Using the Kerr Effect to Characterize the Macrostructures of Synthetic Polymers. *J. Polym. Sci. B Polym. Phys.* **2015,** *53* (3), 155-166.
22. Liu, S.; Sen, A., Syntheses of Syndiotactic-Polystyrene-graft-Poly(methyl methacrylate), Syndiotactic-Polystyrene-graft-Poly(methyl acrylate), and Syndiotactic-Polystyrene-graft-Atactic-Polystyrene with Defined Structures by Atom Transfer Radical Polymerization. *Macromolecules* **2000,** *33* (14), 5106-5110.
23. Gao, Y.; Li, H. M., Synthesis and Characterization of Acetylated Syndiotactic Polystyrene. *Polym. Int.* **2004,** *53* (10), 1436-1441.

24. Weiss, R. A.; Turner, S. R.; Lundberg, R. D., Sulfonated Polystyrene Ionomers Prepared by Emulsion Copolymerization of Styrene and Sodium Styrene Sulfonate. *J. Polym. Sci. A Polym. Chem.* **1985,** *23* (2), 525-533.
25. Weiss, R. A.; Lundberg, R. D.; Turner, S. R., Comparisons of Styrene Ionomers Prepared by Sulfonating Polystyrene and Copolymerizing Styrene with Styrene Sulfonate. *J. Polym. Sci. A Polym. Chem.* **1985,** *23* (2), 549-568.
26. Annunziata, L.; Sarazin, Y.; Duc, M.; Carpentier, J. F., Well-defined Syndiotactic Polystyrene-b-Atactic Polystyrene Stereoblock Polymers. *Macromol. Rapid Comm.* **2011,** *32* (9-10), 751-757.
27. Shin, J.; Chang, Y.; Nguyen, T. L. T.; Noh, S. K.; Bae, C., Hydrophilic Functionalization of Syndiotactic Polystyrene via a Combination of Electrophilic Bromination and Suzuki–Miyaura Reaction. *J. Polym. Sci. A Polym. Chem.* **2010,** *48* (19), 4335-4343.
28. Howe, D. H.; McDaniel, R. M.; Magenau, A. J. D., From Click Chemistry to Cross-Coupling: Designer Polymers from One Efficient Reaction. *Macromolecules* **2017,** *50* (20), 8010-8018.
29. Shen, Q.; Hartwig, J. F., Palladium- Catalyzed Coupling of Ammonia and Lithium Amide with Aryl Halides. *J. Am. Chem. Soc.* **2006,** *128* (31), 10028-10029.
30. Ilavsky, J.; Zhang, F.; Andrews, R. N.; Kuzmenko, I.; Jemian, P. R.; Levine, L. E.; Allen, A. J., Development of combined microstructure and structure characterization facility for in situ and operando studies at the Advanced Photon Source. *J. Appl. Crystallogr.* **2018,** *51* (3), 867-882.
31. Ilavsky, J.; Zhang, F.; Allen, A. J.; Levine, L. E.; Jemian, P. R.; Long, G. G., Ultra-Small-Angle X-ray Scattering Instrument at the Advanced Photon Source: History, Recent Development, and Current Status. *Metall. Mater. Trans. A* **2013,** *44* (1), 68-76.
32. Ilavsky, J., Nika: software for two-dimensional data reduction. *J. Appl. Crystallogr.* **2012,** *45* (2), 324-328.
33. Ilavsky, J.; Jemian, P. R., Irena: tool suite for modeling and analysis of small-angle scattering. *J. Appl. Crystallogr.* **2009,** *42* (2), 347-353.
34. Guo, F.; Jiao, N.; Jiang, L.; Li, Y.; Hou, Z., Scandium-Catalyzed Syndiospecific Polymerization of Halide-Substituted Styrenes and Their Copolymerization with Styrene. *Macromolecules* **2017,** *50* (21), 8398-8405.

35. Gurarslan, R.; Gurarslan, A.; Tonelli, A. E., Characterizing Polymers with Heterogeneous Micro- and Macrostructures. *J. Polym. Sci. B Polym. Phys.* **2015,** *53* (6), 409-414.
36. Hardrict, S. N.; Gurarslan, R.; Galvin, C. J.; Gracz, H.; Roy, D.; Sumerlin, B. S.; Genzer, J.; Tonelli, A. E., Characterizing Polymer Macrostructures by Identifying and Locating Microstructures Along Their Chains with the Kerr Effect. *J. Polym. Sci. B Polym. Phys.* **2013,** *51* (9), 735-741.
37. Gurarslan, R.; Tonelli, A. E., An Unexpected Stereochemical Bias in the RAFT Syntheses of Styrene/p-Bromostyrene Copolymers Uncovered by the Kerr Effect. *Polymer* **2016,** *89*, 50-54.
38. Yang, J. C.; Jablonsky, M. J.; Mays, J. W., NMR and FT-IR Studies of Sulfonated Styrene-based Homopolymers and Copolymers. *Polymer* **2002,** *43* (19), 5125-5132.
39. Dickinson, L. C.; Weiss, R.; Wnek, G. E., NMR Characterization of Sulfonation Blockiness in Copoly(styrene−sulfonated styrene). *Macromolecules* **2001,** *34* (9), 3108-3110.
40. Chang, B.; Zeigler, R.; Hiltner, A., Chlorinated High Density Polyethylene. I. Chain Characterization. *Polym. Eng. Sci.* **1988,** *28* (18), 1167-1172.
41. Wang, Z.; Liu, D.; Cui, D., Statistically Syndioselective Coordination (Co) polymerization of 4-Methylthiostyrene. *Macromolecules* **2016,** *49* (3), 781-787.
42. Liu, D.; Wang, M.; Wang, Z.; Wu, C.; Pan, Y.; Cui, D., Stereoselective Copolymerization of Unprotected Polar and Nonpolar Styrenes by an Yttrium Precursor: Control of Polar-Group Distribution and Mechanism. *Angew. Chem.* **2017,** *129* (10), 2758-2763.
43. Annunziata, L.; Monasse, B.; Rizzo, P.; Guerra, G.; Duc, M.; Carpentier, J.-F., On the Crystallization Behavior of Syndiotactic-b-Atactic Polystyrene Stereodiblock Copolymers, Atactic/Syndiotactic Polystyrene Blends, and aPS/sPS Blends Modified with sPS-b-aPS. *Mater. Chem. Phys.* **2013,** *141* (2–3), 891-902.
44. Gianotti, G.; Valvassori, A., Fusion Enthalpy and Entropy of Syndiotactic Polystyrene. *Polymer* **1990,** *31* (3), 473-475.
45. Tonelli, A. E.; Jhon, Y. K.; Genzer, J., Glass Transition Temperatures of Styrene/4-BrStyrene Copolymers with Variable Co-Monomer Compositions and Sequence Distributions. *Macromolecules* **2010,** *43* (16), 6912.
46. Wang, H.; Wu, C.; Cui, D.; Men, Y., Lamella thickness Dependence of Crystal Modification Selection in the Syndiotactic Polystyrene γ-to-α/β Phase Transition Process. *Macromolecules* **2018,** *51* (2), 497-503.

47. Woo, E. M.; Sun, Y. S.; Yang, C. P., Polymorphism, thermal behavior, and crystal stability in syndiotactic polystyrene vs. its miscible blends. *Prog. Polym. Sci.* **2001,** *26* (6), 945-983.
48. Girolamo Del Mauro, A. D.; Loffredo, F.; Venditto, V.; Longo, P.; Guerra, G., Polymorphic Behavior of Syndiotactic Poly(p-chlorostyrene) and Styrene/p-Chlorostyrene Cosyndiotactic Random Copolymers. *Macromolecules* **2003,** *36* (20), 7577-7584.
49. Xu, H.; Ince, B. S.; Cebe, P., Development of the Crystallinity and Rigid Amorphous Fraction in Cold-crystallized Isotactic Polystyrene. *J. Polym. Sci. B Polym. Phys.* **2003,** *41* (23), 3026-3036.
50. De Rosa, C.; Guerra, G.; Petraccone, V.; Pirozzi, B., Crystal Structure of the Emptied Clathrate Form (δe Form) of Syndiotactic Polystyrene. *Macromolecules* **1997,** *30* (14), 4147-4152.
51. Flory, P. J., Theory of Crystallization in Copolymers. *T. Faraday Soc.* **1955,** *51* (0), 848-857.
52. Daniel, C.; Avallone, A.; Guerra, G., Syndiotactic polystyrene physical gels: Guest influence on structural order in molecular complex domains and gel transparency. *Macromolecules* **2006,** *39* (22), 7578-7582.

Chapter 3.

High Resolution Comonomer Sequencing of Brominated Syndiotactic Polystyrene using ^{13}C NMR spectroscopy and Computer Simulations

Kristen F. Noble, Samantha J. Talley, Gregory B. Fahs, Diego Troya, and Robert B. Moore

3.1. Abstract

This work demonstrates the first high-resolution comonomer sequencing of brominated syndiotactic polystyrene (sPS-*co*-sPS-Br) copolymers based on pentad assignments of the quaternary carbon region of the nuclear magnetic resonance (NMR) spectrum. To develop a comonomer sequencing method, copolymers were prepared using a post-polymerization bromination method carried out in the heterogeneous gel-state and homogeneous solution-state to produce a matched set of copolymers containing 6−30 mol% *p*-bromostyrene units. Characterization of the quaternary carbon spectrum using heteronuclear multiple bond correlation (HMBC) spectroscopy, electronic structure calculations, and simulated statistically random copolymers, revealed that the peaks in the quaternary carbon region could be assigned to styrene and brominated styrene (Br-Sty) units that exist in the center of a unique sequence of five monomers (i.e., a pentad) along the copolymer chain (e.g., ssssb where s = styrene and b = brominated styrene). Using the comonomer sequencing method, peak assignments have been established for all 20 unique pentad sequences that are possible for a copolymer that contains two different monomers. Comparison of the pentad sequence distributions of the brominated copolymers, calculated from the relative area of the peaks in the NMR spectrum, revealed that the gel-state Blocky copolymers have higher degrees of blockiness and significantly larger fractions of bbbbb pentad at relatively low Br-contents (i.e., 29 mol% Br). From the pentad sequence

distributions of the brominated copolymers, simulated average copolymer chains were developed, in order to obtain a deeper understanding of the relationship between the sPS/solvent gel morphology and the copolymer microstructure and degree of blockiness resulting from heterogeneous functionalization. The simulated average chains correctly predict that the Blocky copolymers contain a higher prevalence of crystallizable sPS segments, based on the copolymer microstructure and distribution of block lengths in the simulated chains, and confirmed by experimental results obtained from differential scanning calorimetry (DSC) experiments. Thus, the simulated average chains appear to be representative of average chains in their respective Blocky samples. The simulated average chains of the Blocky copolymers also predict the presence of long blocks of consecutive styrene units along the copolymer chains of at least 39 units, which is in excellent agreement with the estimated number of styrene units in a crystalline stem within the sPS/carbon tetrachloride (CCl_4) gel network of approximately 38−40 units, determined from analysis of the intercrystalline scattering feature in the small-angle X-ray scattering (SAXS) profile of the as prepared sPS/CCl_4 gel. This work thus affirms that during gel-state bromination, functionalizing reagent is impeded from reacting with monomers in the crystalline component of the gel network, producing copolymers with long runs of un-functionalized styrene units that originate from the crystalline stems within the crystalline lamellae.

3.2. Introduction

The physical properties of polystyrene (PS)-based copolymers depend upon the microstructure of the polymer chains, i.e., the tacticity of the repeating units and the sequence distribution of the monomers.[1-7] In syndiotactic polystyrene (sPS), the styrene units are arranged in a regular stereochemical configuration, such that the phenyl rings alternate from side to side with respect to the carbon chain, which is confirmed by sharp signals in the ^{13}C nuclear magnetic

resonance (NMR) spectrum. This stereoregularity allows the chain segments to adopt an ordered conformation and form crystalline regions. Nevertheless, for sPS-based copolymers, functional groups attached to the styrene phenyl ring can act as physical defects along the polymer chains, which limits copolymer crystallizability.[2,8,9] Recently, we demonstrated a new post-polymerization functionalization method carried out in the heterogeneous gel state that is capable of preparing *semicrystalline* brominated syndiotactic polystyrene (sPS-co-sPS-Br) copolymers with relatively high Br-content (i.e., 29 mol% Br).[8] The gel-state bromination process is believed to restrict brominating reagent to monomers well removed from the crystalline component of the gel network, preserving long runs of consecutive styrene units along the chains. The gel-state brominated copolymers are more crystalline, more crystallizable, and crystallize faster than their random copolymer analogs prepared by a conventional solution-state bromination method, even at relatively high degrees of functionality. This crystallization behavior is attributed to a significant degree of non-randomness in the distribution of comonomers along the copolymer chain, which herein will be described as a copolymer with a "blocky" microstructure. To develop a deeper understanding of the relationship between the sPS/solvent gel morphology and the copolymer microstructure and degree of blockiness, the current work is focused on the development of the first high-resolution comonomer sequencing of sPS-*co*-sPS-Br copolymers by ^{13}C NMR spectroscopy.

The NMR signal of the phenyl ring quaternary (C(1)) carbon in PS and its phenyl-ring substituted derivatives exhibits high sensitivity to monomer addition stereochemistry (i.e., tacticity),[10-17] composition,[18,19] and comonomer sequence distribution.[7,9,20,21] Nevertheless, due to complexities in the C(1) resonances that arise from stereoirregularity and the chemical similarity of para-substituted styrene monomers, attempts by others to evaluate the comonomer sequence

distribution of atactic polystyrene (aPS)-based copolymers by NMR have been generally unsuccessful.[3,22-28] Our syndiotactic sPS-*co*-sPS-Br copolymers, with high tactic purity, exhibit high-resolution of the quaternary carbon resonances for styrene (C(1)) and brominated styrene (Br-Sty, C(1′)) monomers that is now understood to be sensitive to neighboring monomers, which permits copolymer sequencing.[7,9,19] This sensitivity is at the pentad level, i.e., the resonance frequency of a particular C(1) or C(1′) signal depends on the identity of that particular monomer's neighboring and next-neighboring monomers in the polymer chain, such that every possible pentad combination of monomers presents a distinct chemical shift for the central C(1) or C(1′) nucleus.

Assignment of the C(1) resonances to stereosequences or, for some syndiotactic PS copolymers, dyad or triad comonomer sequences, has been achieved by comparing the relative peak areas of the C(1) resonances to either Bernoullian[13-17] (i.e., statistically random) or first- or second-order Markov (i.e., statistically non-random) models.[7,9,29] For example, Hardwood et al.[11,30,31] simulated polymer epimerization using a Monte-Carlo method to count the frequency of triad scombinations in simulated epimerized chains in order to assign triad stereosequences in partially epimerized isotactic polystyrene (iPS) samples. Using Bernoullian and hemiisotactic statistical methods to simulate homopolymer chains with a broad range of isotactic content, Miller[32] was able to predict the elastomeric properties of polypropylene (PP) samples based on the presence of crystallizable isotactic blocks in theoretical PP copolymers and pentad sequence distributions from experiment. Model compounds of PS or its derivatives, i.e., oligomers of a parent polymer, have also been used to assign stereosequences of the C(1) resonance.[10,18]

Cui et al.[9] were recently able to assign the C(1) resonances in a syndiotactic styrene-co-4-methylthiostyrene copolymer to triad combinations of monomers based on the conformity of the relative peak areas to first-order Markov statistics. These statistical models are particularly relevant

for copolymers prepared by direct polymerization methods, where the catalyst and monomer reactivity ratio often control the stereoregularity and composition of the growing polymer chain. Systematic changes to the monomer feed ratio or reaction time effect monomer conversion and thus, the relative peak areas observed in the ^{13}C NMR spectrum can be compared to statistical probabilities in order to make peak assignments.[7,9,29] For some copolymers, two dimensional (2D) heteronuclear NMR spectroscopy techniques may prove useful for identifying peaks that arise from specific monomers.[20,26,27]

From the distribution of comonomer sequences, obtained from the relative area of the peaks in the ^{13}C NMR spectrum, the copolymer block character (i.e., blockiness) and average block length of consecutive like monomers may be determined based on Bernoullian statistics.[33-35] These calculated values are a useful addition to comonomer sequencing in that they provide deeper insight into the copolymer microstructure, which may help to explain observed differences in copolymer crystallization behavior and morphology for samples with similar comonomer content. For example, Randall[33] was able to calculate the average block length of isotactic PP segments in amorphous and crystalline polypropylenes to investigate PP crystallizability.

In this work, ^{13}C NMR spectroscopy was used to investigate the copolymer microstructure and comonomer sequence distribution of ring brominated sPS copolymers prepared by a post-polymerization functionalization method carried out in the heterogenous gel state. Gels of crystallizable homopolymers (e.g., sPS) are composed of tightly packed chain segments in lamellar crystallites that act as physical cross-links bound together by a percolating network of solvent swollen amorphous chains.[36-40] When functionalizing reagent is introduced to the heterogeneous gel network, it is believed to be sterically excluded from reacting with monomer units in the crystalline component and thus, only reacts with monomers in the accessible interconnecting

amorphous component. Using this straightforward post-polymerization functionalization approach, the resulting copolymer is likely to contain separate segments of randomly functionalized "blocks" and un-functionalized "blocks" originating from monomer units that were isolated within crystalline domains of the gel.[8,41,42] Thus, the block lengths of consecutive styrene units in the gel-state functionalized copolymers are anticipated to correspond with the average number of styrene units in a crystalline stem within the crystalline lamellae of the gel network.

This work reports the first high-resolution comonomer sequencing of sPS-*co*-sPS-Br copolymers based on pentad assignments of the quaternary carbon region of the quantitative ^{13}C NMR spectrum. The purpose of this research was to develop a comonomer sequencing method for brominated sPS copolymers in order to obtain a deeper understanding of the relationship between the sPS/solvent gel morphology and the copolymer microstructure and degree of blockiness that results from post-polymerization functionalization in the gel state. To develop the comonomer sequencing method, two series of copolymers were prepared in a matched set containing 6-30 mol% *p*-bromostyrene units using a post-polymerization functionalization method carried out in the homogenous solution-state (Random) and heterogeneous gel-state (Blocky). The comonomer sequencing method was investigated using band selective gradient heteronuclear multiple bond correlation (bsgHMBC) spectroscopy, electronic structure calculations, and simulated random copolymers. Based on the experimentally-determined pentad sequence distributions, obtained from this comonomer sequencing method, simulated average chains were generated to predict the copolymer microstructure and distribution of block lengths in the brominated copolymers. To help rationalize the effect of copolymer microstructure and degree of blockiness on the crystallization behavior of the gel-state functionalized copolymers, differential scanning calorimetry was used to investigate copolymer crystallizability, X-ray scattering techniques were used to estimate the

average lamella thickness in the brominated copolymers, and these experimental data were compared to the block length distributions in the simulated average chains. X-ray scattering techniques were also used to estimate the average number of styrene units in a crystalline stem within the sPS/solvent gel network. This work affirms that post-polymerization functionalization carried out in the heterogenous gel state produces copolymers with long runs of un-functionalized styrene units that originate from the crystalline stems within the crystalline lamellae of the gel network. Given the ability to control the precise morphology of the semicrystalline gel network, specifically through changing the polymer concentration,[43] gelation solvent,[36-38,44] and/or gelation conditions,[45] the broader scope of this work is to use the comonomer sequencing method and simulations to predict the copolymer microstructure and degree of blockiness of other sPS-based copolymers for the tailored design of new functional materials.

3.3. Experimental Section

3.3.1. Sample preparation

The preparation of the Random and Blocky sPS-co-sPS-Br copolymers by homogeneous and heterogeneous post-polymerization bromination methods, respectively, is described in **Chapter 2**.[8] Briefly, the Random copolymers (R-*x*%) were prepared by introducing a stock solution of bromine (Br_2) in 1,1,2,2-tetrachloroethane (TCE) to a solution of sPS homopolymer (Questra® 102, 300,000 g mol^{-1} weight average molecular weight) in TCE. The reaction was carried out in the dark under argon and the molar ratio of Br_2 to styrene monomer was varied to control the degree of bromination. The Random copolymers have *p*-bromostyrene (Br-Sty) compositions of approximately x = 6, 16, 18, and 31 mol%, determined by ^{1}H NMR spectroscopy. The Blocky copolymers (B-*x*%) were prepared by introducing a stock solution of Br_2 in

1,2-dichloromethane (DCM) to small pieces of a 10 w/v% sPS / carbon tetrachloride (CCl_4) gel suspended in DCM. The reaction was carried out in the dark under argon and the reaction time was varied to control the degree of bromination. The Blocky copolymers have Br-Sty compositions of approximately x = 6, 15, 21, and 29 mol%. A 10 w/v% sPS/CCl_4 gel was prepared for ultra-small-angle (USAXS) and small-angle X-ray scattering (SAXS) experiments by dissolving sPS pellets in CCl_4 at 120-140 °C in a pressure vessel, capturing a fraction of the 10 w/v% sPS/CCl_4 solution in a thin-walled, 3 mm outer diameter glass tube, and removing from heat to promote gel formation. A 10 w/v% sPS/CCl_4 was prepared for wide-angle X-ray diffraction (WAXD) experiments by dissolving sPS pellets in CCl_4 at 120-140 °C in a pressure vessel, followed by removing from heat to promote gel formation. The gel was stored at room temperature for ca. 24 h to mimic the conditions prior to gel-state bromination. Then, the gel was broken into pieces with a spatula and immediately dried under vacuum at 70 °C for ca. 24 h. Melt-crystallized samples of the sPS homopolymer and the Random and Blocky copolymers were prepared by annealing the samples at 300 °C (or 325 °C for Blocky B-29%) for 5 min to erase thermal history, followed by isothermal crystallization for 2 h at 190 °C.

3.3.2. NMR spectroscopy

Microstructure analysis and comonomer sequencing of the sPS-*co*-sPS-Br copolymers was carried out using nuclear magnetic resonance (NMR) spectroscopy. ^{1}H-^{13}C band-selective gradient heteronuclear multiple bond correlation (bsgHMBC) experiments were recorded at room temperature in 1,1,2,2-tetrachlorethane-d_2 (TCE-d_2) on an Agilent U4-DD2 400 MHz spectrometer. Spin-lattice relaxation time, T_1, experiments for ^{13}C were measured at room temperature in TCE-d_2 on a Bruker Avance II 500 MHz NMR spectrometer equipped with an LN2 prodigy cryogenic BBO probe using inversion recovery with a power gated decoupling pulse

sequence (t1irpg). This pulse program produces a serial file (parameter mode = 2D), therefore the T_1 experiment was carried out in a 2D mode with size of fid (32768, 9), 8 scans per increment, 40 sec relaxation delay, and 9 variable delays (0.1, 0.2, 0.4, 0.8, 1.6, 3.2, 6.4, 12.8, 25.6 sec) from the variable delay list. The acquired data was processed using Topspin 3.2 software and T_1 was calculated by an area fitting method. The calculated T_1 values for the quaternary carbon of sPS homopolymer (C(1)) and a Random R-93% copolymer (C(1′)) were 0.68 sec and 0.71 sec, respectively. Quantitative ^{13}C NMR experiments were recorded at room temperature in TCE-d_2 on a Bruker Avance II 500 MHz spectrometer equipped with a LN2 Prodigy cryogenic BBO probe using a C13IG pulse program, proton decoupling (NOE−), 6 sec relaxation delay, 7680 scans per increment, O1P of 95, and sweep width of 150 ppm. The Line Fitting function in Mestrelab Research's MestReNova x64 software was used to deconvolute and integrate the multiple peaks in the quaternary carbon region of the ^{13}C NMR spectrum. The deconvolution method is discussed in more detail in the Results and discussion section.

3.3.3. Thermal properties

Copolymer crystallizability was probed used differential scanning calorimetry (DSC, TA Instruments DSC Q2000) under continuous nitrogen flow. Samples were first annealed at 300 °C (325 °C for Blocky B-29%) for 3 min to erase thermal history, then cooled to 0 °C at −10 °C min^{-1}, followed by heating at 10 °C min^{-1}. TA Instruments Universal Analysis software was used to determine the area under the melting endotherm (ΔH_f).

3.3.4. X-ray scattering

X-ray scattering techniques were used to characterize the morphology of a 10 w/v% sPS/CCl_4 gel. Ultra-small angle (USAXS) and small-angle (SAXS) X-ray scattering experiments

were performed at the Advanced Photon Source beamline 9ID-C at Argonne National Laboratory.[46-48] The USAXS instrument was configured in standard mode with an X-ray energy of 21 keV (λ = 0.5895 Å), X-ray photon flux of ca. 1013 mm^{-2} s^{-1}, and a combined scattering vector, *q*, range of 0.0001–1.3 $Å^{-1}$ ($q = 4\pi/\lambda \sin(\theta)$, where λ is the wavelength and θ is one-half of the scattering angle). The desmeared USAXS and SAXS profiles were acquired sequentially and merged into a single data set using the Irena SAS package.[49] SAXS experiments were performed on melt-crystallized samples of the sPS homopolymer and the Random and Blocky copolymers using a Rigaku S-Max 3000 3 pinhole SAXS system equipped with a rotating anode that emits X-rays with a wavelength of 0.154 nm (Cu Kα). The sample-to-detector distance was 1605 mm. The *q* range was calibrated using a silver behenate standard. Two-dimensional SAXS patterns were obtained using a fully integrated 2D multiwire, proportional counting, gas-filled detector with an exposure time of 2 h. The SAXS data were analyzed using the SAXSGUI software package to obtain radially integrated SAXS intensity versus *q*. The center-to-center intercrystalline domain spacing, i.e., long period (L_p), and average crystal thickness were calculated from the crystalline scattering feature of Lorentz-corrected SAXS profiles using the one-dimensional (1D) correlation function and a linear two-phase model. Wide-angle X-ray diffraction (WAXD) experiments were performed using a Rigaku MiniFlex II X-ray diffractometer emitting X-rays with a wavelength of 0.154 nm ($Cu K_\alpha$). Samples were scanned from 5° to 40° 2θ at a scan rate of 0.250° 2θ min^{-1} and a sampling window of 0.050° 2θ at a potential of 30 kV and a current of 15 mA. The WAXD data was analyzed using the PDXL 2 software package to obtain WAXD intensity *versus* 2θ profiles. The volume fraction of crystallinity, $\%X_c$, was calculated from the WAXD profile through deconvolution of the crystalline and amorphous contributions and integration, according to **Equation 1**:

$$\%X_c = \frac{I_c}{I_c + I_a} \quad (1)$$

where I_c and I_a are the integrated intensities of the crystalline and amorphous contributions, respectively. To deconvolute the WAXD profile, the crystalline reflections and amorphous contributions were individually fit using Gaussian functions.

3.3.5. Comonomer sequence counting in simulated random copolymer chains

Simulated random copolymer chains were generated using a code created in-house with MATLAB® R2017a programming software. For each desired Br-content, the code simulates 1000 homopolymer chains of 1442 monomer units (based on our sPS sample, M_w = 300K; Đ = 2.0) and selects monomers along the chain at random up to the desired degree of bromination. Along each chain, the frequency of each triad sequence (e.g., SSS, BBB, etc.) and pentad sequence (e.g., SSSSS, BBBBB, *etc*.) is counted. The prevalence of each of the 6 unique triad sequences and 20 unique pentad sequences is calculated by dividing the frequency of a particular sequence by the total number of triad or pentad sequences, respectively, in the chain, which is discussed in more detail below in the Results and discussion section.

3.3.6. Theoretical quaternary carbon chemical shifts

Theoretical chemical shifts of the quaternary carbon nuclei in the 6 unique triad sequences were computed using electronic structure calculations. The calculation model consisted of three consecutive monomers terminated by two ethyl capping units. Geometry optimizations and harmonic frequencies were obtained using the B3LYP density functional and the def2svp basis set as implemented in Gaussian 09.[50] NMR shielding tensors were computed using the Gauche Invariant Atomic Orbital formalism also in Gaussian. The reported chemical shifts for the

quaternary carbon nuclei of the central monomer in the triads were obtained via reference to the isotropic shielding of an internal tetramethylsilane standard calculated at the same level of theory.

3.3.7. Simulated average copolymer chains based on the experimental pentad sequence distributions

Simulated chains that represent the average copolymer chain sequence in the Random and Blocky copolymers, were created using a Fortran code created in-house. Chains are simulated from a short sequence of un-functionalized styrene units by subsequent additions of short sequences of un-functionalized and functionalized styrene units to the chain end. The rationalization for the specific short sequence that is added during each addition step is based on the difference between the average pentad sequence distribution of the simulated chain and the pentad sequence distribution from the NMR data and is discussed in more detail below in the Results and discussion section.

3.4. Results and Discussion

3.4.1. ^{13}C NMR spectroscopy and comonomer sequence distribution

Quantitative ^{13}C NMR spectroscopy was used to investigate the microstructure and comonomer sequence distribution of the solution-state (Random, R-x%) and gel-state (Blocky, B-x%) sPS-*co*-sPS-Br copolymers. For comparison, the Random and Blocky copolymers were prepared in a matched set of approximately x = 6, 15, 20, and 30 mol% brominated styrene (Br-Sty) units, determined from the ^{1}H NMR spectra.[8] **Figure 3.1** compares the high-resolution, quaternary carbon (C(1) and C(1′)) NMR spectra of the sPS homopolymer and the Random and Blocky copolymers. The sPS homopolymer exhibits a single peak at 145.15 ppm that corresponds to the C(1) resonance of an un-functionalized styrene unit. Upon *para*-substitution of the styrene phenyl

rings with bromine, new resonances appear in the ^{13}C NMR spectrum. For the Random copolymers, the new peaks increase in intensity with increasing Br-content. The multiple peaks in the sPS-*co*-sPS-Br copolymers signify through-bond communication between neighboring styrene and Br-Sty monomers and provides a unique fingerprint of the copolymer microstructure originating from the specific comonomer sequence distribution. For the Blocky copolymers, the quaternary carbon peak distributions and intensities differ discernibly from their Random analogs at all degrees of bromination, which is emphasized by the new resonance in Blocky B-21% and B-29% at 143.1−143.3 ppm. These differences in peak distribution and intensity unambiguously show that copolymers prepared by gel-state bromination have a different comonomer sequence distribution compared to their solution-state analogs.

The peaks in the quaternary carbon region appear to be clustered into 6 groups, which are labeled A−F in **Figure 3.1** and are clearly observed in the spectrum of Random R-31%. The observed number of groups is in excellent agreement with the 6 unique triad combinations (8 total combinations) that are possible in a copolymer that contains two different monomers (i.e., S**S**S, [S**S**B/B**S**S], B**S**B, S**B**S, [B**B**S/S**B**B], and B**B**B, where S = styrene and B = Br-Sty). Thus, each group appears to originate from the quaternary carbon nucleus of a styrene or Br-Sty unit that exists in the center of a unique sequence of at least three monomers, *i.e.*, a triad, along the copolymer chain.

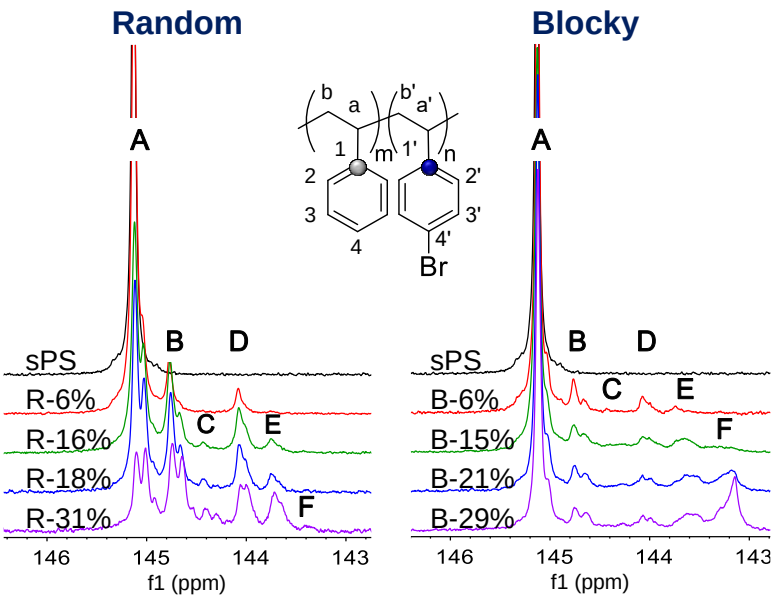

Figure 3.1. The quaternary carbon region of the ^{13}C NMR spectra for the (left) Random and (right) Blocky copolymers increasing in degree of bromination from top to bottom. The spectra were recorded at room temperature and are referenced to TCE-d_2 and normalized over 127.0–132.5 ppm for comparison.

The source of the quaternary carbon resonances as originating from either a styrene or Br-Sty unit was investigated by bsgHMBC spectroscopy. The quaternary carbon and aromatic H(3)/H(4)/H(3′) proton regions of the bsgHMBC spectra for Random R-31% and Blocky B-29% are presented in **Figure 3.2**. For both R-31% and B-29%, the quaternary carbon resonances in the 144-145 ppm range are correlated to the H(3) and/or H(4) protons, indicating that these resonances originate from an un-functionalized styrene unit, C(1). The carbon resonances at lower frequency, in the 143-144 ppm range, are correlated to the H(3′) proton, and thus originate from a Br-Sty unit, C(1′). Therefore, groups A−C were assigned to un-functionalized styrene units and groups D−F were assigned to Br-Sty units.

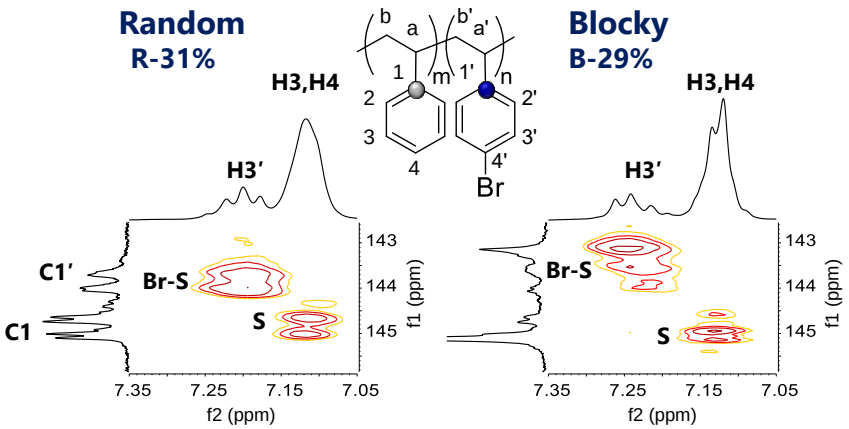

Figure 3.2. The quaternary carbon region of the bsgHMBC spectra for the (left) Random R-31% and (right) Blocky B-29% copolymers recorded in TCE-d_2 at 25 °C.

In order to further assign groups A-F to specific triad sequences of monomers, electronic structure calculations were used to compute theoretical chemical shifts for the quaternary carbon nuclei of the central unit in each of the 6 unique triad sequences. **Figure 3.3** shows the optimized structure of the 6 unique triad sequences end-capped with ethyl units, and the computed chemical shifts. According to the density functional theory (DFT), the chemical shift of the quaternary carbon nucleus of the central styrene or Br-Sty unit in each triad sequence decreases in the following order: S**S**S > [S**S**B/B**S**S] > B**S**B >S**B**S > [B**B**S/S**B**B] > B**B**B. Thus, the quaternary carbon nucleus of a Br-Sty unit is predicted to resonate at a lower frequency than a styrene unit, consistent with the results from the bsgHMBC experiments (see **Figure 3.2**). In addition, the resonance frequency of a styrene or Br-Sty unit decreases with an increasing number of Br-Sty neighbors. This result strongly suggests that bromination of the C(4) carbon of the phenyl ring shields the quaternary carbon nucleus of styrene and neighboring styrene units from an applied external magnetic field. Based on the results of the electronic structure calculations, the bsgHMBC experiments, and previous evidence of the low frequency chemical shift of the quaternary carbon nucleus of a syndiotactic poly(4-bromostyrene) homopolymer[19] (C(1′) = 143.1 ppm), groups A−F were assigned accordingly: A = SSS; B = SSB/BSS; C = BSB; D = SBS; E = SBB/BBS; and F =

BBB. From these assignments, it is clear that the Blocky B-29% copolymer has a larger fraction of BBB triad sequences along its chains relative to the Random R-31% analog (see **Figure 3.1**), despite their similar Br-content. Thus, solution-state bromination results in a relatively low abundance of BBB triad at 31 mol% Br.

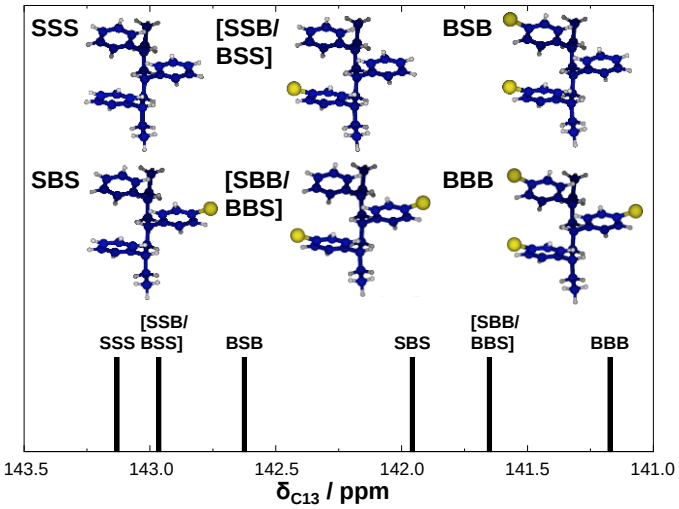

Figure 3.3. Theoretical chemical shifts for the quaternary carbon nuclei of the central monomer unit in the 6 unique triad sequences computed using electronic structure calculations. Geometry optimizations and harmonic frequencies were obtained using the B3LYP density functional and the def2svp basis set as implemented in Gaussian 09.[50] NMR shielding tensors were computed using the Gauche Invariant Atomic Orbital formalism, also in Gaussian. The reported chemical shifts are referenced to the isotropic shielding of an internal tetramethylsilane standard calculated at the same level of theory.

Within groups A−F, the quaternary carbon NMR spectra in **Figure 3.1** display multiple peaks, demonstrating that the quaternary carbon nucleus is capable of communicating with its neighboring *and* next-neighboring styrene and Br-Sty unit. Thus, the individual peaks in the NMR spectrum appear to originate from the quaternary carbon nucleus of a styrene or Br-Sty unit that exists at the center of a sequence of five monomers, i.e., a pentad, along the copolymer chain. **Table 3.1** provides the 20 unique pentad combinations (32 total combinations) that are possible for a copolymer that contains two different monomers, grouped by triad combination and organized by group assignment, A−F. The pentads in each group are arranged from top to bottom in order of increasing number of Br-Sty units that exist two units away from the central styrene or

Br-Sty unit. For the [SSB/BSS]- and [SBB/BBS]-based pentads with one next-neighboring Br-Sty unit, there are two possible pentad permutations, the [bssbs/sssbb], [bsbbs/ssbbb] and [bsbbs/sbbsb], [ssbbb/bbbss] pentads, which are arbitrarily arranged in order of increasing number of consecutive Br-Sty units. Based on the results of the theoretical chemical shifts from electronic structure calculations, which implies that bromination of a neighboring styrene unit shifts the resonance of a central styrene or Br-Sty unit to lower frequency, this order represents the order anticipated for the chemical shifts of the pentad sequences, where the sssss and bbbbb pentads represent the highest and lowest frequency peaks, respectively, in the NMR spectrum.

Table 3.1 Triad and pentad comonomer sequences organized by group assignment, A−F. Styrene = S or s; Br-Sty = B or b.

	Comonomer Sequence	
Group	**Triad**	**Pentad**
A	SSS	s **s s s** s s s s s b / b s s s s b s s s b
B	SSB / BSS	s **s s b** s / s **b s s** s s b s s b / b s s b s s s s b b / b b s s s b b s s b / b s s b b
C	BSB	s **b s b** s b b s b s / s b s b b b b s b b
D	SBS	s **s b s** s s s b s b / b s b s s b s b s b
E	BBS / SBB	s **s b b** s / s **b b s** s s b b s b / b s b b s s s b b b / b b b s s b b b s b / b s b b b
F	BBB	s **b b b** s s b b b b / b b b b s b b b b b

The order of the pentad sequences in the NMR spectrum was investigated by calculating the average pentad sequence distribution in simulated random copolymers using a code created

in-house. The code simulates 1000 homopolymer chains of 1442 monomer units (based on our sPS sample, M_w = 300K; Đ = 2.0) and selects monomers along the chain at random up to the desired degree of bromination. Along each chain, the frequency of each unique pentad sequence (e.g., sssss, bbbbb, *etc.*) is counted, starting at the first unit and moving one unit at a time along the chain. For the 12 pentads with symmetric sequences (e.g., sbbsb and bsbbs), frequencies are added together to conform with the experimental results from NMR. The prevalence of the 20 unique pentad sequences is then calculated by dividing the frequency of each unique pentad sequence by the total number of pentad sequences in the chain. The prevalence of these 20 pentads represents the pentad sequence distribution of the chain. The average pentad sequence distribution of 1000 simulated random copolymers with 31 mol% Br-content (Simulated r-31%) was calculated to compare to the NMR spectrum of Random R-31%.

In order to compare the pentad sequence distribution of Simulated r-31% to R-31%, the NMR spectrum of R-31% was decomposed into its separate additive peak components using the Line Fitting function in Mestrelab Research's MestReNova x64 software. This deconvolution process was assisted by analyzing the NMR spectrum of a Random R-47% copolymer, in which the chemical shift of 20 peaks were easily identified (see **Figure S3.1**). These chemical shifts were then used to approximate the position of the peaks in the spectrum of R-31%.

Figure 3.4(a) compares the average pentad sequence distribution of Simulated r-31% to the NMR spectrum of Random R-31%. For Simulated r-31%, pentads are arranged from left to right according to the top to bottom order of the pentad sequences presented in **Table 3.1**, and are aligned with the peaks observed in the R-31% NMR spectrum. It is worth noting that the average prevalences of the pentad sequences with two possible permutations are not significantly different (*P([bssbs/sbssb]) ≡ P([sssbb/bbsss])*, $p = 0.645 > \alpha = 0.05$; *P([bsbbs/sbbsb]) ≡ P([ssbbb/bbbss])*,

p = 0.250 > α = 0.05, calculated using a two-tailed two-sample t-test). Thus, the assignment of these pentads is extraneous to the overall order of the pentads in the NMR spectrum. Based on the order of the pentad sequences presented in **Table 3.1**, the relative intensities of the pentads in the Simulated r-31% appear to be in excellent agreement with the experimental Random R-31% spectrum. **Figure 3.4(b)** demonstrates the average pentad sequence distribution of Simulated r-31% converted into a theoretical quaternary carbon NMR spectrum using the Lorentzian function (line-width at half-max ($LW_{1/2}$) = 8.9 Hz, determined from the best fit). Again, the theoretical NMR spectrum is strikingly similar to the R-31% NMR spectrum, confirming that the order of the pentad sequences in **Table 3.1** accurately predicts the order of the pentad sequences in the quaternary carbon NMR spectrum.

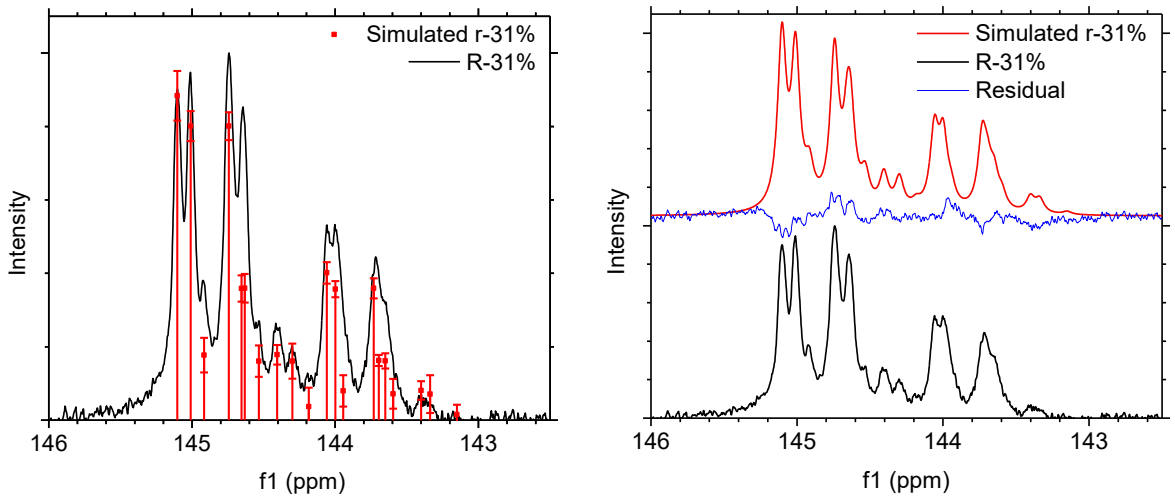

Figure 3.4. (a) The quaternary carbon spectrum of the Random R-31% copolymer (black line) overlaid with the average pentad sequence distribution from 1000 theoretical random copolymers with 31 mol% Br-content (Simulated r-31%, red vertical lines). **(b)** In red, the quaternary carbon spectrum of Simulated r-31% calculated by applying a Lorentzian function ($LW_{1/2}$ = 8.9 Hz). In black, the NMR spectrum of Random R-31% and in blue, the residual of the Simulated r-31% spectrum subtracted from the R-31% spectrum.

The deconvoluted quaternary carbon NMR spectra of the Random R-31% and Blocky B-29% copolymers with triad assignments and several pentad assignments are shown in **Figure 3.5**. For comparison, the spectra are normalized to the same relative intensity. The complete pentad

assignments and their chemical shifts are provided in **Table S3.1**. The R-31% copolymer contains peaks with a broad distribution of intensities. In contrast, the B-29% contains an intense peak for the sssss pentad and a relatively intense peak for the bbbbb pentad. This initial microstructural analysis of the NMR spectrum confirms that the bromination method manipulates the copolymer sequence; gel-state bromination produces sPS-*co*-sPS-Br copolymers with non-random, i.e., blocky distributions of functional groups along the chains.

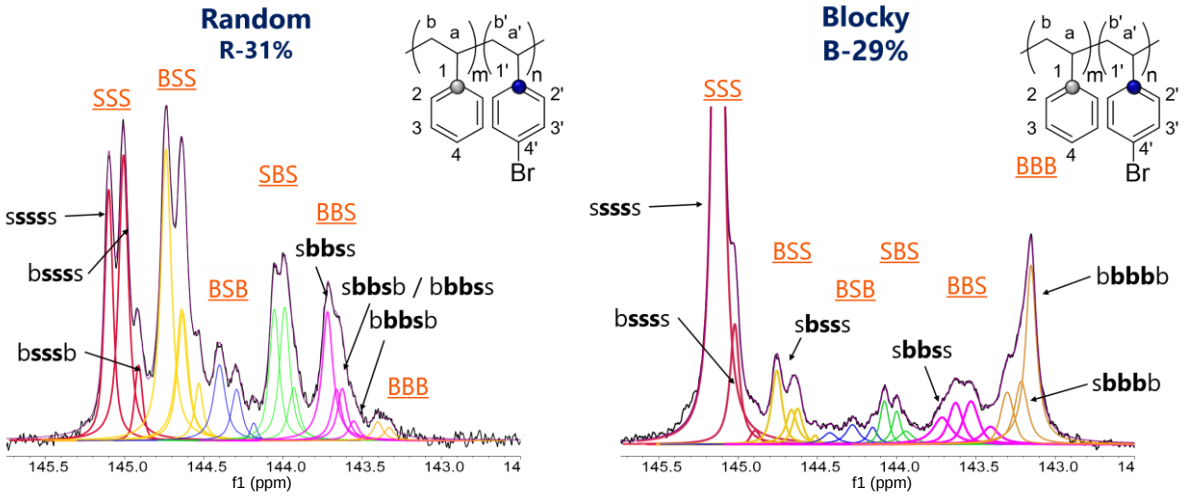

Figure 3.5. The quaternary carbon spectra of the (left) Random R-31% and (right) Blocky B-29% with peak fitting and assignments for the triad combinations and several of the pentad combinations.

With the peaks in the quaternary carbon region of the NMR spectrum assigned to specific pentad sequences, the pentad sequence distribution of each Random and Blocky copolymer was calculated from the ratio of the area under each peak to the total area of the quaternary carbon region (142.9−145.6 ppm). From the pentad sequence distributions, the approximate triad sequence distributions were tabulated, shown in **Table 3.2**. As expected for the Random copolymers, as degree of bromination increases the prevalence of SSS triads decreases and the prevalence of the BSB, SBS, [SSB/BSS], and [SBB/BBS] triads increases. The BBB triad sequence is observed only in the Random R-31% copolymer and comprises approximately 1% of the triad sequence distribution. In contrast, for the Blocky copolymers, the prevalence of SSS triads

decreases to a lesser extent with increasing Br-content. In addition, above 6 mol% Br, the prevalences of the BSB, SBS, [SSB/BSS] and [SBB/BBS] triads remain relatively unchanged, and the prevalence of the BBB triad increases substantially with increasing Br-content. The larger fraction of SSS and BBB triads in the Blocky copolymers again, strongly supports that these copolymers have a blocky microstructure compared to their Random copolymer analogs.

Table 3.2. Triad sequence distributions in the Random and Blocky copolymers, calculated from the peak integration of the quaternary carbon NMR spectra.

Sample	SSS	SSB/BSS	BSB	SBS	SBB/BBS	BBB
B-6%	87%	7%	<0.5%	4%	1%	0%
B-15%	72%	9%	4%	6%	6%	3%
B-21%	65%	8%	4%	5%	8%	10%
B-29%	57%	8%	3%	5%	8%	19%
R-6%	85%	10%	<0.5%	5%	<0.5%	0%
R-16%	59%	24%	2%	12%	4%	0%
R-18%	54%	26%	3%	13%	4%	0%
R-31%	31%	32%	7%	16%	12%	1%

3.4.2. Copolymer block character analysis

The degree of blockiness in the Blocky samples was characterized by the copolymer block character,[34] average length of consecutive styrene units (n_S) and Br-sty units (n_B),[33] and the average number of blocks per 100 monomer units (N), calculated from the triad sequence distributions.[51] Based on Bernoullian probabilities, the block character (R) is determined using **Equation 2**.

$$R = \frac{4(P_{SS})(P_{BB})}{(P_{SB})^2} \qquad \text{where:} \qquad \begin{aligned} P_{SS} &= \text{SSS} + \tfrac{1}{2}\,\text{SSB} \\ P_{BB} &= \text{BBB} + \tfrac{1}{2}\,\text{SBB} \\ P_{BS} &= 1 - P_{SS} - P_{BB} \end{aligned} \qquad \textbf{(2)}$$

For a copolymer with a Bernoullian (i.e., random) sequence distribution, R is equal to unity. For a block-like copolymer, R is greater than unity and for a copolymer that tends toward alternation, R is less than unity. The block character of the Random and Blocky samples and the average block character of simulated random copolymers are compared in **Figure 3.6**. For the simulated copolymers, R values range from 0.98-1.00, affirming that the simulations produce copolymers

with random comonomer sequence distributions. For the Random samples, the *R* values vary between 0.54 (R-6%) and 0.66 (R-16%), which is similar to that expected for a random copolymer, though these data suggest that in solution, there may be some tendency to inhibit the bromination of a styrene unit that neighbors a Br-Sty unit. This intriguing observation that bromination in solution may proceed with inequivalent reaction probabilities will be the subject of further investigations. In distinct contrast to the Random copolymers, the Blocky copolymers have *R* values that range from ca. 3 in B-6% to ca. 25 in B-29%, which confirms that the Blocky copolymers have a block-like microstructure, i.e., a high degree of blockiness, even at low Br-content. Interestingly, *R* also increases considerably with increasing Br-content, demonstrating an increase in the prevalence of consecutive styrene and consecutive Br-Sty "blocks" along the chains. Thus, the large block character of Blocky B-29% may indicate that the B-29% copolymer microstructure is somewhat reminiscent of a multi-block copolymer.

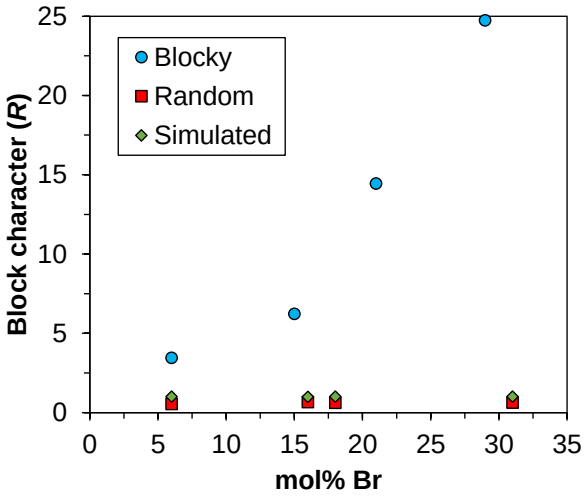

Figure 3.6. The block character (*R*) of the Random (R-x%), Blocky (B-x%), and simulated random (S-x%) copolymers with respect to Br-content (x = Br-content).

To obtain deeper insight into the potential lengths of the styrene and Br-Sty "blocks," in the Blocky copolymers, the average length of consecutive styrene units (n_S) and Br-sty (n_B) units

and average number of blocks per 100 monomer units (*N*) were calculated according to **Equations 3**, **4**, and **5**, respectively.

$$n_S = \frac{SSS + [SSB/BSS] + BSB}{BSB + \frac{1}{2}[SSB/BSS]} \quad \textbf{(3)}$$

$$n_B = \frac{BBB + [BBS/SBB] + SBS}{SBS + \frac{1}{2}[BBS/SBB]} \quad \textbf{(4)}$$

$$N = \frac{200}{n_S + n_B} \quad \textbf{(5)}$$

The average block lengths of consecutive styrene and Br-sty units for the Random and Blocky copolymers, and the average block length for 1000 simulated random copolymers (S-x%) are compared in **Table 3.3**. At approximately 6 mol% Br, the Random R-6% has an n_S value of ca. 18 units, which is in good agreement with the n_S value for a statistically random copolymer (S-6%) of ca. 17 units (based on a copolymer with 1442 monomer units per chain). In contrast, the Blocky B-6% has a much longer n_S of ca. 23 units, which demonstrates that the B-6% has a higher degree of blockiness than its random analog, even at this relatively low degree of functionalization. This result strongly implies that the heterogeneous functionalization is capable of producing copolymers with non-random distributions of functional groups along the chain at low Br-content. For the Random samples with greater than 6 mol% Br, the n_S and n_B values are consistent with that anticipated for a copolymer with a random microstructure, while the Blocky samples with more than 6 mol% Br have relatively long n_S of ca. 10 units. The presence of relatively steady values of n_S in the Blocky samples from 15-29 mol% Br is believed to indicate a non-homogeneous distribution of "blocks" of consecutive styrene units, where contributions from comparatively long and comparatively short blocks of consecutive styrene units result in an intermediate average block length.[33] This bimodal distribution would be consistent with the comonomer distribution

anticipated for a copolymer prepared via post-polymerization bromination in the gel state, in which the gel-state functionalized copolymer is likely to contain separate segments of un-functionalized blocks that originate from the crystalline component of the gel network and randomly functionalized segments that originate from the amorphous component. If this anticipated segmented structure is correct, then the steady increase in n_B from ca. 1 unit in Blocky B-6% to ca. 4 units in Blocky B-29% is suggestive of an increasing density of Br-Sty units in the randomly functionalized blocks with increasing Br-content.

The *N* values in **Table 3.3** represent the average number of blocks of consecutive styrene and Br-Sty units per 100 monomer units in a chain, where a block is at least one unit. For the simulated random copolymers, *N* increases with increasing Br-content, which results from an increasing number of styrene blocks that are terminated at each end by a Br-Sty unit. The Random copolymers exhibit *N* values that are similar to that of the simulated random copolymers. In distinct contrast, the Blocky samples have remarkably low values of *N* even at high Br-content, which suggests that the Blocky copolymers contain fewer relatively long blocks of consecutive styrene units along the chain. Interestingly, Blocky B-15% has the highest *N* value, i.e., the most blocks per 100 monomer units in the Blocky copolymer series. *N* then decreases between 15 mol% Br and 29 mol% Br, which correlates well with the observed increase in n_B, i.e., the average block length of consecutive Br-Sty units. These data are consistent with a blocky copolymer microstructure that consists of long blocks of un-functionalized styrene units and randomly functionalized segments that contain blocks of consecutive Br-Sty units that increase in length with increasing Br-content.

Table 3.3. The average length of consecutive styrene (n_S), and Br-Sty (n_B) and average number of blocks per 100 monomer units (N) for the Random (R-x%), Blocky (B-x%), and simulated random (S-x%) copolymers with respect to Br-content (x = Br-content).

Sample	n_S	n_B	N
B-6%	23.2	1.2	8.2
B-15%	9.7	1.7	17.5
B-21%	9.7	2.7	16.2
B-29%	10.1	3.8	14.4
R-6%	18.2	1.0	10.4
R-16%	6.0	1.1	28.0
R-18%	5.2	1.1	31.4
R-31%	3.0	1.3	46.2
S-6%	16.6	1.1	11.3
S-16%	6.2	1.2	27.0
S-18%	5.5	1.2	29.6
S-31%	3.2	1.4	42.8

3.4.3. Simulated average chains of the sPS-co-sPS-Br copolymers

The pentad sequence distribution provides a fingerprint of the copolymer microstructure and represents the average comonomer sequence distribution along a chain. Using this useful sequence information, a code was developed in-house using Fortran software to predict the average copolymer chain sequence in each of the Random and Blocky copolymers. The copolymer chain is simulated starting with a short sequence of un-functionalized styrene units, followed by subsequent additions of short sequences of un-functionalized and functionalized styrene units to the chain end. The short sequence that is added in each addition step keeps the difference between the experimentally-determined pentad distribution and the pentad distribution of the simulated chain at a minimum. Sequences of 1, 3, 5, 7, 9, 11, and 13 monomers were tested to investigate the addition process. Sequences of 7 monomers were found to minimize the residuals with respect to the experiment. Thus, the simulated chain is started with a short sequence of 7 un-functionalized styrene units and blocks of 7 units are added sequentially. To add a block to the end of the chain, all possible heptad combinations (2^7 or 128) are added in turn and the deviation between the pentad

distribution of the intermediate chain and the experimental results is analyzed. The heptad combination that minimizes the residuals with respect to the experiment is then added to the chain. The process is repeated until the chain length reaches 1442 monomers (based on our sPS sample, M_w = 300K; Đ = 2.0). It is worth noting that the degree of functionalization in the chain is not a parameter of the simulation, yet the simulated chains naturally exhibit Br-Sty compositions that are in good agreement with experiment. Also, the simulated average chains exhibit pentad sequence distributions that deviate by less than one percent from the experimentally-determined pentad sequence distributions.

Figure 3.7 compares the simulated average chains of Random R-31% and Blocky B-29%. The root-mean-square deviations (RMSD) between the simulated and experimental pentad sequence distributions for the simulated average R-31% and B-29% chains are 0.67% and 0.57%, respectively. By inspection, it is clear that the simulated average chain of Random R-31% contains frequent short blocks of consecutive styrene units (grey circles) and noticeably shorter and infrequent blocks of two or more consecutive Br-Sty units (blue circles). In distinct contrast, the simulated Blocky B-29% chain exhibits numerous long blocks of styrene units and relatively long blocks of consecutive Br-Sty units. Overall, the average chains have decidedly different microstructures; the simulated R-31% has a more random microstructure and the simulated B-29% has a considerably non-random, i.e., blocky microstructure. For the simulated average chains of Random 6-18 mol% Br and Blocky 6-21 mol% Br, see **Figure S3.2**.

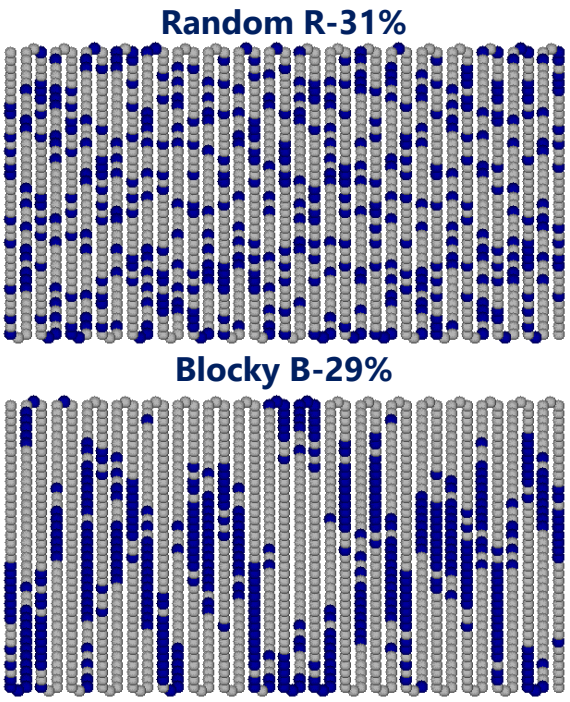

Figure 3.7. Simulated average copolymer chains of (top) Random R-31% and (bottom) Blocky B-29% created through an iterative process that minimizes the difference between the pentad sequence distribution of the simulated chain and the respective data from experiment. Styrene units = grey circles; Br-Sty units = blue circles.

The simulated average chains provide further insight into the copolymer microstructure and distribution of block lengths that are predicted to exist in copolymers prepared by a post-polymerization bromination method carried out in the gel state. The distribution of block lengths in the simulated Random and Blocky average chains was quantified by the weight fraction of styrene units (w_{Sty}) in blocks of at least block length, n, shown in **Figure 3.8**. (For block lengths represented by frequency in the simulated average chains, see **Figure S3.3** and **Figure S3.4**.) For n = 1, all styrene units in the chain are accounted for, which corresponds to a w_{Sty} of 100 wt%. As n increases, the w_{Sty} in blocks of at least n decreases. A w_{Sty} of 50 wt% is half the mass of styrene in the chain. The simulated Random R-6% average chain exhibits 50 wt% of its styrene in blocks of 20-41 units. In comparison, the average chain of Blocky B-6% exhibits half its mass of styrene in longer blocks of 28-67 units, which demonstrates its greater block character compared to its Random analog. This result suggests that heterogeneous functionalization is capable of producing

copolymers with non-random distributions of functional groups along the chain, even at low Br-content. Above 6 mol% Br in the simulated Random average chains, the length of the longest styrene block decreases from 17 to 12 and 9 units for R-16%, R-18%, and R-31%, respectively, and half the mass exists in short blocks of 1- 10, 9, and 5 units, respectively, as expected for copolymers with random microstructures. In contrast, the simulated Blocky average chains with 15, 21, and 29 mol% Br, display half their mass of styrene in long blocks of *at least* 28, 26, and 23 units, respectively, and contain at least one block that is 39 styrene units or longer. These long blocks of consecutive styrene units in the simulated Blocky chains are noteworthy given that the estimated average length of a crystalline stem in the s(2/1)2 helical form of the sPS crystal structure is 26 units, which will be discussed in more detail below in the Analysis subsection of the Results and discussion.[52] The blockiness of the simulated Blocky average chains, even at 6 mol% Br, suggests that during gel-state bromination, crystalline stems in the crystalline component of the gel network are inaccessible to functionalizing reagent and are preserved as long segments of un-functionalized styrene units along the copolymer chains.

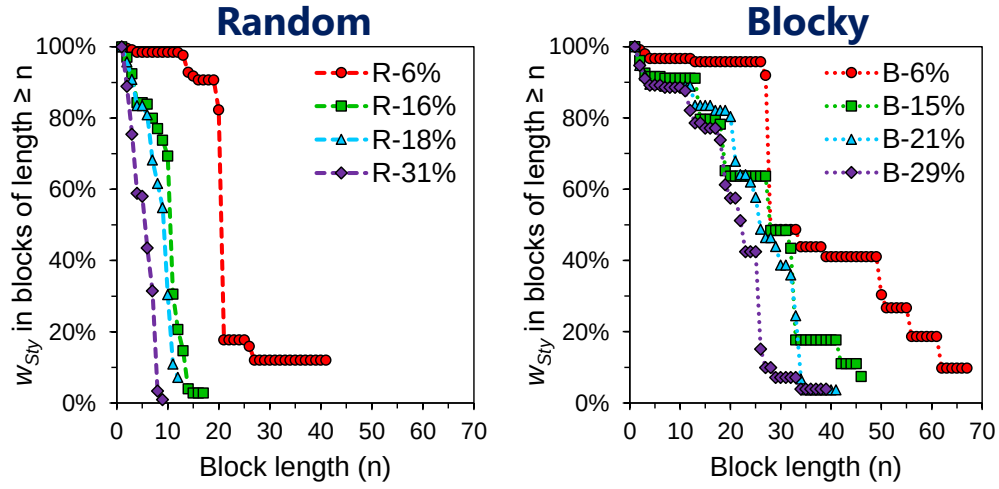

Figure 3.8. Predicted weight fraction of styrene units (w_{Sty}) in blocks of at least block length, *n*, versus block length from the simulated average chains of the (left) Random and (right) Blocky copolymers. Dashed lines are shown to guide the eye.

3.4.4. Analysis of the simulated average chains with respect to experimental results

The simulated average chains have provided further insight into the effect of copolymer microstructure and degree of blockiness on copolymer crystallization behavior after solution-state and gel-state functionalization. **Figure 3.9** shows the weight percent crystallinity, X_c of the sPS homopolymer and the Random and Blocky copolymers after slow cooling (−10 °C min^{-1}) conditions from the melt, calculated from the area under the melting endotherm (ΔH_f) with respect to the heat of fusion of 100% crystalline pure sPS (ΔH_f° = 79.3 J g^{-1}). At approximately 6 mol% Br, both the Random and Blocky copolymers are less crystalline, relative to pure sPS. Bromine groups attached to sPS act as physical defects along the polymer chains, limiting crystallizability and lamella thickness.[2,8] It is not surprising then that the Random and Blocky series show a depression in X_c, with increasing Br-content as a consequence of both shorter crystallizable segments (i.e., runs of consecutive styrene units of sufficient length) and a lower frequency of crystallizable segments along the polymer chains. Nevertheless, it is important to note that the Blocky copolymers demonstrate a much greater aptitude for crystallization compared to their Random analogs, despite their analogous Br-contents. For example, the Blocky B-21% copolymer yields a degree of crystallinity of X_c = 16% that constitutes 50% of the crystallinity of pure sPS, compared to X_c = 0% for the lower Br-content Random R-18%, which did not crystallize under the thermal conditions of this experiment. The much greater crystallizability of the Blocky copolymers is strongly suggestive of a highly blocky microstructure, consistent with the comonomer sequence distributions in the simulated average chains (see **Figure 3.7**).

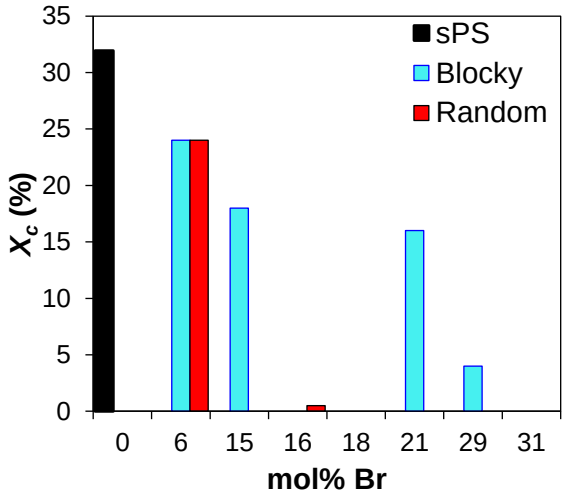

Figure 3.9. The (a) weight percent crystallinity (X_c) of the sPS homopolymer and the Random and Blocky copolymers after slow cooling (−10 °C min^{-1}) from the melt, measured by differential scanning calorimetry.

According to Flory's theory of crystallization in copolymers[53], the probability (P_ζ) that a randomly selected styrene unit along a chain exists in a crystallizable chain segment of at least ζ styrene units is given by:

$$P_\zeta = \sum_j P_{\zeta,j} = \sum_{j=\zeta}^{\infty} \frac{(j - \zeta + 1) \times w_j}{j} \qquad (6)$$

where w_j is the probability that a unit chosen at random is a styrene unit in a sequence of length j, calculated by multiplying the molar fraction of styrene units (X_{Sty}) by the fraction of styrene units occurring in j sequences (j_{Sty}). For this work, ζ is defined as 28 monomer units, the average number of styrene monomers in one crystalline stem of an sPS crystallite.[52] **Figure 3.10** compares the P_ζ values calculated for the simulated Random and Blocky average chains. For the simulated Random average chains, the probability of selecting a crystallizable styrene monomer (i.e., a monomer within a defect-free sequence of 28 monomer units) decreases from P_ζ = 4% in the simulated R-6% average chain to P_ζ = 0% in the simulated Random average chains with at least 16 mol% Br. This infrequency of crystallizable styrene monomers at 16 mol% Br is in excellent agreement with the

experimentally-determined crystallizability of Random R-16%, which exhibits less than 1 wt% crystallinity after conditions of slow cooling (−10 °C min^{-1}). Nevertheless, it is recognized that crystallizability is dependent on the thermal conditions of the experiment and that styrene blocks shorter than 28 units is possible, which is discussed in more detail below.

In contrast to the predicted crystallization behavior of the Random copolymers prepared by a solution-state functionalization method, the simulated Blocky average chains, retain greater than 1% probability that a randomly selected styrene monomer exists in a crystallizable segment, even at 29 mol% Br. This non-zero probability of encountering a defect-free stem is in good agreement with the greater crystallizability of the Blocky copolymers compared to their Random analogs (see **Figure 3.9**). The agreement between crystallization behavior observed in experiment and the block length distributions of the simulated average chains validates the basis of our modeling method and strongly suggests that restricting accessibility of the functionalizing reagent to monomers in the amorphous component of the gel network is capable of producing copolymers with a high prevalence of crystallizable homopolymer segments.

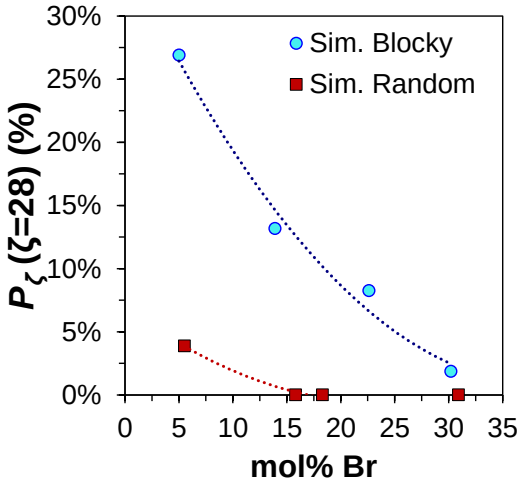

Figure 3.10. Probability that a randomly selected styrene unit in the simulated Blocky (circles) and simulated Random (squares) chains exists in a crystallizable chain segment, ζ, of at least 28 styrene units. Dashed lines are included to guide the eye.

To estimate the average number of styrene units in a crystalline stem in the crystallizable copolymers, copolymer morphology was probed using small-angle X-ray scattering (SAXS). The SAXS profiles of the sPS homopolymer and the Random and Blocky copolymers after 2 h isothermal crystallization from the melt at 190 °C are compared in **Figure S3.5**. The SAXS profile of the sPS homopolymer shows a scattering feature in the range of 0.3 $nm^{-1} < q < 0.5$ nm^{-1} that is consistent with intercrystalline scattering observed previously in sPS.[54] The Random R-6% and R-16%, and the Blocky B-6%, B-15%, and B-21% samples also exhibit intercrystalline scattering over a range of q values from 0.1 $nm^{-1} < q < 0.5$ nm^{-1}. The observed shift in the intercrystalline scattering feature to lower q with increasing Br-content is indicative of an increase in the center-to-center intercrystalline domain spacing, i.e., the long period (L_p). The long period represents the sum of the thicknesses of the crystalline lamellae, l_c, and the interlamellar amorphous region, l_a ($L_p = l_c + l_a$). The d-spacing of the scattering peak in the Lorentz-corrected SAXS profiles was used to estimate the L_p values from Bragg's law ($d_{Bragg} = 2\pi/q$). Assuming a linear two-phase model, the l_c may be estimated from the product of L_p and the volume fraction of crystallinity ($\%X_c$) within the material. The average lamella thickness was also estimated from the 1-D correlation function. Both approaches produced similar results for the estimated average lamella thickness and are useful for probing the average number of styrene units contained in a crystalline stem along the copolymer chain. The results of the linear two-phase approach (columns 2-7) and the 1-D correlation function (columns 8-9) are provided in **Table S** 3.2.

For the melt-crystallized sPS homopolymer and all of the Random and Blocky copolymers that demonstrate intercrystalline scattering, the estimated average thickness of the crystalline lamellae is ca. 4.5−5 nm (see **Table S** 3.2). The average number of consecutive styrene units in a crystalline stem was estimated from the average lamella thickness, based on the α-form planar

zigzag structure of sPS with 2 monomer units per identity period (c-axis dimension = 0.51 nm).[55] All of the crystallizable samples exhibit crystalline stems of approximately 17-20 consecutive styrene units, which is consistent with block lengths observed in the simulated average chains of the respective Random and Blocky copolymers (see **Figure 3.8**). It is worth noting that for pure sPS and potentially for the low Br-content Random, and the Blocky copolymers, melt crystallization at 190 °C may favor a high rate of nucleation and thus, the formation of thinner crystallites.[52,56,57] While the SAXS analysis may therefore underestimate the true maximum average lamella thickness that is possible for these samples, these data still provide a useful initial approximation of the minimum average length of consecutive styrene units that are present in the brominated copolymers. An investigation into the polymorphic composition of the brominated copolymers at different isothermal crystallization obtained from WAXD experiments is beyond the scope of this manuscript and will be the subject of further investigations. The simulated average chains appear to be in good agreement with the morphology of the semicrystalline Random and Blocky copolymers and thus provide a useful visual representation of the copolymer microstructures.

3.4.5. Relationship between gel morphology and copolymer microstructure

To develop a deeper understanding of the relationship between the sPS gel morphology and the copolymer microstructure and degree of blockiness obtained after gel-state functionalization, X-ray scattering techniques were used to probe the morphology of the as 10 w/v% sPS/CCl_4 gel. The merged ultra-small-angle (USAXS) and small-angle X-ray scattering (SAXS) profiles is shown in **Figure 3.11(a)**. To the author's knowledge, this is the first reported USAXS profile of an sPS/solvent gel. The wide-angle X-ray diffraction (WAXD) profile of the as prepared 10 w/v% sPS/CCl_4 gel is provided in **Figure 3.11(b)**. The WAXD profile exhibits

crystalline reflections that are consistent with the s(2/1)2 helical conformation of the δ-form crystal structure of sPS, which is expected for an sPS/solvent gel.[40,58,59] The USAXS/SAXS profile demonstrates two scattering features, a high q scattering feature at 0.2 nm^{-1} < q < 0.7 nm^{-1} that exhibits q^{-4} dependence and a low q scattering feature between 0.006−0.07 nm^{-1} that exhibits q^{-3} dependence in the Porod region between 0.07−0.15 nm^{-1}. The excess scattering at high q is consistent with intercrystalline scattering that has been observed previously in sPS.[54] The d-spacing of this scattering feature, obtained from the Lorentz-corrected SAXS profile, is 0.342 nm^{-1}. The low q scattering feature is strongly suggestive of a large-scale mass fractal-type structure and is attributed to clusters of ordered crystallites.[38] Thus, the presence of these two scattering features is strongly suggestive of an sPS/CCl_4 gel morphology consisting of clusters of crystallites that act as physical cross-links bound together by a percolating network of solvent swollen amorphous chains, forming a three-dimensional (3D) network.[36-40]

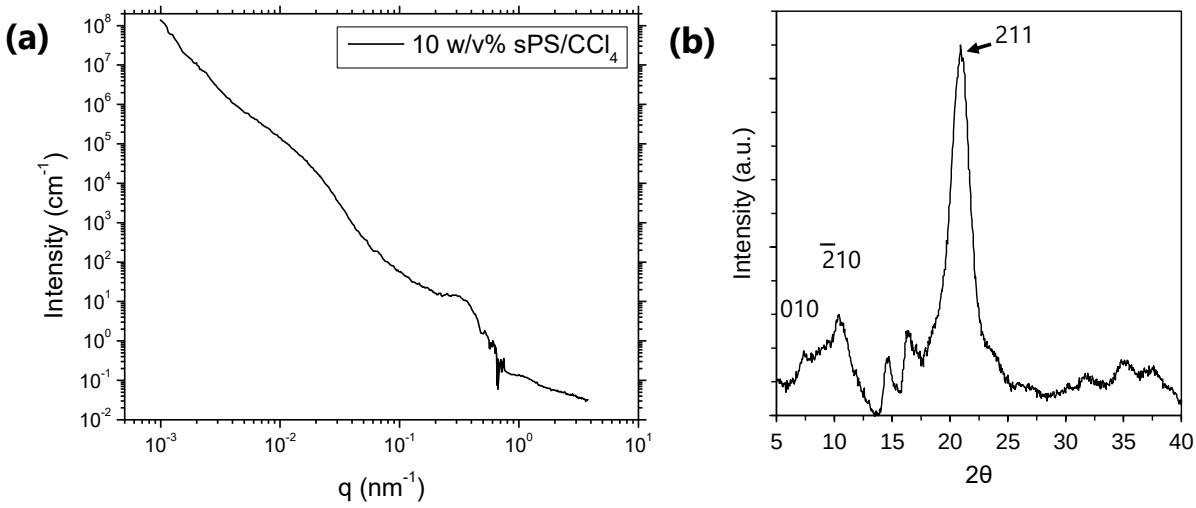

Figure 3.11. The (a) USAXS/SAXS and (b) WAXD profiles of an as prepared 10 w/v% sPS/CCl_4 gel. For the WAXD experiment the gel was dried under vacuum at 70 °C for ca. 24 h prior to analysis. For the WAXD profile of a 10 w/v% sPS/CCl_4 gel stirred in DCM, the bromination reaction solvent, see **Figure S3.6**.

The estimated average lamella thickness in the crystalline component of the gel network was calculated using the method described earlier in **subsection 3.4.4** of the Results and discussion

section. The results of the SAXS analysis of the intercrystalline domain spacing is provided in **Table S** 3.2. For the linear two-phase approach, two methods were used to calculate the $\%X_c$ of a desiccated sPS/CCl_4 gel: 1) DSC, obtained from the first heating trace through integration of the melting endotherm (see **Figure S3.7**); and 2) WAXD, obtained through deconvolution of the crystalline and amorphous contributions and integration. Again, the linear two-phase model approach and the 1-D correlation approach produced similar results. The estimated average lamella thickness in the 10 w/v% sPS/CCl_4 gel was ca. 7.3−8.5 nm. From the average lamella thickness, the average number of consecutive styrene units in a crystalline stem was calculated, based on the helical conformation of the δ-form crystal structure of sPS with 4 monomer units per identity period (c-axis dimension = 0.77 nm).[55] The average crystalline stem in the crystalline lamellae of the gel network contains ca. 38−40 consecutive styrene units. This is in excellent agreement with the block lengths predicted by the simulated average chains of the Blocky copolymers. Remarkably, all of the Blocky simulated average chains contain one or more blocks of consecutive styrene units that is at least 39 styrene units long, even the Blocky B-29% (see **Figure 3.8** and **Figure S3.3**). In comparison, only the simulated average chain of the low Br-content Random R-6% contains blocks of consecutive styrene units of at least 40 units. This result provides strong evidence that the predicted long blocks in the simulated Blocky average chains are not present by random chance and thus originate from the crystalline stems in the crystalline lamellae of the gel network.

3.5. Conclusions

This work demonstrates the first high-resolution comonomer sequencing of brominated sPS copolymers based on pentad assignments of the quaternary carbon region of the quantitative ^{13}C NMR spectrum. The purpose of this research was to develop a comonomer sequencing method

to obtain a deeper understanding of the relationship between the sPS/CCl_4 gel morphology and the copolymer microstructure and degree of blockiness in copolymers prepared by a heterogenous gel-state functionalization method. Using bsgHMBC spectroscopy, electronic structure calculations, and simulated random copolymers, a comonomer sequencing method was successfully developed. As a result, every peak in the quaternary carbon region of the NMR spectrum could be assigned to a styrene or Br-Sty unit in the center of a unique combination of five monomer units, i.e., a pentad sequence. Collectively, all 20 unique pentad sequences that are possible for a copolymer that contains two different monomers were identified, which demonstrates the high sensitivity of the quaternary carbon of styrene and Br-Sty to comonomer sequence.

Based on the comonomer sequence distribution of the Random and Blocky samples, gel-state bromination has been proven to produce copolymers with a higher degree of blockiness and a higher prevalence of long blocks of consecutive styrene units in a blocky microstructure. Simulated average chains of the Random and Blocky copolymers, generated from the comonomer sequence distributions, predict correctly that the Blocky copolymers also contain a higher prevalence of crystallizable sPS segments, confirmed by the greater crystallizability of the Blocky copolymers determined from DSC experiments. Thus, the simulated average chains appear to be representative of average chains in their respective Blocky samples. The excellent agreement between the predicted long blocks of consecutive styrene units of at least 39 styrene in the simulated Blocky average chains and the estimated number of styrene units in a crystalline stem within the sPS/CCl_4 gel network of ca. 38−40 units, affirms that during gel-state bromination, functionalizing reagent is impeded from reacting with monomers in the crystalline component of the gel network, producing copolymers with long blocks of un-functionalized styrene units that originate from the crystalline stems within the crystalline lamellae.

This work thus provides a deeper understanding of the relationship between the sPS/CCl_4 gel morphology and the copolymer microstructure and degree of blockiness. We anticipate that the ability to control the precise morphology of the semicrystalline gel network of sPS/solvent gels, specifically through changing the polymer concentration,[43] gelation solvent,[36-38,44] and/or gelation conditions,[45] will provide avenues of further investigation into tailoring the degree of blockiness in sPS-based copolymers. Future efforts will also focus on developing a method to simulate the post-polymerization functionalization in the gel state using the gel morphology as a template, to ultimately be able to predict the copolymer microstructure and degree of blockiness of copolymers prepared from sPS/solvent gels and other semi-crystalline homopolymers that form thermoreversible gels. The broader scope of this work is to use the comonomer sequencing method and simulations to predict the copolymer microstructure and degree of blockiness of other sPS-based copolymers for the tailored design of new functional materials.

3.6. Acknowledgements

This material is based upon work supported by the National Science Foundation under Grant No. DMR-1809291. Advanced Research Computing at Virginia Tech is gratefully acknowledged for providing computational resources and technical support that have contributed to the results reported within this manuscript. This research used resources of the Advanced Photon Source, a U.S. Department of Energy (DOE) Office of Science User Facility operated for the DOE Office of Science by Argonne National Laboratory under Contract No. DE-AC02-06CH11357. The authors would like to thank Dr. Jan Ilavsky and acknowledge the use of beamline 9ID-C for all USAXS and SAXS experiments. The authors would also like to thank Dr. Narasimhamurthy Shanaiah and Mr. Ken Knott of Virginia Tech's NMR spectroscopy facility staff, for their guidance.

3.7. Supplemental Information I

The quaternary carbon nuclear magnetic resonance (NMR) spectrum of Random R-47% that has been decomposed into its separate additive peak components using the Line Fitting function in Mestrelab Research's MestReNova x64 software is shown in **Figure S3.1**. In total, 20 peaks were identified, which is consistent with the 20 unique pentad sequences that are possible for a copolymer with two different monomers. The peaks are color-coded by triad sequence.

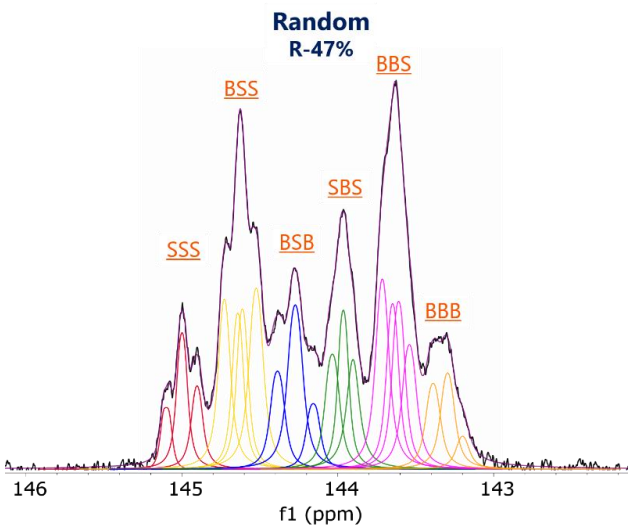

Figure S3.1. The quaternary carbon NMR spectrum of Random R-47% decomposed into its 20 separate additive peak components. The peaks are color-coded and labeled by triad sequence.

The chemical shifts of the quaternary carbon resonances of styrene and brominated styrene (Br-Sty) that exist in the center of unique pentad sequences for the Random R-31% and Blocky B-29% are summarized in **Table S3.1**.

Table S3.1. Chemical shifts of the pentad sequences in the quaternary carbon NMR spectra of Random R-31% and Blocky B-29%.

Pentad combination	Chemical Shift (ppm)	
	Random R-31%	Blocky B-29%
sssss	145.103	145.120
ssssb	145.010	145.014
bsssb	144.915	144.893
sbsss	144.743	144.747
sbssb	144.655	144.650
bbsss	144.631	144.614
bbssb	144.533	144.511
sbsbs	144.405	144.408
bbsbs	144.299	144.273
bbsbb	144.184	144.154
ssbss	144.059	144.071
bsbss	143.999	143.990
bsbsb	143.944	143.904
sbbss	143.732	143.727
sbbsb	143.696	143.647
ssbbb	143.650	143.586
bsbbb	143.596	143.515
sbbbs	143.401	143.377
sbbbb	143.337	143.260
bbbbb	– –	143.151

Table S 3.2

Simulated average chains of the comonomer sequence distribution in the Random and Blocky copolymers are compared in **Figure S3.2**. By inspection, the simulated average chains of the Random and Blocky copolymers with approximately 6 mol% Br, are similar in their comonomer sequence distribution of styrene (grey circles) and Br-Sty (units). Above 6 mol% Br, the simulated Blocky average chains, exhibit noticeably longer and more frequent blocks of two or more consecutive Br-Sty units compared to their Random analogs.

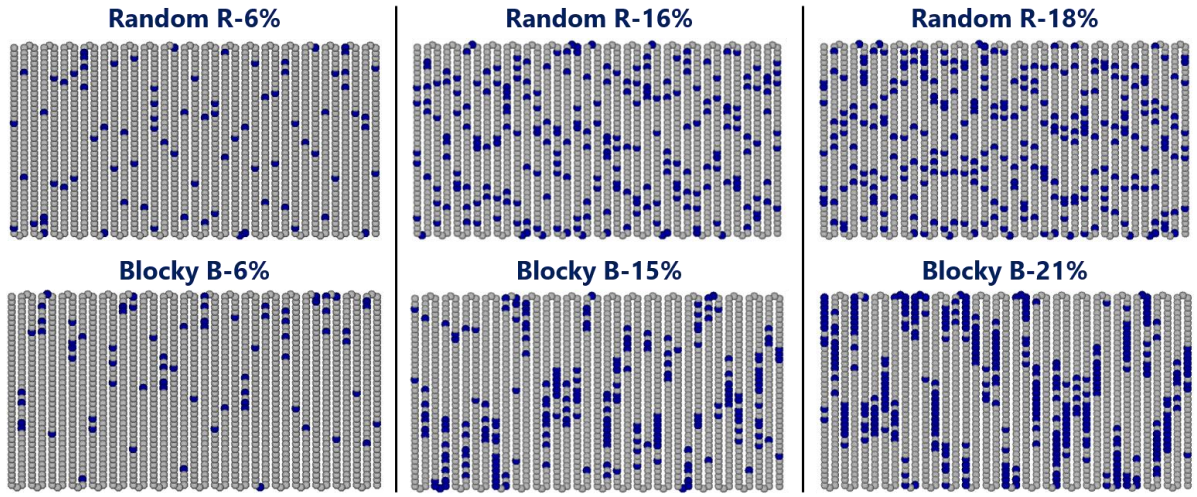

Figure S3.2. Simulated average chains of the (top) Random and (bottom) Blocky copolymers created through an iterative process by minimizing the difference between the pentad sequence distribution of the simulated chain and the experimentally-determined pentad sequence distribution from the quaternary carbon NMR spectra. The root-mean-square deviation (RMSD) between the simulated and experimental results for each chain are: R-6% = 0.24%; R-16% = 0.35%; R-18% = 0.40%; B-6% = 0.37%; B-15% = 0.70%; B-21% = 0.30%. Styrene units = grey circles; Br-Sty units = blue circles.

The distribution of block lengths of consecutive styrene units in the simulated average chains of the Random and Blocky copolymers, represented as frequency *versus* block length, are compared in **Figure S3.3**. Block length frequency was calculated as the number of blocks of consecutive styrene units in a particular length range (e.g., blocks of 6-10 consecutive styrene units) divided by the total number of blocks in the chain. For the simulated Random R-6% average chain, the majority (i.e., 65%) of blocks are 16-20 styrene units and 8% of blocks are ≥ 26 units, noted because 26 monomer units is the average number of units in one crystalline stem of an sPS crystallite.[52] Above 16 mol% Br, the simulated Random average chains exhibit blocks of no longer than 17 styrene units. In contrast, the simulated Blocky average chains exhibit considerably longer blocks, a broader distribution of block lengths, and a relatively substantial fraction of blocks that are at least 26 consecutive styrene units. Remarkably, each of the Blocky simulated average chains has one or more blocks of at least 39 styrene units, which is in excellent agreement with the estimated length of a crystalline stem in the 10 w/v% sPS/CCl_4 gel (see **Table S3.3**).

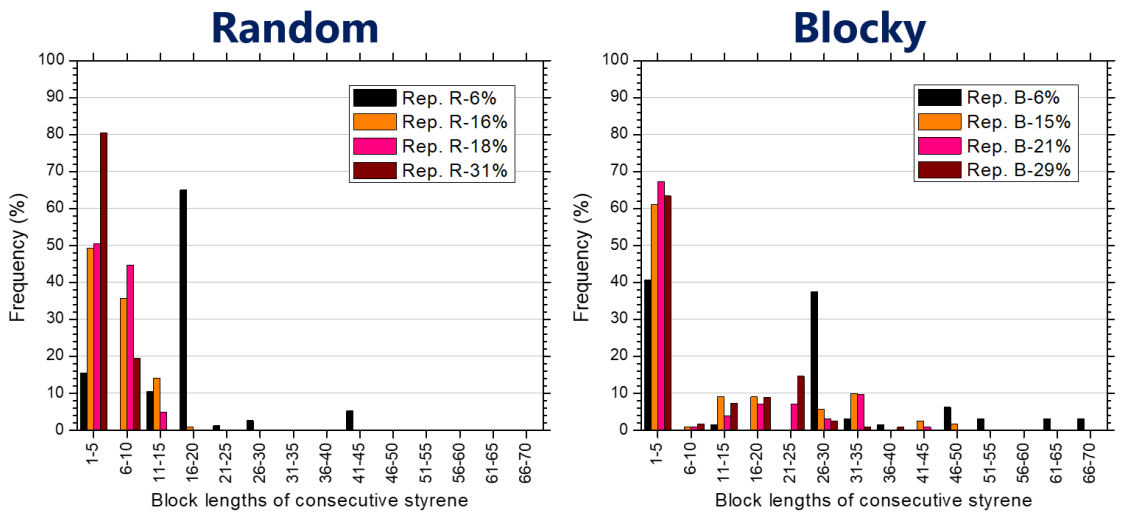

Figure S3.3. The predicted distribution of block lengths of consecutive styrene units from the simulated (left) Random and (right) Blocky average chains, shown as frequency versus block length.

The distribution of block lengths of consecutive Br-Sty units in the simulated average chains of the Random and Blocky copolymers are provided in **Figure S3.4.** Compared to the simulated Random average chains that contain blocks of no more than 4 consecutive Br-Sty units, even at approximately 31 mol% Br, the simulated average chains of the Blocky copolymers contain a broad distribution of block lengths and relatively long blocks. Remarkably, 9% of the Br-Sty blocks in the Blocky B-29% average chain are at least 10 units long.

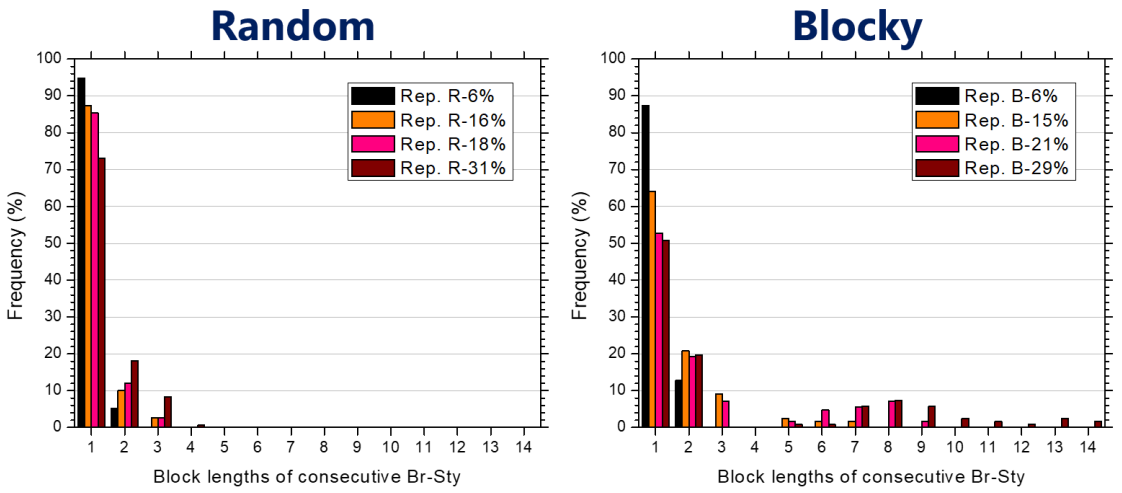

Figure S3.4. The predicted distribution of block lengths of consecutive Br-Sty units in the simulated average chains of the (left) Random and (right) Blocky copolymers, shown as frequency versus block length.

The small-angle X-ray scattering (SAXS) profiles of the sPS homopolymer and the Random and Blocky copolymers after 2 h isothermal crystallization from the melt at 190 °C are compared in **Figure S3.5**. An excess scattering feature is observed in the sPS homopolymer, the Random R-6% and R-16%, and the Blocky B-6%, B-15%, and B-21%, ascribed to intercrystalline scattering.

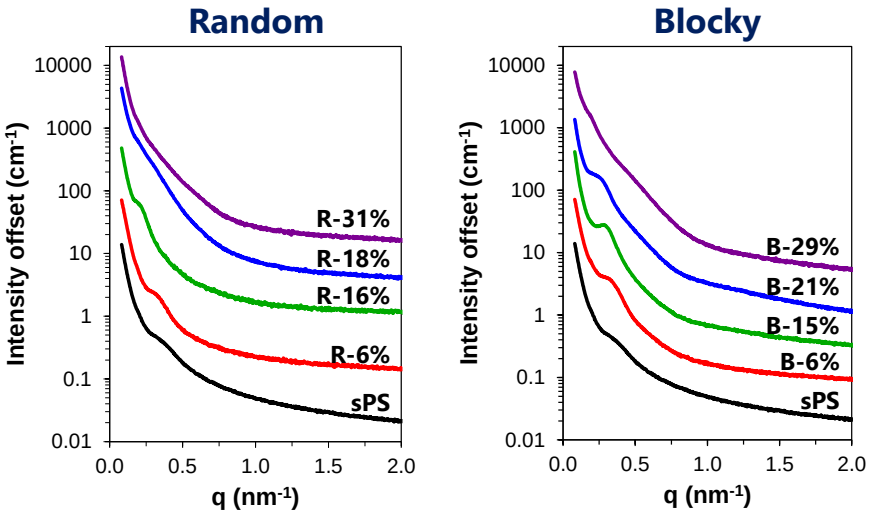

Figure S3.5. SAXS profiles of the (left) Random and (right) Blocky copolymers after 2 h isothermal crystallization at 190 °C.

The SAXS analysis of the intercrystalline domain spacing of the 10 w/v% sPS/CCl_4 gel, sPS homopolymer, and the crystallizable Random and Blocky copolymers is provided in **Table S3.3**. The information in columns 2-7 were derived from a linear two-phase approach and columns 8-9 from the 1-D correlation function. Though Blocky B-29% does crystallize during isothermal crystallization at 190 °C, this sample did not exhibit a strong peak in the SAXS profile. Nevertheless, the copolymer microstructure of B-29% is also so block-like that this sample is known to contain distinct crystallizable segments of both styrene and Br-Sty units,[8] which would have invalidated the SAXS analysis.

Table S3.3. SAXS analysis of the intercrystalline domain spacing of the 10 w/v% sPS/CCl_4 gel, sPS homopolymer, and the Random and Blocky copolymers.

Sample	*d* spacing (nm^{-1})	L_p (nm)	$\%X_c$[a]	l_c (nm)	Avg. # of styrene[b]	l_a (nm)	l_c[c] (nm)	l_a[c] (nm)
sPS	0.389	16.2	32	5.2	20	11.0	5.0	17.8
B-6%	0.337	18.7	29	5.5	21	13.2	5.1	21.9
B-15%	0.315	19.9	22	4.3	17	15.6	4.8	17.1
B-21%	0.273	23.0	19	4.3	17	18.7	4.4	17.2
R-6%	0.337	18.7	29	5.4	21	13.3	4.9	29.3
R-16%	0.214	29.4	18	5.4	21	24.0	--[d]	--[d]
10 w/v% sPS/CCl_4 gel	0.342	18.3	40 (42[e])	7.3 (7.7)	38[f] (40[f])	11.0 (10.7)	8.5	21.8

[a]Fraction of crystallinity determined from the integration of the melting endotherm using DSC ($\Delta H_f°$=79.3 J/g)
[b]Average number of styrene units in a crystalline stem, based on the lamella thickness and the α-form planar zigzag structure of sPS with 2 monomer units per identity period (c-axis dimension = 0.51 nm)[55]
[c]Calculated using the 1-D linear correlation function
[d]A good fit could not be obtained using the linear correlation function
[e]Determined from the integration of the crystalline and amorphous compositions of the WAXD in **Figure 11**
[f]Based on the δ-form s(2/1)2 helical structure (4 monomer units per identity period, c-axis dimension = 0.77 nm)[55]

The wide-angle X-ray diffraction (WAXD) profile of a 10 w/v% sPS/CCl_4 gel stirred in 1,2-dichloromethane (DCM), the bromination reaction solvent, is shown in **Figure S3.6**. This gel was prepared by dissolving sPS pellets in CCl_4 at 120-140 °C in a pressure vessel, followed by removing from heat to promote gel formation. The gel was stored at room temperature for ca. 24 h to mimic the conditions prior to gel-state bromination, then broken into pieces with a spatula, and stirred in DCM for ca. 72 h at room temperature. The gel was filtered and dried under vacuum at 70 °C for ca. 24 h prior to analysis. The WAXD profile is consistent with the s(2/1)2 helical conformation of the δ-form clathrate crystal structure of sPS.[40,58,59] Though there are noticeable differences between the diffraction patterns of the as prepared gel and the gel stirred in DCM, this observed behavior is not surprising. In its helical conformation, sPS is well known to form molecular complexes with guest molecules (i.e., clathrate) that have structures dependent on the chemical nature of the guest.[36,44]

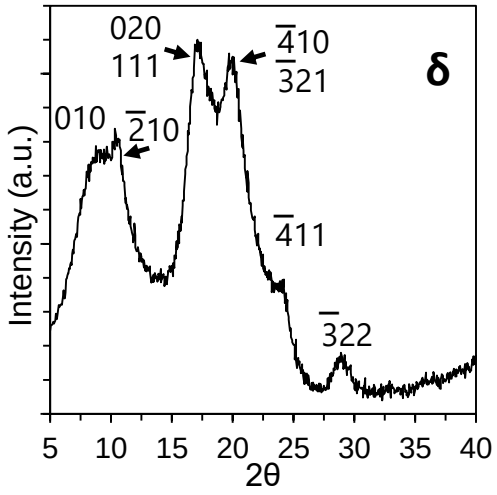

Figure S3.6. The WAXD profile of a 10 w/v% sPS/CCl_4 gel stirred in DCM for 72 h. The gel was dried under vacuum at 70 °C for ca. 24 h prior to analysis.

Figure S3.7 shows the differential scanning calorimetry (DSC) heating trace of a 10 w/v% sPS/CCl_4 gel. The gel was dried under vacuum at 70 °C for ca. 24 h prior to analysis. This is the first heat.

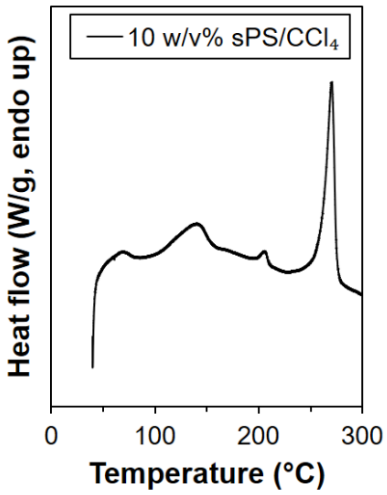

Figure S3.7. DSC first heating trace of a 10 w/v% sPS/CCl_4 that was dried under vacuum at 70 °C for ca. 24 h prior to analysis. Heating rate = 10 °C min^{-1}.

3.8. Supplemental information II

```
!
! This code reads a starting sequence of 1s and 2s and prints the
! sequence that best matches a given pentad distribution
!
! Diego Troya, Virginia Tech June 1, 2018
! Last modification, March 9, 2019
!
      IMPLICIT DOUBLE PRECISION(A-H,O-Z)
      DIMENSION ITAG(32,5)
      DIMENSION SEQ(2,2,2,2,2)    ! All possible sequences, including those symmetric ones
      DIMENSION SEQU(2,2,2,2,2)   ! Symmetry unique ones
      DIMENSION SEQT(2,2,2,2,2)   ! Target sequence
      DIMENSION MONO(99999)
!
! Open file for target distribution
!
      OPEN(UNIT=1,FILE='pentad-target-distribution-block.inp')
      OPEN(UNIT=7,FILE='sequence')
      READ(5,*) NGROWTH1
      READ(5,*) NGROWTH2
      READ(5,*) NGROWTH3
!
      NSTEP=7  ! Grow polymer chain by NSTEP monomers at a time
!
! Initializations
!
      N=0
      DIFFMINN=1.0E10
!
! Read target distribution
!
      WRITE(6,*) 'Target sequence prevalences'
      DO I=1,32
      READ(1,*) (ITAG(I,J),J=1,5)
     .          ,SEQT(ITAG(I,1),ITAG(I,2),ITAG(I,3),ITAG(I,4),ITAG(I,5))
      WRITE(6,99) (ITAG(I,J),J=1,5)
     .          ,SEQT(ITAG(I,1),ITAG(I,2),ITAG(I,3),ITAG(I,4),ITAG(I,5))
      T=T+SEQT(ITAG(I,1),ITAG(I,2),ITAG(I,3),ITAG(I,4),ITAG(I,5))
      END DO
      WRITE(6,*) T
```

```
!
! Grow the chain by NGROWTH segments
!
     NGROWTH=NGROWTH2
     DO NN=1,NGROWTH
!
! Try each of the pentads and see which one minimizes deviation
!
     N=N+NSTEP
     FAC=100./REAL(N-4) ! Normalization factor to turn counts to percent prevalence
     DIFFMIN=1.0E+10
!
! Requires update
!
     DO I1=1,2
     DO I2=1,2
     DO I3=1,2
     DO I4=1,2
     DO I5=1,2
     DO I6=1,2
     DO I7=1,2
!    DO I8=1,2
!    DO I9=1,2
!    DO I10=1,2
!    DO I11=1,2
!    DO I12=1,2
!    DO I13=1,2
       DIFF=0.
       MONO(N-NSTEP+1)=I1
       MONO(N-NSTEP+2)=I2
       MONO(N-NSTEP+3)=I3
       MONO(N-NSTEP+4)=I4
       MONO(N-NSTEP+5)=I5
       MONO(N-NSTEP+6)=I6
       MONO(N-NSTEP+7)=I7
!      MONO(N-NSTEP+8)=I8
!      MONO(N-NSTEP+9)=I9
!      MONO(N-NSTEP+10)=I10
!      MONO(N-NSTEP+11)=I11
!      MONO(N-NSTEP+12)=I12
!      MONO(N-NSTEP+13)=I13
       CALL PENTADS(N,MONO,ITAG,SEQ)
!
```

```
! Symmetrize the pentads
!
      DO I=1,20
       IF(ITAG(I,1).EQ.ITAG(I,5).AND.ITAG(I,2).EQ.ITAG(I,4)) THEN
         SEQU(ITAG(I,1),ITAG(I,2),ITAG(I,3),ITAG(I,4),ITAG(I,5))=
    .     SEQ(ITAG(I,1),ITAG(I,2),ITAG(I,3),ITAG(I,4),ITAG(I,5))
       ELSE
       SEQU(ITAG(I,1),ITAG(I,2),ITAG(I,3),ITAG(I,4),ITAG(I,5))=
    .  SEQ(ITAG(I,1),ITAG(I,2),ITAG(I,3),ITAG(I,4),ITAG(I,5))+
    .  SEQ(ITAG(I,5),ITAG(I,4),ITAG(I,3),ITAG(I,2),ITAG(I,1))
       END IF
!
! Calculate deviation from target in percent
!
       DIFF=DIFF+ABS(
    .  SEQU(ITAG(I,1),ITAG(I,2),ITAG(I,3),ITAG(I,4),ITAG(I,5))*FAC
    .     -SEQT(ITAG(I,1),ITAG(I,2),ITAG(I,3),ITAG(I,4),ITAG(I,5)))
!      WRITE(6,98) I1,I2,I3,I4,I5,
!    . SEQU(ITAG(I,1),ITAG(I,2),ITAG(I,3),ITAG(I,4),ITAG(I,5))*FAC,
!    . SEQT(ITAG(I,1),ITAG(I,2),ITAG(I,3),ITAG(I,4),ITAG(I,5)),
!    . DIFF
      END DO
!
! print
!
!      WRITE(6,98) I1,I2,I3,I4,I5,DIFF
!
! Requires update
!
       IF(DIFF.LT.DIFFMIN) THEN
         DIFFMIN=DIFF
         I1MIN=I1
         I2MIN=I2
         I3MIN=I3
         I4MIN=I4
         I5MIN=I5
         I6MIN=I6
         I7MIN=I7
!        I8MIN=I8
!        I9MIN=I9
!        I10MIN=I10
!        I11MIN=I11
!        I12MIN=I12
```

```
!        I13MIN=I13
         END IF
       END DO  ! 1
       END DO  ! 2
       END DO  ! 3
       END DO  ! 4
       END DO  ! 5
       END DO  ! 6
       END DO  ! 7
!      END DO  ! 8
!      END DO  ! 9
!      END DO  ! 10
!      END DO  ! 11
!      END DO  ! 12
!      END DO  ! 13
!
! Requires update
!
       MONO(N-NSTEP+1)=I1MIN
       MONO(N-NSTEP+2)=I2MIN
       MONO(N-NSTEP+3)=I3MIN
       MONO(N-NSTEP+4)=I4MIN
       MONO(N-NSTEP+5)=I5MIN
       MONO(N-NSTEP+6)=I6MIN
       MONO(N-NSTEP+7)=I7MIN
!      MONO(N-NSTEP+8)=I8MIN
!      MONO(N-NSTEP+9)=I9MIN
!      MONO(N-NSTEP+10)=I10MIN
!      MONO(N-NSTEP+11)=I11MIN
!      MONO(N-NSTEP+12)=I12MIN
!      MONO(N-NSTEP+13)=I13MIN
       WRITE(6,*) 'New pentad',I1MIN,I2MIN,I3MIN,I4MIN,I5MIN,I6MIN,I7MIN
!      .,I8MIN,I9MIN,I10MIN,I11MIN,I12MIN,I13MIN
       WRITE(6,*) 'Diff',DIFFMIN,N
       IF(DIFFMIN.LT.DIFFMINN) DIFFMINN=DIFFMIN
!
! Make one final call to pentads to update the SEQ array in case you are
! terminating here
!
       WRITE(6,*) 'Call to pentads with new sequence'
       CALL PENTADS(N,MONO,ITAG,SEQ)
!
! Symmetrize the pentads
```

```
!
      DO I=1,20
       IF(ITAG(I,1).EQ.ITAG(I,5).AND.ITAG(I,2).EQ.ITAG(I,4)) THEN
         SEQU(ITAG(I,1),ITAG(I,2),ITAG(I,3),ITAG(I,4),ITAG(I,5))=
     .    SEQ(ITAG(I,1),ITAG(I,2),ITAG(I,3),ITAG(I,4),ITAG(I,5))
       ELSE
       SEQU(ITAG(I,1),ITAG(I,2),ITAG(I,3),ITAG(I,4),ITAG(I,5))=
     . SEQ(ITAG(I,1),ITAG(I,2),ITAG(I,3),ITAG(I,4),ITAG(I,5))+
     . SEQ(ITAG(I,5),ITAG(I,4),ITAG(I,3),ITAG(I,2),ITAG(I,1))
       END IF
      END DO
!
! End growth loop
!
     END DO
     WRITE(6,*) 'Absolute lowest difference',DIFFMINN
!
! Print full distribution
!
     WRITE(6,*) 'These are the symmetry-unique pentads'
     WRITE(6,*) N,' monomers',N-4,' pentads'
     S=0
     RMSD=0.0
     DO I=1,20
     WRITE(6,99) (ITAG(I,J),J=1,5)
    .        ,SEQU(ITAG(I,1),ITAG(I,2),ITAG(I,3),ITAG(I,4),ITAG(I,5))
    .        ,SEQU(ITAG(I,1),ITAG(I,2),ITAG(I,3),ITAG(I,4),ITAG(I,5))
    .                                    /REAL(N-4)*100.
    .        ,SEQT(ITAG(I,1),ITAG(I,2),ITAG(I,3),ITAG(I,4),ITAG(I,5))
        S=S+SEQU(ITAG(I,1),ITAG(I,2),ITAG(I,3),ITAG(I,4),ITAG(I,5))
     RMSD=RMSD+
    .(SEQT(ITAG(I,1),ITAG(I,2),ITAG(I,3),ITAG(I,4),ITAG(I,5))-
    .SEQU(ITAG(I,1),ITAG(I,2),ITAG(I,3),ITAG(I,4),ITAG(I,5))
    .                                    /REAL(N-4)*100.)**2
     END DO
     WRITE(6,'("RMSD deviation",1X,F5.3)')SQRT(RMSD/REAL(20-1))
     WRITE(6,*) S,' pentads'
!
     WRITE(6,*) 'These are all the pentads'
     S=0
     DO I=1,32
     WRITE(6,99) (ITAG(I,J),J=1,5)
    .        ,SEQ(ITAG(I,1),ITAG(I,2),ITAG(I,3),ITAG(I,4),ITAG(I,5))
```

```
        S=S+SEQ(ITAG(I,1),ITAG(I,2),ITAG(I,3),ITAG(I,4),ITAG(I,5))
      END DO
      WRITE(6,*) S,' pentads'
!
! Here is the sequence
!
      WRITE(6,*) 'Sequence'
      WRITE(7,*) N
      DO I=1,N
        WRITE(6,*) MONO(I)
        WRITE(7,*) MONO(I)
      END DO
!
 99   FORMAT(5I2,1X,F6.0,1X,2(F8.4,1X))
 98   FORMAT(5I2,1X,F10.4,1X,F8.4,F8.4)
      END
!!!!!!!!!!!!!!!!!!!
      SUBROUTINE PENTADS(N,MONO,ITAG,SEQ)
      IMPLICIT DOUBLE PRECISION(A-H,O-Z)
      DIMENSION ITAG(32,5)
      DIMENSION SEQ(2,2,2,2,2)
      DIMENSION MONO(99999)
!
! Initialize all 32 possible pentad sequences
!
      DO I=1,32
        SEQ(ITAG(I,1),ITAG(I,2),ITAG(I,3),ITAG(I,4),ITAG(I,5))=0.
      END DO
!
! Place yourself at the start of the first pentad and count
!
      DO L=1,N-4
       SEQ(MONO(L),MONO(L+1),MONO(L+2),MONO(L+3),MONO(L+4))=
     . SEQ(MONO(L),MONO(L+1),MONO(L+2),MONO(L+3),MONO(L+4))+1.
      END DO
!
      END
```

3.9. References

1. Liu, S.; Sen, A., Syntheses of Syndiotactic-Polystyrene-Graft-Poly(Methyl Methacrylate), Syndiotactic-Polystyrene-Graft-Poly(Methyl Acrylate), and Syndiotactic-Polystyrene-Graft-Atactic-Polystyrene with Defined Structures by Atom Transfer Radical Polymerization. *Macromolecules* **2000,** *33* (14), 5106-5110.
2. Shin, J.; Chang, Y.; Nguyen, T. L. T.; Noh, S. K.; Bae, C., Hydrophilic Functionalization of Syndiotactic Polystyrene Via a Combination of Electrophilic Bromination and Suzuki–Miyaura Reaction. *J. Polym. Sci., Part A: Polym. Chem.* **2010,** *48* (19), 4335-4343.
3. Semler, J. J.; Jhon, Y. K.; Tonelli, A.; Beevers, M.; Krishnamoorti, R.; Genzer, J., Facile Method of Controlling Monomer Sequence Distributions in Random Copolymers. *Adv. Mater.* **2007,** *19* (19), 2877-2883.
4. Jhon, Y. K.; Semler, J. J.; Genzer, J., Effect of Solvent Quality and Chain Confinement on the Kinetics of Polystyrene Bromination. *Macromolecules* **2008,** *41* (18), 6719-6727.
5. Han, J.; Jeon, B. H.; Ryu, C. Y.; Semler, J. J.; Jhon, Y. K.; Genzer, J., Discriminating among Co-Monomer Sequence Distributions in Random Copolymers Using Interaction Chromatography. *Macromol. Rapid Commun.* **2009,** *30* (18), 1543-1548.
6. Jhon, Y. K.; Semler, J. J.; Genzer, J.; Beevers, M.; Gus' kova, O. A.; Khalatur, P. G.; Khokhlov, A. R., Effect of Comonomer Sequence Distribution on the Adsorption of Random Copolymers onto Impenetrable Flat Surfaces. *Macromolecules* **2009,** *42*, 2843-2853.
7. Liu, D.; Wang, M.; Wang, Z.; Wu, C.; Pan, Y.; Cui, D., Stereoselective Copolymerization of Unprotected Polar and Nonpolar Styrenes by an Yttrium Precursor: Control of Polar-Group Distribution and Mechanism. *Angew. Chem.* **2017,** *129* (10), 2758-2763.
8. Noble, K. F.; Noble, A. M.; Talley, S. J.; Moore, R. B., Blocky Bromination of Syndiotactic Polystyrene Via Post-Polymerization Functionalization in the Heterogeneous Gel State. *Polym. Chem.* **2018,** *9* (41), 5095-5106.
9. Wang, Z.; Liu, D.; Cui, D., Statistically Syndioselective Coordination (Co) Polymerization of 4-Methylthiostyrene. *Macromolecules* **2016,** *49* (3), 781-787.
10. Sato, H.; Tanaka, Y.; Hatada, K., C-13 Nmr Analysis of Polystyrene from Low-Molecular-Weight Model Compounds. *J. Polym. Sci., Part B: Polym. Phys.* **1983,** *21* (9), 1667-1674.

11. Chen, T. K.; Harwood, H. J., Quaternary Aromatic Carbon Resonance Spectra of Epimerized Isotactic Polystyrene. *Makromol Chem Rapid Comm* **1983,** *4* (7), 463-468.
12. Ziaee, F.; Salehi Mobarakeh, H., Effect of Temperature on Polystyrene Tacticity through Para Aromatic Carbon Splitting in 13c Nmr Spectroscopy. *Iran Polym J* **2011,** *20*, 213-221.
13. Suparno, S.; Lacoste, J.; Raynal, S.; Regnier, J.; Schué, F.; Sempere, R.; Sledz, J., Carbon-13 Nuclear Magnetic Resonance Spectroscopy of Polystyrene. *Polym. J.* **1980,** *12*, 861-865.
14. Cheng, H.; Lee, G., Nmr Studies of Polystyrene Tacticity. *Int. J. Polym. Anal. Charact.* **1996,** *2* (4), 439-455.
15. Matsuzaki, K.; Uryu, T.; Seki, T.; Osada, K.; Kawamura, T., Stereoregularity of Polystyrene and Mechanism of Polymerization. *Macromol. Chem. Phys.* **1975,** *176* (10), 3051-3064.
16. Kawamura, T.; Toshima, N.; Matsuzaki, K., Comparison of 13c Nmr Spectra of Polystyrenes Having Various Tacticities and Assignment of the Spectra. *Macromol. Rapid Commun.* **1994,** *15* (6), 479-486.
17. Feil, F.; Harder, S., New Stereochemical Assignments of 13c Nmr Signals for Predominantly Syndiotactic Polystyrene. *Macromolecules* **2003,** *36* (9), 3446-3448.
18. Nguyên-Trân, T. M.; Lauprêtre, F.; Jasse, B., Preparation and 13c Nmr Spectra of Model Compounds for Poly (4-Bromostyrene). *Macromol. Chem. Phys.* **1980,** *181* (1), 125-130.
19. Guo, F.; Jiao, N.; Jiang, L.; Li, Y.; Hou, Z., Scandium-Catalyzed Syndiospecific Polymerization of Halide-Substituted Styrenes and Their Copolymerization with Styrene. *Macromolecules* **2017,** *50* (21), 8398-8405.
20. Brar, A. S.; Puneeta, Synthesis of Styrene/Methyl Methacrylate Copolymers by Atom Transfer Radical Polymerization: 2d Nmr Investigations. *J. Polym. Sci., Part A: Polym. Chem.* **2006,** *44* (6), 2076-2085.
21. Sang, W.; Ma, H.; Wang, Q.; Hao, X.; Zheng, Y.; Wang, Y.; Li, Y., Monomer Sequence Determination in the Living Anionic Copolymerization of Styrene and Asymmetric Bi-Functionalized 1, 1-Diphenylethylene Derivatives. *Polym. Chem.* **2016,** *7* (1), 219-234.
22. Gurarslan, R.; Hardrict, S.; Roy, D.; Galvin, C.; Hill, M. R.; Gracz, H.; Sumerlin, B. S.; Genzer, J.; Tonelli, A., Beyond Microstructures: Using the Kerr Effect to Characterize the Macrostructures of Synthetic Polymers. *J. Polym. Sci., Part B: Polym. Phys.* **2015,** *53* (3), 155-166.

23. Gurarslan, R.; Tonelli, A. E., An Unexpected Stereochemical Bias in the Raft Syntheses of Styrene/P-Bromostyrene Copolymers Uncovered by the Kerr Effect. *Polymer* **2016,** *89*, 50-54.
24. Hardrict, S. N.; Gurarslan, R.; Galvin, C. J.; Gracz, H.; Roy, D.; Sumerlin, B. S.; Genzer, J.; Tonelli, A. E., Characterizing Polymer Macrostructures by Identifying and Locating Microstructures Along Their Chains with the Kerr Effect. *J. Polym. Sci., Part B: Polym. Phys.* **2013,** *51* (9), 735-741.
25. Gurarslan, R.; Gurarslan, A.; Tonelli, A. E., Characterizing Polymers with Heterogeneous Micro- and Macrostructures. *J. Polym. Sci., Part B: Polym. Phys.* **2015,** *53* (6), 409-414.
26. Yang, J. C.; Jablonsky, M. J.; Mays, J. W., Nmr and Ft-Ir Studies of Sulfonated Styrene-Based Homopolymers and Copolymers. *Polymer* **2002,** *43* (19), 5125-5132.
27. Dickinson, L. C.; Weiss, R.; Wnek, G. E., Nmr Characterization of Sulfonation Blockiness in Copoly(Styrene−Sulfonated Styrene). *Macromolecules* **2001,** *34* (9), 3108-3110.
28. Natalello, A.; Alkan, A.; von Tiedemann, P.; Wurm, F. R.; Frey, H., Functional Group Distribution and Gradient Structure Resulting from the Living Anionic Copolymerization of Styrene and Para-but-3-Enyl Styrene. *ACS Macro Lett.* **2014,** *3* (6), 560-564.
29. Zhang, Z.; Dou, Y.; Li, S.; Cui, D., Highly Syndioselective Coordination (Co) Polymerization of Isopropenylstyrene. *Polym. Chem.* **2018**.
30. Shepherd, L.; Chen, T. K.; Harwood, H. J., Epimerization of Isotactic Polystyrene. *Polym. Bull.* **1979,** *1* (6), 445-450.
31. Chen, T. K.; Gerken, T. A.; Harwood, H. J., Methylene Carbon Resonance Spectra of Epimerized Isotactic Polystyrene. *Polym. Bull.* **1980,** *2* (1), 37-42.
32. Miller, S. A., Isotactic Block Length Distribution in Polypropylene: Bernoullian Vs Hemiisotactic. *Macromolecules* **2004,** *37* (11), 3983-3995.
33. Randall, J. C., Carbon-13 Nuclear Magnetic Resonance Quantitative Measurements of Average Sequence Lengths of Like Stereochemical Additions in Polypropylene and Polystyrene. *J. Polym. Sci., Part B: Polym. Phys.* **1976,** *14* (11), 2083-2094.
34. Britton, D.; Heatley, F.; Lovell, P. A., 13c Nmr Spectroscopy Studies of Branching and Sequence Distribution in Copolymers of Vinyl Acetate and N-Butyl Acrylate Prepared by Semibatch Emulsion Copolymerization. *Macromolecules* **2001,** *34* (4), 817-829.

35. Yamadera, R.; Murano, M., The Determination of Randomness in Copolyesters by High Resolution Nuclear Magnetic Resonance. *J. Polym. Sci., Part A: Polym. Chem.* **1967,** *5* (9), 2259-2268.
36. Mochizuki, J.; Sano, T.; Tokami, T.; Itagaki, H., Decisive Properties of Solvent Able to Form Gels with Syndiotactic Polystyrene. *Polymer* **2015,** *67*, 118-127.
37. Shimizu, H.; Wakayama, T.; Wada, R.; Okabe, M.; Tanaka, F., Solvent Effect on Junction Size in Syndiotactic Polystyrene Physical Gel. *Polym. J.* **2005,** *37* (4), 294-298.
38. Kobayashi, M.; Yoshioka, T.; Kozasa, T.; Tashiro, K.; Suzuki, J.; Funahashi, S.; Izumi, Y., Structure of Physical Gels Formed in Syndiotactic Polystyrene/Solvent Systems Studied by Small-Angle Neutron Scattering. *Macromolecules* **1994,** *27* (6), 1349-1354.
39. Roels, T.; Deberdt, F.; Berghmans, H., Solvent Quality and Phase-Stability in Syndiotactic Polystyrene-Solvent Systems. *Macromolecules* **1994,** *27* (21), 6216-6220.
40. Daniel, C.; Guerra, G.; Musto, P., Clathrate Phase in Syndiotactic Polystyrene Gels. *Macromolecules* **2002,** *35* (6), 2243-2251.
41. Fahs, G. B.; Benson, S. D.; Moore, R. B., Blocky Sulfonation of Syndiotactic Polystyrene: A Facile Route toward Tailored Ionomer Architecture Via Postpolymerization Functionalization in the Gel State. *Macromolecules* **2017,** *50* (6), 2387-2396.
42. Anderson, L. J.; Yuan, X.; Fahs, G. B.; Moore, R. B., Blocky Ionomers Via Sulfonation of Poly(Ether Ether Ketone) in the Semicrystalline Gel State. *Macromolecules* **2018,** *51* (16), 6226-6237.
43. Kobayashi, M.; Kozasa, T., Conformational Ordering Process on Physical Gelation of Syndiotactic Polystyrene/Solvent Systems Revealed by Time-Resolved Infrared Spectroscopy. *Appl. Spectrosc.* **1993,** *47* (9), 1417-1424.
44. Daniel, C.; Avallone, A.; Guerra, G., Syndiotactic Polystyrene Physical Gels: Guest Influence on Structural Order in Molecular Complex Domains and Gel Transparency. *Macromolecules* **2006,** *39* (22), 7578-7582.
45. Daniel, C.; Menelle, A.; Brulet, A.; Guenet, J.-M., Thermoreversible Gelation of Syndiotactic Polystyrene in Toluene and Chloroform. *Polymer* **1997,** *38* (16), 4193-4199.
46. Ilavsky, J.; Zhang, F.; Andrews, R. N.; Kuzmenko, I.; Jemian, P. R.; Levine, L. E.; Allen, A. J., Development of Combined Microstructure and Structure Characterization Facility for in

Situ and Operando Studies at the Advanced Photon Source. *J. Appl. Crystallogr.* **2018,** *51* (3), 867-882.

47. Ilavsky, J.; Zhang, F.; Allen, A. J.; Levine, L. E.; Jemian, P. R.; Long, G. G., Ultra-Small-Angle X-Ray Scattering Instrument at the Advanced Photon Source: History, Recent Development, and Current Status. *Metall. Mater. Trans. A* **2013,** *44* (1), 68-76.
48. Ilavsky, J., Nika: Software for Two-Dimensional Data Reduction. *J. Appl. Crystallogr.* **2012,** *45* (2), 324-328.
49. Ilavsky, J.; Jemian, P. R., Irena: Tool Suite for Modeling and Analysis of Small-Angle Scattering. *J. Appl. Crystallogr.* **2009,** *42* (2), 347-353.
50. Frisch, M. J.; Trucks, G. W.; Schlegel, H. B.; Scuseria, G. E.; Robb, M. A.; Cheeseman, J. R.; Scalmani, G.; Barone, V.; Petersson, G. A.; Nakatsuji, H.; Li, X.; Caricato, M.; Marenich, A. V.; Bloino, J.; Janesko, B. G.; Gomperts, R.; Mennucci, B.; Hratchian, H. P.; Ortiz, J. V.; Izmaylov, A. F.; Sonnenberg, J. L.; Williams; Ding, F.; Lipparini, F.; Egidi, F.; Goings, J.; Peng, B.; Petrone, A.; Henderson, T.; Ranasinghe, D.; Zakrzewski, V. G.; Gao, J.; Rega, N.; Zheng, G.; Liang, W.; Hada, M.; Ehara, M.; Toyota, K.; Fukuda, R.; Hasegawa, J.; Ishida, M.; Nakajima, T.; Honda, Y.; Kitao, O.; Nakai, H.; Vreven, T.; Throssell, K.; Montgomery Jr., J. A.; Peralta, J. E.; Ogliaro, F.; Bearpark, M. J.; Heyd, J. J.; Brothers, E. N.; Kudin, K. N.; Staroverov, V. N.; Keith, T. A.; Kobayashi, R.; Normand, J.; Raghavachari, K.; Rendell, A. P.; Burant, J. C.; Iyengar, S. S.; Tomasi, J.; Cossi, M.; Millam, J. M.; Klene, M.; Adamo, C.; Cammi, R.; Ochterski, J. W.; Martin, R. L.; Morokuma, K.; Farkas, O.; Foresman, J. B.; Fox, D. J. *Gaussian 16 Rev. E.01*, Wallingford, CT, 2016.
51. Dasgupta, A.; Garnaik, B., Microstructures of Styrene-Acrylamide Copolymers Using 13c Nmr Spectroscopy. *Polym. J.* **1998,** *30*, 956.
52. Wang, H.; Wu, C.; Cui, D.; Men, Y., Lamellar Thickness Dependence of Crystal Modification Selection in the Syndiotactic Polystyrene Γ-to-A/B Phase Transition Process. *Macromolecules* **2018,** *51* (2), 497-503.
53. Flory, P. J., Theory of Crystallization in Copolymers. *Trans. Faraday Soc.* **1955,** *51* (0), 848-857.
54. Takebe, T.; Yamasaki, K., Crystallization Thermodynamics and Kinetics of Syndiotactic Polystyrene. In *Syndiotactic Polystyrene*, 2009; pp 238-251.

55. Albunia, A. R.; Musto, P.; Guerra, G., Ftir Spectra of Pure Helical Crystalline Phases of Syndiotactic Polystyrene. *Polymer* **2006,** *47* (1), 234-242.
56. Ho, R.-M.; Lin, C.-P.; Tsai, H.-Y.; Woo, E.-M., Metastability Studies of Syndiotactic Polystyrene Polymorphism. *Macromolecules* **2000,** *33* (17), 6517-6526.
57. Sun, Y. S.; Woo, E. M., Correlation between Thermal Behavior and Crystalline Morphology in B-Form Syndiotactic Polystyrene. *Macromol. Chem. Phys.* **2001,** *202* (9), 1557-1568.
58. Guerra, G.; Vitagliano, V. M.; De Rosa, C.; Petraccone, V.; Corradini, P., Polymorphisms in Melt Crystallized Syndiotactic Polystyrene Samples. *Macromolecules* **1990,** *23* (5), 1539-1544.
59. Daniel, C.; Giudice, S.; Guerra, G., Syndiotatic Polystyrene Aerogels with B, Γ, and E Crystalline Phases. *Chem. Mater.* **2009,** *21* (6), 1028-1034.

Chapter 4.

Tailored Chain Sequences of Gel-State Brominated Syndiotactic Polystyrene Copolymers by Changing Gel Morphology

Kristen F. Noble, Diego Troya, and Robert B. Moore

4.1. Abstract

This work demonstrates the post-polymerization bromination of syndiotactic polystyrene (sPS) in the heterogeneous gel state to produce brominated sPS (sPS-co-sPS-Br) copolymers with blocky microstructures and tailored chain sequences. Using a 10 w/v% sPS/carbon tetrachloride (CCl_4) gel and a 10 w/v% sPS/chloroform ($CHCl_3$) gel as templates for the gel-state bromination reactions, semicrystalline blocky copolymers were prepared with degrees of functionality of 6-32 mol% *p*-bromostyrene units. Characterization of the sPS/solvent gels using ultra-small-angle X-ray scattering (USAXS) and small-angle X-ray scattering (SAXS), reveals that the sPS/CCl_4 and sPS/$CHCl_3$ gel networks exhibit different morphologies. The sPS/$CHCl_3$ gel appears to contain loosely packed, unoriented crystallites that are bound together by a percolating network of amorphous chain segments. The sPS/CCl_4 gel morphology is more complex and appears to consist of polymer-rich regions containing clusters of unoriented crystallites bound together by amorphous chain segments, and polymer-poor regions containing a percolating network of amorphous chain segments that link the crystallite clusters together. Based on SAXS analysis of the intercrystalline domain spacing in the gels and assuming a linear two-phase model, the average length of a crystalline stem in a 10 w/v% sPS/CCl_4 and 10 w/v% sPS/$CHCl_3$ gels was estimated as 38-40 and 46-49 styrene units, respectively. Microstructural analysis and comonomer sequencing of the brominated copolymers using ^{13}C nuclear magnetic resonance (NMR) spectroscopy, demonstrates

that the sPS/$CHCl_3$ copolymers contain a high prevalence of styrene "blocks" of at least five consecutive styrene units and a high degree of blockiness. Crystallization behavior of the brominated copolymers, examined using differential scanning calorimetry (DSC), reveals that the sPS/$CHCl_3$ copolymers are more crystallizable during conditions of rapid cooling and crystallize faster at low supercooling relative to their sPS/CCl_4 analogs. Quenched films of the brominated copolymers show micro-phase separated morphologies, with larger domain sizes present in the sPS/$CHCl_3$. These data further support that the sPS/$CHCl_3$ copolymers contain longer, distinct segments of pure sPS and segments of randomly brominated sPS with a greater degree of blockiness compared to their sPS/CCl_4 analogs. To rationalize the effect of gel morphology on the copolymer microstructure and crystallization behavior, simulations of the blocky copolymers were developed, based on the semicrystalline morphologies of the sPS/solvent gels. The results of these simulations predict that the sPS/$CHCl_3$ gel produces copolymers that contain a multiblock-like microstructure, while the sPS/CCl_4 gel produces copolymers that contain a gradient-like blocky microstructure, and thus support the empirical analyses of the gel morphology and copolymer crystallizability. Simulated average chains of the brominated copolymers were generated from experimentally-determined comonomer sequence distributions. The simulated chains were able to predict the copolymer crystallizability observed in the DSC experiments. In addition, the simulated sPS/CCl_4 and sPS/$CHCl_3$ chains were found to contain one or more styrene blocks of at least 38 and 46 styrene units, respectively, in excellent agreement with the estimated average length of a crystalline stem in the respective sPS/solvent gels. These results provide strong evidence that during gel-state bromination, crystalline stems in the crystalline component of the gel network are inaccessible to functionalizing reagent and are preserved as long segments of un-functionalized styrene units along the copolymer chains. Thus, sPS/solvent gels prepared from different solvents

produce semicrystalline blocky sPS-*co*-sPS-Br copolymers with tailored chain sequences and tunable crystallization properties and phase behavior.

4.2. Introduction

Segmented block copolymers are characterized by multiple chemically distinct polymer segments linked together through covalent bonds.[1,2] The individual characteristics of the discrete block segments, for example the chemical nature of the repeating monomers, block lengths and distribution, number of blocks, and chain architectures, govern the chemical and physical properties of the block copolymer.[3-5] Moreover, the thermodynamic incompatibility among the chemically dissimilar blocks often drives self-assembly into well-ordered, micro-phase separated morphologies that can significantly enhance the material properties. Consequently, segmented block copolymers have received tremendous attention with respect to controlled synthesis and customized physical properties with potential uses as nanostructured materials.[6-8] The technological applicability of segmented block copolymers is promising; however, the generally arduous procedures for block copolymer synthesis, often involving inert atmospheric conditions, well-controlled sequential reaction timings, specialized initiators, and high purity monomers and solvents, generally limits the scope of their commercial application.[9]

As a distinct alternative to the complex polymerization mechanisms and synthetic protocols employed in the conventional formation of block copolymers, our recent efforts have demonstrated that blocky copolymer microstructures can be achieved using comparatively simple post-polymerization functionalization chemistries carried out on semicrystalline homopolymers in their heterogeneous gel state.[10-12] Herein, the term "blocky copolymer" will be used as a description of gel-state functionalized copolymers, implying a significant degree of non-randomness in the distribution of comonomers along the copolymer chain.

Gels of crystallizable homopolymers (e.g., sPS) are composed of tightly packed chain segments in lamellar crystallites that act as physical cross-links bound together by a percolating network of solvent swollen amorphous chains.[13-17] When a functionalizing reagent is introduced to the heterogeneous gel network, it is sterically excluded from the crystalline component, and thus only reacts with monomer units in the accessible interconnecting amorphous component. Using this straightforward post-polymerization functionalization approach, the resulting copolymer is likely to contain separate segments of randomly functionalized "blocks" and un-functionalized "blocks" originating from monomer units that were isolated within the crystalline domains of the gel network.

Reports of heterogeneous functionalization reactions in the literature set a precedent for utilizing gel-state reaction conditions to produce copolymers with blocky microstructures and tailored chain sequences. For example, we recently demonstrated that the heterogeneous sulfonation and bromination of sPS and poly(ether ketone) (PEEK) gels, yields copolymers with a blocky distribution of functionalities along the chains.[10-12] The gel-state functionalized sPS and PEEK copolymers demonstrated superior crystallizability and faster crystallization kinetics compared to their solution-state random analogs. Similarly, Venditto and coworkers[18] showed that exposing a gel of semicrystalline syndiotactic polystyrene (sPS) to chlorosulfonic acid results in preferential sulfonation of the gel's amorphous component. While evidence of a blocky microstructure was not directly explored, their heterogeneous method is effectively equivalent to our gel-state approach to produce blocky copolymers.[10,19,20] In earlier work, Borriello and coworkers[21] investigated the post-polymerization sulfonation of solution cast or compression-molded sPS films, evaluating the interplay between sulfonating reagent diffusion and reaction processes on sulfonation heterogeneity across the films. Solution cast films demonstrated uniform

sulfonation, attributed to rapid diffusion of sulfonating reagent through nanoporous phases in the film. In contrast, compression-molded films exhibited a decreasing sulfonation gradient from the film's surface to interior, consistent with slow diffusion of sulfonating reagent into the non-porous, solid-state "bulk" film. The results of their analysis were similar to that observed for the sulfonation of atactic polystyrene (aPS) films.[22] Using results from experiment and simulations, Genzer and coworkers[23-28] have extensively investigated the bromination of aPS in poor solvents, where polymer chains are in a collapsed conformation. In this collapsed state, portions of the chains were effectively shielded from the brominating reagent, resulting in blocky brominated styrene sequences. Others have performed post-polymerization bromination[29] or acetylation[30] on suspended sPS powders, though copolymer microstructure was not investigated in these studies. Ultimately, these results demonstrate that copolymers with a block or blocky microstructure can retain the properties of the pure homopolymer with the added advantage of distinct properties attributed to the functional component. Given the ability to control the precise morphology of the semicrystalline gel network, specifically through changing the polymer concentration, gelation solvent, and/or gelation conditions, copolymers that contain distinct blocks of highly functionalized segments with tunable sequence distributions, chemical composition, and copolymer properties are anticipated.[13-17,31-36]

This work demonstrates the heterogeneous post-polymerization bromination of sPS/carbon tetrachloride (CCl_4) and sPS/chloroform ($CHCl_3$) gels to produce blocky brominated sPS (sPS-co-sPS-Br) copolymers. The purpose of this research was to investigate the relationship between the sPS/solvent gel morphology and the copolymer microstructure, degree of blockiness, and physical properties. The morphology of the sPS/solvent gels was characterized using X-ray scattering techniques. To investigate how the specific distribution of functional groups along the chains

effects the copolymer properties, NMR spectroscopy was used to evaluate the copolymer microstructure and comonomer sequence distribution, X-ray scattering techniques were used to investigate the copolymer morphology, and differential scanning calorimetry (DSC) was used to probe copolymer thermal properties and crystallization kinetics. In order to obtain deeper insight into the effect of gel morphology on copolymer microstructure and crystallization behavior, computer simulations of the blocky microstructure and simulated average chains of the brominated sPS copolymers have been developed. Through this work, heterogeneous gel-state functionalization carried out on sPS/solvent gels with different morphologies is proven to be a facile method to prepare semicrystalline blocky sPS-*co*-sPS-Br copolymers with tailored chain sequences and tunable crystallization properties and phase behavior. Given the wealth of gelation solvents for sPS and other high-performance semicrystalline homopolymers, the broader impact of this fundamental research is to apply this post-polymerization functionalization approach to the tailored design of new functional materials with desirable physical and chemical properties that originate from the tunable blocky microstructure.

4.3. Experimental Section

4.3.1. Materials

Syndiotactic polystyrene (Questra® 102) with a weight average molecular weight (M_w) of 300,000 g mol^{-1} was provided by Dow Chemical Company. Chloroform ($CHCl_3$), 1,2-dichloromethane (DCM), and 1,1,2,2-tetrachloroethane (TCE) were purchased from Fisher Scientific Company. Elemental bromine (Br_2) was obtained from Sigma Aldrich®. The Lewis acid catalyst, ferric(III) chloride ($FeCl_3$), was purchased from VWR International LLC. All chemicals and reagents were used as received.

4.3.2. Sample preparation

Samples of the 10 w/v% sPS/solvent gels and films of the sPS homopolymer and brominated copolymers were prepared for morphological characterization by X-ray scattering techniques. To prepare the 10 w/v% sPS/solvent gels, sPS pellets were dissolved in CCl_4 or $CHCl_3$ at 120−140 °C or 90 °C, respectively, followed by transferring the sPS solution to a thin-walled, 3 mm outer diameter, glass tube that was then sealed and stored at room temperature to promote gel formation. Films were prepared from powders by melt pressing between Kapton sheets at 30 °C above T_m for 20 s at 2200 psi then for 20 s at 4500 psi, followed by quenching in ice water to prevent sPS crystallization. Crystalline films of the sPS homopolymer and brominated copolymers were prepared from the amorphous films by annealing for 1 h at 140 °C. Gel samples were prepared for wide-angle X-ray diffraction (WAXD) experiments by dissolving sPS pellets in solvent in a pressure vessel, followed by removing from heat to promote gel formation. The gels were stored at room temperature for ca. 24 h to mimic the conditions prior to gel-state bromination. The gels were then broken into pieces with a spatula and either immediately dried under vacuum at 70 °C for ca. 24 h or stirred in DCM for ca. 72 h to mimic the bromination reaction, followed by filtering and drying under vacuum at 70 °C for ca. 24 h.

4.3.3. Gel-state bromination

To prepare a 10 w/v% sPS/$CHCl_3$ gel, sPS (2.5 g, 0.83 μmol) pellets were first dissolved in stirred $CHCl_3$ (25 mL) in a pressure vessel at ca. 90 °C, then removed from heat to promote gel formation. A translucent gel formed over a period of at least 6 h and was stored at room temperature for approximately another 24 h prior to use. The post-polymerization functionalization method used to brominate a 10 w/v% sPS/CCl_4 gel is described in **Chapter 2**[12] and was performed on the 10 w/v% sPS/$CHCl_3$ gel with slight modification. Briefly, using a spatula, the gel was broken into

small pieces (ca. 1-3 mm), dispersed in DCM (final sPS concentration of 3 w/v%), and placed in an ice bath. The flask was purged with argon, followed by the addition of $FeCl_3$ (54 mg, 0.33 mmol). After stirring for 30 min, a stock solution of 50 w/w% Br_2 in DCM (2.2 mL, 0.043 mol) was introduced dropwise to the reaction vessel over two hours. The reaction was carried out in the dark under argon at room temperature and terminated after 2.5–6 h from the time of the first stock solution addition, by pouring the suspension into stirred methanol. All samples were purified by dissolving in TCE at reflux, followed by filtration of the warm solutions through a filter paper (Whatman® 1) and precipitation in methanol, which produced white solids. Prior to characterization, samples were ground into homogeneous powders, washed by soxhlet extraction in hot methanol for ca. 24 h, and dried under vacuum at 80 °C for ca. 18 h.

4.3.4. NMR spectroscopy

Microstructural analysis and comonomer sequencing were carried out by nuclear magnetic resonance (NMR) spectroscopy. ^{1}H NMR experiments were recorded at room temperature in deuterated chloroform ($CDCl_3$) on an Agilent U4-DD2 400 MHz spectrometer. Quantitative ^{13}C NMR experiments were recorded at room temperature in 1,1,2,2-tetrachloroethane-d_2 (TCE-d_2) on a Bruker Avance II 500 MHz spectrometer equipped with a LN2 prodigy cryogenic BBO probe using a C13IG pulse program, proton decoupling (NOE−), a relaxation delay of 6 sec, O1P of 95, and a sweep width of 150 ppm. The Line Fitting function in Mestrelab Research's MestReNova x64 software was used to deconvolute and integrate the multiple peaks in the quaternary carbon region of the ^{13}C NMR spectrum. The deconvolution method is discussed in more detail in a **Chapter 3**.[37]

4.3.5. Thermal properties and crystallization kinetics

Copolymer thermal properties and crystallization kinetics were probed using differential scanning calorimetry (DSC, TA Instruments DSC Q2000) operated under continuous nitrogen. To investigate the copolymer crystallizability under specific cooling conditions, samples were first annealed at 300 °C (unless stated otherwise) for 3 min to erase thermal history, then cooled to 0 °C at −60 °C min^{-1} (rapid cool) or −10 °C min^{-1} (slow cool). Isothermal crystallization from the melt was carried out for 2 h at 190 °C. All heating scans were recorded at 10 °C min^{-1}. TA Instruments Universal Analysis software was used to determine glass transition temperatures (T_g), crystallization temperatures at maximum exothermic heat flow (T_c), and melting temperatures at maximum endothermic heat flow (T_m). To ascertain crystallization half-times ($t_{1/2}$), defined as the time at which a material attains 50% of its maximum crystallinity, samples were subjected to isothermal crystallization at specific crystallization temperatures below T_m. Samples were annealed for 5 min at 300 °C (unless stated otherwise) prior to analysis. The isothermal crystallization profiles (heat flow versus time) were analyzed using the following approach (**Equation 1**):

$$\boldsymbol{F_c(t) = \frac{\int_0^t \frac{dH}{dt}\,dt}{\int_0^\infty \frac{dH}{dt}\,dt}} \qquad \textbf{(1)}$$

where $F_c(t)$ is the bulk fractional crystallinity of the functionalized copolymer systems, equal to the heat evolved during isothermal crystallization at a specific time t divided by the total heat evolved during the isothermal crystallization process. The resulting crystallization isotherms (F_c versus time) were used to determine $t_{1/2}$ by extrapolating F_c at 0.5 to the time axis. These $t_{1/2}$ values were used as a comparative measure of the overall rate of bulk crystallization.

4.3.6. X-ray scattering techniques

The morphologies of the sPS/solvent gels, sPS homopolymer, and brominated copolymers were investigated using X-ray scattering techniques. Ultra-small-angle X-ray scattering (USAXS) and small-angle X-ray scattering (SAXS) experiments were performed at the Advanced Photon Source beamline 9ID-C at Argonne National Laboratory. The USAXS instrument was configured in standard mode with an X-ray energy of 21 keV (λ = 0.5895 Å), X-ray photon flux of ca. 1013 mm^{-2} s^{-1}, and a combined q range of 0.0001–1.3 $Å^{-1}$ ($q = 4\pi/\lambda \sin(\theta)$, where λ is the wavelength and θ is one-half of the scattering angle).[38-40] The USAXS and SAXS profiles were acquired sequentially and merged into a single data set using the Irena SAS package.[41] The observed scattering features in the desmeared USAXS/SAXS profiles were analyzed using either the Unified Fit, described in the Irena tool suite,[41] or a linear two-phase model and the one dimensional (1-D) correlation function. Wide-angle X-ray diffraction (WAXD) experiments were performed using a Rigaku MiniFlex II X-ray diffractometer emitting X-rays with a wavelength of 0.154 nm (Cu K_α). Samples were scanned from 5° to 40° 2θ at a scan rate of 0.250° 2θ min^{-1} and a sampling window of 0.050° 2θ at a potential of 30 kV and current of 15 mA. All WAXD data were analyzed using the PDXL 2 software package to obtain WAXD intensity versus 2θ profiles. The volume fraction of crystallinity, $\%X_c$, was calculated from the WAXD profile through deconvolution of the crystalline and amorphous contributions and integration, according to **Equation 2**:

$$\%\boldsymbol{X_c} = \frac{\boldsymbol{I_c}}{\boldsymbol{I_c + I_a}} \qquad \textbf{(2)}$$

where I_c and I_a are the integrated intensities of the crystalline and amorphous contributions, respectively. To deconvolute the WAXD profile, the crystalline reflections and amorphous contributions were individually fit using Gaussian functions. The morphology of melt-crystallized samples was probed by SAXS using a Rigaku S-Max 3000 3 pinhole SAXS system equipped with

a rotating anode that emits X-rays with a wavelength of 0.154 nm (Cu Kα). The sample-to-detector distance was 1605 mm, and the *q*-range was calibrated using a silver behenate standard. Two-dimensional SAXS patterns were obtained using a fully integrated 2D multiwire, proportional counting, gas-filled detector with an exposure time of 2 h. The SAXS data were analyzed using the SAXSGUI software package to obtain radially integrated SAXS intensity versus q profiles. The center-to-center intercrystalline domain spacing, i.e., long period (L_p), and average crystal segment length were calculated from the crystalline scattering feature of the Lorentz-corrected SAXS profiles using the one-dimensional (1D) correlation function and a linear two-phase model.

4.3.7. Simulations of the blocky copolymer microstructure

To rationalize the effect of gel morphology on copolymer microstructure and crystallization behavior, polymer chain sequences with blocky microstructures were simulated using a Fortran code created in-house by Dr. Diego Troya. The blocky microstructure, resulting from functionalization in the semicrystalline gel state, was simulated by first establishing an inaccessible fraction of monomers along a chain, representing crystalline stems in the physical gel, prior to random bromination of the remaining accessible monomers, representing amorphous chain segments in the gel. The rationalization for the inaccessible fraction and inaccessible block lengths used in these simulations is based on the average lamella thickness (l_c) determined from the SAXS profiles of the as prepared gels and the measured degree of crystallinity of the as prepared gels from the WAXD profiles and is discussed in more detail below in the Results and discussion section. For each simulated chain, the prevalence of each unique pentad sequence (e.g., sssss, bbbbb, etc., where s = styrene and b = Br-Sty) is determined and the root-mean-square deviation (RMSD) between the pentad sequence distribution of the simulated chain and the empirical data from ^{13}C NMR spectroscopy is calculated.

4.3.8. Simulated average copolymer chains based on the empirical pentad sequence distributions

Simulated chains that represent the average copolymer chain sequence in the Blocky copolymers, were created using a Fortran code created in house. Chains are simulated from a short sequence of un-functionalized styrene units by subsequent additions of short sequences of un-functionalized and functionalized styrene units to the chain end. The rationalization for the specific short sequence that is added during each addition step is based on the difference between the average pentad sequence distribution of the simulated chain and the pentad sequence distribution from the NMR data and is discussed in more detail below in the Results and discussion section.

4.4. Results and Discussion

4.4.1. The sPS/solvent gel morphology

Images of the 10 w/v% sPS/CCl_4 gel and 10 w/v% sPS/$CHCl_3$ gel, taken approximately 24 h after gelation, are provided in **Figure 4.1**. While both sPS/solvent systems form stable gels established by a simple "tip test" in which no flow was observed upon inversion of the solution-containing vessel, the gels demonstrate strikingly different visible light transparencies. The sPS/CCl_4 gel is opaque, while the sPS/$CHCl_3$ gel is translucent. The gelation kinetics of these solvent systems are also remarkably different. After removal from heat, the sPS/CCl_4 solution develops into a stable gel in under 10 min. In distinct contrast, the sPS/$CHCl_3$ solution forms a translucent gel over a period of at least 6 h.

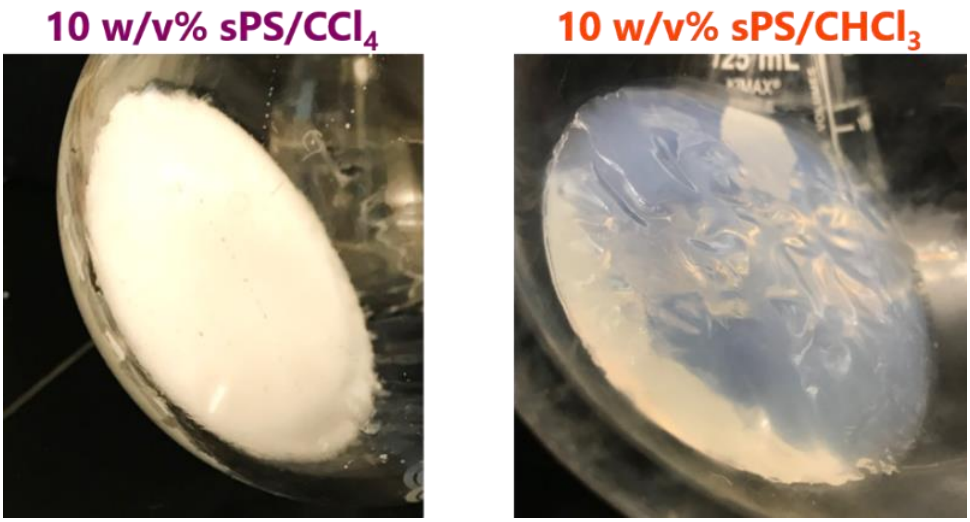

Figure 4.1. Images of a 10 w/v% (left) sPS/CCl_4 gel and (right) sPS/$CHCl_3$ gel.

In order to obtain a deeper understanding of the differences between the sPS/solvent systems, X-ray scattering techniques were used to investigate the sPS/solvent gel morphologies. USAXS/SAXS profiles of the as prepared 10 w/v% sPS/CCl_4 and 10 w/v% sPS/$CHCl_3$ gels are compared in **Figure 4.2**. To the author's knowledge, this is the first reported USAXS profile of an sPS/solvent gel. The wide-angle X-ray diffraction (WAXD) profiles of the sPS/solvent gels are provided in **Figure S4.1**. **Figure 4.2** also shows the USAXS/SAXS profile of an sPS homopolymer film that was quenched from the melt and then annealed for 1 h at 140 °C to promote sPS crystallization. The USAXS/SAXS profile of the sPS homopolymer exhibits a broad scattering feature between 0.3−3 nm^{-1} with q^{-4} dependence in the Porod region between 1−3 nm^{-1} that is attributed to the surface fractal structure of crystalline lamellae.[42] Similarly, both the sPS/CCl_4 gel and sPS/$CHCl_3$ gel show a scattering feature at high q, in the region of 0.2−0.6 nm^{-1} and 0.1−1 nm^{-1}, respectively, each with q^{-4} dependence that is consistent with the crystalline lamellae observed in sPS. In the low q region from 0.001−0.1 nm^{-1}, the sPS/CCl_4 gel shows a second scattering feature in the region from 0.006 $nm^{-1} < q < 0.07$ nm^{-1} with q^{-3} dependence in the Porod region between 0.07−0.15 nm^{-1}. The presence of this feature strongly implies that the sPS/CCl_4

gel has large-scale mass fractal-type structure that is attributed to clusters of crystallites that are randomly dispersed by solvent swollen amorphous chains. Thus, the crystallite clusters are expected to act as physical cross-links bound together by a percolating network of solvent swollen amorphous chains that together form the three-dimensional (3D) gel network.[13-17] In contrast, the sPS/$CHCl_3$ gel is featureless at low q with $q^{-0.67}$ dependence that is indicative of disorder between the boundaries of the crystalline and solvent swollen amorphous components. Based on these results and previous investigations of the sPS/$CHCl_3$ gel morphology by Kobayashi et al.[15,31] using small-angle neutron scattering (SANS) experiments, it appears that the 3D network of the sPS/$CHCl_3$ gel contains loosely packed crystallites that are tied together by amorphous chains. For the Kratky plots (i.e., $I(q) \times q^2$ *versus* q) of the sPS/solvent gels see **Figure S4.1**.

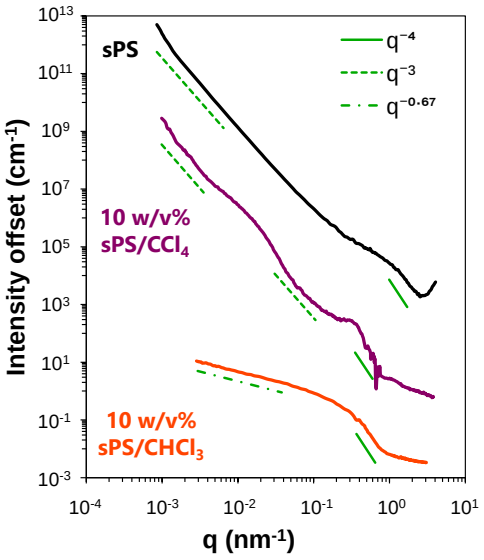

Figure 4.2. USAXS/SAXS profiles of the sPS homopolymer that was quenched from the melt and annealed for 1 h at 140 °C and the as prepared 10 w/v% sPS/CCl_4 and 10 w/v% sPS/$CHCl_3$ gels. For clarity, the scattering profiles are vertically offset. The green lines were added to demonstrate the power law scattering.

The geometry of the sPS/solvent gel networks was further investigated by estimating the center-to-center intercrystalline domain spacing, i.e., long period (L_p), from the d-spacing at the peak of the high q scattering feature in the Lorentz-corrected SAXS profile using Bragg's law ($d_{Bragg} = 2\pi/q$). The long period represents the sum of the thickness of the crystalline lamella, l_c,

and the thickness of the interlamellar amorphous region, l_a ($L_p = l_c + l_a$). Assuming a linear two-phase model, an estimated l_c may be obtained from the product of L_p and the volume fraction of crystallinity ($\%X_c$) within the material. For each gel, $\%X_c$ was ca. 40-42%, determined from the crystalline and amorphous contributions in the WAXD profile (see **Figure S4.2**) and the area of the melting endotherm in the DSC heating trace (see **Figure S4.3**). The results of the SAXS analysis are summarized in **Table 4.1**. Compared to the sPS/CCl_4 gel, which has a L_p value of ca. 18.3 nm and an estimated average lamella thickness of ca. 7.5 nm, the sPS/$CHCl_3$ gel exhibits a slightly larger average center-to-center intercrystalline domain spacing and lamella thickness of ca. 22.2 nm and 9.1 nm, respectively. Thus, it appears that the polymer-solvent interactions in the sPS/$CHCl_3$ system that facilitate relatively slow gelation kinetics also favor the formation of relatively thick crystallites. For each sPS/solvent gel, the average number of styrene units in a crystalline stem was estimated, based on the s(2/1)2 helical conformation of the δ-form crystal structure of sPS with 4 monomer units per identity period (c-axis dimension = 0.77 nm). The sPS/$CHCl_3$ gel exhibits slightly longer crystalline stems of ca. 46-49 styrene units, compared to ca. 38-40 styrene units in the sPS/CCl_4 gel.

Table 4.1. SAXS analysis of the intercrystalline domain spacing in the 10 w/v% sPS/CCl_4 and sPS/$CHCl_3$ gels.

Sample	q (nm^{-1})	L_p (nm)	$\%X_c$	l_c (nm)	Estimated units in a crystalline stem[c]	l_a (nm)
10 w/v% sPS/CCl_4	0.342	18.3	40[a] (42)[b]	7.3 (7.7)	38 (40)	11.0 (10.7)
10 w/v% sPS/$CHCl_3$	0.283	22.2	40[a] (42)[b]	8.8 (9.4)	46 (49)	13.4 (12.8)

[a]Calculated from the area under the melting endotherm in the DSC first heating trace of the sPS/solvent gel. The gel was dried under vacuum at 70 °C for ca. 24 h prior to analysis.
[b]Calculated from the area of the crystalline contribution divided by the area of the amorphous contribution in the WAXD profile of the dried sPS/solvent gel, prepared by the method described above. All values in parentheses are based on the results from the WAXD analysis.
[c]Average number of styrene units in a crystalline stem of thickness l_c, based on the helical conformation of the δ-form crystal structure of sPS with 4 styrene units per identity period (c-axis dimension = 0.77 nm).[43]

Based on the appearance, gelation kinetics, and SAXS analysis of the 10 w/v% sPS/CCl_4 and sPS/$CHCl_3$ gels, and the characteristic fibrillar network structure of sPS/solvent gels,[32,35]

schematic representations of the gel morphologies were developed, shown in **Figure 4.3**. The sPS/solvent gels contain extended crystalline stems in tightly packed crystallites that are tied together by a percolating network of amorphous chain segments.[32,35] In the sPS/CCl_4 gel, two distinct regions are represented, a polymer-rich region that contains clusters of unoriented crystallites tied together by amorphous chain segments, and a polymer-poor region that consists of a percolating network of amorphous chain segments, linking the crystallite clusters together. Styrene units exist in the sPS/CCl_4 gel in three distinct environments, as part of the: (1) crystalline stems in the crystalline component; (2) tightly packed amorphous chain segments between crystallites in the polymer-rich region, and; (3) loosely packed amorphous chain segments in the polymer poor region. In contrast, the sPS/$CHCl_3$ gel is represented by a random dispersion of unoriented crystallites that are bound together by a percolating network of amorphous chain segments. Thus, styrene units exist in the sPS/$CHCl_3$ gel in two distinct environments, as either part of the crystalline stems or the amorphous tie chains. Through the introduction of brominating reagent to these different sPS/solvent gel morphologies, sPS-*co*-sPS-Br copolymers with tailored chain sequences were anticipated.

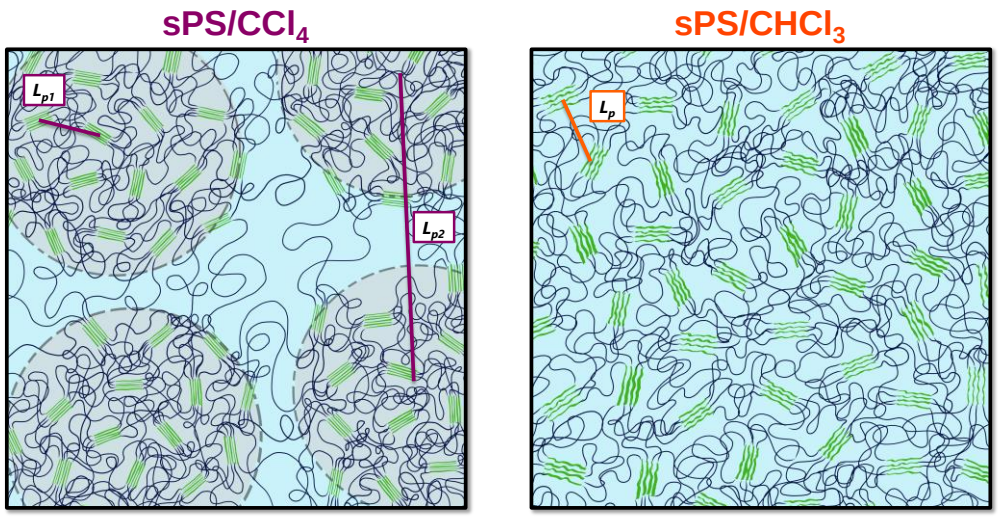

Figure 4.3. Schematic representations of the (left) 10 w/v% sPS/CCl_4 gel and (right) 10 w/v% sPS/$CHCl_3$ gel morphology. Short green lines = crystalline stems in the crystallites; long blue squiggly lines = amorphous polymer chains; grey circles = crystallite clusters. The dimensions of the high q scattering (L_p) and low q scattering (L_{p2}) features are indicated by colored lines. Images are not drawn to a precise scale.

4.4.2. Microstructural analysis using NMR spectroscopy

To investigate the copolymer microstructure of the gel-state functionalized, *i.e.*, Blocky, sPS-*co*-sPS-Br copolymers, samples were prepared from the 10 w/v% sPS/CCl_4 gel (CaT-x%) and 10 w/v% sPS/$CHCl_3$ gel (CH-x%) in a matched set of approximately x = 6, 15, 20, and 30 mol% *para*-bromostyrene (Br-Sty) units and analyzed by NMR spectroscopy. It is worth noting that 29 mol% Br was the maximum degree of functionalization that could be obtained from the 10 w/v% sPS/CCl_4 gel. The ^{1}H NMR spectra of the sPS homopolymer and the sPS/CCl_4 and sPS/$CHCl_3$ copolymers are shown in **Figure 4.4**. Compared to pure sPS, new proton resonances appear in the ^{1}H NMR spectrum of the brominated copolymers at 1.23, 1.58−1.75, 6.27−6.28, and 7.11−7.22 ppm, corresponding to the methylene (H(b′)) and methine (H(a′)) protons, and the aromatic protons (H(2′) and (H(3′)) of brominated styrene (Br-Sty) monomers, respectively.[12] For all samples, the ratio of the total peak areas of the methylene (H(b), H(b′)) and methine (H(a), H(a′)) protons was approximately 2:1, which indicates the absence of backbone bromination. The Br-content (mol% Br) was derived from the fraction of *ortho*-proton resonances of Br-Sty monomers (H(2′),

6.27−6.38 ppm) to the total area of styrene (H(2′)) and Br-Sty *ortho*-proton resonances (6.27−6.60 ppm).

Comparing the ^{1}H NMR spectra of the sPS/CCl_4 and sPS/$CHCl_3$ copolymers with similar Br-content reveals slight differences in their peak intensities and ^{1}H chemical shifts. These differences may be the result of differences in Br-content. They may also indicate differences in copolymer microstructure, i.e., the distribution of comonomer sequences along the copolymer chains. Nevertheless, the sensitivity of the ^{1}H nucleus to comonomer sequence is insufficient to warrant further interpretation of the copolymer microstructure from the ^{1}H NMR spectrum.

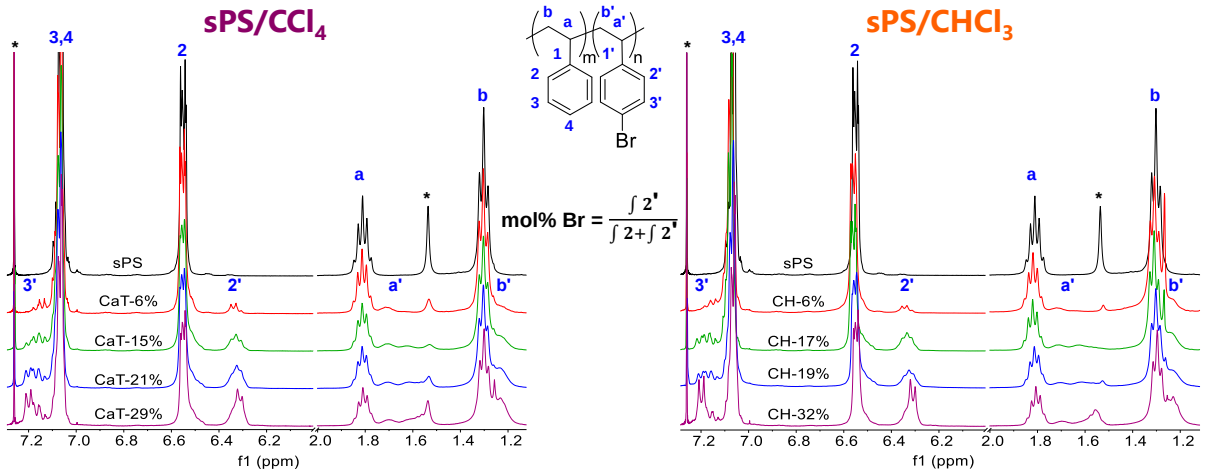

Figure 4.4. ^{1}H NMR spectra of the (left) sPS/CCl_4 and (right) sPS/$CHCl_3$ copolymers increasing in mol% Br from top to bottom. The spectra were recorded at room temperature. For comparison, the spectra are referenced to $CDCl_3$, and normalized over the range 6.27−6.60 ppm. The asterisks (*) indicate solvent resonances.

Quantitative ^{13}C NMR spectroscopy was used to investigate the copolymer microstructure and comonomer sequence distribution of the Blocky copolymers. **Figure 4.5** shows the aromatic region of the high-resolution ^{13}C NMR spectra for the sPS homopolymer and the sPS/CCl_4 and sPS/$CHCl_3$ copolymers. For the full ^{13}C NMR spectrum, see **Figure S4.4**. Upon *para*-substitution of the styrene phenyl ring with bromine, new carbon resonances appear in the ^{13}C NMR spectrum. The new resonances at 129.2 ppm and 130.9 ppm are assigned, respectively, to the *ortho*-(C(2′)) and *meta*-carbons (C(3′)) of brominated phenyl rings. The multiple new resonances in the regions

from 118.8−119.5 ppm and 145.15−143.15 ppm are attributed to the Br-substituted phenyl carbons (C−Br, C(4′)) and the quaternary phenyl carbons of un-brominated (C(1)) and brominated (C(1′)) monomers, respectively. For both the sPS/CCl_4 and sPS/$CHCl_3$ copolymers, the distribution and intensities of the peaks in the quaternary carbon and C−Br regions are highly dependent on Br-content (see **Figure S4.5**). The presence of multiple peaks in these regions signifies through-bond communication between neighboring styrene and Br-Sty monomers and provide a unique fingerprint of the copolymer microstructure originating from the specific comonomer sequence distribution.

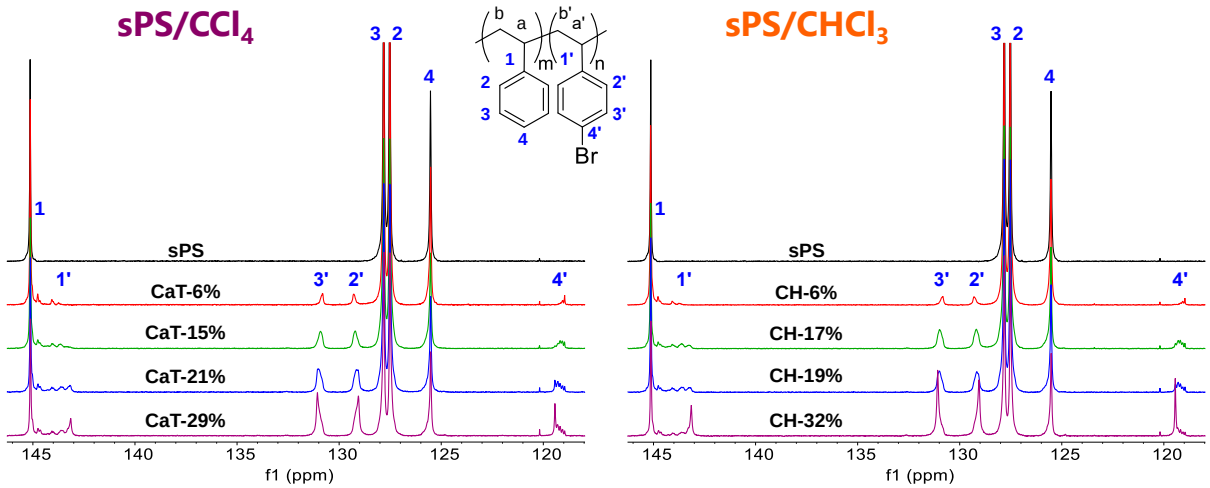

Figure 4.5. The aromatic region of the ^{13}C NMR spectra of the sPS homopolymer and the Blocky brominated copolymers prepared from (left) sPS/CCl_4 gels and (right) sPS/$CHCl_3$ gels, increasing in degree of bromination from top to bottom. The spectra were recorded at room temperature. For comparison, the spectra are referenced to TCE-d_2 and normalized over 127.0–132.5 ppm.

In Chapter 3,[37] a comonomer sequencing method was introduced to assign each peak in the quaternary carbon spectrum of the sPS-*co*-sPS-Br copolymers to a styrene or Br-Sty unit that exists in the center of a unique sequence of five monomers, i.e., a pentad, along the copolymer chain (e.g., ssssb were s = styrene and b = Br-Sty). **Figure 4.6** shows the quaternary carbon spectra of sPS/CCl_4 CaT-29% and sPS/$CHCl_3$ CH-32% decomposed into their twenty separate additive peak components. Each peak represents one of the twenty unique pentad combinations that are possible

for a copolymer with two different monomers. Several of these peaks are assigned to pentad sequences in **Figure 4.6**. For the complete pentad assignments and their approximate chemical shifts, see **Table S4.1**. The color of each peak identifies the unique combination of three monomers in the center of the assigned pentad, i.e., the triad sequence, labeled above the spectrum in **Figure 4.6**. From these assignments, it is clear that the CaT-29% and CH-32% copolymers contain large fractions of both SSS and BBB triads, which is unusual for a statistically random sPS-*co*-sPS-Br copolymer with approximately 31 mol% Br-content.[37] These results strongly suggest that gel-state functionalization is capable of producing copolymers with non-random, i.e., blocky, distributions of functional groups along the chains in a blocky microstructure.

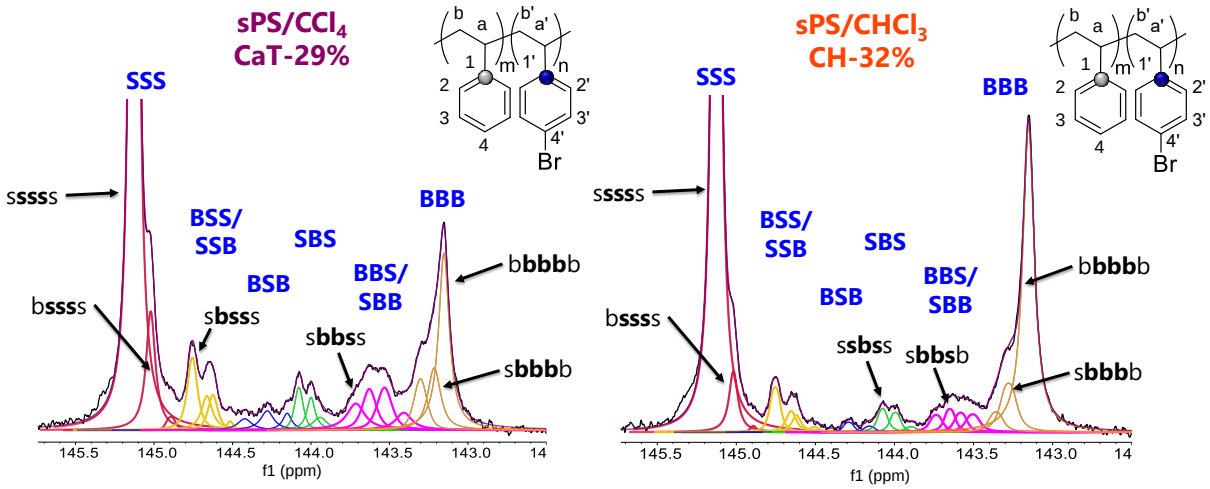

Figure 4.6. The quaternary carbon spectra of (left) sPS/CCl_4 CaT-29% and (right) sPS/$CHCl_3$ CH-32% decomposed into their separate additive pentad peak components with triad assignments and several pentad assignments. The peaks are color-coded by triad combination: SSS = red; BSS/SSB = yellow; BSB = blue; SBS = green; BBS/SBB = magenta; BBB = orange.

To investigate the copolymer microstructure of the Blocky copolymers, pentad sequence distributions were calculated from the ratio of the area under each quaternary carbon peak to the total area of the quaternary carbon region (142.9−145.6 ppm) in the ^{13}C NMR spectrum. **Figure 4.7** compares the fraction of styrene pentad (sssss) in the sPS/CCl_4 and sPS/$CHCl_3$ copolymers with respect to Br-content. At 6 mol% Br, the sPS/CCl_4 and sPS/$CHCl_3$ samples exhibit a similar fraction of sssss pentad. With increasing Br-content, the amount of sssss pentad decreases in both

series, as expected. It is worth noting that this observed decrease in sssss pentad composition is inconsequential compared to the decrease in the fraction of sssss pentad observed in brominated sPS copolymers with random microstructures. For example, a random copolymer with 31 mol% Br-content (R-31%) contains just 14% sssss pentad compared to 51% and 53% in the sPS/CCl_4 CaT-29% and sPS/$CHCl_3$ CH-32% copolymers, respectively. These data confirm that the gel-state functionalization method is capable of producing copolymers with a significant degree of non-randomness in the distribution of comonomers along the copolymer chains in blocky microstructure. Above 6 mol% Br, the sPS/$CHCl_3$ contain a larger fraction of sssss pentad relative to their sPS/CCl_4 analogs. Thus, it appears that the sPS/$CHCl_3$ gel morphology, in which styrene units are expected to exist in two distinct environments within the gel network, produces copolymers with a higher prevalence of styrene "blocks" of at least five consecutive styrene units.

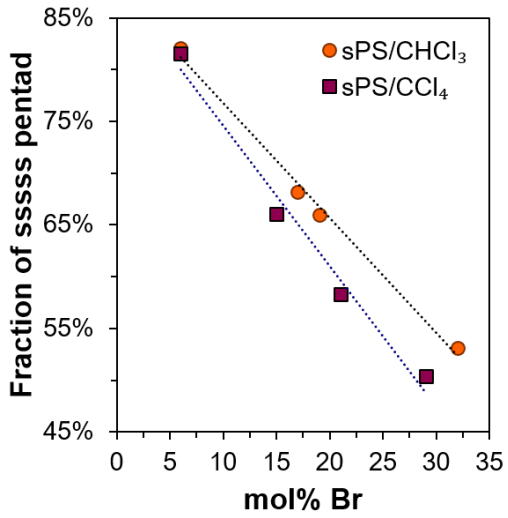

Figure 4.7. Fraction of styrene pentad (sssss) with respect to Br-content in the sPS/CCl_4 and sPS/$CHCl_3$ copolymers calculated from the integration of the quaternary carbon NMR spectra.

The degree of blockiness in the sPS/$CHCl_3$ copolymers has been characterized by the copolymer block character (*R*), calculated based on Bernoullian probability statistics according to **Equation 3**.[44]

$$R = \frac{4(P_{SS})(P_{BB})}{(P_{SB})^2} \qquad \text{where:} \qquad \begin{aligned} P_{SS} &= \text{SSS} + \tfrac{1}{2}\,[\text{SSB/BSS}] \\ P_{BB} &= \text{BBB} + \tfrac{1}{2}\,[\text{SBB/BBS}] \\ P_{BS} &= 1 - P_{SS} - P_{BB} \end{aligned} \qquad \textbf{(3)}$$

Here, P is the probability that a polymer chain contains an SS (P_{SS}), BB (P_{BB}), or BS/SB (P_{BS}) dyad, respectively. The dyad probabilities are obtained from the pentad sequence distribution and are calculated from the fraction of SSS, [SSB/BSS], [SBB/BBS], and BBB triad sequences in each copolymer. For a copolymer with a Bernoullian (*i.e.*, random) sequence distribution, R is equal to unity. A copolymer with a block-like distribution of functional groups along the chain will have an R value greater than unity. The block characters of the sPS/CCl_4 and sPS/$CHCl_3$ copolymers are compared in **Figure 4.8.** For reference, the average block characters of simulated random copolymers are also provided, determined using a random number generation method that is described in **Chapter 2**.[37] The average R values of the simulated random copolymers range from 0.98−1.00, as expected for copolymers that have random distributions of functional groups along their chains. For the sPS/CCl_4 and sPS/$CHCl_3$ samples, R is much greater than unity and increases with increasing Br-content. These results demonstrate that the sPS/CCl_4 and sPS/$CHCl_3$ copolymers have block-like character, even at low Br-content.

Comparing the R values of the sPS/CCl_4 and sPS/$CHCl_3$ samples with similar Br-content reveals that the sPS/$CHCl_3$ copolymers exhibit greater R values, even at 6 mol% Br. Thus, the sPS/$CHCl_3$ copolymers have on average more consecutive styrene units and more consecutive Br-sty units, *i.e.* are more block-like, than their blocky sPS/CCl_4 analogs. Remarkably, the sPS/$CHCl_3$ CH-32% exhibits an R value of ca. 98 (not shown in **Figure 4.8** for clarity), which is approximately three times greater than that of CaT-29%, demonstrating the high degree of blockiness along the copolymer chains in CH-32%. The quantitative insight into the copolymer microstructure obtained from ^{13}C NMR spectroscopy, strongly suggests that the sPS/solvent gel

morphology can be used to tailor the chain sequence of an sPS-*co*-sPS-Br copolymer via a post-polymerization functionalization method; the clustered crystallite morphology of the sPS/CCl_4 gel produces copolymers with a blocky microstructure, while the dispersed crystallite morphology of the sPS/$CHCl_3$ gel produces copolymers with a multiblock-like microstructure, defined here as a polymer chain that contains long "blocks" of un-functionalized styrene units that are separated uniformly by randomly functionalized "blocks" (see **Figure 4.1**).

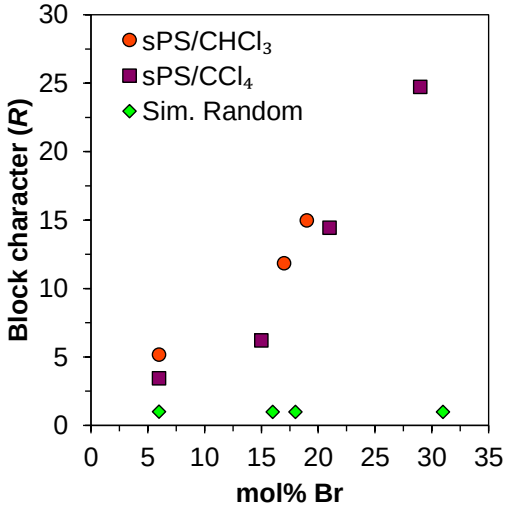

Figure 4.8. The block character (*R*) of the copolymers prepared from sPS/$CHCl_3$ gels (circles) and sPS/CCl_4 gels (squares) with comparison to the average *R* values of 1000 simulated random copolymers (diamonds). $R_{CH\text{-}32\%}$ is 98 (not shown for clarity). The *R* values are calculated from the integration of the quaternary carbon NMR spectra. *R* values greater than one demonstrate block-like character.

4.4.3. Thermal transitions

The effect of sPS/solvent gel morphology on copolymer crystallization behavior was investigated by comparing the thermal transitions and crystallinity of the Blocky copolymers provided by DSC experiments. **Figure 4.9** compares the DSC heating traces of the sPS homopolymer and the sPS/CCl_4 and sPS/$CHCl_3$ copolymers after rapid cooling from the melt at −60 °C min^{-1} to 0 °C. The heating trace of sPS exhibits two endothermic events, the glass transition at 98 °C and an intense melting endotherm at 269 °C. At approximately 6 mol% Br, both the sPS/CCl_4 and sPS/$CHCl_3$ samples crystallize during cooling and show depression in their melting

temperatures, T_m, relative to pure sPS. Bromine groups attached to a crystallizable polymer can act as physical defects along the polymer chains, limiting crystallizability and lamella thickness.[12] It is not surprising then that both the Blocky copolymer series show a depression in T_m with increasing Br-content as a consequence of shorter crystallizable chain segments and thus thinner crystallites.[30,45-47] Nonetheless, it is important to note that melting point depression occurs to a greater extent in the sPS/CCl_4 samples compared to the sPS/$CHCl_3$ samples, despite having approximately the same Br-content (see **Figure S4.6**).

Remarkably, the heating trace of sPS/$CHCl_3$ CH-32% exhibits two distinct melting endotherms, a low temperature endotherm at 226 °C and a higher temperature endotherm at 315 °C (**Figure 4.9**). The low temperature endotherm, which we will denote $T_{m,A}$, is consistent with the melting of thin crystallites composed of short chain sequences of styrene units. The high temperature endotherm, which we will denote $T_{m,B}$, is well above the melting temperature of pure sPS.[48] Based on this DSC result and previous evidence of the crystallization of halogenated sPS,[49,50] $T_{m,B}$ is attributed to the melting of crystallites that contain distinct sequences of Br-Sty units. Thus, it appears that CH-32%, which has approximately one Br-Sty unit for every two styrene monomers, contains polymer chains with runs of styrene units and runs of Br-sty units of significant length that are capable of crystallizing upon rapid cooling from the melt. The presence of two melting endotherms suggests that the "blockiness" that originates from functionalization of the sPS/$CHCl_3$ gel system is somewhat reminiscent of the distribution of comonomers in a conventional multiblock copolymer. In contrast, the sPS/CCl_4 CaT-29% sample shows just one melting endotherm at ca. 270 °C. This T_m is higher than that anticipated for the melting of crystallites composed of styrene units and deviates from the observed trend in melting point depression for the sPS/CCl_4 samples. Thus, in CaT-29%, crystallites composed of Br-Sty units

appear to form preferentially over crystallites of styrene units during heating after conditions of rapid cooling. The melting behaviors of the CH-32% and CaT-29% demonstrate that the gel-state bromination process is capable of producing copolymers that contain distinct sequences of Br-Sty units in segments of significant length irrespective of the gel morphology. However, the superior crystallizability of CH-32% strongly suggests that the sPS/$CHCl_3$ gel morphology is capable of producing copolymers with fewer defects along the chain in a multiblock-like microstructure.

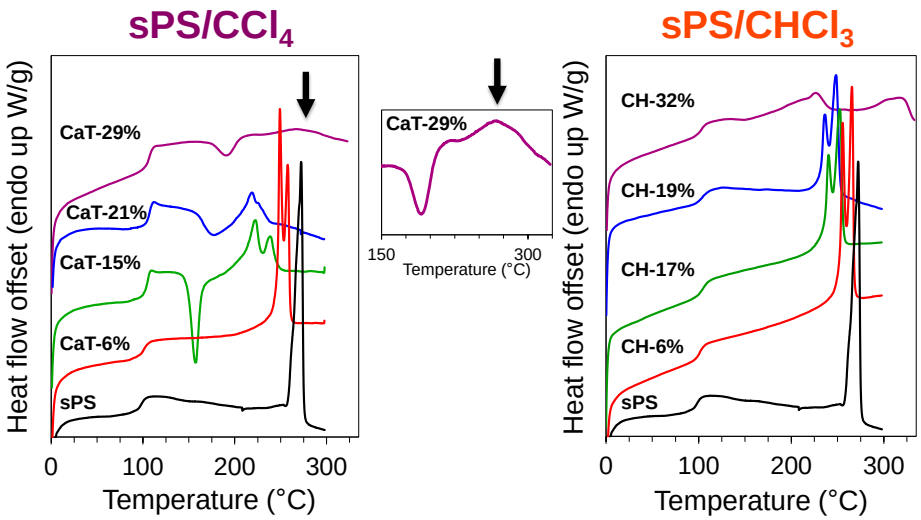

Figure 4.9. DSC heating traces of the sPS homopolymer and the (left) sPS/CCl_4 and (right) sPS/$CHCl_3$ copolymers after rapid cooling from the melt at −60 °C min^{-1}. The melt temperature was 300 °C for samples with less than 25 mol%, 325 °C for CaT-29%, and 335 °C for CH-32%. Heating rate: 10 °C min^{-1}. Center: CaT-29%, indicating the high temperature melting endotherm.

At 17-19 mol% Br, the sPS/$CHCl_3$ copolymers exhibit crystallization during rapid cooling (−60 °C min^{-1}). In distinct contrast, the heating traces of the sPS/CCl_4 samples with greater than 6 mol% Br contain an exothermic event between 150-200 °C (**Figure 4.9**), ascribed to cold crystallization during heating. Cold crystallization following a rapid cool is attributed to a reduction in the rate of crystallization.[30,46] Under slow cooling conditions (−10 °C min^{-1}), the crystallization exotherm, T_c, of the sPS/CCl_4 samples decreases in temperature and intensity with increasing Br-content, which also reflects a reduction in the rate of crystallization (see **Figure S4.7**). By comparison, the sPS/$CHCl_3$ copolymers exhibit crystallization point depression to a

lesser extent (**Figure S4.7**). This thermal behavior strongly suggests that the sPS/$CHCl_3$ copolymer chains contain a more block-like distribution of bromine defects and a higher prevalence of crystallizable styrene segments (i.e., runs of consecutive styrene units of sufficient length), relative to their sPS/CCl_4 copolymer analogs.

To further examine the effect of sPS/solvent gel morphology on copolymer crystallizability, the weight percent crystallinity (%X_c) was calculated from the total area under the melting endotherm (ΔH_f) with respect to the heat of fusion of 100% crystalline pure sPS[48] (ΔH_f° = 79.3 J g^{-1}). The thermal properties and %X_c of the sPS homopolymer and Blocky copolymers after rapid cooling (−60 °C min^{-1}), slow cooling (−10 °C min^{-1}), and 2 h melt crystallization at 190 °C are summarized in **Table 4.2**. For the sPS/CCl_4 samples, the glass transition temperature, T_g, increases with increasing degree of bromination, which is consistent with the findings of Genzer et al.[51] and attributed to hindered rotations of the bulky *p*-bromostyrene units in the amorphous component. Similarly, after rapid cooling conditions the sPS/$CHCl_3$ samples exhibit an increase in T_g. Interestingly, after conditions of slow cooling, during which crystalline chain segments are likely to reorganize and form more perfect crystallites,[33,52] the T_g in the sPS/$CHCl_3$ samples was relatively unchanged. Br-Sty units are expected to be excluded from the crystalline lamellae of sPS crystallites and therefore reside in the amorphous component (if not contained in sequences of crystalline Br-Sty units). While the concentration of Br-Sty units in the amorphous component of the sPS/$CHCl_3$ copolymers is therefore expected to be similar to that of the sPS/CCl_4 copolymers, the observed difference in T_g behavior suggests that the blockiness along the chains in the sPS/$CHCl_3$ copolymer can result in greater thermal expansion, i.e., free volume in the amorphous component.[53]

The crystallizability of the sPS/CCl_4 and sPS/$CHCl_3$ copolymers during conditions of slow cooling and isothermal crystallization is remarkable. For example, after isothermal crystallization at 190 °C, the sPS/CCl_4 CaT-21% and sPS/$CHCl_3$ CH-19% samples yield a degree of crystallinity of $\%X_c$ = 19% and 22%, respectively, that constitutes 59% and 69% of the crystallinity of pure sPS. This crystallization behavior is strongly suggestive of a highly blocky microstructure, in which bromine defects exist in distinct segments along the copolymer chains.[12,30,45] Nevertheless, during rapid cooling conditions, the sPS/$CHCl_3$ copolymers crystallize at lower supercooling (higher crystallization temperatures, T_c) than their sPS/CCl_4 analogs, which signifies faster rates of crystallization. In addition, the sPS/$CHCl_3$ copolymers exhibit greater crystallinity and higher T_m values, indicating that thicker and/or more perfect crystallites form during conditions of rapid cooling. Again, this observed thermal behavior strongly implies a highly block-like distribution of Br-sty defects along the copolymer chains in the sPS/$CHCl_3$ copolymers. For WAXD profiles of the sPS homopolymer and the Blocky brominated copolymers after isothermal crystallization at 190 °C see **Figure S4.8**

Table 4.2 Thermal properties and weight percent crystallinity of the sPS homopolymer and the sPS/$CHCl_3$ (CH-x%) and sPS/CCl_4 (CaT-x%) copolymers measured using DSC.

	After rapid cooling at −60 °C min^{-1}				After slow cooling at −10 °C min^{-1}				After 2 h melt crystallization at 190 °C	
Sample	T_g (°C)	T_{m1} (°C)	T_c (°C)[a]	X_c (%)	T_g (°C)	T_{m1} (°C)	T_c (°C)[a]	X_c (%)	T_{m1} (°C)	X_c (%)
sPS	99	269	224	31	100	270	237	32	270	32
CH-6%	101	256	198	27	101	247	220	27	256	31
CH-17%	105	240	190	23	102	240	206	22	239	25
CH-19%	105	236	189	20	101	238	205	19	237	22
CH-32%	103	211 (305)	170 (252)	6 ([b])	98	221 (313)	184 (284)	8 ([b])	205 (305)	10 ([b])
CaT-6%	103	249	200	25	102	249	215	24	249	29
CaT-15%	107	225	171	14	106	234	187	18	234	22
CaT-21%	105	216	--	11	105	222	180	16	222	19
CaT-29%	109	(267)	--	([b])	107	213	--	4	218	5

T_g = glass transition temperature; T_{m1} = temperature of the first maximum endothermic heat flow; [a]T_c = temperature of the maximum exothermic heat flow during the cooling scan. Values in parentheses correspond to the high melting endotherm ($T_{m,B}$) observed in CaT-29% and CH-32%. X_c = weight percent crystallinity derived from the area under the melting endotherm (ΔH_f) and the heat of fusion of 100% crystalline pure sPS ($\Delta \boldsymbol{H_f^\circ}$) according to the relationship $X_c = \frac{\boldsymbol{\Delta H_f}}{\boldsymbol{\Delta H_f^o}} \times \mathbf{100}\%$. Dashes (--) indicate no thermal transition detected. [b]The X_c for $T_{m,b}$ is not reported. All samples below 29 mol% Br-content were heated to 300 °C and annealed for 3-5 min prior to cooling to erase thermal history. Samples CaT-29% and CH-32% were annealed at 325 °C and 335 °C, respectively.

4.4.4. Crystallization kinetics

How the distribution of bromine defects along the chains affects the crystallization kinetics of the Blocky copolymers was investigated by subjecting the sPS/$CHCl_3$ and sPS/CCl_4 samples to isothermal crystallization at specific temperatures below T_m. To achieve rapid crystallization, chain segments of sufficient length, i.e., stems, of uninterrupted styrene units are required to assemble into stable crystalline domains. Br-Sty monomers encountered at the crystal growth front are structural defects that are consequently excluded from attaching to the growing crystallite. This process of rejection of a defective stem and diffusion of a new stem to the melt-crystal interface ultimately slows the rate of crystallization. The crystallization half-time, $t_{1/2}$, *versus* temperature profiles of the sPS/CCl_4 and sPS/$CHCl_3$ samples are compared in **Figure 4.10**. It should be recognized that for both Blocky copolymer series fast crystallization kinetics (i.e., shorter $t_{1/2}$ times) are observed compared to the crystallization kinetics of statistically random sPS-*co*-sPS-Br copolymers of the same Br-content, attributed to the effects of copolymer microstructure on the probability of encountering a defective stem.[12] The blocky microstructure provides a higher prevalence of crystallizable stems along the polymer chains. With more crystallizable stems, the blocky microstructure minimizes the time-consuming rejection/replacement process and is thus capable of crystallizing in a shorter period of time.

Comparing the $t_{1/2}$ of the Blocky copolymers reveals that at approximately 6 mol% Br, both the sPS/CCl_4 and sPS/$CHCl_3$ samples crystallize relatively fast and at low supercooling (i.e., high temperature). However, above 6 mol% Br, the sPS/$CHCl_3$ copolymers show remarkable crystallization kinetics, crystallizing faster at lower supercooling than their sPS/CCl_4 copolymer analogs. Even the sPS/$CHCl_3$ CH-32% sample, which has approximately one Br-Sty for every two styrene monomers, exhibits a $t_{1/2}$ at 185 °C of just 0.26 min. The intriguing differences in

crystallization kinetics between the sPS/CCl_4 and sPS/$CHCl_3$ samples suggest that the primary microstructure, *i.e.*, the length, frequency, and distribution of crystallizable stems and defective stems along the copolymer chain, effects the probability of encountering a defective stem at the crystal growth front.

The observed differences in the thermal properties and crystallization behavior of the sPS/CCl_4 and sPS/$CHCl_3$ copolymers, strongly suggest that the copolymer's primary microstructure is inherited from the morphology of the crystalline and amorphous components of the parent sPS/solvent gel during the gel-state functionalization reaction. Based on the proposed gel morphology of the sPS/$CHCl_3$ gel, in which crystallites are evenly dispersed by amorphous chain segments (see **Figure 4.1**), it seems reasonable that upon introduction of brominating reagent to the sPS/$CHCl_3$ gel network, the reagent will be sterically excluded from reacting with styrene monomers in the crystalline component and will react readily with styrene monomers in the accessible amorphous component. A copolymer chain from the sPS/$CHCl_3$ gel network is therefore expected to contain crystallizable stems in un-functionalized styrene "blocks" that are separated uniformly by defective stems in randomly functionalized "blocks," with a multiblock-like primary microstructure. Consequently, following attachment of a crystallizable stem along the chain to a crystal growth surface, a subsequent defective stem would be encountered and excluded at the growth front, forming a fold that would bring another crystallizable stem close to the crystal surface. Thus, with crystallizable stems spaced uniformly along a chain and in close proximity to the crystal growth surface, the time-consuming rejection/replacement process would be minimized, resulting in rapid crystallization kinetics, as observed in the empirical data.[54,55]

Compared to the morphology of the sPS/$CHCl_3$ gel, the sPS/CCl_4 gel morphology is highly complex (see **Figure 4.1**). The sPS/CCl_4 gel is expected to contain crystallites that are bound

together by tightly packed amorphous chain segments in polymer-rich regions and by loosely packed amorphous chain segments in polymer-poor regions. Based on this proposed gel morphology, it seems reasonable that when functionalizing reagent is introduced to the sPS/CCl_4 gel network, it will be sterically excluded from reacting with styrene monomers in the crystalline component, will have restricted access to styrene monomers along amorphous chain segments in the polymer-rich regions, and will react readily with styrene monomers in the polymer-poor regions. A copolymer chain from the sPS/CCl_4 gel network is therefore expected to contain crystallizable stems in un-functionalized styrene "blocks" that are separated by compositionally diverse, randomly functionalized "blocks" originating from the two unique amorphous environments within the gel network. Thus, it may be appropriate to describe the sPS/CCl_4 copolymers as having a gradient-like primary blocky microstructure, in which indiscrete boundaries exist between the un-functionalized styrene "blocks" and randomly functionalized "blocks." This gradient-like blocky microstructure is expected to contain a broad distribution of crystallizable stem lengths and defective stem lengths, resulting in a higher probability of encountering a defective stem at the crystal growth front and thus yielding slower crystallization kinetics, as observed in the isothermal crystallization experiments. Overall, the observed differences in the thermal properties and crystallization behavior of the sPS/CCl_4 and sPS/$CHCl_3$ copolymers, reveals that the sPS/solvent gel morphology produces copolymers with tailored chain sequences; the sPS/$CHCl_3$ gel morphology is capable of producing copolymers with fewer defects along the chain, consistent with a multiblock-like microstructure.

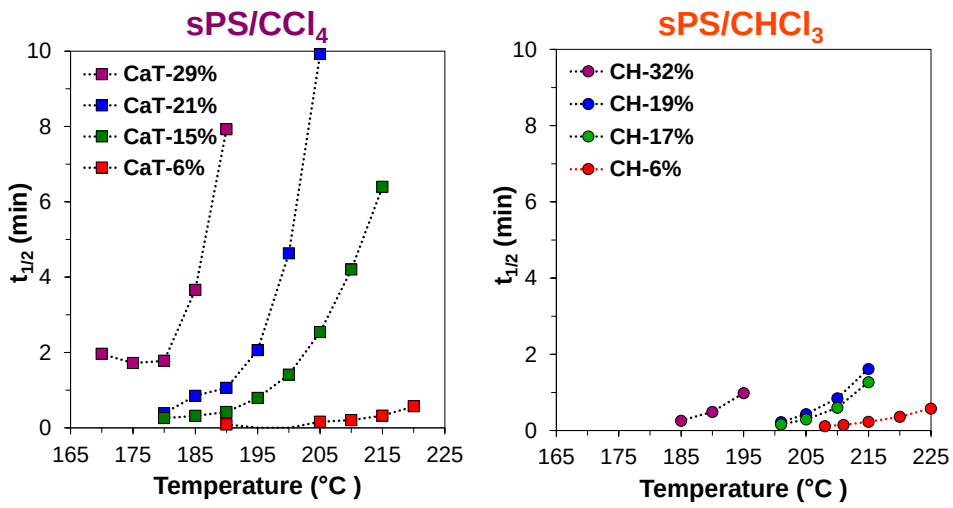

Figure 4.10. Crystallization half-time ($t_{1/2}$) versus temperature profiles for the (left) sPS/CCl_4 and (right) sPS/$CHCl_3$ copolymers. Prior to isothermal crystallization, samples were annealed for 5 min at 300 °C (or 335 °C for CH-32%). The results for CaT-29% are after annealing at 300 °C. This sample showed signs of decomposition (*i.e.*, a decrease in T_g) after repeated annealing at 325 °C.

4.4.5. Morphological characterization of the low Br-content Blocky copolymers

The primary copolymer microstructure was further investigated by probing the polymorphic composition of the low Br-content sPS/CCl_4 CaT-6% and sPS/$CHCl_3$ CH-6% samples using WAXD experiments. **Figure 4.11** compares the WAXD profiles of the sPS homopolymer and the CaT-6% and CH-6% copolymers after the samples were cooled rapidly (−60 °C min^{-1}) from the melt to 0 °C, and after 2 h isothermal crystallization (I) at 190 °C (high supercooling) and 230 °C (relatively low supercooling). The WAXD profiles of the sPS homopolymer contain crystalline reflections that are attributed to the α- and β-form crystal structures of sPS.[56] Pure sPS is well-known to form a mixture of polymorphs and to have a polymorphic composition that is temperature and time dependent.[56-59] During melt crystallization at high supercooling and dynamic cooling at fast rates, nucleation of the α-form lamellae is favored, demonstrated by the intense crystalline reflection at $2\theta = 11.6°$ ([hkl] =300)[56] in the WAXD profiles of pure sPS after isothermal crystallization at 190 °C and rapid cooling. The α-form lamella has been characterized by a disordered fold surface of loosely looped (fringed

micelle-like) polymer chains.[48] During low supercooling conditions (above 260 °C in pure sPS), nucleation of the thermodynamically favorable β-form crystal structure is favored. In addition, during melt crystallization, the α-form lamella has been shown to transform into the β-form lamella via a melt/re-crystallization process that has been recognized to follow crystal thickening.[33,48,58,59] The crystalline reflection at $2\theta = 12.2°$ ([hkl] = 040)[56] in the I-230 °C WAXD profiles of sPS and CH-6% is characteristic of the β polymorph. The β-form lamella is characterized by relatively thick crystallites with a disordered fold surface of non-adjacently reentering (switchboard-like) polymer chains.[48]

The WAXD profiles of the low Br-content Blocky copolymers contain crystalline reflections that occur at approximately the same 2θ as observed in pure sPS and are thus attributed to a combination of α- and β-form crystal structures. Notably, for the sPS/CCl_4 CaT-6% and sPS/$CHCl_3$ CH-6% copolymers, the crystalline reflections at $2\theta = 11.6°$ and 12.2° differ in intensity and breadth depending on the crystallization conditions, which indicates differences in their polymorphic compositions and crystalline chain order, respectively. After conditions of rapid cooling, both the CaT-6% and CH-6% samples exhibit an intense reflection at ca. 11.6°, attributed to α-form crystallites. It is important to note that upon dynamic cooling at −60 °C min^{-1} to 190 °C, the Blocky samples crystallize at a rate that exceeds the limits of detection for the DSC instrument (see **Figure 4.10**). Thus, the rapid cooling profile appears to represent the polymorphic composition of the Blocky copolymers just after crystallization. Upon isothermal crystallization at 190 °C, the intensity of the reflection at ca. 12.2° from the β polymorph increases in both the CaT-6% and CH-6% copolymers. The presence of β-form crystallites after 2 h melt crystallization at 190 °C is suggestive of crystallite thickening and α to β transformation.[33,58] For the CaT-6% copolymer, the intensity of the reflection at 12.2° is similar to that observed in the pure sPS

homopolymer. In contrast, the CH-6% I-190 °C profile exhibits two broad and intense overlapping reflections at ca. 11.6° and 12.2°. After melt crystallization at 230 °C, the CH-6% profile exhibits sharper and more intense reflections at 11.6° and 12.2° relative to CaT-6%, which may indicate that disordered crystalline stems in CH-6% that formed during the initial crystallization process, are capable of re-organizing to more ordered crystallites during low supercooling conditions.[59]

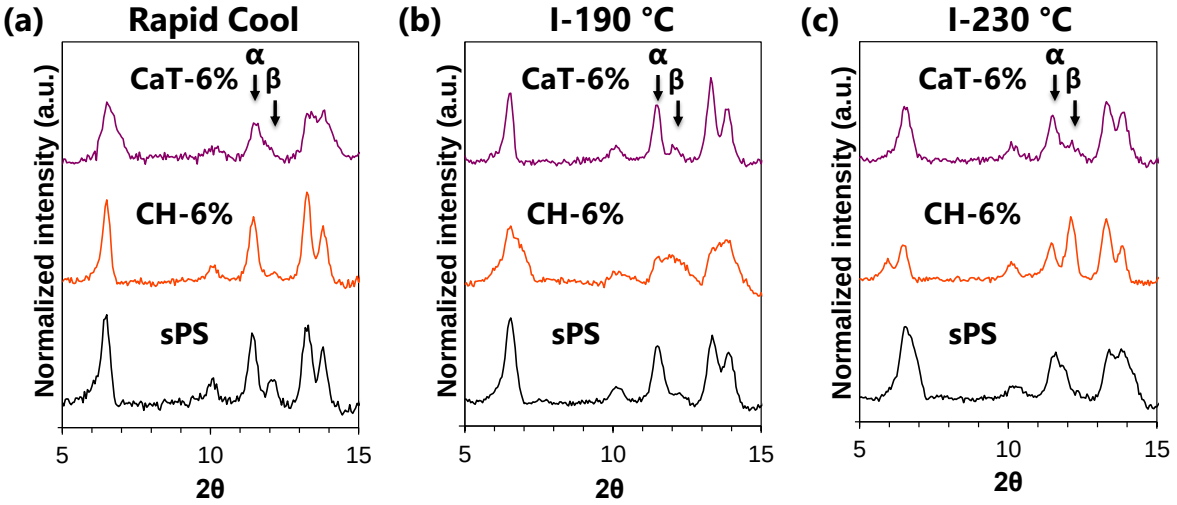

Figure 4.11. WAXD profiles of the sPS homopolymer, and the low Br-content sPS/$CHCl_3$ CH-6% and sPS/CCl_4 CaT-6% copolymers after (a) rapid cooling (−60 °C min^{-1}) from the melt to 0 °C, and 2 h isothermal (I) crystallization at (b) 190 °C and (c) 230 °C.

The polymorphic composition of the sPS homopolymer and the Blocky copolymers was quantified from the relative areas of the diffraction peaks observed at 2θ = 11.6° and 12.2° according to the empirical relationship derived by Guerra et al.,[56] shown in **Equation 4**. The fraction of crystallites in the *α*-form (P_a) is equal to:

$$P_a = \frac{1.8 \times \frac{A_{11.6}}{A_{12.2}}}{1 + 1.8 \times \frac{A_{11.6}}{A_{12.2}}} \quad (4)$$

where $A_{11.6}$ and $A_{12.2}$ are the integrated areas of the diffraction peaks at 2θ = 11.6°and 12.2°, respectively. The P_a values for the sPS homopolymer and the CaT-6% and CH-6% copolymers are summarized in **Table 4.3**. After rapid cooling and isothermal crystallization conditions, the

sPS homopolymer contains a large fraction of α-form crystallites of approximately 80-90%. Similarly, the Blocky copolymers contain over 90% α-form crystallites after rapid cooling. However, after conditions of isothermal crystallization, the fraction of α-form crystallites decreases in both the CaT-6% and CH-6% copolymers, indicating that the blocky microstructure of the gel-state functionalized copolymers promotes the formation of the β polymorph. After melt crystallization at 230 °C, the CH-6% copolymer remarkably contains approximately twice as much of the β polymorph as the CaT-6% copolymers and four times as much of the β polymorph as pure sPS. These data demonstrate that the primary microstructure of the CH-6% copolymer produces an unusually large fraction of the thermodynamically favorable β polymorph during conditions of low and high supercooling. Based on the characteristics of the β-form crystals, it seems reasonable to believe that the CH-6% copolymer contains long, crystallizable stems in even longer uniform blocks of un-functionalized styrene units that allows for crystal thickening and polymorphic transformation from the α-form crystal structure to the β-form crystal structure. In contrast, the CaT-6% copolymer is expected to contain crystallizable stems and defective stems with a broad range of lengths in a gradient-like blocky microstructure, which could limit crystal thickening and thus limit α to β transformations. Further analysis into this intriguing crystallization behavior via mechanical testing to probe chain folding and the fold surface energies of the crystallites will be the subject for future investigations. The DSC heating traces of the sPS homopolymer and the CaT-6% and CH-6% copolymers after rapid cooling, and isothermal crystallization at 190 °C and 230 °C are provided in **Figure S4.9**.

Table 4.3. The fraction of α-form crystallites (P_α) in the sPS homopolymer and the low Br-content Blocky copolymers after rapid cooling (−60 °C min^{-1}) from the melt to 0 °C and 2 h isothermal crystallization at 190 °C and 230 °C.

Crystallization Temperature (°C)	P_α		
	sPS	CH-6%	CaT-6%
Rapid cool to 0 °C	83%	92%	96%
190	90%	68%	87%
230	90%	57%	78%

4.4.6. Morphological characterization of amorphous Blocky copolymer films

USAXS/SAXS experiments were used to investigate the morphology of amorphous films of the Blocky copolymers. The USAXS/SAXS profiles of the sPS/CCl_4 CaT-15% and sPS/$CHCl_3$ CH-17% copolymers, recorded from amorphous films of the samples before and after annealing the films for 1 h at 140 °C, are shown in **Figure 4.12**. For reference, the profile of a solution-state brominated, i.e., random, copolymer containing 16 mol% *p*-bromostyrene units (R-16%) is also provided. The scattering profile of the amorphous random R-16% copolymer is featureless with a q^{-4} dependence between 0.002−0.06 nm^{-1}. This profile is consistent with an amorphous sPS homopolymer and demonstrates a homogeneous, phase-mixed morphology.[12] In contrast, the amorphous films of the CaT-15% and CH-17% copolymers exhibit excess scattering from a large-scale morphological feature at low q, between 0.01−0.2 nm^{-1} and 0.008−0.08 nm^{-1}, respectively. The dimensions of the low q feature were determined using the Unified Fit. For the CaT-15% and CH-17% copolymers, respectively, the low q feature fits to dimensions of ca. 32 nm and 72 nm and is consistent with a micro-phase separated morphology. The presence of this feature strongly suggests that the "blockiness" originating from the gel-state functionalization is sufficient to drive phase development that is somewhat reminiscent of conventional block copolymer phase behavior. The physical and molecular origins of this large-scale feature observed in the USAXS profiles of the CaT-15% and CH-17% copolymers are attributed to a thermodynamic immiscibility between

the electron-dense, randomly brominated sPS segments and the pure runs of un-functionalized sPS within the blocky microstructure of the functionalized chains.

After annealing the amorphous films at 140 °C, above the glass transition temperature of pure sPS, the low *q* scattering feature remains in the USAXS/SAXS profiles of the Blocky copolymers and a new high *q* scattering feature is observed. This high *q* feature is attributed to intercrystalline scattering from crystalline lamellae.[42] The absence of this feature in R-16% demonstrates that this sample, in its phase-mixed state, was unable to crystallize during the thermal conditions of this experiment. These results support that micro-phase separated domains exist in the Blocky copolymers and thus facilitate crystallization of un-functionalized styrene segments within the pure sPS phase domains.

Comparing the domain sizes of the low *q* scattering features in the CaT-15% and CH-17% samples reveals that the CH-17% copolymer exhibits relatively large phase domains. In investigations of multiblock copolymers that contain block length heterogeneities and micro-phase separated morphologies, the copolymers with longer average block lengths often demonstrate larger domain sizes resulting from a greater number of segments of effective block length participating in the micro-phase domains.[60-63] Thus, the large domain size in CH-17% strongly suggests that this sample contains longer blocks of pure sPS and a greater degree of blockiness relative to CaT-15%. These data from the morphological characterization are in excellent agreement with the results of the microstructural analysis and crystallization behavior experiments and support that the sPS/$CHCl_3$ gel is capable of producing copolymers that contain a high degree of blockiness in a multiblock-like microstructure.

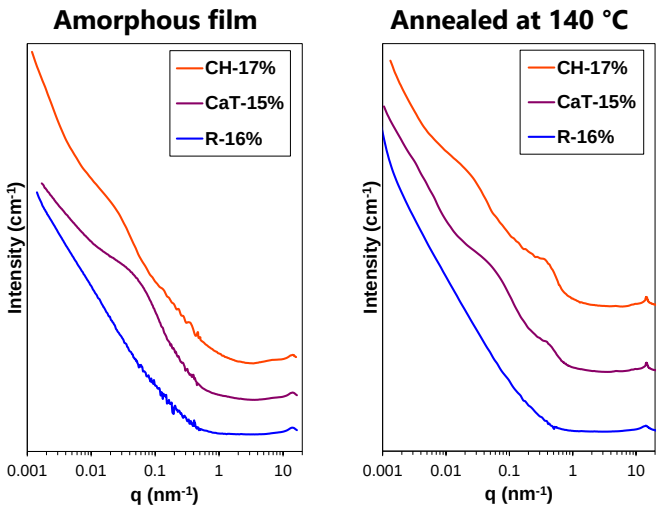

Figure 4.12. USAXS/SAXS profiles taken from (left) amorphous films and (right) amorphous films annealed for 1 h at 140 °C, of the blocky sPS/$CHCl_3$ CH-17% and sPS/CCl_4 CaT-15% copolymers and a solution-state brominated (i.e., random) copolymer that contains 16 mol% p-bromostyrene units (R-16%). Films were prepared from powders by melt pressing between Kapton sheets at 30 °C above T_m for 20 s at 2200 psi then for 20 s at 4500 psi, followed by quenching in ice water to prevent sPS crystallization. For clarity, the scattering profiles are vertically offset.

4.4.7. Simulations of the blocky microstructure of the sPS-*co*-sPS-Br copolymers

To help rationalize the effect of the sPS/solvent gel morphology on the copolymer microstructure and crystallization behavior, simulations of blocky copolymers were developed. The blocky microstructure resulting from functionalization in the gel state, was simulated by first establishing an inaccessible fraction of monomers along a chain prior to random bromination of the remaining accessible fraction. Based on the results of our microstructural analysis and the crystallization behavior of the gel-state brominated copolymers, which provide support for our hypothesis that functionalizing reagent is sterically restricted to the solvent swollen amorphous chains within the semicrystalline gels, the inaccessible fraction of monomers was chosen to represent the fraction of monomers that are isolated within and in close proximity to the crystalline component of the gel network. From the WAXD analysis of the as prepared gels, the crystalline fraction (%X_c) within the 10 w/v% sPS/CCl_4 and 10 w/v% sPS/$CHCl_3$ gels was determined to be approximately 42% (see **Table 4.1**). In addition, it should be recognized that chain segments in close proximity to the crystallites that emanate directly from the basal surfaces of the crystallite

may be locally restricted in their conformations (i.e., a rigid amorphous fraction), which could also limit reagent accessibility. Based on the measurements of Cebe and coworkers,[64] the rigid amorphous fraction for sPS is estimated to be 11%. Thus, the anticipated size of the inaccessible fraction within the heterogeneous gel networks was estimated to be at least 53%.

The simulated blocky microstructure is constructed from a polymer chain of 1442 styrene monomers (based on our sPS sample, M_w = 300 K; $Đ$ = 2.0) by distributing a specified number of inaccessible "blocks" of styrene monomers along the polymer chain, establishing the inaccessible fraction. To place a block, a monomer is first randomly selected along the polymer chain. Next, that monomer and a specified number of its subsequent monomers are removed from the list of functionalizable monomers, resulting in an inaccessible block. From the SAXS analysis of the as prepared gels, the inaccessible block length of the 10 w/v% sPS/CCl_4 and 10 w/v% sPS/$CHCl_3$ gels was anticipated to be at least 38 and 46 styrene units, respectively (see **Table 4.1**). The process of selecting monomers for the inaccessible fraction is repeated until a specified number of blocks has been distributed along the polymer chain. It is important to note that this process can produce blocks that overlap, resulting in blocky chain microstructures that contain a broad range of sizes for the inaccessible fraction as well as inaccessible segments of un-functionalized styrene monomers that are longer than the specified block length. Lastly, with the inaccessible blocks of the inaccessible fraction set, the remaining monomers within the accessible fraction are functionalized by random choice up to the desired degree of bromination.

For the specified degree of bromination, the simulation generates 1000 different blocky chain microstructures of randomly distributed blocks, each containing 999 randomly functionalized copolymer chains, and calculates the pentad sequence distribution of each simulated chain and the root-mean-square deviation (RMSD) between the pentad sequence distribution of

the simulated chain and that obtained empirically from the quaternary carbon NMR spectrum. For the sPS/CCl_4 copolymer chains, the parameters of the simulations were tested by systematically changing the number and length of the inaccessible blocks distributed along the chain. Using a block length of 39 monomers, the number of inaccessible blocks was set to 16, 20, 24, and 26, which corresponds to predicted inaccessible fractions of approximately 43%, 54%, 65%, and 70%, respectively. For all sPS/CCl_4 copolymers, the simulated blocky chain microstructures containing 26 randomly distributed blocks were found to minimize the residuals with respect to experiment. This result was attributed to a large average inaccessible fraction of 51 ± 4%, which is in good agreement with the size of the inaccessible fraction predicted for the sPS/CCl_4 gel network of ca. 53%. Keeping the predicted inaccessible fraction in the simulated blocky chain microstructures at approximately 70%, the block length was set to 26, 39, 47, 52, 104, 128, 170, 204, 312, 330, and 512 monomers. From this list, the shortest block length that minimized the residuals with respect to experiment was 47 monomers. This block length is in good agreement with the average length of a crystalline stem in the sPS/CCl_4 gel of 38-40 monomers and supports that the functionalizing reagent has restricted access to monomers close to the basal surfaces of the crystallite. Thus, a block length of 47 monomers and a predicted inaccessible fraction of approximately 70%, or 22 inaccessible blocks, were chosen to simulate the sPS/CCl_4 copolymer chains as a first approximation of the copolymer microstructure. For the sPS/$CHCl_3$ copolymer chains, the parameters consisted of a block length of 54 monomers (one crystalline stem + 8 monomers) and a predicted inaccessible fraction of approximately 67%, or 18 inaccessible blocks. These parameters for the sPS/$CHCl_3$ copolymer chains are based on the results of the systematic investigation of the sPS/CCl_4 simulated chains and provide a useful first approximation of the sPS/$CHCl_3$ copolymer microstructure.

In order to investigate the relationship between the sPS/solvent gel morphology and copolymer microstructure and crystallization behavior, three block length conditions were investigated, 1 × block length, 1.5 × block length, and 2 × block length, where the block length for the simulated sPS/CCl_4 and the sPS/$CHCl_3$ chains was 47 and 54 monomers, respectively. **Figure 4.13** shows the average RMSD for the simulated sPS/CCl_4 CaT-15% and CaT-21%, and the sPS/$CHCl_3$ CH-17% and CH-19% with respect to the block length conditions. For a summary of the parameters and results of the blocky copolymer microstructure simulations for the sPS/CCl_4 CaT-15% and sPS/$CHCl_3$ CH-19%, see **Figure S4.10**. The CaT-15% and CaT-21% exhibit average RMSD of approximately 0.5-0.6% and 1.4%, respectively. These average RMSD are independent of the inaccessible block length, remaining approximately the same with increasing block length. Thus, the length of the inaccessible blocks along the chain did not affect the residuals between the pentad sequence distribution of the simulated chains and that obtained from experiment. Based on these results, it appears that the sPS/CCl_4 copolymers can contain a high degree of variability in the way Br-Sty groups are distributed along the chains. This behavior is consistent with the gradient-like blocky microstructure described earlier for the sPS/CCl_4 copolymers, where the copolymer chains are expected to contain runs of un-functionalized styrene that are separated by compositionally diverse runs of randomly functionalized styrene. In contrast, for the sPS/$CHCl_3$ simulated chains, the average RMSD decreases from ca. 2% at one block length to ca. 1% at two block lengths. Thus, it appears that the sPS/$CHCl_3$ copolymers contain a low degree of variability in the way Br-Sty groups are distributed along the chains, consistent with the multiblock-like microstructure described earlier for the sPS/$CHCl_3$ copolymers, where the copolymer chains are expected to contain runs of un-functionalized styrene that are separated uniformly from runs of randomly functionalized styrene. While these results also suggest that

within the crystallites of the sPS/$CHCl_3$ gel, an attached crystalline stem is capable of forming at least one chain fold, further analysis of potential chain folding in the sPS/solvent gels and in the brominated copolymers will need to be probed using mechanical testing and will be a subject for future investigations.

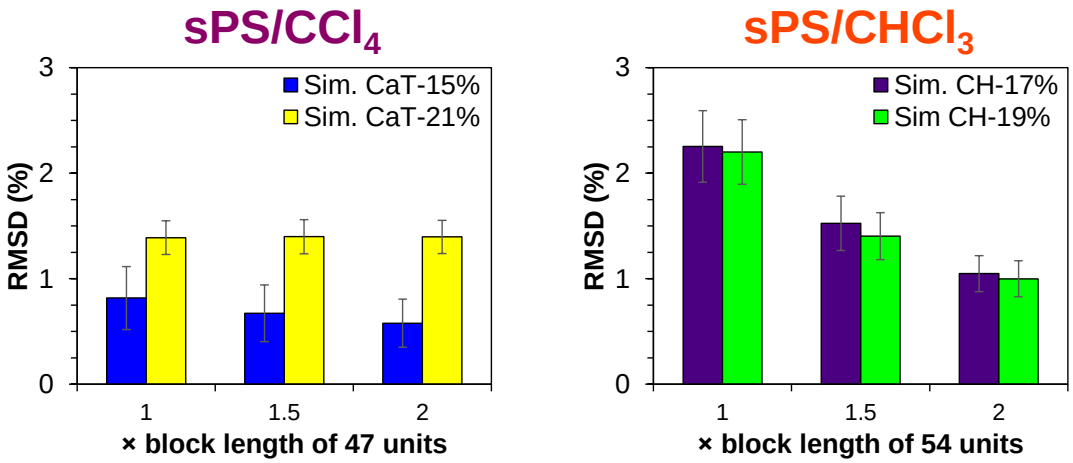

Figure 4.13. Average RMSD between the pentad sequence distribution of the simulated chains and experiment with respect to the number of monomers in an inaccessible block for the simulated (left) sPS/CCl_4 and (right) sPS/$CHCl_3$ copolymers of intermediate Br-content. Values along the x-axis are multiplied by the estimated number of styrene units in one inaccessible block of 47 and 54 monomers, respectively. Average RMSD was calculated from the 5 out of 1000 blocky chain microstructures that produced the smallest RMSD (999 simulated chains per blocky chain microstructure). The error bars represent the standard error of the average RMSD.

4.4.8. Simulated average chains with comparison to the empirical crystallization behavior

The pentad sequence distribution obtained from the quaternary carbon NMR spectrum provides a unique fingerprint of the copolymer microstructure that originates from the average comonomer sequence distribution in the Blocky copolymers. Using this useful sequence information, a computer code was developed to predict the average copolymer chain sequence in each of the sPS/CCl_4 and sPS/$CHCl_3$ copolymers. The Fortran code is described in Chapter 3.[37] Briefly, the copolymer chain is simulated starting with a sequence of 7 un-functionalized styrene units, followed by subsequent additions of un-functionalized and functionalized styrene units to the chain end in 7 monomer long blocks. The block that is added in each addition step keeps the difference between the empirical pentad sequence distribution and that of the intermediate

simulated chain at a minimum. To add a block to the chain end, all possible heptad combinations of un-functionalized and functionalized styrene units (2^7 or 128) are added in turn and the deviation between the pentad distribution of the intermediate simulated chain and the experimental results is analyzed. The heptad combination that minimizes the residuals with respect to the experiment is then added to the chain. This process is repeated until the chain length reaches 1442 monomers (based on our sPS sample, M_w = 300K; Đ = 2.0). It is worth noting that the degree of functionalization in the chain is not a parameter of the simulation, yet the simulated chains naturally exhibit Br-Sty compositions that are in good agreement with experiment. In addition, the simulated average chains exhibit pentad sequence distributions that deviate by less than one percent from the empirical pentad sequence distributions, with one exception. The simulated sPS/$CHCl_3$ CH-32% average chain has an RMSD of 1.28%, resulting from a large (ca. 4%) underrepresentation of the bbbbb pentad in the simulated chain.

Figure 4.14 compares the simulated average chains of sPS/CCl_4 CaT-21% and sPS/$CHCl_3$ CH-19%. The simulated chains of the sPS/CCl_4 CaT-6%, 15%, and 29% and the sPS/$CHCl_3$ CH-6%, 17%, and 32% are provided in **Figure S4.11**. For the CaT-21% and CH-19% average chains, the RMSD between the simulated and empirical pentad sequence distributions are 0.31% and 0.61%, respectively. Thus, the simulated chains are expected to be representative of the average copolymer sequence in these brominated copolymers. By visual inspection, no obvious differences in the distributions of block lengths of consecutive styrene and consecutive Br-Sty units in the simulated CaT-21% and CH-19% chains are immediately apparent. Both chains exhibit numerous long "blocks" of consecutive styrene units (grey circles) and "blocks" of two or more consecutive Br-Sty units (blue circles). Overall, the average chains have considerably non-random,

i.e., blocky microstructures, consistent with the results obtained from the microstructural analysis using ^{13}C NMR spectroscopy.

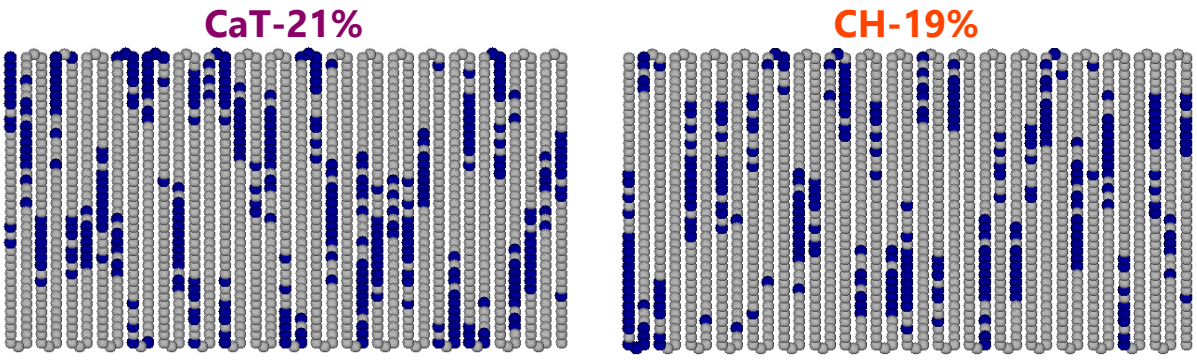

Figure 4.14. Simulated average chains of the sPS/CCl_4 CaT-21% and sPS/$CHCl_3$ CH-19% copolymers created through an iterative process that minimizes the difference between the pentad sequence distribution of the simulated chain and the respective data from experiment. Styrene units = grey circles; Br-Sty units = blue circles.

The distribution of block lengths of consecutive styrene units in the simulated chains represents the length of styrene blocks that are predicted to exist in the gel-state functionalized copolymers. **Figure 4.15** compares the distribution of styrene blocks in the simulated sPS/CCl_4 and sPS/$CHCl_3$ chains, quantified by weight fraction of styrene units (w_{Sty}) in blocks of at least block length, n. Using this method, $n = 1$ accounts for all styrene units in the chain and corresponds to a w_{Sty} of 100 wt%. As n increases, the w_{Sty} in blocks of at least n decreases. A w_{Sty} of 50 wt% represents half the mass of styrene in the chain. (For styrene and Br-Sty block lengths represented as frequency *versus* block length, see **Figure S4.12** and **Figure S4.13**, respectively.) At low Br-content, the simulated sPS/CCl_4 CaT-6% average chain contains long styrene blocks of up to 67 monomers. Above 6 mol%, the length of the longest blocks decreases to 46, 41, and 39 monomers in the simulated CaT-15%, 21%, and 29% chains, respectively. Nevertheless, half the mass of styrene units in the simulated sPS/CCl_4 chains is retained in blocks of at least 23 monomers. The presence of these long blocks is in excellent agreement with the experimentally-determined estimated average length of a crystalline stem in the sPS/CCl_4 copolymers of at least 17 styrene units, based on SAXS analysis of the average lamella thickness in the melt crystallized

samples (see **Table S4.1**). For a discussion on the estimated average lamella thickness in the sPS/CCl_4 and sPS/$CHCl_3$ copolymer series after 2 h isothermal crystallization at 190 °C, see the Supplementary Information and **Figure S4.14**.

The simulated sPS/$CHCl_3$ chains retain half their mass of styrene units in slightly longer blocks of at least 27 monomers. In addition, a large fraction (10% or more) of the styrene units in the sPS/$CHCl_3$ chains exist in blocks of at least 46 monomers. It is important to note that all of the sPS/CCl_4 and sPS/$CHCl_3$ simulated average chains contain one or more styrene blocks of at least 38 and 46 styrene units, respectively, in excellent agreement with the estimated length of a crystalline stem in the 10 w/v% sPS/CCl_4 and 10 w/v% sPS/$CHCl_3$ gels (see **Table 4.1**). These results strongly support that during gel-state bromination, crystalline stems in the crystalline component of the gel network are inaccessible to functionalizing reagent and are preserved as long segments of un-functionalized styrene units along the copolymer chains.

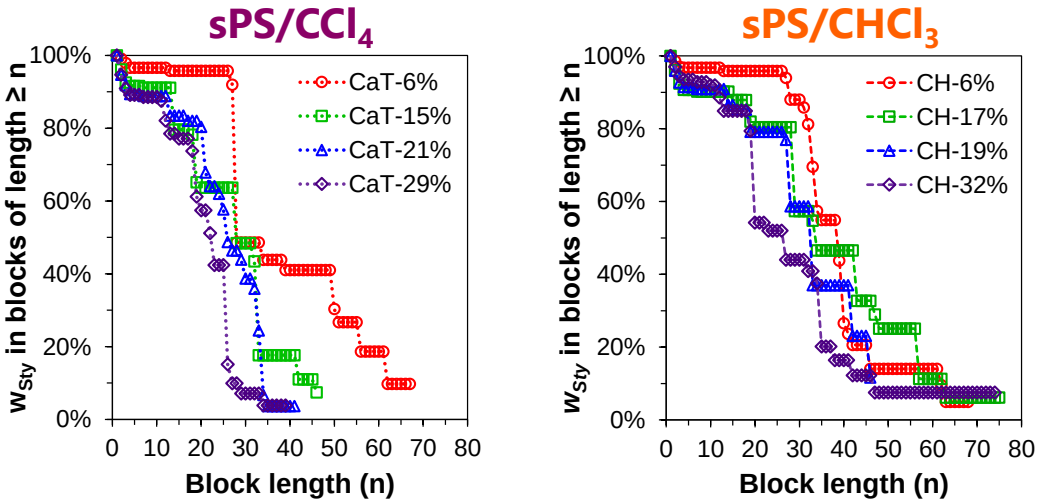

Figure 4.15. Predicted weight fraction of styrene units (w_{Sty}) in blocks of at least block length, *n*, versus block length from the simulated average chains of the (left) sPS/CCl_4 and (right) sPS/$CHCl_3$ copolymers. Dashed lines are shown to guide the eye.

The distribution of block lengths in the simulated average chains provides further insight into the crystallization behavior of the empirical Blocky copolymers. According to Flory's theory

of crystallization in copolymers,[65] the probability (P_ζ) that a randomly selected styrene unit along a chain exists in a crystallizable chain segment of at least ζ styrene units is given by:

$$P_\zeta = \sum_j P_{\zeta,j} = \sum_{j=\zeta}^{\infty} \frac{(j - \zeta + 1) \times w_j}{j} \quad \textbf{(5)}$$

where w_j is the probability that a unit chosen at random is a styrene unit in a sequence of length j, calculated by multiplying the molar fraction of styrene units (X_{Sty}) by the fraction of styrene units occurring in j sequences (j_{Sty}). For this work, ζ is defined as 28 monomer units, the average number of styrene monomers in one crystalline stem of an sPS crystallite, based on the *trans*-planar zigzag conformation of the *α*- and *β*-form crystal structures of sPS with 2 monomers per identity period and an average lamella thickness of 7.2 nm (*c*-axis dimension = 0.51 nm).[52]

The probability of randomly selecting a crystallizable styrene monomer (i.e., a monomer within a defect-free sequence of 28 monomer units) in the sPS/CCl_4 and sPS/$CHCl_3$ simulated chains is compared in **Figure 4.16**. At approximately 6 mol% Br, the simulated sPS/CCl_4 CaT-6% average chain exhibits a P_ζ value of 22%. Above 6 mol% Br, the P_ζ values rapidly decline with increasing Br-content in the sPS/CCl_4 average chains. Nevertheless, there is at least a 1% probability that a randomly selected styrene monomer exists in a crystallizable segment, even at high Br-content. This non-zero probability of encountering a defect-free stem is in good agreement with the crystallizability of the sPS/CCl_4 CaT-29% copolymer. It should also be recognized that the crystallization of styrene segments shorter than 28 units is possible, which is supported by the significant crystallizability (**Table 4.2**) observed in the sPS/CCl_4 CaT-21% copolymer.

Compared to the predicted behavior of the sPS/CCl_4 copolymers, the simulated sPS/$CHCl_3$ copolymers exhibit larger P_ζ values and retain at least 9% of their styrene monomers in crystallizable segments, even at 32 mol% Br. These results of the simulations are in excellent

agreement with the high crystallizability and rapid crystallization kinetics observed for the empirical sPS/$CHCl_3$ copolymers. For example, the sPS/$CHCl_3$ CH-32% is capable of rapidly crystallizing ($t_{1/2}$ = 1 min) to a degree of 10 wt% during isothermal crystallization at 190 °C. Thus, the consistency between the block length distributions of the simulated average chains and the empirical crystallization behavior validates the basis of our modeling method and strongly suggests that the morphology of the sPS/$CHCl_3$ gel network is capable of producing copolymers with a high prevalence of crystallizable homopolymer segments.

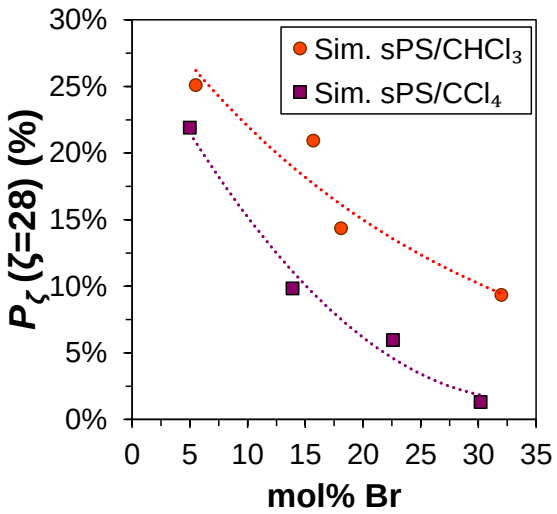

Figure 4.16. Probability (P_ζ) that a randomly selected styrene unit in the simulated sPS/$CHCl_3$ (circles) and sPS/CCl_4 (squares) chains exists in a crystallizable chain segment, ζ, of at least 28 styrene units. Dashed lines are included to guide the eye.

4.5. Conclusions

This work demonstrates the post-polymerization bromination of sPS in the heterogeneous gel state to produce sPS-co-sPS-Br copolymers with blocky microstructures and tailored chain sequences. The purpose of this research was to a develop a structure-property relationship between the sPS/solvent gel morphology and the brominated sPS copolymers. Using 10 w/v% sPS/CCl_4 and sPS/$CHCl_3$ gels as templates for the gel-state bromination reactions, semicrystalline blocky copolymers were prepared with high degrees of functionality. Morphological characterization of

the sPS/solvent gels provided by X-ray scattering techniques, reveals that the sPS/$CHCl_3$ gel likely contains randomly dispersed and unoriented crystallites that are bound together by a percolating network of amorphous chain segments. The proposed sPS/CCl_4 gel morphology is more complex and consists of polymer-rich regions that contain clusters of unoriented crystallites tied together by amorphous chain segments and polymer-poor regions that contain a percolating network of amorphous chain segments, linking the crystallite clusters together. Based on the microstructural analysis of the sPS/CCl_4 and sPS/$CHCl_3$ copolymers provided by NMR spectroscopy, the sPS/$CHCl_3$ gel was found to produce sPS-*co*-sPS-Br copolymers with a high prevalence of styrene "blocks" of at least five consecutive styrene units and a high degree of blockiness. The sPS/$CHCl_3$ copolymers demonstrated superior crystallizability during conditions of rapid cooling and faster crystallization kinetics at lower supercooling compared to their sPS/CCl_4 copolymer analogs. Remarkably, the 10 w/v% sPS/$CHCl_3$ gel produced a crystallizable 32 mol% Br copolymer that contained distinct sequences of styrene units and Br-Sty units in segments of significant length that allowed for crystallization during dynamic cooling conditions, demonstrating that the sPS/$CHCl_3$ gel morphology favorably affects the bromination reaction to produce copolymers with fewer defects along the chains.

When the brominating reagent is introduced into the heterogeneous gel network, it is excluded from the crystalline component and reacts with styrene monomers in the amorphous component. Based on the crystallization behavior and morphology of the Blocky copolymers and the proposed morphology of the sPS/$CHCl_3$ gel, it appears that the sPS/$CHCl_3$ gel is capable of producing copolymers that contain crystallizable stems in un-functionalized styrene "blocks" that are separated uniformly by defective stems in randomly functionalized "blocks" in a multiblock-like microstructure. In contrast, the more complex sPS/CCl_4 gel morphology appears to produce

copolymers that contain a gradient-like blocky microstructure in which indiscrete boundaries exist between the un-functionalized styrene "blocks" and randomly functionalized "blocks." The systematic investigations of the simulated blocky copolymer microstructures predict that the sPS/$CHCl_3$ copolymers contain long blocks of un-functionalized styrene units and a low degree of variability in the way Br-Sty groups are distributed along the chains. This finding is in excellent agreement with the results obtained from the microstructural analysis, crystallization behavior experiments, and morphological characterization, and supports that the sPS/$CHCl_3$ copolymers contain a multiblock-like microstructure. For the simulated sPS/CCl_4 blocky copolymer microstructures, the systematic investigation predicts that the sPS/CCl_4 copolymers contain a high degree of variability in the way Br-Sty groups are distributed along the chains, which again supports the gradient-like blocky microstructure suggested by the experimentally-determined results. Thus, these simulations strongly suggest that the sPS/solvent gel can tune the comonomer sequence distribution and physical properties of the blocky copolymers, directed by the sPS/solvent gel morphology.

Simulated average chains of the Blocky copolymers, generated from the empirical pentad sequence distributions, predict that the sPS/$CHCl_3$ copolymers contain a higher prevalence of crystallizable sPS segments, consistent with the rapid crystallization kinetics of the sPS/$CHCl_3$ copolymers provided by DSC experiments. Thus, the simulated average chains appear to be representative of average chains in their respective Blocky samples. Remarkably, the simulated sPS/CCl_4 and sPS/$CHCl_3$ chains contain one or more styrene blocks of at least 38 and 46 styrene units, respectively, in excellent agreement with the estimated average length of a crystalline stem in the 10 w/v% sPS/CCl_4 and 10 w/v% sPS/$CHCl_3$ gels of ca. 38-40 and 46-49 styrene units. These results strongly support that during gel-state bromination, crystalline stems in the crystalline

component of the gel network are inaccessible to functionalizing reagent and are preserved as long segments of un-functionalized styrene units along the copolymer chains.

This work provides a fundamental investigation of the post-polymerization bromination of sPS, demonstrating that blocky sPS-*co*-sPS-Br copolymers with tailored chain sequences can be prepared using a straightforward physical method of post-polymerization functionalization in the heterogeneous gel state by changing the sPS/solvent gel morphology. Through this work, a relationship has been established between the sPS/solvent gel morphology and the copolymer microstructure, degree of blockiness, and physical properties that result from gel-state functionalization. Given the dependence of sPS/solvent gel morphology on the gelation solvent,[13] temperature,[32,35,36] and concentration,[15,31] we anticipate that the sPS/solvent gel will present avenues of further investigation into controlling the degree of blockiness in sPS-based copolymers. This research also lays the groundwork to synthesize other sPS-based copolymers with tailored chain sequences and useful functionalities through simple substitution of the labile bromine functional groups.

4.6. Acknowledgements

This material is based upon work supported by the National Science Foundation under Grant No. DMR-1809291. Advanced Research Computing at Virginia Tech is gratefully acknowledged for providing computational resources and technical support that have contributed to the results reported within this manuscript. This research used resources of the Advanced Photon Source, a U.S. Department of Energy (DOE) Office of Science User Facility operated for the DOE Office of Science by Argonne National Laboratory under Contract No. DE-AC02-06CH11357. The authors would like to thank Dr. Jan Ilavsky and acknowledge the use of beamline 9ID-C. The

authors would like to thank Virginia Tech undergraduate student Peter M. Moberg for assisting with sample preparation.

4.7. Supplementary Information

Figure S4.1 compares the Kratky plots (i.e., $I(q) \times q^2$ *versus* q) of the 10 w/v% sPS/carbon tetrachloride (CCl_4) and 10 w/v% sPS/chloroform ($CHCl_3$) gels obtained from the USAXS/SAXS profiles. The maximum observed at approximately 0.3 nm^{-1} in both plots is indicative of a gel network.[15] For the sPS/CCl_4 gel, the plateau region from 1 $nm^{-1} < q < 2$ nm^{-1} is characteristic of a rigid rod-like chains. The positive slope in the Kratky plot of the sPS/$CHCl_3$ gel at $q > 1$ nm^{-1} is suggestive of a loosely packed gel network.

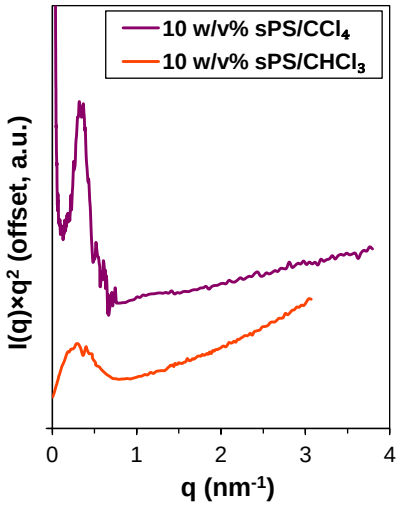

Figure S4.1. Kratky plot of the scattering intensity function for the 10 w/v% sPS/CCl_4 and 10 w/v% sPS/$CHCl_3$ gels.

Figure S4.2 shows the wide-angle X-ray diffraction patterns of the 10 w/v% sPS/CCl_4 and 10 w/v% sPS/$CHCl_3$ gels as prepared and after stirring in 1,2-dichloromethane (DCM), the bromination reaction solvent, for 72 h at room temperature to mimic the reaction conditions. All of the profiles exhibit crystalline reflections that are consistent with the s(2/1)2 helical conformation of the δ-form crystal structure of sPS, as expected for an sPS gel.[17,56,66] Though there are noticeable differences between the diffraction patterns of the gels, as prepared and stirred in DCM, this observed behavior is not surprising, bearing in mind that in its helical conformation, sPS is well known to form molecular complexes with guest molecules (i.e., clathrate) whose fine

structures depend on the chemical nature of the guest.[13,32] It is worth noting that the relatively sharp and intense crystalline reflection in the as prepared 10 w/v% sPS/CCl_4 gel at 2θ = 21°, assigned to the [hkl] = 211 plane nonequatorial to the chain axis, implies that the chain axes in the sPS/CCl_4 gel are highly ordered.[17] Thus, these data suggest that the crystalline lamellae of the sPS/CCl_4 gel contain extended, rigid rod-like crystalline stems that are likely to impede chain-folding.

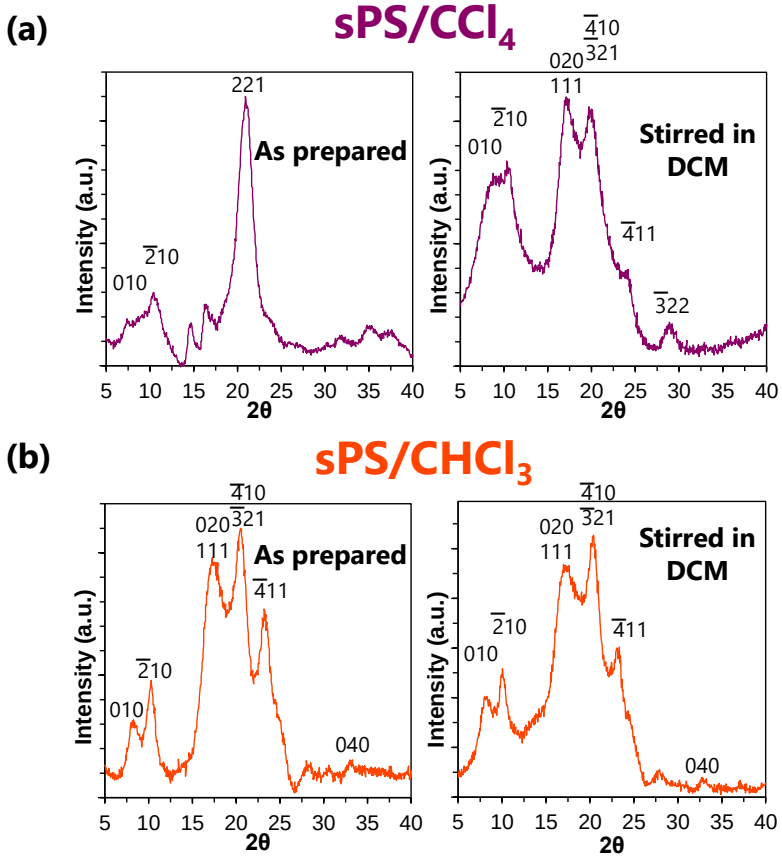

Figure S4.2. WAXD profiles of the (a) 10 w/v% sPS/CCl_4 gel and (b) 10 w/v% sPS/$CHCl_3$ gel (left) as prepared and (right) after stirring in DCM, the bromination reaction solvent, for approximately 72 h at room temperature. The gels were dried under vacuum at 70 °C for ca. 24 h prior to analysis.

The differential scanning calorimetry (DSC) first heating trace of the 10 w/v% sPS/CCl_4 and 10 w/v% sPS/$CHCl_3$ gel are shown in **Figure S4.3**. The gels were dried under vacuum at 70 °C for ca. 24 h prior to analysis. Both heating traces exhibit three heat flow events, the glass

transition at around 100 °C that is overlapped by the $\delta \rightarrow \gamma$ transformation, the $\gamma \rightarrow \alpha$ transformation that occurs at approximately 200 °C, and the melting endotherm at 271 °C.[67] For each gel, the weight percent crystallinity (%X_c) was derived from the area under the melting endotherm (ΔH_f) and the heat of fusion of 100% crystalline pure sPS (ΔH_f°).

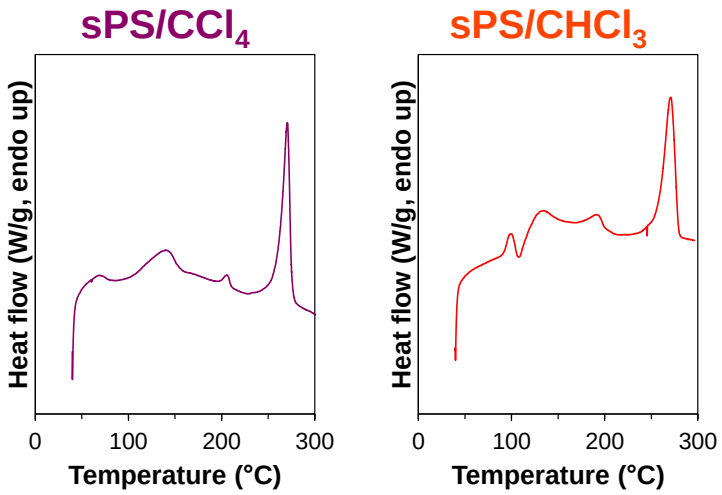

Figure S4.3. The DSC first heating traces of the (left) 10 w/v% sPS/CCl_4 and (right) 10 w/v% sPS/$CHCl_3$ gels. The gels were prepared and stored at room temperature for ca. 24 h, followed by drying under vacuum at 70 °C for ca. 24 h prior to analysis.

The full quantitative ^{13}C NMR spectra of the sPS homopolymer, sPS/CCl_4 CaT-21% and sPS/$CHCl_3$ CH-19% are shown in **Figure S4.4**. The spectra were recorded in 1,1,2,2-tetrachloroethane-d_2 (TCE-d_2) at room temperature using a C13IG pulse program, proton decoupling (NOE−), a relaxation delay of 6 sec, O1P of 95, and a sweep width of 150 ppm.

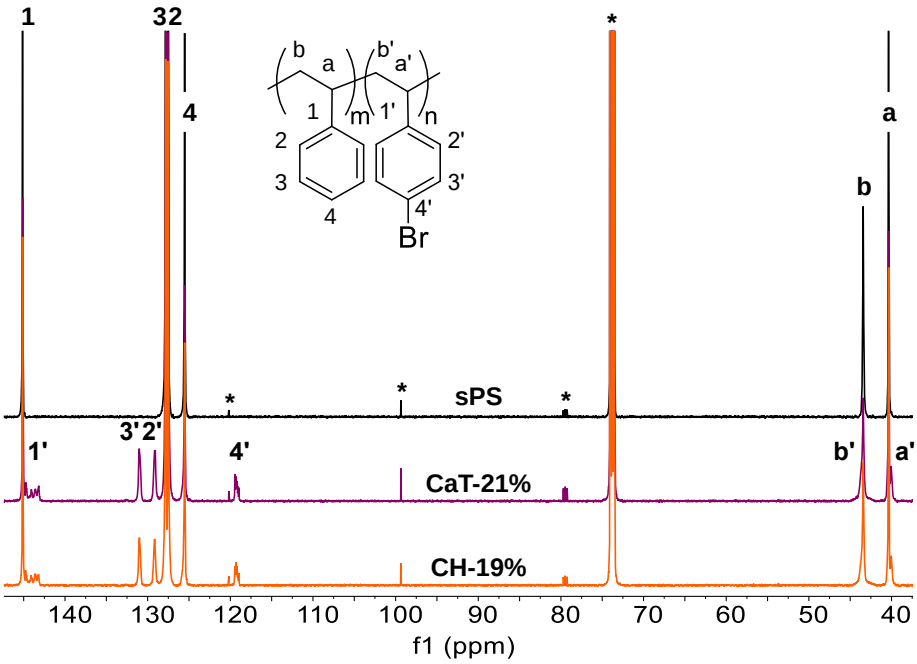

Figure S4.4. Full ^{13}C NMR spectra of the sPS homopolymer and the sPS/CCl_4 CaT-21% and sPS/$CHCl_3$ CH-19% copolymers. The spectra were recorded at room temperature and are referenced to TCE-d_2 and normalized over the range 127.0-132.5 ppm. Asterisks (*) indicate solvent resonances.

The quaternary carbon and Br-substituted phenyl carbon regions of the ^{13}C NMR spectra of the sPS homopolymer and sPS/CCl_4 and sPS/$CHCl_3$ copolymers are shown in **Figure S4.5**. For comparison, the y-axis scales are close to the same intensity. The presence of multiple peaks in these regions signifies through-bond communication between neighboring styrene and Br-Sty monomers and likely provide a unique fingerprint of the copolymer microstructure originating from the specific comonomer sequence distribution.

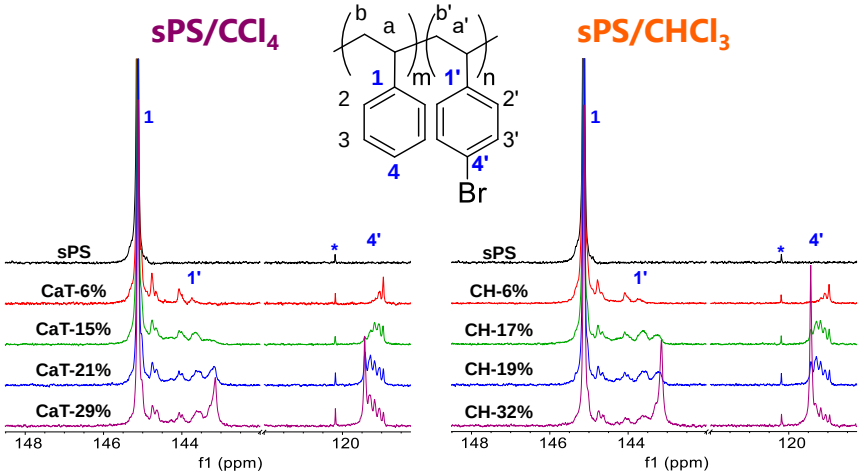

Figure S4.5. The quaternary carbon and Br-substituted phenyl carbon regions of the ^{13}C NMR spectra of the sPS homopolymer and the Blocky brominated copolymers prepared from (left) sPS/CCl_4 gels and (right) sPS/$CHCl_3$ gels increasing in degree of bromination from top to bottom. Recorded at 25 °C, referenced to TCE-d_2, and normalized over 127.0–132.5 ppm.

Figure S4.6 compares the melting temperatures, T_m, of the sPS homopolymer and the sPS/CCl_4 and sPS/$CHCl_3$ copolymers obtained from the differential scanning calorimetry (DSC) heating trace after rapid cooling from the melt at −60 °C min^{-1}. Melting temperature is defined here as the first (T_{m1}) and second (T_{m2}) peak maximum of the melting endotherm that results from crystallites composed of un-functionalized styrene units. Comparison of the T_m for the sPS/$CHCl_3$ and sPS/CCl_4 copolymers reveals that the sPS/$CHCl_3$ samples melt at higher temperatures, which strongly suggests that the sPS/$CHCl_3$ copolymers form thicker crystallites that contain longer runs of consecutive styrene units relative to their sPS/CCl_4 analogs.

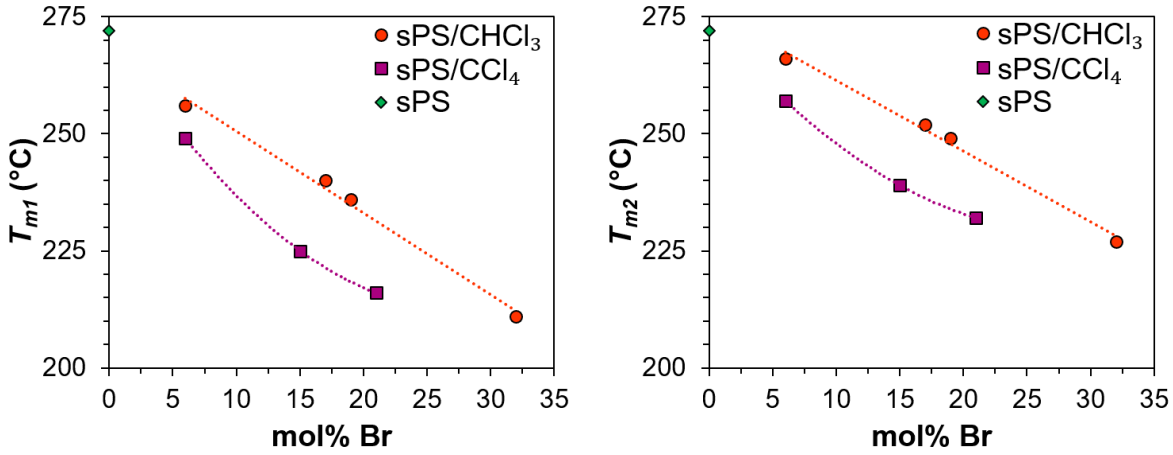

Figure S4.6. The (left) first melting temperature (T_{m1}) and (right) second melting temperature (T_{m2}) with respect to Br-content for the sPS homopolymer and the sPS/CCl_4 and sPS/$CHCl_3$ copolymers after samples were cooled from the melt at −60 °C min^{-1}. The melting temperature is defined here as the melting endotherm peak maximum for crystallites composed of un-functionalized styrene units. Dashed lines are shown to guide the eye.

DSC thermograms of the sPS homopolymer and the sPS/CCl_4 and sPS/$CHCl_3$ copolymers during slow cooling from the melt at −10 °C min^{-1} are shown in **Figure S4.7**. For both series, the crystallization exotherm, T_c, decreases in temperature and intensity with increasing Br-content, which reflects a reduction in the rate of crystallization.[30,46] For the sPS/$CHCl_3$ samples, the T_c occur at lower supercooling (higher temperatures) compared to their sPS/CCl_4 analogs, demonstrating that the sPS/$CHCl_3$ copolymers crystallize at a faster rate. The high temperature crystallization exotherms at above 235 °C in sPS/$CHCl_3$ CH-32% and sPS/CCl_4 CaT-29% are

attributed to the crystallization of distinct sequences of Br-Sty units. The presence of two crystallization exotherms in the CH-32% copolymer demonstrates that the CH-32% polymer chains contain runs of styrene units and runs of Br-sty units of significant length that are capable of crystallizing during slow cooling conditions. In contrast, the CaT-29% exhibits only one crystallization exotherm, demonstrating that runs of styrene units along the polymer chains in CaT-29% do not crystallize under these conditions.

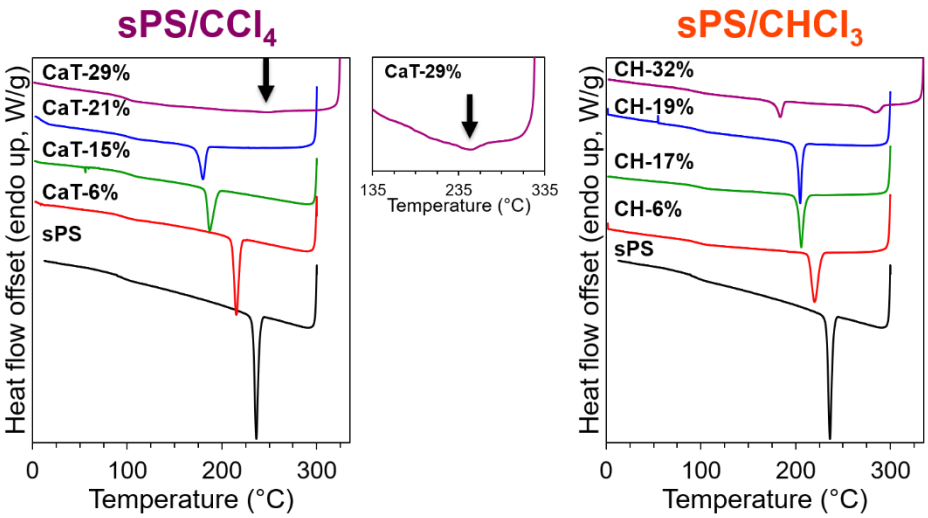

Figure S4.7. DSC cooling traces of the sPS homopolymer and the (dashed lines) sPS/CCl_4 and (solid lines) sPS/$CHCl_3$ copolymers during slow cooling from the melt at −10 °C min^{-1}. Center: CaT-29% indicating the high temperature crystallization exotherm.

To further investigate the crystallinity of the Blocky copolymers, samples were melt-crystallized at 190 °C for 2 h and analyzed by wide-angle X-ray diffraction (WAXD). **Figure S4.8** compares the normalized diffraction patterns of the sPS homopolymer and the sPS/CCl_4 and sPS/$CHCl_3$ copolymers after isothermal crystallization. The diffractograms of the sPS/CCl_4 and sPS/$CHCl_3$ samples with approximately 6-21 mol% Br contain crystalline reflections that are consistent with the diffraction pattern of the melt-crystallized sPS homopolymer. For the sPS/$CHCl_3$ CH-32% and sPS/CCl_4 CaT-29% copolymers, a new crystalline reflection is observed at ca. $2\theta = 19.3°$ that appears to originate from the unit cell of Br-Sty crystallites.[49]

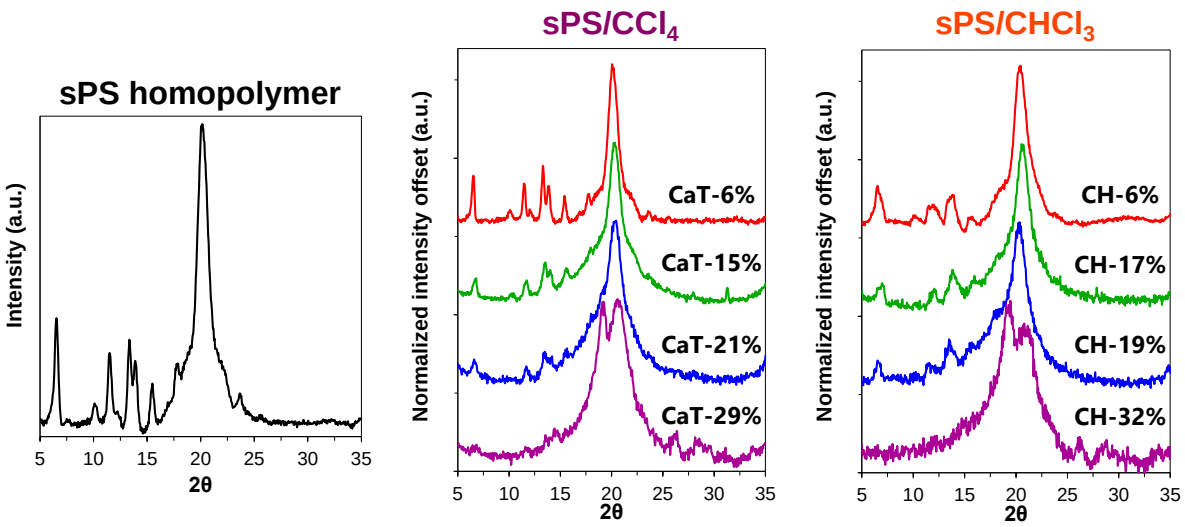

Figure S4.8. WAXD profiles of the (left) sPS/CCl_4 and (right) sPS/$CHCl_3$ copolymers after 2 h melt crystallization at 190 °C. Profiles of the copolymers are normalized by maximum intensity and offset for clarity.

Figure S4.9 shows the heating traces of the sPS homopolymer and the low Br-content sPS/$CHCl_3$ CH-6% and sPS/CCl_4 CaT-6% copolymers after rapid cooling from the melt at −60 °C min^{-1}, and after 2 h isothermal crystallization (I) at 230 °C and 190 °C. The heating traces exhibit intense melting endotherms with multiple peaks that result from the complex polymorphism of sPS. For all of the samples, the heating trace after rapid cooling is remarkably similar to the heating trace after isothermal crystallization at 190 °C, while isothermal crystallization at 230 °C (lower supercooling) produces more complex melting behavior. Based on the polymorphic composition analysis of the WAXD profiles, this complex melting behavior is attributed to a combination of chain re-organization to form more perfect crystallites and α to β transformations (see **Figure 4.11**).[33,48,58,59]

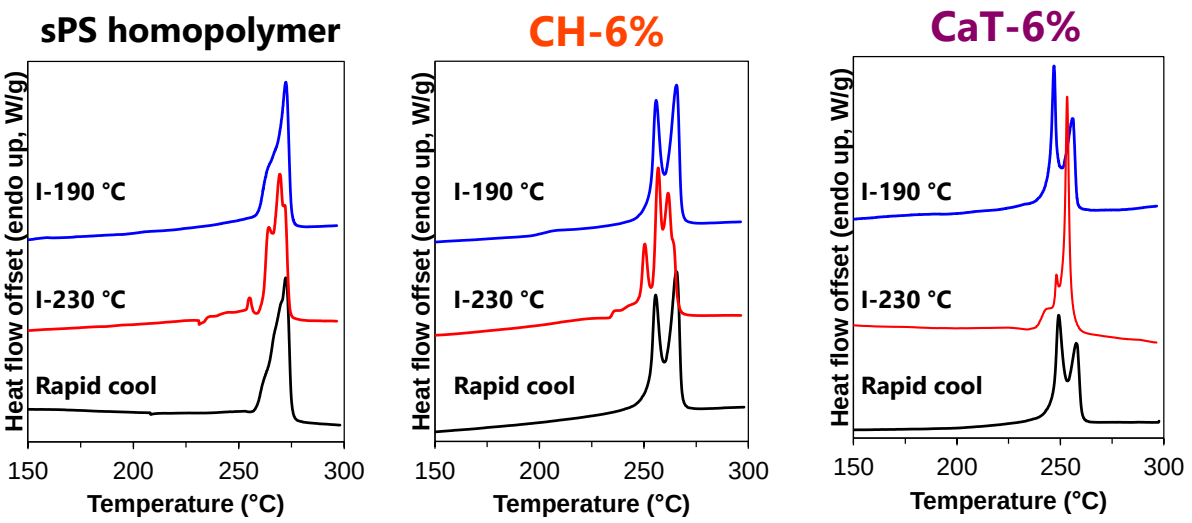

Figure S4.9. DSC heating traces of the (left) sPS homopolymer, and the (center) sPS/$CHCl_3$ CH-6% and (right) sPS/CCl_4 CaT-6% copolymers after (bottom) rapid cooling from the melt at −60 °C min^{-1}, and after 2 h isothermal crystallization (I) at (center) 230 °C and (top) 190 °C. Heating rate = 10 °C min^{-1}.

Figure S4.10 summarizes the parameters and results of the blocky copolymer microstructure simulations for sPS/CCl4 CaT-15% and sPS/CHCl3 CH-19%. Three conditions were investigated: A = 1 × block length; B = 1.5 × block length; and C = 2 × block length. For each condition, 1000 different blocky chain microstructures were constructed by randomly distributing blocks along a chain to form an inaccessible fraction. For each blocky chain microstructure, 999 copolymer chains were generated by functionalizing the remaining monomers within the accessible fraction by random choice up to the desired degree of bromination. For the CaT-15% blocky copolymer simulations, the average RMSD demonstrate that the length of the inaccessible block does not affect the residuals between the pentad sequence distribution of the simulated chains and the experimentally-determined results. In contrast, for the CH-19% blocky copolymer simulations, the average RMSD decreases with increasing length of the inaccessible block. While these results may suggest that within the crystallites of the sPS/$CHCl_3$ gel, an attached crystalline stem has at least one chain fold, further analysis of the chain folding and fold surface energies of the crystallites in the sPS/solvent gels using mechanical testing will be useful for

obtaining deeper insight into the relationship between gel morphology and copolymer microstructure and crystallization behavior and will be the subject for future investigations.

(a)

Parameters and results	sPS/CCl_4: Br-content = 15%			
	A	B	C	Minimum RMSD
Block length	47	71	94	71
Number of blocks	22	14	10	14
Average RMSD	0.8 ± 0.3%	0.7 ± 0.3%	0.6 ± 0.2%	0.45 ± 0.08%
Average size of the inaccessible fraction	61 ± 1%	63 ± 2%	63 ± 1%	67%

Styrene
Inaccessible styrene
Br-Sty

(b) Minimum RMSD block placement

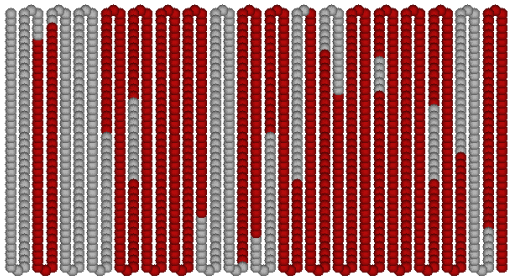

(c) Minimum RMSD simulated chain – 0.08%

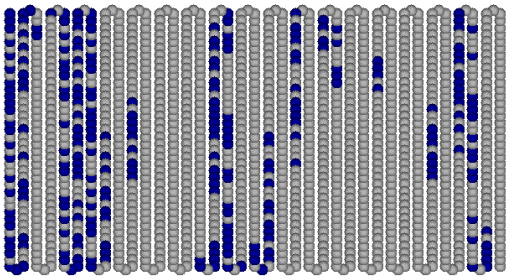

(a)

Parameters and results	sPS/$CHCl_3$: Br-content = 19%			
	1	1.5	2	Minimum RMSD
Block length	54	81	108	108
Number of blocks	22	14	10	10
Average RMSD	2.2 ± 0.3%	1.4 ± 0.2%	1.0 ± 0.2%	0.85 ± 0.07%
Average size of the inaccessible fraction	57 ± 1%	62 ± 1%	65 ± 1%	67%

Styrene
Inaccessible styrene
Br-Sty

(b) Minimum RMSD block placement

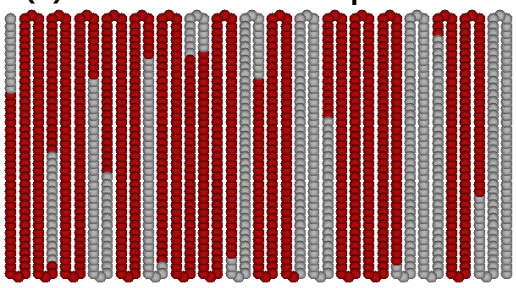

(c) Minimum RMSD simulated chain – 0.62%

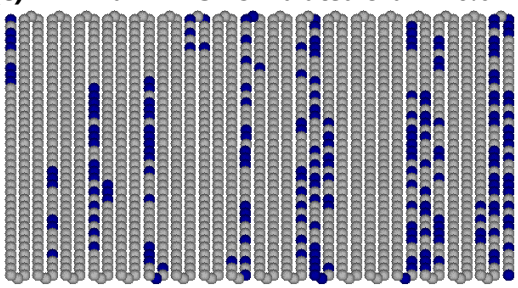

Figure S4.10. Summary of the parameters and results from the blocky copolymer microstructure simulations for (top) sPS/CCl_4 CaT-15% and (bottom) sPS/$CHCl_3$ CH-19%. (a) The parameters used to simulate the copolymer chains and the results of these analyses. For each condition, A−C, 1000 different blocky copolymer microstructures were constructed, each consisting of 999 copolymer chains that contain the desired degree of bromination. Inaccessible fraction = number of inaccessible styrene (red circles) divided by the total number of units in the chain (1442). The average and standard error are calculated from the five inaccessible fractions that produced copolymer chains with the smallest average RMSD. (b) The block distribution of the inaccessible fraction that produced the minimum average RMSD. (c) The simulated copolymer chain with the smallest RMSD.

Simulated average chains of the sPS/CCl_4 and sPS/$CHCl_3$ copolymers, created through an iterative process that minimizes the difference between the pentad sequence distribution of the simulated chain and the respective data from experiment, are provided in **Figure S4.11**. All of the chains exhibit noticeably non-random distributions of Br-Sty units in a blocky microstructure. By visual inspection of the sPS/CCl_4 and sPS/$CHCl_3$ chains with similar Br-content, no discernible differences in the distributions of block lengths of consecutive styrene or consecutive Br-Sty units are immediately apparent.

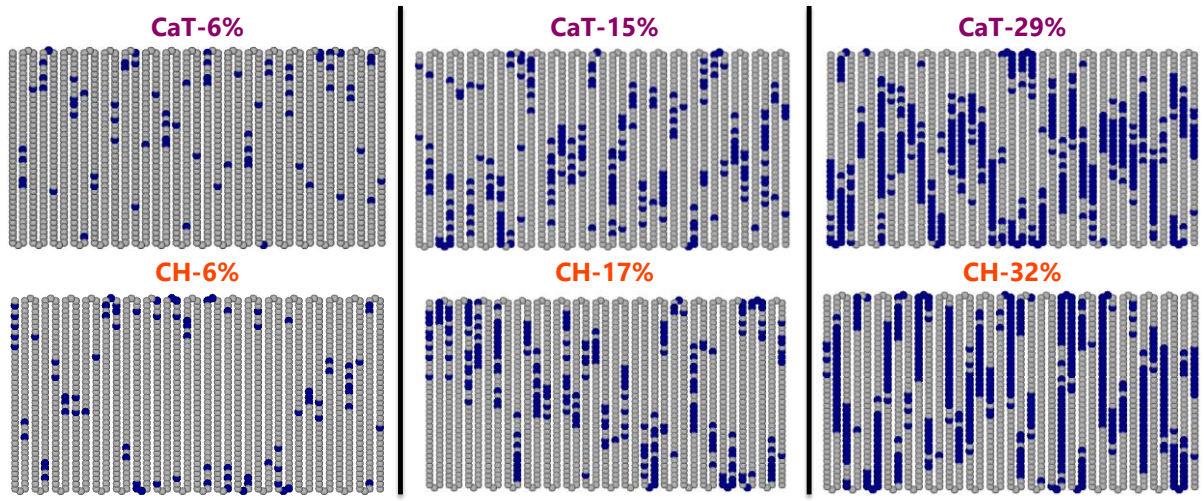

Figure S4.11. Simulated average chains of the (top) sPS/CCl_4 copolymers and the (bottom) sPS/$CHCl_3$ copolymers, created through an iterative process that minimizes the difference between the pentad sequence distribution of the simulated chain and the respective data from experiment. The root-mean-square deviation (RMSD) between the simulated and experimental results are: CaT-6% = 0.37%; CaT-15% = 0.70%; CaT-29% = 0.57%; CH-6% = 0.35%; CH-17% = 0.79%; CH-32% = 1.28%. Styrene units = grey circles; Br-Sty units = blue circles.

Figure S4.12 compares the frequency of block lengths in the sPS/CCl_4 and sPS/$CHCl_3$ simulated average chains. The block length frequency was calculated as the number of blocks of consecutive styrene units in a particular length range (e.g., blocks of 6-10 consecutive styrene units) divided by the total number of blocks in the chain. While this approach of quantifying the distribution of block lengths by frequency is somewhat misleading because the total number of blocks differs between the chains, this approach enables a direct comparison between the length of the blocks in the sPS/CCl_4 and sPS/$CHCl_3$ simulated chains of similar Br-content. It is clear

from **Figure S4.12** that the low Br-content sPS/CCl_4 CaT-6% and sPS/$CHCl_3$ CH-6% average chains contain long styrene blocks of 66-70 monomers. Above 6 mol% in the sPS/CCl_4 chains, the length of the longest blocks decreases. Though even CaT-29%, the sPS/CCl_4 chains contain one or more styrene blocks of at least 39 styrene units, in excellent agreement with the estimated length of a crystalline stem in the 10 w/v% sPS/CCl_4 gel of approximately 38-40 styrene units. Comparison of the block lengths in the sPS/$CHCl_3$ chains to their sPS/CCl_4 analogs reveals that the sPS/$CHCl_3$ chains contain longer styrene blocks. In addition, all of the sPS/$CHCl_3$ simulated chains contain one or more blocks of at least 46 styrene units, again in excellent agreement with the estimated length of a crystalline stem in the 10 w/v% sPS/CCl_4 gel of approximately 46-49 styrene units. Remarkably, the CH-32% simulated average chain exhibits 10% of its styrene units in blocks of at least 46 monomers (see **Figure 4.6**). These results support that the crystalline stems in the sPS/solvent gels are inaccessible to brominating reagent and are thus preserved as long segments of un-functionalized styrene units along the copolymer chains. These data also strongly suggest that the sPS/solvent gel morphology can be used to tailor the chain sequence of copolymers prepared by a heterogeneous gel-state functionalization method.

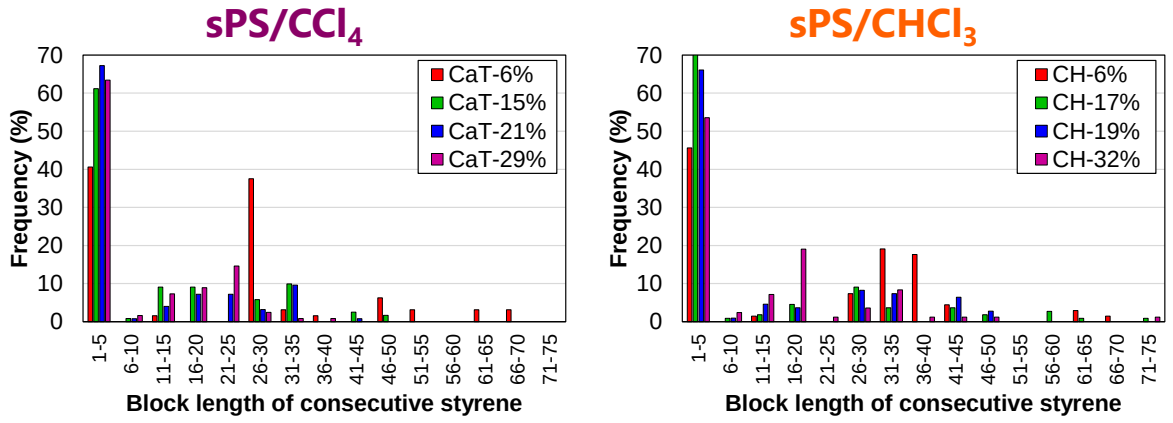

Figure S4.12. The predicted distribution of block lengths of consecutive styrene units from the simulated average chains of the (left) sPS/CCl_4 and (right) sPS/$CHCl_3$ copolymers, represented as frequency versus block length.

Figure S4.13 compares the frequency of block lengths of consecutive Br-Sty units in the simulated chains of the sPS/CCl_4 and sPS/$CHCl_3$ copolymers. Comparing the sPS/$CHCl_3$ chains to their sPS/CCl_4 analogs reveals that the simulated chains have similar distributions of Br-Sty block lengths, with the exception of CH-32%. The simulated CH-32% average chain contains very long Br-Sty blocks of 16-27 monomers. Nevertheless, the long blocks of 6-10 monomers in the chains with approximately 15-21 mol% Br are remarkable, considering the relatively low Br-content of these copolymers. For example, a copolymer with 21 mol% Br-content contains approximately one Br-Sty for every four styrene monomers. These results support that the gel-state bromination process is capable of producing a copolymer microstructure that can contain distinct sequences of Br-Sty units in blocks of significant length.

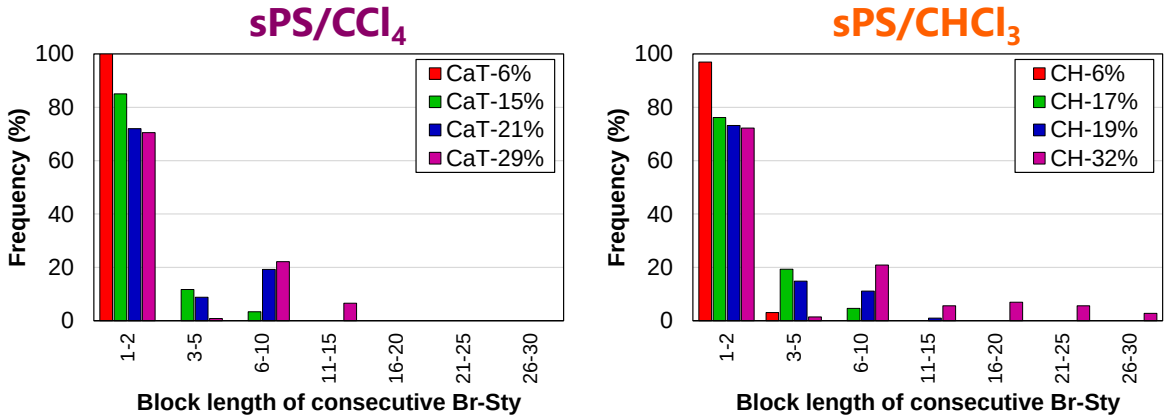

Figure S4.13. The predicted distribution of block lengths of consecutive Br-Sty units from the simulated average chains of the (left) sPS/CCl_4 and (right) sPS/$CHCl_3$ copolymers, represented as frequency versus block length.

Small-angle X-ray scattering (SAXS) was used to estimate the average lamella thickness in the melt crystallized Blocky copolymers. The SAXS profiles of the sPS homopolymer and the sPS/CCl_4 and sPS/$CHCl_3$ copolymers after 2 h isothermal crystallization at 190 °C are compared in **Figure S4.14**. The SAXS profile of the sPS homopolymer shows a low intensity, excess scattering feature in the range of 0.3 $nm^{-1} < q < 0.5$ nm^{-1} that is consistent with intercrystalline scattering observed previously in sPS.[42] The sPS/CCl_4 copolymers with 6-21 mol% Br and all of

the sPS/$CHCl_3$ copolymers also exhibit intercrystalline scattering over a range of q values from ca. 0.1 nm^{-1} < q < 0.5 nm^{-1}. The increased intensity of this excess scattering feature (i.e., Bragg peak) indicates greater periodicity in the distance, d, between scattering features. The observed shift in the Bragg peak to lower q with increasing Br-content is indicative of an increase in the center-to-center intercrystalline domain spacing, i.e., the long period (L_p).

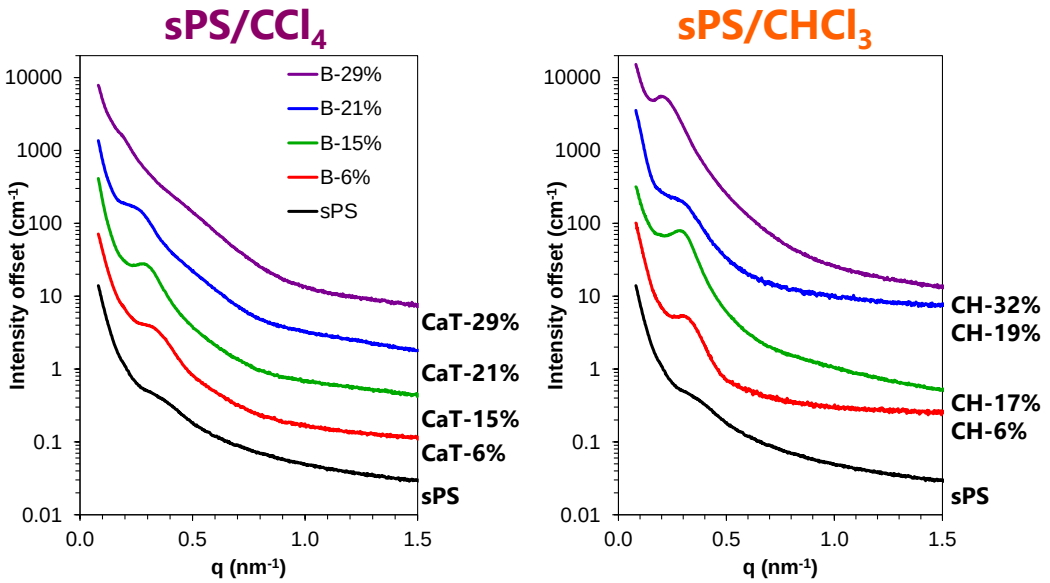

Figure S4.14. SAXS profiles of the sPS homopolymer and the (left) sPS/CCl_4 and (right) sPS/$CHCl_3$ copolymers after 2 h isothermal crystallization at 190 °C. Profiles are offset for clarity.

The long period (L_p) of the Bragg peak was analyzed by assuming a linear two-phase model, as described earlier in **subsection 4.4.1** of the Results and discussion section. Using this approach, the average lamella thickness (l_c) was estimated by multiplying L_p by the weight percent crystallinity (%X_c) in each sample after isothermal crystallization at 190 °C. The %X_c values were determined from the area under the melting endotherm (ΔH_f) in the subsequent DSC heating trace. The average lamella thickness was also estimated from the 1-D correlation function. Both approaches produced similar results, which are provided in **Table S4.1**. The results of the SAXS analysis are similar for the sPS/CCl_4 and sPS/$CHCl_3$ copolymers. Both series generally show an increase in L_p and l_a and a decrease in l_c with increasing Br-content, as expected for an sPS

copolymer that contains Br-Sty defects and is thus only capable of forming thinner crystallites. In addition, the Blocky copolymers with similar Br-content exhibit similar l_c values.

It is important to note that for pure sPS and at least for the low Br-content sPS/CCl_4 and sPS/$CHCl_3$ copolymers, melt crystallization at 190 °C appears to favor the nucleation of the α polymorph and thus potentially the formation of thinner crystallites (see **Table 4.3**). While the SAXS analysis may therefore underestimate the true maximum l_c that is possible for these samples, these data still provide a useful initial approximation of the minimum average lamella thickness.

Table S4.1. SAXS analysis of the intercrystalline domain spacing in the sPS homopolymer and the sPS/CCl_4 and sPS/$CHCl_3$ copolymers after 2 h isothermal crystallization at 190 °C.

	Linear two-phase model						**1-D correlation function**	
Sample	***d*-spacing (nm^{-1})**	**L_p (nm)**	**$\%X_c$ [a]**	**l_c (nm)**	***Avg. # of styrene*[b]**	**l_a (nm)**	**l_c (nm)**	**l_a (nm)**
sPS	0.389	16.2	32	5.2	20	11.0	5.0	17.8
CaT-6%	0.337	18.7	29	5.5	21	13.2	5.1	21.9
CaT-15%	0.315	19.9	22	4.3	17	15.6	4.8	17.1
CaT-21%	0.273	23.0	19	4.3	17	18.7	4.4	17.2
CaT-29%	—	—	—	—	—	—	—	—
CH-6%	0.325	19.3	31	6.0	24	13.3	5.0	25.4
CH-17%	0.308	20.4	25	5.1	20	15.3	6.0	13.1
CH-19%	0.315	19.9	22	4.3	17	15.6	4.6	28.6
CH-32%	0.237	26.5	4	1.2	5	25.3	6.1	19.6

[a] Weight percent crystallinity calculated from the area under the melting endotherm (ΔH_f) in the DSC heating trace ($\Delta H_f°$=79.3 J/g).

[b]Average number of styrene units in a crystalline stem, based on the lamella thickness and the planar zigzag conformation of sPS with 2 monomer units per identity period (c-axis dimension = 0.51 nm).[43]

4.8. References

1. Hadjichristidis, N.; Pispas, S.; Floudas, G. A., *Block Copolymers: Synthetic Strategies, Physical Properties, and Applications*. John Wiley and Sons: New York, 2002.
2. Hamley, I. W., *The Physics of Block Copolymers*. Oxford University Press: New York, 1998.
3. Lee, M.; Park, J. K.; Lee, H.-S.; Lane, O.; Moore, R. B.; McGrath, J. E.; Baird, D. G., Effects of Block Length and Solution-Casting Conditions on the Final Morphology and Properties of Disulfonated Poly(Arylene Ether Sulfone) Multiblock Copolymer Films for Proton Exchange Membranes. *Polymer* **2009,** *50*, 6129-6138.
4. Leibler, L., Theory of Microphase Separation in Block Copolymers. *Macromolecules* **1980,** *13* (6), 1602-1617.
5. Dobrynin, A. V.; Leibler, L., Theory of Polydisperse Multiblock Copolymers. *Macromolecules* **1997,** *30*, 4756-4765.
6. Bates, F. S.; Fredrickson, G. H., Block Copolymers - Designer Soft Materials. *Phys. Today* **1999,** *52* (2), 32-38.
7. Lodge, T. P., Block Copolymers: Past Successes and Future Challenges. *Macromol. Chem. Phys.* **2003,** *204* (2), 265-273.
8. Ruzette, A.-V.; Leibler, L., Block Copolymers in Tomorrow's Plastics. *Nat. Mater.* **2005,** *4* (1), 19-31.
9. Domski, G. J.; Rose, J. M.; Coates, G. W.; Bolig, A. D.; Brookhart, M., Living Alkene Polymerization: New Methods for the Precision Synthesis of Polyolefins. *Prog. Polym. Sci.* **2007,** *32* (1), 30-92.
10. Fahs, G. B.; Benson, S. D.; Moore, R. B., Blocky Sulfonation of Syndiotactic Polystyrene: A Facile Route toward Tailored Ionomer Architecture Via Postpolymerization Functionalization in the Gel State. *Macromolecules* **2017,** *50* (6), 2387-2396.
11. Anderson, L. J.; Yuan, X.; Fahs, G. B.; Moore, R. B., Blocky Ionomers Via Sulfonation of Poly(Ether Ether Ketone) in the Semicrystalline Gel State. *Macromolecules* **2018,** *51* (16), 6226-6237.
12. Noble, K. F.; Noble, A. M.; Talley, S. J.; Moore, R. B., Blocky Bromination of Syndiotactic Polystyrene Via Post-Polymerization Functionalization in the Heterogeneous Gel State. *Polym. Chem.* **2018,** *9* (41), 5095-5106.

13. Mochizuki, J.; Sano, T.; Tokami, T.; Itagaki, H., Decisive Properties of Solvent Able to Form Gels with Syndiotactic Polystyrene. *Polymer* **2015,** *67*, 118-127.
14. Shimizu, H.; Wakayama, T.; Wada, R.; Okabe, M.; Tanaka, F., Solvent Effect on Junction Size in Syndiotactic Polystyrene Physical Gel. *Polym. J.* **2005,** *37* (4), 294-298.
15. Kobayashi, M.; Yoshioka, T.; Kozasa, T.; Tashiro, K.; Suzuki, J.; Funahashi, S.; Izumi, Y., Structure of Physical Gels Formed in Syndiotactic Polystyrene/Solvent Systems Studied by Small-Angle Neutron Scattering. *Macromolecules* **1994,** *27* (6), 1349-1354.
16. Roels, T.; Deberdt, F.; Berghmans, H., Solvent Quality and Phase-Stability in Syndiotactic Polystyrene-Solvent Systems. *Macromolecules* **1994,** *27* (21), 6216-6220.
17. Daniel, C.; Guerra, G.; Musto, P., Clathrate Phase in Syndiotactic Polystyrene Gels. *Macromolecules* **2002,** *35* (6), 2243-2251.
18. Venditto, V.; Pellegrino, M.; Califano, R.; Guerra, G.; Daniel, C.; Ambrosio, L.; Borriello, A., Monolithic Polymeric Aerogels with Vocs Sorbent Nanoporous Crystalline and Water Sorbent Amorphous Phases. *ACS Appl. Mater. Inter.* **2015,** *7* (2), 1318-1326.
19. Benson, S. D.; Moore, R. B., Crystallization Behavior of Non-Random Sulfonated Syndiotactic Polystyrene. *Polym. Prepr.* **2009,** *50* (2), 182.
20. Benson, S. D. The Effect of Nanoscale Particles and Ionomer Architecture on the Crystallization Behavior of Sulfonated Syndiotactic Polystyrene. Dissertation, Virginia Polytechnic Institute and State University, Blacksburg, VA, 2010.
21. Borriello, A.; Agoretti, P.; Ambrosio, L.; Fasano, G.; Pellegrino, M.; Venditto, V.; Guerra, G., Syndiotactic Polystyrene Films with Sulfonated Amorphous Phase and Nanoporous Crystalline Phase. *Chem. Mater.* **2009,** *21* (14), 3191-3196.
22. Gibson, H. W.; Bailey, F. C., Chemical Modification of Polymers. 13. Sulfonation of Polystyrene Surfaces. *Macromolecules* **1980,** *13* (1), 34-41.
23. Semler, J. J.; Jhon, Y. K.; Tonelli, A.; Beevers, M.; Krishnamoorti, R.; Genzer, J., Facile Method of Controlling Monomer Sequence Distributions in Random Copolymers. *Adv. Mater.* **2007,** *19* (19), 2877-2883.
24. Jhon, Y. K.; Semler, J. J.; Genzer, J., Effect of Solvent Quality and Chain Confinement on the Kinetics of Polystyrene Bromination. *Macromolecules* **2008,** *41* (18), 6719-6727.

25. Strickland, L. A.; Hall, C. K.; Genzer, J., Design of Copolymers with Tunable Randomness Using Discontinuous Molecular Dynamics Simulation. *Macromolecules* **2009,** *42* (22), 9063-9071.
26. Han, J.; Jeon, B. H.; Ryu, C. Y.; Semler, J. J.; Jhon, Y. K.; Genzer, J., Discriminating among Co-Monomer Sequence Distributions in Random Copolymers Using Interaction Chromatography. *Macromol. Rapid Comm.* **2009,** *30* (18), 1543-1548.
27. Jhon, Y. K.; Semler, J. J.; Genzer, J.; Beevers, M.; Gus' kova, O. A.; Khalatur, P. G.; Khokhlov, A. R., Effect of Comonomer Sequence Distribution on the Adsorption of Random Copolymers onto Impenetrable Flat Surfaces. *Macromolecules* **2009,** *42*, 2843-2853.
28. Gurarslan, R.; Hardrict, S.; Roy, D.; Galvin, C.; Hill, M. R.; Gracz, H.; Sumerlin, B. S.; Genzer, J.; Tonelli, A., Beyond Microstructures: Using the Kerr Effect to Characterize the Macrostructures of Synthetic Polymers. *J. Polym. Sci. B Polym. Phys.* **2015,** *53* (3), 155-166.
29. Liu, S.; Sen, A., Syntheses of Syndiotactic-Polystyrene-Graft-Poly(Methyl Methacrylate), Syndiotactic-Polystyrene-Graft-Poly(Methyl Acrylate), and Syndiotactic-Polystyrene-Graft-Atactic-Polystyrene with Defined Structures by Atom Transfer Radical Polymerization. *Macromolecules* **2000,** *33* (14), 5106-5110.
30. Gao, Y.; Li, H. M., Synthesis and Characterization of Acetylated Syndiotactic Polystyrene. *Polym. Int.* **2004,** *53* (10), 1436-1441.
31. Kobayashi, M.; Kozasa, T., Conformational Ordering Process on Physical Gelation of Syndiotactic Polystyrene/Solvent Systems Revealed by Time-Resolved Infrared Spectroscopy. *Appl. Spectrosc.* **1993,** *47* (9), 1417-1424.
32. Daniel, C.; Avallone, A.; Guerra, G., Syndiotactic Polystyrene Physical Gels: Guest Influence on Structural Order in Molecular Complex Domains and Gel Transparency. *Macromolecules* **2006,** *39* (22), 7578-7582.
33. Gowd, E. B.; Tashiro, K.; Ramesh, C., Structural Phase Transitions of Syndiotactic Polystyrene. *Prog. Polym. Sci.* **2009,** *34* (3), 280-315.
34. Kobayashi, M.; Nakaoki, T.; Ishihara, N., Molecular Conformation in Glasses and Gels of Syndiotactic and Isotactic Polystyrenes. *Macromolecules* **1990,** *23* (1), 78-83.
35. Daniel, C.; Menelle, A.; Brulet, A.; Guenet, J.-M., Thermoreversible Gelation of Syndiotactic Polystyrene in Toluene and Chloroform. *Polymer* **1997,** *38* (16), 4193-4199.

36. Prasad, A.; Mandelkern, L., The Thermoreversible Gelation of Syndiotactic Polystyrene. *Macromolecules* **1990,** *23* (23), 5041-5043.
37. Noble, K. F.; Talley, S. J.; Fahs, G. B.; Troya, D.; Moore, R. B., High-Resolution Comonomer Sequencing of Sps-Co-Sps-Br Copolymers Using ^{13}c Nmr Spectroscopy, Simulations, and Small-Angle X-Ray Scattering. *Manuscript in progress.*
38. Ilavsky, J.; Zhang, F.; Andrews, R. N.; Kuzmenko, I.; Jemian, P. R.; Levine, L. E.; Allen, A. J., Development of Combined Microstructure and Structure Characterization Facility for in Situ and Operando Studies at the Advanced Photon Source. *J. Appl. Crystallogr.* **2018,** *51* (3), 867-882.
39. Ilavsky, J.; Zhang, F.; Allen, A. J.; Levine, L. E.; Jemian, P. R.; Long, G. G., Ultra-Small-Angle X-Ray Scattering Instrument at the Advanced Photon Source: History, Recent Development, and Current Status. *Metall. Mater. Trans. A* **2013,** *44* (1), 68-76.
40. Ilavsky, J., Nika: Software for Two-Dimensional Data Reduction. *J. Appl. Crystallogr.* **2012,** *45* (2), 324-328.
41. Ilavsky, J.; Jemian, P. R., Irena: Tool Suite for Modeling and Analysis of Small-Angle Scattering. *J. Appl. Crystallogr.* **2009,** *42* (2), 347-353.
42. Takebe, T.; Yamasaki, K., Crystallization Thermodynamics and Kinetics of Syndiotactic Polystyrene. In *Syndiotactic Polystyrene*, 2009; pp 238-251.
43. Albunia, A. R.; Musto, P.; Guerra, G., Ftir Spectra of Pure Helical Crystalline Phases of Syndiotactic Polystyrene. *Polymer* **2006,** *47* (1), 234-242.
44. Britton, D.; Heatley, F.; Lovell, P. A., 13c Nmr Spectroscopy Studies of Branching and Sequence Distribution in Copolymers of Vinyl Acetate and N-Butyl Acrylate Prepared by Semibatch Emulsion Copolymerization. *Macromolecules* **2001,** *34* (4), 817-829.
45. Shin, J.; Chang, Y.; Nguyen, T. L. T.; Noh, S. K.; Bae, C., Hydrophilic Functionalization of Syndiotactic Polystyrene Via a Combination of Electrophilic Bromination and Suzuki–Miyaura Reaction. *J. Polym. Sci., Part A: Polym. Chem.* **2010,** *48* (19), 4335-4343.
46. Annunziata, L.; Sarazin, Y.; Duc, M.; Carpentier, J. F., Well-Defined Syndiotactic Polystyrene-B-Atactic Polystyrene Stereoblock Polymers. *Macromol. Rapid Commun.* **2011,** *32* (9-10), 751-757.
47. Annunziata, L.; Monasse, B.; Rizzo, P.; Guerra, G.; Duc, M.; Carpentier, J.-F., On the Crystallization Behavior of Syndiotactic-B-Atactic Polystyrene Stereodiblock Copolymers,

Atactic/Syndiotactic Polystyrene Blends, and Aps/Sps Blends Modified with Sps-B-Aps. *Mater. Chem. Phys.* **2013,** *141* (2–3), 891-902.

48. Su, C.; Jeng, U.; Chen, S.; Cheng, C.-Y.; Lee, J.-J.; Lai, Y.-H.; Su, W.; Tsai, J.; Su, A., Thermodynamic Characterization of Polymorphs in Bulk-Crystallized Syndiotactic Polystyrene Via Small/Wide-Angle X-Ray Scattering and Differential Scanning Calorimetry. *Macromolecules* **2009,** *42* (12), 4200-4207.
49. Girolamo Del Mauro, A. D.; Loffredo, F.; Venditto, V.; Longo, P.; Guerra, G., Polymorphic Behavior of Syndiotactic Poly(P-Chlorostyrene) and Styrene/P-Chlorostyrene Cosyndiotactic Random Copolymers. *Macromolecules* **2003,** *36* (20), 7577-7584.
50. Guo, F.; Jiao, N.; Jiang, L.; Li, Y.; Hou, Z., Scandium-Catalyzed Syndiospecific Polymerization of Halide-Substituted Styrenes and Their Copolymerization with Styrene. *Macromolecules* **2017,** *50* (21), 8398-8405.
51. Tonelli, A. E.; Jhon, Y. K.; Genzer, J., Glass Transition Temperatures of Styrene/4-Brstyrene Copolymers with Variable Co-Monomer Compositions and Sequence Distributions. *Macromolecules* **2010,** *43* (16), 6912.
52. Wang, H.; Wu, C.; Cui, D.; Men, Y., Lamellar Thickness Dependence of Crystal Modification Selection in the Syndiotactic Polystyrene Γ-to-A/B Phase Transition Process. *Macromolecules* **2018,** *51* (2), 497-503.
53. Strobl, G. R.; Bendler, J. T.; Kambour, R. P.; Shultz, A. R., Thermally Reversible Phase Separation in Polystyrene/Poly(Styrene-Co-4-Bromostyrene) Blends. *Macromolecules* **1986,** *19* (11), 2683-2689.
54. Khokhlov, A. R.; Khalatur, P. G., Protein-Like Copolymers: Computer Simulation. *Physica A* **1998,** *249* (1–4), 253-261.
55. Krishnaswamy, R. K.; Yang, Q.; Fernandez-Ballester, L.; Kornfield, J. A., Effect of the Distribution of Short-Chain Branches on Crystallization Kinetics and Mechanical Properties of High-Density Polyethylene. *Macromolecules* **2008,** *41* (5), 1693-1704.
56. Guerra, G.; Vitagliano, V. M.; De Rosa, C.; Petraccone, V.; Corradini, P., Polymorphisms in Melt Crystallized Syndiotactic Polystyrene Samples. *Macromolecules* **1990,** *23* (5), 1539-1544.
57. Woo, E. M.; Sun, Y. S.; Yang, C. P., Polymorphism, Thermal Behavior, and Crystal Stability in Syndiotactic Polystyrene Vs. Its Miscible Blends. *Prog. Polym. Sci.* **2001,** *26* (6), 945-983.

58. Sun, Y. S.; Woo, E. M., Correlation between Thermal Behavior and Crystalline Morphology in B-Form Syndiotactic Polystyrene. *Macromol. Chem. Phys.* **2001,** *202* (9), 1557-1568.
59. Ho, R.-M.; Lin, C.-P.; Tsai, H.-Y.; Woo, E.-M., Metastability Studies of Syndiotactic Polystyrene Polymorphism. *Macromolecules* **2000,** *33* (17), 6517-6526.
60. Gurarslan, R.; Tonelli, A. E., Do We Need to Know and Can We Determine the Complete Macrostructures of Synthetic Polymers? *Prog. Polym. Sci.* **2016**.
61. Higaki, Y.; Suzuki, K.; Kiyoshima, Y.; Toda, T.; Nishiura, M.; Ohta, N.; Masunaga, H.; Hou, Z.; Takahara, A., Molecular Aggregation States and Physical Properties of Syndiotactic Polystyrene/Hydrogenated Polyisoprene Multiblock Copolymers with Crystalline Hard Domain. *Macromolecules* **2017,** *50* (16), 6184-6191.
62. Tong, Z.-Z.; Huang, J.; Zhou, B.; Xu, J.-T.; Fan, Z.-Q., Chain Microstructure, Crystallization, and Morphology of Olefinic Blocky Copolymers. *Macromol. Chem. Phys.* **2013,** *214* (5), 605-616.
63. Bates, F. S.; Fredrickson, G. H., Block Copolymer Thermodynamics: Theory and Experiment. *Annu. Rev. Phys. Chem.* **1990,** *41* (1), 525-557.
64. Xu, H.; Ince, B. S.; Cebe, P., Development of the Crystallinity and Rigid Amorphous Fraction in Cold-Crystallized Isotactic Polystyrene. *J. Polym. Sci., Part B: Polym. Phys.* **2003,** *41* (23), 3026-3036.
65. Flory, P. J., Theory of Crystallization in Copolymers. *Trans. Faraday Soc.* **1955,** *51* (0), 848-857.
66. Daniel, C.; Giudice, S.; Guerra, G., Syndiotatic Polystyrene Aerogels with B, Γ, and E Crystalline Phases. *Chem. Mater.* **2009,** *21* (6), 1028-1034.
67. Cheng, Y.-W.; Wang, C., Solvent-Induced Crystallization of Electrospun Syndiotactic Polystyrene Nanofibers and Its Reversible Desorption/Sorption of Volatile Organic Vapors. *J. Polym. Res.* **2016,** *23* (11), 234.

Chapter 5.

Blocky Bromination of Syndiotactic Polystyrene via Post-Polymerization Functionalization in the Powder State, a Control Study

Kristen F. Noble, Helen T. Tran, Diego Troya, and Robert B. Moore

5.1. Abstract

This work is a fundamental investigation into the post-polymerization bromination of syndiotactic polystyrene (sPS) in the heterogeneous powder and gel states, which are shown to produce non-random, i.e., blocky, brominated sPS (sPS-*co*-sPS-Br) copolymers. Morphological characterization of the heterogeneous reaction states provided by X-ray scattering techniques shows that the sPS powder contains the γ-form crystal phase and densely packed polymer chains. In contrast, the 10 w/v% sPS/chloroform ($CHCl_3$) gel is composed of loosely packed δ-form crystals that act as physical cross-links bound together by a percolating network of solvent swollen amorphous chains. To evaluate the effect of heterogeneous reaction state on copolymer microstructure and crystallization behavior, a set of copolymers were prepared from the powder-state (Powder) and gel-state (Gel). The degree of bromination and reaction rate were evaluated using ^{1}H nuclear magnetic resonance (NMR) spectroscopy. In contrast to the dense powder-state, which shows limited functionalization of up to 12 mol% *p*-bromostyrene (Br-Sty) units, the gel-state produces copolymers with up to 32 mol% Br in less than one-third of the reaction time. Microstructural analysis and comonomer sequencing of the brominated copolymers, provided by quantitative ^{13}C nuclear magnetic resonance (NMR) spectroscopy, reveal that the Gel copolymers contain a higher prevalence of styrene "blocks" of at least five consecutive styrene units and a higher degree of blockiness. Crystallization behavior of the brominated copolymers, examined

using differential scanning calorimetry (DSC), demonstrates that at 7 mol% Br, the Gel copolymer crystallizes and melts at higher temperatures and exhibits faster crystallization kinetics at lower supercooling relative to its 7 mol% Br Powder analog. Simulated average chains of the brominated copolymers, generated from the experimentally-determined comonomer sequences distributions, predict that the Gel copolymers contain a higher prevalence of crystallizable sPS segments, consistent with the Gel copolymers' rapid crystallization kinetics. Thus, the simulated average chains appear to be representative of average chains in their respective brominated copolymers and support that the gel state favorably affects the bromination reaction, producing blocky copolymers with a high degree of blockiness and fewer defects along the chains.

5.2. Introduction

Block copolymers are a class of macromolecules, characterized by two or more chemically distinct polymer segments linked together through covalent bonds.[1,2] The technological applicability of block copolymers is promising as a result of their remarkable properties that stem from the individual character or function of their discrete blocks. The chemical nature of the different repeating monomers in the blocks, the number of blocks, block lengths, and sequence distributions define the copolymer's operative physical and chemical properties.[3-5] Moreover, thermodynamic immiscibility between chemically dissimilar blocks, often drives self-assembly into well-ordered, micro-phase separated morphologies that can significantly enhance the material properties. Block copolymers have received tremendous attention with respect to controlled synthesis, tailored morphological development, and customized physical properties with potential uses for self-assembled, nanostructured materials; [6-8] however, the generally arduous procedures for block copolymer synthesis, often involving inert atmospheric conditions, well-controlled,

sequential reaction timings, specialized initiators, and high purity monomers and solvents, generally limits the scope of their commercial application.[9]

As a distinct alternative to the complex polymerization mechanisms and synthetic protocols employed in the conventional formation of block copolymers, blocky copolymer microstructures can be achieved using post-polymerization functionalization methods carried out in heterogeneous reaction states. Herein, the term "blocky copolymer" will be used as a description of copolymers that contain a significant degree of non-randomness in the distribution of comonomers along their chains. Genzer and coworkers[10-15] have used empirical data and simulations to extensively investigated the bromination of atactic polystyrene (aPS) in poor solvents, where polymer chains are in a collapsed conformation. In this collapsed state, portions of the chains were effectively shielded from the brominating reagent, resulting in blocky brominated styrene sequences. Others have performed post-polymerization bromination[16] or acetylation[17] on suspended syndiotactic polystyrene (sPS) powders, though copolymer microstructure was not investigated in these studies. Borriello and coworkers[18] investigated the post-polymerization sulfonation of solution cast or compression-molded syndiotactic polystyrene (sPS) films, evaluating the interplay between sulfonating reagent diffusion and reaction processes on sulfonation heterogeneity across the films. Solution cast films demonstrated uniform sulfonation, attributed to rapid diffusion of sulfonating reagent through nanoporous phases in the film. In contrast, compression-molded films exhibited a decreasing sulfonation gradient from the film's surface to interior, consistent with slow diffusion of sulfonating reagent into the non-porous, solid-state "bulk" film. The results of their analysis were similar to that observed for the sulfonation of aPS films.[19] Recently, we demonstrated that the heterogeneous sulfonation and bromination of sPS and poly(ether ether ketone) (PEEK) gels, yields copolymers with a blocky distribution of functionalities along the chains.[20-22] The gel-state

functionalized sPS and PEEK copolymers demonstrated superior crystallizability and faster crystallization kinetics compared to their solution-state random analogs.

The powder state of crystallizable homopolymers (e.g., sPS) is defined by a dense polymer matrix of tightly packed chain segments in lamellar crystals and amorphous chain segments.[23] In contrast, gels of crystallizable homopolymers are composed of tightly packed chain segments in lamellar crystals that act as physical cross-links bound together by a percolating network of solvent swollen amorphous chains.[24-28] When a functionalizing reagent is introduced to the heterogeneous gel network, it is sterically excluded from the crystalline component, and thus only reacts with monomer units in the accessible interconnecting amorphous component. Using this straightforward post-polymerization functionalization approach, the resulting copolymer has been shown to contain separate segments of randomly functionalized "blocks" and un-functionalized "blocks" originating from monomer units that were isolated within the crystalline domains of the gel network.[29]

This work is a fundamental investigation into the post-polymerization bromination of syndiotactic polystyrene (sPS) in the heterogeneous powder and gel states. The purpose of this research was to determine the impact of heterogeneous reaction state on copolymer microstructure, degree of blockiness, and crystallization behavior. Morphological characterization of the sPS powder and a 10 w/v% sPS/$CHCl_3$ gel was provided by X-ray scattering techniques. To investigate how the heterogeneous reaction state effects the copolymer properties, nuclear magnetic resonance (NMR) spectroscopy was used to evaluate the copolymer microstructure and comonomer sequence distribution, differential scanning calorimetry (DSC) was used to probe the copolymer thermal properties and crystallization kinetics, and X-ray scattering techniques were used to investigate the copolymer morphology. In order to obtain deeper insight into the copolymer microstructure and

crystallization behavior, simulated average chains of the brominated copolymers were developed, based on the experimentally-determined distribution of pentad sequences obtained from the quantitative ^{13}C NMR spectra. Through this work, heterogeneous gel-state functionalization is proven to be a superior approach to preparing semicrystalline, blocky brominated sPS copolymers with relatively high functional group content, high degrees of blockiness, and fewer defects along the chains.

5.3. Experimental Section

5.3.1. Materials

Syndiotactic polystyrene (Questra® 102, M_w = 300K g mol^{-1}) was obtained from Dow Chemical Company. The solvents, chloroform ($CHCl_3$), 1,2-dichloromethane (DCM), and 1,1,2,2-tetrachloroethane (TCE) were purchased from Fisher Scientific Company. Bromine (Br_2) was purchased from Sigma Aldrich®. The Lewis acid catalyst, ferric(III) chloride ($FeCl_3$) was obtained from VWR International LLC. All chemicals and reagents were used as received. Solution-state brominated (i.e., Random) copolymers that contain 6, 11, and 16 mol% Br were prepared as described previously in **Chapter 2**.[21]

5.3.2. Gel-state bromination

To prepare a 10 w/v% sPS/$CHCl_3$ gel, sPS (2.5 g, 0.83 μmol) pellets were first dissolved in stirred $CHCl_3$ (25 mL) in a pressure vessel at ca. 90 °C, then removed from heat to promote gel formation. A translucent gel formed over a period of at least 6 h and was stored at room temperature for approximately another 24 h. Using a spatula, the gel was broken into small pieces (ca. 1-3 mm), dispersed in DCM (final sPS concentration of 3 w/v%), and placed in an ice bath. The flask was purged with argon, followed by the addition of $FeCl_3$ (54 mg, 0.33 mmol). After stirring for 30

min, a stock solution of 50 w/w% Br_2 in DCM (2.2 mL, 0.043 mol) was introduced dropwise to the reaction vessel over two hours. The reaction was carried out in the dark under argon at room temperature and terminated after 2.5–6 h from the time of the first stock solution addition, by pouring the suspension into stirred methanol. All samples were purified by dissolving in TCE at reflux, followed by filtration of the warm solutions through a filter paper (Whatman® 1) and precipitation in methanol, which produced white solids. Prior to characterization, samples were ground into homogeneous powders, washed by soxhlet extraction in hot methanol for ca. 24 h, and dried under vacuum at 80 °C for ca. 18 h.

5.3.3. Powder-state bromination

The sPS powder was prepared from sPS pellets by first dissolving the pellets in TCE (ca. 5 w/v%) in a round bottom flask at 150°C, followed by precipitation by slow pouring into stirred methanol (2 L). The recovered white solid was washed by soxhlet extraction in hot methanol for ca. 24 h and dried in a vacuum oven at 80°C for ca. 18 h. Using a mortar and pestle, the sPS homopolymer was ground into a fine powder. The post-polymerization functionalization method used to brominate the sPS powder follows the same method used to prepare copolymers from the 10 w/v% sPS/$CHCl_3$ gel. The sPS powder (2.5 g, 0.83 μmol) was transferred to a round bottom flask and dispersed in DCM (final sPS concentration of 2 w/v%). After addition of $FeCl_3$ (54 mg, 0.33 mmol), the flask was placed in an ice bath and purged with argon for 30 min. To brominate, a bromine stock solution of 50 w/w% Br_2 in DCM (2.2 mL, 0.043 mol) was added dropwise to the reaction vessel over two hours. The reaction was carried out in the dark under argon at room temperature. To control the degree of bromination, reactions were stopped after 19, 31, 69, and 96 hours by pouring the suspensions into stirred methanol. The samples were purified by dissolving in TCE, filtering, and precipitating in methanol to recover a white to off-white product. Before

analysis the samples were ground into homogeneous powders, washed by soxhlet extraction in hot methanol for ca. 24 h, and dried under vacuum at 80°C for ca. 18 h.

5.3.4. Sample preparation

A 10 w/v% sPS/$CHCl_3$ gel was prepared for morphological characterization by X-ray scattering techniques. To prepare the gel, sPS pellets were dissolved in $CHCl_3$ at 90 °C in a pressure vessel, followed by transferring the sPS solution to a thin-walled, 3 mm outer diameter, glass tube that was then sealed and stored at room temperature to promote gel formation. For wide-angle X-ray diffraction (WAXD) experiments, a 10 w/v% sPS/$CHCl_3$ gel was prepared and stored at room temperature for ca. 24 h to mimic the conditions prior to gel-state bromination, then broken into pieces with a spatula and dried under vacuum at 70 °C for ca. 24 h.

5.3.5. NMR spectroscopy

Microstructure analysis was carried out using nuclear magnetic resonance (NMR) spectroscopy. ^{1}H NMR experiments were recorded at room temperature in deuterated chloroform ($CDCl_3$) on an Agilent U4-DD2 400 MHz spectrometer. Quantitative ^{13}C NMR experiments were recorded at room temperature in TCE-d_2 on a Bruker Avance II 500 MHz spectrometer (C13IG parameter set, proton decoupled, relaxation delay of 6 s, O1P of 95, and sweep width of 150 ppm). Quantitative ^{13}C NMR experiments were recorded at room temperature in 1,1,2,2-tetrachloroethane-d_2 (TCE-d_2) on a Bruker Avance II 500 MHz spectrometer equipped with a LN2 prodigy cryogenic BBO probe using a C13IG pulse program, proton decoupling (NOE−), a relaxation delay of 6 sec, O1P of 95, and a sweep width of 150 ppm. The Line Fitting function in Mestrelab Research's MestReNova x64 software was used to deconvolute and integrate the

multiple peaks in the quaternary carbon region of the ^{13}C NMR spectrum. The deconvolution method is discussed in more detail in **Chapter 3**.[30]

5.3.6. Thermal properties and crystallization kinetics

Copolymer thermal transitions, crystallinity, and crystallization kinetics were investigated using differential scanning calorimetry (DSC, TA Instrument DSC Q2000) under continuous nitrogen flow to minimize polymer degradation. TA Instruments Universal Analysis software was used to determine crystallization. To probe the copolymer crystallizability under specific cooling conditions, samples were first annealed at 300 °C for 3-5 min to erase any thermal history, then cooled to 0 °C at −60 °C min^{-1} (rapid cooling), −10 °C min^{-1} (slow cooling), or rapidly cooled at −60 °C min^{-1} and held at 190 °C for 2 h to induce crystallization from the melt. All heating scans were recorded at 10 °C min^{-1}. TA Instruments Universal Analysis software was used to determine the glass transition temperatures (T_g), crystallization temperatures at maximum exothermic heat flow (T_c), and melting temperatures at maximum endothermic heat flow (T_m). To determine the crystallization half-times ($t_{1/2}$), defined as the time at which a material attains 50% of its maximum crystallinity, samples were melt-crystallized at specific crystallization temperatures below their T_m. The isothermal crystallization profiles (heat flow versus time) were analyzed using the following approach (**Equation 1**):

$$\boldsymbol{F_c(t) = \frac{\int_0^t \frac{dH}{dt}\,dt}{\int_0^\infty \frac{dH}{dt}\,dt}} \qquad \textbf{(1)}$$

where $F_c(t)$ is the bulk fractional crystallinity of the functionalized copolymer systems, equal to the heat evolved during isothermal crystallization at a specific time *t* divided by the total heat evolved during the isothermal crystallization process. The $t_{1/2}$ were determined from the resulting

crystallization isotherms (F_c versus time) by extrapolating F_c at 0.5 to the time axis. These $t_{1/2}$ values were used as a comparative measure of the overall rate of bulk crystallization.

5.3.7. X-ray scattering techniques

The morphology of the sPS powder, 10 w/v% sPS/$CHCl_3$ gel, and the brominated copolymers was investigated using X-ray scattering techniques. Ultra-small-angle X-ray scattering (USAXS) and small-angle X-ray scattering (SAXS) experiments were performed at the Advanced Photon Source beamline 9ID-C at Argonne National Laboratory. The USAXS instrument was configured in standard mode with an X-ray energy of 21 keV (λ = 0.5895 Å), X-ray photon flux of ca. 1013 mm^{-2} s^{-1}, and a combined q range of 0.0001–1.3 $Å^{-1}$ ($q = 4\pi/\lambda \sin(\theta)$, where λ is the wavelength and θ is one-half of the scattering angle).[31-33] The USAXS and SAXS profiles were acquired sequentially and merged into a single data set using the Irena SAS package.[34] SAXS experiments were performed in-house using a Rigaku S-Max 3000 3 pinhole SAXS system equipped with a rotating anode that emits X-rays with a wavelength of 0.154 nm (Cu Kα). The sample-to-detector distance was 1605 mm, and the q-range was calibrated using a silver behenate standard. Two-dimensional SAXS patterns were obtained using a fully integrated 2D multiwire, proportional counting, gas-filled detector with an exposure time of 2 h. The SAXS data were analyzed using the SAXSGUI software package to obtain radially integrated SAXS intensity versus q profiles. The center-to-center intercrystalline domain spacing, i.e., long period (L_p), and average crystal segment length were calculated from the crystalline scattering feature of the Lorentz-corrected SAXS profiles by assuming a linear two-phase model. Wide-angle X-ray diffraction (WAXD) experiments were performed using a Rigaku MiniFlex II X-ray diffractometer emitting X-rays with a wavelength of 0.154 nm (Cu K_α). The sPS powder, sPS/$CHCl_3$ gel, and brominated copolymer samples were scanned from 5° to 40° 2θ at a scan rate of 0.250° 2θ min^{-1}

with a sampling window of 0.050° 2θ and at a potential of 30 kV and current of 15 mA. All WAXD data were analyzed using the PDXL 2 software package to obtain WAXD intensity versus 2θ profiles.

5.3.8. Simulated random copolymer chains

Simulated chains with random copolymer microstructures were generated using a code created in-house with MATLAB® R2017a programming software. For each degree of functionalization, 1000 homopolymer chains of 1442 monomer units (based on our sPS sample, M_w = 300 K; $Đ$ = 2.0) are simulated. To construct the random microstructure, monomers along the chain are selected at random up to the desired degree of bromination. For each simulated polymer chain, the length and frequency of consecutive styrene units and the prevalence of each unique triad (e.g., SSS, BBB, etc. where s = styrene and b = Br-Sty) and pentad sequence (e.g., sssss, bbbbb, etc.) are calculated.

5.3.9. Simulated average copolymer chains based on the empirical pentad sequence distributions

Simulated chains that represent the average copolymer chain sequence in the Blocky copolymers, were created using a Fortran code created in house. Chains are simulated from a short sequence of un-functionalized styrene units by subsequent additions of short sequences of un-functionalized and functionalized styrene units to the chain end. The rationalization for the specific short sequence that is added during each addition step is based on the difference between the average pentad sequence distribution of the simulated chain and the pentad sequence distribution from the NMR data and is discussed in more detail below in the Results and discussion section.

5.4. Results and Discussion

5.4.1. Morphological characterization of the sPS powder and sPS/$CHCl_3$ gel

Images of the sPS powder and a 10 w/v% sPS/$CHCl_3$ gel are compared in **Figure 5.1**. The sPS powder consists of white particles that scatter visible light and exhibit a broad distribution of sizes (see **Figure S5.1**). The sPS/$CHCl_3$ gel is a translucent solid that can be cut into small pieces with a spatula. The difference in appearance of the sPS samples strongly suggests that the sPS powder contains densely packed polymer chains.[23]

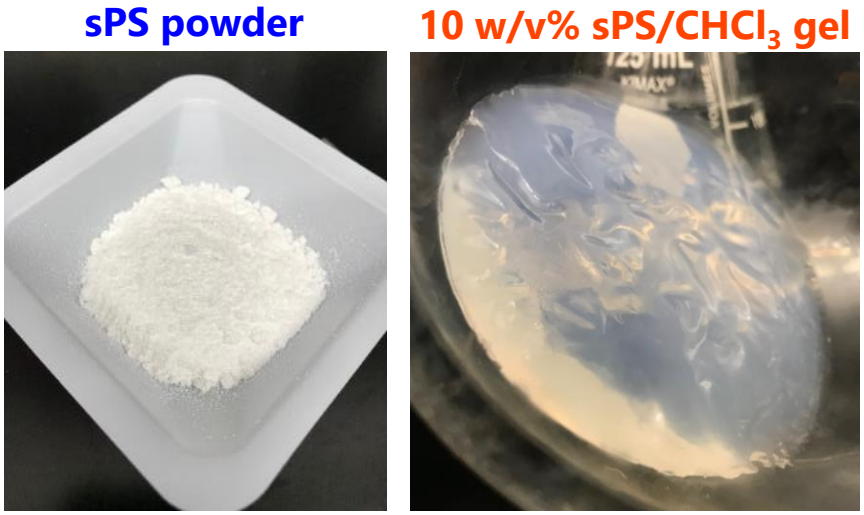

Figure 5.1. Images of the (left) sPS powder and a (right) 10 w/v% sPS/$CHCl_3$ gel.

The morphology of the sPS powder and sPS/$CHCl_3$ gel was characterized using X-ray scattering techniques and differential scanning calorimetry (see **Figure S5.2**). The ultra-small angle X-ray scattering (USAXS) and small-angle X-ray scattering (SAXS) profiles of the 10 w/v% sPS/$CHCl_3$ gel and the sPS powder are compared in **Figure 5.2**. The scattering profile of the sPS/$CHCl_3$ gel shows a scattering feature in the region of $0.1 < q < 1$ nm^{-1} that exhibits q^{-4} dependence and is attributed to surface fractal structure of crystalline lamellae in the semicrystalline physical gel.[35] At low q, the scattering fits to a $q^{-0.67}$ dependence that is indicative

of disorder between the boundaries of the crystalline and amorphous components. The sPS/$CHCl_3$ gel can thus be defined by loosely packed crystals that are tied together by a percolating network of solvent swollen amorphous chains. Conversely, the scattering profile of the sPS powder is featureless with q^{-4} dependence in the range from 0.1−2 nm^{-1}. This behavior demonstrates that the difference between the electron density of the crystalline component and the amorphous component of the sPS powder lacks periodicity and suggests that polymer chains in the powder are packed tightly together.

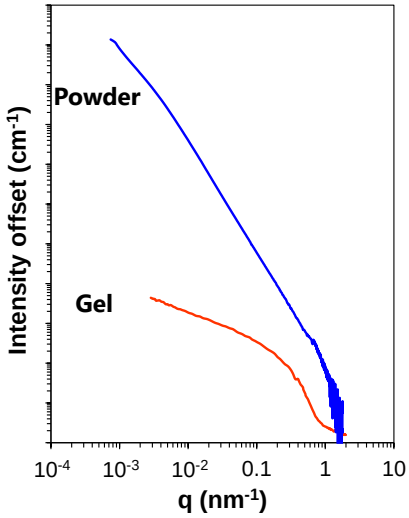

Figure 5.2. USAXS/SAXS profiles of the sPS powder and the 10 w/v% sPS/$CHCl_3$ gel. Profiles are offset for clarity.

Figure 5.3 compares the wide-angle X-ray diffraction (WAXD) profiles of the sPS powder and 10 w/v% sPS/$CHCl_3$ gel. The WAXD profile of the sPS/$CHCl_3$ gel exhibits crystalline reflections that are consistent with the s(2/1)2 helical conformation of the δ-form crystal structure of sPS.[28,36,37] The sPS powder shows crystalline reflections that are characteristic of the γ-form crystal structure.[36] It is worth noting that the γ-form is obtained from the nanoporous δ-form by annealing, and was anticipated for the sPS powder based on the powder preparation conditions. According to Daniel and co-workers,[38] an sPS powder in the γ-form contains less than 1% of the surface area of a δ-form sPS aerogel (based on the two parameter Brunauer-Emmett-Teller

method) as a result of dense packing of chains in the amorphous and crystalline components. The introduction of brominating reagent to the dense sPS powder was therefore expected to produce copolymers with a low degree of functionalization, as a result of limited access to monomers deep within the powder particles. In addition, the powder and gel reaction states were expected to produce copolymers with different microstructures and comonomer sequences.

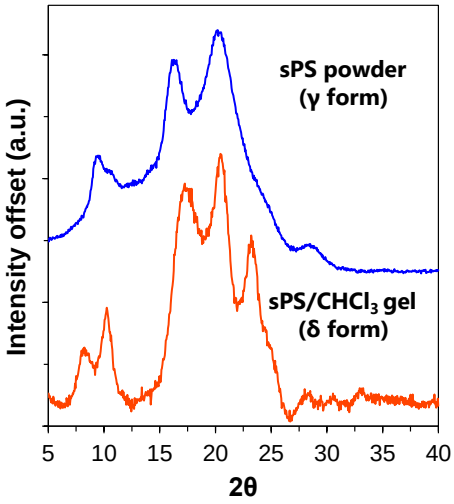

Figure 5.3. WAXD profiles of the sPS powder and 10 w/v% sPS/$CHCl_3$ gel, offset for clarity. Samples were dried under vacuum at 70 °C for ca. 24 h prior to analysis.

5.4.2. Microstructural analysis using NMR spectroscopy

The copolymer microstructure of the powder-state (Powder, P-x%) and gel-state (Gel, CH-x%) brominated copolymers was analyzed by NMR spectroscopy. The ^{1}H NMR spectra of the sPS homopolymer and the Powder and Gel copolymers with reaction times are shown in **Figure 5.4**. Compared to pure sPS, new proton resonances appear in the ^{1}H NMR spectra of the brominated copolymers at 1.23, 1.58−1.75, 6.27−6.28, and 7.11−7.22 ppm, corresponding to the methylene (H(b′)) and methine (H(a′)) protons, and the aromatic protons (H(2′) and (H(3′)) of brominated styrene (Br-Sty) monomers, respectively.[21] Integration of the total peak areas of the aliphatic protons shows that the ratio of the methylene (H(b), H(b′)) to methine (H(a), H(a′))

protons is approximately 2:1, which indicates that bromination occurred exclusively on the styrene phenyl ring, as anticipated. The Br-content (mol% Br) was derived from the fraction of *ortho*-proton resonances of Br-Sty monomers (H(2′), 6.27−6.38 ppm) to the total area of styrene (H(2′)) and Br-Sty *ortho*-proton resonances (6.27−6.60 ppm).

Comparing the reaction times and Br-contents of the Powder and Gel copolymers provided by the ^{1}H NMR spectra, reveals that the rate of bromination in the powder state is considerably slower than that in the gel state. For example, 19 h were required to reach 7% functionalization in the powder state, while in the gel state just 5.75 h were required to reach 32% bromination, demonstrating a greater than threefold increase in Br-content relative to the Powder P-7% copolymer in less than one-third of the time. In addition, the Br-content of the Powder copolymers was limited to 12 mol% Br and was obtained after a long reaction time of 31 h. It should be recognized that the reaction solvent can affect the swelling of the sPS powder, and thus was expected to affect the accessibility of bromine to monomer units within the sPS particles. The effect of solvent quality on the degree of functionalization was investigated by carrying out the heterogeneous powder-state bromination reaction for 96 h using $CHCl_3$ and DCM as reaction solvents. The reaction carried out in $CHCl_3$ produced copolymers with a greater degree of functionalization of 15 mol% Br, compared to the 12 mol% Br copolymers prepared in DCM, the common reaction solvent (see **Figure S5.3**). These results strongly suggest that when bromine is introduced to the dense sPS powder, it is sterically restricted from reacting with monomers in the core of the particle that are far removed from the particle surface and reacts with monomers at and near the particle surface.

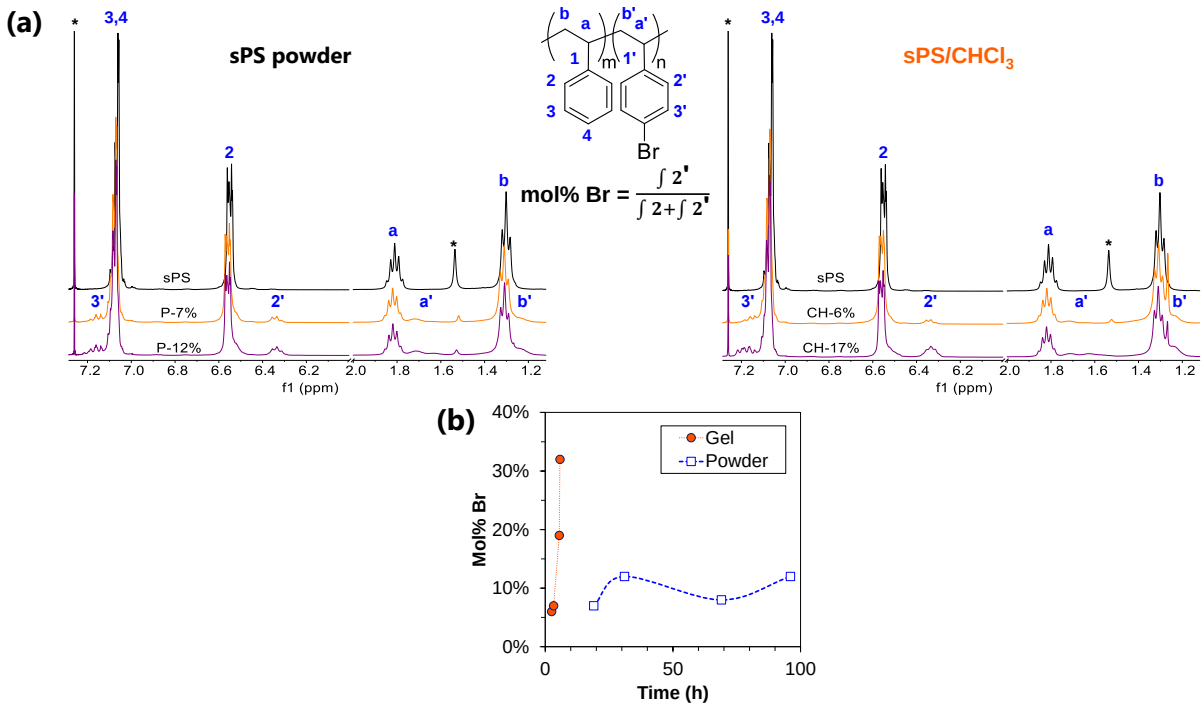

Figure 5.4. (a) ^{1}H NMR spectra of the sPS homopolymer and the powder-state (Powder) and gel-state (Gel) brominated copolymers increasing in reaction time from top to bottom. For comparison, the spectra are referenced to $CDCl_3$ and normalized over 6.27−6.60 ppm. The asterisks (*) indicate solvent resonances. (b) Mol% Br *versus* reaction time for the powder- and gel-state reactions.

To investigate the effect of heterogeneous reaction state on copolymer microstructure, quantitative ^{13}C NMR spectroscopy was used to analyze the comonomer sequence distribution of the brominated copolymers. **Figure S5.4** shows the full high-resolution ^{13}C NMR spectra of the sPS homopolymer and the Powder and Gel copolymers. Upon *para*-substitution of the styrene phenyl ring with bromine, new carbon resonances appear in the ^{13}C NMR spectrum. The new resonances at 40.0 and 43.6 ppm are attributed, respectively, to the methine (C(a′)) and methylene (C(b′)) carbons of Br-Sty monomers. The new resonances at 129.2 ppm and 130.9 ppm are assigned, respectively, to the *ortho*-(C(2′)) and *meta*-carbons (C(3′)) of brominated phenyl rings. The multiple new resonances in the regions from 118.8−119.5 ppm and 145.15−143.15 ppm are attributed to the Br-substituted phenyl carbons (C−Br, C(4′)) and the quaternary phenyl carbons of un-brominated (C(1)) and brominated (C(1′)) monomers, respectively. For both the Powder and Gel copolymers, the distribution and intensities of the peaks in the quaternary carbon and C−Br

regions are highly dependent on Br-content. The presence of multiple peaks in these regions signifies through-bond communication between neighboring styrene and Br-Sty monomers and provide a unique fingerprint of the copolymer microstructure originating from the specific comonomer sequence distribution.

In **Chapter 3**,[30] a comonomer sequencing method was introduced to assign each peak in the quaternary carbon spectrum of the sPS-*co*-sPS-Br copolymers to a styrene or Br-Sty unit that exists in the center of a unique sequence of five monomers, i.e., a pentad, along the copolymer chain (e.g., ssssb were s = styrene and b = Br-Sty). Using this method, the quaternary carbon spectra of the Powder and Gel copolymers have been decomposed into their separate additive peak components. The quaternary carbon spectra of the Powder P-7% and Gel CH-6% copolymer are shown in **Figure 5.5**. The peaks in the spectra are color-coded by triad sequence and several of the peaks are assigned to pentad sequences. For an example of a complete pentad sequence assignment for an sPS-*co*-sPS-Br copolymer, see **Table S3.1**. By visual inspection, the peak distributions and intensities between the P-7% and CH-6% copolymers appear to be different.

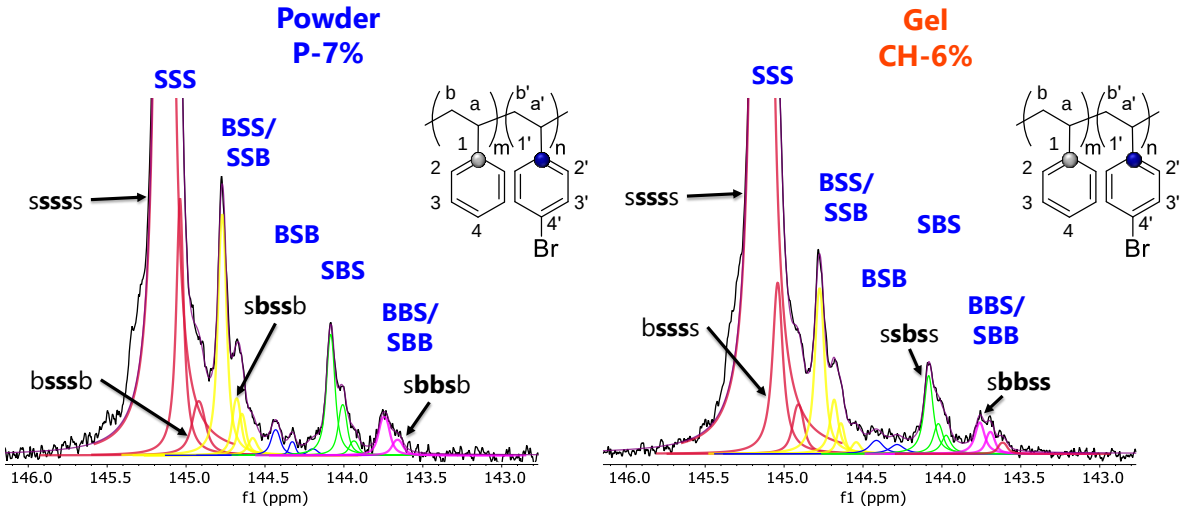

Figure 5.5. The quaternary ^{13}C NMR spectra of the (left) Powder P-7% and (right) Gel CH-6% copolymers decomposed into their separate additive pentad peak components with triad assignments and several pentad assignments. The peaks are color-coded by triad combination: SSS = red; BSS/SSB = yellow; BSB = blue; SBS = green; BBS/SBB = magenta; BBB = orange.

The distribution of pentad sequences in the brominated copolymers was calculated from the ratio of the area under each quaternary carbon peak to the total area of the quaternary carbon region (142.9−145.6 ppm) in the ^{13}C NMR spectrum. **Figure 5.6** compares the fraction of styrene pentads (sssss) in the Powder and Gel copolymers and the average fraction of sssss in 1000 simulated random copolymer chains of similar Br-content. At approximately 7 mol% Br, both the Powder P-7% and Gel CH-6% copolymers contain a larger fraction of sssss pentad than the simulated random copolymers with 6% Br-content. Above 6 mol% Br, the amount of sssss pentad in the copolymers decreases, as expected. Nevertheless, the fraction of sssss pentad in the simulated random copolymers decreases more rapidly than in the Powder and Gel samples. These results demonstrate that the Powder and Gel copolymers exhibit non-random, i.e., blocky distributions of Br-Sty units along their chains even at relatively low Br-content, as anticipated for copolymers prepared from heterogeneous reaction states.[10,11,21,39] Comparing the Powder and Gel copolymers with greater than 6 mol% Br reveals that the Gel CH-17% copolymer contains a larger fraction of sssss pentad compared to the lower Br-content P-12% copolymer. These data demonstrate that the sPS/$CHCl_3$ gel produces copolymers with a higher prevalence of styrene "blocks" of at least five consecutive styrene units relative to the dense sPS powder.

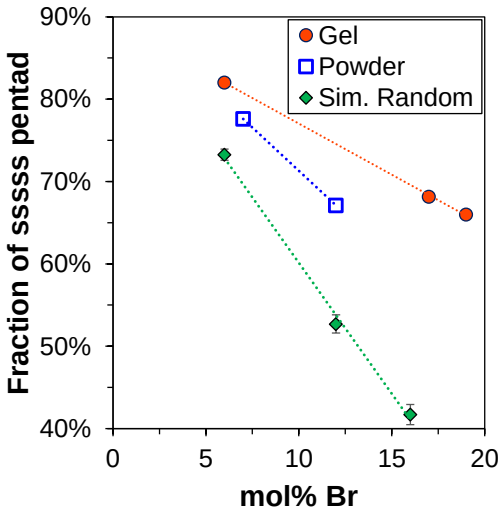

Figure 5.6. Fraction of styrene pentad (sssss) in the of the Powder and Gel copolymers with comparison to that of 1000 simulated random copolymer chains with similar Br-content. The error bars represent one standard deviation. The empirical data are calculated from the integration of the quaternary carbon NMR spectra. Dashed lines are included to guide the eye.

The degree of blockiness in the brominated copolymers has been characterized by the copolymer block character (R). Based on Bernoullian probability statistics,[40] expressed by **Equation 2**,

$$R = \frac{4(P_{SS})(P_{BB})}{(P_{SB})^2} \qquad \text{where:} \qquad \begin{aligned} P_{SS} &= \text{SSS} + \tfrac{1}{2}\,[\text{SSB/BSS}] \\ P_{BB} &= \text{BBB} + \tfrac{1}{2}\,[\text{SBB/BBS}] \\ P_{BS} &= 1 - P_{SS} - P_{BB} \end{aligned} \qquad \textbf{(2)}$$

where, P is the probability that a polymer chain contains an SS (P_{SS}), BB (P_{BB}), or BS/SB (P_{BS}) dyad, respectively. The dyad probabilities are obtained from the pentad sequence distribution based on the fraction of SSS, [SSB/BSS], [SBB/BBS], and BBB triad sequences in each copolymer. For a copolymer with a Bernoullian (*i.e.*, random) sequence distribution, R is equal to unity. A copolymer with a block-like distribution of functional groups along the chain will have an R value greater than unity. The block characters of the Powder and Gel copolymers are compared in **Figure 5.7**. For reference, the average block characters of simulated random copolymer chains of similar Br-content are also provided. The average R values of the simulated

random chains range from 0.98−1.03, as expected for copolymers that have a random distribution of functional groups. For the Powder and Gel copolymers, *R* is greater than unity and increases with increasing Br-content. Thus, the Powder and Gel copolymers have block-like character, even at low Br-content.

Comparing the *R* values of the Gel and Powder copolymers reveals that Gel CH-6% exhibits a greater block character than both the Powder P-7% and P-12% copolymers. Thus, this low Br-content Gel copolymer contains on average more consecutive styrene units and more consecutive Br-sty units, *i.e.* is more block-like, than its Powder analogs. The quantitative insight into the copolymer microstructure obtained from ^{13}C NMR spectroscopy, strongly suggests that the sPS/$CHCl_3$ gel produces copolymers with a higher degree of blockiness than the dense sPS powder.

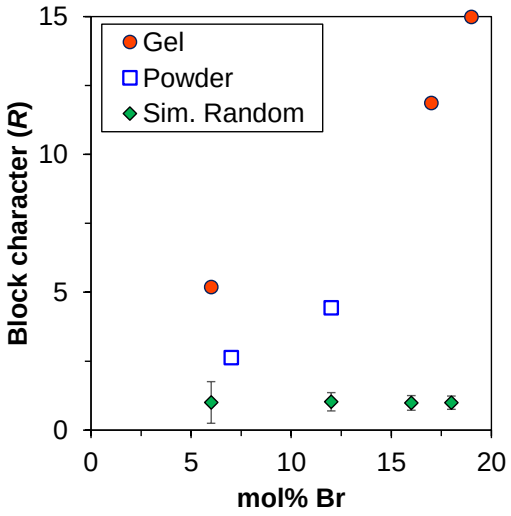

Figure 5.7. The block character (*R*) of the Gel and Powder copolymers with comparison to the average *R* values of 1000 simulated random copolymer chains. The error bars represent one standard deviation. The empirical *R* values are calculated from the integration of the quaternary carbon NMR spectra. *R* values greater than one demonstrate block-like character.

The pentad sequence distributions of the brominated copolymers also provide deeper insight into the potential run lengths of styrene and Br-Sty along the copolymer chains. The average length of consecutive styrene units (n_S) and Br-sty (n_B) units and the average number of

blocks per 100 monomer units (*N*) were calculated according to **Equations 3**, **4**, and **5**, respectively.

$$\boldsymbol{n_S = \frac{SSS + [SSB/BSS] + BSB}{BSB + \frac{1}{2}[SSB/BSS]}} \quad \textbf{(3)}$$

$$n_B = \frac{BBB + [BBS/SBB] + SBS}{SBS + \frac{1}{2}[BBS/SBB]} \quad \textbf{(4)}$$

$$N = \frac{200}{n_S + n_B} \quad \textbf{(5)}$$

For these calculations, a block is defined as one or more consecutive like units. It is worth noting that this method can provide only an estimate of the potential block lengths in the blocky brominated copolymers, as the calculations cannot accurately account for a bimodal distribution of very long and very short blocks. The average run lengths and *N* values for the Powder and Gel copolymers and simulated random copolymer chains (Sim. R-x%) are compared in **Table 5.1**. For the simulated random chains with 6% Br-content, the n_s and *N* values are 17 and 11, respectively. At 12% functionalization, the n_s value decreases substantially to 8 consecutive styrene units and the *N* value increases substantially to 21 blocks per 100 monomers as a consequence of shorter styrene blocks. Compared to the simulated random chains, both the Powder and Gel copolymers exhibit larger n_s values and smaller *N* values, consistent with a blocky microstructure. At approximately 7 mol% Br, the Powder P-7% exhibits an n_S value of ca. 19 units and an *N* value of ca. 10 blocks per 100 monomers. At higher Br-content, the Powder P-12% contains shorter runs of consecutive styrene units that are terminated at each end by Br-Sty units, resulting in a larger *N* value of 16. In comparison, both the Gel CH-6% and CH-17% copolymers contain longer average run lengths of consecutive styrene units and fewer numbers of blocks relative to their respective

Powder copolymer analogs. These data suggest that gel-state functionalization produces copolymers with longer runs of pure sPS compared to functionalization in the powder state.

Table 5.1. The average length of consecutive styrene (n_S), and Br-Sty (n_B) and average number of blocks per 100 monomer units (N) for the Powder (P-x%), Gel (CH-x%), copolymers (x = mol% Br).

Sample	n_S	n_B	N
P-7%	19	1	10
P-12%	11	1	16
CH-6%	27	1	7
CH-17%	12	2	14
Sim. R-6%	17	1	11
Sim. R-12%	8	1	21

5.4.3. Thermal transitions

Figure 5.8 shows the DSC heating traces of the sPS homopolymer and the Powder and Gel copolymers after slow cooling from the melt to 0 °C at −10 °C min^{-1}. For reference, the heating traces of solution-state brominated copolymers (Random, R-x%) with 6 and 11 mol% Br (R-6% and R-11%, respectively), are also included. The heating trace of sPS exhibits two endothermic events, the glass transition at 100 °C and an intense melting endotherm at 270 °C. At approximately 7 mol% Br, the brominated copolymers crystallize during cooling and show depression in their melting temperatures, T_m, relative to pure sPS. Bromine groups attached to a crystallizable polymer can act as physical defects along the polymer chains, limiting crystallizability and lamella thickness. It is not surprising then that the brominated copolymers show a depression in T_m, as a consequence of shorter crystallizable chain segments and thus thinner crystals.[17,41-43] Interestingly, the Powder P-7% copolymer exhibits a first melting endotherm peak (T_{m1}) at lower temperature than the melting endotherm peak in the Random R-6% copolymer. These data suggest that the P-7% copolymer contains some fraction of crystals that are thinner, i.e., contain shorter crystalline segments of consecutive styrene units, than exhibited by the R-6% sample. Further analysis of this

intriguing behavior using high-temperature gel permeation chromatography to probe the Powder copolymer polydispersity will be the subject for future investigations.

At high Br-content, the melting point depression occurs to a greater extent in the Random R-11% copolymer compared to the Powder and Gel copolymers, demonstrating a non-random, i.e., blocky, distribution of Br-Sty units along the copolymer chains in the P-12% and CH-17% copolymers (see **Figure S5.5**). Remarkably, the Gel CH-17% copolymer exhibits a higher melting temperature than the lower Br-content Powder P-12% copolymer. This result strongly implies that the CH-17% contains thick crystals with long runs of consecutive styrene units that would require a high degree of blockiness along its copolymer chains.

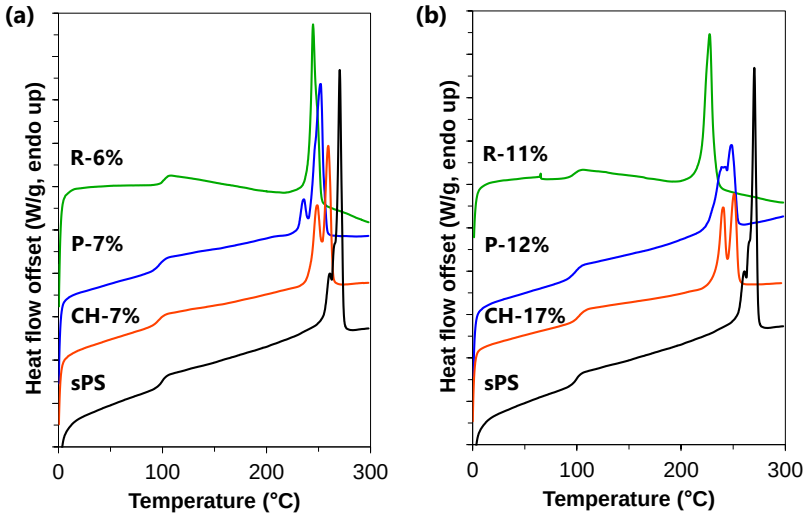

Figure 5.8. DSC heating scans of the sPS homopolymer the (a) low Br-content and (b) high Br-content Powder, Gel, and Random copolymers after slow cooling from the melt (300 °C) at −10 °C min^{-1}. Heating rate: 10 °C min^{-1}.

To further examine the effect of the heterogenous reaction state on copolymer crystallizability, the weight percent crystallinity (%X_c) was calculated from the total area under the melting endotherm (ΔH_f) with respect to the heat of fusion of 100% crystalline pure sPS[44] (ΔH_f° = 79.3 J g^{-1}). The thermal properties and %X_c of the sPS homopolymer and brominated copolymers after rapid cooling (−60 °C min^{-1}) and 2 h melt crystallization at 190 °C are summarized in **Table 5.2**. At low Br-content, the Powder P-7% and Gel CH-7% copolymers exhibit greater crystallinity

than their Random R-6% analog, which demonstrates the blocky microstructure of the Powder and Gel copolymers, even at low Br-content.[21] Comparing the crystallization behavior of the Powder and Gel copolymers reveals that the brominated copolymer analogs exhibit similar crystallinity. However, it is important to note that the Gel copolymers crystallize (T_c) and melt (T_m) at higher temperatures relative to their Powder analogs. This observed thermal behavior in the Gel samples strongly suggests a greater degree of blockiness in the distribution of Br-Sty defects along the Gel copolymer chains. While the CH-17% appears to exhibit remarkable crystallinity given its higher degree of functionalization relative to P-12%, a Gel sample that contains 12 mol% Br will need to be prepared in order to characterize the thermal properties of the P-12% copolymer. For WAXD profiles of the sPS homopolymer and the brominated copolymers after isothermal crystallization at 190 °C, see **Figure S5.6**.

Table 5.2. Thermal properties and weight percent crystallinity of the sPS homopolymer and the Powder (P-*x*%), Gel (CH-*x*%), and Random (R-x%) copolymers measured using DSC.

Sample	After rapid cooling at −60 °C min^{-1}				After 2 h isothermal crystallization at 190 °C	
	T_g(°C)	T_m(°C)	T_c(°C)	X_c(%)	T_m(°C)	X_c(%)
sPS	99	269	224	31	270	32
P-7%	96	245	193	28	245	33
P-12%	98	238	187	27	239	28
CH-7%	97	251	205	28	250	32
CH-17%	105	240	190	23	239	25
R-6%	103	244	180	25	245	29
R-11%	100	228	160	24	230	28

T_g = glass transition temperature; T_{m1} = temperature of the first maximum endothermic heat flow; ^aT_c = temperature of the maximum exothermic heat flow during the cooling scan, X_c = weight percent crystallinity derived from the area under the melting endotherm (ΔH_f) and the heat of fusion of 100% crystalline pure sPS (ΔH_f°) according to the relationship $X_c = \frac{\Delta H_f}{\Delta H_f^o} \times 100\%$. Dashes (--) indicate no thermal transition detected. All samples were heated to 300 °C and annealed for 3-5 min prior to cooling to erase thermal history.

5.4.4. Crystallization kinetics

How the distribution of bromine defects along the chains affects the crystallization kinetics of the Powder copolymers was investigated by subjecting the Powder and Gel samples to isothermal crystallization at specific temperatures below T_m. To achieve rapid crystallization, chain segments of sufficient length, i.e., stems, of uninterrupted styrene units are required to assemble into stable crystalline domains. Br-Sty monomers encountered at the crystal growth front are structural defects that are consequently excluded from attaching to the growing crystallite. This process of rejection of a defective stem and diffusion of a new stem to the melt-crystal interface ultimately slows the rate of crystallization. The crystallization half-time, $t_{1/2}$, *versus* temperature profiles of the Powder and Gel copolymers are compared in **Figure 5.9**. For reference, the $t_{1/2}$ values of the Random copolymers with 6 and 11 mol% Br (R-6% and R-11%, respectively) are also provided. At approximately 7 mol% Br, the Powder P-7% exhibits similar $t_{1/2}$ values to that of the Random R-6% copolymer throughout the isothermal crystallization temperature series. In contrast, the Gel CH-7% copolymer demonstrates faster crystallization kinetics (i.e., shorter $t_{1/2}$ times) and at lower supercooling compared to its Powder and Random analogs. Above 7 mol% Br, both the Powder and Gel copolymers crystallize at low supercooling and demonstrate shorter $t_{1/2}$ than the Random R-11% copolymer, attributed to the blocky microstructure of the Powder and Gel copolymers that provides a higher prevalence of crystallizable stems along the polymer chains.[21] With more crystallizable stems, the blocky microstructure minimizes the time-consuming rejection/replacement process and is thus capable of crystallizing in a shorter period of time. Remarkably, the Powder P-12% copolymer exhibits similar $t_{1/2}$ times to the P-7% copolymer, suggesting that the Powder copolymers contain a similar fraction of crystallizable stems despite their 5% difference in Br-content. The P-12% copolymer also exhibits similar $t_{1/2}$ times to the

greater Br-content Gel CH-17% copolymer. The crystallization behavior of the brominated copolymers strongly support that the Gel copolymers contain a blocky microstructure with a high degree of blockiness and a large fraction of crystallizable stems.

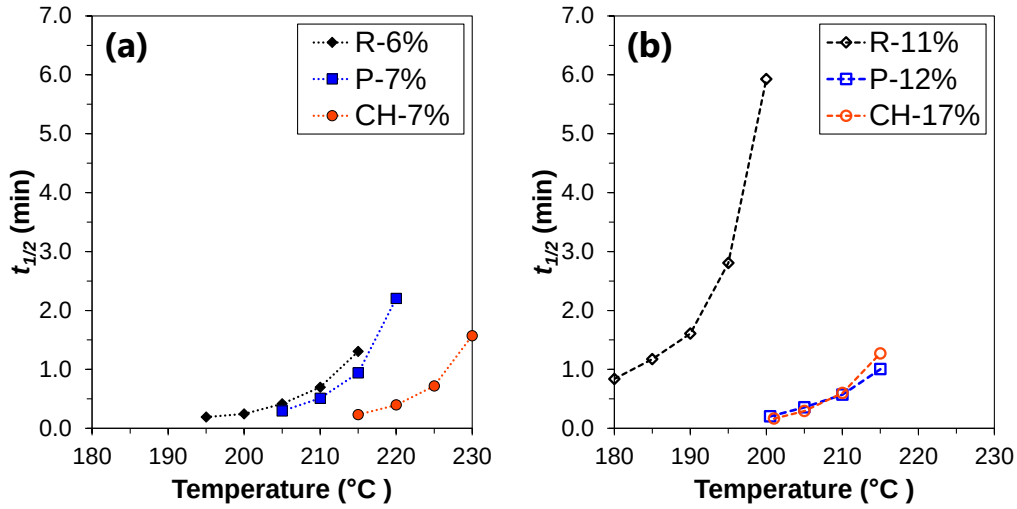

Figure 5.9. Crystallization half-time ($t_{1/2}$) *versus* temperature profiles for the Random, Powder, and Gel copolymers of (a) low Br-content and (b) high Br-content. Prior to isothermal crystallization, samples were annealed for 5 min at 300 °C. Dashed lines are included to guide the eye.

5.4.5. Morphological characterization of the brominated copolymers

The morphology of the brominated copolymers was investigated using small-angle X-ray scattering (SAXS). The SAXS profiles of the sPS homopolymer and the Powder and Gel copolymers after 2 h isothermal crystallization from the melt at 190 °C are compared in **Figure 5.10**. The SAXS profile of the sPS homopolymer shows a low intensity, excess scattering feature in the range of 0.3 $nm^{-1} < q < 0.5$ nm^{-1} that is consistent with intercrystalline scattering observed previously in sPS.[35] The Powder and Gel copolymers exhibit intercrystalline scattering over a range of q values from 0.1 $nm^{-1} < q < 0.5$ nm^{-1}. The increased intensity of this excess scattering feature (i.e., Bragg peak) with higher Br-content indicates greater periodicity in the distance, d, between scattering features. The observed shift in the Bragg peak to lower q with increasing Br-content is indicative of an increase in the center-to-center intercrystalline domain spacing, i.e., the long period (L_p).

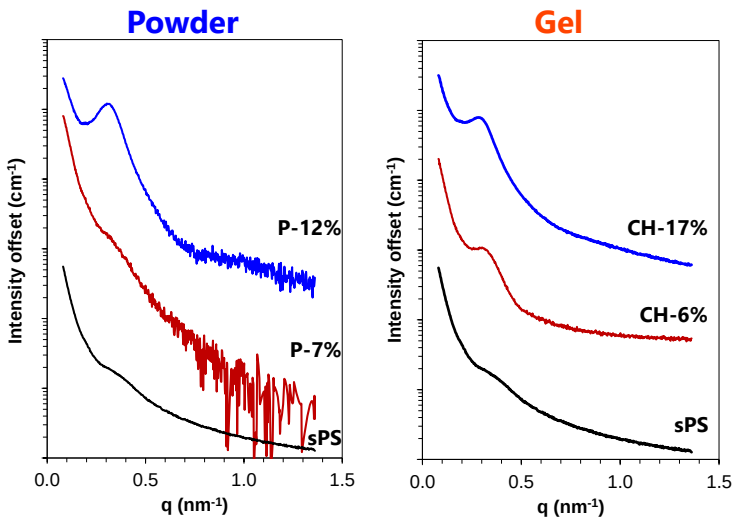

Figure 5.10. SAXS profiles of the sPS homopolymer and the (left) Powder and (right) Gel copolymers after 2 h isothermal crystallization at 190 °C. Profiles are offset for clarity.

The long period in the melt-crystallized samples of the brominated copolymers was estimated from the *d*-spacing at the peak of the high *q* scattering feature in the Lorentz-corrected SAXS profiles using Bragg's law ($d_{Bragg} = 2\pi/q$). The long period represents the sum of the thickness of the crystalline lamellae, l_c, and the thickness of the interlamellar amorphous region, l_a ($L_p = l_c + l_a$). Assuming a linear two-phase model, an estimated l_c may be obtained from the product of L_p and the volume fraction of crystallinity ($\%X_c$) within the material. The results of the SAXS analysis are summarized in **Table S5.1**. The sPS homopolymer exhibits a L_p value of ca. 16.2. nm. For the brominated copolymers, the L_p values are greater than 16.2 nm, as anticipated. Bromine groups attached to sPS act as physical defects along the polymer chains, resulting in fewer crystallizable chain segments and a larger fraction of amorphous chain segments. Thus, the average thickness of the amorphous components, l_a, in the brominated copolymers increases with increasing Br-content. Meanwhile, the brominated copolymers exhibit average lamella thicknesses, l_c, that are similar to that of pure sPS. It is worth noting that for pure sPS and for the low Br-content brominated copolymers, melt crystallization at 190 °C is known to favor the nucleation of the α polymorph, and thus the formation of thinner crystals (see **subsection 4.4.5**).

While the SAXS analysis may therefore underestimate the true maximum l_c that is possible for these samples, these data still provide a useful initial approximation of the minimum average lamella thickness.

From the l_c values in the brominated copolymers, the average number of styrene units in a crystalline stem has been estimated, based on the α-form planar zigzag structure of sPS with 2 monomer units per identity period (c-axis dimension = 0.51 nm).[45] The brominated copolymers exhibit similar crystalline stem lengths of approximately 20-26 styrene units. As will be demonstrated below in the Simulated average chains section, these crystalline stem lengths are in good agreement with the run lengths of styrene units that are predicted to exist in the brominated copolymers based on simulations of average chain sequences in the Powder and Gel copolymers.

5.4.6. Simulated average chains with comparison to the empirical crystallization behavior

The pentad sequence distribution obtained from the quaternary carbon NMR spectrum provides a unique fingerprint of the copolymer microstructure that originates from the average comonomer sequence distribution in the brominated copolymers. Using this useful sequence information, a computer code was developed to predict the average copolymer chain sequence in each of the Powder and Gel copolymers.[30] Briefly, the copolymer chain is simulated starting with a sequence of 7 un-functionalized styrene units, followed by subsequent additions of un-functionalized and functionalized styrene units to the chain end in 7 monomer long blocks. The block that is added in each addition step keeps the difference between the empirical pentad sequence distribution and that of the intermediate simulated chain at a minimum. To add a block to the chain end, all possible heptad combinations of un-functionalized and functionalized styrene units (2^7 or 128) are added in turn and the deviation between the pentad distribution of the intermediate simulated chain and the experimental results is analyzed. The heptad combination

that minimizes the residuals with respect to the experiment is then added to the chain. This process is repeated until the chain length reaches 1442 monomers (based on our sPS sample, M_w = 300K; Đ = 2.0). It is worth noting that the degree of functionalization in the chain is not a parameter of the simulation, yet the simulated chains naturally exhibit Br-Sty compositions that are in good agreement with experiment. In addition, the simulated average chains exhibit pentad sequence distributions that deviate by less than one percent from the empirical pentad sequence distributions.

The simulated average chains of the Powder P-7% and Gel CH-6% copolymers are compared in **Figure 5.11** (for the simulated chains of the Powder P-12% and Gel CH-17% see **Figure S5.7**). The root-mean-square deviation (RMSD) between the simulated and empirical pentad sequence distributions of the P-7% and CH-6% average chains are 0.43% and 0.35%, respectively. Thus, the simulated chains are expected to be representative of average copolymer sequences in these brominated copolymers. Both chains exhibit numerous long "blocks" of consecutive styrene units (grey circles) and short segments of 1-3 Br-Sty units (blue circles). By visual inspection, no obvious differences exist in the distribution of block lengths of consecutive styrene and consecutive Br-Sty units in these simulated chains.

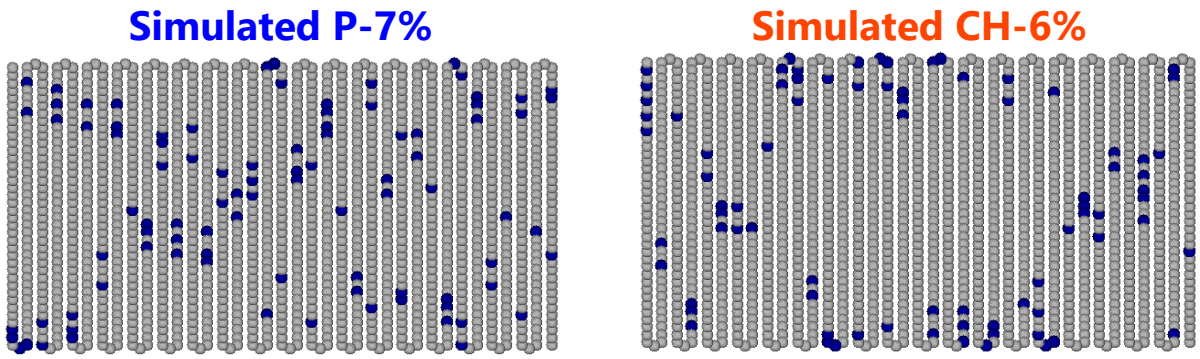

Figure 5.11. Simulated average chains of the Powder P-7% and Gel CH-6% copolymers created through an iterative process that minimizes the difference between the pentad sequence distribution of the simulated chain and the respective experimentally-determined data. Styrene units = grey circles; Br-Sty units = blue circles. The root-mean-square deviation (RMSD) between simulated and empirical: P-7% = 0.43%; CH-6% = 0.35%.

The distribution of block lengths of consecutive styrene units in the simulated chains represents the length of styrene blocks that are predicted to exist in the brominated copolymers. **Figure 5.12** compares the distribution of styrene block lengths in the simulated Powder and Gel average chains, quantified by weight fraction of styrene units (w_{Sty}) in blocks of at least block length, *n*. Using this method, $n = 1$ accounts for all styrene units in the chain and corresponds to a w_{Sty} of 100 wt%. As *n* increases, the w_{Sty} in blocks of at least *n* decreases. A w_{Sty} of 50 wt% represents half the mass of styrene in the chain. For reference, the average distribution of block lengths in 1000 simulated random copolymer chains (Sim. R-x%) with x = 7%, 12%, and 17% Br-content are also included. The Sim. R-7% reveals that truly random copolymer chains with 7% functionalization would contain half their mass of styrene in blocks of 24 units and 1 wt% styrene in long blocks of at least 90 units. Compared to the distribution of block lengths in the Sim. R-7%, the simulated Powder P-7% and Gel CH-6% average chains contain larger mass fractions of styrene in long blocks of at least 10 to 32 and 39 styrene units, respectively. These data strongly suggest that the low Br-content Powder and Gel copolymers contain a blocky microstructure. For the simulated P-7% average chain, the longest blocks of consecutive styrene are 37 units. In contrast, the simulated Gel CH-6% chain contains much longer blocks of up to 70 units. Thus, the Gel CH-6% copolymer is predicted to exhibit a higher degree of blockiness compared to its Powder analog. Interestingly, the shorter block lengths predicted in the Powder P-7% chain also support that the P-7% copolymer would contain thinner crystals than observed in the low Br-content Gel sample, which was suggested earlier by the DSC experiments (see **Figure 5.8**).

At higher Br-content, both the simulated Powder P-12% and Gel CH-17% average chains exhibit large mass fractions of styrene in blocks longer than that predicted for truly random chains of the same Br-content. This again supports that the Powder and Gel copolymers have blocky

microstructures. It is worth noting however that the deviation in block length distribution between the P-12% average chain and the average 12 mol% Br random chains (Sim. R-12%) is substantially less than the difference between the CH-17% and Sim. R-17% chains. Remarkably, the simulated CH-17% average chain contains half its mass of styrene in long blocks of at least 34 styrene units and a long block of 75 units, while a truly random copolymer with 17% Br-content would contain less than 1 wt% styrene in blocks of at least 39 units. The block length distribution in the simulated average chains thus strongly suggest that the Gel copolymers contain longer runs of consecutive styrene units than their Powder analogs and have a higher degree of blockiness along their chains.

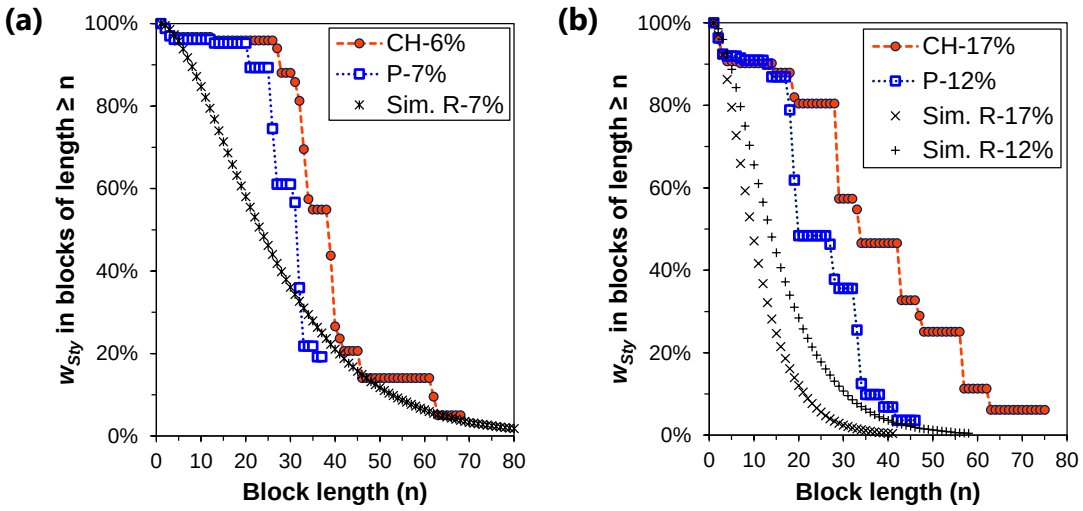

Figure 5.12. Predicted weight fraction of styrene units (w_{Sty}) in blocks of at least block length, *n*, versus block length for the simulated average chains of the (a) low Br-content and (b) high Br-content Gel and Powder copolymers and the average of 1000 simulated random copolymer chains of similar Br-content (Sim. R-x%). Dashed lines are shown to guide the eye.

The distribution of block lengths in the simulated average chains provides further insight into the crystallization behavior of the empirical brominated copolymers. According to Flory's theory of crystallization in copolymers,[46] the probability (P_ζ) that a randomly selected styrene unit along a chain exists in a crystallizable chain segment of at least ζ styrene units is given by (**Equation 6**),

$$P_{\zeta} = \sum_{j} P_{\zeta,j} = \sum_{j=\zeta}^{\infty} \frac{(j - \zeta + 1) \times w_j}{j} \quad \textbf{(6)}$$

where w_j is the probability that a unit chosen at random is a styrene unit in a sequence of length j, calculated by multiplying the molar fraction of styrene units (X_{Sty}) by the fraction of styrene units occurring in j sequences (j_{Sty}). For this work, ζ is defined as 28 monomer units, the average number of styrene monomers in one crystalline stem of an sPS crystal, based on the *trans*-planar zigzag conformation of the α- and β-form crystal structures of sPS with 2 monomers per identity period and an average lamella thickness of 7.2 nm (c-axis dimension = 0.51 nm).[47]

As shown in **Figure 5.13**, the probability of randomly selecting a crystallizable styrene monomer (i.e., a monomer within a defect-free sequence of 28 monomer units) rapidly declines in the simulated random copolymers from ca. 31% at 4% Br-content to below 1% at 16% Br-content. At approximately 7 mol% Br, the simulated Powder P-7% average chain exhibits a P_{ζ} value of ca. 10%, which is slightly less than that expected for a truly random copolymer with the same Br-content. The simulated Gel CH-6% average chain exhibits a much greater P_{ζ} value of ca. 25%, that is similar to that predicted for the simulated random chains. For a better comparison, this analysis should be repeated using the CH-7% copolymer sample. At high Br-content, the simulated Powder P-12% chain predicts that 7% of styrene units exist in crystallizable segments, which is greater than the probability of the truly random chains and reveals the predicted blocky microstructure for the P-12% copolymer.

In contrast to the predicted behavior of the Powder and random copolymer chains, the high Br-content Gel copolymers retain approximately 14% of their styrene monomers in crystallizable segments, even at 18 mol% Br. These results of the simulations are in excellent agreement with the rapid crystallization kinetics observed for the empirical Gel copolymers. For example, the Gel

CH-17% sample is capable of crystallizing with a $t_{1/2}$ of 0.6 s during isothermal crystallization at a low supercooling of 210 °C. Thus, the consistency between the block length distributions of the simulated average chains and the empirical crystallization behavior validates the basis of our modeling method and strongly suggests that the Gel copolymers contain a higher prevalence of crystallizable sPS homopolymer segments than their Powder analogs.

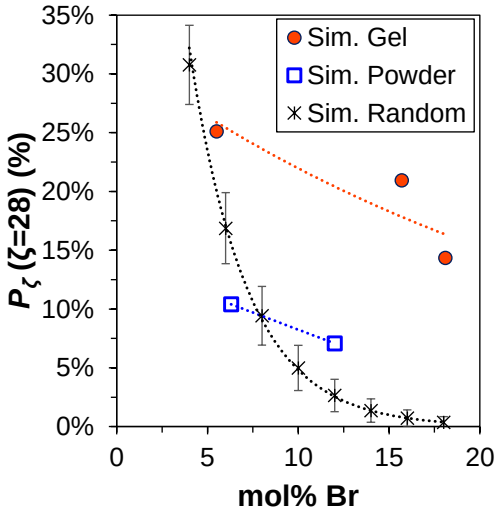

Figure 5.13. Probability (P_ζ) that a randomly selected styrene unit exists in a crystallizable chain segment, ζ, of at least 28 styrene units for the simulated Gel and Powder average chains and the average results for 1000 simulated random copolymer chains. Dashed lines are included to guide the eye.

5.5. Conclusions

This work demonstrates the bromination of sPS in the heterogeneous powder and gel states to produce sPS-*co*-sPS-Br copolymers with blocky microstructures. The purpose of this research was to determine the impact of heterogeneous reaction state on copolymer microstructure, degree of blockiness, and crystallization behavior. Morphological characterization of the heterogeneous reaction states provided by X-ray scattering techniques showed that the sPS powder contains a dense γ-form crystal phase and tightly packed polymer chains. In contrast, the 10 w/v% sPS/$CHCl_3$ gel exhibits a nanoporous δ-form crystal phase and is composed of loosely packed crystals that are tied together by a percolating network of solvent swollen amorphous chains. The heterogeneous

powder-state required long reaction times and produced copolymers with a relatively low degree of functionalization of up to 12 mol% Br. In contrast, using our heterogeneous gel-state bromination method, a copolymer with 32 mol% Br was realized in one-third of the time. When the brominating reagent is introduced into the heterogeneous gel network, it is excluded from the crystalline component and reacts with styrene monomers in the amorphous component. In the sPS powder, the polymer chains in the crystalline and amorphous components are packed tightly together. Thus, when functionalizing reagent is introduced to the dense sPS powder it is sterically restricted from reacting with monomers that are far removed from the particle surface and reacts with monomers at and near the particle surface, resulting in a limited degree of functionalization.

Based on the microstructural analysis of the Powder and Gel copolymers provided by NMR spectroscopy, the sPS/$CHCl_3$ gel produced brominated copolymers with a higher prevalence of styrene "blocks" of at least five consecutive styrene units and a higher degree of blockiness. At low Br-content, the Gel CH-7% copolymer crystallizes (T_c) and melts (T_m) at higher temperatures and demonstrates faster crystallization kinetics at lower supercooling relative to its Powder P-7% analog. Remarkably, the CH-17% copolymer exhibits similar crystallization behavior to the lower Br-content P-12% copolymer, demonstrating that even at high Br-content, the Gel CH-17% copolymer has a high degree of blockiness and few defects along its chains. Simulated average chains of the brominated copolymers, generated from the empirical pentad sequence distributions, predict that the Gel copolymers contain a higher prevalence of crystallizable sPS segments, consistent with the rapid crystallization kinetics of the Gel copolymers provided by DSC experiments. Thus, the simulated average chains appear to be representative of average chains and support that the gel state favorably affects the bromination reaction, producing blocky copolymers with fewer defects along the chains.

This work provides a fundamental investigation of the post-polymerization bromination of sPS in heterogeneous reaction states, demonstrating that the gel state is capable of producing blocky brominated copolymers with a higher degree of blockiness and higher functional group content relative to the powder state. Given the dependence of sPS/solvent gel morphology on the gelation solvent,[24] temperature,[48-50] and concentration,[26,51] we anticipate that the sPS/solvent gel will present avenues of further investigation into controlling the degree of blockiness in sPS-based copolymers. This research also establishes that post-polymerization functionalization carried out on gel-forming semi-crystalline polymers is a facile approach to polymer design and synthesis that will be useful in the development of next-generation functionalized materials that would otherwise be inaccessible using heterogeneous powder state reaction methods.

5.6. Acknowledgements

This material is based upon work supported by the National Science Foundation under Grant No. DMR-1809291. Advanced Research Computing at Virginia Tech is gratefully acknowledged for providing computational resources and technical support that have contributed to the results reported within this manuscript. This research used resources of the Advanced Photon Source, a U.S. Department of Energy (DOE) Office of Science User Facility operated for the DOE Office of Science by Argonne National Laboratory under Contract No. DE-AC02-06CH11357. The authors would like to thank Dr. Jan Ilavsky and acknowledge the use of beamline 9ID-C.

5.7. Supplementary Information

Figure S5.1 shows a polarized light micrograph of sPS particles along with a histogram and normal distribution of the estimated sPS particle diameters provided by ImageJ software. The micrograph reveals that the sPS particle sizes are irregular. In addition, some particles appear to be clumped together that may otherwise be separate particles if suspended in a non-solvent. The calculated average particle diameter is 31 ± 25 μm, based on rough estimates of the particle diameters and considering only particles in the range from 4−120 μm. Using this estimated average particle diameter, the average surface area of an sPS particle was found to be $3 \pm 2 \times 10^3$ μm^2, which would contain approximately 10 ± 6 billion styrene units (estimated molecular area of a styrene monomer = 3.16×10^{-7} μm^2)[52] or 0.004 ± 0.003% of the total styrene per particle.

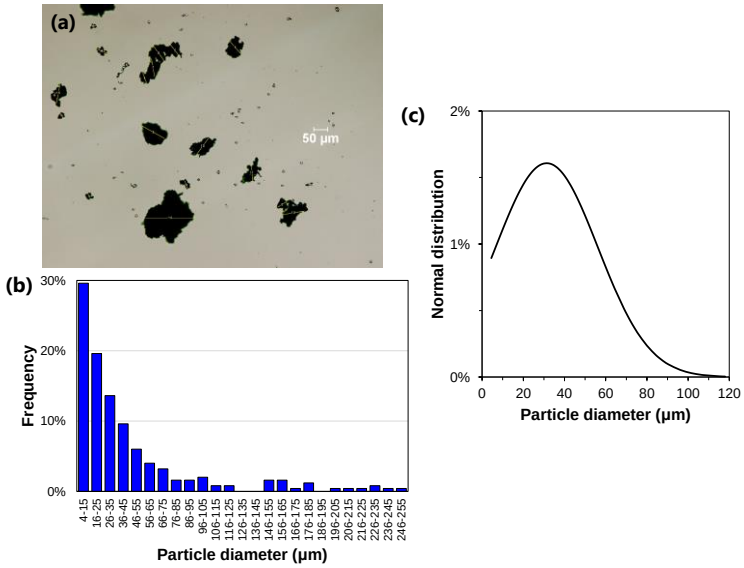

Figure S5.1. (a) A micrograph of sPS particles that has been analyzed using ImageJ software. The (b) histogram and (c) normal distribution of the estimated sPS particle diameters obtained from the ImageJ analysis. Based on particles with diameters in the range from 4-120 μm, the average particle diameter was 31 ± 25 μm.

The differential scanning calorimetry (DSC) first heating trace of the sPS powder and 10 w/v% sPS/$CHCl_3$ gel are shown in **Figure S5.2**. Four heat flow events are observed in the heating traces, the glass transition, T_g, at around 100 °C, the $\delta \rightarrow \gamma$ transformation that occurs just after the

T_g of the sPS powder and overlaps the T_g of the sPS/$CHCl_3$ gel, the $\gamma \rightarrow \alpha$ transformation that occurs at approximately 200 °C, and the melting endotherm at ca. 271 °C.[53]

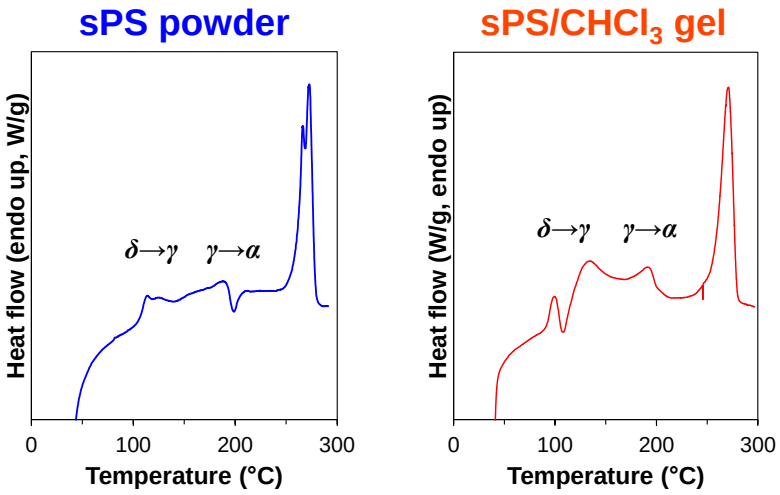

Figure S5.2. DSC first heating traces of the (left) sPS powder and (right) 10 w/v% sPS/$CHCl_3$ gel. The gel sample was dried under vacuum at 70 °C for ca. 24 h prior to analysis. Heating rate = 10 °C min^{-1}.

Figure S5.3 shows the ^1H NMR spectra of two Powder samples that were prepared by reacting sPS powder with Br_2 for 96 h using dichloromethane (DCM) or chloroform ($CHCl_3$) as the reaction solvents. Compared to the reaction carried out in DCM which produced a copolymer with 12 mol% Br-content, the reaction carried out in $CHCl_3$ resulted in a copolymer with 15 mol% Br. These data demonstrate that the degree of functionalization is dependent upon the reaction solvent, and thus on the accessibility of functionalization reagent to monomer units within the sPS powder.

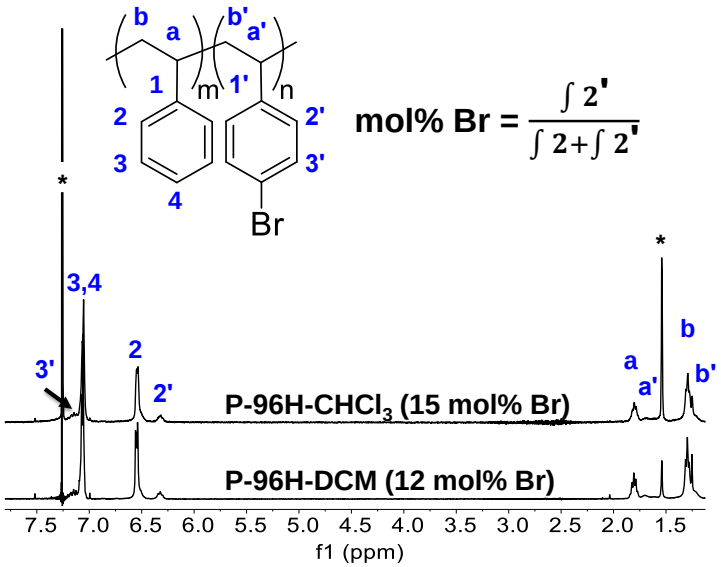

Figure S5.3. ^{1}H NMR spectra of the Powder P-96H-$CHCl_3$ and P-96H-DCM copolymers. Samples were prepared by reacting sPS powder with Br_2 for 96 h using (top) $CHCl_3$ and (bottom) DCM as reaction solvents.

The quantitative ^{13}C NMR spectra of the sPS homopolymer and the Powder and Gel copolymers are compared in **Figure S5.4**. The sharp and intense peak at approximately 145.15 ppm is attributed to the resonance from a quaternary carbon nucleus of an un-functionalized styrene unit (C(1)) that exists in the center of a combination of five consecutive styrene units, i.e., a pentad of styrene units (sssss, where s = styrene), along a polymer chain.

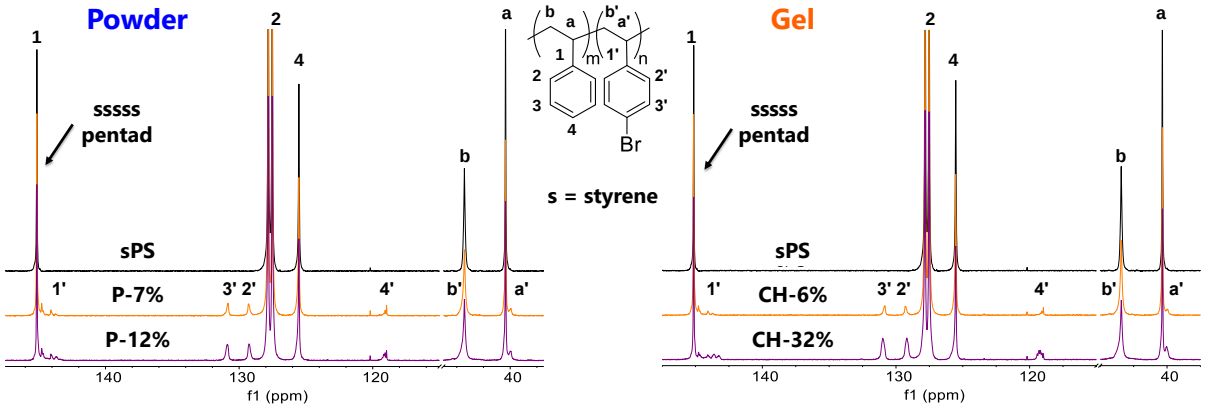

Figure S5.4. Quantitative ^{13}C NMR spectra of the sPS homopolymer and the (left) Powder and (right) Gel copolymers increasing in degree of bromination from top to bottom. For comparison, spectra are referenced to TCE-d_2 and normalized over 127.0−132.5 ppm.

Figure S5.5 compares the melting temperatures, T_m, of the sPS homopolymer and the Powder, Gel, and Random copolymers obtained from the differential scanning calorimetry (DSC)

heating trace after rapid cooling from the melt at −60 °C min^{-1}. Melting temperature is defined here as the first (T_{m1}) and second (T_{m2}) peak maximum of the melting endotherm that results from crystallites composed of un-functionalized styrene units. The Powder and Gel copolymers exhibit higher melting temperatures relative to the Random copolymers. Comparison of the T_m for the Powder and Gel copolymers reveals that the Gel samples melt at higher temperatures, which strongly suggests that the Gel copolymers form thicker crystallites that contain longer runs of consecutive styrene units relative to their Powder analogs.

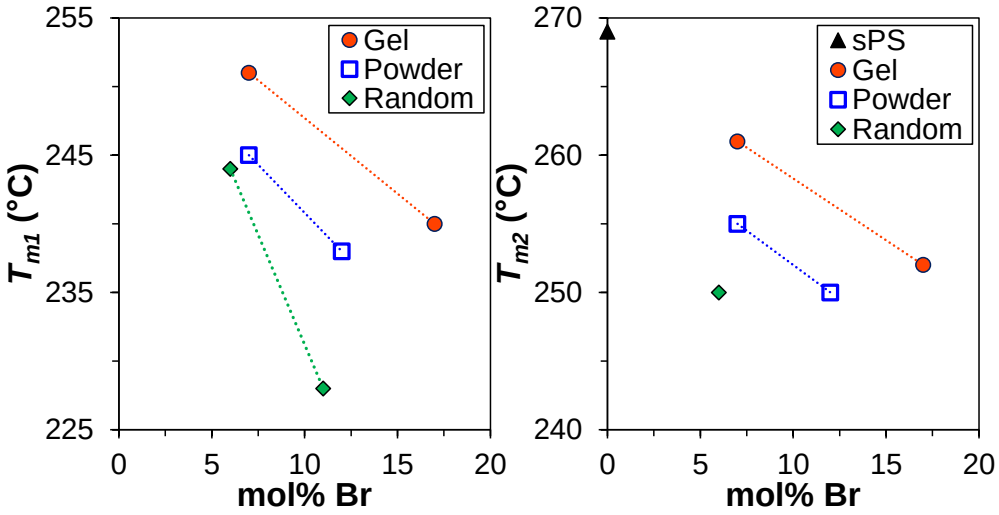

Figure S5.5. The (left) first melting temperature (T_{m1}) and (right) second melting temperature (T_{m2}) for the sPS homopolymer and the Gel, Powder, and Random copolymers after samples were cooled from the melt at −60 °C min^{-1}. The melting temperature is defined here as the melting endotherm peak maximum for crystallites composed of un-functionalized styrene units. Dashed lines are shown to guide the eye.

The wide-angle X-ray diffraction (WAXD) profiles of the sPS homopolymer, and the Powder, Gel, and Random copolymers after 2 h isothermal crystallization at 190 °C are shown in **Figure S5.6**. The crystalline reflections observed in the diffractograms of the brominated copolymers are consistent with the diffraction pattern of the melt-crystallized sPS homopolymer sample.

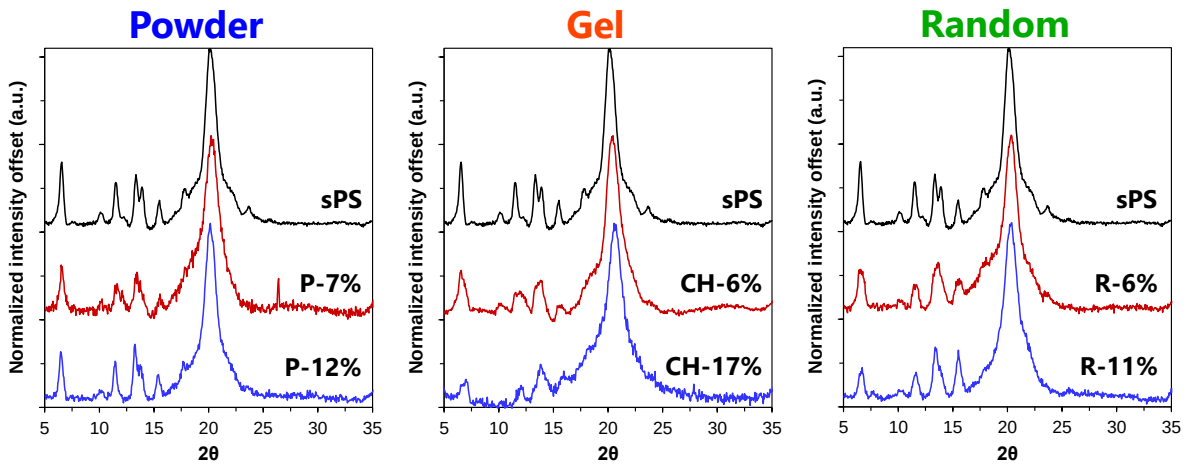

Figure S5.6. Normalized WAXD profiles of the sPS homopolymer and the (left) Powder, (center) Gel, and (right) Random copolymers after isothermal crystallization for 2 h at 190 °C. Diffractograms are offset for clarity.

The long period (L_p) of the Bragg peak in the small-angle X-ray scattering (SAXS) profiles of the sPS homopolymer and the Powder and Gel copolymers was analyzed by assuming a linear two-phase model. The results of the SAXS analysis of the intercrystalline domain spacing for the sPS homopolymer and the Powder, Gel, and Random copolymers are summarized in **Table S5.1**. Samples were melt-crystallized for 2 h at 190 °C prior to analysis.

Table S5.1. SAXS analysis of the intercrystalline domain spacing in the sPS homopolymer and the Powder, Gel, and Random copolymers after 2 h isothermal crystallization at 190 °C.

Sample	*d* spacing (nm^{-1})	L_p (nm)	$\%X_c$ [a]	l_c (nm) [a]	Avg. # units in a crystalline stem	l_a (nm) [a]
sPS	0.389	16.2	32	5.2	20	11.0
P-7%	0.315	19.9	33	6.6	26	13.3
P-12%	0.320	19.6	28	5.5	22	14.1
CH-6%	0.325	19.3	31	6.0	24	13.3
CH-17%	0.308	20.4	25	5.1	20	15.3
R-6%	0.337	18.7	29	5.4	21	13.3

[a] Weight percent crystallinity calculated from the area under the melting endotherm (ΔH_f) in the DSC heating trace ($\Delta H_f°$=79.3 J/g).
[b]Average number of styrene units in a crystalline stem, based on the lamella thickness and the planar zigzag conformation of sPS with 2 monomer units per identity period (c-axis dimension = 0.51 nm).[45]

Simulated average chains of the Powder P-12% and Gel CH-17% copolymers, created through an iterative process that minimizes the difference between the pentad sequence

distribution of the simulated chain and the respective data from experiment, are provided in **Figure S5.7**. The simulated chains exhibit noticeably non-random distributions of Br-Sty units in a blocky microstructure.

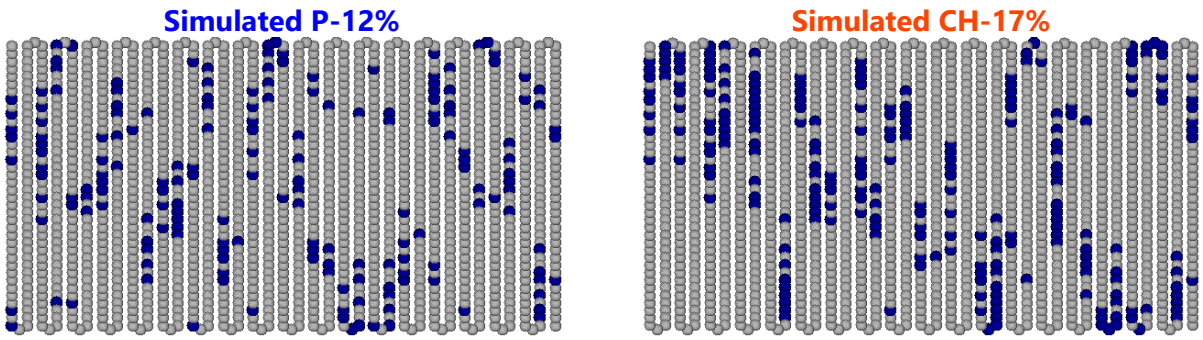

Figure S5.7. Simulated average chains of the (left) Powder P-12% and (right) Gel CH-17% copolymers created through an iterative process that minimizes the difference between the pentad sequence distribution of the simulated chain and the respective experimentally-determined data. Styrene units = grey circles; Br-Sty units = blue circles. The root-mean-square deviation (RMSD) between simulated and empirical: P-12% = 0.47%; CH-17% = 0.79%.

5.8. References

1. Hadjichristidis, N.; Pispas, S.; Floudas, G. A., *Block Copolymers: Synthetic Strategies, Physical Properties, and Applications*. John Wiley and Sons: New York, 2002.
2. Hamley, I. W., *The Physics of Block Copolymers*. Oxford University Press: New York, 1998.
3. Lee, M.; Park, J. K.; Lee, H.-S.; Lane, O.; Moore, R. B.; McGrath, J. E.; Baird, D. G., Effects of Block Length and Solution-Casting Conditions on the Final Morphology and Properties of Disulfonated Poly(Arylene Ether Sulfone) Multiblock Copolymer Films for Proton Exchange Membranes. *Polymer* **2009,** *50*, 6129-6138.
4. Leibler, L., Theory of Microphase Separation in Block Copolymers. *Macromolecules* **1980,** *13* (6), 1602-1617.
5. Dobrynin, A. V.; Leibler, L., Theory of Polydisperse Multiblock Copolymers. *Macromolecules* **1997,** *30*, 4756-4765.
6. Bates, F. S.; Fredrickson, G. H., Block Copolymers - Designer Soft Materials. *Phys. Today* **1999,** *52* (2), 32-38.
7. Lodge, T. P., Block Copolymers: Past Successes and Future Challenges. *Macromol. Chem. Phys.* **2003,** *204* (2), 265-273.
8. Ruzette, A.-V.; Leibler, L., Block Copolymers in Tomorrow's Plastics. *Nat. Mater.* **2005,** *4* (1), 19-31.
9. Domski, G. J.; Rose, J. M.; Coates, G. W.; Bolig, A. D.; Brookhart, M., Living Alkene Polymerization: New Methods for the Precision Synthesis of Polyolefins. *Prog. Polym. Sci.* **2007,** *32* (1), 30-92.
10. Semler, J. J.; Jhon, Y. K.; Tonelli, A.; Beevers, M.; Krishnamoorti, R.; Genzer, J., Facile Method of Controlling Monomer Sequence Distributions in Random Copolymers. *Adv. Mater.* **2007,** *19* (19), 2877-2883.
11. Jhon, Y. K.; Semler, J. J.; Genzer, J., Effect of Solvent Quality and Chain Confinement on the Kinetics of Polystyrene Bromination. *Macromolecules* **2008,** *41* (18), 6719-6727.
12. Strickland, L. A.; Hall, C. K.; Genzer, J., Design of Copolymers with Tunable Randomness Using Discontinuous Molecular Dynamics Simulation. *Macromolecules* **2009,** *42* (22), 9063-9071.

13. Han, J.; Jeon, B. H.; Ryu, C. Y.; Semler, J. J.; Jhon, Y. K.; Genzer, J., Discriminating among Co-Monomer Sequence Distributions in Random Copolymers Using Interaction Chromatography. *Macromol. Rapid Comm.* **2009,** *30* (18), 1543-1548.
14. Jhon, Y. K.; Semler, J. J.; Genzer, J.; Beevers, M.; Gus' kova, O. A.; Khalatur, P. G.; Khokhlov, A. R., Effect of Comonomer Sequence Distribution on the Adsorption of Random Copolymers onto Impenetrable Flat Surfaces. *Macromolecules* **2009,** *42*, 2843-2853.
15. Gurarslan, R.; Hardrict, S.; Roy, D.; Galvin, C.; Hill, M. R.; Gracz, H.; Sumerlin, B. S.; Genzer, J.; Tonelli, A., Beyond Microstructures: Using the Kerr Effect to Characterize the Macrostructures of Synthetic Polymers. *J. Polym. Sci. B Polym. Phys.* **2015,** *53* (3), 155-166.
16. Liu, S.; Sen, A., Syntheses of Syndiotactic-Polystyrene-Graft-Poly(Methyl Methacrylate), Syndiotactic-Polystyrene-Graft-Poly(Methyl Acrylate), and Syndiotactic-Polystyrene-Graft-Atactic-Polystyrene with Defined Structures by Atom Transfer Radical Polymerization. *Macromolecules* **2000,** *33* (14), 5106-5110.
17. Gao, Y.; Li, H. M., Synthesis and Characterization of Acetylated Syndiotactic Polystyrene. *Polym. Int.* **2004,** *53* (10), 1436-1441.
18. Borriello, A.; Agoretti, P.; Ambrosio, L.; Fasano, G.; Pellegrino, M.; Venditto, V.; Guerra, G., Syndiotactic Polystyrene Films with Sulfonated Amorphous Phase and Nanoporous Crystalline Phase. *Chem. Mater.* **2009,** *21* (14), 3191-3196.
19. Gibson, H. W.; Bailey, F. C., Chemical Modification of Polymers. 13. Sulfonation of Polystyrene Surfaces. *Macromolecules* **1980,** *13* (1), 34-41.
20. Fahs, G. B.; Benson, S. D.; Moore, R. B., Blocky Sulfonation of Syndiotactic Polystyrene: A Facile Route toward Tailored Ionomer Architecture Via Postpolymerization Functionalization in the Gel State. *Macromolecules* **2017,** *50* (6), 2387-2396.
21. Noble, K. F.; Noble, A. M.; Talley, S. J.; Moore, R. B., Blocky Bromination of Syndiotactic Polystyrene Via Post-Polymerization Functionalization in the Heterogeneous Gel State. *Polym. Chem.* **2018,** *9* (41), 5095-5106.
22. Anderson, L. J.; Yuan, X.; Fahs, G. B.; Moore, R. B., Blocky Ionomers Via Sulfonation of Poly(Ether Ether Ketone) in the Semicrystalline Gel State. *Macromolecules* **2018,** *51* (16), 6226-6237.
23. Daniel, C.; Longo, S.; Ricciardi, R.; Reverchon, E.; Guerra, G., Monolithic Nanoporous Crystalline Aerogels. *Macromol. Rapid Commun.* **2013,** *34* (15), 1194-1207.

24. Mochizuki, J.; Sano, T.; Tokami, T.; Itagaki, H., Decisive Properties of Solvent Able to Form Gels with Syndiotactic Polystyrene. *Polymer* **2015,** *67*, 118-127.
25. Shimizu, H.; Wakayama, T.; Wada, R.; Okabe, M.; Tanaka, F., Solvent Effect on Junction Size in Syndiotactic Polystyrene Physical Gel. *Polym. J.* **2005,** *37* (4), 294-298.
26. Kobayashi, M.; Yoshioka, T.; Kozasa, T.; Tashiro, K.; Suzuki, J.; Funahashi, S.; Izumi, Y., Structure of Physical Gels Formed in Syndiotactic Polystyrene/Solvent Systems Studied by Small-Angle Neutron Scattering. *Macromolecules* **1994,** *27* (6), 1349-1354.
27. Roels, T.; Deberdt, F.; Berghmans, H., Solvent Quality and Phase-Stability in Syndiotactic Polystyrene-Solvent Systems. *Macromolecules* **1994,** *27* (21), 6216-6220.
28. Daniel, C.; Guerra, G.; Musto, P., Clathrate Phase in Syndiotactic Polystyrene Gels. *Macromolecules* **2002,** *35* (6), 2243-2251.
29. Noble, K. F.; Troya, D.; Moore, R. B., Tailored Chain Sequences of Gel-State Brominated Syndiotactic Polystyrene Copolymers by Changing Gel Morphology. *Manuscript in progress.*
30. Noble, K. F.; Talley, S. J.; Fahs, G. B.; Troya, D.; Moore, R. B., High-Resolution Comonomer Sequencing of Sps-Co-Sps-Br Copolymers Using ^{13}c Nmr Spectroscopy, Simulations, and Small-Angle X-Ray Scattering. *Manuscript in progress.*
31. Ilavsky, J.; Zhang, F.; Andrews, R. N.; Kuzmenko, I.; Jemian, P. R.; Levine, L. E.; Allen, A. J., Development of Combined Microstructure and Structure Characterization Facility for in Situ and Operando Studies at the Advanced Photon Source. *J. Appl. Crystallogr.* **2018,** *51* (3), 867-882.
32. Ilavsky, J.; Zhang, F.; Allen, A. J.; Levine, L. E.; Jemian, P. R.; Long, G. G., Ultra-Small-Angle X-Ray Scattering Instrument at the Advanced Photon Source: History, Recent Development, and Current Status. *Metall. Mater. Trans. A* **2013,** *44* (1), 68-76.
33. Ilavsky, J., Nika: Software for Two-Dimensional Data Reduction. *J. Appl. Crystallogr.* **2012,** *45* (2), 324-328.
34. Ilavsky, J.; Jemian, P. R., Irena: Tool Suite for Modeling and Analysis of Small-Angle Scattering. *J. Appl. Crystallogr.* **2009,** *42* (2), 347-353.
35. Takebe, T.; Yamasaki, K., Crystallization Thermodynamics and Kinetics of Syndiotactic Polystyrene. In *Syndiotactic Polystyrene*, 2009; pp 238-251.

36. Guerra, G.; Vitagliano, V. M.; De Rosa, C.; Petraccone, V.; Corradini, P., Polymorphisms in Melt Crystallized Syndiotactic Polystyrene Samples. *Macromolecules* **1990,** *23* (5), 1539-1544.
37. Daniel, C.; Giudice, S.; Guerra, G., Syndiotatic Polystyrene Aerogels with B, Γ, and E Crystalline Phases. *Chem. Mater.* **2009,** *21* (6), 1028-1034.
38. Daniel, C.; Sannino, D.; Guerra, G., Syndiotactic Polystyrene Aerogels: Adsorption in Amorphous Pores and Absorption in Crystalline Nanocavities. *Chem. Mater.* **2008,** *20* (2), 577-582.
39. Venditto, V.; Pellegrino, M.; Califano, R.; Guerra, G.; Daniel, C.; Ambrosio, L.; Borriello, A., Monolithic Polymeric Aerogels with Vocs Sorbent Nanoporous Crystalline and Water Sorbent Amorphous Phases. *ACS Appl. Mater. Inter.* **2015,** *7* (2), 1318-1326.
40. Britton, D.; Heatley, F.; Lovell, P. A., 13c Nmr Spectroscopy Studies of Branching and Sequence Distribution in Copolymers of Vinyl Acetate and N-Butyl Acrylate Prepared by Semibatch Emulsion Copolymerization. *Macromolecules* **2001,** *34* (4), 817-829.
41. Shin, J.; Chang, Y.; Nguyen, T. L. T.; Noh, S. K.; Bae, C., Hydrophilic Functionalization of Syndiotactic Polystyrene Via a Combination of Electrophilic Bromination and Suzuki–Miyaura Reaction. *J. Polym. Sci., Part A: Polym. Chem.* **2010,** *48* (19), 4335-4343.
42. Annunziata, L.; Sarazin, Y.; Duc, M.; Carpentier, J. F., Well-Defined Syndiotactic Polystyrene-B-Atactic Polystyrene Stereoblock Polymers. *Macromol. Rapid Commun.* **2011,** *32* (9-10), 751-757.
43. Annunziata, L.; Monasse, B.; Rizzo, P.; Guerra, G.; Duc, M.; Carpentier, J.-F., On the Crystallization Behavior of Syndiotactic-B-Atactic Polystyrene Stereodiblock Copolymers, Atactic/Syndiotactic Polystyrene Blends, and Aps/Sps Blends Modified with Sps-B-Aps. *Mater. Chem. Phys.* **2013,** *141* (2–3), 891-902.
44. Su, C.; Jeng, U.; Chen, S.; Cheng, C.-Y.; Lee, J.-J.; Lai, Y.-H.; Su, W.; Tsai, J.; Su, A., Thermodynamic Characterization of Polymorphs in Bulk-Crystallized Syndiotactic Polystyrene Via Small/Wide-Angle X-Ray Scattering and Differential Scanning Calorimetry. *Macromolecules* **2009,** *42* (12), 4200-4207.
45. Albunia, A. R.; Musto, P.; Guerra, G., Ftir Spectra of Pure Helical Crystalline Phases of Syndiotactic Polystyrene. *Polymer* **2006,** *47* (1), 234-242.

46. Flory, P. J., Theory of Crystallization in Copolymers. *Trans. Faraday Soc.* **1955,** *51* (0), 848-857.
47. Wang, H.; Wu, C.; Cui, D.; Men, Y., Lamellar Thickness Dependence of Crystal Modification Selection in the Syndiotactic Polystyrene Γ-to-A/B Phase Transition Process. *Macromolecules* **2018,** *51* (2), 497-503.
48. Daniel, C.; Avallone, A.; Guerra, G., Syndiotactic Polystyrene Physical Gels: Guest Influence on Structural Order in Molecular Complex Domains and Gel Transparency. *Macromolecules* **2006,** *39* (22), 7578-7582.
49. Prasad, A.; Mandelkern, L., The Thermoreversible Gelation of Syndiotactic Polystyrene. *Macromolecules* **1990,** *23* (23), 5041-5043.
50. Daniel, C.; Menelle, A.; Brulet, A.; Guenet, J.-M., Thermoreversible Gelation of Syndiotactic Polystyrene in Toluene and Chloroform. *Polymer* **1997,** *38* (16), 4193-4199.
51. Kobayashi, M.; Kozasa, T., Conformational Ordering Process on Physical Gelation of Syndiotactic Polystyrene/Solvent Systems Revealed by Time-Resolved Infrared Spectroscopy. *Appl. Spectrosc.* **1993,** *47* (9), 1417-1424.
52. Megiel, E.; Kaim, A., Molecular Geometry and Electronic Structure of Molecules in Free-Radical Copolymerization of Styrene and Methyl Methacrylate Derived from Density Functional Calculations. *J. Polym. Sci., Part A: Polym. Chem.* **2001,** *39* (21), 3761-3769.
53. Cheng, Y.-W.; Wang, C., Solvent-Induced Crystallization of Electrospun Syndiotactic Polystyrene Nanofibers and Its Reversible Desorption/Sorption of Volatile Organic Vapors. *J. Polym. Res.* **2016,** *23* (11), 234.

Chapter 6.

Conclusions and Suggested Future Work

6.1. Conclusions

This work demonstrates the bromination of sPS in the homogeneous solution-state and heterogeneous gel and powder states to produce random and blocky sPS-co-sPS-Br copolymers, respectively. The purpose of this research was to prepare semicrystalline blocky copolymers with relatively high degrees of functionality using a facile post-polymerization functionalization method. Using our heterogeneous gel-state bromination method, a crystallizable 32 mol% Br copolymer was prepared in less than 6 h, demonstrating that gel-state functionalization favorably affects the bromination reaction to produce a blocky microstructure. In comparison, the powder-state bromination method produced copolymers with a limited degree of functionalization of up to 12 mol% Br and required a threefold longer reaction time than the gel-state method. In the powder-state, the polymer chains in the crystalline and amorphous components are packed tightly together. Thus, when functionalizing reagent is introduced to the dense sPS powder it is sterically restricted from reacting with monomers that are far removed from the surface of the particle and reacts with monomers at and near the particle surface, resulting in a limited degree of functionalization. In contrast, within the heterogenous gel network brominating reagent is excluded from monomers in the tightly packed crystalline component and reacts with styrene monomers in the solvent swollen amorphous component, resulting in a high degree of functionalization in a short period of time.

Microstructural analysis of the solution-state and heterogeneous gel- and powder-state brominated copolymers was provided by quantitative ^{13}C NMR spectroscopy. This research reports the first high-resolution comonomer sequencing of brominated sPS copolymers.

BsgHMBC spectroscopy, electronic structure calculations, and simulated random copolymer chains were used to develop the comonomer sequencing method. Using this method, every peak in the quaternary carbon region of the NMR spectrum was assigned to a styrene or Br-Sty unit in the center of a unique combination of five monomer units, i.e., a pentad sequence along the chain. Through this microstructural analysis, the heterogeneous reaction states have been proven to produce copolymers with block-like character relative to their solution-state random analogs. In addition, gel-state bromination produces copolymers with a higher degree of blockiness and a higher prevalence of styrene "blocks" of at least five consecutive styrene units compared to the powder-state reaction method.

Morphological characterization of quenched films of the gel-state functionalized copolymers provided by USAXS/SAXS, support that distinct segments of pure sPS and randomly brominated sPS in the gel-state blocky copolymers are capable of producing a micro-phase separated morphology that is attributed to thermodynamic immiscibility. Thus, the blockiness originating from the gel-state functionalization method is sufficient to drive phase development that is somewhat reminiscent of conventional block copolymer phase behavior. The gel-state copolymers also demonstrate superior crystallizability and faster crystallization kinetics at lower supercooling compared to their solution-state random analogs. The microstructure of simulated chains with random and blocky copolymers, affirm that restricting access of the functionalizing reagent to monomers well removed from the crystalline fraction of the gel network, produces copolymers with a greater prevalence of crystallizable sPS segments, which is advantageous for preserving desired crystallizability of the resulting blocky copolymers.

This work further aimed to develop a structure-property relationship between the sPS/solvent gel morphology and the gel-state blocky brominated copolymers. Gels of

crystallizable homopolymers are composed of tightly packed chain segments in lamellar crystallites that act as physical cross-links bound together by a percolating network of solvent swollen amorphous chains. Morphological characterization of a 10 w/v% sPS/$CHCl_3$ gel and a 10 w/v% sPS/CCl_4 gel provided by X-ray scattering techniques, demonstrated that the sPS/$CHCl_3$ gel contains randomly dispersed and unoriented crystallites that are loosely bound together by the percolating network of amorphous chain segments. The sPS/CCl_4 gel morphology is more complex, consisting of polymer-rich regions that contain clusters of unoriented crystallites and amorphous tie chains, and polymer-poor regions comprised of the percolating network of amorphous chain segments, which link the crystallite clusters together. Microstructural analysis of the gel-state brominated copolymers revealed that the sPS/$CHCl_3$ gel produces brominated copolymers with a higher prevalence of styrene "blocks" of at least five consecutive styrene units and a higher degree of blockiness. The copolymers derived from the sPS/$CHCl_3$ gel also exhibited superior crystallizability during conditions of rapid cooling and faster crystallization kinetics at lower supercooling compared to their sPS/CCl_4 copolymer analogs. Remarkably, the 10 w/v% sPS/$CHCl_3$ gel produced a crystallizable 32 mol% Br copolymer that contained distinct sequences of styrene units and Br-Sty units in segments of significant length that allowed for crystallization during dynamic cooling conditions, demonstrating that the sPS/$CHCl_3$ gel morphology favorably affected the bromination reaction to produce copolymers with fewer defects along the chains in a multiblock-like microstructure. In contrast, the more complex sPS/CCl_4 gel morphology appears to produce copolymers that contain a gradient-like blocky microstructure in which indiscrete boundaries exist between un-functionalized styrene "blocks" and randomly functionalized "blocks." The presence of large micro-phase domains in the quenched film of a 17 mol% Br sPS/$CHCl_3$ copolymer characterized by USAXS/SAXS experiments, also supports that the

sPS/$CHCl_3$ gel is capable of producing copolymers with a high degree of blockiness in a multiblock-like microstructure.

To help rationalize the effect of the sPS/solvent gel morphology on the copolymer microstructure and crystallization behavior, simulated chains of the sPS/CCl_4 and sPS/$CHCl_3$ copolymer microstructures were developed. A systematic investigation of the inaccessible block lengths in the simulated blocky chains predicted that the sPS/$CHCl_3$ copolymers contain long blocks of un-functionalized styrene units and a low degree of variability in the way Br-Sty groups are distributed along the chains. This finding is in excellent agreement with the results obtained from the microstructural analysis, crystallization behavior experiments, and morphological characterization, and supports that the sPS/$CHCl_3$ copolymers contain a multiblock-like microstructure. For the simulated sPS/CCl_4 blocky copolymer microstructures, the systematic investigation predicts that the sPS/CCl_4 copolymers contain a higher degree of variability in the way Br-Sty groups are distributed along the chains, which again supports the gradient-like blocky microstructure suggested by the empirical results. Thus, these simulations strongly suggest that the sPS/solvent gel morphology produces copolymers with tailored comonomer sequence distributions.

Simulated average chains of the sPS/CCl_4 and sPS/$CHCl_3$ copolymers created from the empirical pentad sequence distributions, predict that long blocks of consecutive styrene units of at least 38 and 46 styrene units, respectively, exist along the chains, in excellent agreement with the estimated number of styrene units in a crystalline stem within the sPS/solvent gel networks. These results provide strong evidence that the long blocks of un-functionalized styrene units in the gel-state brominated copolymers originate from the crystalline stems within the crystalline lamellae of the gel network.

This work provides a fundamental investigation of the post-polymerization bromination of sPS, demonstrating that blocky brominated copolymers can be prepared using a straightforward physical method of post-polymerization functionalization in the heterogeneous gel state. Furthermore, the gel state was found to produce blocky copolymers with higher degrees of blockiness and higher functional group content than the powder state. Perhaps the most noteworthy contribution of this research is that it demonstrates that blocky copolymers with tailored chain sequences, degrees of blockiness, and crystallization behaviors can be prepared using the gel-state method by simply changing the sPS/solvent gel morphology. Given the dependence of sPS/solvent gel morphology on gelation temperature[1-3] and polymer concentration,[4,5] we anticipate that the sPS/solvent gel will present avenues of further investigation into controlling the degree of blockiness in sPS-based copolymers. The broader impact of this research is that it clearly establishes gel-state functionalization as a physical approach to the controlled synthesis of blocky copolymers with tailored microstructures, which was previously believed to be restricted to pure synthetic chemistry. This facile gel-state approach to polymer design and synthesis will be useful in the development of next-generation functionalized materials. As an advancement to the manner in which micro-phase separated structures are created, these tailored materials will greatly enhance the convenience of block copolymers for a wide variety of applications including structural and biomechanical materials, and polymeric membranes for energy conversion and water purification systems.

6.2. Suggested future work

6.2.1. Tuning copolymer properties by changing the sPS/solvent gel polymer concentration

This dissertation work has proven that blocky brominated sPS copolymers can be prepared with tailored microstructures and tunable crystallization behaviors simply by changing the sPS gelation solvent. While this finding is relevant for sPS, few other semicrystalline polymers are capable of forming semicrystalline thermoreversible gels in a broad range of solvents.[6,7] Given the ability to control the morphology of the semicrystalline gel network by changing the polymer concentration,[4,5,8] copolymers should be prepared from an sPS/solvent gel system using a broad range of polymer concentrations in order to develop a deeper understanding of the relationship between gel morphology and copolymer microstructure, degree of blockiness, and crystallization behavior.

The sPS/solvent gel morphology can be probed using USAXS/SAXS techniques. **Figure 6.1** shows the USAXS/SAXS profiles for a series of sPS/$CHCl_3$ and sPS/1,2,4-trichlorobenzene (TCB) gels ranging in polymer concentration from 5.0−15.0 w/v%. These data were recorded at the Advanced Photon Source beamline 9ID-C at Argonne National Laboratory. The USAXS/SAXS profiles of the sPS/$CHCl_3$ gels exhibit a scattering feature in the range from 0.1 $nm^{-1} < q < 1\ nm^{-1}$ that is attributed to intercrystalline scattering. This feature increases slightly in intensity with increasing polymer concentration, which may indicate greater ordering between crystallites at higher polymer concentrations. The USAXS/SAXS profiles of the sPS/TCB gels exhibit two scattering features, a high q scattering feature from $0.2\ nm^{-1} < q < 1\ nm^{-1}$ and a low q scattering feature from 0.01−0.2 nm^{-1}. The high q scattering feature is consistent with the scattering present in the sPS/$CHCl_3$ gels from intercrystalline scattering. The low q scattering feature is similar to that observed in the 10 w/v% sPS/CCl_4 gel and is attributed to clusters of crystallites

that are randomly dispersed by solvent swollen amorphous chains (see **Figure 4.3**). This low *q* feature becomes more prominent at high polymer content, suggestive of greater ordering between the crystallite clusters. Given the more distinct changes in the gel morphology of the sPS/TCB gel series, it appears that the sPS/TCB gels would provide valuable insight into the effect of polymer concentration on copolymer microstructure and properties.

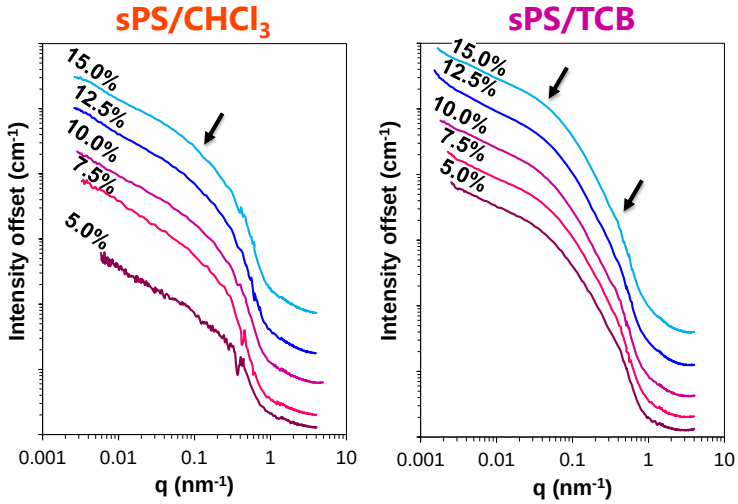

Figure 6.1. USAXS/SAXS profiles for a series of (left) sPS/$CHCl_3$ and (right) sPS/TCB gels increasing in polymer concentration from bottom to top. Profiles are offset for clarity. The arrows indicate the excess scattering features.

6.2.2. Polymorphism and mechanical properties of blocky brominated sPS copolymers

In **Chapter 4**, low Br-content copolymers prepared from sPS/CCl_4 and sPS/$CHCl_3$ gels were shown to exhibit different crystallization behavior and polymorphism. After isothermal crystallization experiments at temperatures below the melting temperature, the sPS/$CHCl_3$ CH-6% copolymer exhibited a larger fraction of the thermodynamically favored *β*-form of sPS relative to the sPS/CCl_4 CaT-6% copolymer. This difference was believed to stem from the primary copolymer microstructure inherited from the sPS/solvent gel morphology during the post-polymerization bromination reaction. The sPS/$CHCl_3$ gel morphology appears to favorably affect the bromination reaction to produce copolymers with fewer defects along the chains that allows for crystallizable segments to organize and re-organize from the melt during isothermal conditions.

To obtain deeper insight into the effect of the copolymer primary microstructure on copolymer crystallization behavior, future work should include tensile testing of melt-crystallized films of the low-Br content sPS/CCl_4 and sPS/$CHCl_3$ copolymers using dynamic mechanical analysis. Krishnaswamy et al.[9] reported the tensile properties of blends of short and long chain high-density polyethylene (HDPE) with short-chain branches and found that the short-chain branched long chain HDPE contained a larger fraction of interlamellar tie-chains that prevented the polymer from deforming to high strains and allowed the polymer to carry greater stresses. Interlamellar tie chains are expected to be more prominent in the sPS/CCl_4 copolymers, based on the large fraction of the α-form polymorph in which loosely looped polymer chains have been reported.[10] The crystal growth during isothermal crystallization in the gel-state functionalized copolymers should also be investigated using polarized light microscopy.

6.2.3. Blocky alkylation via post-polymerization functionalization in the gel-state

As introduced in **Chapter 2**, this research lays the groundwork to synthesize other sPS-based blocky copolymers with useful functionalities through substitution of the labile bromine functional groups.[11-13] For example, to investigate the effect of functional group distribution on self-assembly, a H-bonding side chain could be installed on the styrene phenyl ring through a palladium catalyzed Suzuki-Miyaura cross-coupling reaction using a functionalized phenylboronic acid.[11] The blocky copolymer microstructure can also be used as a template for further reactions, such as sulfonation of the brominated sPS copolymer using sulfuric acid to realize an amphiphilic blocky ionomer.[14,15] This researcher is however, interested in another functionalization reaction that would produce a copolymer with an alkyl halide side chain instead of an aryl halide functional group, without the use of a transition metal catalyst. The method shown in **Scheme 6.1**, has been reported by Jeon and co-workers[16] for sPS and proceeds by a Friedel-Crafts reaction between the

styrene phenyl ring and a bromoalkylated tertiary alcohol using triflic acid as a superacid catalyst. Using this approach, a labile primary halide is installed pendant to the polymer backbone. As will be discussed in **Appendix C**, nucleophilic substitution of the halide with an amine functional group would allow for covalent attachment of a ruthenium(II)-polypyridyl chromophore to a blocky brominated sPS copolymer for the purpose of investigating the effect of proximity on the chromophore's energy and electron transfer properties. The polymer support also provides a means to remove the chromophore from a solvent in order to investigate the chromophore stability after ultraviolet and visible light exposure.

Scheme 6.1. Bromoalkylation of sPS using a superacid catalyst.

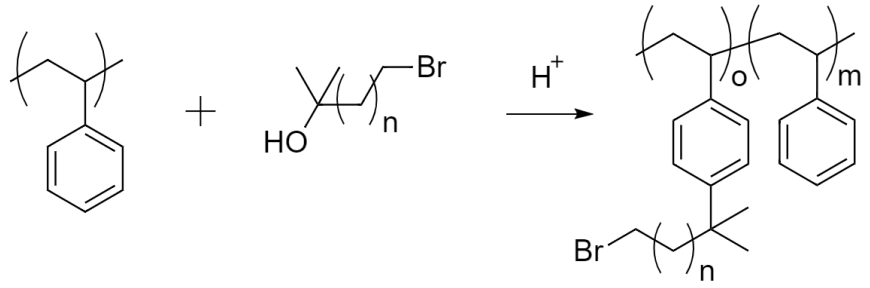

6.3. References

1. Daniel, C.; Avallone, A.; Guerra, G., Syndiotactic Polystyrene Physical Gels: Guest Influence on Structural Order in Molecular Complex Domains and Gel Transparency. *Macromolecules* **2006,** *39* (22), 7578-7582.
2. Prasad, A.; Mandelkern, L., The Thermoreversible Gelation of Syndiotactic Polystyrene. *Macromolecules* **1990,** *23* (23), 5041-5043.
3. Daniel, C.; Menelle, A.; Brulet, A.; Guenet, J.-M., Thermoreversible Gelation of Syndiotactic Polystyrene in Toluene and Chloroform. *Polymer* **1997,** *38* (16), 4193-4199.
4. Kobayashi, M.; Kozasa, T., Conformational Ordering Process on Physical Gelation of Syndiotactic Polystyrene/Solvent Systems Revealed by Time-Resolved Infrared Spectroscopy. *Appl. Spectrosc.* **1993,** *47* (9), 1417-1424.
5. Kobayashi, M.; Yoshioka, T.; Kozasa, T.; Tashiro, K.; Suzuki, J.; Funahashi, S.; Izumi, Y., Structure of Physical Gels Formed in Syndiotactic Polystyrene/Solvent Systems Studied by Small-Angle Neutron Scattering. *Macromolecules* **1994,** *27* (6), 1349-1354.
6. Talley, S. J.; Yuan, X.; Moore, R. B., Thermoreversible Gelation of Poly (Ether Ether Ketone). *ACS Macro Lett.* **2017,** *6*, 262-266.
7. Sundararajan, P. R., *Physical Aspects of Polymer Self-Assembly*. John Wiley & Sons, Inc.: 2016.
8. Prasad, A.; Marand, H.; Mandelkern, L., Supermolecular Morphology of Thermoreversible Gels Formed from Homogeneous and Heterogeneous Solutions. *J. Polym. Sci., Part B: Polym. Phys.* **1993,** *31* (12), 1819-1835.
9. Krishnaswamy, R. K.; Yang, Q.; Fernandez-Ballester, L.; Kornfield, J. A., Effect of the Distribution of Short-Chain Branches on Crystallization Kinetics and Mechanical Properties of High-Density Polyethylene. *Macromolecules* **2008,** *41* (5), 1693-1704.
10. Gowd, E. B.; Tashiro, K.; Ramesh, C., Structural Phase Transitions of Syndiotactic Polystyrene. *Prog. Polym. Sci.* **2009,** *34* (3), 280-315.
11. Shin, J.; Chang, Y.; Nguyen, T. L. T.; Noh, S. K.; Bae, C., Hydrophilic Functionalization of Syndiotactic Polystyrene Via a Combination of Electrophilic Bromination and Suzuki–Miyaura Reaction. *J. Polym. Sci., Part A: Polym. Chem.* **2010,** *48* (19), 4335-4343.

12. Howe, D. H.; McDaniel, R. M.; Magenau, A. J. D., From Click Chemistry to Cross-Coupling: Designer Polymers from One Efficient Reaction. *Macromolecules* **2017,** *50* (20), 8010-8018.
13. Shen, Q.; Hartwig, J. F., Palladium-Catalyzed Coupling of Ammonia and Lithium Amide with Aryl Halides. *J. Am. Chem. Soc.* **2006,** *128* (31), 10028-10029.
14. Fahs, G. B.; Benson, S. D.; Moore, R. B., Blocky Sulfonation of Syndiotactic Polystyrene: A Facile Route toward Tailored Ionomer Architecture Via Postpolymerization Functionalization in the Gel State. *Macromolecules* **2017,** *50* (6), 2387-2396.
15. Anderson, L. J.; Moore, R. B., Sulfonation of Blocky Brominated Peek to Prepare Hydrophilic-Hydrophobic Blocky Copolymers for Efficient Proton Conduction. *Solid State Ionics* **2019,** *336*, 47-56.
16. Jeon, J. Y.; Umstead, Z.; Kangovi, G. N.; Lee, S.; Bae, C., Functionalization of Syndiotactic Polystyrene Via Superacid-Catalyzed Friedel–Crafts Alkylation. *Top. Catal.* **2018,** *61* (7), 610-615.

Appendix A.

Sample Preparation and Instrument Methods

A.1. Sample preparation

Prior to characterization, all brominated syndiotactic polystyrene (sPS-co-sPS-Br) copolymer samples were purified by dissolving in 1,1,2,2-tetrachloroethane (TCE) at reflux, filtering hot to remove catalyst impurities, and precipitating by slow pouring into stirring methanol. Samples were ground into homogenous powders, washed by soxhlet extraction in hot methanol for *ca.* 24 h., and dried under vacuum at 70-110 °C for *ca.* 18 h. Gels were prepared in round bottom flasks in an oil bath to ensure uniform heating and complete dissolution. To prepare a 10 w/v% sPS/carbon tetrachloride (CCl_4) gel for analysis by ultra-small-angle X-ray scattering (USAXS) and small-angle X-ray scattering (SAXS) experiments, a thin-walled NMR tube was suspended within a pressure vessel in order to collect the warm solution prior to gelation, demonstrated in **Figure A.1**. After dissolution, the NMR tube was dipped into the solution using an external magnet and removed from heat to promote gelation. After the pressure vessel cooled to room temperature the tube was removed and sealed with heat to prevent solvent evaporation.

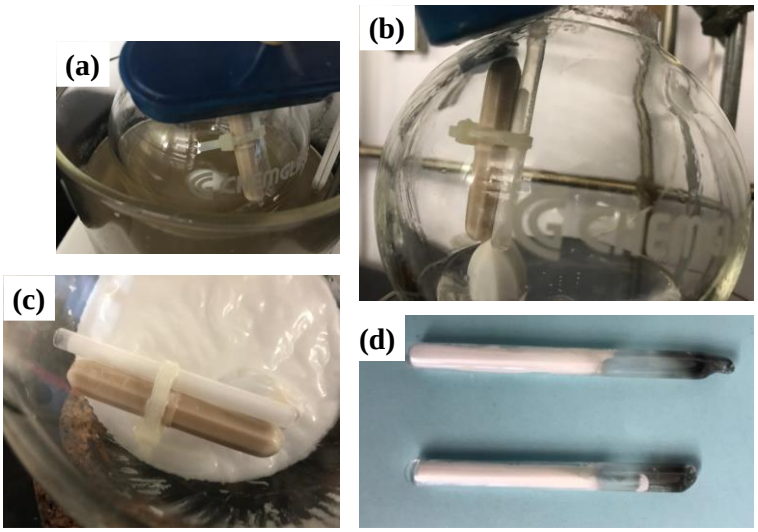

Figure A.1. Pictures demonstrating the preparation of a 10 w/v% sPS/CCl_4 gel inside of a pressure vessel. (a) The NMR tube is suspended in the pressure vessel (b) dipped into the solution (c) and removed from heat to promote gelation. (d) The tube is sealed with heat to prevent solvent evaporation.

A.2. Instrument methods

A.2.1. Thermogravimetric analysis

Thermogravimetric analysis (TGA) experiments were conducted using a TA Instruments TGA Q500 thermogravimetric analyzer. The sample mass ranged from 4-7 mg. Samples were heated from room temperature up to 600 °C at 10 °C min^{-1} under continuous nitrogen flow.

A.2.2. High temperature gel permeation chromatography

High temperature gel permeation chromatography (HT GPC) experiments were conducted using an Agilent 1260 Infinity II Multi-detector GPC/SEC system equipped with four detectors: refractive index, viscometry, and light scattering at 15° and 90°. Samples were prepared at approximately 0.2 w/v% by dissolving in 1,2,4-trichlorobenzene at elevated temperature with perturbation. The general instrument and sample parameters are provided in **Table A.1**.

Table A.1. Parameters for high temperature gel permeation chromatography experiments.

Sample Information	Injection number	1
	Injection volume (µL)	100
	Concentration (mg/mL)	2
	dn/dc (mL/g)	0.1
	UV extinction coefficient [(mg/mL)$^{-1}$][cm^{-1}]	1
	Mp (g/mol)	100000
	IV (dL/g)	0.5
	Mark-Houwink K ((10e-5) dL/g)	14.1
	Mark-Houwink Alpha	0.7
Sample Instrument Conditions	Eluent	1,2,4-trichlorobenzene
	Eluent refractive index	1
	Set flow rate (mL/min)	1
	LS wavelength (nm)	650
	Laser power (%)	0
	Set detector temperature (°C)	0
	Actual detector temperature (°C)	0
	Actual flow rate (mL/min)	0
Sample Collection Parameters	Number of channels	4
	Run length (mins)	45.01666667
	Delay time (secs)	0
	Sampling interval (secs)	1
	Number of data points	2701
Sample DLS Parameters	Eluent refractive index	1
	Eluent viscosity (P)	0.0089
	DLS correlator run time (secs)	5
	DLS Clip Time (µs)	100
	DLS R^2	0.4
Sample Channel Information	Detector type	Detector units
	RI	mV
	LS 15°	mV
	LS 90°	mV
	VS DP	mV

A.2.3. Differential scanning calorimetry

A.2.3.1. Materials, instrumentation, and sample preparation

Tzero aluminum pans and lids were purchased from TA Instruments. Differential scanning calorimetry (DSC) experiments were carried out using a TA Instruments DSC Q2000 under continuous nitrogen flow. The sample mass for copolymer thermal transition experiments ranged from 5-10 mg. For the crystallization kinetics experiments, the mass of each sample ranged from 8-14 mg.

A.2.3.2. DSC methods

Table A.2 shows the general method log to investigate the crystallizability and crystallinity of an sPS homopolymer and the brominated sPS copolymers. During method development, an initial annealing step at 140 °C was found to improve the overall reproducibility of the experiments, possibly by removing residual solvent from the sample. For the Blocky copolymers with at least 29 mol% Br, the annealing temperature was increased to 320 °C.

Table A.2. General method log for the differential scanning calorimetry thermal transitions experiments.

1: Ramp 20.00°C/min to 140.00°C
2: Equilibrate at 140.00°C
3: Isothermal for 3.00 min
4: Ramp 60.00°C/min to 40.00°C
5: Equilibrate at 40.00°C
6: Data storage: On
7: Ramp 10.00°C/min to 300.00°C
8: Mark end of cycle 0
9: Isothermal for 3.00 min
10: Mark end of cycle 0
11: Ramp 60.00°C/min to 0.00°C
12: Mark end of cycle 0
13: Equilibrate at 0.00°C
14: Mark end of cycle 0
15: Ramp 10.00°C/min to 300.00°C
16: Mark end of cycle 0
17: Isothermal for 3.00 min
18: Mark end of cycle 0
19: Ramp 10.00°C/min to 0.00°C
20: Mark end of cycle 0
21: Equilibrate at 0.00°C
22: Mark end of cycle 0
23: Ramp 10.00°C/min to 300.00°C
24: Mark end of cycle 0
25: Isothermal for 5.00 min
26: Mark end of cycle 0
27: Ramp 60.00°C/min to 190.00°C
28: Isothermal for 120.00 min
29: Mark end of cycle 0
30: Ramp 60.00°C/min to 120.00°C
31: Equilibrate at 120.00°C
32: Mark end of cycle 0
33: Ramp 10.00°C/min to 300.00°C
34: Mark end of cycle 0
35: Data storage: Off
36: End of method

Table A.3 shows the general method log to investigate the isothermal crystallization kinetics of the brominated sPS copolymers. For each sample, the crystallization temperatures and times were initially determined based on the anticipated copolymer microstructure and degree of functionalization. For the Blocky copolymers with at least 29 mol% Br, the annealing temperature was increased to at least 320 °C.

Table A.3. General method log for the differential scanning calorimetry crystallization kinetics experiments.

1: Ramp 20.00°C/min to 140.00°C
2: Equilibrate at 140.00°C
3: Isothermal for 3.00 min
4: Ramp 60.00°C/min to 40.00°C
5: Equilibrate at 40.00°C
6: Data storage: On
7: Ramp 20.00°C/min to 300.00°C
8: Mark end of cycle 0
9: Equilibrate at 300.00°C
10: Isothermal for 5.00 min
11: Mark end of cycle 0
12: Ramp 60.00°C/min to 195.00°C
13: Isothermal for 15.00 min
14: Mark end of cycle 0
15: Ramp 60.00°C/min to 0.00°C
16: Equilibrate at 0.00°C
17: Isothermal for 5.00 min
18: Mark end of cycle 0
…Repeat steps 7-18 at various crystallization temperatures and times (steps 12-13)
90: Mark end of cycle 0
91: Data storage: Off
92: End of method

The isothermal crystallization profiles (heat flow *versus* time) were analyzed using TA Instruments Universal Analysis software to ascertain crystallization half-times. An example of the method used to integrate the crystallization exotherm is shown in **Figure A.2**. First, the crystallization profile was zoomed in around the exothermic event to ensure the consistency in choosing the minimum and maximum times. The minimum was selected as the time at which the heat flow initially decreased. The maximum selected was the latest time before the linear peak integration would cross over the heat flow curve. The exothermic event was integrated using a running integral in area percent mode.

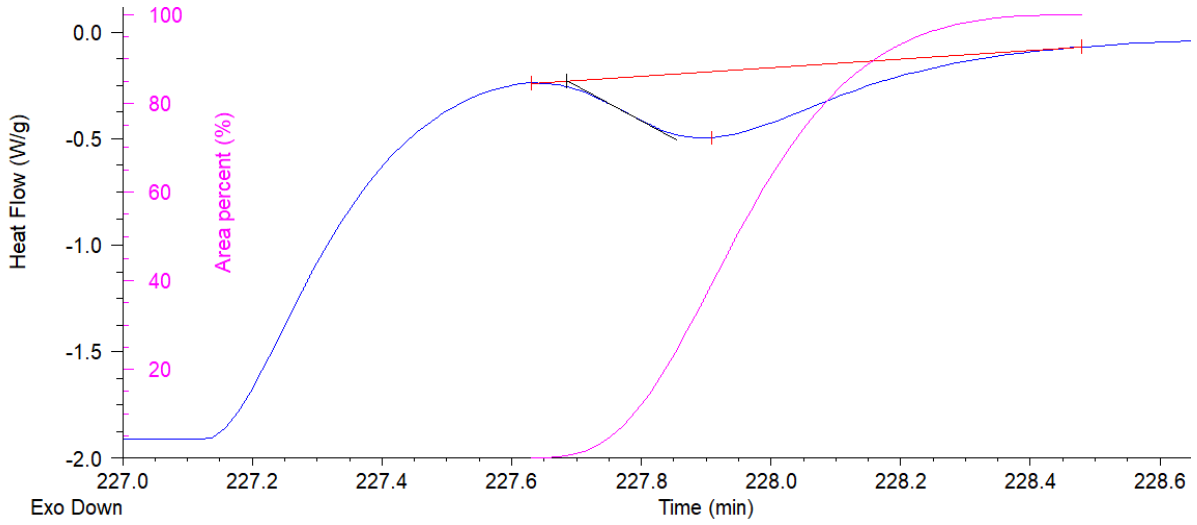

Figure A.2. DSC isothermal crystallization trace showing the method used to integrate the crystallization exotherm.

A.2.4. Wide-angle X-ray diffraction

Melt-crystallized samples were prepared for characterization by wide-angle X-ray diffraction (WAXD) experiments using the DSC instrument. Samples should be crushed into a homogeneous powder prior to analysis. WAXD experiments were performed using a Rigaku MiniFlex II X-ray diffractometer emitting X-rays with a wavelength of 0.154 nm (Cu K_α). Samples were scanned from 5° to 40° 2θ at a scan rate of 0.250° 2θ min^{-1} and a sampling window of 0.050° 2θ at a potential of 30 kV and a current of 15 mA. The WAXD data was analyzed using the PDXL 2 software package to obtain WAXD intensity *versus* 2θ profiles.

A.2.5. Nuclear magnetic resonance spectroscopy

A.2.5.1. Materials

Deuterated chloroform ($CDCl_3$) was purchased from Cambridge Isotope Laboratories, Inc. 1,1,2,2-tetrachloroethane-d_2 (TCE-d_2) was obtained from Sigma Aldrich®. NMR samples were prepared in 5 mm outer diameter, thin-walled (0.43 mm) 7” NMR sample tubes (class B glass) purchased from Wilmad-LabGlass.

A.2.5.2. One-dimensional NMR experiment methods

Quantitative ^{1}H NMR experiments were recorded at room temperature in $CDCl_3$ on an Agilent U4-DD2 400 MHz spectrometer using the parameters summarized in **Table A.4**. Mestrelab Research's MestReNova software was used to process the NMR spectra. All spectra were phase corrected using the automatic phase correction option, baseline corrected using the Bernstein Polynomial Fit method (polynomial order = 3), and referenced to $CDCl_3$ (chemical shift = 7.260 ppm). To prepare a sample for ^{1}H NMR, *ca.* 10 mg of sample was dissolved in 610 μL $CDCl_3$ with stirring in a one-dram vial at ca. 50 °C and transferred by pipet to an NMR sample tube.

Table A.4. Quantitative ^{1}H NMR experiment parameters.

Parameter	Value
Pulse Sequence	s2pul
Experiment	1D
Number of Scans	64
Receiver Gain	44 dB
Relaxation Delay	5 s
Pulse Width	1.6622 μs
Acquisition Time	2.5559 s
Spectrometer Frequency	399.87 MHz
Spectral Width	6410.3 Hz
Lowest Frequency	-796.3 Hz
Nucleus	1H

Samples were prepared for ^{13}C NMR, by dissolving about *ca.* 50 mg of sample in 530 uL TCE-d_2 with stirring in a one-dram vial at *ca.* 100 °C and transferred by pipet to an NMR sample tube. Quantitative ^{13}C NMR experiments were recorded at room temperature in TCE-d_2 on a Bruker Avance II 500 MHz NMR spectrometer equipped with an LN2 prodigy cryogenic BBO probe using the parameters summarized in **Table A.5**. Mestrelab Research's MestReNova software was used to process the NMR spectra. All spectra were phase corrected using the

automatic phase correction option, baseline corrected using the Whittaker Smoother method with a Filter of 17.21 Hz and autodetected Smooth Factor, and referenced to TCE-d_2 (chemical shift = 73.780 ppm).

Table A.5. Quantitative ^{13}C NMR experiment parameters

Parameter	Value
Pulse Sequence Inverse-gated decoupling experiment that provides a decoupled spectrum without NOE	zgig30
Parameter Set	C13IG
Experiment	1D
Number of Scans	7680
Receiver Gain	215.1
Relaxation Delay	6 s
Pulse Width	11 μs
Acquisition Time	1.7433 s
Spectrometer Frequency	125.78 MHz
Spectral Width	18797 Hz (150 ppm)
Lowest Frequency	3266.9
Transmitter Frequency Offset (O1P)	95 ppm
Nucleus	13C

A.2.5.3. Two-dimensional NMR experiment methods

For all two-dimensional NMR experiments, the NMR spectra were processed using Mestrelab Research's MestReNova software. All spectra were phase corrected using the automatic phase correction option, baseline corrected using the Bernstein Polynomial Fit method (polynomial order = 3), and referenced to the appropriate solvent. Manual phase correction and the graphic reference option were performed as required. Samples were prepared for the two-dimensional homonuclear gradient double quantum filtered correlation spectroscopy (gDQCOSY) experiments by dissolving *ca.* 10 mg of sample in 610 μL solvent with stirring in a one-dram vial at ca. 50 °C, followed by transferring by pipet to an NMR sample tube. The gDQCOSY

experiments were recorded in either $CDCl_3$ or TCE-d_2 on an Agilent U4-DD2 400 MHz spectrometer using the parameters summarized in **Table A.6**.

Table A.6. gDQCOSY experiment parameters.

Parameter	Value
Pulse Sequence	gDQCOSY
Experiment	DQF-COSY
Number of Scans	8
Receiver Gain	40 dB
Relaxation Delay	1 s
Pulse Width	6.8 μs
Acquisition Time	0.5636 s
Spectrometer Frequency	399.87 MHz, 399.87 MHz
Spectral Width	3633.7 Hz 3633.7 Hz
Lowest Frequency	-402.0 Hz, -389.9 Hz
Nucleus	1H, 1H

Samples were prepared for the two-dimensional heteronuclear NMR experiments by dissolving about *ca.* 50 mg of sample in 530 uL TCE-d_2 with stirring in a one-dram vial at *ca.* 100 °C and transferred by pipet to an NMR sample tube. Gradient heteronuclear single quantum coherence (gHSQC) recorded at room temperature in TCE-d_2 on an Agilent U4-DD2 400 MHz spectrometer using the parameters summarized in

Table A.7. Parameters for the gHSQC experiments.

Parameter	Value
Pulse Sequence	gHSQCAD
Experiment	HSQC-EDITED
Number of Scans	8
Receiver Gain	24 dB
Relaxation Delay	1 s
Pulse Width	6.8 μs
Acquisition Time	0.1597 s
Spectrometer Frequency	399.87 MHz, 100.56 MHz
Spectral Width	6410.3 Hz, 20110.6 Hz
Lowest Frequency	-1300.2 Hz, -1747.3 Hz
Nucleus	1H, 13C

Band-selective gradient heteronuclear multiple bond correlation (bsgHMBC) were recorded at room temperature in TCE-d_2 on an Agilent U4-DD2 400 MHz spectrometer using the parameters summarized in **Table A.8**.

Table A.8. Parameters for the bsgHMBC experiments.

Parameter	Value
Pulse Sequence	bsgHMBC
Experiment	Unknown
Number of Scans	32
Receiver Gain	24 dB
Relaxation Delay	1 s
Pulse Width	6.8 μs
Acquisition Time	0.1597 s
Spectrometer Frequency	399.87 MHz, 100.56 MHz
Spectral Width	6410.3 Hz, 4021.9 Hz
Lowest Frequency	-1304.4 Hz, 10903.0 Hz
Nucleus	1H, 13C

Appendix B.

Additional Results and Discussion

B.1. Introduction

This Appendix includes experiments, results, and discussions related to the brominated syndiotactic polystyrene (sPS-co-sPS-Br) copolymers that were not otherwise discussed in Chapters 3-6. These experiments investigate the stability and homogeneity of the gel-state (Blocky) brominated copolymers prepared from a 10 w/v% sPS/carbon tetrachloride (CCl_4) gel (CaT-x%, where x = 6, 15, 21, and 29) or a 10 w/v% sPS/chloroform ($CHCl_3$) gel (CH-x%, where x = 6, 17, 19, and 32). For an explanation of the bromination reaction conditions see **Chapter 2**.

B.2. Results and Discussion

The molecular weight and polydispersity of the brominated copolymers was investigate using high temperature gel permeation chromatography (HT GPC) conducted on an Agilent 1260 Infinity II Multi-detector GPC/SEC system equipped with four detectors: refractive index, viscometry, and light scattering at 15° and 90°. Prior to analysis, samples were prepared at approximately 0.2 w/v% by dissolving in 1,2,4-trichlorobenzene at elevated temperature with perturbation. A calibration curve was constructed using nine polystyrene standards ranging in molecular weight (M_p) from 1,440−3,187,000 g mol^{-1}. The calibration curve is provided in **Figure B.1**, along with the molecular weight at peak maximum (M_p) and polydispersity index (PDI) results for the sPS homopolymer and the brominated copolymers. The sPS homopolymer exhibited an M_p value of close to 400,000 g mol^{-1} and a PDI value of 2.5, as anticipated based on the sample specifications provided by Dow Chemical Company. In general, the M_p values of the Blocky

sPS/CCl_4 and sPS/$CHCl_3$ and the solution-state (Random) copolymers were smaller than that of the pure sPS homopolymer, ca. 335,000−365,000 g mol^{-1}, and the PDI values were in the range from 2−3. While the decrease in M_p is unexpected and suggests that post-polymerization bromination resulted in chain degradation, which is consistent with the observations of Shin and co-workers,[1] there was no evidence of a second population of lower molecular weight polymer eluting from the GPC column at longer time. It is worth noting that when these data were being collected there were several issues with the HT GPC instrument. For each sample, the detector response was less than 100 mV and typically around 20 mV. In addition, the light scattering and viscometry detectors were unreliable. We recommend reanalyzing these samples in the future using another HT GPC instrument.

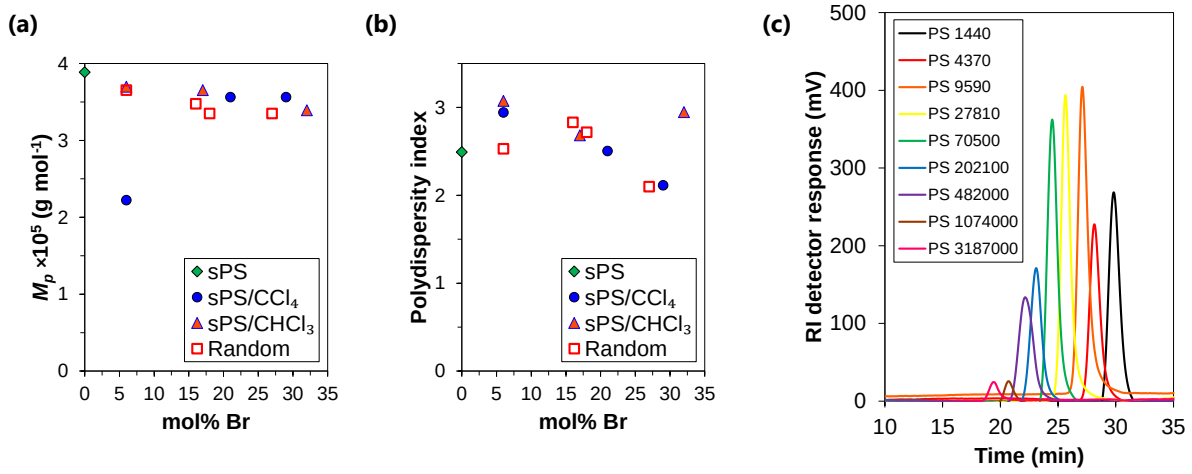

Figure B.1. Results from the HT-GPC analysis for the sPS homopolymer and the gel-state Blocky sPS/CCl_4 and sPS/$CHCl_3$ and solution-state Random copolymers. (a) Molecular weight of the peak maximum (M_p) and (b) polydispersity index (PDI) with respect to Br-content, and (c) the calibration curve prepared using polystyrene (PS) standards. The molecular weight of the standards is included in the sample name.

Thermogravimetric analysis (TGA) was used to investigate the thermal stability of the brominated copolymers in inert atmospheric conditions. TGA experiments were recorded on a TA Instruments TGA Q500 thermogravimetric analyzer with a heating profile from room temperature up to 600 °C at 10 °C min^{-1} under continuous nitrogen flow. The TGA results and decomposition temperatures at a weight loss of 5 wt% ($T_{d,5\%}$) for the sPS homopolymer and the Random and

Blocky sPS/CCl_4 copolymers are reported in **Figure B.2**. The pure sPS homopolymer and brominated copolymers exhibit single stage decomposition profiles. All of the samples decompose between 350−400 °C. In addition, the $T_{d,5\%}$ values are similar for all samples and do not show a trend with respect to degree of bromination, as expected based on the similar decomposition temperatures reported for sPS and brominated sPS copolymers in the literature.[2,3] For the Random R-6% sample, a slightly higher $T_{d,5\%}$ was observed relative to the other samples and this sample did not decompose fully, which suggests that R-6% contained a thermally stable contaminant. Thus, the purification process appears to be very important to the polymer thermal stability.

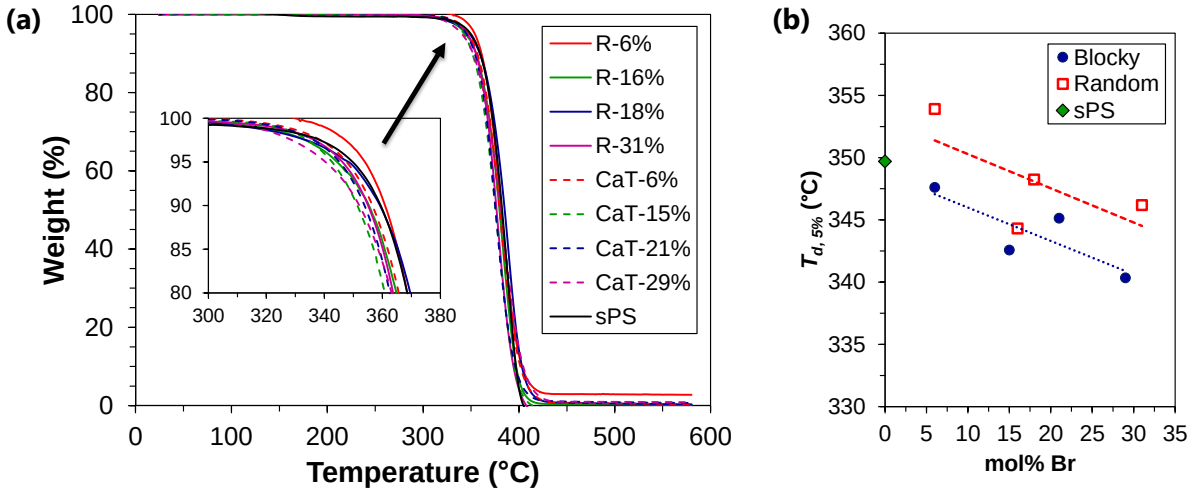

Figure B.2. Thermogravimetric analysis of the sPS homopolymer and the Random and Blocky copolymers. (a) Weight percent *versus* temperature (Inset: weight percent at temperatures close to the decomposition temperature) (b) decomposition temperature at a weight loss of 5 wt% ($T_{d,5\%}$) with respect to Br-content.

The nuclear magnetic resonance (NMR) spectrum provides an overall average of the copolymer microstructure, i.e., the distribution of short-range comonomer sequences along the polymer chains; however, NMR cannot be used to distinguish between heterogeneities along or among polymer chains.[4] Consequently, a mixture of pure sPS and a highly brominated sPS copolymer that contains an overall Br-content similar to that of a brominated copolymer sample would exhibit the same NMR spectrum as the brominated copolymer sample if their overall microstructures were also the same. To investigate the copolymer microstructure of the Blocky

copolymers, a mixture of pure sPS and a 47 mol% Br random copolymer, R-47%, was prepared with a total Br-content of 25 mol%, designated as M-25%. **Figure B.3** shows the ^{1}H NMR spectrum of random R-47%, the mixture M-25%, the sPS homopolymer, and the Blocky CaT-29% and Random R-31% copolymers. The spectrum of the sPS homopolymer contains four sharp and intense peaks from the methylene, methine, and aromatic protons. Compared to pure sPS, the brominated sPS copolymers exhibit new proton resonances at 1.23, 1.55−1.75, 6.27−6.38, and 7.11−7.22 ppm, corresponding to the methylene (H(b′)) and methine (H(a′)) protons, and the aromatic protons (H(2′) and H(3′)) of brominated styrene (Br-Sty) monomers, respectively. In the aliphatic region of the R-47% NMR spectrum, two distinct broad peaks are present in the range from 1.55−1.75 ppm, demonstrating that Br-Sty units exist in two distinct environments along the chain. Based on the anticipated high prevalence of Br-Sty dyads (BB) and triads (BBB) in the R-47% copolymer, the peak at ca. 1.70 ppm is assigned to a Br-Sty unit with one Br-Sty neighbor (H(a_1')) and the peak at ca. 1.60 ppm is assigned to a Br-Sty unit with two Br-Sty neighbors (H(a'_2)). Remarkably, the H(a_1') and H(a_2') peaks in the mixture M-25% and Blocky CaT-29% copolymer are similar in intensity. In addition, both the M-25% and CaT-29% samples contain sharp proton resonances similar to that of pure sPS and indicative of a high prevalence of styrene triads (SSS). In contrast, the Random R-31% sample contains broad un-brominated styrene resonances, consistent with a low prevalence of pure homopolymer segments, as expected for a random copolymer. It is worth noting here that multiple NMR samples of the same brominated copolymers were found to produce consistent spectra, ruling out heterogeneities as a possible source of the disparities between the samples. Thus, these results strongly suggest that the Blocky CaT-29% copolymer has a similar copolymer microstructure to that of the M-25% mixture. The

homogeneity of the CaT-29% copolymer chains, however cannot be determined based on the NMR spectrum.

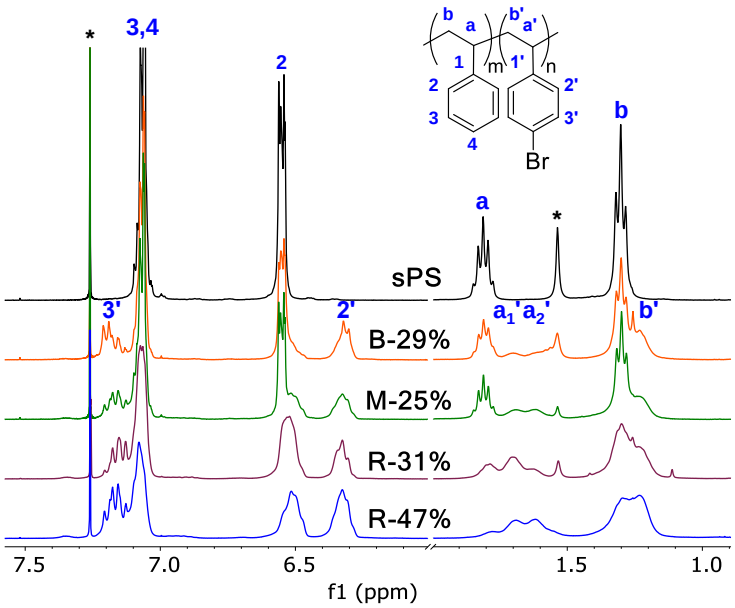

Figure B.3. ^{1}H NMR spectra of the sPS homopolymer and the Blocky CaT-29%, Random R-31% and R-47%, and a mixture of samples R-47% and sPS, denoted as M-25%. For comparison, spectra are referenced to $CDCl_3$ and normalized over 6.25−6.65 ppm. The asterisks (*) indicate solvent resonances.

To investigate the homogeneity of the Blocky CaT-29% copolymer, the thermal properties of the brominated copolymers and the mixture M-25% were analyzed using differential scanning calorimetry (DSC). The M-25% sample was prepared from a solution of the R-47% copolymer and the sPS homopolymer by drying in air followed by drying under vacuum to remove the solvent. DSC thermograms of the sPS homopolymer, Blocky CaT-29% and Random R-31% copolymers, and the mixture M-25% after slow cooling from the melt (300 °C) to 0 °C at −10 °C min^{-1} are compared in **Figure B.4**. The heating trace of pure sPS displays two endothermic events, the glass transition at 100 °C and an intense melting endotherm at 272 °C. At 31 mol% Br, the Random R-31% copolymer does not crystallize under the thermal conditions of the experiment, as expected for a brominated sPS copolymer with a high Br-content. Bromine groups act as physical defects along the polymer chains, limiting the copolymer crystallizability. Remarkably, the Blocky CaT-29% copolymer exhibits cold crystallization, T_c, at ca. 165 °C, followed by a low temperature

melting endotherm, T_m, at ca. 208 °C, attributed to the melting of crystallites composed of pure sPS segments. The depression in T_m is a consequence of shorter crystallizable chain segments and thus thinner crystallites. The mixture M-25% displays one T_m at 272 °C, in excellent agreement with pure sPS. The absence of a second melting endotherm in the M-25% heating trace demonstrates that the brominated copolymer component of the mixture was unable to crystallize upon slow cooling and subsequent heating. In addition, the ability of the pure sPS component to form thick crystallites was unaffected by the presence of the brominated copolymer component. These data strongly suggest that the Blocky CaT-29% copolymer is a homogeneous mixture of brominated copolymer chains with long segments of un-functionalized styrene "blocks" and segments of randomly functionalized "blocks" in a blocky microstructure. While the results are not expected to change, it would be worth reanalyzing the mixture in the future, beginning with the preparation of a new sample.

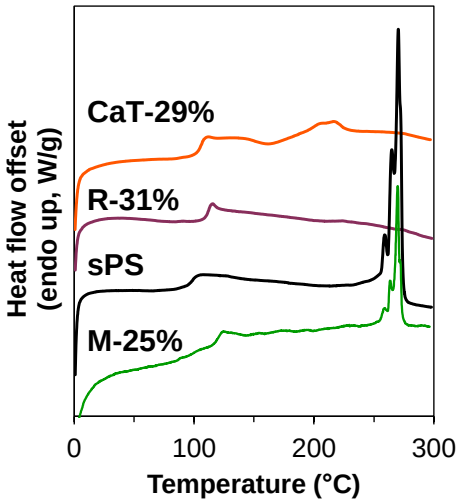

Figure B.4. DSC heating traces of the sPS homopolymer, the Blocky CaT-29% and Random R-31% copolymers and a mixture of a random R-47% copolymer and pure sPS, denoted as M-25% after slow cooling from the melt (300 °C) at −10 °C min^{-1}. Heating rate: 10 °C min^{-1}.

The crystallizability of Br-Sty segments in the Blocky CaT-29% and CH-32% copolymers was investigated by preparing a highly brominated random copolymer using the solution state

bromination method described in **Chapter 2**. The random copolymer, designated as R-93%, contained 93 mol% *p*-bromostyrene units, calculated from the ^{1}H NMR spectrum shown in **Figure B.5**

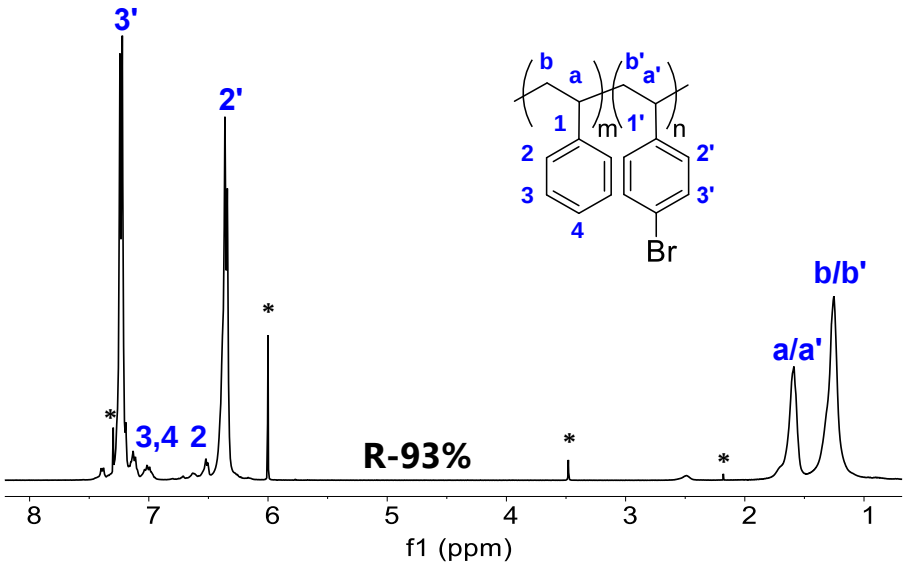

Figure B.5. ^{1}H NMR spectrum of a highly brominated random copolymer, designated as R-93%. The asterisks (*) indicate solvent resonances.

The crystallization behavior, measured by DSC, and wide-angle X-ray diffraction (WAXD) profiles of the random R-93% copolymer and the sPS homopolymer are compared in **Figure B.6**. Prior to analysis, the samples were washed by soxhlet extraction in hot methanol for ca. 24 h and dried under vacuum at 70 °C for ca. 18 h. In the first heat of the sPS homopolymer, crystallite melting is observed at ca. 272 °C. Conversely, the R-93% copolymer exhibits an endothermic event at ca. 306 °C that is well above the equilibrium melting temperature of pure sPS of 282 °C ($T^{\circ}_{m,\alpha}$) (see **Figure B.6a**).[5] Upon cooling R-93% from the melt, a crystallization exotherm is observed at ca. 257 °C, above the crystallization temperature of pure sPS at 238 °C (see **Figure B.6b**). The crystallization and melting in R-93% is attributed to the melting of crystallites composed of Br-Sty segments. The WAXD profile of R-93% after rapid cooling from the melt at −60 °C min^{-1} shows a crystalline reflection at 2θ = 19.4° that is not observed in the

WAXD profile of pure sPS (see **Figure B.6c**). This crystallization reflection is consistent with new reflection observed in the WAXD profiles of the CaT-29% and CH-32% copolymers and confirms that Br-Sty segments in the gel-state functionalized copolymers with high Br-content are crystallizable.

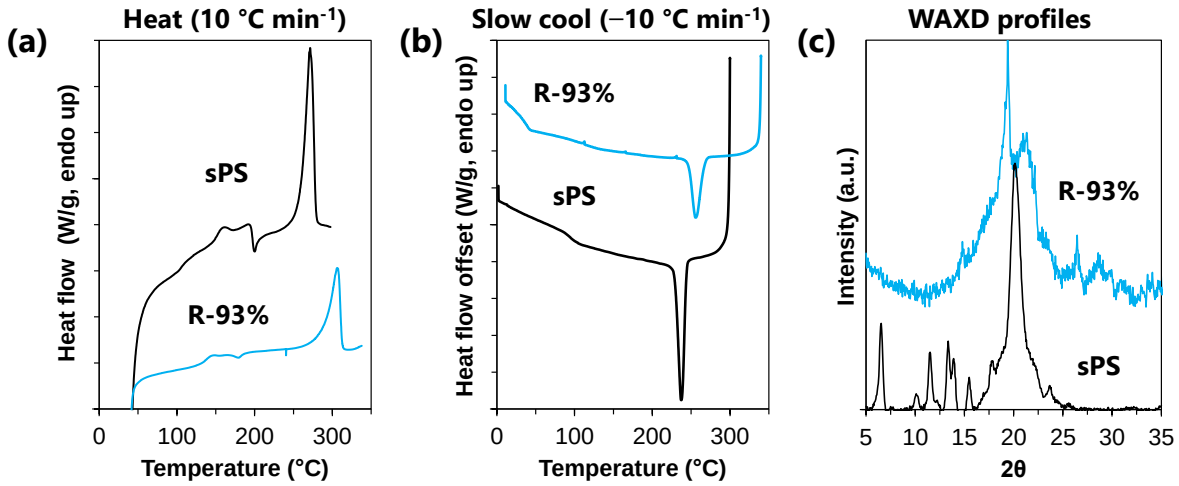

Figure B.6. (a) Heat after annealing at 140 °C for 3 min and cooling to 40 °C, (b) slow cool after the heating trace, and (c) WAXD profiles, of the sPS homopolymer and the random R-93% copolymer. The WAXD profile of R-93% is after rapid cooling from the melt at (−60 °C min^{-1}). The WAXD profile of sPS is after 2 h melt crystallization at 190 °C.

B.3. References

1. Shin, J.; Chang, Y.; Nguyen, T. L. T.; Noh, S. K.; Bae, C., Hydrophilic Functionalization of Syndiotactic Polystyrene Via a Combination of Electrophilic Bromination and Suzuki–Miyaura Reaction. *J. Polym. Sci., Part A: Polym. Chem.* **2010,** *48* (19), 4335-4343.
2. Şenocak, A.; Alkan, C.; Karadağ, A., Thermal Decomposition and a Kinetic Study of Poly (Para-Substituted Styrene) S. *Am J Analyt Chem* **2016,** *7* (03), 246.
3. Boinon, B.; Abboud, W.; Bouras, A.; Ainad-Tabet, D., Kinetics of the Thermal Degradation of Partially Para-Brominated Polystyrenes. *Polym. Degrad. Stab.* **1993,** *42* (1), 75-80.
4. Gurarslan, R.; Gurarslan, A.; Tonelli, A. E., Characterizing Polymers with Heterogeneous Micro- and Macrostructures. *J. Polym. Sci., Part B: Polym. Phys.* **2015,** *53* (6), 409-414.
5. Woo, E. M.; Sun, Y. S.; Yang, C. P., Polymorphism, Thermal Behavior, and Crystal Stability in Syndiotactic Polystyrene Vs. Its Miscible Blends. *Prog. Polym. Sci.* **2001,** *26* (6), 945-983.

Appendix C.

Basic Principles of Quantitative Nuclear Magnetic Resonance Spectroscopy

C.1. Introduction to nuclear magnetic resonance

Nuclear magnetic resonance (NMR) spectroscopy was used to investigate the copolymer microstructure, i.e., the distribution of short-range comonomer sequences along the polymer chains. This dissertation relies heavily on the analysis of quantitative ^{13}C NMR spectra. In **Chapter 3**, a comonomer sequencing method was developed that used quantitative ^{13}C NMR and two-dimensional NMR spectroscopy techniques. This method was used to analyze the copolymer microstructure and comonomer sequence of brominated syndiotactic polystyrene (sPS-*co*-sPS-Br) copolymers. The purpose of this chapter is to introduce the basic principles and theory that are relevant to quantitative NMR spectroscopy and the general requirements for optimizing the accuracy of peak integration. For additional information, the reader may be interested in T. D. W. Claridge's 2016, *High-Resolution NMR Techniques in Organic Chemistry*[1] and R.N. Ibbett's 1993, *NMR Spectroscopy of Polymers.*[2] For a detailed discussion of the method used to assign resonances in the copolymer NMR spectrum to specific comonomer sequences, see the introduction of **Chapter 3**.

C.1.1. Nuclear spin and magnetic moment

The nucleus contains neutrons and positively charged protons that spin, giving the nucleus angular momentum, *P*, which generates a magnetic field. Thus, the nucleus can behave like a tiny magnet that can interact with an applied external magnetic field. Nuclear spin defines the total angular momentum of the nucleus and is represented by the symbol, *I*. The nuclear spin, *I*, is determined by the number of unpaired protons and neutrons in the nucleus, where each unpaired

subatomic particle contributes a spin of ½. For example, the ^{13}C isotope contains six protons, six neutrons, and one unpaired neutron, and has an $I = ½$. The much more abundant ^{1}H isotope also has a nuclear spin of ½, resulting from its one proton and zero neutrons. The ^{12}C isotope possesses the same number of protons and neutrons and thus has zero net nuclear spin, $I = 0$. Nuclei with I value greater than zero have net spin and their angular momentum (P) and charge give rise to an associated magnetic moment, μ, defined by **Equation 1**.

$$\mu = \gamma P \quad \textbf{(1)}$$

The γ term is the magnetogyric ratio of a given nuclide, a constant that provides a measure of the nuclide's magnetic strength. The γ values for ^{1}H and ^{13}C are 26.75×10^{7} rad $T^{-1}s^{-1}$ and 6.73×10^{7} rad $T^{-1}s^{-1}$ (T = Tesla), respectively.[1] Expressed as a ratio, γ_H/γ_C is ca. 4. Thus, the magnetic strength of a ^{1}H nucleus is approximately four times greater than that of a ^{13}C nucleus. The magnetic moment is a measure of the tendency of the nucleus' axis of rotation to align in the direction of an external magnetic field.[3]

C.1.2. Basic principles of nuclear magnetic resonance The angular momentum, P, and magnetic moment, μ, are vector quantities. Depending on the nuclide, the magnetic moment has a specific number of allowed orientations, designated as spin states. The number of spin states is equal to $2I + 1$. Thus, $I = ½$ (spin-½) nuclei have two possible spin states, which are conventionally denoted as α ($I_z = +½$) and β ($I_z = -½$). In the absence of an external magnetic field, the magnetic moments of the nuclei are randomly oriented, and the spin states are degenerate, demonstrated in **Figure C.1(a)**. Conversely, when placed in an applied external magnetic field (B_0), the magnetic moments orient themselves relative to the field in the quantized spin states. **Figure C.1(b)** shows an example of spin-½ nuclei in an applied external magnetic field, where the magnetic moments of the nuclei are oriented either in the direction of B_0, the lower energy spin state (α), or opposite to B_0, the

higher energy spin state (β). The images in **Figure C.1** are a simplification of the classical mechanical model of nuclear spin.

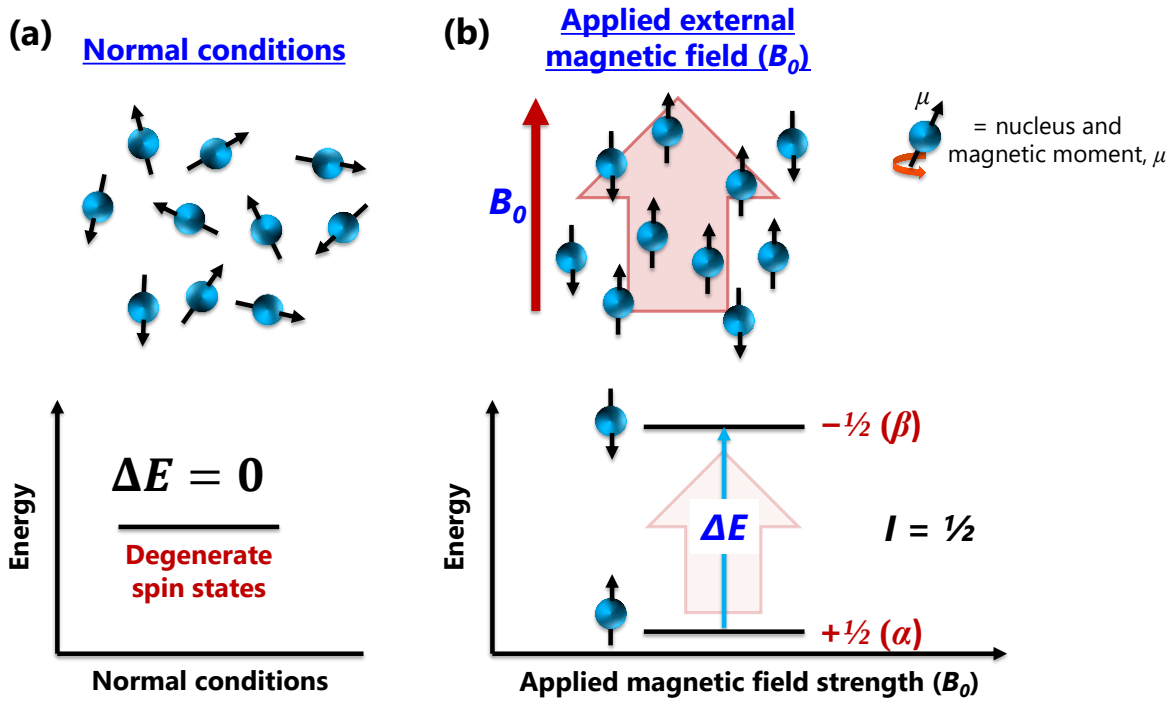

Figure C.1. (top) Pictorial representations of nuclei and (bottom) energy diagrams for spin-½ nuclei during (a) normal conditions where the magnetic moments are randomly oriented and (b) when the nuclei are placed in an applied external magnetic field, B_o, where the magnetic moments align relative to B_o in quantized spin states.

While **Figure C.1(b)** depicts the direction of the magnetic moments as either parallel or antiparallel to B_0, the torque exerted by B_0 on the nucleus actually causes the magnetic moment to move in precession, i.e., in a circular path, about the direction of the magnetic field. This motion is analogous to that of a spinning top. The angular velocity (ν) of the precession, also called the Larmor frequency or resonance frequency, is dependent on the magnetogyric ratio, γ, of the nuclide and the strength of B_0, and is defined in **Equation 2**.

$$\boldsymbol{\nu = \frac{\gamma B_0}{2\pi}} \qquad \textbf{(2)}$$

The operating frequency of an NMR spectrometer is defined by the resonance frequency of the ^{1}H nucleus. For example, ^{1}H nuclei in a 400 MHz spectrometer resonate at 400 MHz. The ^{13}C nuclei

in the same spectrometer resonate at 100 MHz because the magnetogyric ratio of ^{13}C is one-fourth that of ^{1}H.

The resonance frequency is directly related to the energy difference between the spin states, since $\Delta E = h\nu$, where h is Plank's constant. This relationship demonstrates that an $I > 0$ nucleus positioned in an applied external magnetic field and subsequently exposed to radiation possessing the same energy as ΔE, can absorb that energy, producing a change, often referred to as a "flip," in its nuclear spin from the low energy state to the high energy state. This perturbation of the nucleus that is driven by selective absorption of electromagnetic radiation is called nuclear magnetic resonance (NMR) and is depicted in **Figure C.2**. Nuclides with I > 0 values that experience NMR are defined as NMR active.

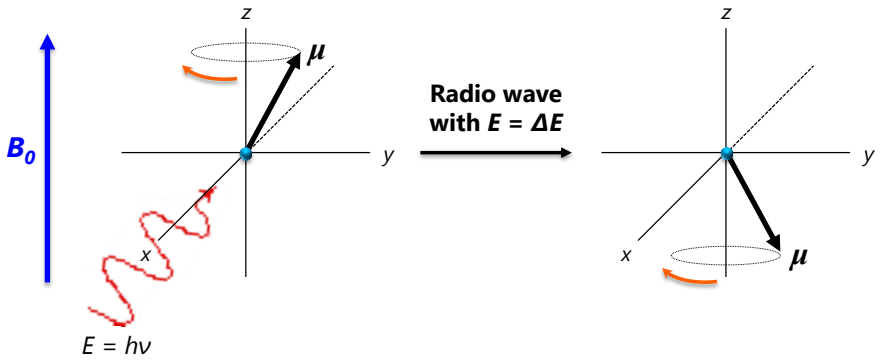

Figure C.2. Vector model of the nuclear magnetic resonance phenomenon in which a nucleus that is placed in an applied external magnetic field (B_0) absorbs high frequency radio waves that possess the same energy as ΔE, resulting in a change in the spin state of the nucleus.

The resonance frequency of an NMR active nucleus, and thus the energy difference between the spin states, is also dependent on the nucleus' electronic environment. Electrons, like protons and neutrons, possess spin and act as a cloud of miniscule magnets surrounding the nucleus. The electron cloud produces a localized magnetic field that opposes the direction of B_0, effectively shielding the nucleus from the full effect of the applied external magnetic field. Atoms and groups of atoms that are directly attached or in close proximity to the nucleus can also shield

the nucleus from B_0. As the effective magnetic field, B_{eff}, experienced by the nucleus decreases, the resonance frequency of the nucleus decreases and the energy difference between the spin states decreases. Conversely, neighboring atoms can also draw the electron cloud away from its nucleus, exposing the nucleus to more of B_0 and increasing ΔE. The resonance frequencies of NMR active nuclides are therefore sensitive to the structure of the molecules within a sample. These slight changes in resonance frequency between nuclides in different electronic environments can be detected using NMR spectroscopy.

C.2. Nuclear magnetic resonance spectroscopy

NMR spectroscopy is a technique used to obtain detailed information about a molecule's structure. In an NMR spectroscopy experiment, a sample is placed in an applied external magnetic field (B_0) in a spinning sample holder to optimize the sample homogeneity and magnetic field homogeneity. The NMR active nuclei exist in the magnetic field at thermal equilibrium and orient with respect to B_0 in the low or high energy spin states according to a Boltzmann distribution,[4] in which there is a slightly greater probability that a nuclear spin will orient toward the low energy state. This majority can be represented as a net magnetization vector, M, in the direction of B_0, shown in **Figure C.3**. The net magnetization exists only in the direction of the magnetic field (longitudinal direction) because the nuclear spins precess out of phase. Thus, the phase incoherence produces zero net magnetization in the x,y plane (transverse direction). When the sample is exposed to a polychromatic radiofrequency pulse, B_1, possessing the same frequencies as the resonance frequencies of the nuclei in the sample, the radiation is absorbed causing the nuclear spins to precess in phase and reducing the population difference between spin states, demonstrated on the right in **Figure C.3**. The phase coherent bundle precesses at the resonance

frequency of the nuclei, moving the net magnetization into the x,y plane, represented as M_y. The magnitude of M_y depends on the initial population difference between the spin states. As the nuclear spins relax ("spin flip") from the excited state to the ground state, the precessing and decaying M_y component of the net magnetization vector is detected as a voltage that is induced in a pickup coil surrounding the sample holder.

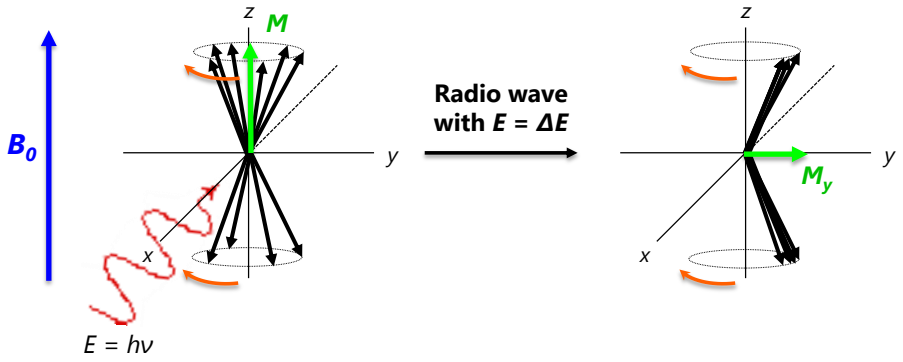

Figure C.3. Vector model of multiple nuclei in a sample before a radiofrequency pulse when the magnetic moments are out of phase and after a radiofrequency pulse, demonstrating nuclear magnetic resonance and the oscillation of the magnetic moments in phase.

Relaxation of nuclear spins occurs through interactions between the nuclei in the excited state and local molecular motions that are oscillating at the same resonance frequency. This relaxation process, called *spin-lattice (longitudinal) relaxation*, T_1, results in a change in the spin state population that reestablishes the equilibrium state. The "spin flipped" magnetic moments enter the ground state slightly out of phase with the oscillating phase coherent bundle, which lowers the magnitude of M_y. In addition, nuclear spins oscillating in the original bundle tend to precess at slightly faster or slower frequencies than the average resonance frequency due to different local magnetic fields experienced by the nuclei as well as energy exchange processes between spins (i.e., mutual "spin flips"). Different resonance frequencies result from inhomogeneities in B_0 (reduced by shimming) and intramolecular and intermolecular interactions in the sample. Loss of phase coherence through this relaxation process, called *spin-spin*

(transverse) relaxation, T_2, occurs in the transverse direction and returns the net magnetization vector to the longitudinal direction.

The NMR signal is recorded after the radiofrequency (RF) pulse as a voltage response in the time domain and is termed the free induction decay (FID). A simple FID signal is shown in **Figure C.4**. The FID begins as an intense, oscillating sinusoidal wave that decays exponentially over time due to the loss of magnetization in the x,y plane. The FID is digitized and Fourier transformed to represent the NMR signal as a frequency domain spectrum, shown on the right in **Figure C.4**. The frequency scale is reported as a chemical shift, where the resonance frequency of the nucleus is referenced to a standard in the magnetic field and is therefore independent of B_0. Chemical shift is calculated as the difference between the absolute resonance frequency of the sample (ν_{sample}) and the absolute resonance frequency of a reference (ν_{ref}) divided by ν_{ref} and is expressed in parts per million (ppm). The NMR spectrum in **Figure C.4** contains a single resonance (peak), demonstrating that all of the nuclides of interest in the sample are resonating at the same frequency and must therefore exist in the same electronic environment. As discussed previously, most samples contain NMR active nuclei that exist in different electronic environments, based on the molecular structure of the sample. These chemically distinct nuclei precess at their respective resonance frequencies that can be observed as multiple peaks in the NMR spectrum.

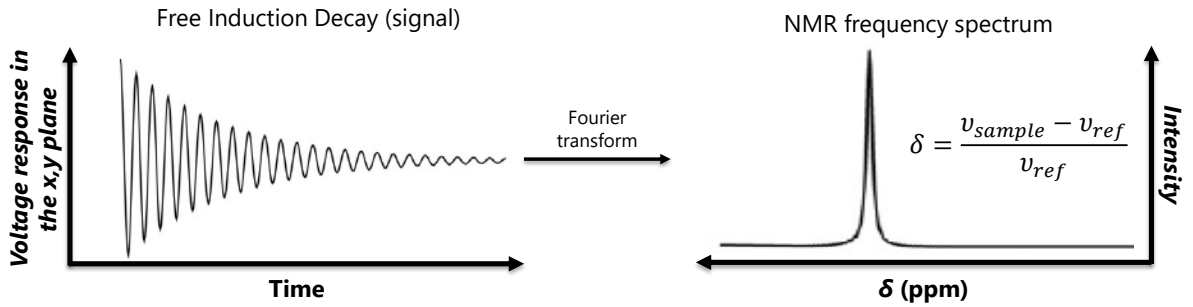

Figure C.4. (left) The observable free induction decay NMR signal and (right) the intensity *versus* frequency spectrum of the NMR signal produced after digitization and a Fourier transform.

The peaks in the NMR spectrum fit to a Lorentzian line shape, based on the exponential decay of the FID. The linewidth of each peak is inversely proportional to the spin-spin relaxation time, T_2, since rapid loss of phase coherence (short T_2) corresponds to greater frequency differences between the nuclear spins and thus broader lines in the frequency domain. Spin-lattice relaxation (T_1) contributes to the weakening of the phase coherence. Therefore, T_2 is never longer than T_1.

The T_1 and T_2 are dependent on the solution viscosity and the rate of molecular motions, demonstrated in **Figure C.5**. Molecular motion is defined here by the rotational correlation time, τ_c, which is the time required to rotate through an angle of one radian. The τ_c values increase with molecular size. In low viscosity solutions of small molecules, the average rates of molecular motions are much faster than the resonance frequencies of the nuclei and only a small fraction of the motions possess the proper frequency to produce relaxation. Rapid tumbling therefore corresponds to inefficient relaxation and very long T_1 and T_2 times, which generates narrow linewidths. The small molecule region is therefore often referred to as the extreme narrowing limit. An increase in viscosity, produced by lowering the temperature of the solution or increasing the sample concentration, results in shorter relaxation times and hence broader peaks. The T_1 reaches a minimum and the T_2 plateaus when the molecular motion of the sample matches the resonance frequency of the nuclide. At larger τ_c values the T_1 increases while the T_2 continues to decrease due to efficient energy exchange processes that are stimulated by low frequency fluctuations in the sample. Thus, the NMR spectrum of large molecules, polymers, and proteins contain relatively broad linewidths compared to small molecules. The multiple linewidths within an NMR spectrum can also vary depending on the molecular origin of the resonances. For example, in segmented copolymers or tactically impure homopolymers, polymer chain segments that are more flexible

and tumble faster can possess long T_2 and relatively narrow peaks, while more rigid chain segments that tumble slower can have shorter relaxation times and broader peaks.[5,6] Line broadening can reduce the resolution of the NMR spectrum and therefore the qualitative and quantitative robustness of an NMR spectroscopy experiment.

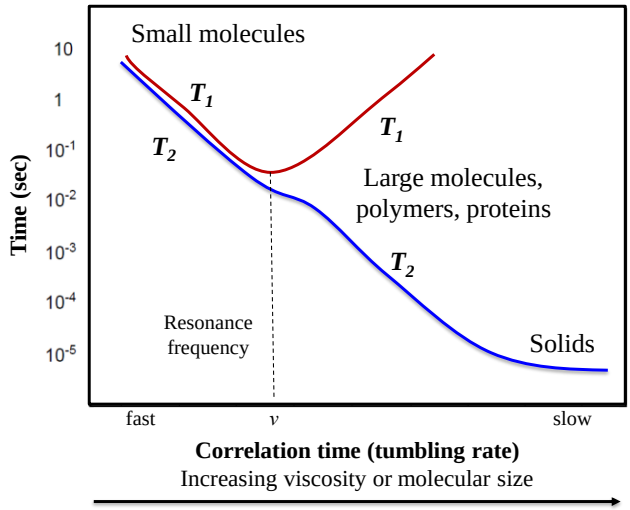

Figure C.5. Schematic representation of the dependence of T_1 and T_2 on the correlation time (tumbling rate) and molecular size for a spin-½ nucleus. Adapted with permission from .[1]

C.3. Quantitative NMR spectroscopy

C.3.1. General requirements for quantitative NMR experiments

For every NMR active nucleus probed in an NMR experiment, if the population difference of its equilibrium state is reestablished between each radiofrequency (RF) pulse, then the relative area of its signal in the NMR spectrum will be proportional to the number of nuclei of that type in the sample. Thus, the peaks in the NMR spectrum can be integrated to obtain quantitative information about the structure of the molecule. For most routine NMR experiments, the accuracy of peak integration is typically within 10−20%;[7] however, the integration accuracy can be improved significantly through experiment design and spectrum processing.

Prior to an NMR experiment, the external magnetic field is shimmed to optimize its homogeneity throughout the sample. Inhomogeneities in the magnetic field decrease the spin-spin relaxation time (T_2) and produce line broadening and asymmetric line shapes in the NMR spectrum. Shimming is typically performed using shimming coils that are located inside of the NMR spectrometer. The signal of a properly shimmed standard will have a line width at half maximum ($LW_{1/2}$) of less than 1 Hz. The shimming process can be performed manually, though it is often integrated into the automated routine of the instrument software.

During the NMR pulse sequence, a relaxation delay is added after every pulse to allow the equilibrium state to be reestablished. The duration of the relaxation delay is typically set to at least 5×(longest T_1) in the sample to ensure that at least 99% of the magnetization has recovered from the x,y plane before the next RF pulse. Spin-lattice relaxation times (T_1) are measured using a multiple-pulse inversion recovery sequence experiment in which a 180° RF pulse is applied followed by a 90° RF pulse after a period of time, τ.[1] The experiment is repeated with increasing values of τ to monitor the inversion recovery of the net magnetization vector. For each nonequivalent nucleus, the T_1 is determined from a plot of $\ln(M_0 - M_t)$ versus τ where M_0 is the equilibrium magnetization, M_t is the intensity of the detected magnetization, and the slope is equal to T_1^{-1}.

Pulses are repeated to improve the signal to noise ratio (*S/N*) of the NMR spectrum. A sufficiently large *S/N* is needed to support a high level of integration accuracy in an experiment. The *S/N* is proportional to the square root of the number of scans or pulses, *n*, performed on the sample. The *S/N* also increases with the strength of B_0.

The acquisition time (*at*) of the FID signal and spectral width (sw, also called the sweep width) are parameters that affect the peak resolution, i.e., the smallest frequency difference at

which signals can be distinguished. Digital resolution (*res*) of an NMR spectrum is inversely proportional to the acquisition time of the FID signal, which is the allotted time to collect the FID. The optimal acquisition time captures the full exponential decay of the FID. Acquisition times that are longer than the full decay of the FID result in a greater number of data points (*np*) and greater resolution according to **Equation 3**. However, a long *at* adds time to the experiment and extra data points produce noise in the spectrum and should therefore be eliminated.

$$\boldsymbol{res = \frac{1}{at} = \frac{2sw}{np}} \qquad \textbf{(3)}$$

Resolution is also dependent on the spectral width (*sw*, also termed sweep width), which is the frequency range over which a nuclide resonates depending on its electronic environment. For the ^{1}H nucleus, the spectral width is approximately 10-ppm. The ^{13}C nucleus has a much larger spectral width of approximately 200 ppm. Therefore, the separation of signals in a ^{13}C NMR spectrum can resonate over a much broader frequency range than that observed in a ^{1}H NMR spectrum. The spectral width can be reduced in an NMR experiment to improve the digital resolution; however, it must be at least 10% larger on each end of the spectrum to avoid filtering effects that can reduce the intensity of peaks near the spectrum edges. While chemical shift (ppm) is independent of B_0, the resonance frequency in Hertz depends on the strength of the magnetic field. For example, a 10-ppm frequency range contains 1000 Hz on a 100 MHz spectrometer (100 Hz ppm^{-1}), while the same range on a 500 MHz spectrometer contains 5000 Hz (500 MHz ppm^{-1}). Thus, increasing the spectrometer operating frequency also improves the signal resolution. When adjusting the *sw*, the *np* should also be adjusted to reduce the *at* and avoid increasing the spectral noise.

After the NMR signal has been recorded, the frequency domain spectrum must be processed to adjust errors in the phase and remove distortions in the baseline that are produced during the digitization and Fourier transform of the FID. The unprocessed spectrum often contains

a mixture of absorptive and dispersive signals. Absorptive signals lie entirely above the baseline, while dispersive signals contain a portion of their signal below the baseline. Phase correction converts the spectrum to a purely absorptive signal. Baseline correction removes distortions in the baseline. Phase correction and baseline correction can be performed manually or automatically using NMR data processing software.

The peaks in the NMR spectrum can be integrated using NMR data processing software to obtain the relative peak areas for quantitative analysis. According to Claridge,[7] deconvolution using NMR software "may reduce operator bias in integral definition and may prove to be more reliable in the presence of baseline noise or other low-level artefacts, or when resonances experience overlap with a neighboring peak and are not sufficiently resolved for integration" (pg. 140).

C.3.2. Quantitative ^{13}C NMR spectroscopy and the Nuclear Overhauser Effect

Signal intensity in broadband proton-decoupled ^{13}C NMR spectra is greatly complicated by the nuclear Overhauser effect (NOE). The NOE is a dipolar (through-space) coupling interaction between ^{1}H and ^{13}C nuclei that results in enhancement or suppression of signals in the ^{13}C NMR spectrum as a result of the continuous broadband saturation of the ^{1}H nuclei. Under conditions of saturation, the population difference between spin states is zero and the nuclear spins precess out of phase, producing zero net magnetization in the x,y-plane (signal loss). Saturation often occurs with ^{1}H nuclei because P_α and P_β are similar at equilibrium and the spin-lattice relaxation times (T_1) are relatively long, reducing the likelihood of full recovery between pulses.

The equilibrium state of the ^{1}H nuclei is recovered after saturation by spin-lattice relaxation processes that produce a change in the spin state population of dipolar coupled ^{13}C nuclei. Relaxation of a ^{1}H nucleus that induces the relaxation of a ^{13}C nucleus ($\beta\beta \rightarrow \alpha\alpha$) increases the

natural population difference of the ^{13}C equilibrium state, resulting in enhanced signal intensity (positive NOE). Conversely, relaxation of a ^{1}H nucleus that induces the excitation of a ^{13}C nucleus ($\beta\alpha \rightarrow \alpha\beta$) decreases the natural population difference, which suppresses the signal intensity (negative NOE).

Spin-lattice relaxation processes are induced by fluctuating magnetic fields generated by the rotational motion of neighboring molecules oscillating at the same resonance frequency. Thus, the NOE pathway that is favored depends on the rates of molecules tumbling in the sample. Rapid molecular tumbling (short τ_c) favors the positive NOE pathway and thus signal enhancement. Slow molecular tumbling (long τ_c), for example by large molecules and polymers, favors the negative NOE pathway and signal suppression. The NOE is also distance dependent and is therefore often used to provide insight into the three-dimensional structure of a molecule.

It is worth noting for clarity that the NOE is not responsible for the signal splitting observed in a ^{1}H NMR spectrum.[8] Signal splitting, caused by scalar (through-bond) coupling, is an intramolecular phenomenon in which the nuclear spins of neighboring nuclides interact and impact the effective magnetic field (B_{eff}) experienced by the nucleus. For example, H_A, interacting with the nuclear spins of a neighboring chemically-distinct will resonate at a slightly larger resonance frequency when the H_A and H_B spins are aligned and a slightly smaller resonance frequency when the spins are opposed. The splitting pattern depends on the number of chemically-distinct neighbors and the relative population of the spin states. Dipolar couplings typically due not produce observable splitting because the relaxation and excitation transitions (e.g., $\beta\alpha \rightarrow \alpha\beta$) involved have the same energy. Standard ^{13}C NMR spectroscopy experiments are ^{1}H-decoupled to remove the scalar coupling and thus the peak splitting caused by ^{1}H–^{13}C interactions.

In order to obtain quantitative ^{13}C NMR spectra, the NOE must be suppressed to ensure the accuracy of the peak integration. The NOE suppression is achieved using an inverse gated proton decoupling technique that applies a broad-bandwidth decoupling field of several kilohertz to remove the spin coupling between neighboring ^{1}H and ^{13}C nuclei.[2] The decoupling field is switched on only during the time the FID is being acquired (acquisition time) and is switched off during the relaxation delay when equilibrium is reestablished. Using this technique, any NOE that does occur during the acquisition time does not influence the detected transverse signal because the NOE only affects the longitudinal magnetization. Thus, the decoupled spectrum can be recorded without NOE enhancement.

C.4. Other considerations for the quantitative NMR spectroscopy of polymers

Polymers are composed of a large number of NMR active nuclei that can exist in different chemical environments depending on many factors that include the monomer structure, polymer tactic purity, intermolecular interactions, functional group content, and chain conformations.[2] In addition, the resonance frequencies of nuclei depend on temperature and solvent, which can be varied to improve peak resolution and can also provide insight into molecular interactions.[9] One-dimensional and two-dimensional NMR spectroscopy experiments are commonly used to investigate polymer composition, end group substituents, and branching as well as polymer dynamics and conformations. The ^{13}C nuclei of polymers are also highly sensitive to short-range segmental motions of the local sequence structure, which is useful for the analysis of tacticity and comonomer sequence in copolymers.[6,10,11] In **Chapter 3**, the development of a comonomer sequencing method using quantitative ^{13}C NMR and two-dimensional NMR spectroscopy

techniques is discussed. The comonomer sequencing method was used to analyze the copolymer microstructure and comonomer sequence of brominated syndiotactic polystyrene copolymers.

C.5. References

1. Claridge, T. D. W., Chapter 2 - Introducing High-Resolution Nmr. In *High-Resolution Nmr Techniques in Organic Chemistry (Third Edition)*, Claridge, T. D. W., Ed. Elsevier: Boston, 2016; pp 11-59.
2. *Nmr Spectroscopy of Polymers*. 1st ed.; Springer Science+Business Media Dordrecht: New Delhi, 1993.
3. Magnetic Resonance. In *Encyclopædia Britannica*, Encyclopædia Britannica, inc.: 2011.
4. Boltzmann Factor. $P(A)/P(B) = E^{(\Delta e/Kt)}$ Where, $P(A)$ and $P(B)$ Are the Probabilities of the Two States, Δe Is the Energy Difference between States, K Is the Boltzmann Constant, and T Is Temperature.
5. Bain, A.; Eaton, D.; Hamielec, A.; Mlekuz, M.; Sayer, B., Line Broadening in the Carbon-13 Nmr Spectra of Cross-Linked Polymers. *Macromolecules* **1989,** *22* (9), 3561-3564.
6. Gronski, W.; Quack, G.; Murayama, N.; Elgert, K. F., Dependence of Local Chain Motions on the Sequence Structure of Cis-(1,4-1,2)-Polybutadiene as Revealed by 13c Spin-Lattice Relaxation. *Die Makromolekulare Chemie* **1975,** *176* (12), 3605-3608.
7. Claridge, T. D. W., Chapter 4 - One-Dimensional Techniques. In *High-Resolution Nmr Techniques in Organic Chemistry (Third Edition)*, Claridge, T. D. W., Ed. Elsevier: Boston, 2016; pp 133-169.
8. Claridge, T. D. W., Chapter 9 - Correlations through Space: The Nuclear Overhauser Effect. In *High-Resolution Nmr Techniques in Organic Chemistry (Third Edition)*, Claridge, T. D. W., Ed. Elsevier: Boston, 2016; pp 315-380.
9. Ziaee, F.; Salehi Mobarakeh, H., Effect of Temperature on Polystyrene Tacticity through Para Aromatic Carbon Splitting in 13c Nmr Spectroscopy. *Iran Polym J* **2011,** *20*, 213-221.
10. Randall, J. C., The Distribution of Stereochemical Configurations in Polystyrene as Observed with 13c Nmr. *J. Polym. Sci., Part B: Polym. Phys.* **1975,** *13* (5), 889-899.
11. Randall, J. C.; Ruff, C. J.; Kelchtermans, M., 13c Nmr Microstructure Determinations of Low-Density Polyethylene Homopolymers and Copolymers. *Recl. Trav. Chim. Pays-Bas* **1991,** *110* (12), 543-552.

Appendix D.

Carbon-Based Electrode Materials as Supports in Electrocatalytic, Photocatalytic, and Photoelectrocatalytic Applications

Kristen F. Noble, Robert B. Moore, Karen J. Brewer

D.1. Introduction to water reduction photocatalysis

Global interest in hydrogen (H_2) as a renewable and sustainable alternative to fossil fuels reinforces the importance of developing efficient water splitting systems. Photocatalytic systems show promise in this area when satisfying the following requirements: (1) the photocatalytic molecules and/or materials absorb light appreciably and are able to drive water oxidation and water reduction reactions, (2) energy loss from electron−hole recombination and excited state deactivation pathways is minimal, and (3) the photocatalyst components are stable in aqueous media.[1] In this work, the photocatalytic system will be simplified by reducing molecular collisions through covalent binding of a water reduction catalyst to an electrically conductive carbon nanofiber (CNF) electron donor source. Insight will be gained on electron transfer processes using this intramolecular electron source, with applications in water splitting. This review is focused on carbon-based electrode materials as supports in electrocatalytic, photocatalytic, and photoelectrocatalytic applications, and polymer-supported transition metal catalysts and photosensitizers, beginning with a brief overview of solar energy conversion, water splitting, and photocatalytic H_2 production.

D.1.1. Broader context: global energy demand

As global energy demand increases, stringent regulations are being placed on the use of unsustainable, carbon-based energy sources with the goal of diminishing environmental changes that threaten future standards of living. Despite global efforts to promote the use of sustainable resources (e.g. wind, hydro, geothermal, and solar), fossil fuels continue to dominate global energy consumption, accounting for 78% of energy consumed worldwide in 2012. Meanwhile, renewables contributed less than one-fifth to energy consumption and solar accounted for only a few tenths of a percent.[2]

Solar is an inexhaustible source of energy and an alternative solution to global concerns over the use of unsustainable resources. Incident solar radiation provides 4.3×10^{20} J every hour. If this energy could be stored and converted into electricity, the current global energy demand could be met for an entire year (3.4×10^{20} J).[2,3] Nevertheless, uneconomical, low efficiency materials currently available for solar energy conversion applications limit solar energy use.

D.1.2. **Solar energy-to-chemical energy conversion**

The sun's energy can be converted into electrical energy directly and/or stored as chemical energy in molecular bonds. Light-driven molecular bond formation and cleavage provides a source of sustainable fuels, necessary for uninterrupted energy availability in the absence of incident solar radiation. Hydrogen (H_2) is a particularly attractive alternative fuel because it can be produced photocatalytically through water splitting and converted back into water in an energy rich, exothermic combustion reaction ($\Delta H°_{comb}$ = −143 kJ/g) without forming environmentally detrimental carbon-based byproducts.[4] Furthermore, the energy density per gram of H_2 burned in the combustion reaction is nearly double that of other small molecule fuel sources (excluding

nuclear-based fuels). Improving the efficiency of photocatalytic H_2 production from water is a dedicated area of research.[5-7]

D.1.2.1. Electrochemistry of water splitting

Water electrolysis to H_2 and oxygen (O_2) through multi-electron transfer requires a minimum energy input of 1.23 eV under standard reaction conditions (pH = 0, 25 °C, and 1 atm, referenced to a normal hydrogen electrode (NHE)), demonstrated in **Equations 1-3**.[8]

$$2\ H_2O\ (l) \rightarrow 4\ H^+\ (aq) + O_2\ (g) + 4\ e^- \qquad E = -1.23\ V\ vs\ NHE \qquad (1)$$

$$4\ e^- + 4\ H^+\ (aq) \rightarrow 2\ H_2\ (g) \qquad E = 0.00\ V\ vs\ NHE \qquad (2)$$

$$\textbf{Overall:} \quad \mathbf{2\ H_2O\ (l) \rightarrow 2\ H_2\ (g) + O_2\ (g)} \qquad \mathbf{E = -1.23\ V\ vs\ NHE} \qquad \mathbf{(3)}$$

The sun provides sufficient energy to drive water splitting, however, water does not absorb at or above the 1.23 eV (i.e., 1008 nm) required for bond formation and cleavage.[4] Water splitting can be realized indirectly using photocatalysts that absorb the sun's energy and transfer that energy to water via photoexcited electrons and photogenerated holes that reduce and oxidize water, respectively. Efficient water splitting requires photocatalysts that are stable in aqueous media and absorb light appreciably above 1.23 eV to account for kinetic barriers in the electron transfer processes.[9] Electron−hole recombination and excited state deactivation pathways (e.g., quenching by ground state O_2 via energy transfer[10]) reduce photocatalyst efficiency. In addition, the inability of homogeneous photocatalysts to separate H_2 and O_2 reduces overall efficiency due to photoproduct recombination, which increases the cost of H_2 recovery. Heterogeneous photocatalytic systems that spatially separate water reduction and water oxidation catalysts using electron and proton conducting materials are imperative to realizing efficient photocatalytic water splitting.

D.1.2.2. Photocatalytic water reduction to H_2

Hydrogen can be evolved from water through photocatalytic water reduction using a water reduction catalyst (WRC) and an electron donor source. Multi-electron water reduction requires accumulation of two reducing equivalents at the WRC for delivery to water or protons. Photoinitiated electron collection at the catalyst can be achieved by incorporating a photosensitizer with an electron relay (**Figure D.1**). The photosensitizer absorbs light and is oxidatively quenched by the electron relay, which shuttles an electron to the catalyst. The electron donor is necessary to regenerate the oxidation state of the photosensitizer and introduce the second electron required for H_2 production. Water is the ideal electron donor, however stronger reducing agents are typically required to effectively reduce the photosensitizer and continue the photocatalytic cycle. Efficient photocatalysis requires appreciable absorption of UV and/or visible light by the photosensitizer, catalyst stability in multiple oxidation states, and favorable forward electron transfer kinetics with respect to excited state deactivation pathways and back electron transfer reactions.[6]

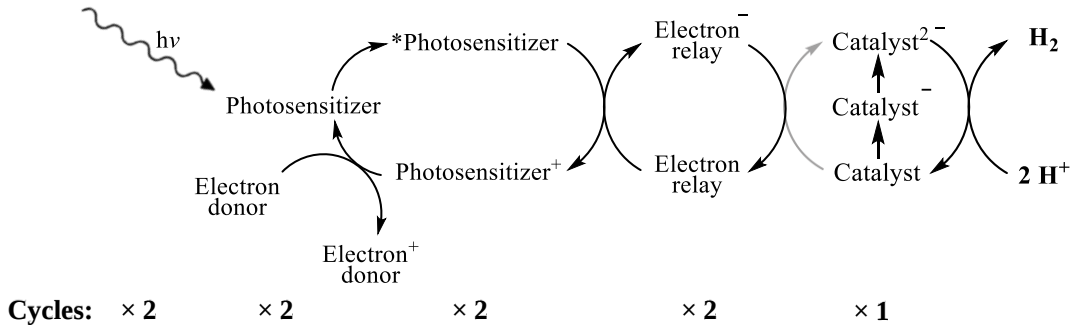

Figure D.1. Light-driven water reduction to H_2 via photoinitiated electron collection of two reducing equivalents at a water reduction catalyst. The curved light gray arrow demonstrates the catalyst transition to doubly reduced through a singly reduced intermediate. *hν* = photoexcitation; * = excited state.

D.1.3. Photocatalysts for H_2 production

D.1.3.1. Multicomponent water reduction catalysts involving bimolecular interactions

Water reduction photocatalysts are well established in the literature.[5,6,11-15] Early multicomponent systems utilized $[Ru(bpy)_3]^{2+}$ (bpy = 2,2′-bipyridine) as a photosensitizer, $[Rh(bpy)_3]^{3+}$ as an electron relay (ER), colloidal platinum (Pt) as a reactive metal catalyst, and triethanolamine (TEOA) as a sacrificial electron donor (ED).[16,17] These molecular components interact through diffusion-controlled intermolecular collisions to transfer electrons to water or protons for H_2 production. $[Ru(bpy)_3]^{2+}$ and related polypyridyl analogs absorb strongly in the UV and visible light ($\epsilon \geq 14{,}000$ in aqueous solution) regions with high excitation quantum yields, producing long-lived excited states ideal for driving redox chemistry (**Figure D**.2).[18-22] Light absorption by $[Ru(bpy)_3]^{2+}$ results in excitation of a formally Ru-based (Ru(dπ)) electron to a formally bpy-based (bpy(π*)) anti-bonding orbital, forming a singlet metal-to-ligand charge transfer (^{1}MLCT) excited state ($[Ru(bpy)_3]^{2+}$*). Spin-orbit coupling with the Ru center facilitates an electron spin flip, allowing population of the lower energy ^{3}MLCT excited state with near unit efficiency.[22] $[Ru(bpy)_3]^{2+}$ is a stronger reducing agent and oxidizing agent in the ^{3}MLCT excited state than in the ground state. Oxidative quenching of the ^{3}MLCT excited state by $[Rh(bpy)_3]^{3+}$ and electron transfer to water or protons produces 22.4 mL of H_2 over 45 h (λ_{irr} = 450 ± 20 nm), totaling 80 turnovers per $[Rh(bpy)_3]^{3+}$.[16] An inherent shortcoming of multicomponent systems is the efficient excited state deactivation pathways and back electron transfer reactions that occur up to two orders of magnitude faster than diffusion-controlled excited state quenching by the ER or ED.[23] Incorporation of photocatalyst components into covalently coordinated assemblies drastically reduces diffusion-controlled electron transfer and improves overall catalyst efficiency.

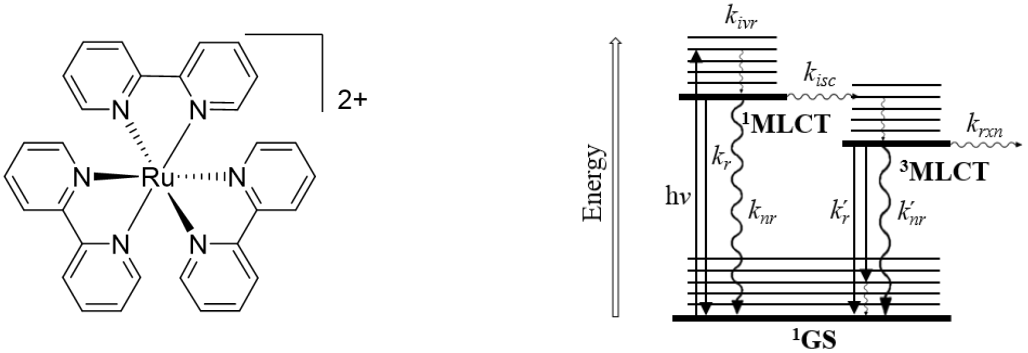

Figure D.2. (**left**) Molecular structure of $[Ru(bpy)_3]^{2+}$ (bpy = 2,2′-bipyridine). (**right**) Simplified Jablonski diagram. GS = ground state; MLCT = metal-to-ligand charge transfer excited state; *hν* = photoexcitation; *k* = rate constant; k_r = radiative decay by fluorescence; *kŕ* = radiative decay by phosphorescence; k_{nr} = non-radiative decay by internal conversion (IC); k'_{nr} = non-radiative decay by intersystem crossing; k_{isc} = intersystem crossing; k_{ivr} = intramolecular vibrational redistribution; k_{rxn} = photocatalytic reaction.

D.1.3.2. Supramolecular photocatalysts

Supramolecular photocatalysts are molecular assemblies that perform light-driven chemical reactions through interactions among covalently bound components, each with a specific purpose that contributes to the overall function of the complex.[24] Photoinitiated electron collectors (PECs) are a type of supramolecular photocatalyst that maintain molecular stability upon collection of reducing equivalents at a reactive center.[6] The ability of a supramolecular complex to function as a PEC depends on the photophysical properties of the selected components and the order of assembly. For example, $[\{(bpy)_2Ru(dpp)\}_2RhCl_2]^{5+}$ (dpp = 2,3-bis(2-pyridyl)pyrazine), synthesized by Brewer et al. in 2007, was the first reported supramolecular PEC to photocatalytically produce H_2 from water in the presence of organic solvent and an electron donor.[25,26] This complex consists of two Ru^{II} photosensitizers with bpy terminal ligands (TL) coordinated to a central Rh reactive metal center through bis-bidentate dpp bridging ligands (BL) (**Figure D.3**). Within this complex, molecular orbital energetics direct electron transfer from the formally Ru(dπ) highest occupied molecular orbital (HOMO) ($Ru^{II/III}$ = + 1.63 V) to the formally Rh(dσ*) lowest unoccupied molecular orbital (LUMO) ($Rh^{III/II/I}$ = − 0.37 V). Stabilization of the dpp(π*) orbital ($dpp^{0/-}$ = − 0.76 V) via σ-donation to the electropositive metal center facilitates the

intramolecular electron transfer (potentials vs Ag/AgCl in deoxygenated CH_3CN). Electron collection in the Rh(dσ*) anti-bonding orbital causes Jahn-Teller distortion and induces halide loss upon formation of the Rh^I square planar species, hypothesized to be the active form of the catalyst.[26,27] Changing the terminal ligand structure and the halide ligand coordinated to Rh results in an optimized turnover number (TON) of 1300 over 46 h under irradiation at 460 nm.[27-31]

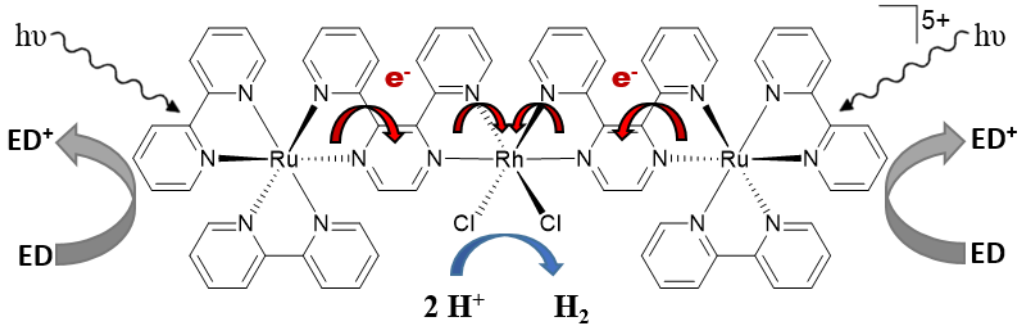

Figure D.3. $[\{(bpy)_2Ru(dpp)\}_2RhCl_2]^{5+}$ (bpy = 2,2′-bipyridine; dpp = 2,3-bis(2-pyridyl)pyrazine), used as a water reduction photocatalyst.[26] *hν* = photoexcitation; ED = electron donor; red arrows = intramolecular electron transfer.

The electron donor plays a critical role in photocatalyst efficiency. Reductive quenching of the Ru(dπ)→dpp(π*) ^{3}MLCT excited state fills the orbital vacancy resulting from photoexcitation and facilitates transfer of the excited electron toward the reactive metal center.[25] The rate of reductive quenching (k_q) is diffusion controlled, demonstrated by an increase in photocatalyst efficiency with increasing electron donor concentration.[26] Excited state deactivation pathways and back electron transfer reactions, assisted by relatively slow solvent reorganization, continue to compete effectively with reductive quenching.[25] Therefore, photocatalysis is carried out with a large excess of electron donor.

In photocatalytic water reduction, the electron donor is typically an organic molecule that reacts irreversibly upon electron loss.[9] Aqueous electron donors are typically less efficient at competing with the rapid excited state non-radiative decay kinetics observed in aqueous media. The increase in k_{nr} is thought to be a consequence of quenching by water through electrostatic

interactions between the excited state dipole and high frequency O−H bond vibrations (~ 3500 cm^{-1}).[32] Coupling an electron donor to the supramolecular architecture via ligand modification may increase k_q as to compete with k_{nr} and excited state deactivation. However, back electron transfer reactions and the limited number of electron donor species per photocatalyst make a reductive quencher-photocatalyst complex only practical for mechanistic insight.[33,34] Replacing the solution-based electron donor with a carbon-based electrode material will provide a source of electrons and support the photocatalyst during photocatalysis. In addition, electrons can be delivered to the material by an applied potential or through electron transfer from a water oxidation catalyst to realize photocatalytic water splitting.

D.2. Carbon-based electrode material supports

Carbon-based electrode materials (e.g. CNFs, carbon nanotubes (CNTs), and activated carbon (AC)) have proven useful as counter electrodes for solar photovoltaics,[35-38] membrane supports[39] and electrodes[40-46] for fuel cells, catalysts[47,48], and catalyst supports[49,50] for numerous applications. Their relatively low cost, high specific surface area, and remarkable stability, mechanical properties, and electron conductivity have attracted much attention in water splitting applications.[46,49] Versatile and well-established methods for functionalizing the surface of carbon materials have also broadened carbon-based material applications.[51] This section of the review focuses on carbon-supported catalysts for electrocatalytic, photocatalytic, and photoelectrocatalytic water splitting.

D.2.1. Carbon-based electrode supports in electrocatalytic water oxidation and reduction

Catalysts supported on carbon-based electrodes for electrocatalytic water oxidation and water reduction applications typically exhibit increased catalyst stability and enhanced

catalyst efficiency.[13,52-54] Artero et al. suggest that catalyst stability increases due to optimization in the supply of electrons between the electrode and covalently bound catalysts, which limits the lifetime of reduced/oxidized catalyst intermediates and diminishes degradative side reactions.[52] In addition, covalent attachment of the catalyst to the electrode surface enhances catalyst dispersion, shown in **Figure D.4**, and diminishes catalyst deactivation by reducing intermolecular collisions.[52,55,56]

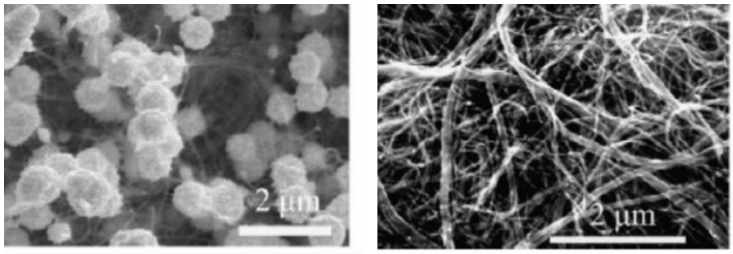

Figure D.4. (**left**) SEM image of Pt particles electrodeposited on untreated CNTs and (right) SEM image of Pt electrodeposited on CNTs functionalized with carboxyl groups from electrochemical reduction of a diazonium salt. Reproduced with permission from Elsevier.[56]

Using an electrocatalyst-CNT covalent assembly scheme, Artero et al. demonstrated for the first time a diimine−dioxime cobalt (Co) catalyst having high electrocatalytic activity for H_2 production from a fully aqueous, mildly acidic solution (pH = 4). Catalyst immobilization was realized by surface functionalization of the CNTs via electrochemical reduction of an aryldiazonium salt, followed by azide−alkyne cycloaddition catalyzed by a copper(I) (Cu^I) catalyst. The CNT-supported Co catalyst exhibited a high turnover frequency (TOF), ca. 8,000 (± 5%) h^{-1} per catalyst (ca. 2.2 s^{-1}), at an overpotential of 590 mV with a stable current density of ca. 1 mA cm^{-2} over 4 h. Catalyst stability was maintained over seven hours of cycling at – 590 mV vs RHE (reversible hydrogen electrode) and after 55,000 (± 5%) turnovers.

The water oxidation catalyst, [Cp*IrCl(4-NH_2-bpy)] (Cp* = pentamethylcyclo-pentadienyl), immobilized on a glassy carbon electrode (GCE) also demonstrated enhanced catalyst efficiency in comparison to the same catalyst in solution.[54] This water oxidation catalyst

(WOC) exhibited a TOF of 0.113 s^{-1} at an overpotential of 660 mV, with a current density of 14.2 μA cm^{-2} and TON of 644 after 1 h, while the same catalyst in solution obtained only ca. 150 turnovers after 7.5 h. The efficiency of the GCE−supported WOC decreased rapidly after 1 h of electrolysis due to corrosion of the GCE. Electrode corrosion by water, facilitated by high oxidative potentials, is a major challenge in electrocatalysis carried out in aqueous environments.[53-55] Carbon materials with high graphitization (sp^2 hybridization) and hydrophobic character (e.g. CNFs and CNTs) exhibit enhanced corrosion resistance, making them more suitable than GC as catalyst supports in electrocatalytic applications.[49,57]

CNFs and CNTs have exceptionally high specific surface areas that promote high catalyst loading.[13,53] Palacin et al. found that using multi-walled CNTs (MWCNTs) to immobilize a nickel (Ni) diphosphine-based WRC enhances catalyst loading by nearly two orders of magnitude relative to an indium tin oxide (ITO) electrode (1.5 (± 0.5) nmol cm^{-2} : 0.045 (± 0.015) nmol cm^{-2}), demonstrated by a large current response in cyclic voltammetry (CV).[13] The MWCNT−supported Ni-catalyst achieved 20,000 (± 30%) turnovers in 1 h with a sustained current of 2 mA cm^{-2} at 500 mV overpotential in an acidified acetonitrile (CH_3CN) solution. Exceptional stability and catalyst efficiency was also observed in aqueous media (0.5 M H_2SO_4) after coating the Ni-functionalized MWCNTs in Nafion®, a commercially available proton exchange membrane. A steady current density of 4 mA cm^{-2} and more than 100,000 (± 30%) turnovers were achieved in 10 h at low overpotential (300 mV). High catalyst loading does not ensure greater efficiency for the appended catalyst, as demonstrated by Roberts et al. in a study of the same Ni catalyst covalently attached to a GCE.[55] A significant reduction in TOF for the surface bound Ni catalyst at a surface concentration of 0.13 nmol cm^{-2} (28 s^{-1}) was observed, relative to unbound catalyst in acidic CH_3CN solution (> 540 s^{-1}), though consistency between reaction conditions for these experiments

was not apparent. Decreased catalyst efficiency at high surface concentrations has been contributed to steric crowding, catalyst deactivation via intermolecular interactions, a reduced effective number of active catalyst sites, and slow or inhibited electron transfer between catalyst and the electrode.[52,54-56] High specific surface area electrode materials still present an advantage over lower surface area electrodes since higher catalyst loading with greater catalyst dispersion can be achieved using these materials given the same unit area.

D.2.2. Carbon-supported catalysts in photocatalytic and photoelectrocatalytic water splitting

Carbon-based electrode materials utilized as scaffolds in semiconductor-based photocatalytic and photoelectrochemical systems have been shown to improve charge separation, reduce charge-transfer resistance, and suppress electron−hole recombination, resulting in enhanced catalyst efficiency.[48,58] The high specific surface area of carbon materials also promotes catalyst dispersion and maximizes the number of active catalyst sites.[48,56,58,59] Kamat et al. observed a nearly two-fold increase in photoconversion efficiency for a photoelectrochemical cell composed of TiO_2 nanoparticles dispersed on SWCNT films.[48] Incident photon conversion to charge carrier conversion efficiency (IPCE) increased from 7.36% under 350 nm irradiation and 0 V vs SCE to 16% with incorporation of the SWCNT scaffold support under the same reaction conditions. A small increase in photoelectrocatalytic efficiency was also observed (0.09% to 0.20%). The authors note that charge separation efficiency in SWCNT networks under visible excitation was low and did not contribute to the photocatalytic activity of the SWCNT/TiO_2 composites. The incorporation of activated carbon (AC) into a mesoporous Pt/TiO_2/AC nanocomposites, in the presence of a sacrificial reagent, increased photocatalytic H_2 production by 10% over Pt/TiO_2 photocatalysts.[58] The AC surface was functionalized by acid treatment to

oxidize the carbon surface and improve TiO_2 dispersion. The mesoporous Pt/TiO_2/AC nanocomposites exhibited enhanced rates of H_2 production, possibly from adsorption of the sacrificial reagent to the AC surface, keeping the reagent nearer to the TiO_2 surface. These results demonstrate the usefulness of carbon-based electrode materials for enhancing electrocatalyst and photocatalyst performance.

D.2.3. Functionalizing carbon-based electrode materials for catalyst attachment

Functionalizing carbon-based electrode materials for covalent attachment of molecular catalysts can be realized using well-established methods provided in the literature.[51,60,61] For water splitting applications that use carbon electrode supports, carbon surface modification is most often achieved by either acid treatment,[58,62] Hassner addition of azide from iodine azide (IN_3),[55] or electrochemical reduction of aryldiazonium salts.[13,52-54,63] Acid treatment is an oxidation process using strong acids (e.g. HNO_3 and H_2SO_4) to introduce oxygen-containing functional groups (e.g. –OH, – COOH, etc.) to the carbon surface.[62] This method produces a surface that is difficult to characterize and creates defects in the electrode surface that impede electronic conductivity.[64] Hassner addition forms a monolayer of azide functional groups on the carbon surface via ionic addition of IN_3, which limits the utility of this method to catalysts containing functional groups that react with azide (e.g. alkynes).[55,61] IN_3 is a dangerous explosive, and thus a non-ideal reagent for surface modification. Electrochemical reduction of aryldiazonium salts is the most frequently used surface modification method because of the wide variety of aryldiazonium salts that have been shown to attach to the carbon electrode surface.[13,52-54,63] In this reaction, a potential bias applied to the electrode reduces the aryldiazonium salt to a radical and liberates nitrogen gas (N_2). The radical then reacts with the electrode surface forming a C−C bond (**Figure D**.5).[60] The degree of functionalization can be controlled by varying the concentration of starting material. This

method produces very stable surfaces, important for electrocatalytic and photocatalytic water splitting applications.[53,63]

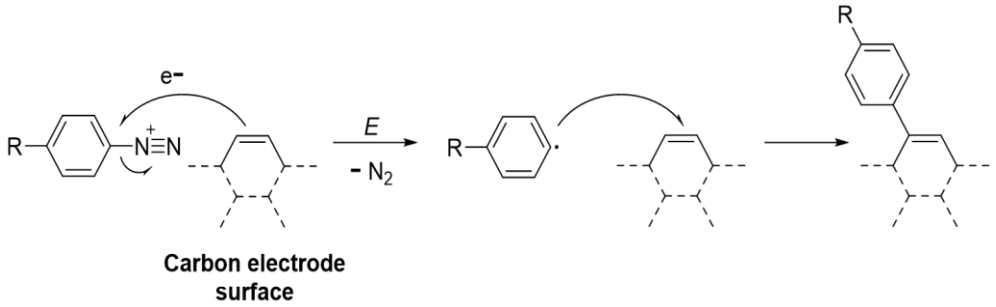

Figure D.5. Mechanism for electrochemical reduction of an aryl diazonium salt to a carbon electrode surface.[60] *E* = applied potential.

D.3. Polymer supported photosensitizers and photocatalysts

Before assembling a photocatalyst/carbon-based electrode complex, it is necessary to first investigate the behavior and stability of the photosensitizer and catalyst on a polymer support, in order to obtain deeper insight into the structure-function relationship of the full supramolecular photocatalyst assembly. In particular, random and block, or block-like, copolymers can be useful supports for investigating how the spatial separation of the photosensitizers or catalysts effects their photophysical properties and function.

Covalent attachment of transition metal photosensitizers to a polymer support has been shown to facilitate energy and electron transfer between photosensitizers when the photosensitizers are assembled in close spatial proximity.[65-68] Through-space energy transfer and electron transfer can occur when sufficient orbital overlap exists between molecules. Tunable energy transfer was observed by Waters et al.[69] in a self-assembled, coiled-coil peptide scaffold of Ru^{II}- and Os^{II}-polypyridyl complexes. In this study, metal complexes were loaded onto specific residues in the repeating heptad peptide sequence to control the distance between complexes. Remarkably, energy transfer was only observed when the metalopeptide was in its coiled-coil tertiary structure,

demonstrating the need for close contact between the complexes to facilitate $*Ru^{II} \rightarrow Os^{II}$ energy transfer. As the distance between complexes decreased, the rate of energy transfer increased, consistent with distance dependent, through space energy transfer. The energy and electron transfer processes exhibit directionality, based on the relative energies of occupied and unoccupied molecular orbitals. Papanikolas and co-workers[66,69] showed that polymer supported Ru^{II}- and Os^{II}-polypyridyl complexes experience energy and electron transfer that occurs through the photosensitized Ru^{II} complexes, $*Ru^{\boldsymbol{II}}$**,** to an $Os^{\mathbf{II}}$ complex, driven by the lower energy orbital vacancy in Os^{II}.

Recently, Thanneeru et al.[70] reported that a Cu-coordinated random copolymer experienced polymer-promoted cooperative catalysis, where the near proximity of the catalysts generated by the random distribution along the polymer chains, enhanced the catalytic function. The Cu-polymer demonstrated up to an eight-fold enhancement in activity compared to a Cu-monomer complex. The researchers noted that block copolymer supports were not explored due to the generally arduous procedures required to synthesize block copolymers. Nevertheless, this work suggests that catalysts supported on block or block-like copolymers will exhibit further enhancement in their catalytic function.

Block copolymers have been extensively investigated for the preparation of well-defined metal nanostructures, based on their well-ordered, micro-phase separated morphologies stemming from the immiscibility between the chemically dissimilar blocks.[71,72] In these studies, the metal was typically incorporated into the block copolymer through selective coordination to one of the comonomers. Casting a film of a metal-block copolymer solution produced a pattern of metal nanostructures localized within one of the well-defined nanoscale domains. Often, the polymer is used only as a template and removed by pyrolysis followed by calcination to generate a metal

nanopattern on the surface. Block copolymers also have unique properties that originate from the individual character or function of their discrete blocks that in combination with the metal guest particles can be useful in the design of advanced materials.[73]

D.4. Conclusions

As global interest in H_2 fuel increases, improving the efficiency of renewable, non-carbon-based water splitting systems remains a critical challenge. Photoinitiated electron collectors that consist of supramolecular water reduction catalysts and are capable of producing H_2 from water in the presence of an electron donor are a positive step toward addressing the global need for a solar energy-based H_2 fuel source. The current supramolecular WRC assemblies can be further simplified by covalently attaching the WRC to a carbon-based electrode material to rationalize the effect of the sacrificial electron donor on catalyst efficiency and to obtain a deeper understanding of photocatalytic water splitting under tunable environmental conditions.[52,54,55] Covalent binding of the catalyst to an electrically conductive surface is expected to improve catalyst dispersion and reduce catalyst deactivation through intermolecular collisions. Charge separation in the carbon material is also expected to suppress back electron transfer reactions from the catalyst. Thus, the WRC-carbon-based electrode assembly is anticipated to demonstrate improved catalyst stability and enhanced overall catalyst efficiency compared to an analogous WRC in solution. The photosensitizer and photocatalyst can also be linked to a polymer support, where the behavior and stability of the complexes can be investigated in order to obtain deeper insight into the structure-function relationship of the full supramolecular photocatalyst assembly.

D.5. Research statement and objectives

The purpose of this research is to investigate the electron transfer rate and efficiency of Ru^{II},Rh^{III} supramolecular photocatalysts that are attached to a material capable of donating electrons to the catalyst, with the goal of understanding how these electron and proton transfer processes impact catalyst function. As a first step in this work, the focus will be to attach the Ru^{II} photosensitizer and the bimetallic catalyst to a polystyrene support in order to understand how the spatial separation of the photosensitizers along the polymer chain affects the photophysical properties and stability. Specific objectives and fundamental questions of this research are as follows.

- Synthesize novel Ru^{II}- and $Ru^{II}Rh^{III}$-polypyridyl complexes with carboxylic acid substituents to provide a site for covalent attachment to a polystyrene-based support
- Covalently attach the photosensitizer to the polymer support and explore analytical methods to fully characterize the complex
- Rationalize the effect of comonomer sequence distribution on the photophysical properties of the photosensitizer
    - How does covalently attaching the photosensitizer to a polymer support impact the photosensitizer photophysical properties?
    - How does the spatial distribution of the photosensitizer along the copolymer chain impact the photosensitizer photophysical properties?
- Synthesize novel Ru^{II}- and $Ru^{II}Rh^{III}$-polypyridyl complexes with an alkyne substituent to provide a site for covalent attachment of the complex to a functionalized CNF
- Covalently attach the photosensitizer and photocatalyst to the CNF and explore analytical methods to fully characterize the complex
- Develop a fundamental understanding of the physical and chemical interactions that take place between the photocatalyst and the CNF
    - How does covalent attachment of the photocatalyst impact catalyst function?
    - How does catalyst loading impact catalyst function?
    - How does applying an external potential to the CNF impact catalyst function?

D.6. Preliminary results

D.6.1. Synthesis and characterization of tris-heteroleptic Ru^{II}-polypyridyl complexes with Ph_2phen, dpp, and bpy or dcbpy ligands

Tris-heteroleptic Ru^{II}-polypyridyl complexes were prepared using modified literature procedures, starting with the synthesis of a Ru-dimer complex and adding each bidentate ligand in subsequent reaction steps.[74-76] The reactions for the synthesis of the Ru-dimer, $[Ru(BZ)Cl_2]_2$ (BZ = benzene), and the monosubstituted complexes [(BZ)(bpy)RuCl]Cl (bpy = 2,2′-bipyridine) and [(BZ)(dcbpy)RuCl]Cl (dcbpy = 2,2′-bipyridine-4,4′-dicarboxylic acid) are provided in **Scheme D.1**. The Ru-dimer was synthesized from the reaction of $RuCl_3 \cdot H_2O$ and 1,3-cyclohexadiene in ethanol (EtOH) at reflux.[74] After 4 h a brown precipitate had formed. The precipitate was filtered, washed with methanol, and dried under vacuum. The reaction of the Ru-dimer with two equivalence of bpy terminal ligand (TL) in refluxing methanol produced the monosubstituted [(BZ)(bpy)RuCl]Cl complex after 3 h and was followed by removing the solvent under vacuum.[75] The product was purified by dissolving in methanol and precipitating in hexanes with a yield of 98%. The product was a pale-orange powder. Synthesizing the monosubstituted [(BZ)(dcbpy)-RuCl]Cl complex required deprotonation of the dcbpy TL with a base. After the reaction, the addition of acid precipitated the unreacted ligand, which was removed by filtering through a sintered glass funnel. The product was dried under vacuum and purified by dissolving in methanol and precipitating in hexanes, producing a pale-yellow powder in 58% yield. Looking back at the literature procedure,[75] the monosubstituted reactions may also be performed at room temperature.

Scheme D.1. Reaction scheme for the synthesis of the dimer $[Ru(BZ)Cl_2]_2$ and the monosubstituted complexes [(BZ)(bpy)RuCl]Cl (bpy = 2,2′-bipyridine) and [(BZ)(dcbpy)RuCl]Cl.

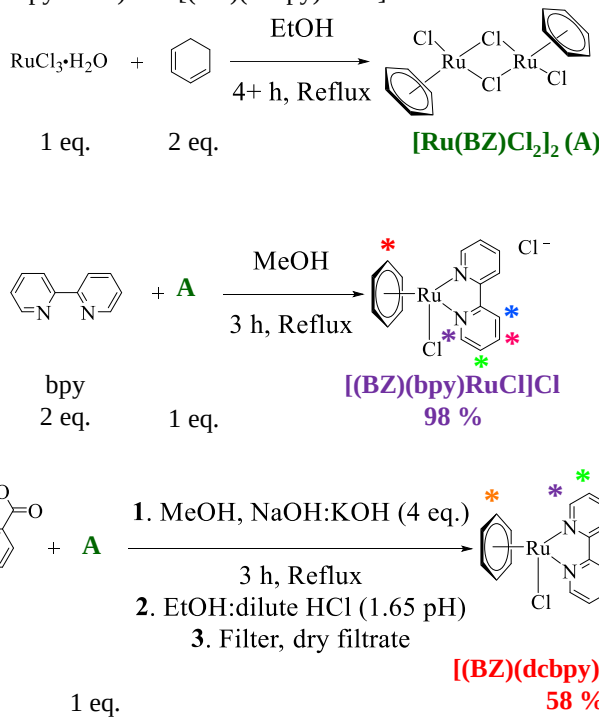

The Ru-dimer and monosubstituted complexes were characterized using ^1H nuclear magnetic resonance (NMR) spectroscopy. The aromatic regions of the NMR spectrum for the Ru-dimer, bpy and dcbpy ligands, and the [(BZ)(bpy)RuCl]Cl and [(BZ)(dcbpy)RuCl]Cl complexes are compared in **Figure D.6**. The Ru-dimer contains a single peak from the benzene aromatic protons. Coordination of the bpy or dcbpy ligands to a Ru-center produces a downfield shift in the benzene protons, indicating that the protons are deshielded by ligand coordination. The benzene protons are deshielded to a greater extent by the electron withdrawing carboxylic acid groups of dcbpy, as expected. The NMR spectra of the monosubstituted complexes exhibit a 1:1 ratio of ligand to benzene. In addition, there is no indication of unbound ligand in the monosubstituted complexes. The set of doublets in the [(BZ)(dcbpy)RuCl]Cl around 7.9 ppm may be from an impurity. This sample was used without further purification.

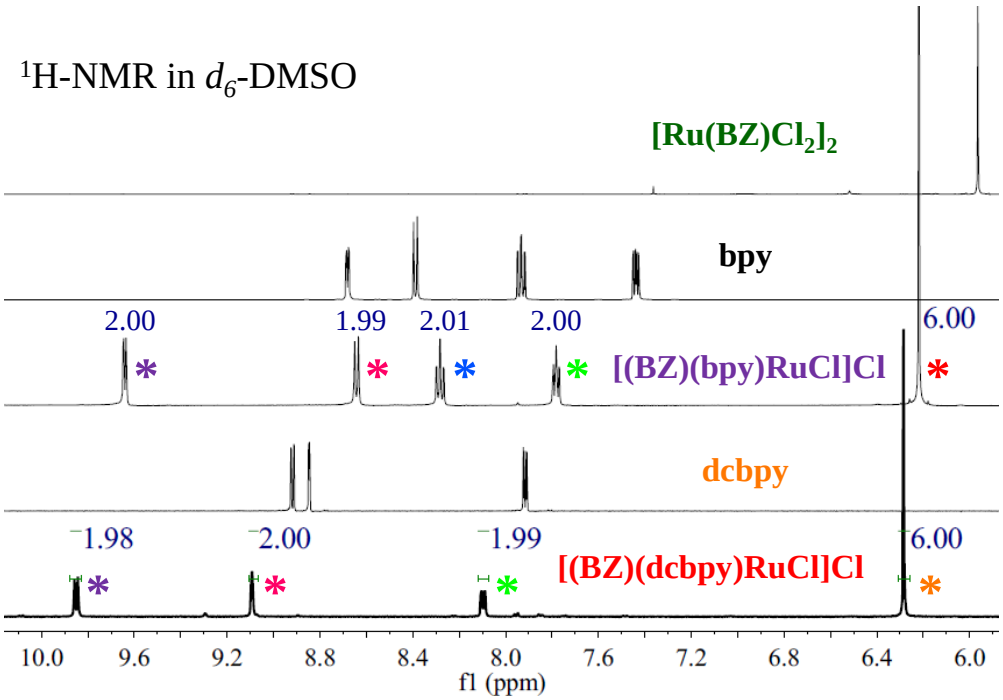

Figure D.6. ^{1}H NMR spectra of the (top to bottom) [Ru(BZ)Cl$_2$]$_2$ dimer, bpy ligand, [(BZ)(bpy)RuCl]Cl, dcbpy ligand, and [(BZ)(dcbpy)RuCl]Cl. BZ = benzene; bpy = 2,2′-bipyridine; dcbpy = 2,2′-bipyridine-4,4′-dicarboxylic acid. Referenced to d_6-DMSO. The asterisks correspond to the asterisks included in **Scheme C.1**.

The monosubstituted complexes were subsequently reacted with Ph$_2$phen (4,7-diphenyl-1,10-phenanthroline) TL to produce the disubstituted *cis*-[(X$_2$bpy)(Ph$_2$phenRuCl$_2$] complexes (X = H, COOH) according to the reaction procedure in **Scheme D.2**.[77] The monosubstituted complexes were reacted with one equivalent of Ph$_2$phen in dimethyl formamide (DMF) and 1,4-dioxane in the presence of a chloride salt to reduce the likelihood of forming the trisubstituted impurity. To recover the product, the solutions were added dropwise to a large excess of stirring acetone, which resulted in precipitation of a purple powder. The *cis*-[(bpy)(Ph$_2$phenRuCl$_2$] reaction showed excellent success with LiCl and could be purified using column chromatography with deactivated alumina as the stationary phase and acetonitrile (CH$_3$CN), chloroform (CHCl$_3$) and acetone as the mobile phase in a 1:0.8:0.2 ratio by volume (v/v). The synthesis of *cis*-[(dcbpy)(Ph$_2$phenRuCl$_2$] using tetrabutylammonium chloride (TBACl) proved to be more successful than with LiCl. In the presence of the LiCl salt, the product did not precipitate in acetone

and remained as an oily residue at the bottom of the Erlenmeyer flask. These results suggest that the bulky TBA^+ cation more effectively neutralizes the charge on the ligand, potentially through ionic interactions with the delocalized electrons on the COO^- group. The carboxylated complex was difficult to purify by column chromatography. A silica gel stationary phase with a CH_3CN:$CHCl_3$:MeOH (0.05 M TBACl) (2:1:0.7 by volume) mobile phase appeared to separate the product from the excess ligand and other impurities. While non-chromatographic techniques were not explored in the purification of this complex, protonation of the carboxylate ligand may result in the precipitation of the hydrated disubstituted complex and should be investigated in the future. Fractions collected from the column chromatography that did not demonstrate emission from the trisubstituted impurity after excitation at 460 nm were combined and dried in vacuum.

Scheme D.2. Reaction scheme for the preparation of *cis*-[(X_2bpy)(Ph_2phen$RuCl_2$] (X = H, COOH).

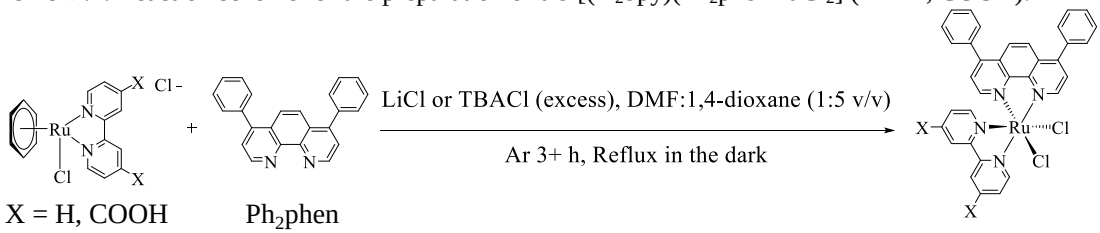

X = H, COOH
1 eq.

Ph_2phen
1 eq.

cis-[(X_2bpy)(Ph_2phen)$RuCl_2$]

Finally, the disubstituted complexes were reacted with dpp (2,3-bis(2-pyridyl)pyrazine) bridging ligand to produce the tris-heteroleptic [(X_2bpy)(Ph_2phen)Ru(dpp)]$(PF_6)_2$ complexes (X = H, COOH), according to **Scheme D.3**. The disubstituted complexes were reacted in refluxing ethanol:water (2:1 v/v, EtOH:H_2O) with an excess of dpp to reduce the probability of forming the bimetallic impurity. To recover the product, the solutions were added dropwise to a 0.1 M NH_4PF_6(*aq*) solution, resulting in precipitation. The products were filtered, dissolved in a minimal amount of acetone, and precipitated in diethyl ether, affording orange powders. Column chromatography was performed to purify the [(bpy)(Ph_2phen)Ru(dpp)]$(PF_6)_2$, using deactivated alumina as the stationary phase and toluene:CH_3CN (0.05 M NH_4PF_6) (3:2 v/v) as the mobile phase

(electrospray ionization mass spectrometry ((+)ESI-MS): $[M-PF_6]^+$ calcd: 969.10, found: 969.16). The $[(dcbpy)(Ph_2phen)Ru(dpp)](PF_6)_2$ complex was purified using a silica gel stationary phase and EtOH:H_2O (0.05 M NH_4PF_6) (1:1 v/v) mobile phase ((+)ESI-MS: $[M-PF_6]^+$ calcd: 1057.10, found: 1057.15). The mass spectra are included in **Figure SD.1**.

Scheme D.3. Reaction scheme for the preparation of $[(X_2bpy)(Ph_2phenRu(dpp)](PF_6)_2$ (X = H, COOH).

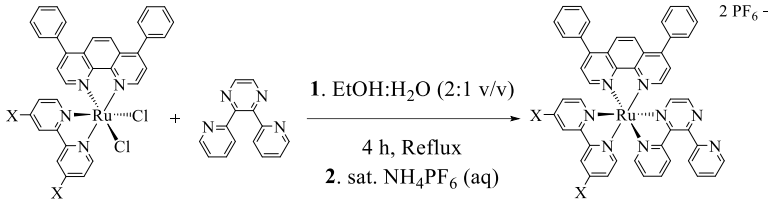

X = H, COOH (1 eq.) dpp (excess) **$[(X_2bpy)(Ph_2phen)Ru(dpp)](PF_6)_2$**

The tris-heteroleptic complexes, referred to herein as Bpy and Dcbpy, were characterized using electrochemistry to probe the electronic transitions, and electronic absorption spectroscopy and emission spectroscopy to investigate the photophysical properties. The instrumentation and methods are described in **subsection D.8.1**. The cyclic voltammograms (CV) of Bpy and Dcbpy are compared in **Figure D.7**. Scanning oxidatively, the CV of Bpy contains a reversible oxidation at E½ = +1.39 V and two reversible reductions at E½ = −1.03 V and −1.40 V (all vs Ag/AgCl), attributed to the $Ru^{II/III}$ oxidation and ligand-based reductions, respectively. The Dcbpy complex shows a reversible oxidation at E½ = +1.53 V that is preceded by an irreversible oxidation at E½ = +1.32 V. Based on the structure of Dcbpy, the irreversible oxidation is tentatively assigned to the oxidation of a carboxylate functional group on the dcbpy ligand. Continuing to scan reductively, a reversible reduction is observed at E½ = −1.03 V, attributed to a ligand-based reduction. The second ligand-based reduction appears to be masked by a rapid increase in the current at below −1.2 V. The rapid increase in current may be catalytic current from the reduction of water molecules that were around the carboxylate functional groups.[78]

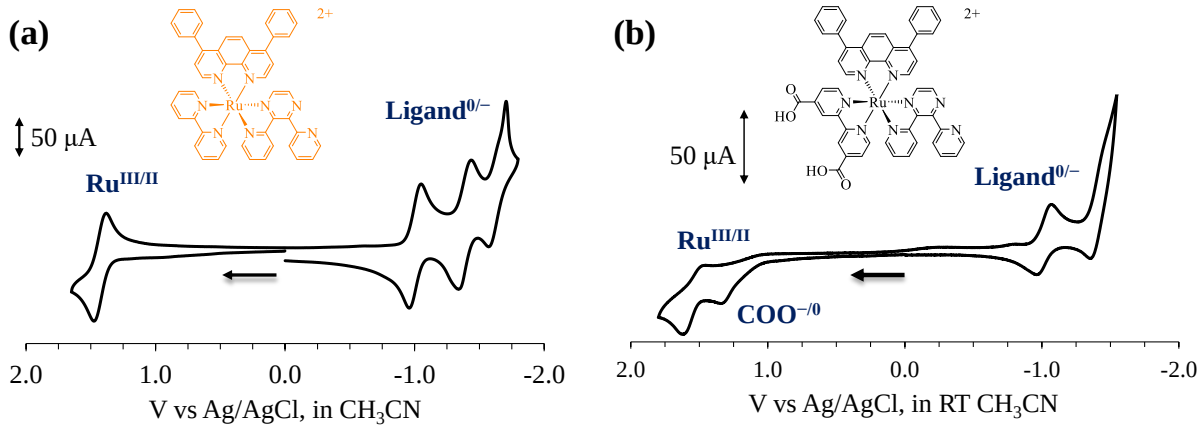

Figure D.7. Cyclic voltammograms of the (a) $[(bpy)(Ph_2phen)Ru(dpp)](PF_6)_2$ ($E½$ = +1.39 V ($Ru^{II/III}$), −1.03 V ($dpp^{0/–}$), −1.40 V ($Ph_2phen^{0/–}$) vs Ag/AgCl, and (b) $[(dcbpy)(Ph_2phen)Ru(dpp)](PF_6)_2$ ($E½$ = +1.53 V ($Ru^{II/III}$), −1.03 V ($dpp^{0/–}$), −1.42 V ($Ph_2phen^{0/–}$); ox. = +1.32 V ($COO^{–/0}$) vs Ag/AgCl. Recorded in CH_3CN with 0.1 M $TBAPF_6$ supporting electrolyte, a Pt disc working, Pt wire auxiliary, Ag/AgCl (3 M NaCl) reference and rate of 100 mV s^{-1}.

In order to obtain further insight into the effect of terminal ligand substitution on the electrochemical properties, the tris-heteroleptic complexes were compared to a model complex with two Ph_2phen terminal ligands, $[(Ph_2phen)_2Ru(dpp)](PF_6)_2$, synthesized by Mongelli and Brewer.[79] **Figure D.8(b)** compares the square wave voltammograms (SWV) of the $[(X_2bpy)(Ph_2phen)$-$Ru(dpp)](PF_6)_2$ complexes (X = H, COOH) and the $[(Ph_2phen)_2Ru(dpp)](PF_6)_2$, referred to herein as Ph_2phen. The electrochemical properties of the Bpy complex are similar to Ph_2phen. Both complexes exhibit a Ru-based oxidation at +1.39 V (vs Ag/AgCl for all). Conversely, in the Dcbpy complex the Ru-based oxidation occurs at a more positive potential than in the model. These data suggest that the electron withdrawing carboxylic acid functional groups decrease the electron density on the metal center, which in turn stabilizes the Ru-based HOMO, making it more energy intensive to remove an electron. All of the monometallic complexes show a first ligand-based reduction at ca. −1.03 V and is therefore assigned to $dpp^{0/–}$. The second ligand reduction occurs at ca. −1.40 V in every complex and is therefore tentatively assigned to $Ph_2phen^{0/–}$, based on the similar reduction potential in the model. The second ligand reduction in the Bpy and Dcbpy complexes occurs at a slightly more negative

potential, suggesting that the ph$_2$phen ligand possess a lower energy LUMO and is thus easier to reduce.

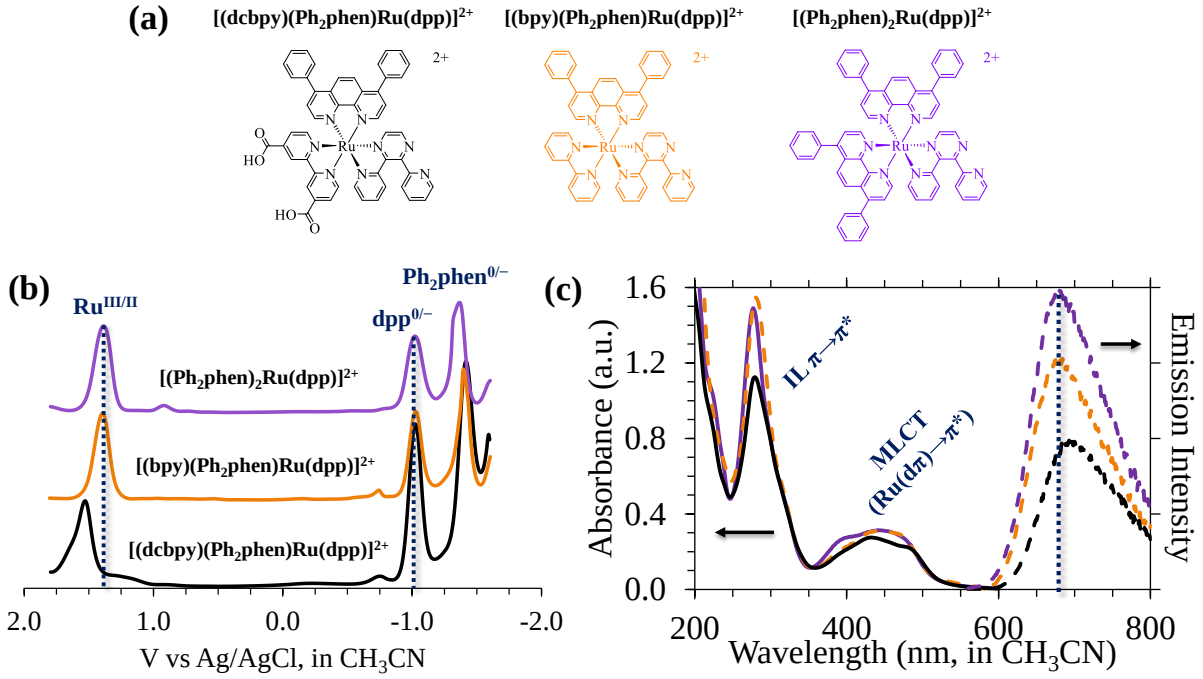

Figure D.8. (a) Structures of the tris-heteroleptic [(X$_2$bpy)(Ph$_2$phen)Ru(dpp)](PF$_6$)$_2$ complexes (X = H, COOH) and the previously synthesized [(Ph$_2$phen)$_2$Ru(dpp)](PF$_6$)$_2$ complex. (b) Square wave voltammograms in CH$_3$CN with 0.1 M TBAPF$_6$ supporting electrolyte (Pt disc working, Pt wire auxiliary, Ag/AgCl (3 M NaCl) reference and rate of 100 mV s^{-1}) and (c) electronic absorption spectra (absorbance matched at 450 nm) and emission spectra of the complexes in (a) recorded in CH$_3$CN (λ_{ex} = 450 nm).

The electronic absorption and emission spectra of the Bpy, Dcbpy, and Ph$_2$phen complexes, absorbance matched at 490 nm, are compared in **Figure D.8(c)**. The monometallic complexes exhibit similar absorption properties, with UV absorption (250 – 320 nm), attributed to overlapping intraligand $\pi\rightarrow\pi^*$ transitions, and visible absorption (350 – 500 nm), attributed to overlapping ^{1}MLCT Ru(dπ)→ligand π^* transitions. The lowest energy transition at ca. 485 nm is assigned to the Ru(dπ)→dpp(π^*) charge transfer transition, based on the model complex. The observed differences in the absorption spectra are attributed to differences in the molar absorptivity of the intraligand and ^{1}MCLT transitions, as expected for different complexes. After excitation with 490 nm light, the monometallic complexes exhibit an intense emission at approximately 670 nm. While

the Dcbpy complex shows a lower emission intensity, not enough is understood about the charge of this complex (e.g., protonated *versus* deprotonated), therefore more information is needed to interpret these results. The electrochemical and photophysical data demonstrate that the dcbpy terminal ligand does not significantly perturb the photophysical and electronic properties of the Ru photosensitizer and should therefore be a suitable coordination site for covalent attachment to a polymer support.

D.6.2. Synthesis and characterization of a novel Ru,Rh bimetallic complex

A novel Ru,Rh bimetallic complex, $[((dcbpy)(Ph_2phen)Ru(dpp))RhBr_2(Ph_2phen)](PF_6)_3$ was synthesized from Dcbpy using a previously reported method.[28] The reaction is provided in **Scheme SD.1**. The bimetallic complex was synthesized using a building block approach in which the Dcbpy monometallic was reacted with a large excess of $[RhBr_4(Ph_2phen)]$ in refluxing EtOH:H_2O (2:1 v/v) for 3 h and precipitated by slow pouring into an $NH_4PF_6(aq)$ solution. The product was filtered and washed with water and diethyl ether. Herein, the new bimetallic complex will be referred to as trisRuRh. **Figure D.9** compares the electronic absorption spectra of trisRuRh, Dcbpy, and a model bimetallic complex and known photoinitiated electron collector, $[((Ph_2phen)_2Ru(dpp))RhBr_2(Ph_2phen)]^{3+}$.[80] All of the complexes show intense UV absorption from overlapping intraligand $\pi\rightarrow\pi^*$ transitions. The bimetallic complexes have remarkably similar absorption spectrum in the visible region and absorb light throughout the UV and visible spectrum. In addition, the ^{1}MLCT Ru(dπ)→ligand π^* transitions in the bimetallic complexes are red-shifted relative to that of the monometallic complex. These data are consistent with the stabilization of the dpp(π^*) orbital upon coordination to a second electropositive metal center and support that the lowest ^{1}MLCT transition is a Ru(dπ)→dpp(π^*) charge transfer transition. Thus, these results strongly suggest that the novel Ru,Rh bimetallic complex will behave as a photoinitiated electron

collector. In addition, trisRuRh contains carboxylic acid groups that can be used to attach the complex to a polymer support. Further characterization of the trisRuRh complex was not performed because the emission spectrum showed emission upon excitation with 490 nm light that was likely from the monometallic impurity. Attempts to purify the sample using size exclusion chromatography (SEC) with a Sephadex® LH-20 stationary phase and CH_3CN:EtOH (3:2 v/v) mobile phase were unsuccessful. However, new methods of purification should be explored, and the electrochemical and spectroscopic properties should be analyzed in the future.

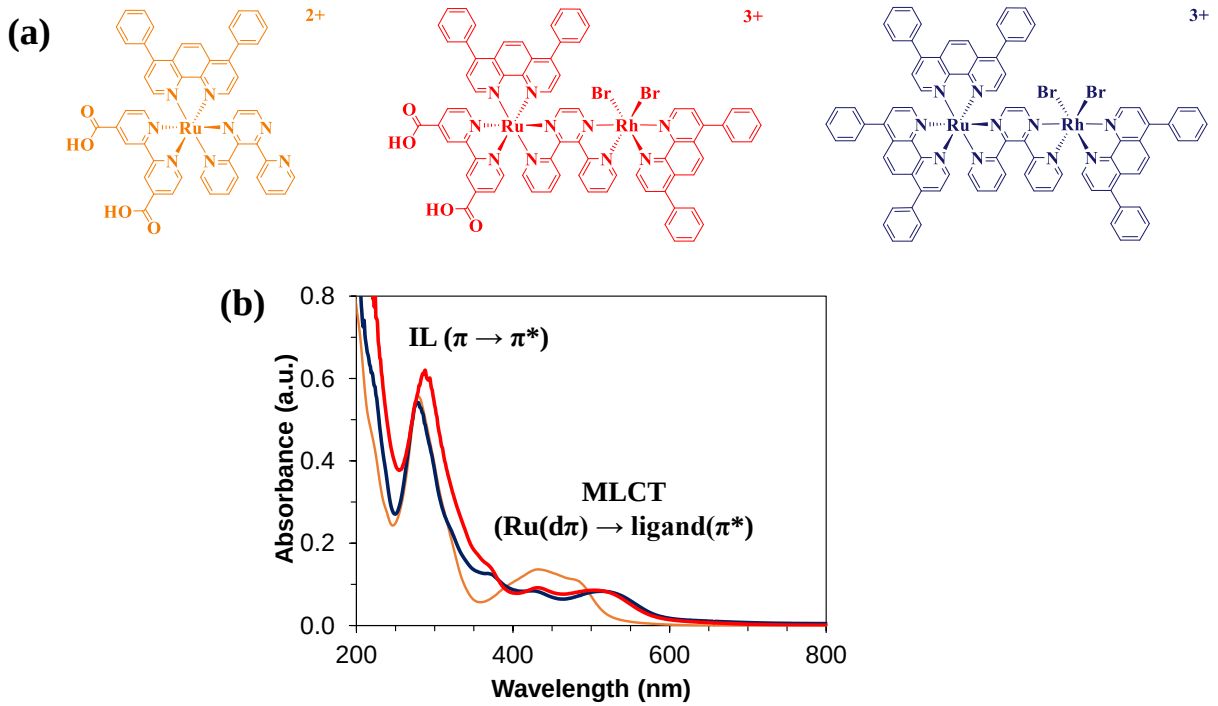

Figure D.9. (a) Structures and (b) electronic absorption spectra of the (left) $[(dcbpy)(Ph_2phen)Ru(dpp)]^{2+}$, (center) $[((dcbpy)(Ph_2phen)Ru(dpp))RhBr_2(Ph_2phen)]^{3+}$, and (right) $[((Ph_2phen)_2Ru(dpp))RhBr_2(Ph_2phen)]^{3+}$ complexes.

D.6.3. Covalent attachment of a photosensitizer to a crosslinked polystyrene resin

To investigate the reversible covalent attachment of a Ru^{II}-polypyridyl photosensitizer to a polymer support, a $[Ru(bpy)_2(Mebpy\text{-}COOH)]^{2+}$ (Ru-OH) model complex was reacted with cross-linked polystyrene resins and the fluorescence of the resin was investigated using a UV light source. **Figure D.10** shows the amidation reaction used to attach Ru-OH to polystyrene rink amide

(PS-RA). This reaction is typically carried out in peptide synthesis procedures and uses HCTU, an aminium coupling reagent, and *N*,*N*-diisopropylethylamine (DIEA). After the reaction, the resin was washed several times. The reaction procedure was repeated using $[Ru(bpy)_3]^{2+}$ as a non-complexing control. Before the reactions, the PS-RA was a white solid. After the reaction with $[Ru(bpy)_3]^{2+}$ the resin was an off-white color and showed no visible fluorescence under irradiation with UV light. In contrast, the PS-RA/Ru-OH complex was bright orange, consistent with the color of the Ru-OH complex, and the resin exhibited strong fluorescence.

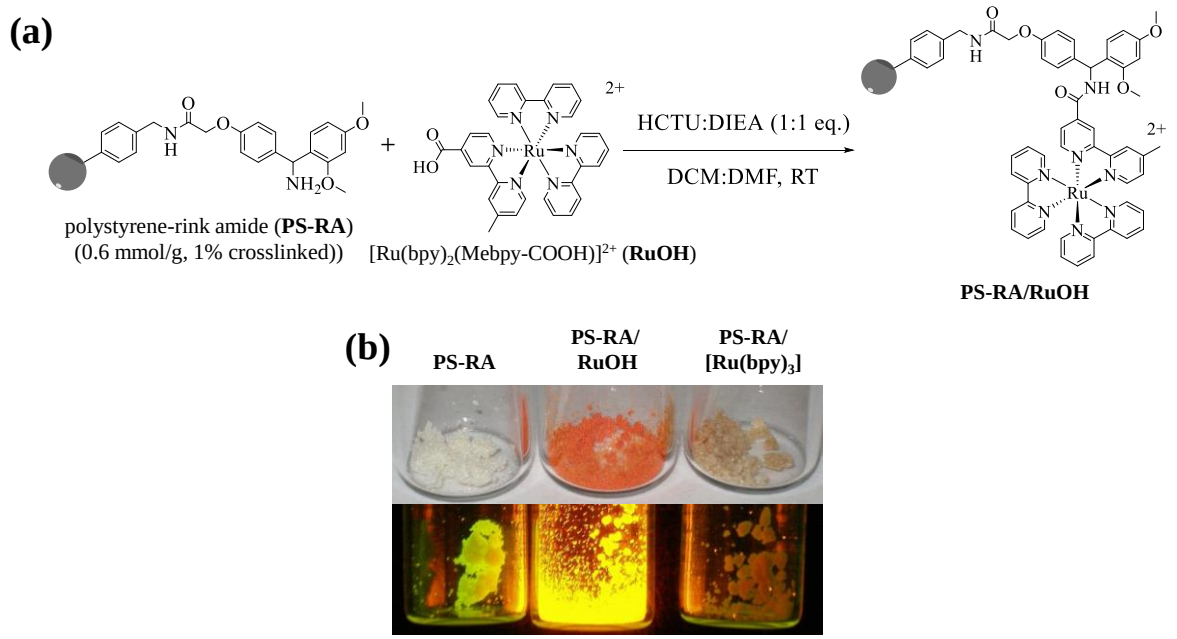

Figure D.10. (a) Reaction scheme for the covalent attachment of $[Ru(bpy)_2(Mebpy\text{-}COOH)]^{2+}$ (bpy = 2,2′-bipyridine; Mebpy-COOH = 4′-methyl-2,2′-bipyridine-4-carboxylic acid) to polystyrene rink amide (PS-RA) and (b) the appearance of PS-RA, the complexed PS-RA/RuOH, and an noncomplexed PS-RA/$[Ru(bpy)_3$ (top) under normal lighting conditions and (bottom) exposed to ultraviolet radiation. HCTU = aminium coupling reagent; DIEA = *N*,*N*-diisopropylethylamine.

The same Ru-OH complex was attached through a glycine linker molecule to another polystyrene resin with a 2-chlorotrityl chloride functional group (2-ClTrt), in order to investigate the cleavage and recovery of the complex from the resin. The glycine residue was incorporated as a marker to show an increase in the mass of the Ru-OH complex after cleavage. The polystyrene resin and cleavage reaction are shown in **Figure D.11**. The reaction used to attach the glycine

residue and Ru-OH complex is provided in **Scheme SD.2**. To remove the Ru-OH complex with the glycine linker, the 2-ClTrt/Ru-Gly was exposed to acetic acid (HOAc) and trifluorethanol (TFE) in dichloromethane (DCM), which breaks the C−O bond between the resin and the Ru-Gly complex. Before any reaction, the resin was an off-white solid and showed a pale-yellow fluorescence. After the reaction with Ru-OH the resin (2-ClTrt/Ru-Gly) was a bright orange and exhibited strong fluorescence. Following the cleavage reaction, the resin returned to an off-white color and showed bright yellow fluorescence, suggesting that the Ru-Gly complex was not completely removed during the reaction. The solution from the cleavage reaction was recovered and analyzed by ESI-MS. The mass spectrum contained a peak with a m/z of 342.27, in excellent agreement with the calculated m/z for the $Ru\text{-}Gly^{2+}$ complex of 342.57. Thus, these data demonstrate that a Ru^{II}-polypyridyl complex can be successfully coordinated to a polystyrene resin through an amide condensation reaction and is stable after cleavage from the resin.

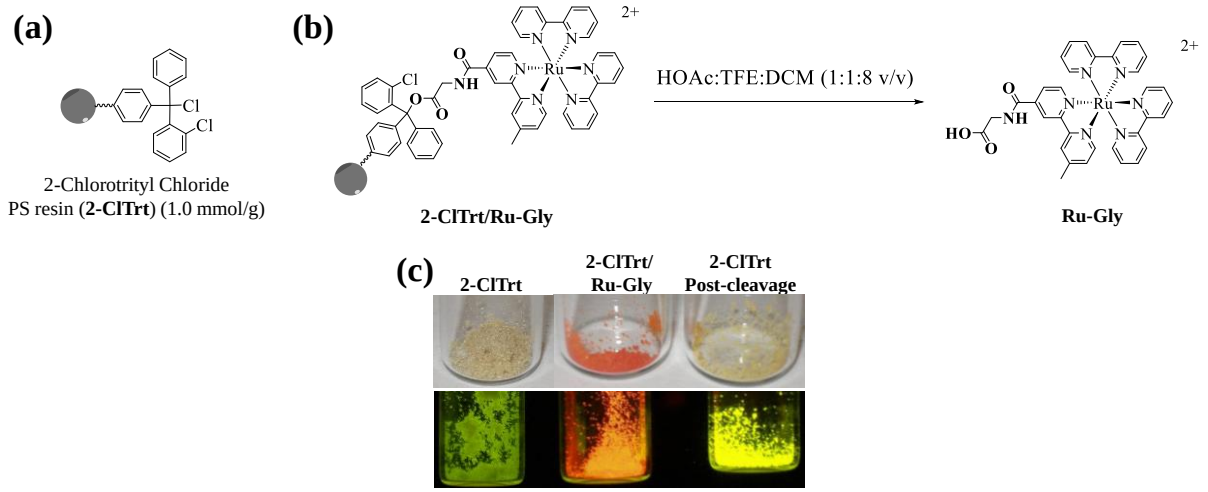

Figure D.11. (a) Structure of the 2-chlorotrityl chloride polystyrene resin (2-ClTrt). (b) Reaction scheme to remove the Ru^{II}-polypyridyl photosensitizer from the polystyrene resin. (c) The appearance of 2-ClTrt, the complexed 2-ClTrt/Ru-Gly, and the resin post-cleavage (top) under normal lighting conditions and (bottom) exposed to ultraviolet radiation. HOAc = acetic acid; TFE = trifluorethanol.

D.6.4. Synthesis and characterization of $[(Mebpy\text{-}COOH)(Ph_2phen)Ru(dpp)](PF_6)_2$

The novel tris-heteroleptic $[(Mebpy\text{-}COOH)(Ph_2phen)Ru(dpp)](PF_6)_2$ complex (Mebpy-COOH 4′-methyl-2,2′-bipyridine-4-carboxylic acid) was synthesized according to a slightly

different procedure proposed by Vougioukalakis et al.,[81] that appears to have been quite successful. The step-by-step reaction is provided in **Scheme D.4**. Starting with the same Ru-dimer that was described previously, the dimer was first reacted with the Ph_2phen ligand. After 4 h, the Mebpy-COOH ligand was then added directly to the reaction vessel in one step and the reaction was continued for another 4 h. The product was precipitated by reducing the solvent volume in vacuum, followed by dropwise addition to diethyl ether to form the disubstituted [(Mebpy-COOH)(Ph_2phen)$RuCl_2$] intermediate. The product was washed with diethyl ether and used without further purification. The dpp bridging ligand was combined with the disubstituted complex and refluxed in EtOH:H_2O (2:1 v/v) for at least 3 h. The crude product was recovered by slow addition to stirred 0.1 M NH_4PF_6(*aq*) solution to afford an orange powder. Size exclusion chromatography was conducted to purify the crude product using a Sephadex® LH-20 stationary phase and CH_3CN:EtOH (3:2 v/v) mobile phase ((+)ESI-MS: calcd: 441.0997, found: 441.1031 [M^{2+}]; calcd: 1027.164 found: 1027.1713 [$M-PF_6]^+$).

Scheme D.4. Reaction scheme to prepare [(Mebpy-COOH)(Ph_2phen)Ru(dpp)]$(PF_6)_2$.

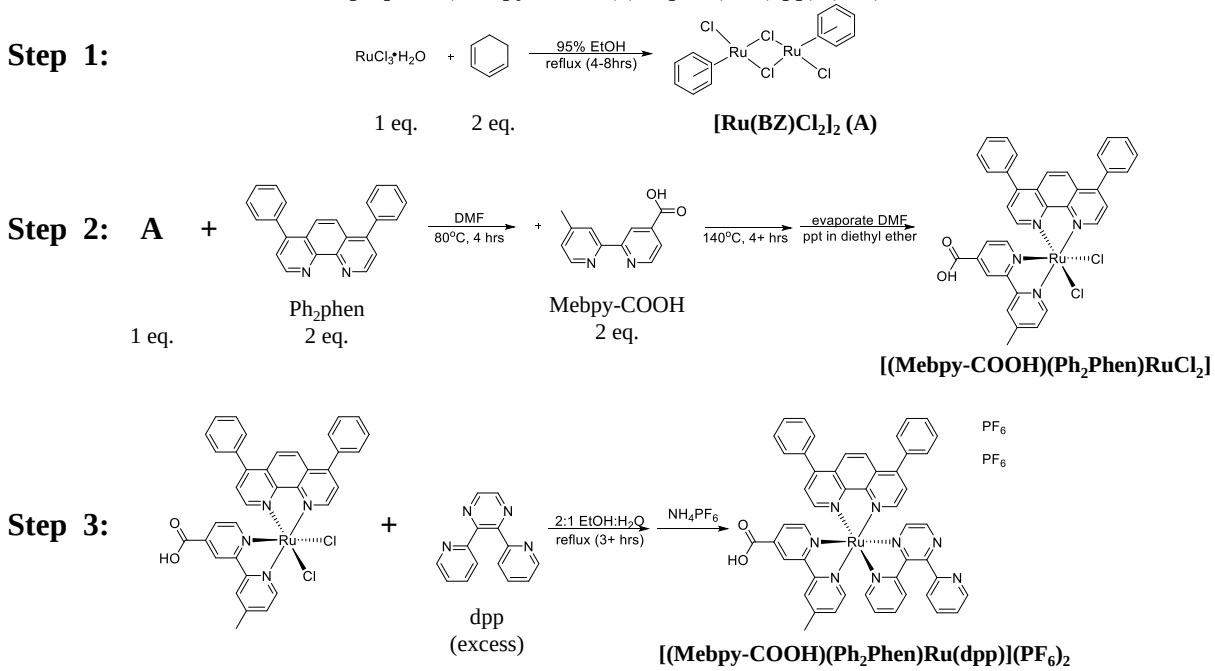

The electrochemical and photophysical properties of the [(Mebpy-COOH)(Ph_2phen)-Ru(dpp)](PF_6)$_2$, were investigated using electrochemistry and electronic absorption and emission spectroscopies. Herein, the complex is referred to as Mebpy-OH. Overall, the properties of Mebpy-OH are consistent with those of the Dcbpy complex with two carboxylic acid functional groups instead of one. The CV and SWV of Mebpy-OH are provided in **Figure D.12(a)**. Scanning oxidatively, a reversible oxidation was observed at E½ = +1.43 V (all vs Ag/AgCl), assigned to a Ru-based oxidation. The metal-based oxidation was preceded by an irreversible oxidation at E½ = +1.35 V, which is consistent with that observed in the CV of Dcbpy and strongly supports that this feature is from the oxidation of the carboxylate functional group on the dcbpy ligand. Two reversible reductions occurred at E½ = −1.06 V and −1.45 V, assigned to the dpp-based and Ph_2phen-based reductions, respectively, based on the ligand reduction potentials of the model Ph_2phen complex. The rapid increase in current below −1.6 V may be catalytic current from the reduction of water molecules that were around the carboxylate functional group.[78] The electronic absorption and emission spectra of the Mebpy-OH are shown in **Figure D.12(b)**. The absorption spectrum contained intense UV absorption, attributed to overlapping intraligand π→π* transitions, and visible absorption, attributed to overlapping ^{1}MLCT Ru(dπ)→ligand π* transitions. After excitation with 450 nm light, the complex showed intense emission at 675 nm. The electrochemical and photophysical properties of Mebpy-OH are consistent with those observed for Dcbpy. These results suggest that the three-step reaction procedure shown in **Scheme D.4** may be a simpler route to achieve a high purity tris-heteroleptic complex that involves fewer purification steps. Unfortunately, this project was abandoned because of the difficulty in synthesizing the Mebpy-COOH terminal ligand.

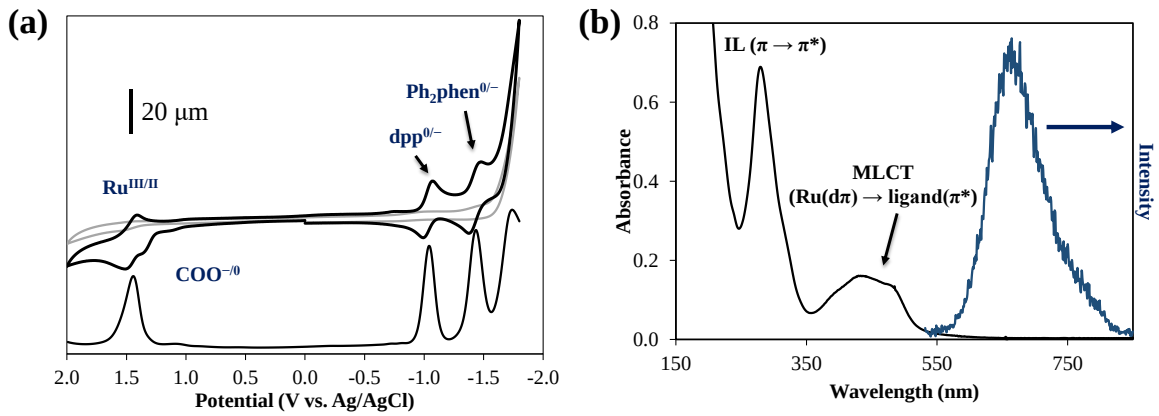

Figure D.12. Characterization of [(Mebpy-COOH)(Ph_2phen)Ru(dpp)](PF_6)$_2$ (Mebpy-COOH = 4′-methyl-2,2′-bipyridine-4-carboxylic acid; Ph_2phen = 4,7-diphenyl-1,10-phenanthroline; dpp = 2,3-bis(2-pyridyl)pyrazine). (a) CV (bold black) and SWV (black) in CH_3CN with 0.1 M $TBAPF_6$ supporting electrolyte (grey = background). E½ = +1.43 V ($Ru^{II/III}$), −1.06 V ($dpp^{0/–}$), −1.45 V ($Ph_2phen^{0/–}$); ox. +1.35 V = $COO^{–/0}$ vs Ag/AgCl(b) Electronic absorption spectrum (black) and emission spectrum (red) in CH_3CN (250 – 320 nm: overlapping ligand π→π* transitions; 350 – 500 nm: overlapping Ru(dπ)→ligand π* transitions; λ_{ex} = 450 nm; λ_{max} = 675 nm).

D.6.5. Synthesis of *cis*-[(X)$_2$RuCl$_2$] complexes

The *cis*-[(Mebpy-COOH)$_2$RuCl$_2$] and *cis*-[(dcbpy)$_2$RuCl$_2$] complexes were synthesized using a modified literature procedure.[82] Briefly, $RuCl_3$•$2H_2O$ (0.229 mmol) and (0.463 mmol) of ligand were refluxed under argon in DMF (8 mL) for 8 h, followed by cooling to room temperature and filtering. According to the literature method, the product should precipitate in acetone after evaporating the solvent under vacuum. When this procedure was performed the products did not precipitate and instead remained as an oily residue at the bottom of the stirred acetone. It was later discovered that reducing the volume of DMF to less than 1-2 mL prevented the precipitation of the product. However, not removing the solvent and pouring into stirred acetone followed by cooling the mixture overnight at 4 °C did result in product precipitation. The product also may have precipitated if added dropwise to stirred acetone. In addition, the volume of DMF used in this reaction was less than recommended. Increasing the reaction volume may have improved product recovery. **Figure D.13** shows the electronic absorption spectrum of each complex. The spectra are similar and exhibit the characteristic intraligand π→π* transitions at 250–340 nm and two Ru(dπ)→ligand π* transitions at 340–450 and 470−630 nm. The *cis*-[(Mebpy-COOH)$_2$RuCl$_2$]

shows greater absorbance at ca. 200 nm, which may be indicative of ligand impurity. Both crude products contained impurities of the $[L_3Ru]Cl_2$ (L = ligand), demonstrated by an intense emission peak at ca. 630 nm after excitation at 450 nm. Attempts were made to remove the impurity using column chromatography techniques with alumina and silica stationary phases and a broad range of solvent systems. The conclusions were that the impurity could not be removed below the detection limit of the fluorometer and there was significant product loss in the process. Looking back on this synthetic approach, the recovered product could have been washed with acetone and used without purification. In addition, purification methods to precipitate the product at its isosbestic point should be investigated in the future.[82]

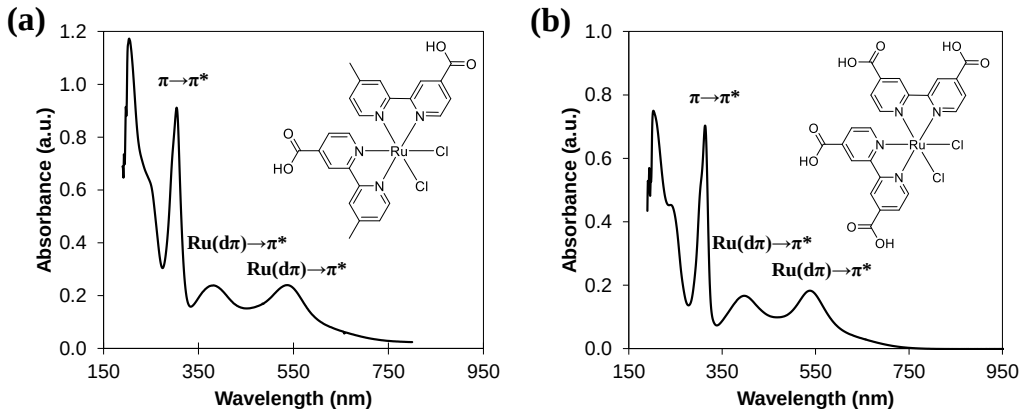

Figure D.13. Electronic absorption spectrum of (a) of *cis*-$[(Mebpy\text{-}COOH)_2RuCl_2]$ and (b) *cis*-$[(dcbpy)_2RuCl_2]$. Mebpy-COOH = 4′-methyl-2,2′-bipyridine-4-carboxylic acid; dcbpy = 2,2′-bipyridine-4,4′-dicarboxylic acid.

D.6.6. Procedure for preparing electrospun carbon fiber mats

Electrospun carbon fiber mats were prepared from a 12% w/w polyacrylonitrile (PAN, 2.1856 g) in DMF (16.0 g) solution using a syringe pump and a rotating cylinder collector. The solution was prepared by combining the two components with heat and stirring overnight. The electrospinning parameters included a distance of ca. 30 cm, syringe volume of 2 mL, flow rate of 0.75 mLh^{-1}, and voltage of +18.01 to +18.35 V. Throughout the electrospinning process the measured relative humidity remained ca. 51% and the temperature was ca. 22 °C. An as prepared

mat is shown in **Figure D.14(a)**. The mat was fluffy and did not role tight at the edges. The mat was cut off the rod using a scalpel blade. After removal from the rod, a glass plate heated to 125°C was used to anneal the fibers with heat treatment for approximately five minutes on each side, as shown in **Figure D.14(b)**. Oxidation was performed in an oven in an air-purged environment. The temperature was increased from room temperature to 260°C at a rate of 5°C/min, followed by heating to 380°C at 1°C/min. At 380°C, the mat was promptly removed and allowed to cool to room temperature in air. The mat was carbonized in a tube furnace by ramping the temperature from room temperature up to 1000°C at 5°/min in a N_2 purged environment followed by cooling to room temperature in the tube furnace. The product was a black, flexible mat as shown in **Figure D.14(c)**.

Figure D.14. Electrospun carbon fiber mat prepared from a 12% w/w solution of polyacrylonitrile (PAN) and DMF (a) as prepared, (b) after annealing at 125 °C for 10 minutes, and (c) after oxidation and carbonization.

D.7. Final remarks and broader impacts

Solar is an inexhaustible source of energy that can be stored as chemical energy through the formation of molecular bonds. The photocatalytic production of hydrogen gas from water splitting is a particularly attractive sustainable process to store solar energy because H_2 can be converted back into water in an energy rich, exothermic combustion reaction without forming environmentally detrimental carbon-based byproducts. Furthermore, the energy density per gram of H_2 burned in the combustion reaction is nearly double that of other small molecule fuel sources

(excluding nuclear-based fuels). Supramolecular photocatalysts have been reported that produce H_2 by reducing water in the presence of a sacrificial electron donor.

This work demonstrates the synthesis of two novel, tris-heteroleptic Ru^{II}-polypyridyl complexes and one novel Ru,Rh bimetallic complex each containing carboxylic acid functional groups that can allow for covalent attachment of the monometallic and bimetallic complexes to a polymer support or electron donor source. The stability of a Ru^{II}-polypyridyl complex to covalent attachment and cleavage from a polystyrene resin was investigated. The complex was stable and could be recovered after cleavage, which supports that the monometallic and bimetallic may be reversibly attached to a polymer in order to simplify the supramolecular photocatalyst assembly. The novel bimetallic complex contained a low energy $Ru(d\pi^*)\rightarrow dpp(\pi^*)$ charge transfer that is expected to direct electrons from the formally $Ru(d\pi)$ HOMO to the $Rh(d\sigma^*)$, as observed previously in similar bimetallic photocatalysts. Overall, the synthesis of the complexes proved to be challenging. The synthetic strategies involved required confidence, patience, significant synthetic skill, and experience, which the researcher did not have when performing this project. Nevertheless, the preliminary results are promising and demonstrate that this work should be continued in the future. Reducing molecular collisions through covalently binding a WRC to an electron donor source will provide valuable insight into electron transfer processes. In addition, the knowledge gained from this continued work will benefit other areas of photocatalysis, as well as the areas of membrane engineering, and fuel cell research.

D.8. Supplementary information

The (+)ESI-MS of the tris-heteroleptic $[(X_2bpy)(Ph_2phen)Ru(dpp)](PF_6)_2$ complexes (X = H, COOH) are provided in **Figure SD.1**.

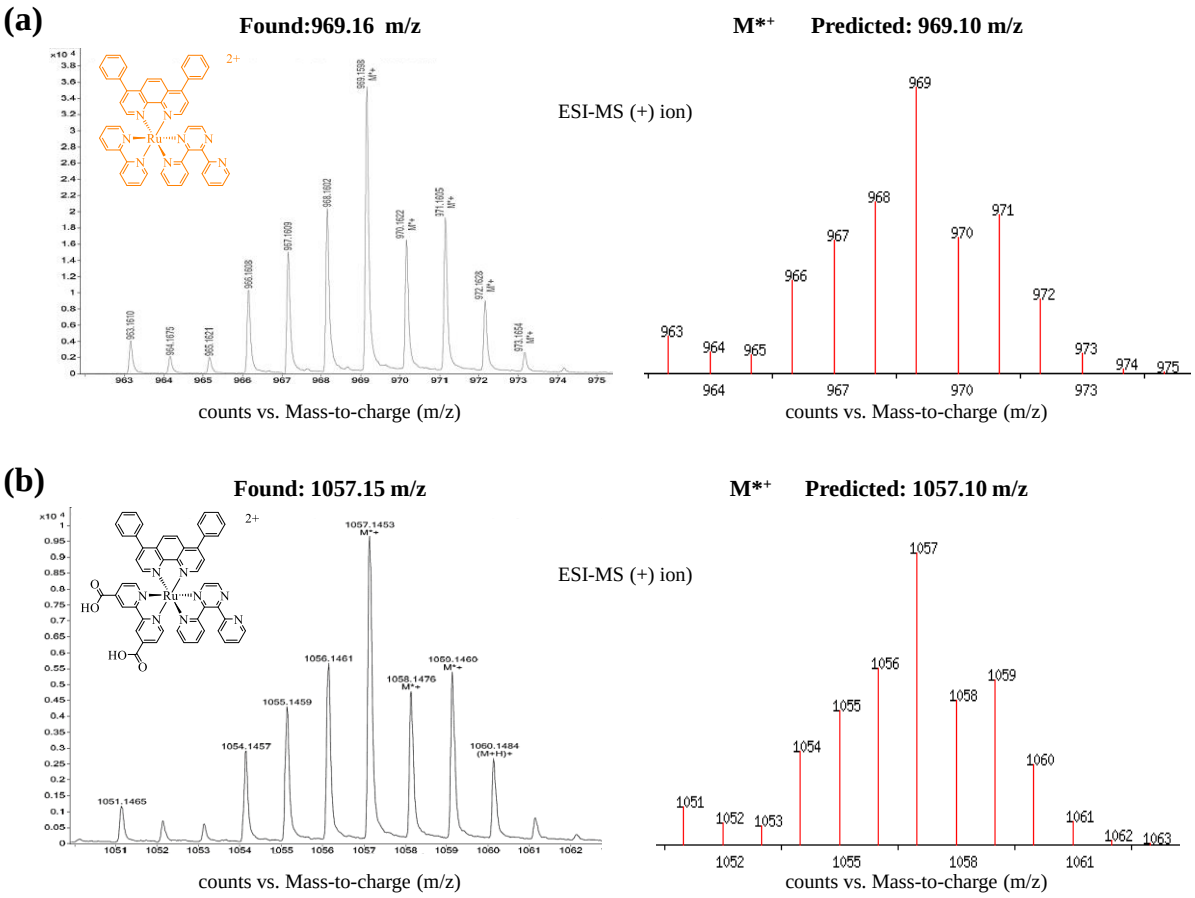

Figure SD.1. (left) mass spectrum and (right) predicted mass spectrum of (a) $[(bpy)(Ph_2phen)Ru(dpp)]^{2+}$ and (b) $[(dcbpy)(Ph_2phen)Ru(dpp)]^{2+}$.

Scheme SD.1 provides the reaction scheme for the synthesis of the novel bimetallic complex, $[((dcbpy)(Ph_2phen)Ru(dpp))RhBr_2(Ph_2phen)](PF_6)_3$.[28] The $[(Ph_2phen)RhBr_4]$ complex was prepared according to Rogers et al.,[80] who reported that this complex should actually be $[(Ph_2phen)RhBr_3(DMF)]$, however the ^1H NMR spectrum did not suggest the complex contained a coordinated DMF molecule.

Scheme SD.1. Reaction scheme for the synthesis of $[((dcbpy)(Ph_2phen)Ru(dpp))RhBr_2(Ph_2phen)](PF_6)_3$.

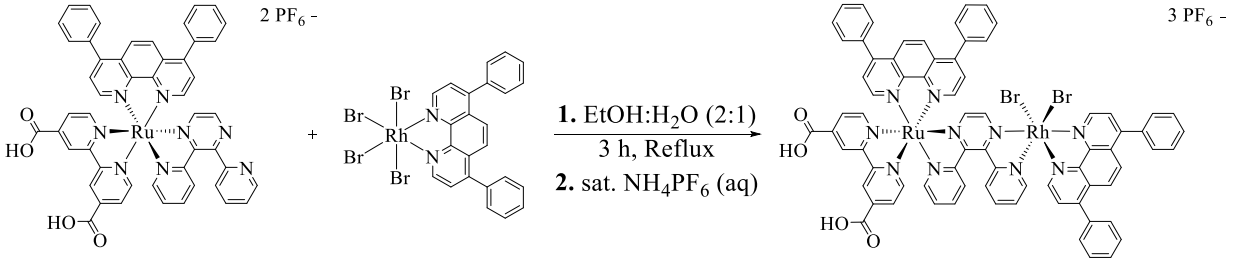

Scheme SD.2 shows the reaction scheme used to attach $[Ru(bpy)_2(Mebpy\text{-}COOH)]^{2+}$ to the 2-chlorotrityl chloride PS resin.[83] This reaction procedure is typically used in peptide synthesis.

Scheme SD.2. Reaction scheme for the covalent attachment of $[Ru(bpy)_2(Mebpy\text{-}COOH)]^{2+}$ (bpy = 2,2′-bipyridine; Mebpy-COOH = 4′-methyl-2,2′-bipyridine-4-carboxylic acid) to 2-chlorotrityl chloride polystyrene resin. DIEA = *N*,*N*-diisopropylethylamine; DCE = 1,2-dichloroethane; HCTU = aminium coupling reagent; Gly = Fmoc protected glycine.

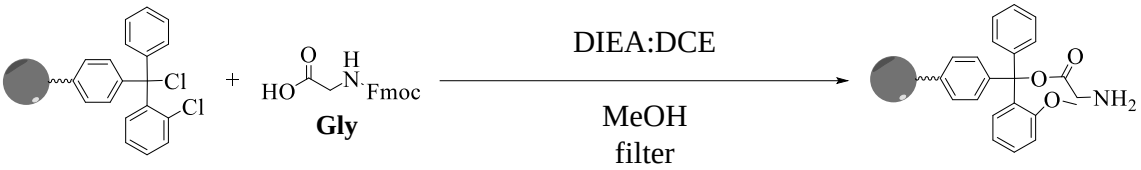

2-Chlorotrityl Chloride
PS resin (**2-ClTrt**) (1.0 mmol/g)

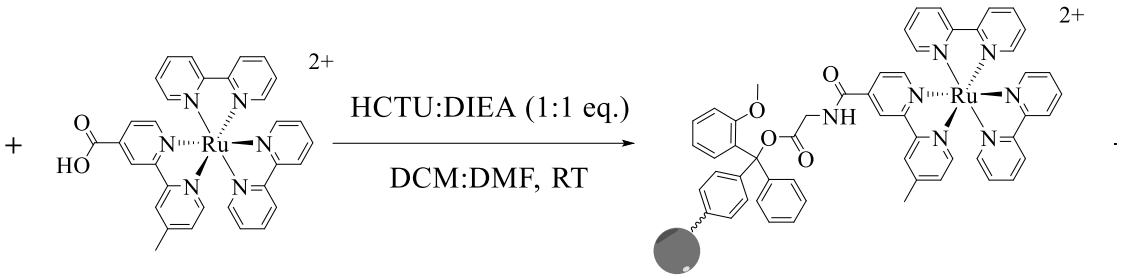

$[(bpy)_2Ru(MebpyCOOH)](PF_6)_2$ (1 eq.)

D.8.1. Instrumentation and methods

^{1}H NMR experiments were recorded at room temperature in d_6-dimethyl sulfoxide (DMSO) on an Agilent U4-DD2 400 MHz spectrometer. Positive ion electrospray ionization mass spectrometry ((+)ESI-MS) experiments were performed by Mr. William Bebout in the Virginia Tech Chemistry Department Analytical Services laboratory using an Agilent Technologies 6220 Accurate-Mass time-of-flight (TOF) instrument with a dual ESI source. Samples were dissolved

in HPLC grade CH_3CN and directly injected into the instrument source through a preloading capillary at +1.2 kV with a flow rate of 0.4 mL min^{-1}, using N_2 gas at a pressure of 60 psi as the inert nebulizing gas, and a charging voltage of 2000 V, fragmentor voltage of 125 V, and skimmer voltage of 65 V. Electrochemistry experiments were conducted in deoxygenated CH_3CN electrolyte solution containing 0.1 M Bu_4NPF_6 using an Epsilon potentiostat (Bioanalytical Systems, Inc.) with a one compartment three electrode cell, glassy Pt disk working electrode, platinum wire auxiliary electrode, and a Ag/AgCl (3 M NaCl) reference electrode. The cyclic voltammetry (CV) experiments were performed at a scan rate of 100 mv s^{-1}. Osteryoung square wave voltammetry (SWV) experiments were performed with a pulse frequency of 15 Hz, pulse time of 30 ms, fixed pulse potential magnitude of 25 mV, and potential step of 4 mV. Electronic absorption spectra were recorded using an Agilent 8453 diode array UV-Vis spectrophotometer with 1 nm resolution and a spectral range of 190 to 1100 nm. Samples were dissolved in room temperature spectral grade CH_3CN and measured in a 1 cm pathlength quartz cuvette (Starna Cells, Inc.; Atascadero, CA, USA).

D.9. References

1. Navarro, R. M.; del Valle, F.; Villoria de la Mano, J. A.; Álvarez-Galván, M. C.; Fierro, J. L. G., Photocatalytic Water Splitting under Visible Light: Concept and Catalysts Development. In *Adv. Chem. Eng.*, Hugo, I. d. L.; Benito Serrano, R., Eds. Academic Press: 2009; Vol. Volume 36, pp 111-143.
2. REN21 *Renewables 2014 Global Status Report*; Paris, 2014.
3. *Report of the Basic Energy Sciences Workshop on Solar Energy Utilization*; 2005.
4. Bard, A. J.; Fox, M. A., Artificial Photosynthesis: Solar Splitting of Water to Hydrogen and Oxygen. *Accounts Chem. Res.* **1995,** *28* (3), 141-145.
5. Losse, S.; Vos, J. G.; Rau, S., Catalytic Hydrogen Production at Cobalt Centres. *Coord. Chem. Rev.* **2010,** *254* (21–22), 2492-2504.
6. Manbeck, G. F.; Brewer, K. J., Photoinitiated Electron Collection in Polyazine Chromophores Coupled to Water Reduction Catalysts for Solar H-2 Production. *Coord. Chem. Rev.* **2013,** *257* (9-10), 1660-1675.
7. Meyer, T. J., Chemical Approaches to Artificial Photosynthesis. *Accounts Chem. Res.* **1989,** *22* (5), 163-170.
8. Bard, A. J.; Faulkner, L. R., *Electrochemical Methods: Fundamentals and Applications*. Wiley: 2000.
9. Pal, U.; Ghosh, S.; Chatterjee, D., Effect of Sacrificial Electron Donors on Hydrogen Generation over Visible Light–Irradiated Nonmetal-Doped Tio2 Photocatalysts. *Transit. Metal Chem.* **2012,** *37* (1), 93-96.
10. Demas, J. N.; Diemente, D.; Harris, E. W., Oxygen Quenching of Charge-Transfer Excited States of Ruthenium(Ii) Complexes. Evidence for Singlet Oxygen Production. *J. Am. Chem. Soc.* **1973,** *95* (20), 6864-6865.
11. Peng, T.; Ke, D.; Cai, P.; Dai, K.; Ma, L.; Zan, L., Influence of Different Ruthenium(Ii) Bipyridyl Complex on the Photocatalytic H2 Evolution over Tio2 Nanoparticles with Mesostructures. *J. Power Sources* **2008,** *180* (1), 498-505.
12. Stoll, T.; Gennari, M.; Fortage, J.; Castillo, C. E.; Rebarz, M.; Sliwa, M.; Poizat, O.; Odobel, F.; Deronzier, A.; Collomb, M.-N., An Efficient Ruii–Rhiii–Ruii Polypyridyl

Photocatalyst for Visible-Light-Driven Hydrogen Production in Aqueous Solution. *Angew. Chem. Int. Edit.* **2014,** *53* (6), 1654-1658.

13. Le Goff, A.; Artero, V.; Jousselme, B.; Tran, P. D.; Guillet, N.; Métayé, R.; Fihri, A.; Palacin, S.; Fontecave, M., From Hydrogenases to Noble Metal–Free Catalytic Nanomaterials for H2 Production and Uptake. *Science* **2009,** *326* (5958), 1384-1387.
14. Matt, B.; Fize, J.; Moussa, J.; Amouri, H.; Pereira, A.; Artero, V.; Izzet, G.; Proust, A., Charge Photo-Accumulation and Photocatalytic Hydrogen Evolution under Visible Light at an Iridium(Iii)-Photosensitized Polyoxotungstate. *Energ. Environ. Sci.* **2013,** *6* (5), 1504-1508.
15. Kiwi, J.; Graetzel, M., Projection, Size Factors, and Reaction Dynamics of Colloidal Redox Catalysts Mediating Light Induced Hydrogen Evolution from Water. *J. Am. Chem. Soc.* **1979,** *101* (24), 7214-7217.
16. Kirch, M.; Lehn, J.-M.; Sauvage, J.-P., Hydrogen Generation by Visible Light Irradiation of Aqueous Solutions of Metal Complexes. An Approach to the Photochemical Conversion and Storage of Solar Energy. *Helv. Chim. Acta* **1979,** *62* (4), 1345-1384.
17. Brown, G. M.; Chan, S. F.; Creutz, C.; Schwarz, H. A.; Sutin, N., Mechanism of the Formation of Dihydrogen from the Photoinduced Reactions of Tris(Bipyridine)Ruthenium(Ii) with Tris(Bipyridine)Rhodium(Iii). *J. Am. Chem. Soc.* **1979,** *101* (25), 7638-7640.
18. Thompson, D. W.; Ito, A.; Meyer, T. J., [Ru(Bpy)3]2+* and Other Remarkable Metal-to-Ligand Charge Transfer (Mlct) Excited States. *Pure Appl. Chem.* **2013,** *85* (7), 1257-1305.
19. Caspar, J. V.; Meyer, T. J., Photochemistry of Tris(2,2'-Bipyridine)Ruthenium(2+) Ion (Ru(Bpy)32+). Solvent Effects. *J. Am. Chem. Soc.* **1983,** *105* (17), 5583-5590.
20. Durham, B.; Caspar, J. V.; Nagle, J. K.; Meyer, T. J., Photochemistry of Tris(2,2'-Bipyridine)Ruthenium(2+) Ion. *J. Am. Chem. Soc.* **1982,** *104* (18), 4803-4810.
21. Van Houten, J.; Watts, R. J., Photochemistry of Tris(2,2'-Bipyridyl)Ruthenium(Ii) in Aqueous Solutions. *Inorg. Chem.* **1978,** *17* (12), 3381-3385.
22. Meyer, T. J., Photochemistry of Metal Coordination Complexes: Metal to Ligand Charge Transfer Excited States. *Pure Appl. Chem.* **1986,** *58* (9), 1193-1206.
23. Anne Fox, M., Photoinduced Electron Transfer in Arranged Media. In *Photoinduced Electron Transfer Iii*, Mattay, J., Ed. Springer Berlin Heidelberg: 1991; Vol. 159, pp 67-101.

24. Balzani, V.; Moggi, L.; Scandola, F., Towards a Supramolecular Photochemistry: Assembly of Molecular Components to Obtain Photochemical Molecular Devices. In *Supramolecular Photochemistry*, Balzani, V., Ed. Springer Netherlands: 1987; Vol. 214, pp 1-28.
25. Elvington, M.; Brewer, K. J., Photoinitiated Electron Collection at a Metal in a Rhodium-Centered Mixed-Metal Supramolecular Complex. *Inorg. Chem.* **2006,** *45* (14), 5242-5244.
26. Elvington, M.; Brown, J.; Arachchige, S. M.; Brewer, K. J., Photocatalytic Hydrogen Production from Water Employing a Ru, Rh, Ru Molecular Device for Photoinitiated Electron Collection. *J. Am. Chem. Soc.* **2007,** *129* (35), 10644-10645.
27. Arachchige, S. M.; Brown, J.; Brewer, K. J., Photochemical Hydrogen Production from Water Using the New Photocatalyst [{(Bpy)2ru(Dpp)}2rhbr2](Pf6)5. *J. Photoch. Photobio. A* **2008,** *197* (1), 13-17.
28. White, T. A.; Whitaker, B. N.; Brewer, K. J., Discovering the Balance of Steric and Electronic Factors Needed to Provide a New Structural Motif for Photocatalytic Hydrogen Production from Water. *J. Am. Chem. Soc.* **2011,** *133* (39), 15332-15334.
29. Arachchige, S. M.; Brown, J. R.; Chang, E.; Jain, A.; Zigler, D. F.; Rangan, K.; Brewer, K. J., Design Considerations for a System for Photocatalytic Hydrogen Production from Water Employing Mixed-Metal Photochemical Molecular Devices for Photoinitiated Electron Collection. *Inorg. Chem.* **2009,** *48* (5), 1989-2000.
30. White, T. A.; Rangan, K.; Brewer, K. J., Synthesis, Characterization, and Study of the Photophysics and Photocatalytic Properties of the Photoinitiated Electron Collector [{(Phen)2ru(Dpp)}2rhbr2](Pf6)5. *J. Photoch. Photobio. A* **2010,** *209* (2–3), 203-209.
31. White, T. A.; Higgins, S. L. H.; Arachchige, S. M.; Brewer, K. J., Efficient Photocatalytic Hydrogen Production in a Single-Component System Using Ru,Rh,Ru Supramolecules Containing 4,7-Diphenyl-1,10-Phenanthroline. *Angew. Chem. Int. Edit.* **2011,** *50* (51), 12209-12213.
32. Chen, P.; Meyer, T. J., Medium Effects on Charge Transfer in Metal Complexes. *Chem. Rev.* **1998,** *98* (4), 1439-1478.
33. Danielson, E.; Elliott, C. M.; Merkert, J. W.; Meyer, T. J., Photochemically Induced Charge Separation at the Molecular Level. A Chromophore-Quencher Complex Containing Both an Electron Donor and an Acceptor. *J. Am. Chem. Soc.* **1987,** *109* (8), 2519-2520.

34. Moore, T. A.; Gust, D.; Mathis, P.; Mialocq, J.-C.; Chachaty, C.; Bensasson, R. V.; Land, E. J.; Doizi, D.; Liddell, P. A.; Lehman, W. R.; Nemeth, G. A.; Moore, A. L., Photodriven Charge Separation in a Carotenoporphyrin-Quinone Triad. *Nature* **1984,** *307* (5952), 630-632.
35. Joshi, P.; Zhang, L.; Chen, Q.; Galipeau, D.; Fong, H.; Qiao, Q., Electrospun Carbon Nanofibers as Low-Cost Counter Electrode for Dye-Sensitized Solar Cells. *ACS Appl. Mat. Interfaces* **2010,** *2* (12), 3572-3577.
36. Park, S.-H.; Jung, H.-R.; Kim, B.-K.; Lee, W.-J., Mwcnt/Mesoporous Carbon Nanofibers Composites Prepared by Electrospinning and Silica Template as Counter Electrodes for Dye-Sensitized Solar Cells. *J. Photoch. Photobio. A* **2012,** *246* (0), 45-49.
37. Veerappan, G.; Bojan, K.; Rhee, S.-W., Sub-Micrometer-Sized Graphite as a Conducting and Catalytic Counter Electrode for Dye-Sensitized Solar Cells. *ACS Appl. Mat. Interfaces* **2011,** *3* (3), 857-862.
38. Park, S.-H.; Jung, H.-R.; Lee, W.-J., Hollow Activated Carbon Nanofibers Prepared by Electrospinning as Counter Electrodes for Dye-Sensitized Solar Cells. *Electrochim. Acta* **2013,** *102* (0), 423-428.
39. Di, Y.; Yang, W.; Li, X.; Zhao, Z.; Wang, M.; Dai, J., Preparation and Characterization of Continuous Carbon Nanofiber-Supported Speek Composite Membranes for Fuel Cell Application. *RSC Adv.* **2014,** *4* (94), 52001-52007.
40. Li, M.; Han, G.; Yang, B., Fabrication of the Catalytic Electrodes for Methanol Oxidation on Electrospinning-Derived Carbon Fibrous Mats. *Electrochem. Commun.* **2008,** *10* (6), 880-883.
41. Li, M.; Zhao, S.; Han, G.; Yang, B., Electrospinning-Derived Carbon Fibrous Mats Improving the Performance of Commercial Pt/C for Methanol Oxidation. *J. Power Sources* **2009,** *191* (2), 351-356.
42. Han, S.; Yun, Y.; Park, K. W.; Sung, Y. E.; Hyeon, T., Simple Solid-Phase Synthesis of Hollow Graphitic Nanoparticles and Their Application to Direct Methanol Fuel Cell Electrodes. *Adv. Mater.* **2003,** *15* (22), 1922-1925.
43. Jhan, J.-Y.; Huang, Y.-W.; Hsu, C.-H.; Teng, H.; Kuo, D.; Kuo, P.-L., Three-Dimensional Network of Graphene Grown with Carbon Nanotubes as Carbon Support for Fuel Cells. *Energy* **2013,** *53* (0), 282-287.

44. Zhang, L.; Kim, J.; Dy, E.; Ban, S.; Tsay, K.-c.; Kawai, H.; Shi, Z.; Zhang, J., Synthesis of Novel Mesoporous Carbon Spheres and Their Supported Fe-Based Electrocatalysts for Pem Fuel Cell Oxygen Reduction Reaction. *Electrochim. Acta* **2013,** *108* (0), 480-485.
45. Shen, Y.; Zhou, Y.; Chen, S.; Yang, F.; Zheng, S.; Hou, H., Carbon Nanofibers Modified Graphite Felt for High Performance Anode in High Substrate Concentration Microbial Fuel Cells. *Sci. World J* **2014**.
46. Kumar, P. S.; Sundaramurthy, J.; Sundarrajan, S.; Babu, V. J.; Singh, G.; Allakhverdiev, S. I.; Ramakrishna, S., Hierarchical Electrospun Nanofibers for Energy Harvesting, Production and Environmental Remediation. *Energ. Environ. Sci.* **2014,** *7* (10), 3192-3222.
47. Cheng, Y.; Xu, C.; Jia, L.; Gale, J. D.; Zhang, L.; Liu, C.; Shen, P. K.; Jiang, S. P., Pristine Carbon Nanotubes as Non-Metal Electrocatalysts for Oxygen Evolution Reaction of Water Splitting. *Appl. Catal. B-Environ.* **2015,** *163* (0), 96-104.
48. Kongkanand, A.; Martínez Domínguez, R.; Kamat, P. V., Single Wall Carbon Nanotube Scaffolds for Photoelectrochemical Solar Cells. Capture and Transport of Photogenerated Electrons. *Nano Lett.* **2007,** *7* (3), 676-680.
49. Serp, P.; Corrias, M.; Kalck, P., Carbon Nanotubes and Nanofibers in Catalysis. *Appl. Catal. A-Gen.* **2003,** *253* (2), 337-358.
50. Planeix, J. M.; Coustel, N.; Coq, B.; Brotons, V.; Kumbhar, P. S.; Dutartre, R.; Geneste, P.; Bernier, P.; Ajayan, P. M., Application of Carbon Nanotubes as Supports in Heterogeneous Catalysis. *J. Am. Chem. Soc.* **1994,** *116* (17), 7935-7936.
51. Wu, H.-C.; Chang, X.; Liu, L.; Zhao, F.; Zhao, Y., Chemistry of Carbon Nanotubes in Biomedical Applications. *J. Mater. Sci.* **2010,** *20* (6), 1036-1052.
52. Andreiadis, E. S.; Jacques, P.-a.; Tran, P. D.; Leyris, A.; Chavarot-kerlidou, M.; Jousselme, B.; Matheron, M.; Pécaut, J.; Palacin, S.; Fontecave, M.; Artero, V., Molecular Engineering of a Cobalt-Based Electrocatalytic Nanomaterial for H2 Evolution under Fully Aqueous Conditions. *Nat. Chem.* **2013,** *5* (1), 48-53.
53. Tong, L.; Gothelid, M.; Sun, L., Oxygen Evolution at Functionalized Carbon Surfaces: A Strategy for Immobilization of Molecular Water Oxidation Catalysts. *Chem. Commun.* **2012,** *48* (80), 10025-10027.

54. deKrafft, K. E.; Wang, C.; Xie, Z.; Su, X.; Hinds, B. J.; Lin, W., Electrochemical Water Oxidation with Carbon-Grafted Iridium Complexes. *ACS Appl. Mat. Interfaces* **2012,** *4* (2), 608-613.
55. Das, A. K.; Engelhard, M. H.; Bullock, R. M.; Roberts, J. A. S., A Hydrogen-Evolving Ni(P2n2)2 Electrocatalyst Covalently Attached to a Glassy Carbon Electrode: Preparation, Characterization, and Catalysis. Comparisons with the Homogeneous Analogue. *Inorg. Chem.* **2014,** *53* (13), 6875-6885.
56. Su, X.; Wu, J.; Hinds, B. J., Catalytic Activity of Ultrathin Pt Films on Aligned Carbon Nanotube Arrays. *Carbon* **2011,** *49* (4), 1145-1150.
57. Oh, H.-S.; Lim, K. H.; Roh, B.; Hwang, I.; Kim, H., Corrosion Resistance and Sintering Effect of Carbon Supports in Polymer Electrolyte Membrane Fuel Cells. *Electrochim. Acta* **2009,** *54* (26), 6515-6521.
58. Hakamizadeh, M.; Afshar, S.; Tadjarodi, A.; Khajavian, R.; Fadaie, M. R.; Bozorgi, B., Improving Hydrogen Production Via Water Splitting over Pt/Tio2/Activated Carbon Nanocomposite. *Int. J. Hydrogen Energ.* **2014,** *39* (14), 7262-7269.
59. Hinnemann, B.; Moses, P. G.; Bonde, J.; Jørgensen, K. P.; Nielsen, J. H.; Horch, S.; Chorkendorff, I.; Nørskov, J. K., Biomimetic Hydrogen Evolution: Mos2 Nanoparticles as Catalyst for Hydrogen Evolution. *J. Am. Chem. Soc.* **2005,** *127* (15), 5308-5309.
60. Allongue, P.; Delamar, M.; Desbat, B.; Fagebaume, O.; Hitmi, R.; Pinson, J.; Savéant, J.-M., Covalent Modification of Carbon Surfaces by Aryl Radicals Generated from the Electrochemical Reduction of Diazonium Salts. *J. Am. Chem. Soc.* **1997,** *119* (1), 201-207.
61. Devadoss, A.; Chidsey, C. E. D., Azide-Modified Graphitic Surfaces for Covalent Attachment of Alkyne-Terminated Molecules by "Click" Chemistry. *J. Am. Chem. Soc.* **2007,** *129* (17), 5370-5371.
62. Liu, Z.; Lin, X.; Lee, J. Y.; Zhang, W.; Han, M.; Gan, L. M., Preparation and Characterization of Platinum-Based Electrocatalysts on Multiwalled Carbon Nanotubes for Proton Exchange Membrane Fuel Cells. *Langmuir* **2002,** *18* (10), 4054-4060.
63. Evrard, D.; Lambert, F.; Policar, C.; Balland, V.; Limoges, B., Electrochemical Functionalization of Carbon Surfaces by Aromatic Azide or Alkyne Molecules: A Versatile Platform for Click Chemistry. *Chem.-Eur. J.* **2008,** *14* (30), 9286-9291.

64. Lin, Z.; Ji, L.; Woodroof, M. D.; Yao, Y.; Krause, W.; Zhang, X., Synthesis and Electrocatalysis of Carbon Nanofiber-Supported Platinum by 1-Ap Functionalization and Polyol Processing Technique. *J. Phys. Chem. C* **2010,** *114* (9), 3791-3797.
65. Fleming, C. N.; Brennaman, M. K.; Papanikolas, J. M.; Meyer, T. J., Efficient, Long-Range Energy Migration in Ruii Polypyridyl Derivatized Polystyrenes in Rigid Media. Antennae for Artificial Photosynthesis. *Dalton T.* **2009,** (20), 3903-3910.
66. Fleming, C. N.; Maxwell, K. A.; DeSimone, J. M.; Meyer, T. J.; Papanikolas, J. M., Ultrafast Excited-State Energy Migration Dynamics in an Efficient Light-Harvesting Antenna Polymer Based on Ru(Ii) and Os(Ii) Polypyridyl Complexes. *J. Am. Chem. Soc.* **2001,** *123* (42), 10336-10347.
67. Friesen, D. A.; Kajita, T.; Danielson, E.; Meyer, T. J., Preparation and Photophysical Properties of Amide-Linked, Polypyridylruthenium-Derivatized Polystyrene. *Inorg. Chem.* **1998,** *37* (11), 2756-2762.
68. Sykora, M.; Maxwell, K. A.; DeSimone, J. M.; Meyer, T. J., Mimicking the Antenna-Electron Transfer Properties of Photosynthesis. *P. Natl. Acad. Sci. USA* **2000,** *97* (14), 7687-7691.
69. Wilger, D. J.; Bettis, S. E.; Materese, C. K.; Minakova, M.; Papoian, G. A.; Papanikolas, J. M.; Waters, M. L., Tunable Energy Transfer Rates Via Control of Primary, Secondary, and Tertiary Structure of a Coiled Coil Peptide Scaffold. *Inorg. Chem.* **2012,** *51* (21), 11324-11338.
70. Thanneeru, S.; Milazzo, N.; Lopes, A.; Wei, Z.; Angeles-Boza, A. M.; He, J., Synthetic Polymers to Promote Cooperative Cu Activity for O2 Activation: Poly Vs Mono. *J. Am. Chem. Soc.* **2019,** *141* (10), 4252-4256.
71. Abd-El-Aziz, A. S.; Manners, I., *Frontiers in Transition Metal-Containing Polymers*. Wiley Online Library: 2007.
72. Förster, S.; Antonietti, M., Amphiphilic Block Copolymers in Structure-Controlled Nanomaterial Hybrids. *Adv. Mater.* **1998,** *10* (3), 195-217.
73. Grubbs, R. B., Hybrid Metal–Polymer Composites from Functional Block Copolymers. *J. Polym. Sci., Part A: Polym. Chem.* **2005,** *43* (19), 4323-4336.
74. Bennett, M. A.; Smith, A. K., Arene Ruthenium(Ii) Complexes Formed by Dehydrogenation of Cyclohexadienes with Ruthenium(Iii) Trichloride. *Dalton T* **1974,** (2), 233-241.
75. Joya, K. S.; DeGroot, H. J. M. Metal Complex and Use as Multi-Electron Catalyst. 2012.

76. Vougioukalakis, G. C.; Stergiopoulos, T.; Kontos, A. G.; Pefkianakis, E. K.; Papadopoulos, K.; Falaras, P., Novel Ru(Ii) Sensitizers Bearing an Unsymmetrical Pyridine-Quinoline Hybrid Ligand with Extended [Small Pi]-Conjugation: Synthesis and Application in Dye-Sensitized Solar Cells. *Dalton T.* **2013,** *42* (18), 6582-6591.
77. Allen, G. H.; White, R. P.; Rillema, D. P.; Meyer, T. J., Synthetic Control of Excited-State Properties. Tris-Chelate Complexes Containing the Ligands 2,2'-Bipyrazine, 2,2'-Bipyridine, and 2,2'-Bipyrimidine. *J. Am. Chem. Soc.* **1984,** *106* (9), 2613-2620.
78. Nickita; Belousoff, M. J.; Bhatt, A. I.; Bond, A. M.; Deacon, G. B.; Gasser, G.; Spiccia, L., Synthesis, Structure, Spectroscopic Properties, and Electrochemical Oxidation of Ruthenium(Ii) Complexes Incorporating Monocarboxylate Bipyridine Ligands. *Inorg. Chem.* **2007,** *46* (21), 8638-8651.
79. Mongelli, M. T.; Brewer, K. J., Synthesis and Study of the Light Absorbing, Redox and Photophysical Properties of Ru(Ii) and Os(Ii) Complexes of 4,7-Diphenyl-1,10-Phenanthroline Containing the Polyazine Bridging Ligand 2,3-Bis(2-Pyridyl)Pyrazine. *Inorg. Chem. Commun.* **2006,** *9* (9), 877-881.
80. Rogers, H. M.; White, T. A.; Stone, B. N.; Arachchige, S. M.; Brewer, K. J., Nonchromophoric Halide Ligand Variation in Polyazine-Bridged Ru(Ii),Rh(Iii) Bimetallic Supramolecules Offering New Insight into Photocatalytic Hydrogen Production from Water. *Inorg. Chem.* **2015**.
81. McCafferty, D. G.; Bishop, B. M.; Wall, C. G.; Hughes, S. G.; Mecklenberg, S. L.; Meyer, T. J.; Erickson, B. W., Synthesis of Redox Derivatives of Lysine and Their Use in Solid-Phase Synthesis of a Light-Harvesting Peptide. *Tetrahedron* **1995,** *51* (4), 1093-1106.
82. Liska, P.; Vlachopoulos, N.; Nazeeruddin, M. K.; Comte, P.; Graetzel, M., Cis-Diaquabis(2,2'-Bipyridyl-4,4'-Dicarboxylate)Ruthenium(Ii) Sensitizes Wide Band Gap Oxide Semiconductors Very Efficiently over a Broad Spectral Range in the Visible. *J. Am. Chem. Soc.* **1988,** *110* (11), 3686-3687.
83. Barlos, K.; Chatzi, O.; Gatos, D.; Stavropoulos, G., 2-Chlorotrityl Chloride Resin. Studies on Anchoring of Fmoc-Amino Acids and Peptide Cleavage. *Int. J. Pept. Protein Res.* **1991,** *37* (6), 513-520.

Appendix E.

Highly-Stable Organo-Lead Halide Perovskites Synthesized Through Green Self-Assembly Process

(*Wu, C.; Li, H.; Yan, Y.; Chi, B.; Felice, K. M.; Moore, R. B.; Magill, B. A.; Mudiyanselage, R. R. H. H.; Khodaparast, G. A.; Sanghadasa, M.; Priya, S., Solar RRL* ***2018,*** *2 (6), 1800052*)

Collaboration with Dr. Congcong Wu, Virginia Tech

E.1. Hydrogen bonding interactions in organo-lead halide perovskite-poly(methyl methacrylate) self-assembled solar cells

Organic-inorganic hybrid perovskite solar cells (PSCs) show unprecedented enhancement in light-electricity conversion efficiency compared to their silicon-based solar cell analogs.[1-4] Nevertheless, the poor long-term stability of PSCs is a critical challenge to their usefulness and implementation. This work demonstrates a highly stable methylammonium lead iodide ($CH_3NH_3PbI_3$, $MAPbI_3$) perovskite prepared using a self-assembly process in which $MAPbI_3$ layered perovskite intermediates are complexed with the hydrophobic polymer, poly(methyl methacrylate) (PMMA).[5] The resulting three-dimensional self-assembly consists of perovskite grains coated along grain boundaries with PMMA that effectively blocks moisture corrosion. To rationalize the effect of $MAPbI_3$ complexation with PMMA on the improved stability of the $MAPbI_3$ perovskite, Fourier transform infrared spectroscopy in attenuated total reflectance (ATR-FTIR) mode was used to investigate the interaction between $MAPbI_3$ and PMMA in the self-assembled PSC. This work was conducted in collaboration with Dr. C. Wu from Professor S. Priya's research group. The starting materials of the PSC were prepared by Dr. C. Wu and provided for characterization.

Figure E.1(a) shows the infrared spectra of methylammonium iodide (CH_3NH_3I, MAI), PMMA, and the complexed MAI-PMMA. Upon complexation of MAI with PMMA, the infrared spectrum of MAI exhibits a shift in the ammonium ion (NH_3^+) bending mode from 1490 cm^{-1} to 1485 cm^{-1}. This shift in frequency is consistent with an elongation of the N−H bond. In addition, vibrations assigned to the C−N stretching mode at 991 cm^{-1} and the CH_3 bending mode at 1406 cm^{-1} shift to 989 cm^{-1} and 1404 cm^{-1}, respectively.[6,7] The frequency shifts in MAI are suggestive of intermolecular hydrogen bonding interactions between MAI and PMMA that originate from a hydrogen in NH_3^+, acting as a Lewis acid electron acceptor, and the carbonyl (C=O) oxygen on PMMA, a well-known Lewis base-type polymer, shown in **Figure E.1(c)**. In the case of $MAPbI_3$, the polar (δ^-) O in the C=O of PMMA can potentially interact with both MA^+ and Pb_2^+.[8] However, the Pb^{2+} cation in $MAPbI_3$ is known to exist as the PbI_3^- anion arranged in an octahedron and is not expected to interact with C=O. In contrast, in the two-dimensional layered perovskite intermediate, MA^+ cations are exposed at the layer surface, favoring the interaction between the permanent dipole moment in MA^+ and the polar C=O bond in PMMA. **Figure E.1(b)** shows the infrared spectra of PMMA, MAI−PMMA, and $MAPbI_3$−PMMA. For both $MAPbI_3$−PMMA and MAI−PMMA, the C=O stretch in PMMA, located at 1721 cm^{-1}, shifts to 1726 cm^{-1}, which strongly suggests that the complexation between PMMA and $MAPbI_3$ is analogous to that of PMMA and MAI. The dipole moment in MA^+ promotes water absorption through hydrogen bonding.[9] Complexation of $MAPbI_3$ with PMMA leads to a monolayer of PMMA anchored between the perovskite grains. The PMMA coating is expected to improve the long-term stability of the perovskite light absorber by isolating the MA^+ cations from water molecules in the air, illustrated in **Figure E.1(d)**.

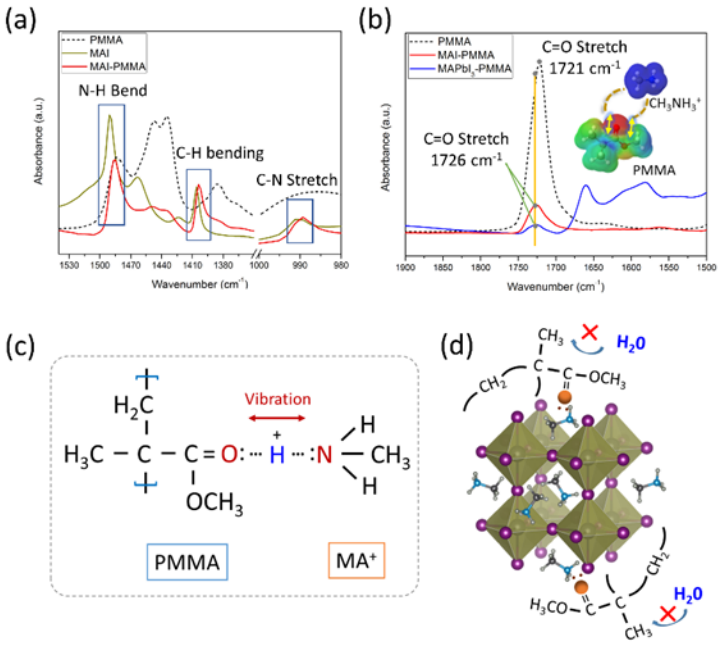

Figure E.1. The complexation of the $MAPbI_3$ perovskite with PMMA. ATR-FTIR of PMMA, MAI, and MAI−PMMA in the regions of (a) 1350−1550 cm^{-1}, highlighting the N−H and C−H bending modes, 908−1000 cm^{-1}, highlighting the C−N stretching mode, and (b) 1500−1900 cm^{-1}, highlighting the carbonyl (C=O) stretching mode. (c) Illustration of the complexation of the carbonyl oxygen of PMMA with the amine group of MA^+. (d) Schematic illustration of the PMMA coating on the outer layer of the perovskite grains that prevents water penetration. Reproduced with permission from John Wiley and Sons.[5]

E.2. References

1. Grätzel, M., The Light and Shade of Perovskite Solar Cells. *Nat. Mater.* **2014,** *13*, 838.
2. Green, M. A.; Ho-Baillie, A.; Snaith, H. J., The Emergence of Perovskite Solar Cells. *Nat. Photonics* **2014,** *8*, 506.
3. Kim, H.-S.; Lee, C.-R.; Im, J.-H.; Lee, K.-B.; Moehl, T.; Marchioro, A.; Moon, S.-J.; Humphry-Baker, R.; Yum, J.-H.; Moser, J. E.; Grätzel, M.; Park, N.-G., Lead Iodide Perovskite Sensitized All-Solid-State Submicron Thin Film Mesoscopic Solar Cell with Efficiency Exceeding 9%. *Scientific reports* **2012,** *2*, 591-591.
4. Snaith, H. J., Perovskites: The Emergence of a New Era for Low-Cost, High-Efficiency Solar Cells. *J. Phys. Chem. Lett.* **2013,** *4* (21), 3623-3630.
5. Wu, C.; Li, H.; Yan, Y.; Chi, B.; Felice, K. M.; Moore, R. B.; Magill, B. A.; Mudiyanselage, R. R. H. H.; Khodaparast, G. A.; Sanghadasa, M.; Priya, S., Highly-Stable Organo-Lead Halide Perovskites Synthesized through Green Self-Assembly Process. *Solar RRL* **2018,** *2* (6), 1800052.
6. Cabana, A.; Sandorfy, C., The Infrared Spectra of Solid Methylammonium Halides. *Spectrochim. Acta* **1962,** *18* (6), 843-861.
7. Patel, J. B.; Milot, R. L.; Wright, A. D.; Herz, L. M.; Johnston, M. B., Formation Dynamics of Ch3nh3pbi3 Perovskite Following Two-Step Layer Deposition. *J. Phys. Chem. Lett.* **2016,** *7* (1), 96-102.
8. Ahn, N.; Son, D.-Y.; Jang, I.-H.; Kang, S. M.; Choi, M.; Park, N.-G., Highly Reproducible Perovskite Solar Cells with Average Efficiency of 18.3% and Best Efficiency of 19.7% Fabricated Via Lewis Base Adduct of Lead(Ii) Iodide. *J. Am. Chem. Soc.* **2015,** *137* (27), 8696-8699.
9. Zhu, Z.; Hadjiev, V. G.; Rong, Y.; Guo, R.; Cao, B.; Tang, Z.; Qin, F.; Li, Y.; Wang, Y.; Hao, F.; Venkatesan, S.; Li, W.; Baldelli, S.; Guloy, A. M.; Fang, H.; Hu, Y.; Yao, Y.; Wang, Z.; Bao, J., Interaction of Organic Cation with Water Molecule in Perovskite Mapbi3: From Dynamic Orientational Disorder to Hydrogen Bonding. *Chem. Mater.* **2016,** *28* (20), 7385-7393.